From Ion Recognition to Antimicrobial Activity: Oxo- and Thiosquaramide-Based Receptors and Transporters

Maynooth University
National University of Ireland Maynooth

A thesis submitted to Maynooth University in fulfilment of the requirements for the degree of

Doctor of Philosophy

By

Xuanyang Luo, M.Sc.

Department of Chemistry,

Maynooth University,

Maynooth,

Co. Kildare, Ireland.

October 2025

Research Supervisor: Dr. Robert Elmes

Head of Department: Prof. Diego Montanger

Table of contents

Declaration

I declare that the work presented in this thesis was carried out in accordance with the regulations of Maynooth University. The work is original, except where indicated by reference and has not been submitted before, in whole or in part, to this or any other university for any other degree.

Signed: Xuanyang Luo Date: 28.10.2025

Xuanyang Luo, M.Sc. (Hons)

Acknowledgements

The PhD has been a journey that the most demanding challenge I have faced so far. Over the past four years, I have been extraordinarily fortunate to be supported by a generous and steadfast community. Their encouragement, guidance, and practical help made it possible for me to reach the finish line. I am deeply grateful to everyone who has been part of this journey. Your support has made all the difference.

First and foremost, I would like to thank my parents for their unwavering love and encouragement. Your support in every aspect of my life allowed me to explore widely, take risks without hesitation, and focus on the work that mattered. I am profoundly lucky to be your son. Words can never fully capture the gratitude I feel, but I trust that you understand the depth of my appreciation. Everything I have achieved rests on the foundation you provided.

I am especially indebted to my supervisor, Prof. Robert Elmes, for giving me the opportunity to join the group as a PhD student and for your guidance in both research and thesis writing. Even during the most difficult times, you offered support and optimism that kept me moving forward. Your personal charisma is something I have long admired. Working under your supervision has been a genuine pleasure, and I feel privileged to have pursued my PhD under your mentorship.

I would extend my sincere thanks to the Department's administrative, technical, and academic staff for their consistent assistance, which made my research possible. In particular, I thank Ria for invaluable advice on health and safety, and Noel for extensive help with laboratory instrumentation. Your expertise and responsiveness kept the laboratory running effectively and enabled me to carry out my experiments smoothly.

I have been fortunate to meet a cohort of friendly and supportive colleagues and lads here. To Luke B., from our very first meeting, your dedication and talent were evident. Thank you for your consistent help on every aspect. Your map guidance on all the wonderful restaurants in Dublin really opened a new world for me. Best of luck to you. To Abhik, although our time working together was brief, your good humour and positivity left a strong impression. I wish you every success in Limerick and in all that follows. To Jordan, thank you for your patience with materials ordering, figure crossed! To Luke M., thank you for your kindness and friendship; the thoughtful note you left upon graduating meant a great deal to me, and I continue to appreciate your support. To Wyne, thank you for your steady patience and practical help. Wishing you all the best. To Gero, thank you for the energy and good spirits you brought to the lab. Gero Gero, you are a hero. To Faz and Stephen, the laboratory was livelier because of you both, thank you for your assistance and camaraderie, and I hope our paths cross again. I am also grateful to Emily, Lea, and Hua for your advice and support, your perspectives and suggestions made the work better and the process more enjoyable.

Meanwhile, to my landlord, thank you for providing me with a lifetime discount at your restaurant; it means I no longer have to worry about cooking.

Finally, to Xiaoling, thank you for your love, encouragement, and patience. You helped me rise from low moments and face challenges with resilience rather than resignation. Your companionship has been a constant source of strength; this thesis would not have been possible without your steady belief in me.

I would also like to acknowledge myself, briefly but sincerely. The past four years brought significant growth alongside periods of pressure and anxiety, and they deepened my understanding of perseverance, balance, and the value of support. I am grateful that I did not give up when the path was steep.

To everyone named here, and to the many others who helped in ways , thank you. This dissertation is, in many ways, a collective achievement, and I am honoured to have shared this journey with you.

Abstract

Ions are indispensable to the maintenance of life, with nearly every biochemical process relying on the recognition, transport, or transformation of anions at some stage. The realisation of this pivotal role has stimulated growing interest in the development of artificial ion receptors, which can be applied in diverse areas such as molecular recognition, sensing, and transmembrane transport with implications for biochemistry and biomedicine. Nevertheless, despite the intense efforts and significant advances in this field, the creation of ion receptors and transporters that are truly functional under biologically relevant conditions remains a major challenge. Critical barriers include the need for sufficient binding affinity in complex aqueous environments, selective recognition in the presence of competing species, and the ability to achieve controlled ion transport across lipid membranes.

In this context, one of the primary objectives of our recent research has been the design and synthesis of new classes of ion receptors, with a particular focus on elucidating the structural and electronic features that enable effective anion binding and recognition. Our strategy emphasises the development of electroneutral, lipophilic molecules that are capable of strongly interacting with target ions such as Zn^{2+} and Cl^-, while maintaining compatibility with hydrophobic membrane environments. Such receptors not only act as efficient carriers for transmembrane ion transport but also open new avenues for modulating biological processes, including the induction of antimicrobial effects. By bridging the gap between supramolecular chemistry and biological function, our work aims to expand the potential of synthetic ion receptors toward practical biomedical applications.

This thesis will open with a literature review (**Chapter 1**) that surveys the development of supramolecular chemistry and research on ion recognition and ion transport. It then elaborates on applications in antibacterial therapy, drug delivery, and tissue repair, before narrowing to the squaramide scaffold, an important motif in supramolecular chemistry, to discuss its recent advances and applications in these areas.

Chapter 2 details the design, synthesis and characterisation of thiosquaramide. These molecules have already been shown to be competent in anion recognition and transport.

In this chapter, we employ UV-vis spectroscopy and fluorimetry to explore their undeveloped cation-recognition capacity. The results reveal that, while exhibiting strong cation recognition and transport, thiosquaramides also engage in co-transport with anions, thereby accelerating anion translocation. Moreover, biological assays corroborate their function as Zn^{2+}-dependent antibacterial agents

Chapter 3 keeps building on the thiosquaramide scaffold, where we appended a fluorophore as a signalling unit to construct fluorescently responsive cation receptors. This chapter describes the design and synthesis of a class of fluorescent receptors derived from thiosquaramide and quinoline, and examines their cation-binding characteristics and fluorescence responses. We find that these quinoline thiosquaramides bind a range of cations and exhibit fluorescence 'turn-on' behaviour. Subsequently, their ion-transport capabilities were evaluated, demonstrating that they likewise retain transport activity under physiological conditions.

Finally, **Chapter 4** builds on the findings of the previous two chapters; this chapter further expands the molecular structure. Our objective was to enhance ionic affinity and selectivity by constructing a preorganized binding cavity. We describe the design and synthesis of a series of novel bipodal molecules derived from both oxosquaramides and thiosquaramides, and we investigate their ion-binding and transport properties

Abbreviations

AcO^-	Acetate
Ba^{2+}	Barium
Br^-	Bromide
Ca^{2+}	Calcium
Cd^{2+}	Cadium
$CDCl_3$	Deuterated chloroform
Cl^-	Chloride
CF_3	Trifluoromethyl
CN^-	Cyanide
Co^{2+}	Cobalt
CO_3^{2-}	Carbonate
COSY	Correlation Spectroscopy
Cu^{2+}	Copper
DCM	Dichloromethane
DMF	Dimethylformamide
DMSO	Dimethylsulfoxide
EDCI	1-Ethyl-3-(3-dimethylaminopropyl)carbodiimide
e.g.	Exempli gratia
eq.	Equivalents
ESI	Electrospray ionisation
Et al.	Et alia
Et_2O	Diethyl ether
EtOAc	Ethyl acetate
EtOH	Ethanol
F^-	Fluoride
H_2O	Water
$H_2PO_4^-$/ PO_4^{3-}	Phosphate

hrs	Hours
HCl	Hydrochloric Acid
Hg^{2+}	Mercury
HMBC	Heteronuclear Multiple Bond Correlation
HRMS	High Resolution Mass Spectrometry
HSAB	Hard and Soft Acids and Bases
HSQC	Heteronuclear Single Quantum Coherence
ICT	Internal Charge Transfer
i.e.	Id est
IR	Infrared Spectroscopy
K	Kelvin
K_a	Binding Constant
Li^+	Lithium
LUV	Large Unilamellar Vesicles
LC-MS	Liquid Chromatography – Mass Spectrometry
MeCN	Acetonitrile
MeOH	Methanol
MHz	Megahertz
mg	Milligram
min	Minute
mL	Millilitre
Na^+	Sodium
Ni^{2+}	Nickel
NO_2	Nitro group
NO_3^-	Nitrate
TEA	Triethylamine
nm	Nanometre
NMR	Nuclear Magnetic Resonance
OH	Hydroxyl group

O_2^{2-}	Peroxide
Pb^{2+}	Lead
PBS	Phosphate-buffered saline
PET	Photoinduced electron transfer
Pet. Ether	Petroleum Ether
ppm	Parts per million
ROS	Reactive Oxygen Species
r.t.	Room Temperature
SO_4^{2-}	Sulphate
TBA	*Tert*-butylammonium
TEA	Triethylamine
TFA	Trifluoracetic Acid
µL	Microlitre
µg	Microgram
UV	Ultraviolet
Vis	Visible
Zn^{2+}	Zinc

Chapter 1: Introduction

1.1 Supramolecular chemistry

1.1.1 The origin of supramolecular chemistry

The origin of supramolecular chemistry can be traced back to the mid-20th century. The initial concept, described as "chemistry beyond the molecule," emphasized the organisation of molecules into functional assemblies through noncovalent interactions such as hydrogen bonding, π–π stacking, electrostatic forces, van der Waals interactions, and hydrophobic effects.

A milestone in this field was the discovery of crown ethers. In 1967, Charles J. Pedersen reported that crown ether molecules could selectively complex metal cations, thereby providing a paradigm for artificial molecular recognition.[1] Subsequently, Jean-Marie Lehn, Donald J. Cram, and Charles J. Pedersen advanced host–guest chemistry, formulating the idea of selective recognition through molecular design, for which they were jointly awarded the Nobel Prize in Chemistry in 1987. Lehn defined supramolecular chemistry as "chemistry beyond the molecule, dealing with organized entities of higher complexity that result from the association of two or more chemical species held together by intermolecular noncovalent interactions."[2–4] This definition marked the transition of supramolecular chemistry from molecular chemistry to a higher level of inquiry, highlighting molecular assembly, self-organization, molecular machines, and the construction of functional materials.

1.1.2 The importance of supramolecular chemistry

As mentioned above, the essence of supramolecular chemistry lies in noncovalent interactions. Although individually weak, these forces can achieve highly selective and controllable molecular recognition when operating in a cooperative and multivalent manner.

The principal types of such interactions include:[5] Hydrogen bonding, one of the most widely employed recognition forces, extensively utilized in anion receptors, molecular self-assembly, and biomimetic systems; Electrostatic interactions, which play a pivotal role in ion recognition and transmembrane transport; π-π stacking and cation–π/anion–π interactions, which are of fundamental importance in aromatic host–guest recognition, molecular devices, and the construction of functional materials; The

hydrophobic effect, a driving force for self-assembly and vesicle formation in aqueous media, often applied to mimic biological membranes; Van der Waals forces, although weak, provide essential stabilization when molecules are in close contact.

In anion recognition, selectivity is unsually controlled by more than one interaction:[6] multiple noncovalent forces in conjunction with the desolvation penalty.[7] The highly directional interactions (*e.g.*, hydrogen bonding) often display relatively high level of anion selectivity because they are acutely sensitive to donor acidity, spatial orientation, and multidentate binding topologies, thereby preferentially 'choose' anions that better match the receptor in size and shape.[8,9] By contrast, electrostatic attraction typically enhances the overall affinity, but it tends to display limited selectivity among different anion types.[10] Meanwhile, π-π interactions can reorder selectivity in certain systems, with particularly pronounced contributions for more polarizable anions.[11,12] In competitive solvents or aqueous media, hydrophobic interaction and Van der Waals force can further enhance binding differences by affecting desolvation costs.[13] Overall, these interactions exhibit a functional "division of labor": directional forces more frequently determine selectivity, whereas nondirectional forces prefer to modity affinity; the ultimate outcome reflects a system-specific balance among anion size and shape, hydrogen-bond acceptor strength, hydration free energy, and polarizability within a given receptor architecture.

These interactions are central to both biological systems and materials science. For example, hydrogen bonding and the hydrophobic effect underlie the formation of DNA double helices and protein folding,[14–17] while electrostatic and π-interactions are ubiquitous in enzyme–substrate recognition and transmembrane transport.[18,19] By judiciously exploiting these noncovalent forces, researchers can design highly selective molecular recognition systems, self-assembled supramolecular materials, and artificial molecular machines, thereby establishing supramolecular chemistry as a critical bridge between chemistry, life sciences, and materials science. As a result, supramolecular chemistry serves as a bridge between fundamental molecular design and applications in biology, medicine, and materials science.

1.2 Ion recognition

Although anion and cation recognition are similar in their formation, their dominant driving forces and the design strategy are different. Anion binding is usually driven by directional hydrogen bonding that often recognize through multidentate H-bond donors such as urea, thiourea, and squaramide motifs.[20,21] This activity is usually further supported by electrostatic stabilization.[22] Because anions are normally strongly hydrated, receptor design must consider the desolvation penalty, geometric complementarity, and preorganization in order to achieve selectivity and sufficient affinity in competitive solvents.[23,24] By contrast, cation binding is usually leading by coordination and ion-dipole interactions, where the cation is 'caught' by lone pairs on donor atoms (*e.g.*, O, N, and S) within the receptor scaffold.[25] Selectivity in such systems often arises from matching the preferred coordination number and the size and shape of the binding cavity.[26] The following sections will discuss representative receptor classes and design principles for both anions (Sections 1.2.1-1.2.2) and for cations (Sections 1.2.3-1.2.4), respectively.

1.2.1 Anion Recognition: Principles and Significance

In supramolecular chemistry, anion recognition refers to the process by which a receptor molecule binds selectively to an anionic guest through noncovalent interactions. Anions play essential roles in chemical, biological, and environmental systems. For example, chloride (Cl^-), sulfate (SO_4^{2-}), phosphate (PO_4^{3-}), carbonate (CO_3^{2-}), peroxide (O_2^{2-}), cyanide (CN^-), and nitrate (NO_3^-) are critical in areas such as water treatment,[27] catalysis,[28] biological ion channels,[29] sensors,[30] ion transport,[31] environmental monitoring,[32] and electrochemical energy storage.[33] In the colorimetric domain, coupling PDA with lateral-flow analysis enables on-site, rapid visual readout of Cd^{2+}.[34] In the electrochemical domain, voltammetric and amperometric measurements using nanomaterial/carbon-modified electrodes achieve highly sensitive, interference-resistant quantification of NO_2^-/NO_3^- in real water matrices.[35] In parallel, many anion sensors operate as reaction-based probes through specific chemical reaction(*i.e.*, a covalent bond) rather than host-guest binding(noncovalent interactions). For example, BODIPY-based organic dye probes deliver selective dual-mode (colorimetric/fluorescent) readouts for F^- and CN^- by reaction based sensing

activity (Figure 1.2.1).[36] In summary, this thesis primarily focuses on supramolecular ion recognition dominated by noncovalent interactions, including hydrogen bonding, electrostatics, π-interactions, the hydrophobic effect, and Van der Waals force. Reaction-based (covalent bond) probes such as that shown in Figure 1.2.1 are mentioned only for comparison.

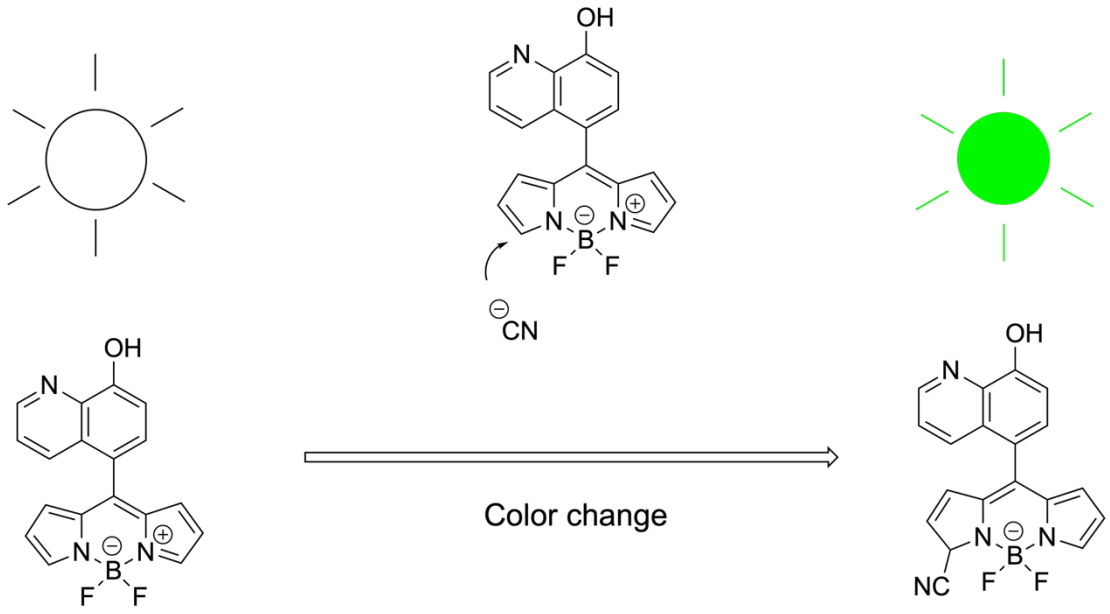

Figure 1.2.1. Example of reaction-based BODIPY probe for selective detection of CN^-.

Consequently, the efficient and selective recognition, sensing, or regulation of anions has become a central focus in supramolecular chemistry. In addition, in some catalytic systems, anions act as substrates, ligands, intermediates, or counterions. Receptors capable of recognizing specific anions may regulate reaction pathways or stabilize intermediates, thereby enhancing catalytic efficiency and selectivity.[37] Moreover, the design and study of selective anion receptors provides insights into fundamental principles such as noncovalent interactions, cooperative effects, solvent influence, conformational preorganization, and desolvation energetics, thereby advancing the theoretical framework of supramolecular chemistry itself.

1.2.2 Anion receptors

In supramolecular chemistry, the study of anion receptors is a promising direction along with significant challenges. Due to their high charge density, pronounced

polarity, and strong hydration shells, anions require receptors not only to provide complementary binding sites but also to balance desolvation penalties, geometric compatibility, and cooperative interactions. Current design strategies typically employ preorganized rigid scaffolds[38,39] and multipoint binding approaches to enhance binding affinity and selectivity toward anions. Moreover, exploiting cooperative or allosteric effects to regulate binding behaviour and introducing vacant coordination positions on a metal centre can also further strengthen coordination capacity.[40]

1.2.2.1 Preorganization of anion receptors.

One of the significant challenges in designing efficient anion receptors is the strong hydration effect of anions. 'The more highly hosts and guests are organized for binding and low solvation prior to their complexation, the more stable will be their complexes. ' This passage is quoted from Cram's Nobel Prize Lecture.[41] Preorganization refers to the situation in which the binding groups of a receptor, such as hydrogen-bond donors, cationic sites, or π-systems, are arranged in an almost ideal geometric configuration prior to binding, thereby closely matching the shape and charge distribution of the target anion. In the absence of preorganization, flexible acyclic receptors undergo substantial conformational rearrangements upon binding, which lead to entropic penalties and additional energy costs, ultimately reducing binding affinity.[42,43] Urea-based hydrogen-bond donors are relatively flexible, whereas squaramides, by virtue of strong conjugation and ring strain, are generally regarded as rigid hydrogen-bonding scaffolds. Compared with urea, squaramides, owing to their higher Brønsted acidity and coplanar, convergent NH hydrogen-bonding geometry, typically deliver larger binding constants and superior selectivity toward halides and polyoxyanions, a trend repeatedly corroborated in head-to-head comparisons and subsequent reviews(Figure 1.2.2).[44]

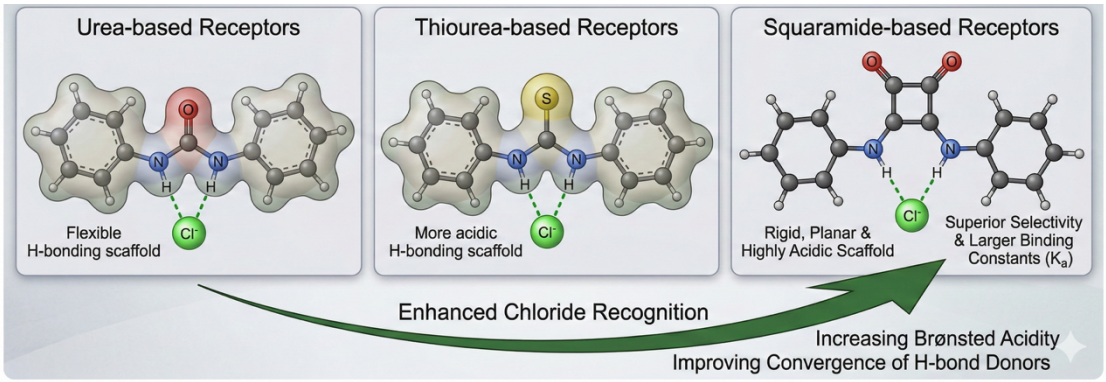

Figure 1.2.2. Graphical abstract of chloride affinity of urea, thiourea and squaramide.[45]

By contrast, rigid cyclic or backbone-constrained receptors are already arranged in favourable spatial conformations prior to binding, requiring minimal conformational changes during complexation, and thus exhibiting higher binding strength and selectivity.[38,39] A more intuitive example is cyclo[2]carbazole[2]pyrrole vs. calix[4]pyrrole.[46] Cyclo[2]carbazole[2]pyrrole is fixed in a pseudo-1,3-alternate conformation, which provides preorganized anion binding site consisting of two pyrrole subunits The conformation of cyclo[2]carbazole[2]pyrrole is locked into a 1,3-alternate, preorganized geometry that establishes a directional anion-binding site centered on the two pyrrole NH groups. Benefiting from this preorganization and a lower host deformation energy, the receptor exhibits higher affinity in DCM for Cl^- than the classical tetrapyrrolic hydrogen-bond receptor calix[4]pyrrole (Figure 1.2.3). Computations attribute this advantage to larger binding energies and reduced host-guest strain of cyclo[2]carbazole[2]pyrrole.

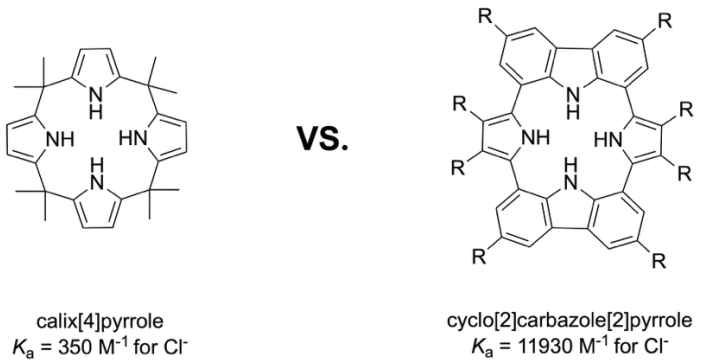

Figure 1.2.3. Comparison of chloride affinity of cyclo[2]carbazole[2]pyrrole and calix[4]pyrrole. Redrawn based on reference 40.[47]

To enable straightforward comparison of binding affinities across different host-guest systems, the association constant K_a is usually reported to quantify the binding strength, where the K_a value of cyclo[2]carbazole[2]pyrrole is much higher than that of calix[4]pyrrole. The association constant is defined as:

$$K_a = \frac{[HG]}{[H][G]}$$

A larger K_a value represents a greater fraction of complex [HG] at equilibrium and therefore stronger binding. Because K_a value usually span several orders of magnitude, sometimes log K_a is used for compact comparison scale. In addition, the dissociation constant K_d is also widely used in biochemistry:

$$K_d = \frac{[H][G]}{[HG]} = \frac{1}{K_a}$$

However, binding strength is more often reported as the association constant K_a to follow supramolecular host-guest convention and to enable direct comparison between different systems.

Preorganization represents a key strategy for achieving high selectivity and elevated binding constants. Therefore, owing to their intrinsic preorganization and structural control, macrocyclic receptors have demonstrated remarkable performance in recent anion recognition studies. Recently, Mohammed and co-workers reviewed the development and applications of macrocyclic host molecules in the field of anion recognition and pointed out their potential applications in sensing, separation, transmembrane transport, and catalysis.[48] Taking the typical macrocyclic receptors reported by Elmes as an example (Figure 1.2.4),[49] their work focused on combining the macrocyclic framework with squaramide units to achieve efficient anion recognition. The study revealed that, owing to their strong hydrogen-bond donor character, squaramide groups can establish highly preorganized binding sites within the macrocyclic scaffold, thereby enabling stable and selective binding of sulfate even in highly competitive aqueous environments.

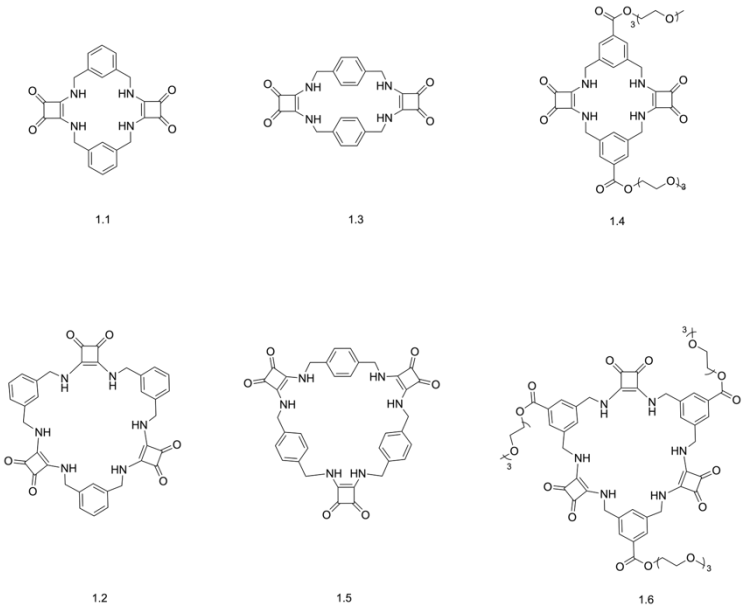

Figure 1.2.4. Macrocyclic squaramides reported by Elmes and co-workers.

1.2.3 Cation Recognition: Principles and Significance

In parallel, cation recognition has also been intensively studied. The importance of cation recognition lies primarily in the pivotal roles played by metal ions in biological and environmental systems.[50] In biology, sodium (Na^+) and potassium (K^+) ions are involved in maintaining cell membrane potential, forming the basis of nerve signal transmission and muscle contraction.[51,52] Calcium ions (Ca^{2+}), as critical signaling molecules, regulate processes such as enzyme activity and apoptosis.[53,54] Magnesium ions (Mg^{2+}) are widely present in nucleic acid and protein structures, contributing to conformational stability and catalytic activity.[55,56] Transition metal ions, such as zinc (Zn^{2+}) and copper (Cu^{2+}), also participate in numerous enzymatic reactions.[57,58] In contrast, toxic metal ions such as lead (Pb^{2+}), cadmium (Cd^{2+}), and mercury (Hg^{2+}) pose severe threats to the environment and human health, making their selective recognition a crucial task in supramolecular chemistry.[59,60] Therefore, cation recognition is not only essential for understanding fundamental biological processes but also holds significant value in medical diagnostics and environmental monitoring. For example, synthetic cation-recognition molecules can modulate protein function by selectively forming complexes with amino acids and peptides.[61]

At the core of cation recognition lies the cooperative effect of noncovalent interactions. Among these, coordination interactions represent the most prevalent mechanism.

Electron-donating atoms (such as O, N, and S) in host molecules can form stable coordination bonds with metal cations.[62] For example, crown ethers utilize the lone pairs of oxygen atoms to selectively bind alkali metal ions, with their recognition efficiency closely related to the cavity size of the macrocycle.[42,63] Beyond coordination, electrostatic interactions and ion–dipole interactions also play critical roles in cation recognition. Particularly in polar environments, negatively charged groups or dipolar moieties can exert strong attractive forces toward cations, thereby enhancing binding affinity.[61,64,65] This has motivated the development of ion-pair receptors that incorporate both anion and cation binding sites. When the cation and anion sites within a single host engage their respective guests concurrently, the Coulombic attraction between the captured ions, together with host-induced conformational and electronic effects, further stabilises the complex.[26,66,67] In low-polarity media or extraction settings, salts frequently exist as contact ion pairs; attempting to "forcibly dissociate" only one constituent ion with a single receptor typically incurs a larger desolvation penalty.[68] By contrast, ion-pair receptors sequester the paired ions in an integrated manner, partially retaining the intrinsic ion-ion interactions.

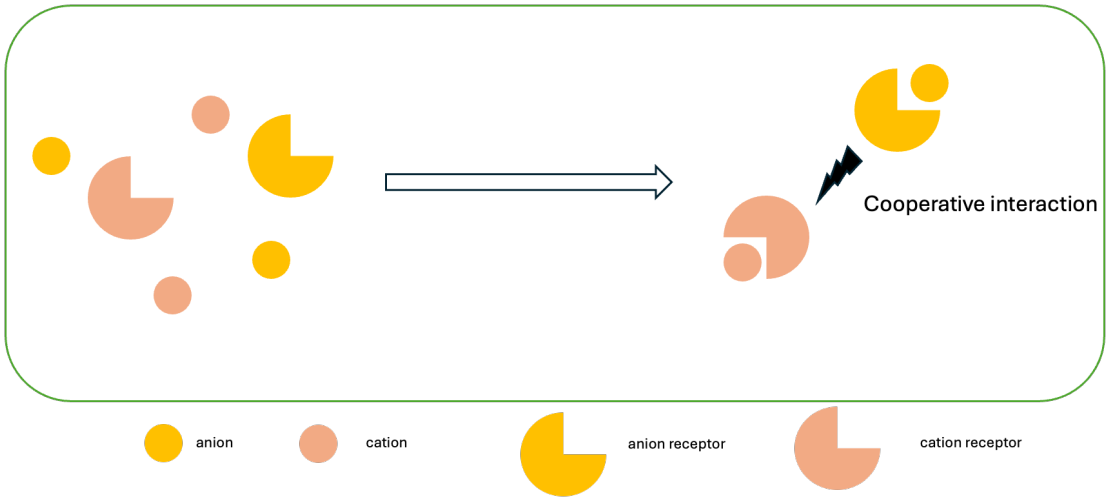

Figure 1.2.6. Schematic illustration of ion pair extraction, showing the cooperative interaction between the complexed anion and complexed cation.

Another important mechanism is cation–π interactions, in which positively charged metal ions are stabilized by the π-electron cloud of aromatic rings. For instance, benzene or indole rings can engage in pronounced cation–π interactions with potassium and ammonium ions.[69,70]

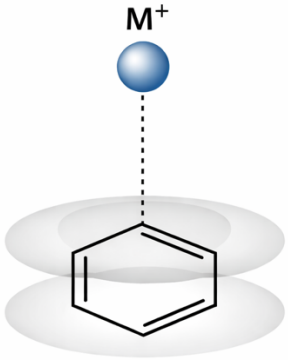

Figure 1.2.7. Schematic of the cation-π interaction between cation and benzene.

Such interactions are widely observed in the function of protein ion channels, and synthetic receptors incorporating aromatic frameworks can mimic and even amplify these effects.[71,72] Finally, hydrogen-bond-assisted binding can also contribute to certain systems. Here, hydrogen-bond donors in the receptor interact with ligand molecules surrounding the cation (such as water or counteranions), thereby indirectly reinforcing the overall binding stability.[73,74] Hydrogen-bond donors and acceptors on the receptor can engage in second-coordination-sphere interactions with either the coordinated waters in the cation's first solvation shell or its counter anion, giving rise to an outer-sphere hydrogen-bond network of the type M-O-H----N or M-O-H----O. This network bridges and preorganizes the host-guest assembly. Materials reported in Derek's early studies exhibited thermal stabilities comparable to prototypical coordination polymers, demonstrating that second-sphere hydrogen bonding constitutes a general supramolecular synthon and design strategy for crystal engineering (Figure 1.2.8).[75]

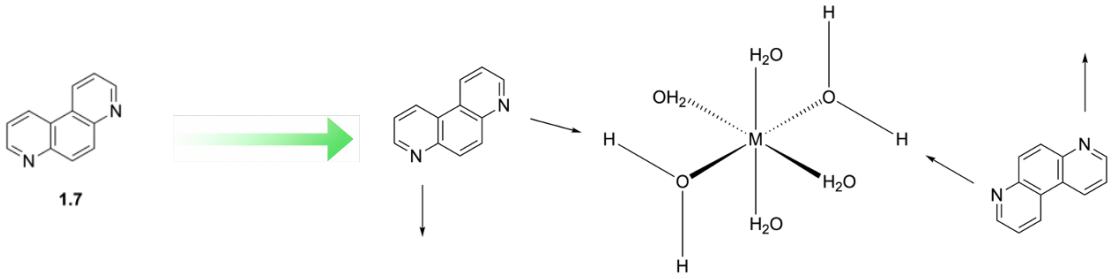

Figure 1.2.8. Illustration of first and second spheres of coordination interaction.[75]

In summary, the significance of cation recognition lies in its broad biological and environmental relevance, while its fundamental mechanisms rely primarily on coordination, electrostatic and ion-dipole interactions, cation-π interactions, and hydrogen-bond-assisted binding. Understanding these interactions not only provides a theoretical foundation for the design of artificial receptors but also establishes the prerequisites for their applications in complex environments.

1.2.4 Cation receptors

The previous discussion has highlighted the importance of cation recognition and its principal mechanisms. However, constructing highly efficient and selective receptors through molecular design remains a central challenge in the development of supramolecular chemistry. An ideal cation receptor should achieve both high affinity and selectivity for target ions under complex conditions, while also exhibiting tunability and potential functional applications. Consequently, multiple design strategies have been proposed, which rely on diverse noncovalent interactions to achieve effective recognition of specific metal ions.

Analogous to anion receptors, the most common approach involves designing receptors based on the matching of cavity size and geometry. Typically, receptors contain one or more cavities to accommodate cations, and thus the size, shape, and spatial arrangement of binding sites directly determine selectivity.[76,77] Furthermore, coordination and multivalent interactions are effective approaches to enhance binding affinity. Incorporating electron-donor atoms with lone pairs into receptor molecules enables the formation of stable coordination with metal ions. To mitigate entropic penalties during binding, the “preorganization” strategy is frequently employed,

whereby rigid backbones or conjugated frameworks are used to restrict molecular flexibility so that the receptor adopts a geometry close to the binding conformation even prior to interaction.[78] For instance, crown ethers coordinate metal ions through the evenly distributed oxygen atoms on their cyclic frameworks,[79,80] their different ring sizes (e.g., 12-crown-4, 15-crown-5, 18-crown-6) preferentially accommodate Li^+, Na^+, and K^+, respectively, thereby achieving remarkable ion selectivity and providing insights for the design of macrocyclic compounds and multidentate ligands. Thomas and co-workers employed UV and IR spectroscopy in a cold ion trap, complemented by DFT calculations, to demonstrate that for smaller metal ions, the crown ether ring undergoes deformation to reduce the metal-oxygen distance and thereby enhance the interaction between the metal and the oxygen atoms. In contrast, larger metal ions cannot fully enter the crown ether cavity. Instead, they remain at the outer side of the ring while keeping one side open to allow further solvation. In the Na^+-**1.8** and K^+-**1.9** complexes, the crown ether adopts the most open conformation and holds the metal ion at the centre of the ether ring, indicating an optimal size match between the crown ether cavity and the metal ion (Figure 1.2.9).[81]

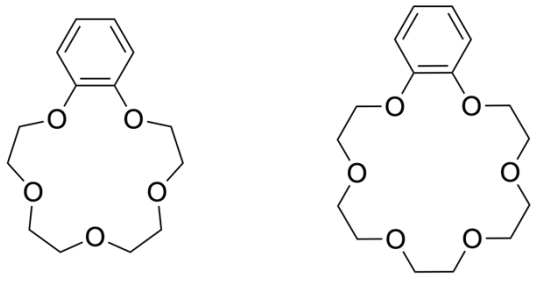

1.8 **1.9**

Figure 1.2.9. Structure and compounds of **1.8**, **1.9**.[81]

In addition, as mentioned in the last part, electrostatic interactions and cation-π interactions can significantly strengthen recognition. Receptors bearing negatively charged groups or strong dipoles can stabilise metal ions through electrostatic attraction, while π-electron clouds in aromatic frameworks engage in cation-π interactions. These interactions, widely observed in biological systems, have also been successfully utilized in artificial receptors. Calixarenes, for instance, exploit their aromatic cavities to establish cooperative cation-π interactions with cations, thereby exhibiting excellent binding performance toward ammonium salts and alkali metal ions. Meadows and colleagues systematically investigated lariat ether ligands bearing

aromatic side chains, revealing the cation-π interactions between alkali metal ions and the aromatic π systems (Figure 1.2.10).[82] Experimental results demonstrated that metal ions can engage in significant interactions with the aromatic rings of the side chains, thereby enhancing the ligand's binding affinity for the ions. The study further showed that the electronic properties and spatial configuration of the aromatic groups directly influence ion selectivity: indole-containing ligands exhibit higher selectivity toward K^+, whereas phenyl-substituted ligands display stronger affinity for Na^+. These findings indicate that incorporating aromatic side chains into crown ether derivatives or lariat ether systems allows precise modulation of alkali metal ion recognition via cation-π interactions, providing an important strategy for the design of highly selective ion receptors.

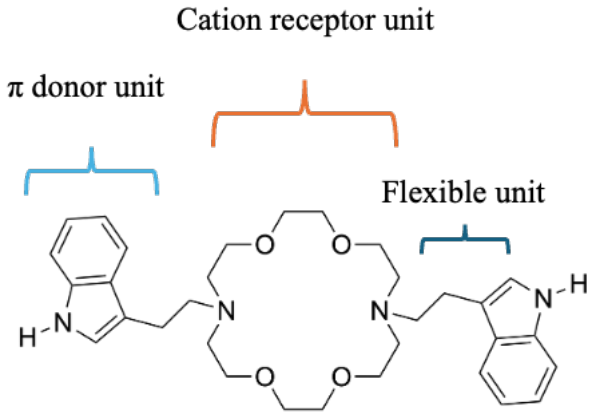

1.10

Figure 1.2.10. Structure of diaza-18-crown-6 derivatives.[82]

Recent studies have also emphasized responsive and functionalized designs. By incorporating photoresponsive, pH-sensitive, or redox-active groups into receptors, it becomes possible to externally regulate the binding process.

For example, photoresponsive crown ethers undergo reversible conformational changes under irradiation, thereby altering their binding capacity for metal ions. Such "stimuli-responsive receptors" not only attract fundamental research interest but also open new avenues for applications in controlled drug release, molecular switches, and functional materials.[83,84] Another representative example is calixarene derivatives,[85] whose aromatic cavities and modifiable hydroxyl rims impart unique advantages in binding metal ions and organic ammonium salts. These cases illustrate the tight

interplay between molecular design and binding mechanisms, while also paving the way for the development of receptor systems based on squaramides and other hydrogen-bond donor frameworks.[30]

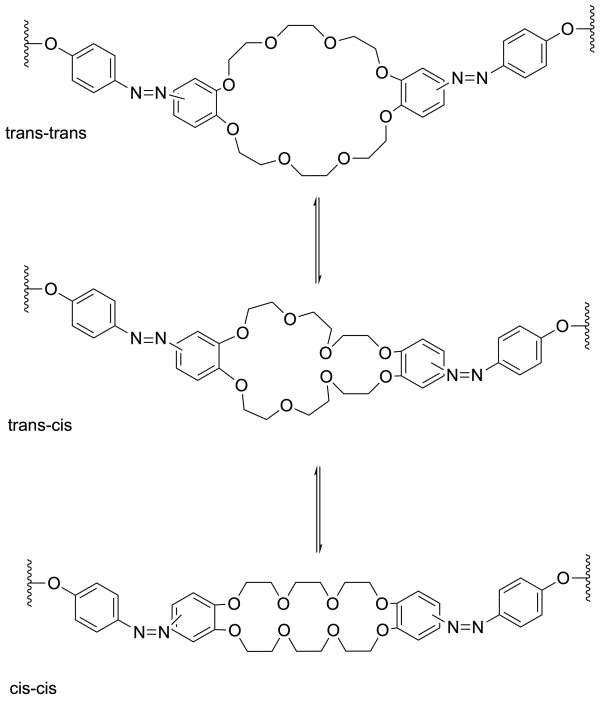

1.11

Figure 1.2.11. Reversible conformational changes of polymer-supported crown ether under irradiation.

In conclusion, the design strategies for cation receptors mainly revolve around spatial matching, multivalent coordination, synergistic noncovalent interactions, and responsive regulation. These design principles are generally applicable and highly versatile across different systems. With the continuous introduction of novel structural motifs and functional groups, cation receptors are expected to play increasingly important roles in biomedicine, environmental monitoring, and smart materials.

1.3 Ion transport

In the previous sections, we have discussed the design principles and recognition capabilities of cation and anion receptors. Whether it involves the selective coordination of cations by crown ethers and cryptands or the hydrogen-bond-based

recognition of anions by urea, thiourea, and squaramide frameworks, the central objective lies in achieving highly selective ion binding. However, in real biological systems, ion regulation depends not merely on binding but further on transmembrane transport processes that enable signal transduction, energy conversion, and maintenance of homeostasis.

Accordingly, in the context of supramolecular chemistry, ion transport is regarded as a functional extension of ion recognition. Recognition provides selectivity, whereas transport provides dynamic functionality. Receptors that can only complex ions in solution remain limited to applications as molecular probes or sensors. However, once they are capable of overcoming energy barriers within a membrane environment and accomplishing a cyclic process of binding-translocation-release, they acquire the potential to mimic natural ion channels and transporters.

Ion transport across membranes is one of the most fundamental and essential processes in living organisms, underlying nearly all cellular activities.[86] From the generation and propagation of nerve impulses to muscle contraction, osmoregulation, and energy metabolism, transmembrane ion movement plays a central role in maintaining homeostasis and physiological balance.[87] For instance, the exchange of sodium (Na^+) and potassium (K^+) ions across membranes forms the molecular basis of neuronal action potentials, while transient fluxes of calcium ions (Ca^{2+}) act as key signaling events that regulate muscle contraction, neurotransmitter release, and gene transcription.[88,89] Meanwhile, chloride ions (Cl^-) are indispensable for maintaining membrane potential and osmotic balance.[90,91]

Natural ion channels and transporters are highly sophisticated biomacromolecules, typically composed of polypeptide chains folded into precise architectures and often associated with cofactors or auxiliary proteins.[92] These systems achieve ion transport with remarkable efficiency and selectivity. For example, potassium channels can discriminate K^+ from Na^+ with a selectivity exceeding 10^4, exhibiting exceptional molecular recognition.[93] However, the structural and functional complexity of these natural molecular machines makes them extremely difficult to reproduce or manipulate under laboratory conditions. Consequently, the development of simplified artificial models has become an important strategy for elucidating the mechanisms of ion translocation.

Within this context, supramolecular chemistry offers a powerful conceptual and methodological framework. By exploiting noncovalent interactions such as hydrogen bonding, electrostatic forces, and π-π interactions, researchers have designed and synthesized artificial ion transporters that can mimic, regulate, or even interfere with ion transport across membranes.[94]

1.3.1 Cation transporters

1.3.1.1 Mechanism of cation transport

Research on cation transporters commenced relatively early. Pressman and co-workers elucidated the mechanism by which valinomycin functions as a K^+-selective carrier, and has been widely used as a prototypical ion carrier.[95] In parallel, Gramicidin A provided one of the earliest protein models for a channel/pore mechanism.[96] Subsequently, Pedersen's discovery of crown ethers established the macrocyclic recognition foundation for synthetic cation channels and carriers.[97]

In general, cations can cross membranes via two principal mechanisms: the carrier mechanism and the channel mechanism. In the carrier mechanism, the carrier complexes the target cation with high affinity to form a "lipophilic complex," which diffuses through the membrane core within the lipid phase. On the opposite side, changes in coordination environment, ionic strength, and/or membrane potential promote ion release, after which the carrier returns to the original side to complete the cycle. A classic example is the highly K^+-selective transport by valinomycin.[95] the eight-coordinate carbonyl geometry in its inner ring provides coordination favorable to K^+, thereby enabling dissolution and diffusion of the "carrier-K^+ complex" in the lipid phase, and markedly enhances the permeability of the mitochondrial inner membrane to K^+.

In contrast, the channel mechanism involves the self-assembly or aggregation of receptors into continuous pores that allow ions to pass through the membrane.[98] Natural minimalist channels such as gramicidin A form stable single-file conduction.[99] Synthetic channels mimic these features and can be engineered for gating (voltage, light, pH, redox) and tailored cation selectivity.[100]

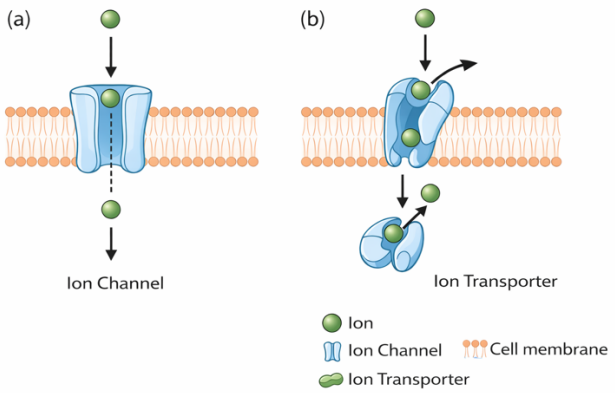

Figure 1.3.1. (a) Ion channels and (b) ion transporters. Reproduced with permission from.

1.3.1.2 The design of cation transporters

Among various artificial cation carriers, crown ethers represent the earliest and most extensively studied class. Their cyclic cavities are highly compatible with the sizes of alkali metal ions, enabling efficient and selective complexation.[101] Because the lipid bilayer is highly hydrophobic, many hydrophilic receptors, despite their excellent ion recognition capabilities, struggle to insert into the membrane environment. Therefore, researchers often introduce hydrophobic modifications to enhance their membrane affinity. Using crown ethers as an example, 18-crown-6 strongly coordinates alkali metal ions but is excessively hydrophilic, hindering its effective entry into phospholipid bilayers. By installing phenyl groups on either side of the crown ether to increase the lipophilicity of the molecule, Stolwijk synthesised a family of dibenzo-18-crown-6 that shows pronounced transmembrane ion-transport efficiency, supporting the necessity of lipophilic modification for effective operation within membrane phases (Figure 1.3.2).[102]

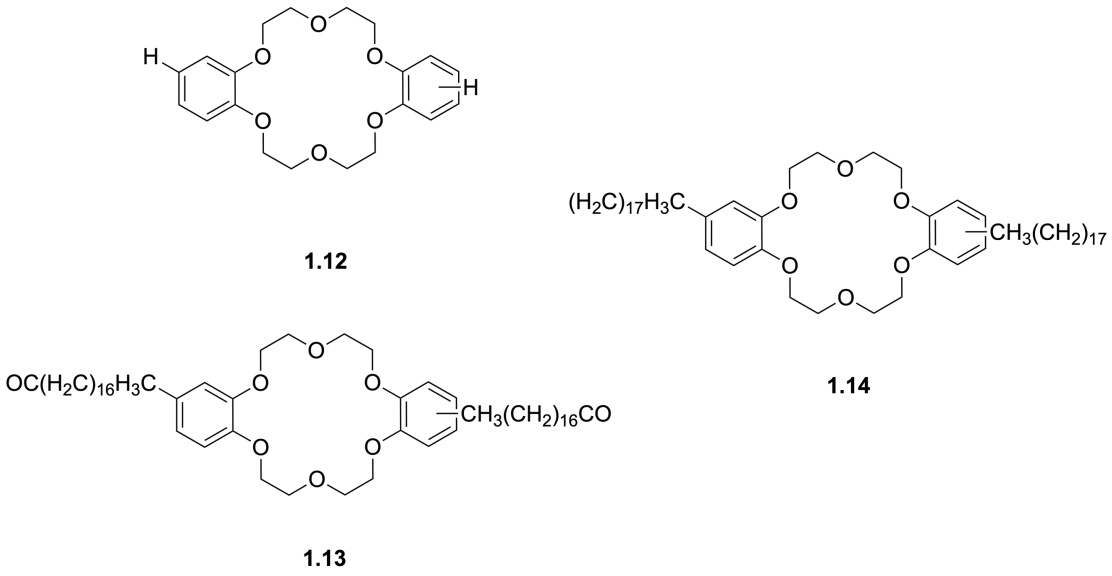

Figure 1.3.2. Structure of dibenzo-18-crown-6.

Beyond cavity size and lipophilic modification, the effective design of artificial cation carriers hinges on a thermodynamics-kinetics balance and membrane compatibility. On the one hand, sufficient affinity is required to bind the ion while maintaining appropriate association and dissociation rates: the key to traversing the lipophilic membrane core is to offset the ion's desolvation free-energy penalty upon transfer from water into the membrane by means of appropriately tailored receptor-ion interactions.[92] Overly strong binding suppresses transmembrane release, whereas insufficient affinity fails to sequester the cation. On the other hand, the overall lipophilicity must be tuned within a productive window: inadequate lipophilicity impedes membrane insertion, whereas excessive lipophilicity promotes aggregation, slows diffusion, and can trigger nonspecific permeability or membrane perturbation.[104] As one of the earliest families of synthetic channel-forming molecules to be systematically investigated, hydraphiles have been shown by ion-selective electrode (ISE) assays to mediate ion conduction in synthetic bilayers. Their channel scaffolds align along the membrane and are terminated with hydrophilic headgroups that stabilise membrane insertion. The electronics and length of the side chains and arms regulate the extent of insertion, aggregation propensity, and channel stability, thereby modulating flux and selectivity. For example, the introduction of electron-rich aromatic side arms engages cation-π interactions with lipid headgroups, markedly enhancing activity. Moreover, in cells and model organisms, hydraphiles elicit biological effects attributable to disruption of ion homeostasis (Figure 1.3.3).[105]

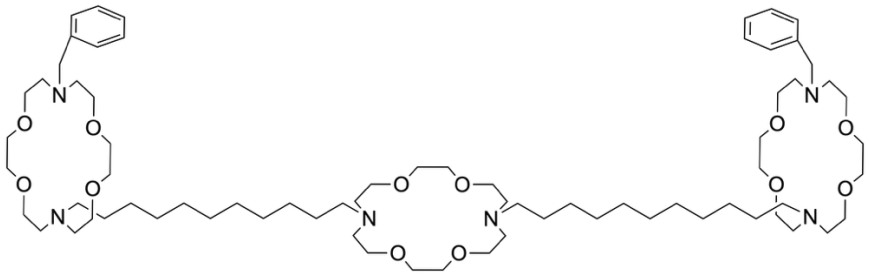

Figure 1.3.3. the structure of hydraphiles reported by Weber.[105]

Leevy et al. synthesised a series of dialkyl diaza-18-crown-6 lariat ethers bearing two alkyl side arms and systematically compared their cation transmembrane transport in liposomes with their biological activities (Figure 1.3.4). These molecules exhibit log P values between 5.5 to 9.2. Sodium-release and membrane-depolarisation assays showed a discontinuous on-off dependence of transport activity on side-chain length. Moreover, the extent of cation transport in liposomes correlated with toxicity toward Escherichia coli, Bacillus and yeast .[106]

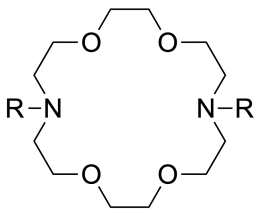

1.15 R= C_8H_{17} **1.19** R= $C_{16}H_{33}$

1.16 R= $C_{10}H_{21}$ **1.20** R= $C1_8H_{37}$

1.17 R= $C_{12}H_{25}$ **1.21** R= COC_9H_{19}

1.18 R= $C_{14}H_{29}$ **1.22** R= $COC_{11}H_{23}$

Figure 1.3.4. The structure of dialkyl diaza-18-crown-6 lariat ethers.[106]

Chen et al. reported a [2]rotaxane molecular shuttle that operates within lipid bilayers (Figure 1.3.5). The carrier comprises an amphiphilic axle bearing three recognition sites, threaded by a dibenzo-24-crown-8 macrocycle, with a benzo-18-crown-6 unit

appended to the ring as a K^+ carrier. This molecule inserts into the membrane and, via stochastic shuttling motion, mediates passive transmembrane ion transport, hence the moniker "molecular cable car." Experimentally, it transports K^+ across giant unilamellar vesicles (GUVs) with EC_{50} value of 1.0 μM. [107]

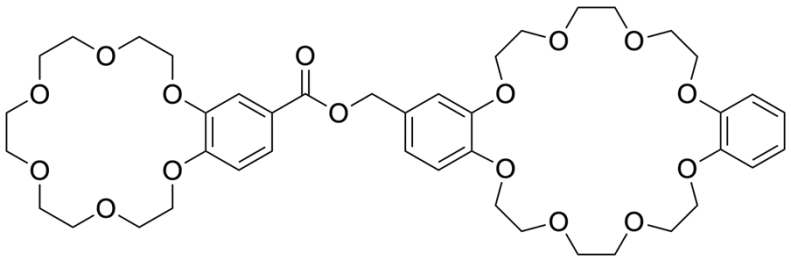

Figure 1.3.5. The structure of [2]rotaxane reported by Chen.[107]

1.3.2 Anion transport

Anion transport across membranes is an indispensable process in biological systems.[108] Similar to cations, anions play central roles in maintaining charge balance, regulating osmotic pressure, and mediating signal transduction. However, their physiological functions are often complex and diverse. For example, chloride ions (Cl^-) are crucial for controlling neuronal excitability and cell volume,[109] and phosphate ions ($H_2PO_4^-/HPO_4^{2-}$) serve not only as essential components in energy metabolism but also as structural building blocks of biomacromolecules such as DNA and RNA.[110] In nature, highly specialised anion channels and transporters have developed to accomplish these tasks. For example, the CLC chloride channel family achieves efficient Cl^- translocation through a finely tuned selectivity filter, while CFTR (cystic fibrosis transmembrane conductance regulator) can mediate the transport of both Cl^- and HCO_3^-.[111,112]

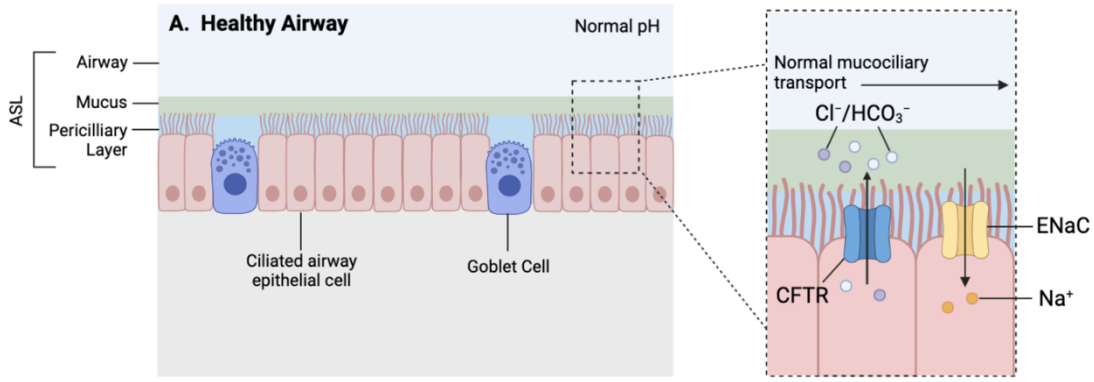

Figure 1.3.6. Schematic illustration of efficient chloride (Cl^-) and bicarbonate (HCO_3^-) transport mediated by the CFTR channel in healthy airways. Licensed under CC BY 4.0.[113]

1.3.3.1 Mechanism of anion transport

Similar to cations, artificial anion transport across membranes can generally proceed via two fundamental mechanisms: the carrier-type and the channel-type pathways.[114] However, due to the distinct physicochemical properties of anions compared with cations, both mechanisms exhibit unique challenges and characteristics in anionic systems.

In the mobile carrier mechanism, receptor molecules form lipophilic complexes with anions through noncovalent interactions and subsequently diffuse across the lipid bilayer to release the bound anion on the opposite side.[115] Unlike cation carriers that mainly rely on coordination bonding, anion carriers typically employ hydrogen bonding, electrostatic interactions, or ion-pair formation for anion binding.[116] For example, urea, thiourea, and squaramide derivatives have been extensively studied as efficient anion transporters owing to their strong hydrogen-bond donor ability.[21,117] Nevertheless, the high hydration energies of anions make dehydration a major energetic barrier, many anions are more strongly hydrated than cations of comparable size, and shedding their hydration shells results in a signigicant free-energy penalty.[118,119] Hence, the receptor must possess sufficient binding affinity to compete with solvation while maintaining reversibility to ensure efficient anion release. Striking the delicate balance between binding strength and reversibility thus represents the central challenge in designing carrier-type anion transporters.

In the anion channel mechanism, molecules self-assemble into transmembrane pores or tubular structures that enable rapid ion migration. Anion channel design requires more stringent structural features: the inner wall of the channel must provide directional hydrogen-bonding sites or localized positive charge distributions to stabilize negatively charged species, whereas the outer surface must remain sufficiently hydrophobic to ensure stable membrane insertion.[120] For example, Montenegro reported a class of self-assembling cyclic peptide nanotubes (SCPNs) as programmable models of artificial ion channels (Figure 1.3.7). These nanotubes are constructed from conformationally planar cyclic-peptide monomers that axially stack via backbone–backbone hydrogen bonding to yield hollow, tubular supramolecular architectures. Both the lumen diameter and the outer-surface chemistry can be precisely dictated by sequence design, thereby endowing the channels with selective transmembrane transport of small molecules and ions.[121]

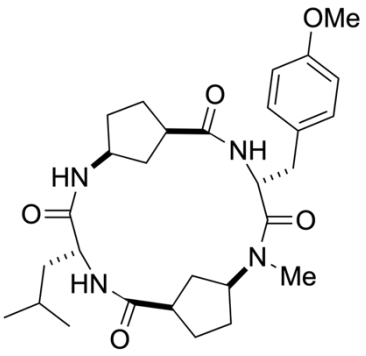

CP18

Figure 1.3.7. Structure of CP18 reported by Montenegro.[121]

1.3.3.2 Anion transporters

Systematic studies of artificial transmembrane anion transport date back to the 1990s. Starting from synthetic/peptide channel motifs, Tomich and co-workers first demonstrated that man-made molecules could mediate efficient migration of chloride (Cl^-) and other anions across lipid membranes.[122,123] Subsequently, the Davis group constructed carrier-type receptors on a cholestane scaffold (e.g., cholapods and cholaphanes) and, through preorganized multi-point hydrogen bonding in concert with a hydrophobic exterior, achieved Cl^- transport in liposomal model membranes as well as cooperative transmembrane co-transport of ion pairs (e.g., Cl^-/K^+). Flux and

selectivity were quantified using HPTS/lucigenin fluorescence probes, membrane depolarization assays, and ion-selective electrodes.[124]

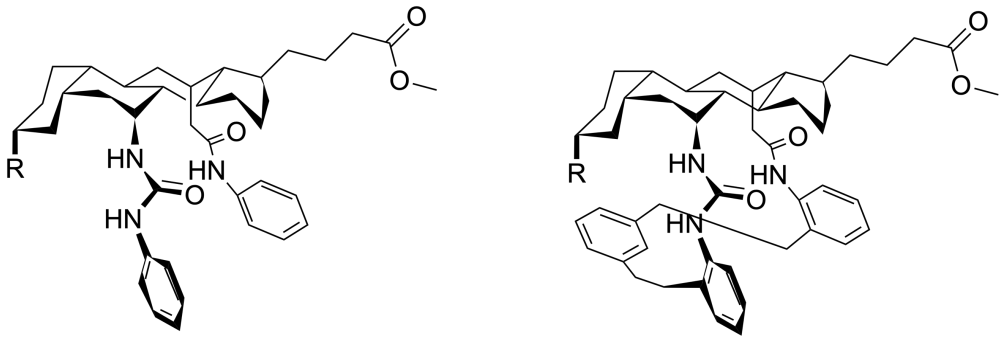

1.23 R= OAc
1.24 R= $NHCOCF_3$

1.25 R= OAc
1.26 R= $NHCOCF_3$

Figure 1.3.8. The structure of cholapods **1.23**-**1.24** and cholaphanes **1.25**-**1.26**. [124]

Building on this, Gale and collaborators systematically developed small-molecule anion carriers based on (thio)urea recognition units (Figure 1.3.9). By increasing NH acidity and enforcing geometric preorganization, they strengthened Hydrogen bonding to Cl^- and, across diverse membrane compositions and pH conditions, demonstrated Cl^-/NO_3^- and Cl^-/HCO_3^- antiport as well as symport behaviours.[125,126] Subsequently, the field of artificial anion channels advanced rapidly, yielding diverse systems based on π-stacked rigid scaffolds and stimuli-responsive molecules. Several of these constructs display fast anion conduction and tunable ion selectivity in both purified lipid membranes and cell-relevant environments, further underscoring their prospects for applications in biomimetic membranes and ion-channel materials.[127]

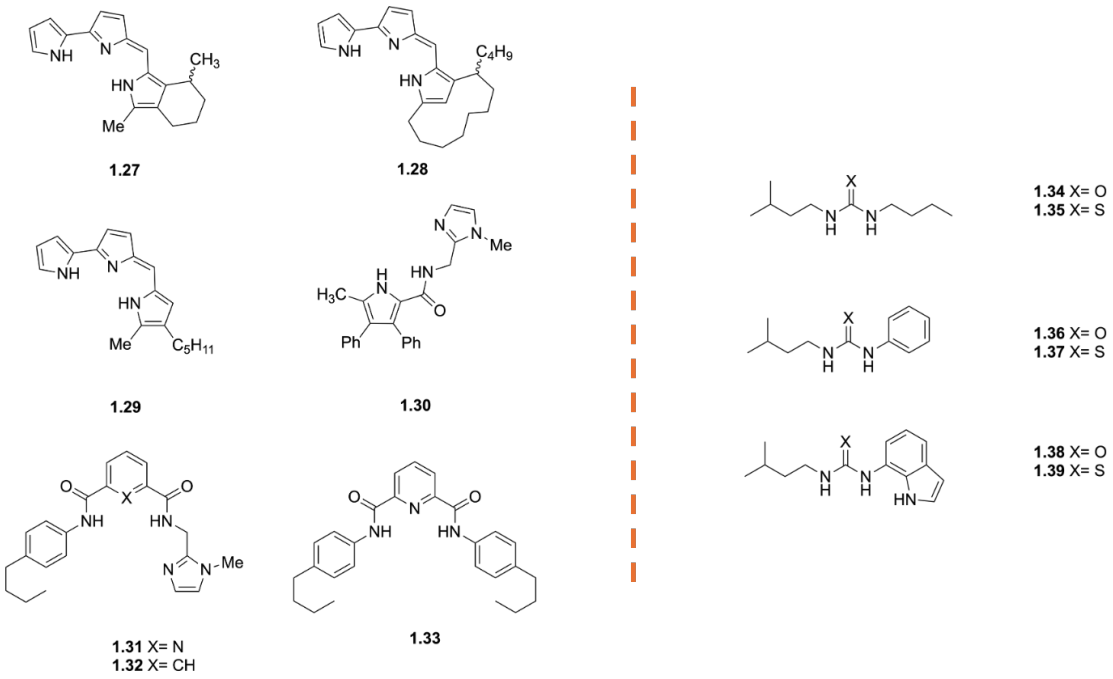

Figure 1.3.9. Structures of urea and thiourea derivatives reported by Gale and co-workers.

Muraoka et al. designed asymmetric, multisegment amphiphilic small molecules **1mer** and **2mer** that insert into preformed lipid bilayers with a defined orientation (Figure 1.3.10). Upon complexation with amine ligands, they assemble into transmembrane supramolecular channels that mediate ion transport. Removal of the ligand switch off the transport activity. Moreover, biomimetic regulation of the synthetic channels by agonistic and antagonistic ligands was demonstrated in both artificial membranes and the biological membranes of living cells.[128]

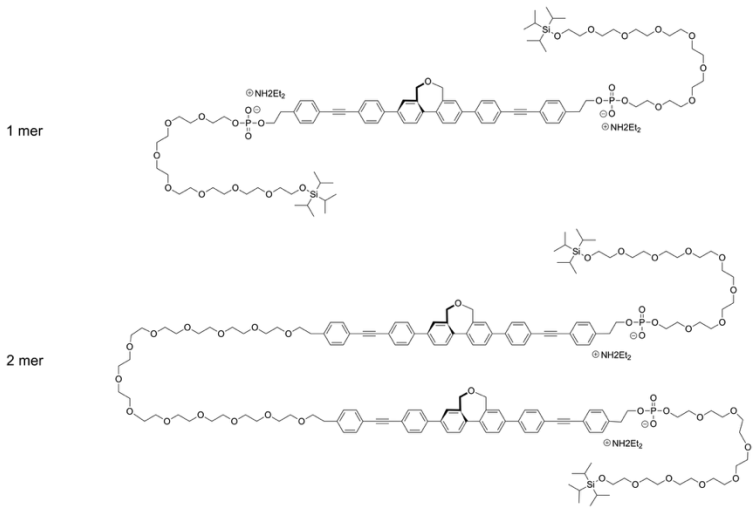

Figure 1.3.10. The structure of multiblock amphiphiles reported by Muraoka.[128]

Busschaert et al. systematically synthesised and characterised a series of thiosquaramides and found that their NH protons are markedly more acidic than those of the corresponding oxosquaramides. Consequently, they are readily deprotonated and rendered inactive under neutral conditions, whereas in acidic media they remain neutral, bind anions, and mediate transmembrane transport, displaying a clear pH-dependent 'switch-on' behaviour. Owing to their more acidic NH donors, thiosquaramides also show stronger anion transport ability than oxosquaramides under acidic conditions (Figure 1.3.11).[129]

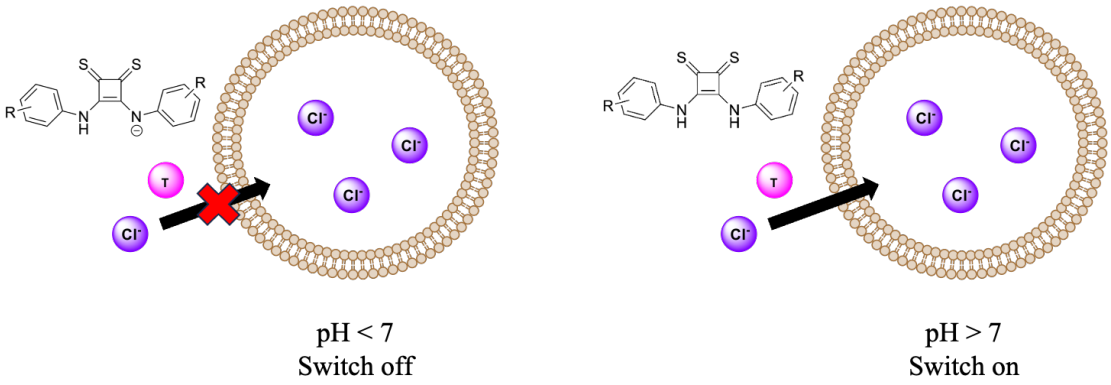

Figure 1.3.11. Graphic abstract of pH-dependent chloride transport behaviour of thiosquaramides.

In summary, the study of artificial anion transport has evolved from simple molecular recognition into a diverse and rapidly advancing field encompassing multiple strategies. There remains substantial room for advancement in this area.

1.4 The Application of Supramolecular Chemistry

The development of supramolecular chemistry has not only provided powerful tools for molecular recognition and ion transport but has also shown great potential in biological and medical applications. Compared with classical small-molecule drugs or macromolecular biopharmaceuticals, supramolecular systems are distinguished by their dynamic tunability driven by noncovalent interactions. This unique characteristic not only confers advantages in recognition and transport but also opens new

possibilities for biological applications such as antimicrobial therapy, drug delivery, and tissue repair. In particular, against the backdrop of globally emerging antibiotic-resistant bacterial strains and the diminishing efficacy of traditional antibiotics, the development of supramolecular-based antimicrobial strategies has become a key interdisciplinary research focus.[130]

The special status of supramolecular chemistry in biology arises primarily from its ability to mimic natural systems. For instance, artificial ion transporters discussed earlier not only replicate the high selectivity and efficiency of natural ion channels but can also achieve functions not found in nature, such as photo-control, pH responsiveness, or metal-ion regulation through structural modification.[100,131,132] This means that supramolecular systems can serve both as biomimetic models to help us understand cellular physiological processes and as molecular tools for biomedical applications. Moreover, the highly designable and controllable nature of supramolecular assemblies enables the fine-tuning of hydrogen-bond donors/acceptors, hydrophobic groups, and responsive units to construct stimuli-responsive or multifunctional molecular materials. Such molecules exhibit adaptability and versatility in complex biological environments that traditional drugs rarely possess.

Conventional antimicrobials typically target biosynthetic machineries (cell-wall assembly, nucleic-acid replication, translation). The rapid spread of multidrug resistance exposes the limits of these modes of action. By contrast, supramolecular systems leverage hydrogen bonding, π–π stacking, electrostatics, and hydrophobic effects to construct materials that disrupt membranes, collapse ion homeostasis, or perturb signaling/metabolic flux, thereby engaging nontraditional antimicrobial targets. Such mechanisms can also potentiate existing antibiotics. For example, synthetic ion channels (such as hydraphiles) have been shown to enhance antibacterial potency when co-administered with sublethal antibiotic doses..

As discussed above, one of the most prominent advantages of supramolecular chemistry in biological applications lies in its dynamic tunability. Many supramolecular assemblies can respond to external stimuli such as pH, light, or redox conditions, enabling spatiotemporal control over their structure and function. For example, photoresponsive supramolecular antimicrobials can release reactive oxygen

species (ROS) upon irradiation at infection sites, achieving localized and controllable antibacterial activity. This “stimulus-response to functional output” paradigm greatly enhances both safety and specificity, underscoring the translational potential of supramolecular chemistry from fundamental research to real-world applications.

Finally, from an interdisciplinary perspective, supramolecular chemistry bridges chemistry, materials science, and life sciences. It not only provides chemical model systems that deepen our understanding of biological processes such as ion transport, cell signaling, and membrane architecture, but also contributes practical strategies to medicine and pharmacy, advancing antimicrobial therapies, tissue regeneration, and intelligent drug delivery systems.

1.4.1 Membrane Regulation and Signal Transduction

The cell membrane serves as the interface between the cell and its external environment, with one of its most critical functions being the regulation of ion and molecular transport across the membrane.[133] The advent of artificial supramolecular transporters has enabled researchers to manipulate ion fluxes at the molecular level.[132,134] For example, Busschaert et al. synthesized a squaramide-based anion carrier and demonstrated that these molecules perturb intracellular chloride levels, thereby elevating lysosomal pH, suppressing autophagy, and inducing apoptosis (Figure 1.4.2). In liposomes they rapidly promote Cl^- efflux/exchange; at 1 mol% the representative compound 3 emptied intravesicular Cl^- in around 120 s. Crucially, compound 3 raised lysosomal pH to around 7.0, inhibited cathepsin B/L, caused concomitant upregulation of LC3-II and p62, and blocked autophagosome-lysosome fusion. By contrast, compounds 5 and 6 triggered apoptosis but, owing to excessive lipophilicity/strong membrane binding, failed to reach lysosomes and thus did not inactivate autophagy. This constitutes the first example of synthetic ion carriers that concurrently disrupt autophagy and induce apoptosis..[135]

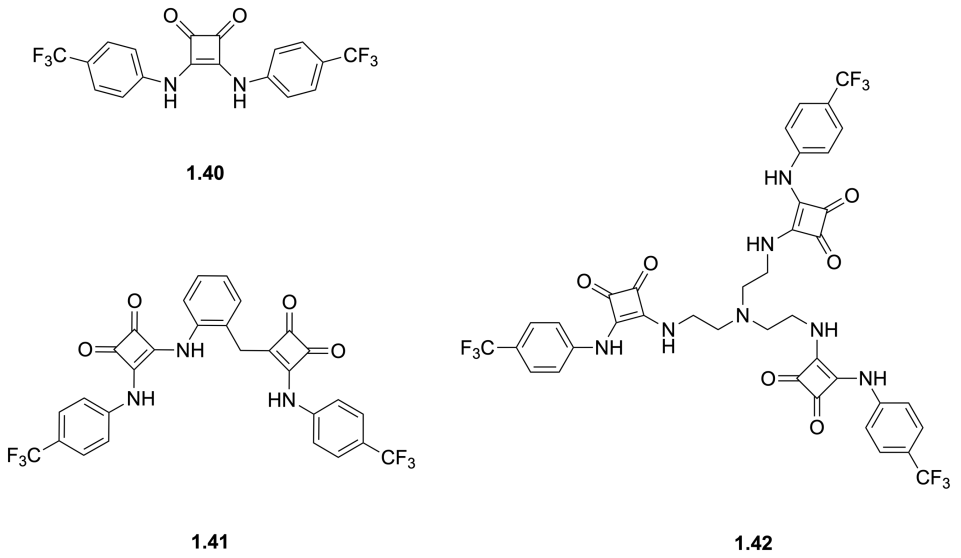

Figure 1.4.2. The structure of squaramides reported by Busschaet.[135]

In addition, supramolecular molecules possess diverse functionalities: they can act as chemical probes to elucidate the mechanisms of specific signalling pathways or be used to modulate cellular processes directly.[136] As discussed earlier, supramolecular systems are capable of inducing intracellular pH shifts or osmotic stress, which may trigger cell apoptosis or other stress responses.[137] Compared with traditional strategies based on genetic regulation or pharmacological intervention, these physicochemical perturbation–driven approaches offer a novel perspective for investigating cellular homeostasis and pathophysiological processes.

1.4.2 Drug Delivery and Targeted Therapy

For drug molecules to exert their therapeutic effects, they often need to cross cellular membranes or be released in a controlled manner within specific biological environments. Supramolecular chemistry provides innovative solutions to these challenges through the construction of self-assembled nanocarriers such as vesicles, micelles, and nanotubes.[121,138,139] Unlike covalent modification strategies, supramolecular systems rely on noncovalent interactions, endowing them with reversibility and stimuli-responsiveness. Host-guest systems based on cyclodextrins, pillar[n]arenes, or cucurbiturils have been proven to be able to encapsulate drug molecules and achieve controlled release in response to environmental cues.[140–143]

Moreover, supramolecular carriers can be engineered for targeted delivery through specific receptor-ligand interactions. For example, folic acid-modified supramolecular nanoparticles can selectively enter tumour cells that overexpress folate receptors, thereby enhancing drug utilization efficiency while minimising side effects.[144] Zhou et al. synthesised biodegradable F127-b-poly(ε-caprolactone) copolymer and decorated their surfaces with folic acid (FA) and β-cyclodextrin (β-CD). Using DOX·HCl as a model drug, pH- (7.4 and 5.0) and temperature-dependent (4, 25 and 37 °C) release behaviour was examined by DLS and AFM. Quantitative comparisons of cellular uptake in HepG2, KB, A549, and fibroblasts by confocal microscopy and flow cytometry demonstrated that FA conjugation markedly enhanced uptake and antitumor activity in folate-receptor-positive cells.[145]

In recent years, researchers have also introduced ion-responsive elements into supramolecular carriers, enabling drug release to be triggered by changes in H^+, Cl^-, or HCO_3^- concentrations. This approach allows precise coupling between drug release behaviour and the microenvironment of pathological sites, offering a promising direction for intelligent and targeted therapeutic systems.[146–148]

1.4.3 Bioimaging and Sensing

The application of supramolecular chemistry in bioimaging and sensing has also grown rapidly in recent years. By rationally designing fluorescent receptor molecules, researchers can achieve selective recognition of specific ions within complex biological environments and monitor them in real time through fluorescence signals.[149] For example, squaramide-based anion probes have been developed for the highly sensitive detection of fluoride ions, while crown ether derivatives are widely employed for sodium and potassium ion recognition and imaging.[150,151] Also, Lasitha et al. reported a series of fluorescent probe by coupling squaramide and Schiff-base motifs.[152] These probes exhibit weak emission in the free state, but display a pronounced ‘turn-on’ fluorescence response upon the addition of Zn^{2+} or Cd^{2+}, particularly when supplied as the corresponding acetates. These systems closely align with the ion recognition principles discussed earlier but extend their utility in biological contexts as visualisation tools.

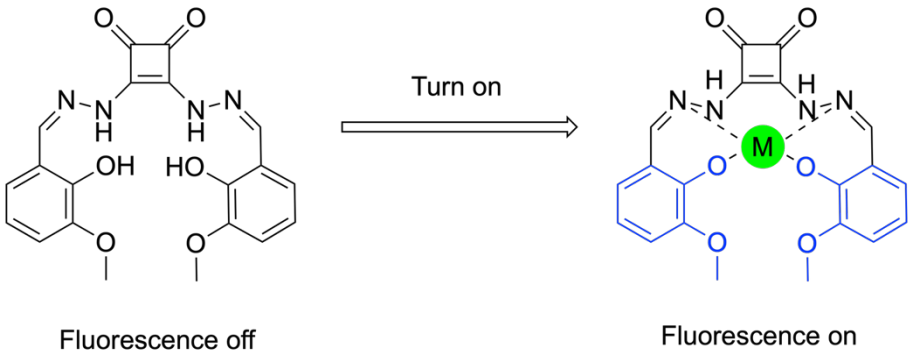

Figure 1.4.4. Illustration of squaramide-Schiff base scaffold based Zn^{2+}/Cd^{2+} fluorescent probe. Redrawn based on reference 149.

More importantly, certain receptor molecules integrate both recognition and transport functionalities. For instance, researchers have reported fluorescent probes capable of binding Zn^{2+} ions while simultaneously promoting their transmembrane transport. Such dual-function systems serve not only as imaging tools but also as active molecular regulators.[153] This supramolecular design concept combining sensing, transport, and regulation, highlights a shift in biochemical research toward smarter and more multifunctional molecular systems.[154]

1.4.4 The application of supramolecular chemistry in the antibacterial field.

Recently, the potential of artificial anion and cation transporters in antibacterial applications has become increasingly evident. Similar to their role in regulating cellular ion flux, these molecules can disrupt bacterial ion homeostasis-a process that many microorganisms rely on for growth and metabolism-thereby inducing cell death.[155,156] For example, squaramide-based Cl^- transporters have been shown to cause electrolyte imbalance within bacterial cells, ultimately leading to growth inhibition.[157,158] This mode of action differs fundamentally from that of traditional antibiotics, which typically target specific biomolecular pathways, and therefore artificial transporters are less prone to resistance caused by genetic mutations. [159] Moreover, cation transporters have exhibited selective bactericidal activity against drug-resistant bacteria, further supporting ion homeostasis as a critical vulnerability for antibacterial intervention.[160,161]

This strategy is similar to natural antimicrobial peptides (AMPs), which kill bacteria by compromising membrane integrity or perturbing membrane potential.[162] However, artificial ion transporters achieve similar bactericidal effects through controlled molecular-level ion transport, offering significantly greater tunability and structural precision.[157,159] Such advantages make artificial supramolecular systems highly promising candidates for the development of next-generation antibacterial agents that operate via non-traditional, physicochemical mechanisms.

Beyond small-molecule ion transporters, supramolecularly assembled antibacterial materials have also emerged as a rapidly developing research direction. For instance, supramolecular hydrogels and surface coatings containing cationic fragments can effectively inhibit bacterial adhesion and biofilm formation, thereby reducing infection risks.[163,164] In contrast to conventional disinfectant coatings, supramolecular materials rely on dynamic noncovalent interactions to maintain their functionality. This feature not only endows them with self-healing properties but also enables stimuli-responsive switching of antibacterial activity under external triggers.

In recent years, researchers have further combined metal ions with supramolecular assemblies to construct hybrid systems possessing long-lasting antibacterial performance.[165,166] For example, silver ion-cucurbituril complexes can release Ag^+ gradually from the material surface while maintaining a stable distribution through host-guest interactions,[167] thereby exhibiting sustained and efficient antibacterial activity. These advances highlight the potential of supramolecular design principles in developing adaptive, durable, and intelligent antibacterial materials that go beyond the limitations of traditional chemical disinfectants.

In summary, supramolecular chemistry exhibits tremendous potential in biological and antimicrobial applications. Its uniqueness lies in the ability to interact with the environment through noncovalent forces, thereby enabling molecular-level intervention in biological processes. Research on ion recognition and transport not only provides valuable models for understanding fundamental biological phenomena but also lays the foundation for the development of artificial regulatory strategies. In the antimicrobial field, supramolecular systems offer novel approaches to combat drug resistance by disrupting membrane integrity and ion homeostasis.

1.5 The Application of Squaramide in Supramolecular Chemistry

Recently, squaramide has attracted widespread research interest. Some examples have been mentioned in the previous sections. By uniting strong ion-recognition capability, structural rigidity, membrane compatibility, and chemical programmability, the squaramide framework is not merely a stronger hydrogen-bond donor, but a pivotal scaffold that integrates efficient molecular recognition with transmembrane functionality. The two NH donors of squaramide adopt a convergent orientation under the constraint of the cyclobutene-1,2-dione core and are conjugated with the adjacent carbonyls, thereby markedly increasing their Brønsted acidity relative to urea and thiourea.[168] Also, squaramides have been shown to display higher ion-binding affinity than their urea and thiourea analogues.[45,169,170] Markedly, even in competing media, squaramides are able to engage in strong interactions with Cl^-, HCO_3^-, and $H_2PO_4^-$.[171–173] In addition, the planar rigidity and intrinsic preorganization of the scaffold confer lower conformational freedom on the core, reducing the conformational penalty upon binding. Meanwhile, the readily tunable side-chain substituents permit systematic structural editing,[174] enabling the application of squaramides as fluorescent dyes, pH-responsive systems, ion transporters, and polymer-encapsulation components et.al.[175–177]

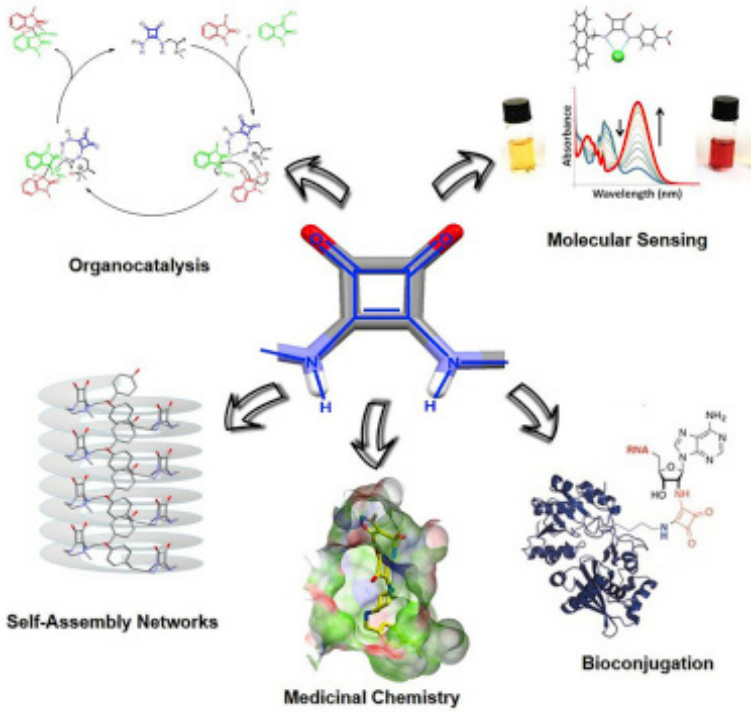

Figure 1.5.1. The application of squaramide in various fields.[30]

Costa et al. reported receptors bearing secondary squaramide binding units that form 1:1 complexes with acetate and other carboxylates in competitive DMSO/water mixtures.[178] This study is widely regarded as the first systematic introduction of squaramides into the field of anion recognition. Subsequently, Busschaert et al. demonstrated that squaramides are able to act as ion carriers in liposomes for Cl^-/HCO_3^- transport (Figure 1.5.2), and display more efficient transport behaviour than the corresponding urea and thiourea derivatives. This is the first example of squaramides as artificial anion transporters.[179] Since then, squaramides have found use across diverse areas. For instance, as noted above, naphthalimide-squaramide conjugates function as fluorescent probes capable of imaging chloride and mediating chloride transport.[180]

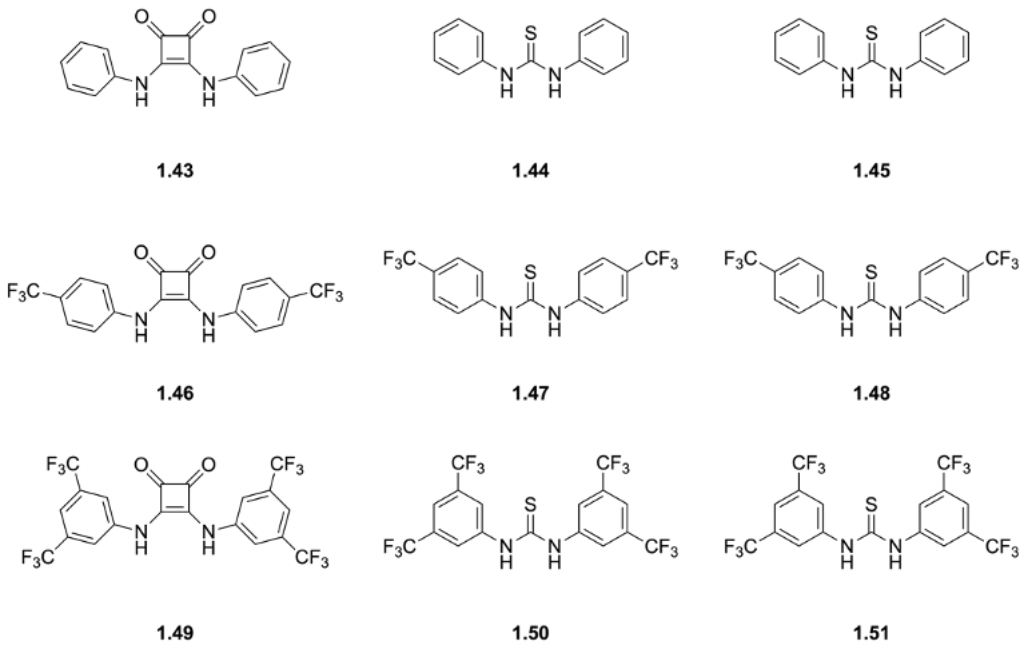

Figure 1.5.2. Structures of squaramide and their (thio)urea derivatives. Graphic abstract of the squaramide acting as anion transporter.[179]

In summary, owing to its various advantages, the squaramide scaffold has distinguished itself across multiple areas of supramolecular chemistry. In the sections that follow, we build on this motif to conduct a series of more in-depth investigations.

1.6 Project Aim

From a supramolecular chemistry perspective, the development of artificial anion transport faces a greater challenge. As discussed in the section on cation recognition, cations generally bind through coordination with lone-pair donors. Anions, however, possess much higher hydration energies, making the dehydration process and subsequent migration into the hydrophobic membrane thermodynamically unfavorable. Consequently, the design of efficient artificial both anion and cation transporters demands molecular precision and functional adaptability to operate effectively within the membrane environment. More importantly, ion transport represents not merely an extension of recognition but the functional realization of receptor chemistry. This process transforms “static molecular recognition” into “dynamic transmembrane function,” marking a crucial step in the evolution of supramolecular chemistry from molecular recognition to functional systems and molecular devices.

Although substantial progress in receptor development has been achieved in recent years, further exploration is still required on the application side of supramolecular chemistry.

Therefore, one of goals of our research has been to develop new classes of efficient receptors and ionophores for both anions and cations, broaden the repertoire of ion-transport scaffolds through synthetic chemistry. In parallel, we will develop new supramolecular frameworks to meet the demands of synthetic receptors in ion imaging and antibacterial applications.

Chapter 2 seeks to address the current gap in cation recognition using thiosquaramides and to evaluate their potential application in ion transport and antibacterial contexts. Building on this, **Chapter 3** will combine thiosquaramides with suitable fluorophores to develop fluorescent probes that integrate ion transport with recognition, to potentially enable cellular imaging. In **Chapter 4**, we will continue to employ squaramide and thiosquaramide scaffolds to design and synthesise complex ion carriers via structural preorganization, to enhance selectivity for single ions and transport efficiency. Meanwhile, elucidate how structural variations modulate transport performance.

Chapter 2: Zinc Dependent Anti-Microbial Activity with Ionophoric Thiosquaramides

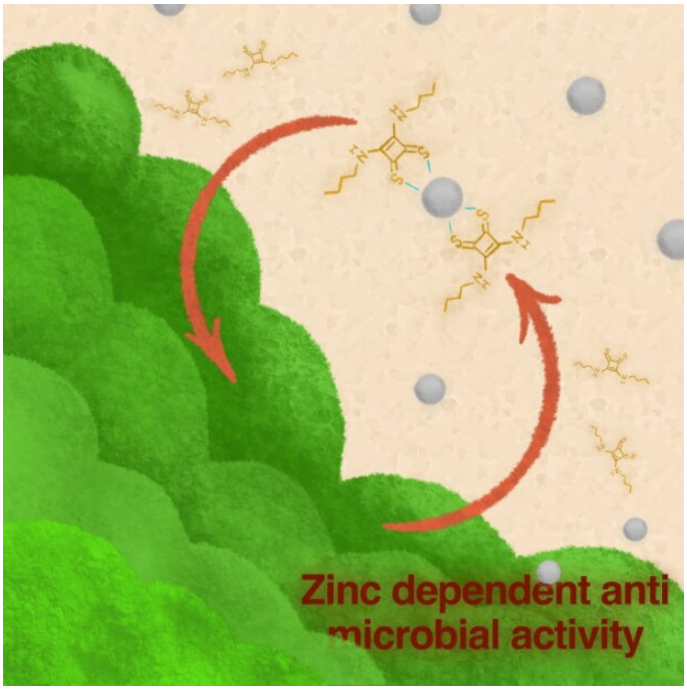

2.1 Introduction

Publication Statement: The work described in this chapter has been published as:

X. Luo, L. E. Brennan, C. S. Hawes, T. Krämer, J. Farragher, S. Robinson, K. Kavanagh and R. B. P. Elmes. Thiosquaramides: dual-function ionophores for Zn^{2+} and Cl^- with ion dependent anti-microbial activity. *Org. Biomol. Chem.*, 2025, **23**, 9142–9151.

As discussed in Chapter 1, Research interest in squaramide has surged in recent years because it has several favourable properties and has applicability in various fields of chemical and biological sciences.[181–183] The application of squaramide, along with their thiosquaramide derivatives, has been explored in, for example, organocatalysis, bioconjugation and sensors.[184–187] To a great degree, The exploitation of squaramide and thiosquarmaide has been developed in the field of anion recognition, sensing and transport.[187,188] The ability of squaramide derivatives to act as anionophores has been exploited for potential anti-cancer and anti-microbial therapeutics.[189,190]

In the meantime, with the favourable H-bond accepting ability, the application of squaramides to act as cation receptors and sensors has aroused attention in several fields. For example, McGouran and co-workers developed a series of nucleoside derivatives based on squaramide and thiosquaramide, which are capable of inhibiting SNM1A (zinc-dependent nuclease involved in the removal of interstrand crosslink lesions from DNA).[191] This kind of compounds were proved to act as SNM1A inhibitors by binding to the active site zinc ions, where thiosquaramide-based compounds displayed higher affinity than oxosquaramide-based compounds.

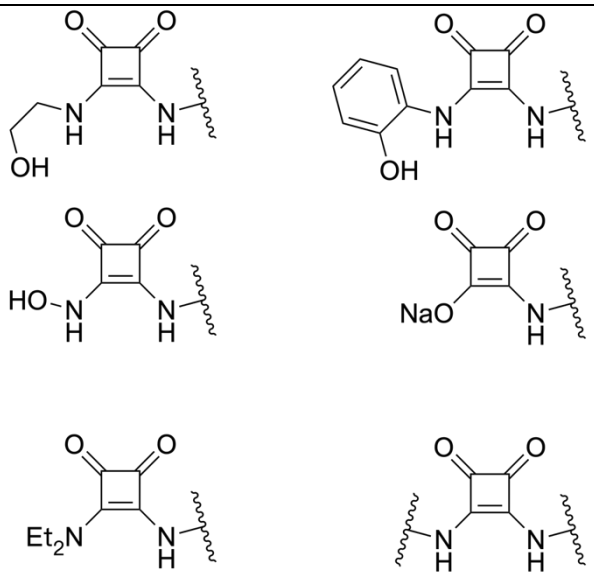

Figure 2.1.1. Structures of designed molecules reported by McGouran.[191]

Recently, Beer and co-workers displayed their work on the synthesis of squaramide-based heteroditopic [2]rotaxanes promoted by the chelation of Lewis basic squaramide carbonyls to sodium cation.[192] The functionalized axle-squaramide motif displayed significant role in ion pair recognition where sodium cation binding through the coordination between two C=O and sodium cation and anion binding through NH H-bond donors replenished by rotaxane motif (Figure 2.1.2). This also demonstrates the squaramide's ability to bind cations.

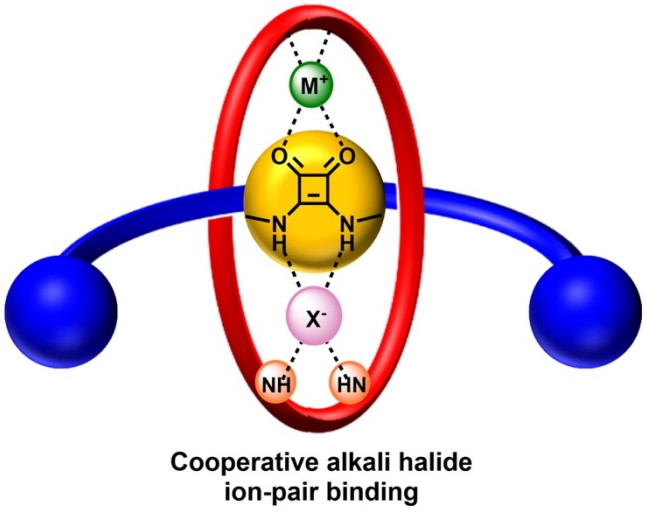

Figure 2.1.2. Ion-pair recognition of axle-squaramide containing [2]rotaxane host system. Reproduced from ref. 194, licensed under CC BY 4.0.[192]

However, so far, no comprehensive spectroscopic research has been conducted to confirm the metal-binding abilities of squaramide derivatives. One of our interests in this field is the synthesis of squaramide-based receptors that display effective ionophoric activities, with potential application in medicinal chemistry. Recently, we have shown that these receptors display potent antimicrobial activity against gram-positive bacteria, including *Staphylococcus aureus* and Methicillin-Resistant Staphylococcus aureus (MRSA), which is due to their ability to disrupt chloride homeostasis efficiently.[158] In the meantime, we also started investigating the potential of oxosquaramide and thiosquaramide to act as ion transporter, especially cation transporter, with the possibility that this activity might also lead to antimicrobial activity. Valkenier and colleagues introduced the first synthetic transmembrane transporters for Cu^+, suggesting the application of Cu^+ ionophores in biomedical therapeutics.[193] Numerous renowned and clinically approved antibiotics, for example valinomycin and monensin, exert their antimicrobial effects by acting as ionophores for Na^+ and K^+ ions.[194,195] Zn^{2+} ionophore is emerging as a promising modality for novel antimicrobial agents through disrupting Zn^{2+} homeostasis to interfere with the process of microbial growth.[196] PBT2 is a zinc ionophore that is safe for human use and has advanced to clinical trials. It functions as a Zn^{2+}/H^+ ionophore, facilitating the exchange of extracellular zinc for intracellular protons in an electroneutral process, resulting in the accumulation of zinc within cells.[197] This zinc accumulation occurs alongside manganese depletion and the production of reactive oxygen species (ROS), which is proposed to ultimately lead to cell death. Combined with zinc, PBT2 exhibits antibacterial activity and disrupts cellular homeostasis in erythromycin-resistant Group A Streptococcus (GAS), methicillin-resistant Staphylococcus aureus (MRSA), and vancomycin-resistant Enterococcus (VRE).[198]

This novel supramolecular strategy for developing antimicrobial agents is a burgeoning area. However, there is a significant need for greater structural diversity among ionophore families to create new antimicrobial medications that operate via unique mechanisms. This is particularly crucial in addressing the current antimicrobial resistance crisis. With these examples in mind, we predicted that squaramide, especially their thiosquaramide derivatives, is capable of binding to metal ions with a high affinity. Meanwhile, we anticipated that squaramides could act as ionophores and display antimicrobial behaviour in the biological field.

2.2 Chapter Objectives

The aims of this Chapter is to synthesise a series of oxosquaramide and their thiosquaramide derivatives. Much of the research in this regard has focused on anion recognition, however, there are no detailed reports to indicate oxosquaramide and thiosquaramide to act as a cation recognition scaffold (Figure 2.2.1). We expected to investigate the effect on the cation binding and anionophoric activity of (thio)squaramide.

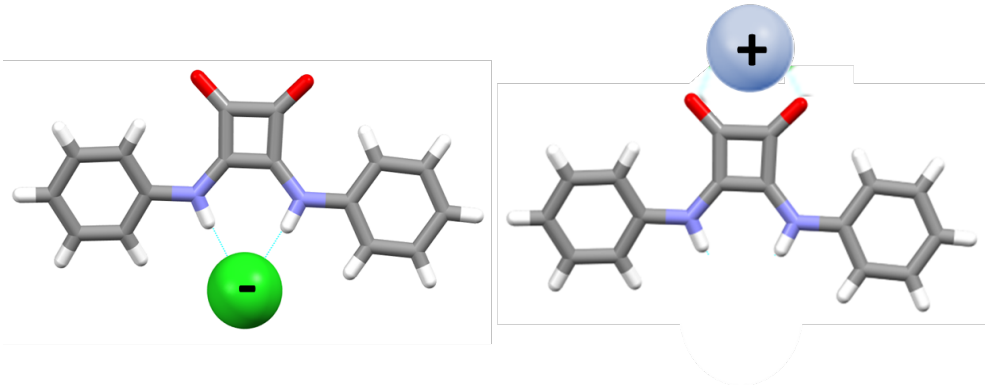

Figure 2.2.1. Schematic representation of squaramide anion recognition and cation recognition.

These targeted molecules were varied by the introduction of different alkyl and phenyl motifs (Figure 2.2.2). Such motifs reported to enhance the ion transport activities of receptors would be included in the structures (*e.g.* -CF_3). Compared to oxosquaramide, thiosquaramide derivates have enhanced acidity and higher lipophilicity. With the efficient anion binding ability and potential cation binding ability,[129,191] thiosquaramide is supposed to display co-transport behaviour between anion and cation. Meanwhile, the introduction of C=S made thiosquaramide a better electron acceptor.[129,199] With this in mind, we envisaged that thiosquaramide would display strong ion transport activity and potential antimicrobial effect. Given that studies on most of these molecules in anion recognition and transport have already been reported,[129] this chapter focuses on evaluating their cation-transport capabilities and their potential co-transport performance.

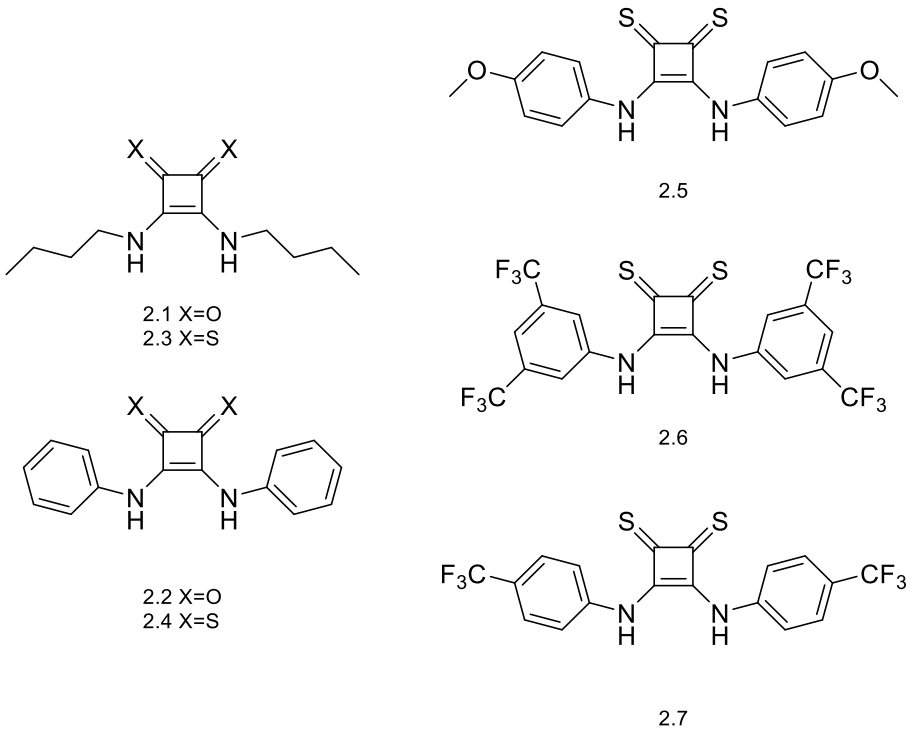

Figure 2.2.2. The chemical structures of the targeted receptors in this work.

2.3 Synthesis of Target Compounds

Oxosquaramides in this study were synthesised by following the method developed by Taylor and co-workers.[200] First steps to form the oxosquaramide using diethyl suqarate and primary amines in the presence of zinc triflate give oxosquaramides **2.1** and **2.2** in 78% and 69% yields, respectively (Scheme 2.3.1). The synthesis of formation is confirmed by ^{1}H NMR and ^{13}C NMR. These values agree well with the previously reported data.

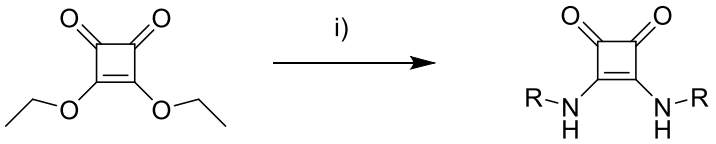

Scheme 2.3.1. Synthetic method for the formation of oxosquarmaide.[200] *Reagnets and conditions*: (i) $Zn(OTf)_2$, NH_2-R, EtOH, 70 °C, overnight.

The formation of thiosquaramide derivatives followed the synthetic protocols developed by Rombola and co-worders.[201] Firstly, we try to generate thiosquaramides by using P_4S_{10} • pyridine to thionate oxosquaramide.[202] However, this method lead to a low yield and the reaction seems to be poorly reproducible, which may be attributable to environmental sensitivity such as moisture. Rawal's method provides an easier method for the synthesis and formation of purer thiosquaramide receptors. The synthesis process began with the synthesis of dicyclopentyl squarate **A1** in 73% yield as a white solid. Then Lawesson's reagent was used to thionate the dicyclopentyl squarate to form the significant intermediate dicyclopentyl thiosquarate **A2** as an orange solid in 71% yield. Thiosquaramides **2.3** - **2.7** was obtained via the reaction between dicyclopentyl thiosquarate **A2** and appropriate primary amine in DCM with acceptable yields from 30% to 70% (Scheme 2.3.2). Notably, in the synthesis of thiosquaramide, we employed an intermediate containing cyclopentyl side chain, rather than the intermediate analogous containing ethoxy side chain that used in the preparation of oxosquaramide. Previous studies have shown that,[201] cyclopentyl-side-chain intermediates exhibit relatively superior operational characteristics and higher reactivity, which is beneficial for the subsequent transformations.

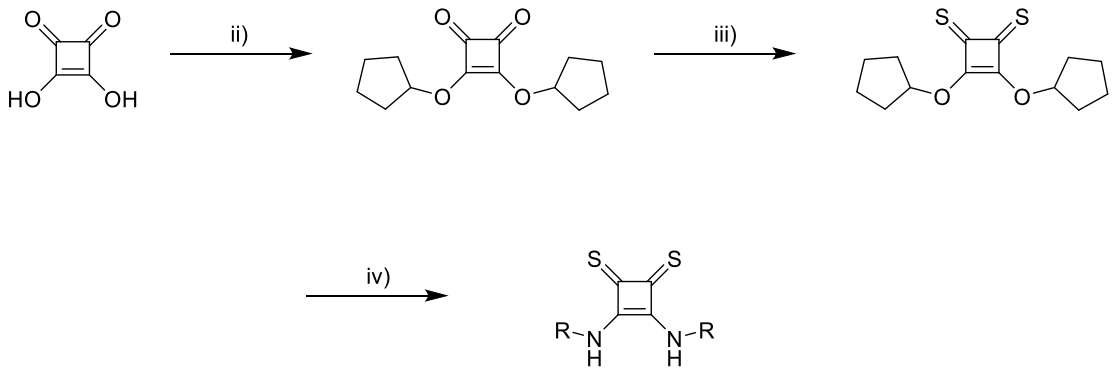

Scheme 2.3.2. The synthesis of thiosquaramides. *Reagnets and conditions*: (ii) cyclopentanol, 120 °C, 12 hr, 73%; (iii) lawesson's reagent, anhydrous DCM, 38 hr, 71%; (iv) substituted amine (NH_2-R), anhydrous DCM, 12 hr, 30 - 70%.

The synthesis of target molecule **2.3**-**2.7** was confirmed by ^{1}H NMR, ^{13}C NMR and High-Resolution Mass Spectrometry (HRMS). The purity was confirmed by LCMS.

As shown in Figure 2.3.2, the respective NH signals of thiosquaramides **2.4** were clearly observed at 10.83 ppm as a broad singlet in ^{1}H NMR spectra, while the signals of phenyl appear from 7.05 to 7.5 ppm. Also, one high peak shown in LCMS spectra along with MS spectra give the mass of 297.2 (Figure 2.3.2). This further supports our successful synthesis.

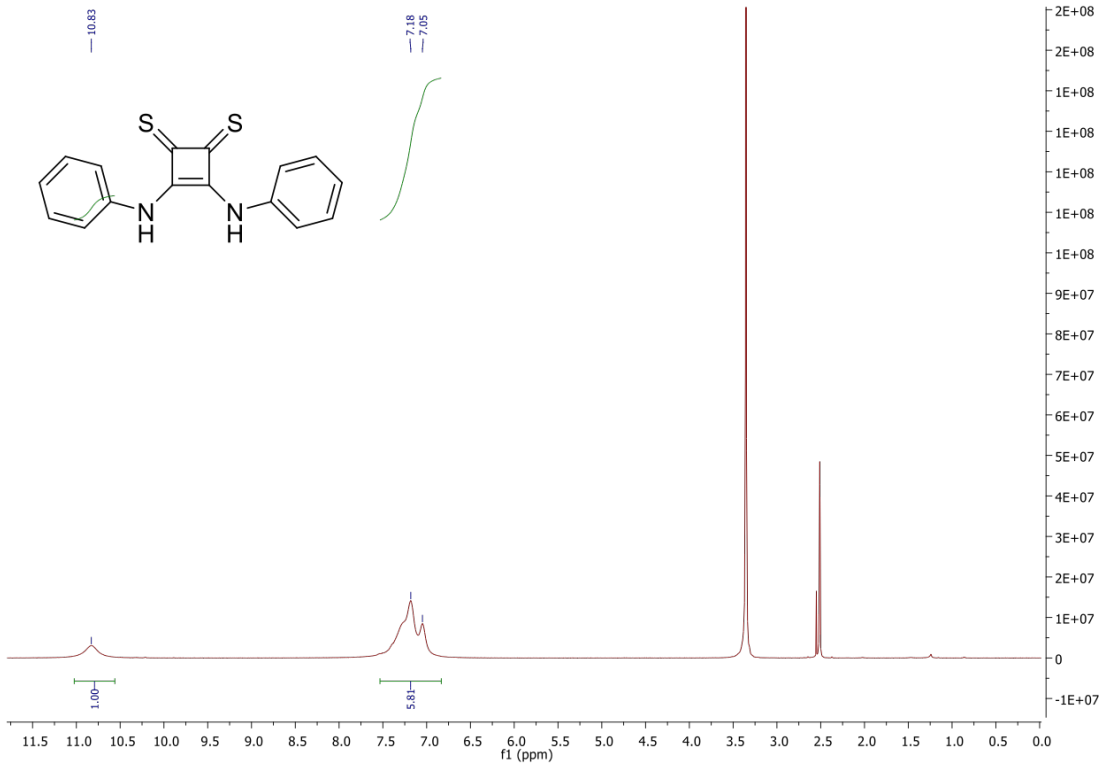

Figure 2.3.1. ^{1}H NMR spectra of **2.4**.

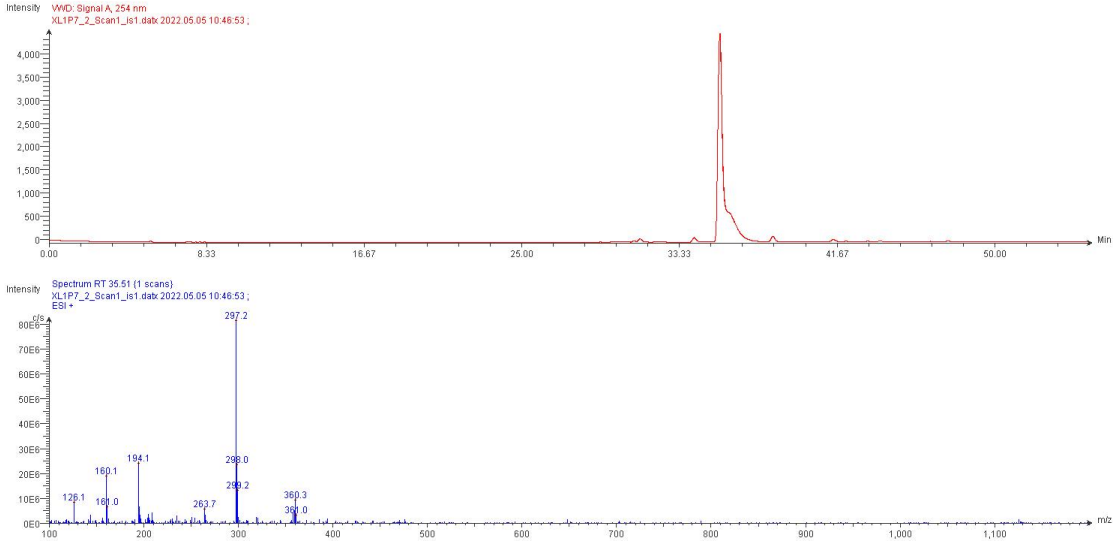

Figure 2.3.2. LCMS spectra of **2.4**.

The comparison between oxosquaramides and thiosquaramide analogues revealed significant differences in the NH signals when measured in DMSO-d_6. For example, oxosquaramide **2.2** gave the chemical shift values for the NH signal at 9.90 ppm, while the NH signal of its thio-derivative **2.4** underwent a significant downfield shift to 10.83 ppm. Furthermore, significant variation was also observed in the ^{13}C NMR spectra. For compound **2.2**, the carbonyl carbon and the cyclobutene carbon exhibited chemical shift values of 182 ppm and 166 ppm, respectively, while compound **2.4** displayed chemical shift values of 208 ppm and 169 ppm for the thiocarbonyl carbon and cyclobutene carbon, respectively (Figure 2.3.3).

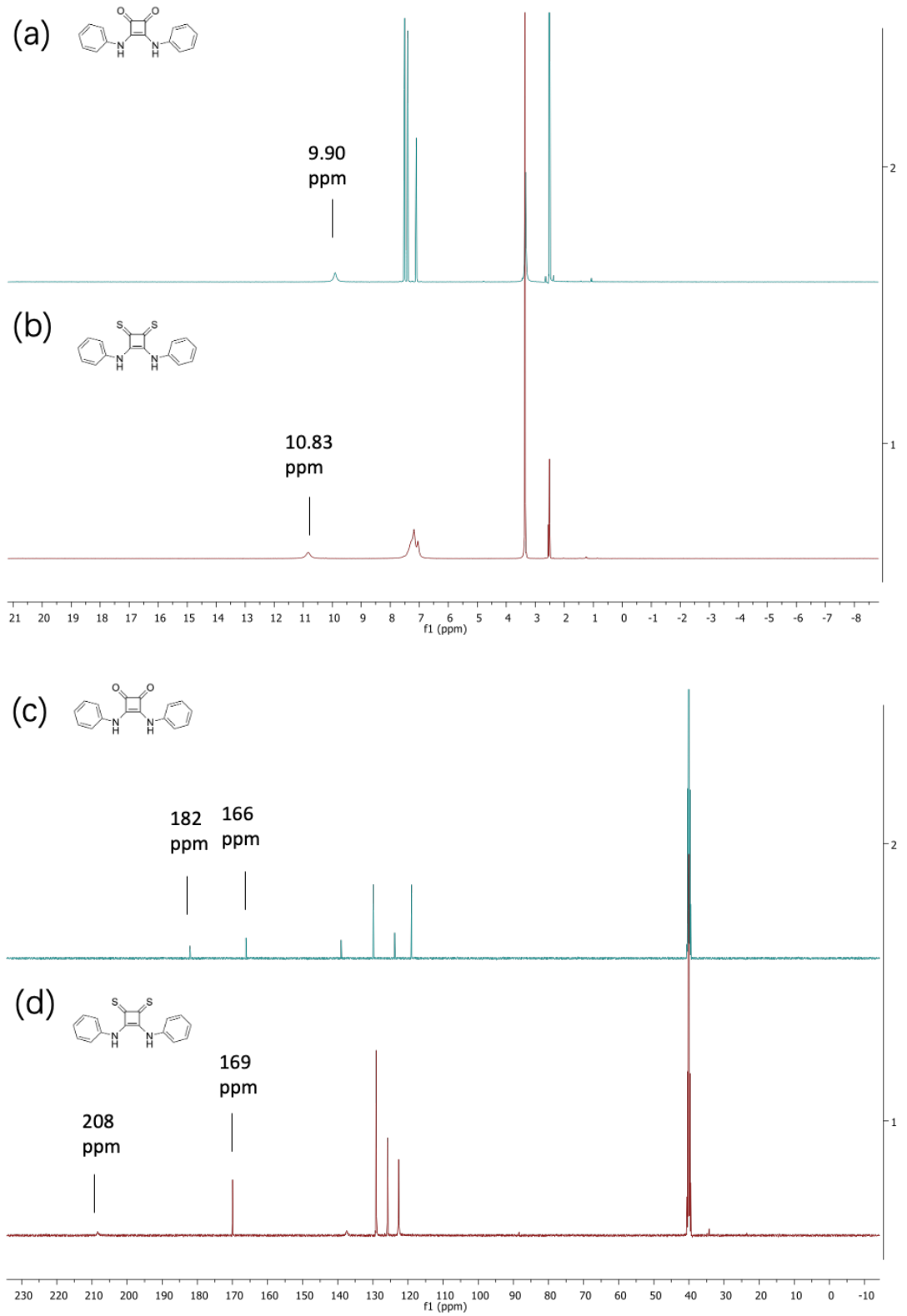

Figure 2.3.3. Comparison of ^{1}H NMR of receptor (a) **2.2** and (b) **2.4**. Comparison of ^{13}C NMR of receptor (c) **2.2** and (d) **2.4**.

2.4 X-Ray Crystallography

Thiosquaramide **2.3** was crystallized from hot MeCN, and its structure was confirmed by single crystal X-ray diffraction analysis (by Dr Chris S. Hawes, Keele University). The analysis revealed that Compound **2.3** forms a one-dimensional hydrogen-bonded chain in the solid state, as illustrated in Figure 2.4.1. This chain consists of $R_2^2(10)$ rings formed between N-H donors and sulfur acceptors, with D···A distances measuring 3.4188(6) Å. Despite the directional nature of these interactions, the peripheral butyl chains do not contribute significant inter-chain interactions. Consequently, there is no transfer of directionality from one chain to the next, resulting in an overall disordered structure with chains extending in both positive and negative b directions.

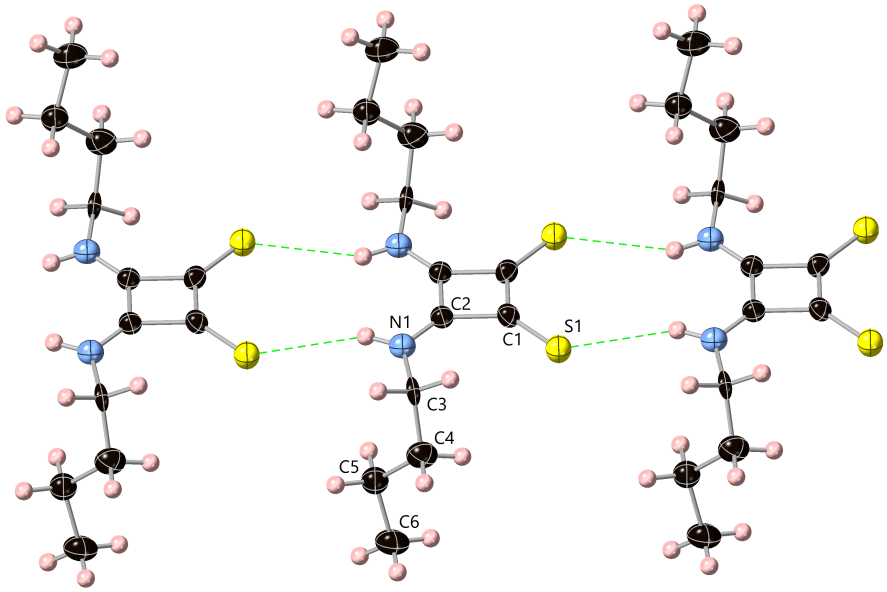

Figure 2.4.1. Structure of compound **2.3**, highlighting the unique heteroatoms while omitting disorder for clarity.

Remarkably, after a sample of compound **2.3** was immersed in water for several weeks, a small amount of a second crystalline phase was detected. The structural model, refined within the trigonal space group R-3, included compound **2.3**, along with butylammonium cations and sulfate anions. The butylammonium cations likely resulted from the gradual hydrolysis and oxidation of **2.3**. The butylammonium cations

are consistent with partial hydrolysis of **2.3** during the soaking period. Given the presence of sulfur in thiosquaramide **2.3**, sulfate may arise from slow oxidative degradation of the sulfur-containing motif. Related thiourea systems are known to form urea and sulfate under oxidative conditions.[203] However, as no sulfate source was intentionally introduced, the origin of sulfate cannot be unambiguously established and sulfate contamination from the soaking medium cannot be excluded. Therefore, we report this result cautiously and avoid proposing a definitive formation pathway in the absence of further evidence. Future experiments such as ion chromatography of the soaking medium and control experiments using freshly prepared sulfate-free water under oxygen-free conditions would help to identify the source of butylammonium and sulfate.

As illustrated in Figure 2.4.2, the overall structure is depicted as a linear arrangement of three sulfate anions, flanked on both ends by three molecules of **2.3**, and surrounded by an equatorial belt of six butylammonium cations.

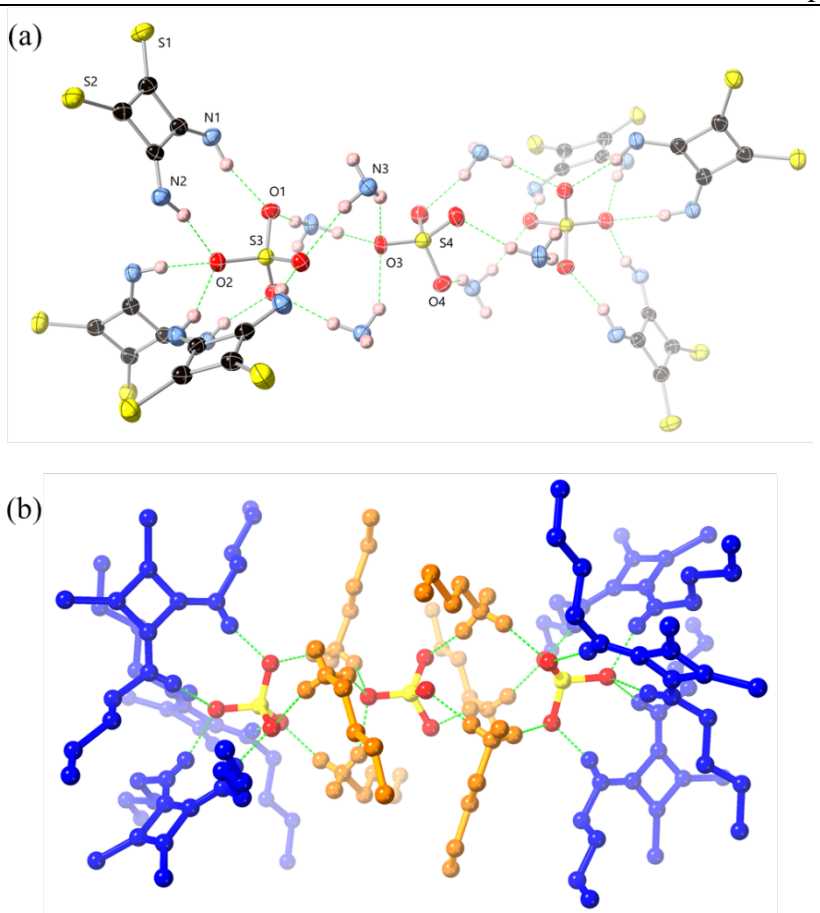

Figure 2.4.2. (a) The core hydrogen-bonded structure of the butylammonium sulfate adduct $(BuNH_3)_6$(**2.3**)$_6(SO_4)_3$, shows unique heteroatoms and excludes all butyl chains for clarity. The atomic displacement parameters (ADPs) are displayed at the 50% probability level. (b) Complete structure of $(BuNH_3)_6$(**2.3**)$_6(SO_4)_3$, with thiosquaramide molecules shown in blue and butylammonium species in orange. Selected hydrogen atoms and disorder in the central sulfate are excluded for clarity.

The hydrogen bonds from the butylammonium cations support the central sulfate and the inner faces of the terminal sulfates, while the thiosquaramides form a three-fold propeller through chelating $R_2^2(9)$ hydrogen bonding interactions with the terminal sulfate groups. This structure resembles the motif seen in tripodal urea-based anion receptors, for example, the sulfate receptor reported by Das.[204] However, the shorter N···O distances in compound **2.3** (2.765(3) and 2.864(3) Å, compared to 2.87–2.90 Å in the urea case) may suggest a higher N-H acidity for the thiosquaramide.

2.5 Photophysical Evaluation

After successfully synthesizing and characterizing squaramides and thiosquaramides, we aimed to carry out a preliminary analysis of the UV/Vis absorption properties of receptors **2.1**-**2.7**. We expected to observe significant differences in their properties and believed this information could be valuable in determining ion binding behavior. In MeCN, we observed an absorption band at 291 nm for **2.1**, while for its thiosquaramide derivative **2.3**, An absorption of two bands with λ_{max} of 274 nm and 388 nm was observed respectively (Figure. 2.5.1 (a)).

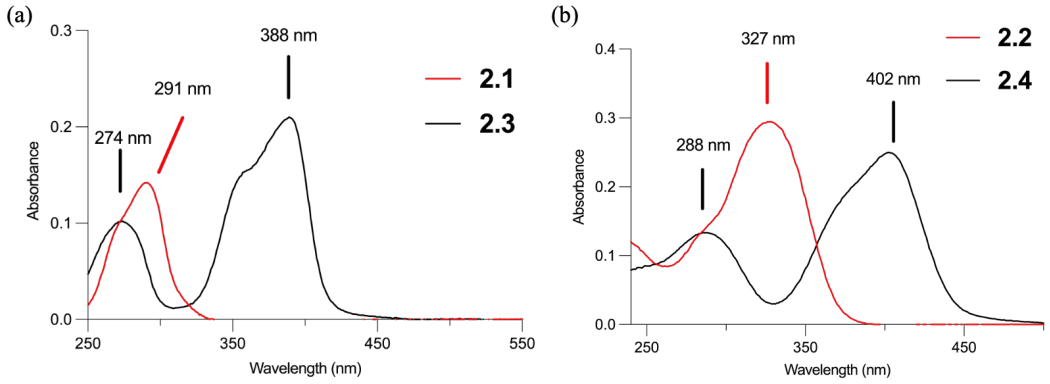

Figure 2.5.1. Uv/Vis spectrum of (a) compounds **2.1**(red) and **2.3**(black) in MeCN (b) compounds **2.2**(red) and **2.4**(black) in MeCN.

Similarly, receptor **2.2** displayed a maximum absorption of 327 nm, while **2.4** exhibited λ_{max} at 288 nm and 402 nm. A notable distinction between the oxo- and thio-derivatives was observed in MeCN, indicating a significant red shift in absorption when the sulfur atoms were included (Figure 2.5.1 (b)). This behaviour is corresponding to the DFT calculation results. This suggests that, compared to C=O, the inclusion of sulfur atoms results in a lower energy level for electronic transitions, which leads to a considerable red shift in λ_{max}.[205] Also, this trend was consistent across all analogues. Additionally, solutions of oxo-squaramides **2.1** and **2.2** appeared colourless, whereas solutions of all thio-derivatives appeared yellow or orange.

In order to further understand the differences between oxosquaramides and thiosquaramides, Time-dependent density functional theory (TD-DFT) calculations

were conducted by Dr Tobias Krämer on models of receptors **2.1**-**2.4**. M06-2x/def2-QZVP was used to simulate the UV absorption characteristics of these models in the 200-500 nm spectral region, in combination with an implicit solvation model to account for the effect of acetonitrile,[206,207] following geometry optimization at the RI-MP2/def2-TZVP level of theory.[208–210] The calculated absorption spectra (Figure 2.5.2) are consistent with the spectral features of the experimental data and accurately reproduce the red shift of the absorption bands for the thio congeners.

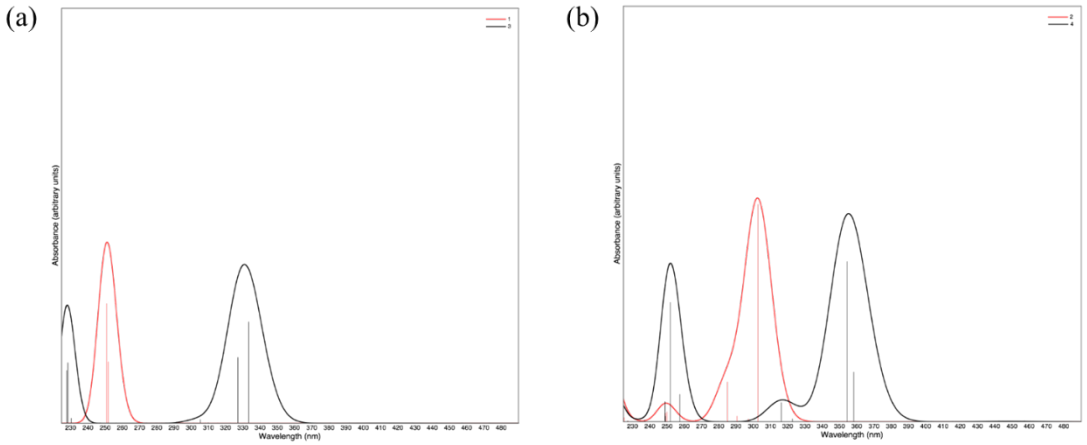

Figure 2.5.2. TD-DFT calculated absorption spectra for receptors (a) **2.1** (red) and **2.3** (black) (b) **2.2** (red) and **2.4** (black)[SMD-CPCM(AcCN)/M06-2X/def2-QZVP].

2.6 Cl^- Binding Studies

Given the observed absorption of these oxo- and thio- squaramides, we anticipated that complexation with either anionic or cationic species might alter their ground state properties. Due to their known affinity for anion binding, we aimed to conduct anion binding titrations to compare the binding activities of the oxo- and thio- analogues in MeCN. Previously, Fabbrizzi and colleagues investigated the binding behavior of a nitro-squaramide analogue using UV/Vis spectrophotometric titration experiments. They demonstrated that the interaction between Cl^- and the NH signals of squaramide leads to a red shift in the absorption spectrum because of the stabilization of one or more excited states.[169]

In our study, we anticipated our compounds might display similar behaviour. Initially, we conducted a comparison of the binding of Cl^- with receptors **2.1**-**2.4** (10 μM). The experiments involved titration in MeCN solution with tetrabutylammonium chloride (TBACl)(Up to 100 equivalents), and all four compounds exhibited a red shift of absorption in their UV/Vis spectrum. As an example, the titration of receptor **2.2** with Cl^- showing a red shift in λ_{max} from 327 nm to 345 nm while the titration of receptor **2.4** with Cl^- showing a red shift in λ_{max} from 399 nm to 415 nm (Figure 2.6.1).

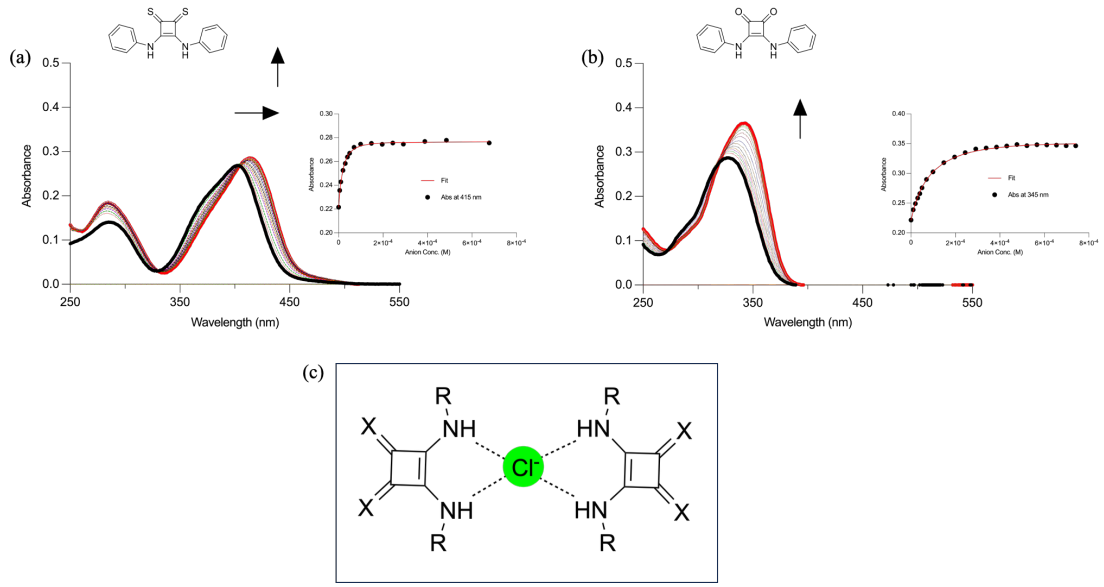

Figure 2.6.1 (a) The UV-vis titration study of **2.4** with Cl^- in MeCN. {insert} Analysis by using Bindfit for absorbance at 415 nm where a 2:1 binding model gave the best fit to the data. (b) The UV-vis titration study of **2.2** with Cl^- in MeCN. {insert} Analysis by using Bindfit for absorbance at 345 nm where a 2:1 binding model gave the best fit to the data.(c) Illustration of 2:1 binding model (ligand-guest-ligand) in MeCN.

The observed changes suggest that Cl^- binding occurred at the squaramide. These changes were then analysed by using the BindFit software v0.5 program, which indicated a 2:1 stoichiometry for all cases.[211,212] BindFit is an open-access online software used to determine binding constants from UV-vis, fluorescence and NMR titration data by fitting the recorded data to common 1:1, 1:2 and 2:1 host-guest binding model. For each dataset, multiple binding models were evaluated and the most appropriate model was selected based on the quality of fit (residuals) and the error

returned by the fitting routine. In our study, the data were best described by a 2:1 binding model: Two receptor molecules encapsulate one single chloride ion to form a sandwich-type host-guest complex (Figure 2.6.1(c)).

Unfortunately, the data for receptor **2.3** could not be fitted due to large errors, likely resulting from self-assembly formation in solution, supported by the crystal structure analysis (Figure 2.4.1). In addition, although we got the crystal structure of **2.3** chain in solid phase, we conducted the concentration study to further confirm the aggregation behaviour of **2.3** in solution. As shown in Figure 2.6.2, at 0.2 mM, two NH peaks were observed around 7 ppm. As the receptor concentration increased, these minor peaks gradually approached one another and ultimately coalesced into one single peak, supporting our hypothesis that **2.3** aggregates in solution.

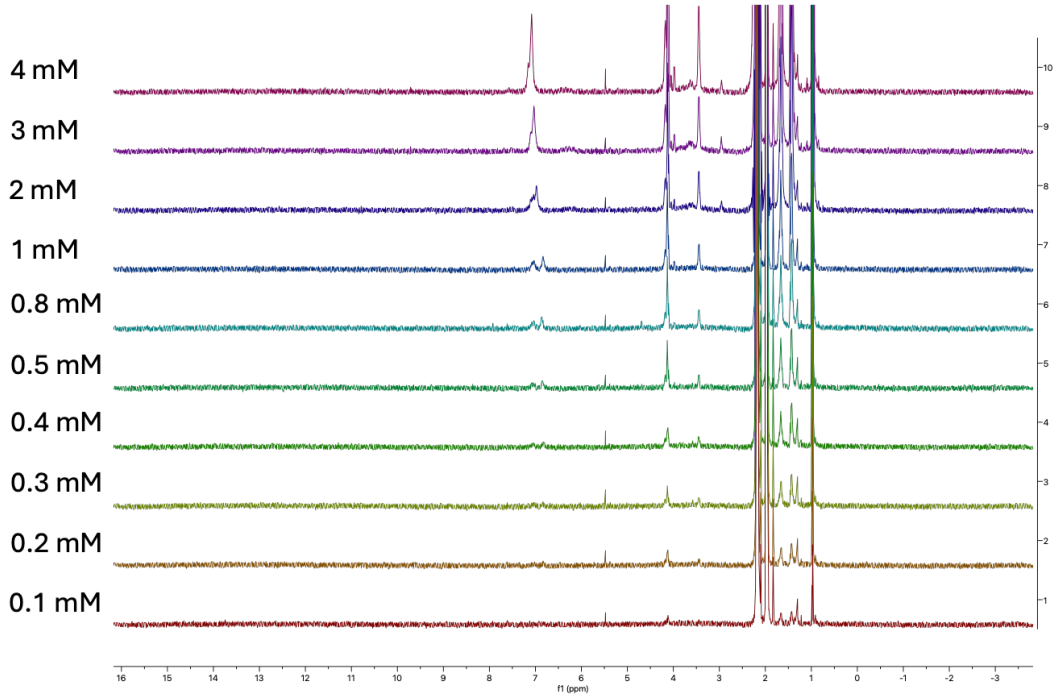

Figure 2.6.2. ^{1}H NMR stackplot of **2.3** in CD_3CN at various concentrations.

A summary of the binding data in Table 2.6.1 shows that receptor **2.4** exhibited the highest affinity for Cl^-, while receptor **2.1** had the lowest. Overall, thiosquaramide derivatives exhibit a higher affinity for Cl^- in MeCN than oxosquaramide derivatives.

Table 2.6.1. Summary of the Cl^- association constant $K_a(M^{-1})$ of receptor **2.1**-**2.7** in MeCN[a]

Receptor	K_{11} (M^{-1})	K_{21} (M^{-1})	Binding mode
2.1	2.5×10^2	0.9×10^2	2:1
2.2	2.6×10^3	5.8×10^4	2:1
2.3	-[b]	-[b]	2:1
2.4	2.1×10^4	5.3×10^4	2:1
2.5	-[b]	-[b]	2:1
2.6	2.1×10^4	4.5×10^5	2:1
2.7	2.3×10^4	6.8×10^4	2:1

a Data fited to a 2:1 binding model with error < 10%. b High errors lead to unreliable K_a value.

Interestingly, Busschaet and co-workers did the similar Cl^- ^1H NMR titration for thiosquaramides but they select 1:1 binding model for analysis. To further confirm the binding interaction between squaramide and Cl^-, we carried out ^1H NMR titration for receptors **2.1**-**2.4** in either CD_3CN or DMSO-d_6 at 298 K. Similar to UV-vis titration experiments, TBACl was selected as chloride source gradually introduced to the solution of receptors (0.4 mM). Interestingly, take **2.4** as an example, the gradually addition of chloride to the receptor solution (DMSO-d_6) leads to the change in chemical shift at 10.86 ppm and a 1:1 binding model gives the best fit, which corresponds to Busschaet's result (Figure 2.6.3). Therefore, we sought to test whether solvent effects modulate the binding mode between the thiosquaramide receptors and anions. Because **2.4** exhibits limited solubility in neat CD_3CN, we employed CD_3CN/ DMSO-d_6 (49:1) as solvent. Under these conditions, **2.4** and chloride preferentially assemble into a 2:1 complex. These are supported by Job's plot (Figure 2.6.4). These results indicate that the choice of solvent exerts a pronounced effect on the binding stoichiometry between the thiosquaramide receptors and chloride.

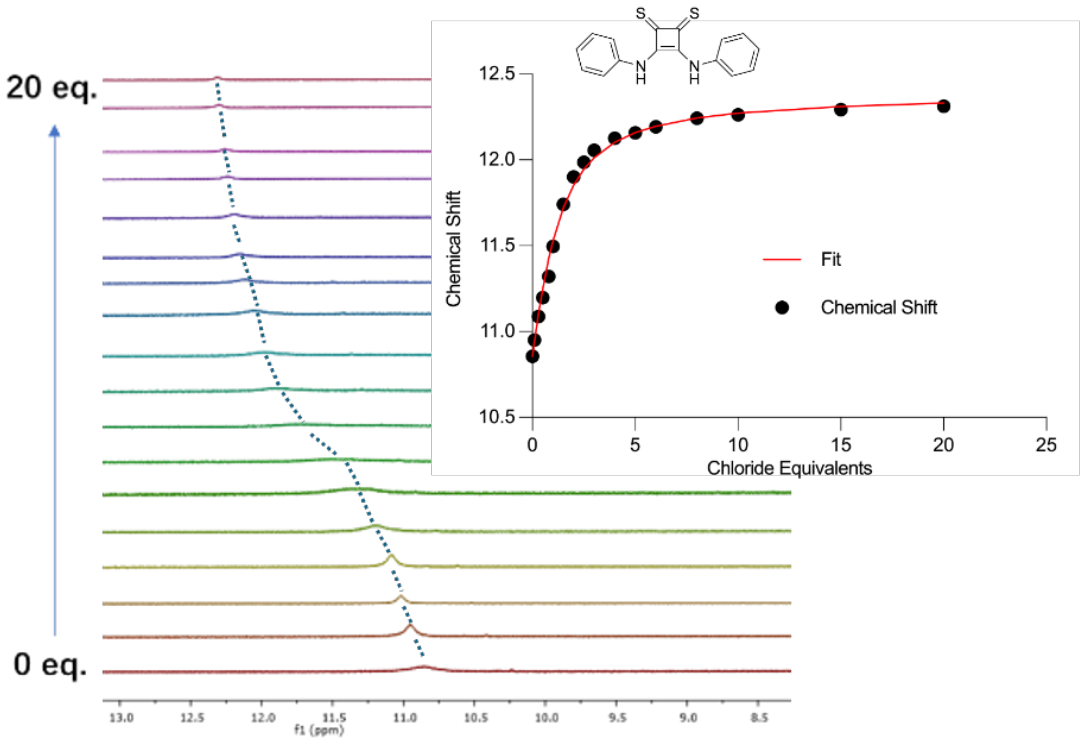

Figure 2.6.3. ^{1}H NMR chloride titration for **2.4** in DMSO-d_6. {Insert} Fitplot for NH proton at 10.86 ppm.

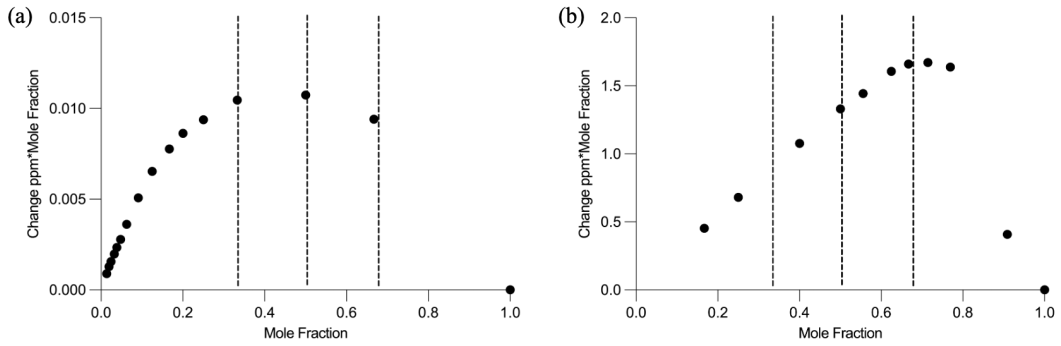

Figure 2.6.4. (a) ^{1}H NMR Job's Plot of **2.4** (0.4 mM) with TBACl in DMSO-d_6 evaluated by the chemical shift changes of the squaramide NH protons. (a) ^{1}H NMR Job's Plot of **2.4** (0.4 mM) with TBACl in CD_3CN/DMSO-d_6 (49:1) evaluated by the chemical shift changes of the squaramide NH protons.

2.7 Metal ions binding studies

As we know, squaramides are widely recognized in the scientific literature for their capacity to act as H-bond donor and acceptors. Consequently, they have been frequently reported as effective binders for anions.[211–214] However, their potential as receptors for binding cations has been relatively underexplored. There are only a few literature instances of this, and to the best of our knowledge, there have been no published research on metal binding with thiosquaramides.[191]

In an initial experiment, given the absence of research on this molecule functioning as a cation receptor, we performed a broad affinity survey against multiple metal ions, containing mono- (Ag^{+}, Li^{+}), di- (Fe^{2+},Co^{2+}, Na^{+}, Ba^{2+}, Cu^{2+}, Ca^{2+}, Ni^{2+}, Zn^{2+}, Cd^{2+}, Hg^{2+}, Pb^{2+}), and trivalent metal ions (Fe^{3+}), in order to establish an initial binding profile. Perchloride metal salts were selected for this test to avoid any interference caused by complexation of the counteranion. 1 equivalent of various metal ions were added to a solution of compound **2.4** (10 μM), and then the UV spectrum was recorded. The results showed that Ni^{2+} and Cu^{2+} lead to the medium change in the absorbance while the most significant changes occurred with the addition of Cd^{2+}, Pb^{2+}, Hg^{2+}, and Zn^{2+} (Figure 2.7.1). In addition, Fe^{2+} and Fe^{3+} exhibited intense absorption bands in the UV region which can overlap any binding-induced spectral changes. Therefore, UV-vis titration was not employed to evaluate their binding in this study. Subsequently, we extend the same experiments to **2.1**-**2.3** with Cd^{2+}, Pb^{2+}, Hg^{2+}, and Zn^{2+} which displayed relatively high affinity. Overall, significant changes in absorbance are observed for **2.3** and **2.4** upon the introduction of these metal ions. However, the addition of these metal ions to oxosquaramide derivatives **2.1** and **2.2** just lead to minimal changes. This indicate that the introduce of sulfur significantly enhances the metal ion affinities of receptors.

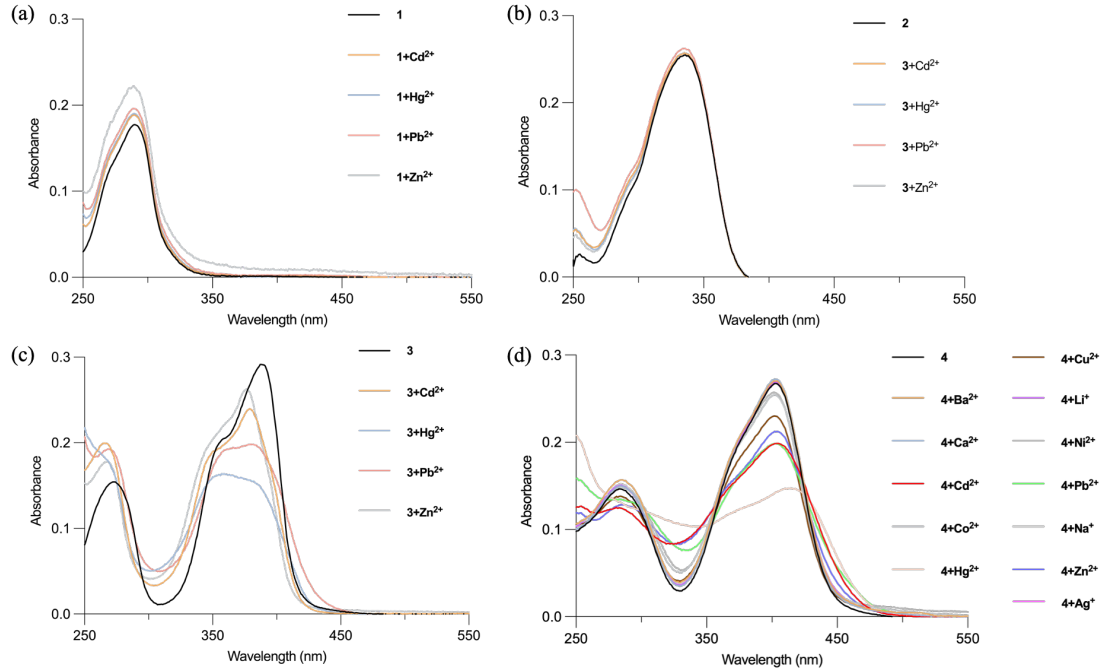

Figure 2.7.1. Metal screen of receptors in MeCN (10 μM) after the addition of 0.5 eq. metal ions (a) **2.1**, (b) **2.2**, (c) **2.3**, (d) **2.4**.

In the meantime, we observed that the addition of metal ions to a thiosquaramide as MeCN solution led to a colour change that is visible to the naked eye. Therefore, colorimetric measurements were conducted for receptor **2.3** - **2.7** (**2.3**, **2.5**, **2.6** and **2.7** were dissolved in MeCN while **2.4** was dissolved in DMSO because of its poor solubility in MeCN). As shown in Figure 2.7.2, after the addition of 1 eq. of metal ions Fe^{3+}, Hg^{2+}, Pb^{2+}, Cd^{2+}, Zn^{2+}, K^{+}, Li^{+}, Ca^{2+}, Na^{+}, Ni^{2+}, Cu^{2+} and Co^{2+} (from left to right) into the solution of thiosquaramide receptors (1 mM), the colour change from orange to yellow was observed as the result of the addition of Pb^{2+}, Cd^{2+} and Zn^{2+} in all cases (even colourless for **2.3**). The addition of a small number of Hg^{2+} led to the same result. However, upon the addition of excess Hg^{2+} (more than 0.5 eq.), the solution containing Hg^{2+} and receptors became cloudy, and a white precipitate formed. This distinct behaviour was observed between all 5 thiosquaramides and Hg^{2+} as well, which may be attributed to a biphasic interaction. The colour changes observed with Fe^{3+}, Ni^{2+}, Cu^{2+}, and Co^{2+} could be attributed to the inherent colour of the metal ion solutions.

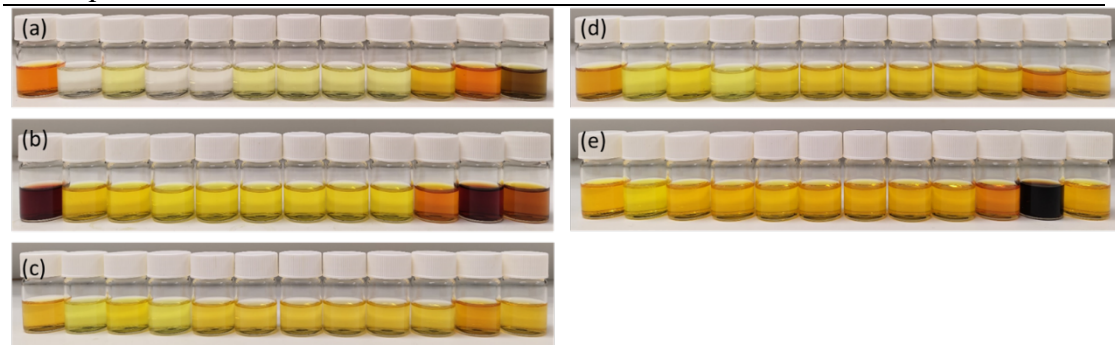

Figure 2.7.2. Colorimetric metal screen for thiosquaramide receptor (a)**2.3** (b)**2.4** (c)**2.5** (d)**2.6** (e)**2.7** in MeCN after the addition of 1 eq. of metal ions.

Therefore, we conducted more detailed titrations with these metals by using UV-vis spectroscopy by adding metal perchlorate salts (Cd^{2+}, Pb^{2+}, Hg^{2+}, Zn^{2+}) to a solution of the receptors in MeCN. Notably, we observed distinct differences in behaviour between oxo squaramides and their thio- analogues. As shown in Figure 2.7.3, receptor **2.2** exhibited minimal changes in the presence of Zn^{2+}, whereas its thiosquaramide analogue receptor **2.4** displayed significant changes in its UV spectrum, resulting in a reduction in absorbance at 404 nm and a simultaneous red-shift to 410 nm, along with a stark increase in absorbance at 330 nm and a decrease at 290 nm. These changes lead to the emergence of two isosbestic points at 305 nm and 354 nm.

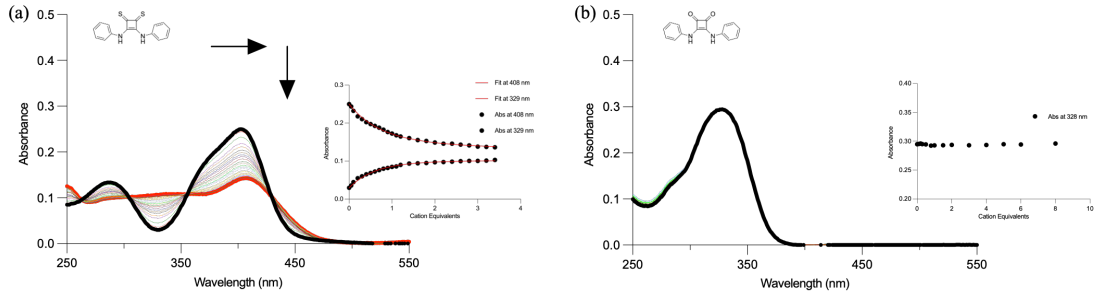

Figure 2.7.2. Uv-vis spectrum of (a) compound **2.4** after the addition of Zn^{2+} in MeCN. {insert} Fitplot for absorbance at 408 nm and 329 nm as a function of Zn^{2+} concentration (b) compound **2.2** after the addition of Zn^{2+} in MeCN. {insert} Fitplot for absorbance at 328 nm as a function of Zn^{2+} concentration.

These results indicate a strong binding of receptor **2.4** to the metal while **2.2** displays no obvious binding behaviour. Similar observations were observed for Cd^{2+} and Pb^{2+}, while Hg^{2+} exhibited complicative binding behaviour with a biphasic interaction, which prevent the fit. This result corresponds to the phenomena observed in colorimetric titration (Figure 2.7.3).

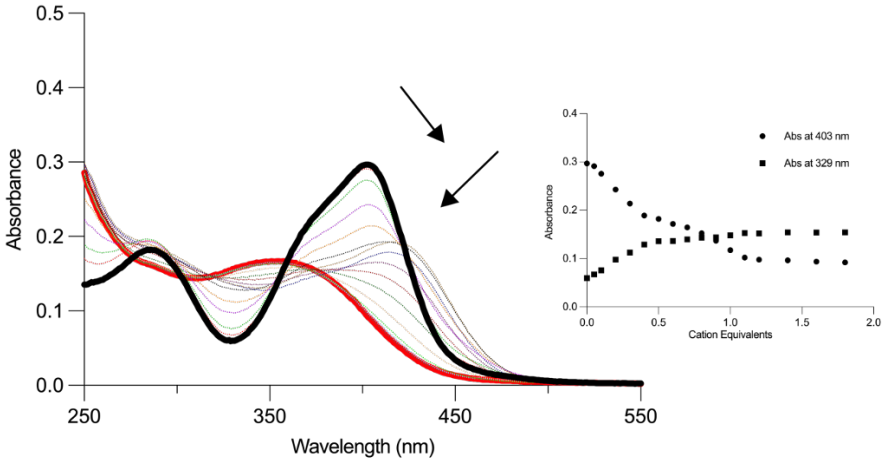

Figure 2.7.3. Uv-vis spectrum of compound **2.4** after the addition of Hg^{2+} in MeCN. {insert} Fitplot for absorbance at 388 nm and 307 nm as a function of Hg^{2+} concentration

To indicate the effect of substituents around the thiosquaramide on the affinity for metal ions, the same titration experiments were conducted for compounds **2.5** – **2.7**. Similar changes to those obtained for compound **2.4** were observed in all cases, which demonstrated compounds **2.5** - **2.7** all showed high affinity for Cd^{2+}, Pb^{2+}, Hg^{2+}, and Zn^{2+}. As shown in Figure 2.7.4, **2.6** displayed significant changes in its UV spectrum after the addition Zn^{2+}, resulting in a reduction in absorbance at 400 nm and a simultaneous red-shift to 418 nm, along with a stark increase in absorbance at 329 nm and a decrease at 279 nm. These changes lead to the emergence of two isosbestic points at 306 nm and 354 nm. The data is fitted to a 2:1 binding model and Job's plot supports the choice.

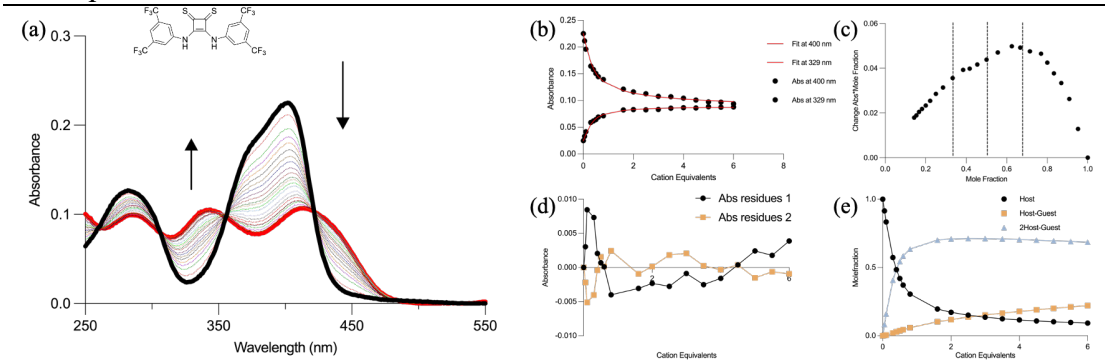

Figure 2.7.4. Uv-vis titration data for **2.6** towards Zn^{2+}. (a) Uv-vis spectra of **2.6**(10 μM in MeCN) upon addition of increasing molar equivalents of Zn^{2+} (0 - 6 eq.). (b) Fitplot of **2.6** towards Zn^{2+} in a 2:1 binding model. (c) Job's plot of Zn^{2+} titration for **2.6**. (d) Residuals plot of **2.6**. (e) Mole fraction plot of Host vs. Host-Guest fraction with increasing guest concentration for **2.6**.

All the data analysis, conducted by using Bindfit, indicated that a 2:1 binding model was fitted in all cases, which is supported by Job's plot. As shown in Table 2.7.1, the association constants $K_a(M^{-1})$ of receptors **2.3**-**2.7** in MeCN were varied from 10^3 to 10^6 M^{-1}, although large error values in metal selectivity or affinity were noted in some cases. These discrepancies in the binding studies may be attributed to competition between the self-assembly of the squaramide subunits and metal recognition. Thiosquaramides have been shown to efficiently assemble through p-p stacking interactions,[215] complicating the thermodynamics of binding and leading to changes that do not align well with the binding model, as productive receptor-ion binding requires prior disruption of the receptor's self-assembly. However, crystal structure analysis confirmed the ability of thiosquaramides to form a 2:1 complex with Cd^{2+} and Pb^{2+}.

Table 2.7.1. Summary of metal ions association constant K_a (M^{-1}) of receptor **2.3**-**2.7** in MeCN[a]

	Zn^{2+}		Pb^{2+}		Cd^{2+}	
Receptor	K_{11} (M^{-1})	K_{12} (M^{-1})	K_{11} (M^{-1})	K_{12} (M^{-1})	K_{11} (M^{-1})	K_{12} (M^{-1})
2.3	1.2×10^3	1.0×10^5	-[b]	-[b]	9.9×10^4	8.2×10^5
2.4	1.3×10^4	8.1×10^5	9.5×10^4	19	5.3×10^5	2.5×10^5
2.5	2.6×10^4	1.9×10^6	4.9×10^3	1.3×10^3	3.0×10^4	1.7×10^5
2.6	5.3×10^4	1.1×10^6	3.1×10^4	2.1×10^4	8.5×10^4	2.6×10^6
2.7	4.6×10^4	1.7×10^6	-[b]	-[b]	2.4×10^5	4.8×10^5

a Data fitted to a 2:1 binding model with error < 17%. b High errors lead to unreliable K_a values

The preliminary colorimetric study and UV–vis screen indicates that thiosquaramides display pronounced responses towards several 2+ metal ions (*e.g.*, Zn^{2+}, Cd^{2+}, Pb^{2+} and Hg^{2+}), whereas the their oxosquaramide analogue shows minimal spectral change upon the addition of these metal ions, proving the strong influence of thionation on metal binding. This selectivity can be explained by the Hard and Soft Acids and Bases (HSAB) concept: Oxygen donors are typical hard bases, whereas sulfur donors are relatively softer bases. For transition-metal ions such as Zn^{2+} and soft acids (Cd^{2+}, Pb^{2+} and Hg^{2+}), sulfur generally affords more stable complexes with them and displays higher coordination affinity than oxygen.

In principle, electron-donating substituents enhance the electron-donor capacity of the sulfur centre, thereby favouring the formation of stronger M···S bonds. However, from the K_a values, it seems that aromatic substituted receptors **2.4**-**2.7** display higher affinities for metal ions than butyl substituted receptor **2.3**. Among **2.4** to **2.7**,

substituents with greater electron-withdrawing character did not produce a discernible trend in binding affinity, either upward or downward. Notably, the interaction between **2.3** and cations need to pay the energetic cost associated with disrupting the one-dimensional hydrogen-bonded chain has to be borne. This may result in low the association constant K_a values when the data are fitted with a conventional 2:1 model. Based on the available data, it is difficult to establish a clear trend in how substituents influence cation-binding propensity. Nevertheless, we have confirmed that the molecule exhibits strong cation affinity.

The chelation of receptor **2.4** with $Pb(ClO_4)_2$ in MeCN produced small yellow plate crystals. As shown in Figure 2.7.4, analysis of these crystals by X-ray diffraction revealed a complex of the form $[Pb(\mathbf{2.4})_2]2ClO_4$ where the asymmetric unit contained two nearly equivalent residues, with the Pb^{2+} ions adopting four coordinate distorted sawhorse geometries. The thiosquaramides exhibited asymmetric chelating coordination modes, which occupied the equatorial positions at much shorter distances than the axial positions (2.782(3) - 2.825(3) Å for equatorial, *vs* 2.915(3) – 3.025(3) Å for the axial positions). Compared to those in the H-bonded sulfate adduct (*ca.* 1.65 Å), the C=S bonds of thiosquaramides did not show obvious lengthening by coordination. The extended structure of $[Pb(\mathbf{2.4})_2]2ClO_4$ revealed further association of $[Pb(\mathbf{2.4})_2]$ dications into discrete tetranuclear assemblies around two central perchlorate anions, with weaker Pb···O contacts involving the open faces of the Pd^{2+} mostly beyond 3 Å in length. Additionally, the remaining perchlorate anions engaged in hydrogen bonding with the thiosquaramide N-H groups, showing more mobility or tendency for disorder than the perchlorate anions bound within the Pb4 tetramer, as indicated by the enlarged ADPs. The stability of this lead structure was not systematically assessed in this study. Nevertheless, the binding experiments were performed on a short timescale, and no obvious precipitation or spectral instability was observed under the conditions employed. A more detailed stability assessment will be part of future work.

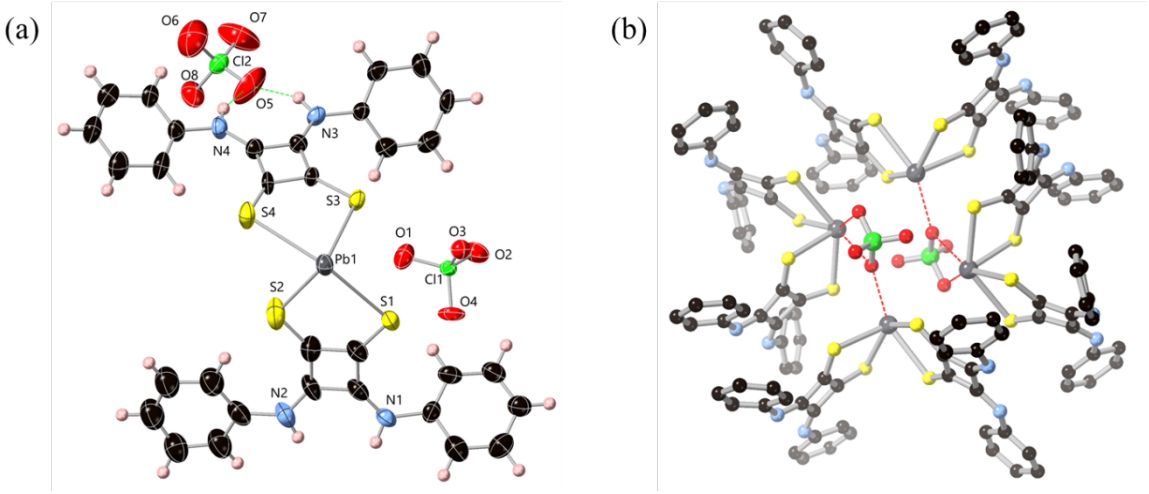

Figure 2.7.4. (a) Representative structure of one of the two unique fragments in **[**Pb(**2.4**)$_2$**]**2ClO$_4$ with heteroatom labelling scheme. ADPs are rendered at the 50% probability level; hydrogen atoms and anion disorder are omitted for clarity. (b) The tetranuclear assembly of **[**Pb **(2.4)**$_2$**]** cations around two central perchlorate anions.

2.8 Zn^{2+} transport studies

As discussed above, we proved the ability of thiosquaramide to chelate metals, prompting us to investigate whether they are capable of metal ion transport. Zinc transport has aroused widespread interest in the field of biology, as it plays a crucial role in many significant biological processes. For instance, recent studies have shown that disturbances in zinc concentrations can lead to neurotoxic processes and impact neuronal functioning.[213] Additionally, zinc ionophores such as quercetin have been found to exhibit antioxidant, anti-inflammatory, and neuroprotective effects in the central nervous system.[216,217] To examine the ability of oxo- and thiosquaramides to act as zinc ionophores, we utilized the FluoZin-3 Liposome assay (Figure 2.8.1). In this step, liposomes consisting of 1-palmitoyl-2-oleoyl-snglycero-3-phosphocholine (POPC) and cholesterol (7:3) were made as a simple membrane tool to mimic cell membranes and FluoZin-3 was encapsulated in the liposomes.[218] FluoZin-3 has been widely used in Zn^{2+} detection due to its fluorescence enhancement upon binding Zn^{2+}.

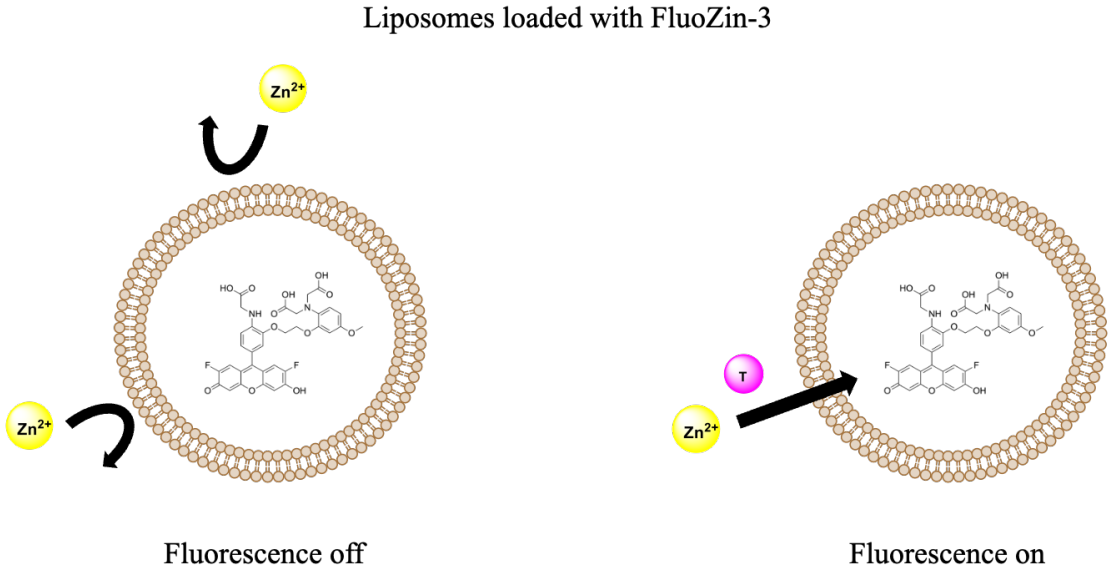

Figure 2.8.1. Concept design of the liposome system for the zinc ionophore activity determination by using FluoZin-3. T represents transporter.

As mentioned above, again we used perchlorate salt as the ion source to avoid any interference caused by the counteranion. Zn^{2+} (0.1 mM, in the form of zinc perchlorate) was added into the liposome solution followed by thiosquaramide receptors and the fluorescence intensity was recorded over time. Our results showed that the addition of thiosquaramide **2.3** - **2.7** led to a rapid increase in fluorescence, indicating the transport of Zn^{2+} inside the liposomes. However, no significant change in fluorescence intensity was observed after the addition of the oxo-squaramide derivatives **2.1** or **2.2**, confirming the importance of thionation for metal transport (Figure 2.8.2).

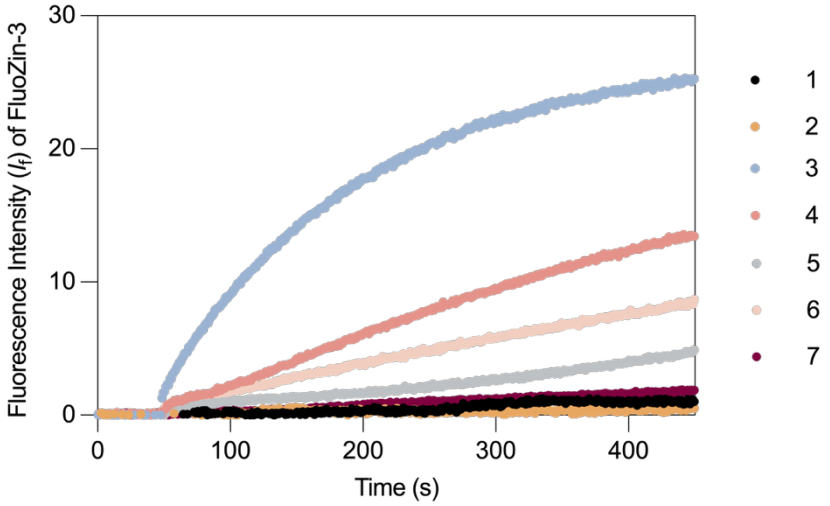

Figure 2.8.2. The fluorescence intensity of liposome loaded FluoZin-3 (in 0.01 M PBS, pH=7.4) after the addition of Zn^{2+}(0.1 mM) followed by **2.1**-**2.7** (0.01 mol%).

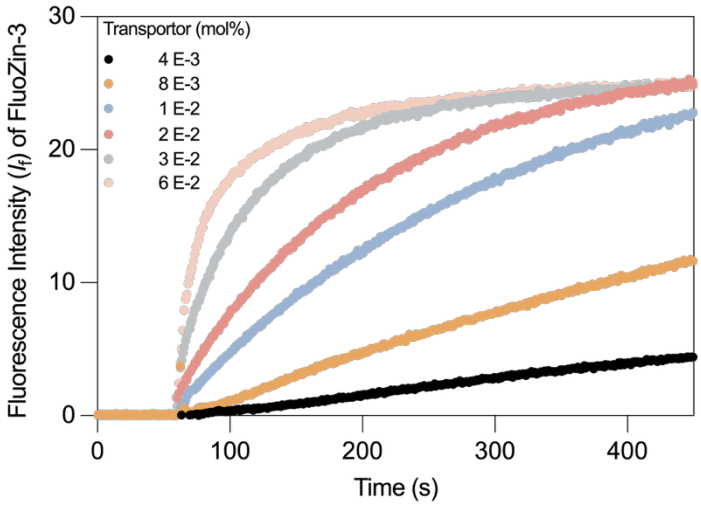

Figure 2.8.3. The dose-dependent change in fluorescence intensity of FluoZin-3 over time of liposomes containing FluoZin-3 in PBS (0.01 M, pH=7.4) upon the addition of $Zn(ClO_4)_2$ (0.1 mM) followed by a pulse of **2.3** at a range of increasing concentrations.

The findings indicated that all 5 thiosquaramide receptors exhibit ionophoric activity at 5 μM, with receptor **2.3** displaying the highest potency. Interestingly, the introduction of electron-withdrawing groups, which typically enhance Cl^- transport,

seems to reduce the efficiency of Zn^{2+} transport. indicating that cation and anion transport exhibit divergent structure-activity relationships. The transport activity of **2.3** was also assessed at various transporter: lipid ratios (Figure 2.8.3), clearly showing that as the proportion of **2.3** increases, so does the transport activity. In summary, in this section, we demonstrate that the molecule possesses strong cation binding affinity while functioning as an effective cation transporter under physiologically relevant conditions. To the best of our knowledge, this is the first report of thiosquaramide-mediated transmembrane transport of Zn^{2+}.

2.9 Cl^- transport studies

Additionally, as **2.4**-**2.7** was proven to be chloride transporter, a lucigenin assay was conducted to investigate the ability of **2.3** to act as Cl^- ionophores simultaneously.[219] In this assay, the vesicles loaded lucigenin were made by using the same method as the above. The principle is similar to FluoZin-3 assay: chloride could be transported into the liposomes and subsequently quench lucigenin (Figure 2.9.1).

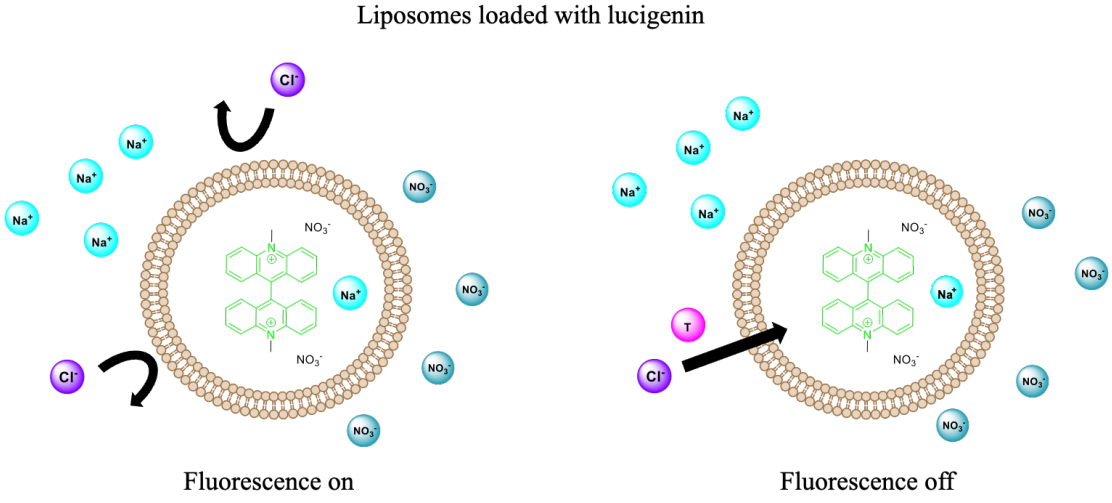

Figure 2.9.1. Concept design of the liposome system for the chloride ionophore activity determination by using lucigenin. T represents transporter.

The solution of **2.3** was added to the solution of LUVs containing lucigenin (0.4 mM in 225 mM $NaNO_3$, pH 7.2), followed by NaCl solution (75 μL, 1 M) which led to a

decrease of intensity. This result clearly suggested compound **2.3** was acting as an efficient anionophore and transporting Cl^- into the vesicles. Furthermore, we observed that the presence of metal ions has the potential to impact the Cl^- transport performance of thiosquaramides. To investigate this, a series of contrast experiments were conducted at different transporter: lipid ratios in the presence of either Zn^{2+} or Na^+. The EC_{50} value at 270 s (*i.e.* the concentration of transporter required to achieve the half effect) was determined using a Hill plot (Figure 2.9.2).

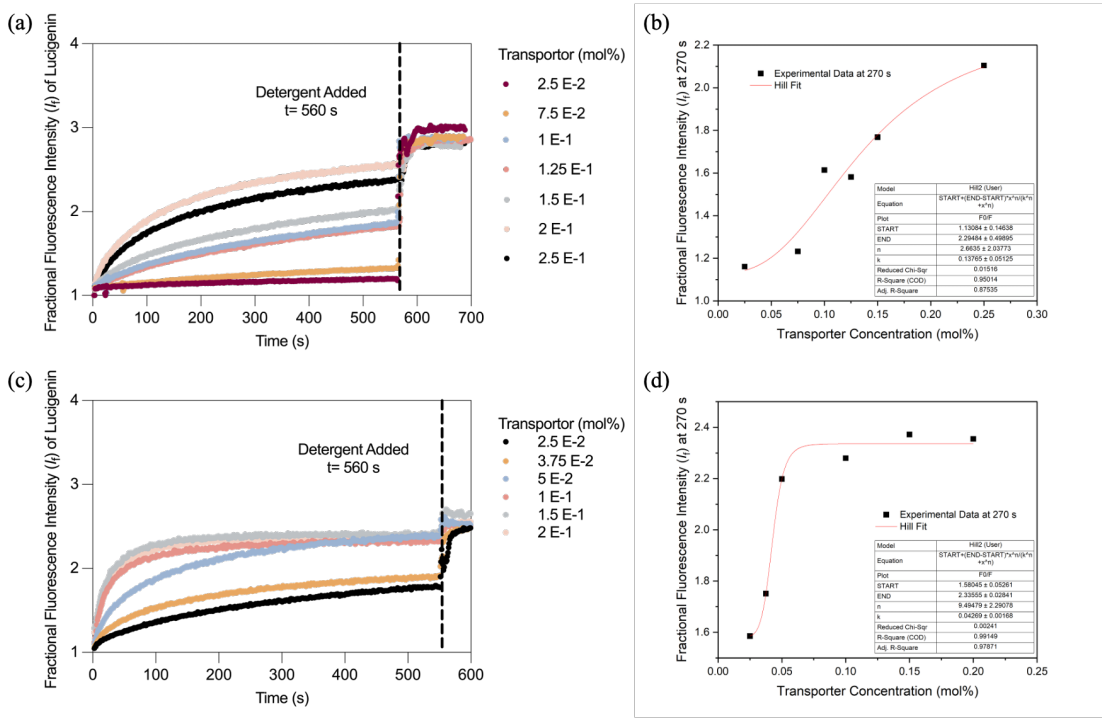

Figure 2.9.2. (a) The change of fractional fluorescent intensity with the addition of **2.3** and NaCl (75 µL, 1 M) to the liposomes containing lucigenin (225 mM $NaNO_3$, pH 7.2) at various transporter concentrations (mol%). (b) Hill plot of the fractional fluorescence intensity of lucigenin recorded at 270 s for each experiment carried out at various transporter concentrations. (c) The change of fractional fluorescent intensity with the addition of **2.3** and $ZnCl_2$ (75 µL, 0.5 M) to the liposomes containing lucigenin (225 mM $NaNO_3$, pH 7.2) at various transporter concentrations (mol%). (d) Hill plot of the fractional fluorescence intensity of lucigenin recorded at 270 s for each experiment carried out at various transporter concentrations.

According to the previous research, the pK_a value of thiosquaramide **2.4** is 7.3 and the Cl^- transport activity of this molecule is switched off at pH 7.2 because of the deprotonation.[20] Therefore, for compound **2.4**, the liposome solution was buffered to pH 4 before the titration. As shown in Table 2.9.1, the EC_{50} value in the presence of Na^+ is approximately three times greater than the EC_{50} value in the presence of Zn^{2+}, indicating that the presence of Zn^{2+} enhances the anion transport activity of thiosquaramide receptor **2.3**. Additionally, experiments for **2.4** yielded similar results that **2.4** exhibits higher anion transport activity in the presence of Zn^{2+} than in the presence of Na^+. Although the aggregation of **2.4** results in the insufficiently rigorous computational data, the big difference of EC_{50} values obtained for **2.3** demonstrated the influence of Zn^{2+} on chloride transport. It's important to note that anion transport activity does not occur in isolation, and there is evidence of co-transport behaviour between anions and cations.

Table 2.9.1 Summary of EC_{50} (mol%) value of **2.3** and **2.4**.

Receptor	Ion	pH	$EC_{50}{}^a$ (mol%)
2.3	$ZnCl_2$	7.2	0.04
	NaCl		0.14
2.4	$ZnCl_2$	4	$EC_{50} < 0.015^b$
	NaCl		$0.018 < EC_{50} < 0.02^b$

a Concentration of receptors required to achieve the half of max effect.

a Concentration of receptors required to obtain the half of max effect. *b* The high value of n obtained in Hill plot results in the inaccurate EC_{50} value, but the approximate value can be estimated.

Furthermore, to further explore the effect of metal ions on the chloride transport ability, we modify the lucigenin assay, where the NO_3^- source of the background solution was replaced with $Zn(NO_3)_2$, $Cu(NO_3)_2$, $Cd(NO_3)_2$, $Ni(NO_3)_2$, or KNO_3, and external chloride pulse was initiated with the corresponding MCl salt, such as $ZnCl_2$, $CuCl_2$

and $CdCl_2$. In order to keep the concentration of NO_3^- the same, the concentration of the nitrate solution for 2+ metal ions was halved (112.5mM, such as $Zn(NO_3)_2$). Similarly, a 0.5 M chloride solution was prepared to ensure a consistent Cl^- concentration for 2+ metal ions. Other conditions were kept as the same.

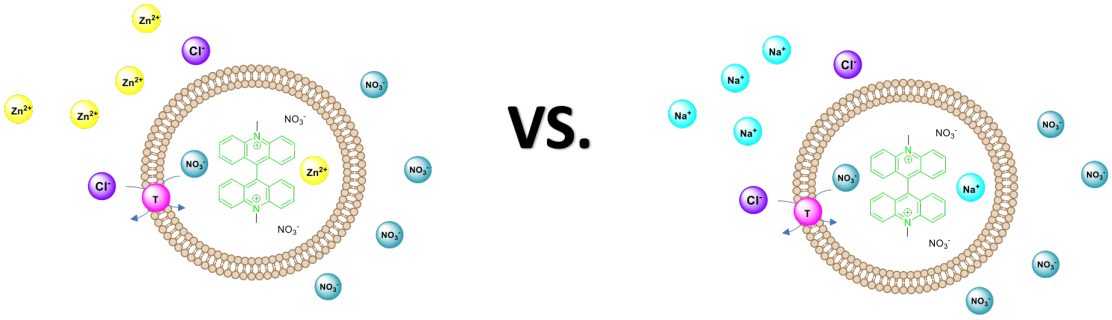

Figure 2.9.3. Concept design of the liposome system for the chloride ionophore activity determination in the presence of different metal ions by modifying lucigenin assay.

This time, we would like to focus on the receptor **2.3**. As shown in Figure 2.9.4 (a), $Zn(NO_3)_2$ is used as solution and $ZnCl_2$ is used as external chloride pulse, while Figure 2.9.4 (b) uses $Cd(NO_3)_2$ as solution and uses $CdCl_2$ as external chloride pulse. In the presence of Zn^{2+}, the chloride transport ability is still active, while in the prescence of Cd^{2+}, there is no transport performance observed.

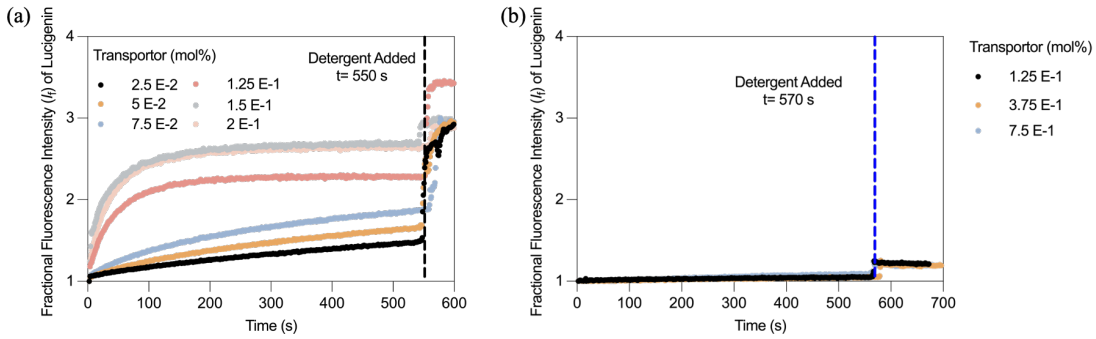

Figure 2.9.4. (a) The change of fractional fluorescent intensity with the addition of **2.3** and $ZnCl_2$ (75 μL, 0.5 M) to the liposomes containing lucigenin (112.5 mM

$Zn(NO_3)_2$) at various transporter concentrations (0.025 – 0.2 mol%). (b) The change of fractional fluorescent intensity with the addition of **3** and $CdCl_2$ (75 μL, 0.5 M) to the liposomes containing lucigenin (112.5 mM $Cd(NO_3)_2$) at various transporter concentrations (0.125 – 0.75 mol%).

To quantify transport efficiency and thereby better compare transport activity of **2.3** in the presence of different ions, we calculated the EC_{50} values under each condition. As shown in Table 2.9.2, in the presence of K^+, Cu^{2+} and Na^+, similar EC_{50} value is obtained, suggesting these cations has minimal effect on chloride transport; In the presence of Ni^{2+}, the EC_{50} value is a little bit higher than the EC_{50} value of that in the presence of of K^+, Cu^{2+} and Na^+, which means Ni^{2+} exerts a measurable inhibitory effect on chloride transport; Subsequently, as mentioned above, in the presence of Cd^{2+}, there is almost no transport behaviour observed. Notably, in the presence of Zn^{2+}, the results show an increase in Cl^- transport efficiency, indicating that a positive cation influence was occurred. Overall, we propose that metal ions with high affinity for the receptor inhibit its chloride-transport activity. By preferentially binding the receptor, high-affinity metals outcompete Cl^- and render the receptor unavailable for chloride binding, thereby reducing transport efficiency, even 'switch off' transport activity.

Table 2.9.2. Summary of the EC_{50} value at 270 s for transporters **2.3** in different conditions

Metal ion	n[a]	EC_{50} (mol%)
Cu^{2+}	3.1	0.27
Zn^{2+}	4.5	0.10
Ni^{2+}	3.1	0.63
Na^+	2.7	0.13
K^+	2.5	0.25
Cd^{2+}	n.a[b]	n.a[b]

a Hill coefficient (n-value) *b* no observed transport behaviour

To further confirm our hypothesis, we performed ^{1}H NMR titration experiments in the presence of Cd^{2+}. Compared to the Cl^- titration of **2.3** (0.4 mM, CD_3CN) in the absence of Cd^{2+}, the addition of Cl^- to a solution of receptor **2.3** (0.4 mM, CD_3CN) in the presence of Cd^{2+} (8 eq.) caused almost no changes in the chemical shift of the NH protons (Figure 2.9.5). In addition, the addition of Cd^{2+} to a solution of **2.3** (0.4 mM, CD_3CN) containing 2 equivalents of chloride will lead to the chemical shift of NH move to downfield, which means the release of chloride (see appendix). This further supports our hypothesis.

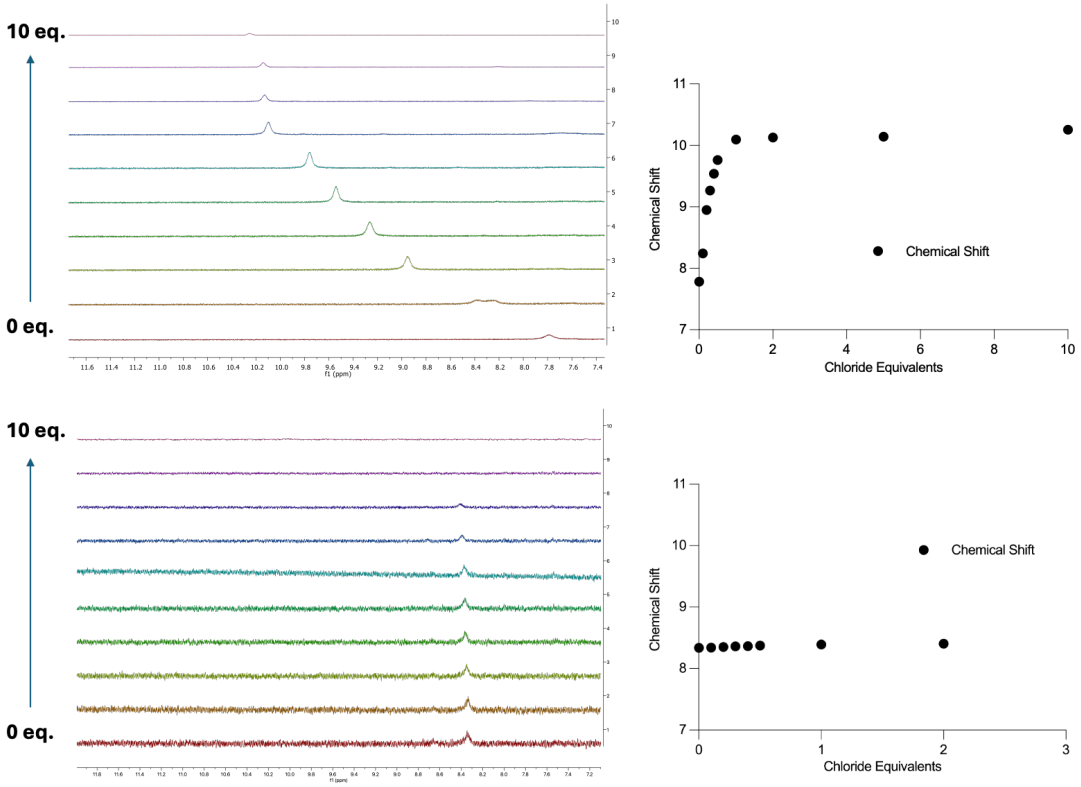

Figure 2.9.5. (a) ^{1}H NMR stackplot of **2.3** with TBACl in CD_3CN in the absence of Cd^{2+}. (b) ^{1}H NMR stackplot of **2.3** with TBACl in CD_3CN in the presence of Cd^{2+} (8 eq.).

Interesting, Zn^{2+} has similar affinity as Cd^{2+} for **2.3**, thus, Zn^{2+} is expected to bind the receptor and thereby inhibit receptor-chloride association, ultimately suppressing Cl^- transport as well. Contrary to this expectation, analysis of the EC_{50} values shown above indicates that Zn^{2+} uniquely enhances Cl^- transport. This suggests that a co-

transport mechanism may be occurring with this metal, where Zn^{2+} and Cl^- are transported concurrently. We conducted an extra transport assay with modified conditions: the vesicles were prepared by following the lucigenin assay, but the lucigenin is replaced by FluoZin-3 to evaluate the Zn^{2+} transport behaviour in 225 mM $NaNO_3$ and $ZnCl_2$ (75 µL, 0.5 M) was used as external pulse. Therefore, the transport behaviour of Zn^{2+} and Cl^- can be compared. As shown in Figure 2.9.6, the time-dependent traces obtained from both the FluoZin-3 and lucigenin assays under comparable background conditions (225 mM $NaNO_3$) exhibit nearly identical kinetics, supporting a coupled Zn^{2+}/Cl^- co-transport process mediated by thiosquaramide receptor **2.3**. Although binding of Zn^{2+} still diminishes the receptor's affinity for chloride and thus exerts a deleterious effect on Cl^- transport, the cotransport effect enhances chloride transport efficiency by an amount sufficient to compensate for this penalty. Consequently, in the presence of Zn^{2+}, a net enhancement of Cl^- transport efficiency is observed.

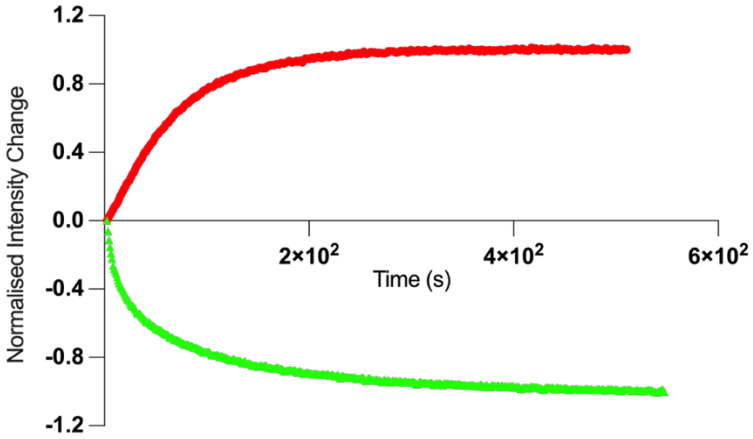

Figure 2.9.6. Normalised Zn^{2+} transport data of FluoZin-3 assays (red) vs. Cl^- transport data of lucigenin assays (green) of **2.3** (0.8 µM) under analogous conditions (225 mM $NaNO_3$).

In addition, Cadmium interference was not investigated in this study. Given the potential of Cd^{2+} to compete for binding, future work will include interference control experiments in the presence of relevant Cd^{2+} concentrations.

2.10 Biological and Imaging Experiments

For further confirmation of **2.3**'s Zn^{2+} ionophoric ability, confocal microscopy was used to observe the activation of FluoZin-3 fluorescence in POPC vesicles (conducted by Dr Luke E. Brennan). The vesicles, suspended in PBS (0.01 M) with an excess of extravesicular Zn^{2+} ions, were imaged before and after adding each thiosquaramide receptor at a final concentration of 10 μM. Images were obtained by using the cumulative acquisition of 30% of each well stemming from the centre of a standard live-cell imaging compatible 96-well plate, using a Leica Stellaris 8 LSCM (WL laser 80% power, $\lambda_{exc/em}$ 494/516 nm, 10x non-immersion objective). The images were then stitched and deconvoluted using the in-house LasX software package. As shown in Figure 2.10.1 (a), vesicles treated with **2.3**-**2.7** for 5 minutes at 10 μM exhibited significantly higher levels of fluorescence compared to untreated vesicles. The intensity values were quantified, and the results showed a substantial increase in FluoZin-3 derived fluorescence when transporters were added to vesicles (up to 26-fold increase, $p < 0.0001$, multiple unpaired t-test).

Building on this result, we aimed to determine whether this Zn^{2+} transport behaviour is efficient in biological activity. As discussed above, we have recently published our findings on the synthesis, characterization, and mechanistic understanding of a series of "squindoles" that demonstrate strong antimicrobial activity through anion transport.[207] It is worth noting that Monensin, Valinomycin, Salinomycin, and lasalocid are known for their potent antimicrobial properties through cation transport mechanisms.[220] We conducted an analysis of the antimicrobial properties of **2.3**-**2.7**. To achieve this, we performed growth inhibition assays. Cultures of Staphylococcus aureus were grown to an early stationary phase and then exposed to each transporter at various concentrations (in the presence of or in the absence of a 2 eq. excess of Zn^{2+}). After 24 hours of incubation at 37°C, we measured bacterial growth by assessing the optical density at 600 nm and compared it to the control.

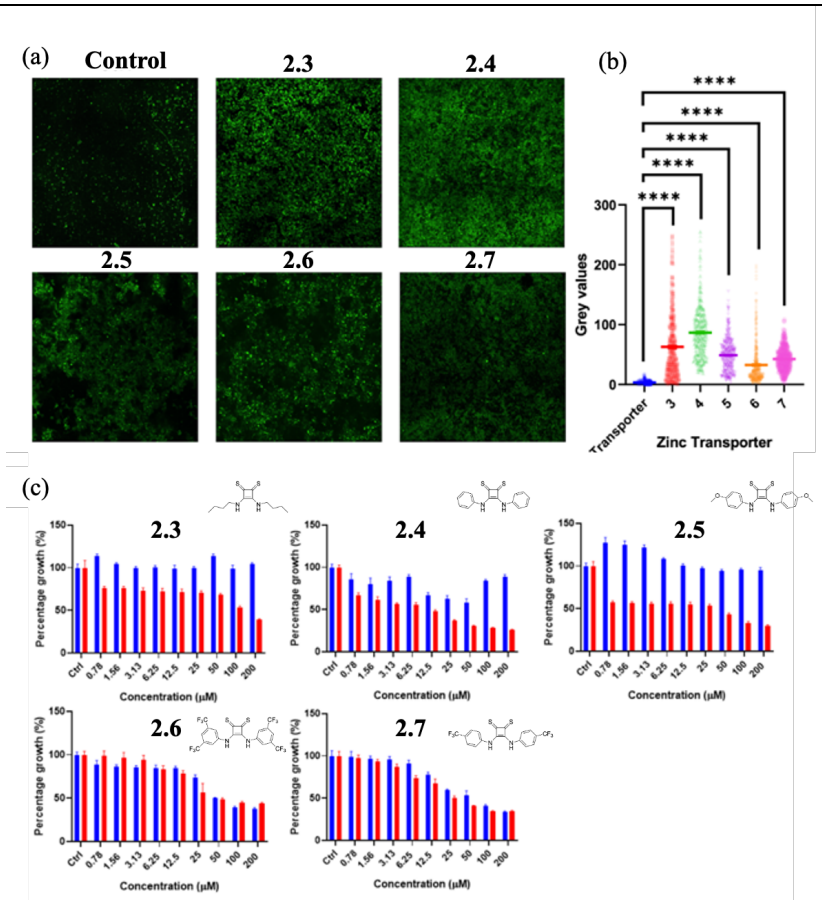

Figure 2.10.1. (a) Confocal laser scanning microscopy of unfixed POPC vesicles, comparing FluoZin-3 fluorescence before and after treatment with receptors **2.3**-**2.7**. (b) Analysis of the fluorescence intensity of FluoZin-3 across a 1000 μM ROI identified as the centre of each image, represented as mean grey values (± SEM) compared to control. (c) Results of growth inhibition assays for **2.3** – **2.7** against *S. aureus*. Blue represented transporter added in the absence of Zn^{2+}. Red represented transporter added with two eq. excess of Zn^{2+}. All results are represented as mean (± SEM) percentage growth relative to the control of three biological replicates.

The IC_{50} values for each compound were determined from growth inhibition data, with IC_{50} representing the minimum concentration of transporter required to inhibit 50% of bacterial growth after 24 hours (Fig. 2.10.1 (C)). As shown in Table 2.10.1, a significant increase in growth inhibition was observed when Zn^{2+} was made available for transport. Compounds **2.3**-**2.5** exhibited a notable increase in growth inhibition, effectively demonstrating a "switch-on" of inhibition when Zn^{2+} was added alongside the transporter. For each of these compounds, there was a shift from minimal activity

in the absence of Zn^{2+} to high levels of antimicrobial activity, with IC_{50} values as low as 9.4 μM for compound **2.4**, when zinc was abundant in the culture media. While not as dramatic, compounds **2.6** and **2.7** also showed a noticeable increase in antimicrobial activity when Zn^{2+} was available for transport in the culture media.

Table 2.10.1. Summary of the IC_{50} concentrations for transporters **2.3**-**2.7** against *S. aureus* in the absence and presence of 2 molar equivalents of Zn^{2+}. n.a = no observed activity.

Receptor	IC_{50} (- Zn^{2+}) (μM)	IC_{50} (+ Zn^{2+}) (μM)
2.3	n.a	100
2.4	n.a	9.4
2.5	n.a	25
2.6	50	33
2.7	50	25

In addition, a preliminary quick single-point screen against *E. coli* did not indicate obvious growth inhibition under the experiment conditions. However, as these observations were not collected as a full, replicated dataset and the raw data were not retained, they are not discussed further, and this chapter focuses on *S. aureus* only.

2.11 Conclusion

In summary, our research demonstrates that thiosquaramides exhibit a strong affinity for metal ions such as Cd^{2+}, Pb^{2+}, Hg^{2+}, and Zn^{2+} compared to oxosquaramides. Additionally, they are capable of binding anionic species such as Cl^-. We observed significant changes in their absorption properties upon complexation, which were further explained through TD-DFT analysis. The addition of metal ions (Cd^{2+}, Pb^{2+}, Hg^{2+}, and Zn^{2+}) to the solution of all 5 thiosquaramide receptors leads to the colour

change which is visible to the naked eye, proving the ability of thiosquaramide to act as potential colorimetric metal detector.

Furthermore, UV-vis and X-ray crystallography confirmed their ability to form 2:1 complexes with these metals. Our FluoZin-3 Liposome assay confirmed the effectiveness of thiosquaramides as potent zinc ionophores, with receptors **2.3** - **2.7** exhibiting rapid and efficient zinc transport at a 0.005 mM concentration, unlike their oxosquaramide counterparts. In addition, thiosquaramide receptors displays enhanced Cl^- transport behaviour in the presence of Zn^{2+}, clearly suggesting the co-transport behaviour is occurring.

Moreover, our evaluation of their antimicrobial activity against *S.aureus* revealed that thiosquaramides **2.3** - **2.5** showed no observed activity, while **2.6** and **2.7** displayed only moderate inhibition (IC_{50}=50 μM) which may arise from the toxicity associated with fluorine-containing species. Upon the addition of Zn^{2+} (2 eq.) to **2.3** - **2.5**, a pronounced Zn^{2+}-dependent 'switch-on' effect was observed, giving IC_{50} values of 100 μM, 9.4 μM, 25 μM, respectively. The inhibition effect of **2.6** (IC_{50}=33 μM) and **2.7** (IC_{50}=25 μM) also increased to some extent in the presence of Zn^{2+}. Therefore, within the scope of the bacterial model examined in this chapter, the Zn^{2+}-dependent growth inhibition activity is consistent with efficient Zn^{2+} transport behaviour in cells, which may enhance antibacterial effects by perturbing ion homeostasis.

Overall, these results present a new ionophoric scaffold that can be leveraged in the development of novel antimicrobial drugs, providing a foundation for further exploration of structural diversity and innovative mechanisms of action within the realm of supramolecular medicinal chemistry. This chapter has served to lay the foundation for efficient thiosquaramide-based ionophores by which we hope to further functionalize these metal transporters in subsequent chapters.

In the future, work of interest should be directed towards the development of efficient ion transporters based on thiosquaramide scaffolds that display high selectivity for specific ions (Figure 2.11.1). The well-organised cavity in the structure is potentially conducive to the specific selection of ions.

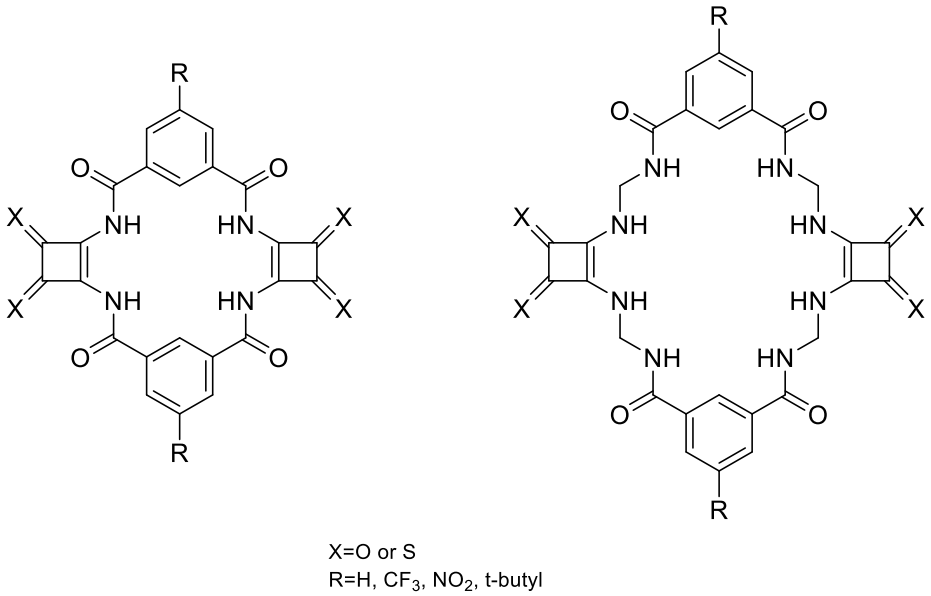

Figure 2.11.1. Potential approaches to the development of thiosquaramide-based ion transporters through the design of a macrocyclic ring with suitable cavity for ions.

Chapter 3: Thiosquaramide-based Fluorescent Metal Sensors

3.1 Introduction

Metal ions have attracted extensive attention due to their significant roles in biological processes. For example, Cu^{2+} participate in the catalysis of dopamine β-hydroxylase,[221,222] influences neural signal transmission and synaptic plasticity, and copper homeostasis imbalance is associated with neurodegenerative diseases such as Alzheimer's and Parkinson's.[223,224] Zn^{2+} act as a regulatory factor for immune cell function and participates in the immune response of organisms, while also playing important roles in embryonic development, cell division, and gonadal function.[225–227] Therefore, the highly sensitive and selective detection of metal ions is of great significance in bioanalysis.

Among various analytical techniques, fluorescent probes have attracted considerable attention due to their high sensitivity, real-time detection capability, and visualization features. Compared with conventional detection methods such as atomic absorption spectroscopy and inductively coupled plasma mass spectrometry, fluorescence-based techniques enable rapid detection under diverse conditions. The design of an efficient fluorescent probe typically comprises two key components: a fluorophore and an ion receptor. As mentioned in the previous chapter, these molecules have been widely employed in ion recognition, sensing, and transmembrane transport owing to their excellent ion-binding capability.[228–230] Based on this feature, Gale and co-workers achieved the synthesis of a class of fluorescent squaramide derivatives by integrating strongly hydrogen-bond-donating squaramide moieties with fluorescent chromophores. These compounds are capable of anion recognition along with transmembrane anion transport functionality, binding chloride ions via hydrogen bonding, and displaying fluorescence modulation. Such properties render them valuable tools for probing the subcellular localisation and pharmacokinetic behaviour of anion transporters in biological systems.[229] The Elmes group has also conducted more in-depth studies on similar structures. They reported two novel squaramide-1,8-naphthalimide conjugates (**SQ1** and **SQ2**) that exhibit unique performance as selective "turn-on" fluorescent probes for bromide (Br^-) detection. These probes display pronounced self-assembly behavior in aqueous/DMSO solutions, and upon increasing temperature, a fluorescence enhancement is observed, arising from a disaggregation-induced emission (DIE) effect (Figure 3.1.1).[230] Subsequently, they further reported the first two squaramide-1,8-naphthalimide conjugates capable of sensing Br^- in

cellulose.[181] Meanwhile, they confirmed that the position of the squaramide unit within the molecule not only influences the self-assembly morphology but also modulates its binding affinity toward different anions.

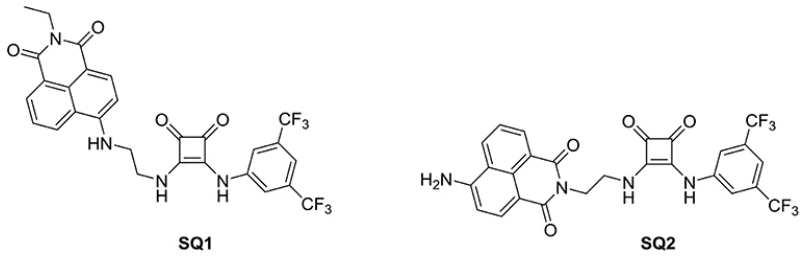

Figure 3.1.1. The structure of SQ1 and SQ2, and graphical abstract of "turn on" fluorescent probes for bromide through a disaggregation-induced response.[230]

Squaramides have also been employed in the design of fluorescent receptor structures for cations. Early investigations showed that squaramide-based receptors are capable of forming stable complexes with tetraalkylammonium compounds (Figure 3.1.2).[231] The observed binding selectivity is attributed to the synergistic influence of molecular size compatibility, hydrophobic microenvironments, and hydrogen-bond geometry. The present work highlights the viability of the squaramide scaffold in cation–anion co-recognition systems, broadening its prospects for applications in molecular recognition and sensor design. Subsequently, they developed an efficient fluorescent probe for the detection of choline-containing phospholipids. The probe molecule recognises the choline cationic headgroup and binds to the intramolecular fluorescent chromophore, resulting in a pronounced fluorescence enhancement signal, thereby enabling the selective detection of the target phospholipids.

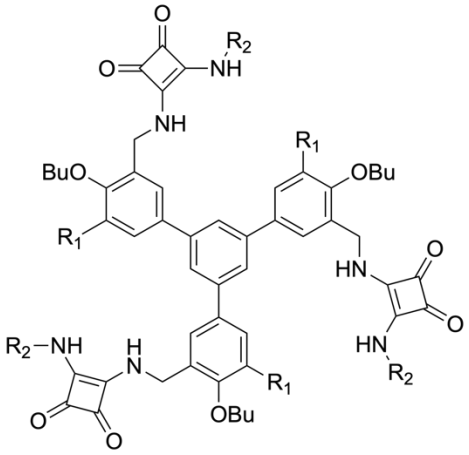

Figure 3.1.2. Structure of squaramido-based tripodal receptor reported by Tomas.

Recently, Wang and co-workers reported two fluorescent probes derived from a squaramide framework, combining the structural characteristics of squaric acid and imine functionalities, which were developed for the selective detection of Cu^{2+} and Cd^{2+} with low detection limits (1.26×10^{-8} M and 2.04×10^{-8} M, respectively). This kind of fluorescent probe displays remarkable sensitivity, rapid response, and robust performance across a wide pH range, together with pronounced resistance to interference.[232]

Research on squaramide in cation recognition have largely focused on the development of ion-pair receptors. Romański et al. reported an ion-pair receptor incorporating pyrene as the fluorescent reporting unit and squaramide as the hydrogen-bonding recognition motif, and investigated the modulation of its fluorescence sensing performance upon complexation with graphene quantum dots (GQDs) (Figure 3.1.3).[233] Recently, a squaramide-based fluorescent cryptand receptor reported by the Romański' group exhibited remarkable selectivity and high binding constants toward zwitterions such as choline and betaine.[234] It was also demonstrated that zwitterions with a high degree of complementarity to the molecular cavity can trigger a stronger fluorescence response.

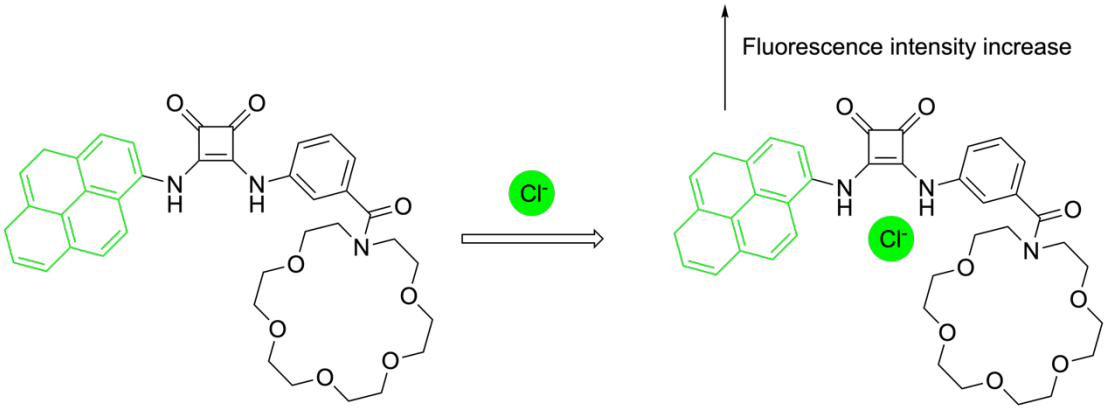

Figure 3.1.3. Graphical abstract of fluorescent sensing of the pyrene-based ion pair receptor reported by Romański.[233]

These macrocyclic squaramide receptors form a preorganized binding cavity through the macrocyclic framework, further enhancing the stability and selectivity of ion-pair binding. Reported macrocyclic receptors have been shown to induce significant fluorescence enhancement upon binding sulfate, achieving "turn-on" sensing, and maintaining high selectivity even in the presence of various common anions such as phosphate, nitrate, and chloride (Figure 3.1.4).[235]

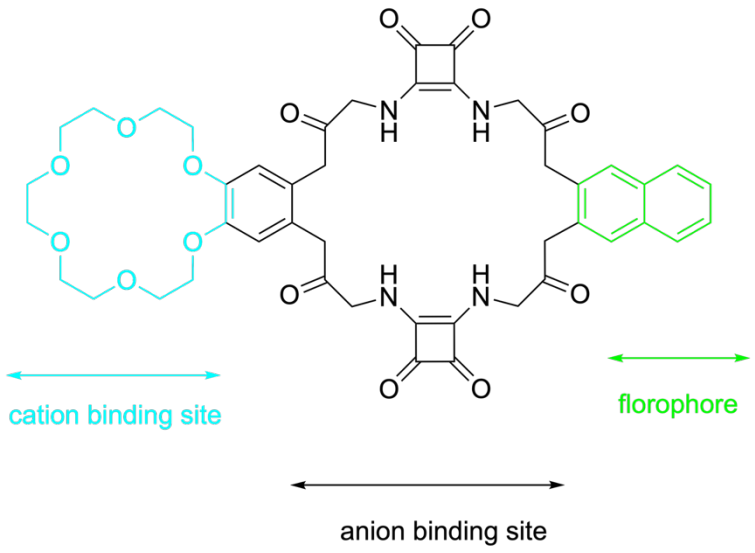

Figure 3.1.4. Graphical abstract of macrocyclic squaramides as ion pair receptors and fluorescent sensors reported by Zaleskaya.[235]

Despite extensive research progress, existing fluorescent probes for metal ions still exhibit several shortcomings. Most fluorescent probes suffer from insufficient selectivity and are susceptible to interference from other ions, while their relatively high detection limits make them unsuitable for trace-level detection. Complex ion-pair probes often have poor water solubility, limiting their application in biological systems, and their multistep synthetic procedures hinder large-scale production. Based on these considerations, the work presented in this chapter aims to design and synthesise a series of novel fluorescent metal-ion receptors, exploited to achieve highly selective and sensitive detection of specific metal ions, while ensuring good aqueous compatibility and synthetic feasibility. In Chapter 2, we demonstrated that thiosquaramides can act as receptors for M^{2+} metal ions. The work presented in this chapter, will explore their potential as a platform for fluorescence ion detection. This work is expected to have potential applications not only to environmental monitoring but may also be extended to fluorescent bioimaging of metal ions. Fluorescent ionophores as "self-reporting" transport platforms. Beyond fluorescence-based ion detection, attaching a fluorophore to an ionophore scaffold provides fluorescent ionophores, which enable direct visualisation of transporter localisation and uptake in membranes and cells, and can help reveal the relationship between their distribution and function. Reviews discussing ion transport in cell have highlighted the value of fluorescent transporters for probing subcellular localisation and pharmacokinetics.[236,237] A representative example is the development of squaramide-based anion transporters consist of a 1,8-naphthalimide fluorophore, which combine transmembrane anion transport with live-cell fluorescence imaging.[229] In this context, the present chapter further explores quinoline-thiosquaramide conjugates as a platform that combines metal binding-induced fluorescence response and liposome-based transport assays, aiming to evaluate whether a single scaffold can act as both a fluorescent sensor and an ionophore.

3.2 Chapter objectives

The objective of this Chapter is to synthesise a series of fluorescent probes based on the thiosquaramide motif that will display sensitive and selective fluorescent responses for metal ions. In Chapter 2, we have discussed the application of thiosquaramide as ion receptors, ion transporters and antibacterial agents. In this chapter, we aim to

design and construct thiosquaramide as a fluorescent receptor capable of metal ion recognition. In our molecular design, quinoline was selected as the fluorophore due to its favourable photophysical and coordination properties. As a scaffold widely used for live-cell imaging, quinoline exhibits good photostability.[238] The quinoline motif contains a built-in binding site that the ring nitrogen (N) can directly coordinate metal ions, which may contribute to the ion recognition. By coupling an appropriate receptor to the quinoline framework to create a donor-acceptor system, PET- or ICT-based switching from a non-emissive to an emissive state is readily achieved, making quinoline suitable as a turn-on fluorescent reporter.[239] In addition, quinoline exhibits a moderate quantum yield, and its emission wavelength typically falls within 440-500 nm. However, by strengthening push-pull electronic interactions and extending π-conjugation, the emission can be shifted into the green and even orange-red region. This facilitates the construction of near-infrared (NIR) emissive probes.[239] The essence of this strategy involves a quinoline fluorophore linked to a thiosquaramide ion receptor with the intention that the ion binding event will lead to a photophysical response. Accordingly, we designed six target molecules that respectively employ 3-quinoline and 6-quinoline as the fluorophores (Figure 3.2.1).

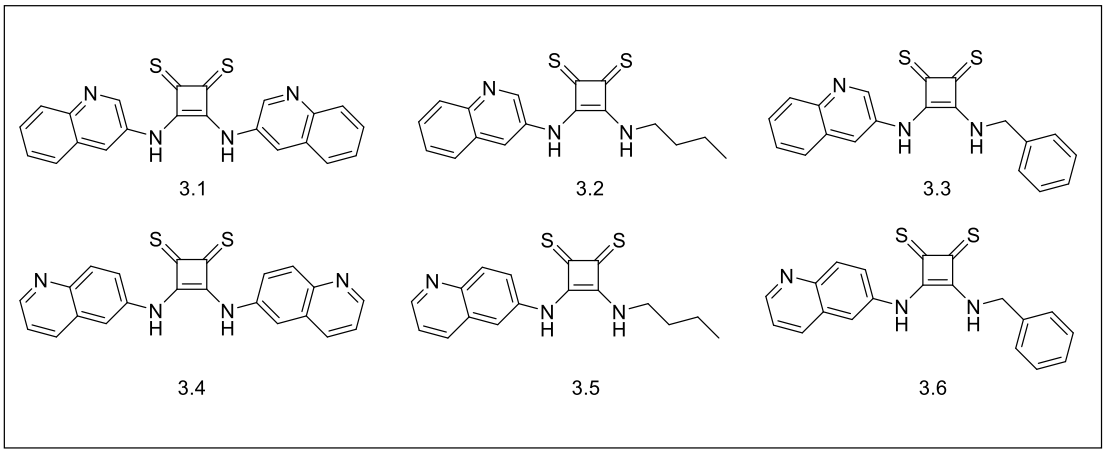

Figure 3.2.1. Structures of target molecules.

We planned to follow a similar synthetic protocol to that described in Chapter 2. Using 3-aminoquinoline as an example, the first step is expected to afford intermediate mono-substituted thiosquarate by adding a single equivalent of 3-aminoquinoline to a

solution of dicyclopentenyl thiosquarate before subsequent reaction of this intermediate with an excess of amine to generate the desired product (Scheme 3.2.1).

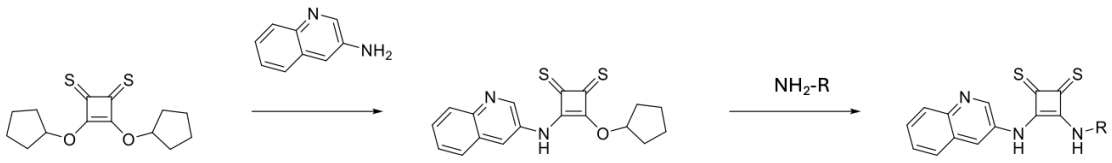

Scheme 3.2.1. Proposed synthetic method of quinoline thiosquaramides.

We expect that the thiosquaramide-based fluorescent receptor derivatives will retain their high affinity toward ions and envisage that a fluorescence response may be observed upon binding with the target ions (Figure 3.2.2).

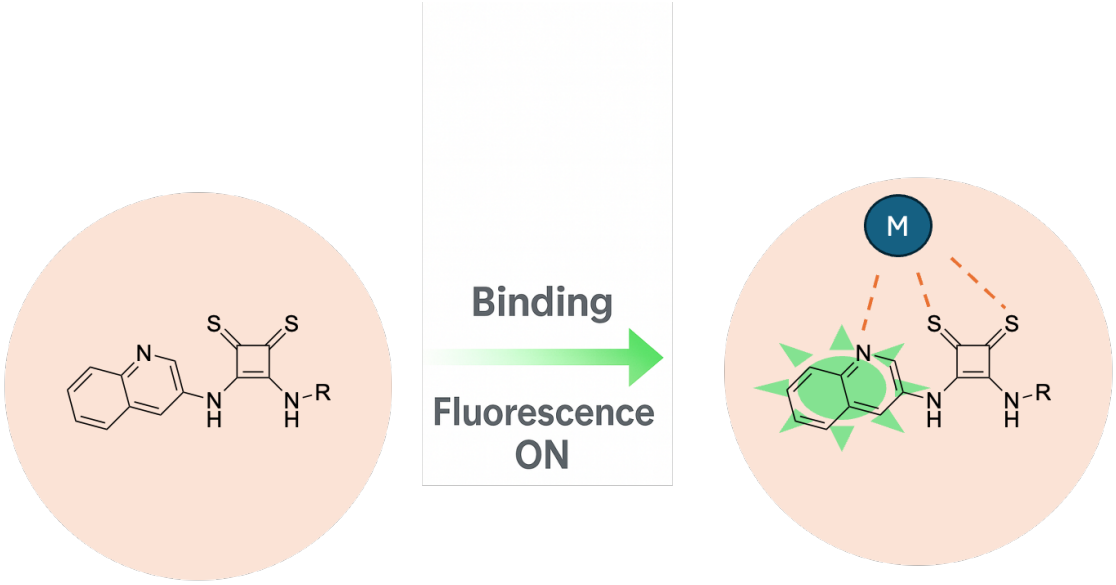

Figure 3.2.2. Schematic of quinoline thiosquaramide fluorescent probe.

Based on the high sensitivity of thiosquaramides toward various ions, we expected that quinoline thiosquaramides may enable the monitoring of trace amounts of ions, specifically M^{2+} ions. Herein, we report the synthesis method for the formation of a series of quinoline thiosquaramide conjugates.

In this Chapter, we will also evaluate their metal-binding ability and fluorescence response behaviour through both NMR and UV-vis titration experiments. Moreover, as we have shown thiosquaramides to be effective ion transporter scaffolds, we anticipate that quinoline-substituted thiosquaramide derivatives should also possess analogous transport behaviour. The FluoZin-3 assay is again employed to evaluate the Zn^{2+} transport behaviour alongside ana analysis of whether such fluorescent molecules can act as 'self-reporting' transporters of the targeted ions.

3.3 Synthesis and characteristics of quinoline thiosquaramide

As discussed in the last section, the synthetic route to quinoline thiosquaramide was expected to be similar to the method employed in Chapter 2.[201] To establish a versatile synthetic route, we initially attempted to employ the first synthetic method. Dicyclopentyl thiosquarate and an aminoquinoline were successfully reacted to generate mono-substituted thiosquarate intermediates **a** and **b**, which then reacted with amine to afford the final product (Scheme 3.3.1). However, this approach leads to the formation of thiosquarain isomers in an approximate 1:1 ratio (Scheme 3.3.1 Method 1). In the synthesis of squaramides, amine is able to attack C=O bond to form squaraine.[200] Therefore, we propose the mechanism of the formation of thiosquaraine should be the same: the amine attack the C=S bond to form 1,3-isomer (shown in the Scheme 3.3.1). Interestingly, in the synthesis of thiosquraramides, the preference is likely also governed by nucleophile reactivity and steric effects. More nucleophilic aliphatic amines can react with thiosquarate core rapidly and seem to show poor regioselectivity, giving an approximate 1:1 ratio of desired products and isomers. In contrast, aromatic amines are less nucleophilic and more sterically constrained, so the reaction is more strongly governed by steric and conformational effects in the competing transition states, which may lead the reaction to form the 1, 2-isomer.

This observation is corresponding to Chapter 2. Notably, In the synthesis of oxosquaramides (shown in Scheme 2.3.1), the use of a Lewis acid catalyst, for example $Zn(OTf)_2$, markedly speed up the condensation reaction and effectively inhibit the formation of isomeric byproducts by protecting the C=O site. However, this strategy was not employed in the synthesis of thiosquaramide. Although this results in the generation of the thiosquarain isomers, the exceptionally strong metal-binding

affinity of thiosquaramide would lead to the direct formation of a host-guest complex upon addition of a metal-based catalyst. Therefore, we prefer to purify the product by column chromatography rather than introducing a catalyst. For **3.1** and **3.6**, the desired products were obtained with yields of 85% and 81% respectively by following method 1.

Although the desired products **3.2** and **3.5** were successfully obtained by chromatography with yields of 31% and 37%, products **3.3** and **3.6** could not be purified by using chromatography due to their limited solubility.

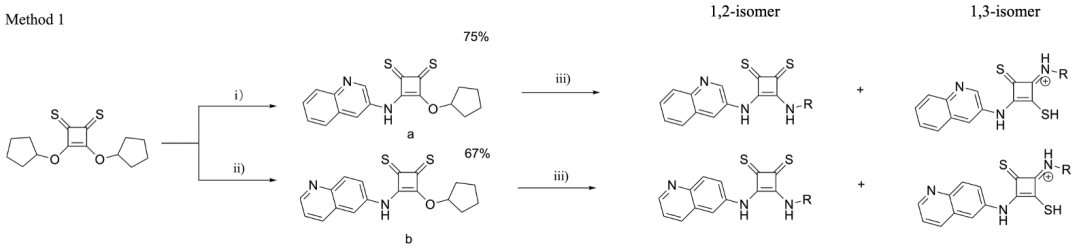

Scheme 3.3.1. Synthetic pathway towards quinoline thiosquaramide. *Reagents and conditions:* (i) anhydrous DCM, 3-aminoquinoline, rt., 4 h; (ii) anhydrous DCM, 6-aminoquinoline, rt., 6 h; (iii) anhydrous DCM, amine, 0 °C – rt., 24 h.

However, we found that the formation of isomers could be prevented by initially preparing a mono-substituted thiosquarate intermediate with an aliphatic amine, followed by the introduction of the desired aminoquinoline. Intermediates **B1** and **B2** were synthesised through the reaction of dicyclopentyl thiosquaramide with respective substituted aliphatic amine in acceptable yields (30% and 33%). Target compounds **3.2**, **3.3**, **3.5** and **3.6** were obtained in varied yields (71% - 85%) through the reaction of **B1** and **B2** with aminoquinoline. The desired diquinoline thiosquaramide **3.1** and **3.4** were generated through a nucleophilic substitution reaction of dicyclopentyl thiosquarate with excess aminoquinoline in 85% and 81% yields, respectively.

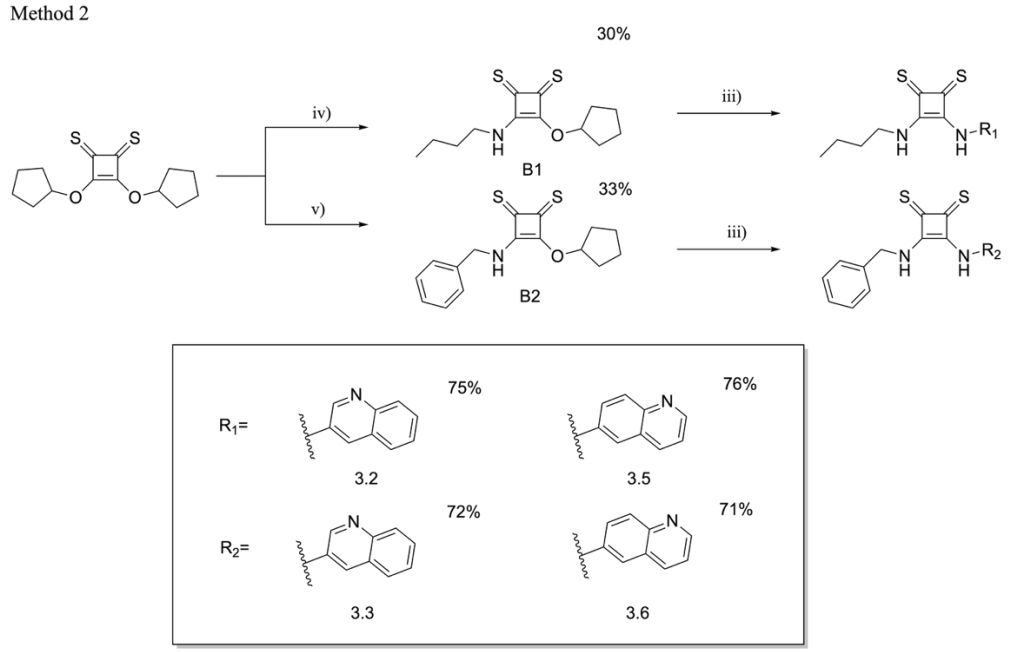

Scheme 3.3.2. Synthetic pathway towards quinoline thiosquaramide. *Reagents and conditions:* (iii) anhydrous DCM, amine, 0 °C – rt., 24 h; (iv) anhydrous DCM, butylamine, 0 °C, 2 h; (v) anhydrous DCM, benzylamine, 0 °C, 2 h.

The successful synthesis of each targeted quinoline thiosquaramides was confirmed by using ^{1}H NMR, ^{13}C NMR and LC-MS (Figure 3.3.2 and appendix). As an example, the synthesis and characterisation of **3.6** is outlined below. Firstly, we synthesised the starting material dicyclopentanyl thiosquarate by using the procedure described in Chapter 2. Subsequently, the reaction of dicyclopentanyl thiosquarte with 0.9 eq. benzylamine afforded intermediate **B2** in 33% yield. As shown in Figure 3.3.2, the signal of phenyl appears at 7.31 – 7.41 ppm, along with methyl hydrogen H1 appearing as a sharp doublet at 5.21 ppm. The methyl phenyl NH peak appears at 10.25 ppm as a singlet and the peaks of cyclopentanyl appears at 1.58 – 2.02 ppm as broad overlapped signals. Owing to the molecular flexibility, rotation of the side chains, and both intra- and intermolecular interactions, a series of additional signals of B2 were observed. For example, the extra methyl phenyl NH peak appears at 10.15 ppm while methyl hydrogen H1 appears as another singlet at 4.58 ppm. This behaviour also observed in the ^{13}C NMR spectrum, where carbon 3 appears at 175.6 and 173.2 ppm and carbon 4 gives two singlets at 183.3 and 182.7 ppm. All the peaks are the same as the previous reported data by Rawal, which supports our successful synthesis.[201]

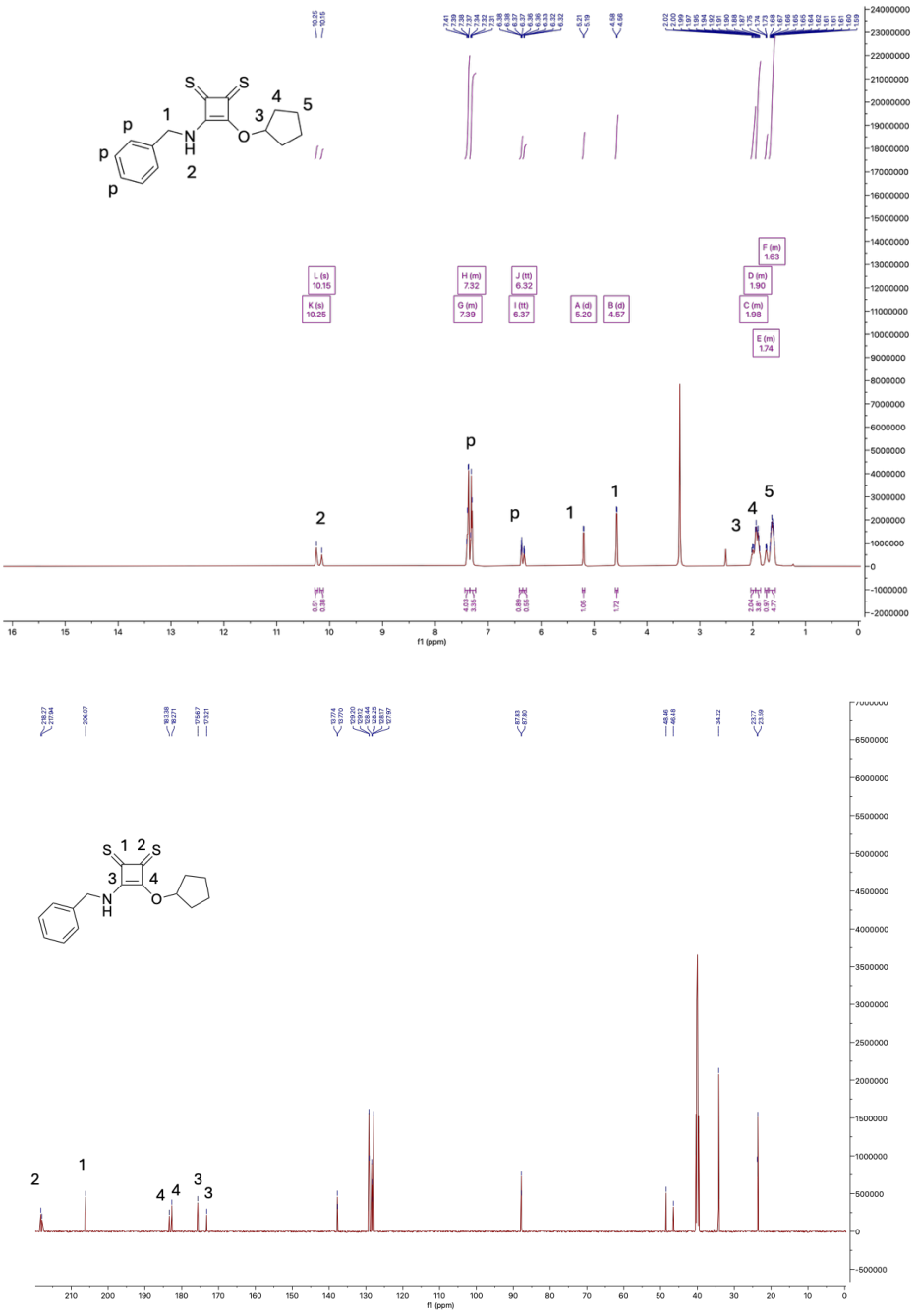

Figure 3.3.2. ^{1}H NMR and ^{13}C NMR spectrum of **B2**.

Finally, target molecule **3.6** was obtained in 72% yields through the reaction of the intermediate B2 with excess 6-aminoquinoline. As would be expected (Figure 3.3.3), the signal of phenyl appears at 7.34 – 7.53 ppm, along with methyl hydrogen H1 appearing as a sharp doublet at 5.39 ppm. Combining COSY experiments, the hydrogen H4 - H9 are able to be assigned. The quinoline NH appears in the most upfield position of the spectrum at 11.03 ppm as a broad singlet, while the methyl

phenyl NH appears at 8.79 ppm as a broad singlet as well. Given the potential similarity of ^{1}H NMR spectra between the targeted molecule and the isomer, ^{13}C NMR spectra is employed to further verify the product structure. As expected, the carbons of the thiosquaramide appears at 208.9 ppm and 169.4 ppm. This offers further evidence in support of our successful synthesis as the ^{13}C NMR of isomers typically shows four distinct peaks in the downfield region.

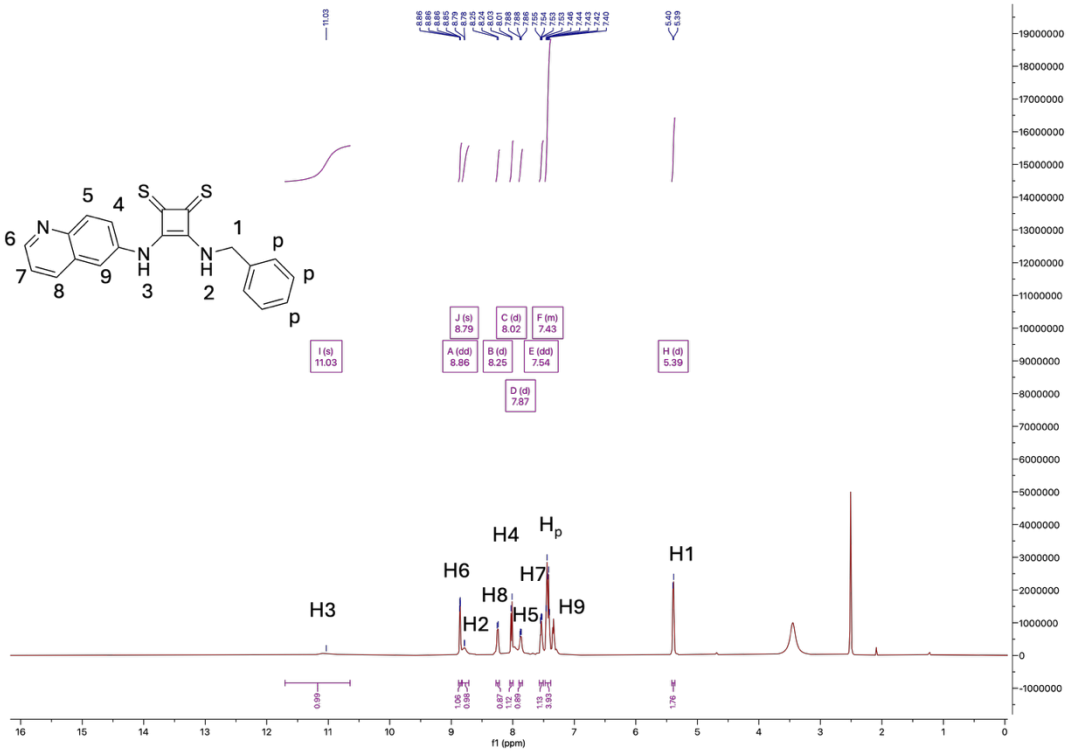

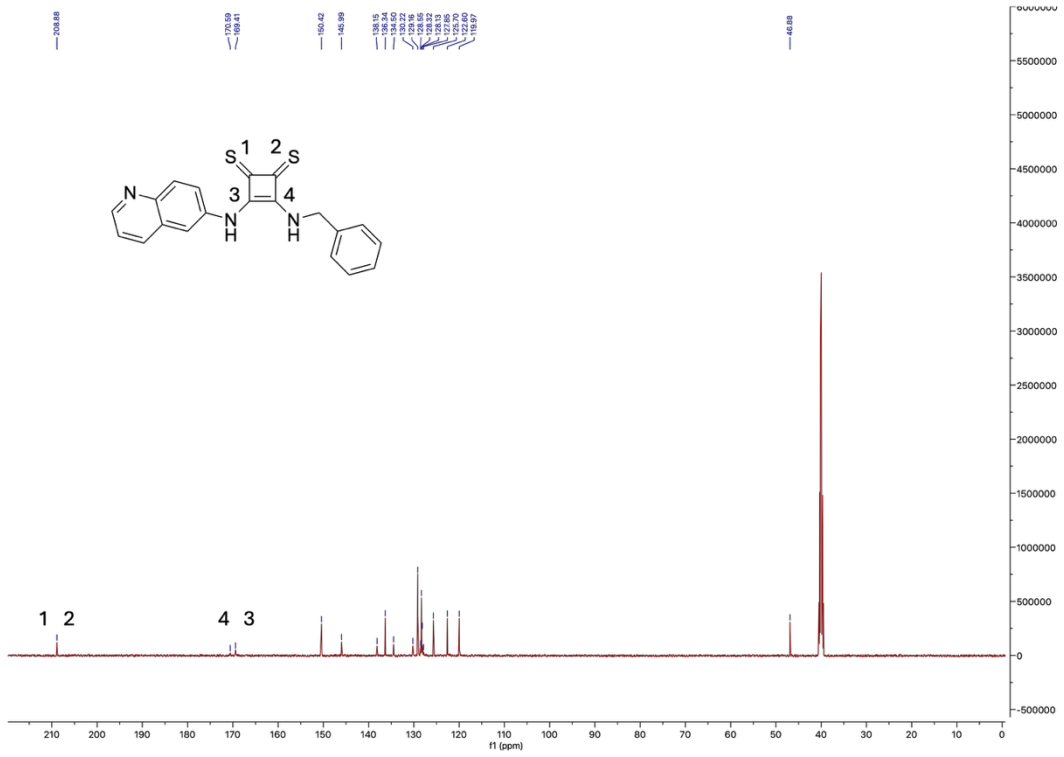

Figure 3.3.3. ^{1}H NMR and ^{13}C NMR spectrum of **3.6**.

Because of the high structural flexibility, sidechain rotations and potential intermolecular hydrogen bonding lead to some minor peaks observed in both ^{1}H NMR and ^{13}C NMR spectra.[240] For example, as shown in ^{13}C NMR, due to the rotation of the flexible methyl phenyl arm, there is a short signal of carbon 4 of the rotamer that appears at 170.5 ppm. This phenomenon is more evident in MeCN solution. Nevertheless, LC-MS and HRMS analyses support the purity of target molecules (Figure 3.3.4 and appendix).

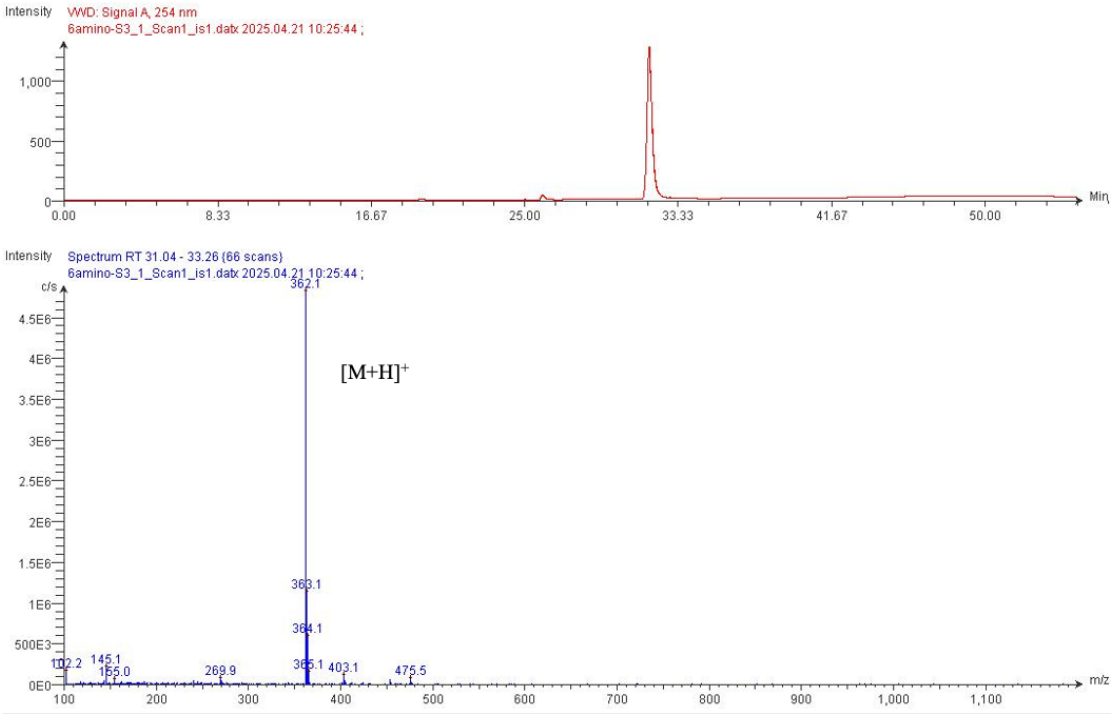

Figure 3.3.4. LC-MS analysis of **3.6**.

3.4 Physical properties.

With the successful synthesis of all target molecules, we next wished to ascertain their ability to bind and sense metal ions, however, prior to assessing the ion-binding capability of the target molecules, we measured the physicochemical properties of each . We first prepared 10 μM solutions of each receptor in MeCN and their UV-Vis spectra were collected over 250 - 500 nm with a data interval of 1 nm. As shown in Figure 3.4.1, because of the similar structure, all these compounds display a similar λ_{max} from 404 nm to 411 nm. The UV-Vis absorption spectrum of 6-aminoquinoline-based thiosquaramide **3.4** exhibits a λ_{max} of 411 nm; The UV-Vis absorption spectrum of **3.6** exhibits a λ_{max} of 404 nm, while two distinct absorption bands are shown at 363 nm and 273 nm. The introduction of an alkyl side chain seems to lead to a slight blue shift of absorbance maxima. Similarly, **3.5** displays a λ_{max} of 408 nm, while two distinct absorption bands are shown at 362 nm and 272 nm. This behaviour may arise because 6-quinoline is directly conjugated with the thiosquaramide scaffold, generating the strongest intramolecular charge transfer (ICT). In contrast, the butyl substituent lacks π-conjugation, which enlarges the HOMO-LUMO gap and thus induces a relatively large blue shift. For the benzyl substituent, partial excitation of the

phenyl moiety occurs; although it is separated from the backbone by a -CH_2- spacer and therefore not fully conjugated, it still produces a red shift relative to butyl. This behaviour was observed on 3-aminoquinoline-based thiosquaramides **3.1**-**3.3** as well.

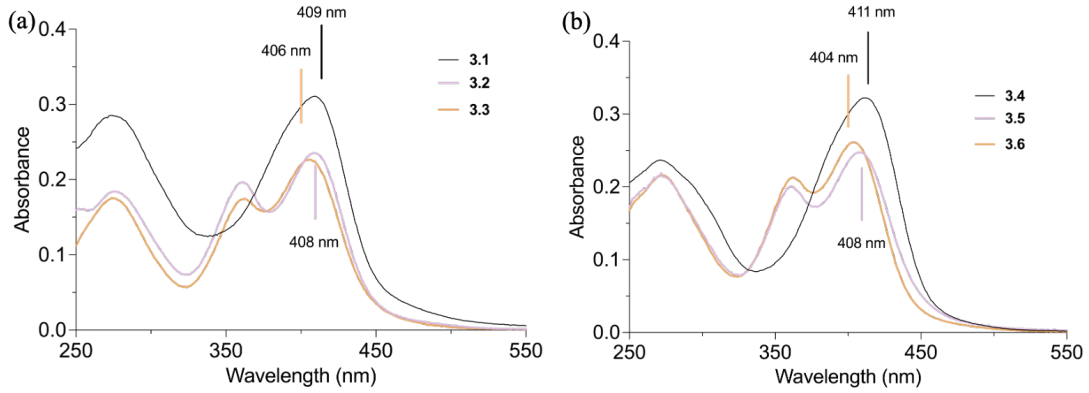

Figure 3.4.1. UV-Vis spectra of **3.1**-**3.6** (10 μM) in MeCN.

In addition, we evaluated the fluorescence properties of the target molecules in the absence of ions. Fluorescence spectra were recorded on a fluorometer at 20 °C using a 1 cm quartz cuvette. Stock solutions of the receptor were prepared in MeCN at 1 mM. The excitation wavelength was chosen from the absorption maximum of the receptor, and emission spectra were collected over 410 - 700 nm with a data interval of 1 nm. The excitation and emission slit widths were 20 nm and 10 nm, respectively. As shown in Figure 3.4.2, only weak emission was observed for the molecules under ion-free conditions. For 3-aminoquinoline-based thiosquaramide **3.1**-**3.3**, a faint emission band was observed at 466 nm, whereas 6-aminoquinoline-based thiosquaramide **3.4**-**3.6** exhibited an emission band at 463 nm. This faint emission may arise from both intermolecular and intramolecular π-stacking interactions of aromatic groups, leading to excimer emission.

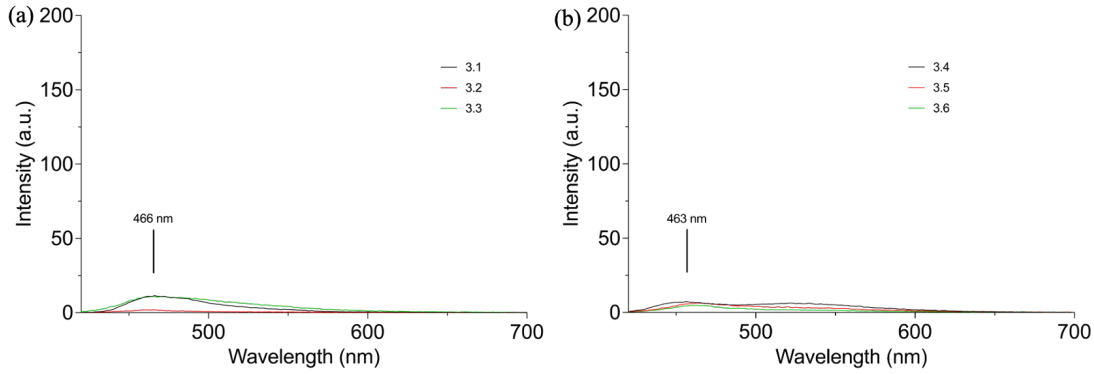

Figure 3.4.2. Emission spectra of (a) 3-aminoquinoline-based thiosquaramide **3.1**-**3.3** and (b) 6-aminoquinoline-based thiosquaramide **3.4**-**3.6**.

3.5 Cation binding studies

Based on the previous work in Chapter 2, the thiosquaramide scaffold has been proven to exhibit high metal affinity for metal toward metal ions in MeCN. We anticipated that quinoline thiosquaramides would be capable of displaying comparable metal binding properties. Moreover, the incorporation of quinoline, whose aromatic ring contains a nitrogen atom may act as an additional coordination site, could further modulate the molecule's binding preference toward specific metal ions. To verify our hypothesis, UV-vis titrations of each compound was conducted to evaluate the degree of association with a range of metal ions. Each compound was dissolved in MeCN to a final concentration of 0.01 mM, followed by the addition of up to 5 equivalents of metal ion solution (1 mM). An initial screening was performed to assess the binding capabilities of **3.6** with various metal ions (Ag^{+}, Ba^{2+}, Ca^{2+}, Cd^{2+}, Co^{2+}, Cu^{2+}, K^{+}, Li^{+}, Na^{+}, Ni^{2+}, Pd^{2+}, Zn^{2+}). After the addition of 1 equivalent of Ag^{+}, Cd^{2+}, Co^{2+}, Cu^{2+}, Ni^{2+}, Pd^{2+} and Zn^{2+}, significant changes were observed. In contrast, there are no changes observed upon addition of Ba^{2+}, Ca^{2+}, K^{+}, Li^{+} and Na^{+}. In addition, we conducted the same preliminary experiments on the other receptors. The results revealed that all these receptors displayed a spectroscopic response to Ag^{+}, Cd^{2+}, Co^{2+}, Cu^{2+}, Ni^{2+}, Pd^{2+} and Zn^{2+}. The UV/Vis screen of receptors **3.4** - **3.6** are shown in Figure 3.5.1 as examples.

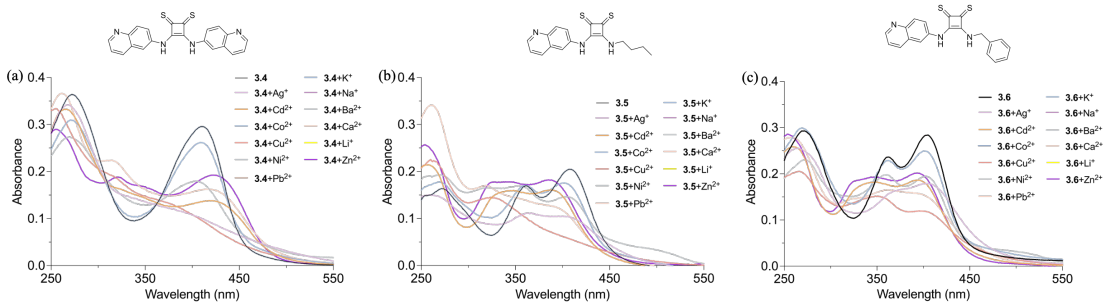

Figure 3.5.1. UV spectra of the addition of 1 eq. different metal ions to a 1 mM receptor solution in MeCN (a) **3.4**; (b) **3.5**; (c) **3.6**.

Subsequently, to explore the response in moe detail, full titrations were conducted by the addition of Ag^{+}, Cd^{2+}, Co^{2+}, Cu^{2+}, Ni^{2+}, Pd^{2+} and Zn^{2+} to **3.6**. Theresults of each titration were then analysed by using the bindfit v0.5 open-access supramolecular analysis tool to measure binding stoichiometry and affinity.[211,212] Similar to the compounds presented in Chapter 2, a 2:1 (host : guest) yielded the best fit in all cases, where, interestingly, the introduction of an extra binding site didn't affect the binding stoichiometry. This result was supported by Job's plot analysis, where the maximum was at the mole fraction of around 0.67 (Figure 3.5.2 (c)). For example, as shown in Figure 3.4.2, upon the initial addition of 0.1 equivalent of Zn^{2+}, a pronounced change in the UV spectrum of receptor **3.6** was observed, whereas the spectrum remained essentially unchanged after the addition of 1 equivalent of Cd^{2+}, indicating saturation of the binding interaction. The addition of 1 eq. Cd^{2+} resulted in significant hypochromism at 404 nm, a blue shift to 390 nm, and pronounced changes at 359 nm and 325 nm, along with the appearance of isosbestic points at 351 nm and 303 nm. These notable spectral changes indicate strong metal–receptor interaction. Similar behaviour was observed for Ag^{+}, Cd^{2+}, Co^{2+}, Cu^{2+}, Ni^{2+} and Pd^{2+}. A summary of the binding properties of **3.6** towards various metals is shown in Table. 3.5.1 showing receptor **3.6** exhibited high sensitivity toward these tested metal ions, yielding association constants (K_a), which can be as high as 10^6 M^{-1}. Again, a 2:1 stoichiometry gave the best fit in all cases, and Job's plot provides compelling evidence in support of our results, indicating that higher-order complexation appears to occur under these experimental conditions. Also, as shown in Figure 3.5.2(a) and (b), a pronounced inflection point appears at 0.5 equivalents, which further substantiates our conclusion. Some datasets exhibit large errors or could not be adequately fitted. As discussed in

Chapter 2, the thiosquaramides self-assemble in solution via hydrogen bonding to form one-dimensional hydrogen-bonded chains or aggregate through π-π stacking. Effective complexation with cations requires prior disruption of these self-assembled structures. However, this process is not captured by the conventional 2:1 (host:guest) binding model, leading to poor or unfittable data.

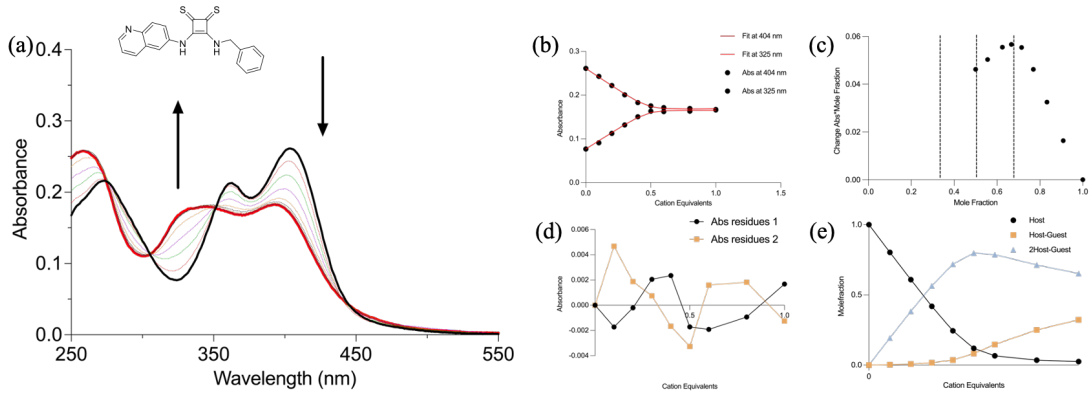

Figure 3.5.2. Uv-vis titration data for **3.6** towards Cd^{2+}. (a) Uv-vis spectra of **3.6**(10 μM in MeCN) upon addition of increasing molar equivalents of Cd^{2+} (0 - 10 eq.). (b) Fitplot of **3.6** towards Cd^{2+} in a 2:1 binding model. (c) Job's plot of Cd^{2+} titration for **3.6**. (d) Residuals plot of **3.6**. (e) Mole fraction plot of Host vs. Host-Guest fraction with increasing guest concentration for **3.6**.

Table 3.5.1. A summary of UV-vis titration results for the binding behaviour of **3.6** towards various metal ions.[a]

Metal ions	K_{11} (M^{-1})	K_{12} (M^{-1})	Binding mode
Ag^{+}	1.3×10^{3}	1.0×10^{5}	2:1
Cd^{2+}	3.6×10^{6}	4.0×10^{6}	2:1
Co^{2+}	-[b]	-[b]	2:1
Cu^{2+}	3.4×10^{3}	9.9×10^{4}	2:1
Ni^{2+}	-[b]	-[b]	2:1
Pd^{2+}	1.5×10^{3}	9.2×10^{3}	2:1
Zn^{2+}	-[b]	-[b]	2:1

a The errors of the K_a value shown in the table are < 25%. b High errors result in unreliable K_a value.

With this preliminary knowledge in hand, we next conducted similar metal ion titration experiments with **3.1** – **3.5**. The results revealed that **3.1** – **3.5** could effectively detect Ag^{+}, Cd^{2+}, Co^{2+}, Cu^{2+}, Ni^{2+}, Pd^{2+} and Zn^{2+} as well and induced similar spectral responses, typically best described again by a 2:1 binding model (See appendix). Subsequently, we focussed on the Zn^{2+} binding behaviour of these compounds as the binding behaviour was found to be most consistent with this ion. As shown in Table 3.5.2, consistent with the previous observations, a portion of the datasets could not be satisfactorily fitted to the model. Nevertheless, comparison between **3.1** and **3.4** suggests that 3-aminoquinoline-based thiosquaramide derivatives seem to exhibit higher affinity for Zn^{2+}.

Table 3.5.2. A summary of UV-vis titration results for the binding behaviour of **3.1**-**3.6** towards Zn^{2+}.[a]

Metal ions	K_{11} (M^{-1})	K_{12} (M^{-1})	Binding mode
3.1	1.0×10^5	9.2×10^5	2:1
3.2	-[b]	-[b]	2:1
3.3	1.4×10^5	3.6×10^5	2:1
3.4	8.0×10^4	3.3×10^5	2:1
3.5	-[b]	-[b]	2:1
3.6	-[b]	-[b]	2:1

a The errors of the K_a value shown in the table are < 25%. b High errors result in unreliable K_a value.

3.6 Fluorescent studies

Having established that compounds **3.1** – **3.6** are capable of metal ion recognition through UV/Vis analysis, we next sought to investigate whether ion binding could also influence their excited-state properties. The fluorescence behaviour of each compound in MeCN upon interaction with the same metal ions was studied, aiming to evaluate their sensing performance. Again, following the method and conditions described in section 3.4, we took compound **3.6** as an example. The compound was dissolved in MeCN to obtain a 1 mM solution. The fluorescence response was monitored by incremental addition of Zn^{2+} (50 mM, Zinc perchlorate) and spectral changes were

recorded accordingly. As shown in Figure 3.6.1, the MeCN solution of **3.6** displayed almost no fluorescent emission on its own. Upon the addition of Zn^{2+}, a new emission peak emerged at 539 nm. Further additions up to 1 equivalent Zn^{2+} resulted in no further changes in fluorescence intensity. This observation corresponds to the UV titration data, which indicate that the binding interaction reaches near saturation upon the addition of 1 eq. Zn^{2+}. We attempted to fit the data to a 2:1 binding model; however, the fitting was unsuccessful in this case, possibly due to the aggregation of the compound, which may have influenced the overall fluorescence output.[241]

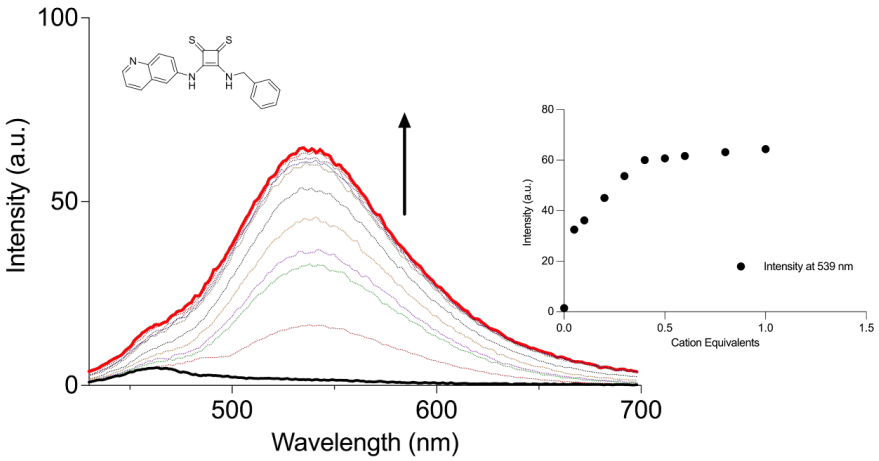

Figure 3.6.1. Zn^{2+}-induced fluorescence response of **3.6** (1 mM) in MeCN. The excitation wavelength was set to λ_ex= 406 nm, and emission was collected over 412 - 700 nm (1 nm interval) with slit widths of 20 nm (Ex) and 10 nm (Em). {insert} Emission intensity at 539 nm plotted against the equivalents of added Zn^{2+}.

According to the findings described in the previous section, **3.6** can associate with various metal ions to form 2:1 complexes. Subsequently, cation titration experiments were conducted to assess its fluorescence response behaviour to a range of metal ions (Ag^{+}, Cd^{2+}, Co^{2+}, Cu^{2+}, Ni^{2+} and Pd^{2+}). Notably, the fluorescence behaviour towards these ions is similar to that observed for Zn^{2+}. As shown in Figure 3.6.2, these ions (1, 10 and 50 equivalents) are capable of inducing an increase in fluorescence intensity, among which Ag^{+}, Cd^{2+}, Co^{2+}, Ni^{2+} and Pd^{2+} exhibit similar intensities, whereas Cu^{2+}

induces a slightly stronger fluorescence response than the other ions. Upon addition of 1 equiv. of the ion, the fluorescence intensity increased markedly and nearly reached its maximum, indicating that the fluorescence of almost all molecules had been switched on. Further addition of excess ions (50 equivalents) afforded only a slight additional increase. We also extended the experiment to Cl^-. Interestingly, although **3.6** is capable of binding Cl^- and forming the receptor-anion complexes, the addition of Cl^- does not switch on the fluorescence of the receptor.

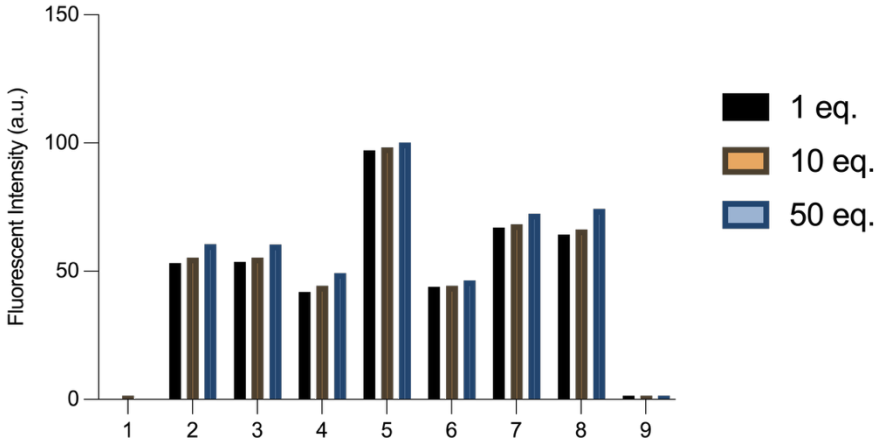

Figure 3.6.2. Fluorescence intensity of **3.6** at 539 nm in MeCN upon addition of 1, 10 and 50 equivalents of various ions. Data set (1) **3.6** (2) **3.6**+Ag^+ (3) **3.6**+Cd^{2+} (4) **3.6**+Co^{2+} (5) **3.6**+ Cu^{2+} (6) **3.6**+Ni^{2+} (7) **3.6**+Pd^{2+} (8) **3.6**+Zn^{2+} (9) **3.6**+Cl^-. Excitation wavelength: 400 nm.

3.7 Anion binding studies

Meanwhile, as discussed in Chapter 2, thiosquaramide has been demonstrated to possess strong anion binding capability.[129,242] We anticipated that quinoline thiosquaramide may exhibit a similar anion binding behaviour. The affinity of each receptor toward Cl^- was evaluated by ^1H NMR titration in DMSO-d_6. Receptor **3.6** was first selected and a 0.4 mM DMSO-d_6 solution was prepared. Upon the addition of Cl^-, a pronounced downfield shift of the NH peaks from 11.01 ppm to 11.62 ppm was observed (Figure 3.7.1), indicating a binding interaction between the thiosquaramide NH proton and Cl^-.

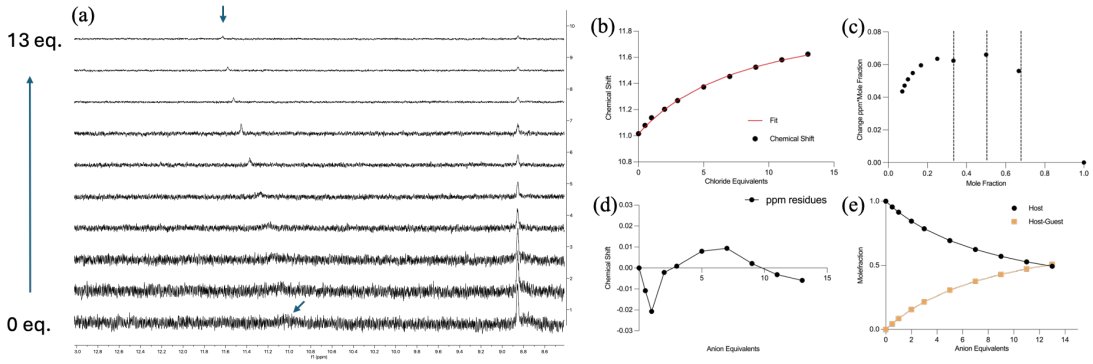

Figure 3.7.1. ^{1}H NMR titration data for **3.6** towards Cl^-. (a) ^{1}H NMR stackplot of **3.6**(0.4 mM in DMSO-d_6) upon addition of increasing molar equivalents of TBACl (0 - 13 eq.). (b) Fitplot of **3.6** towards Cl^- in a 1:1 binding model. (c) Job's plot of Cl^- titration for **3.6**. (d) Residuals plot of **3.6**. (e) Mole fraction plot of Host vs. Host-Guest fraction with increasing guest concentration for **3.6**.

Subsequently, using the same methodology, the chloride-binding properties of samples **3.1** - **3.5** were evaluated, revealing that their affinities for Cl^- were similar to those observed for **3.6**. The binding constants of all these receptors towards Cl- were summarised in Table 3.7.1. The binding affinities of **3.1** - **3.6** were in the range of 230 - 340 M^{-1} and all the errors are below 10%. Overall, the 6-aminoquinoline substituted receptors **3.4** - **3.6** showed higher affinities for chloride than those substituted by the 3-aminoquinoline scaffold (**3.1**-**3.3**). Normally, the more acidic NH group of squaramide derivatives display higher binding affinity for anions. The 3-amino group occupies the β position of the pyridine ring and therefore experiences a stronger influence from the adjacent ring nitrogen, whereas the 6-amino group lies on the benzene ring and is only weakly affected by the ring nitrogen. Therefore, 3-aminoquinoline-based thiosquaramides seem to have more acidic NH. However, 3-aminoquinoline-substituted thiosquaramide derivatives with higher NH acidity exhibited lower binding affinity for Cl^- than 6-aminoquinoline-substituted thiosquaramide derivatives. This unexpected trend might be caused by an unpredictable penalty arising from the high conformational freedom.[129]

Table 3.7.1. A summary of ^{1}H NMR titration results for the binding behaviour of **3.1** - **3.6** towards Cl^-.[a]

	3.1	**3.2**	**3.3**	**3.4**	**3.5**	**3.6**
K_a (M^{-1})	-[b]	230	230	270	340	260

a The error of the *K* value is < 10%. b The disappearance of NH peaks at high anion concentration prevents the calculation of the *K* value.

Furthermore, to compare the chloride affinity of quinoline thiosquaramide and quinoline oxosquaramide, we obtained the oxo analogue (**3.2B**) of **3.2**. Identical ^{1}H NMR titrations established that this molecule binds chloride in a 1:1 model with the K_a value of 246 M^{-1}. Theoretically, the thio analogue **3.2** should exhibit higher NH acidity than oxo analogue (**3.2B**) and thus a stronger binding affinity towards Cl^-. However, the results show that the chloride affinity of **3.2** is reduced relative to the oxo analogue (**3.2B**). This may arise from the penalty of higher conformational freedom of thiosquaramides.[129,243]

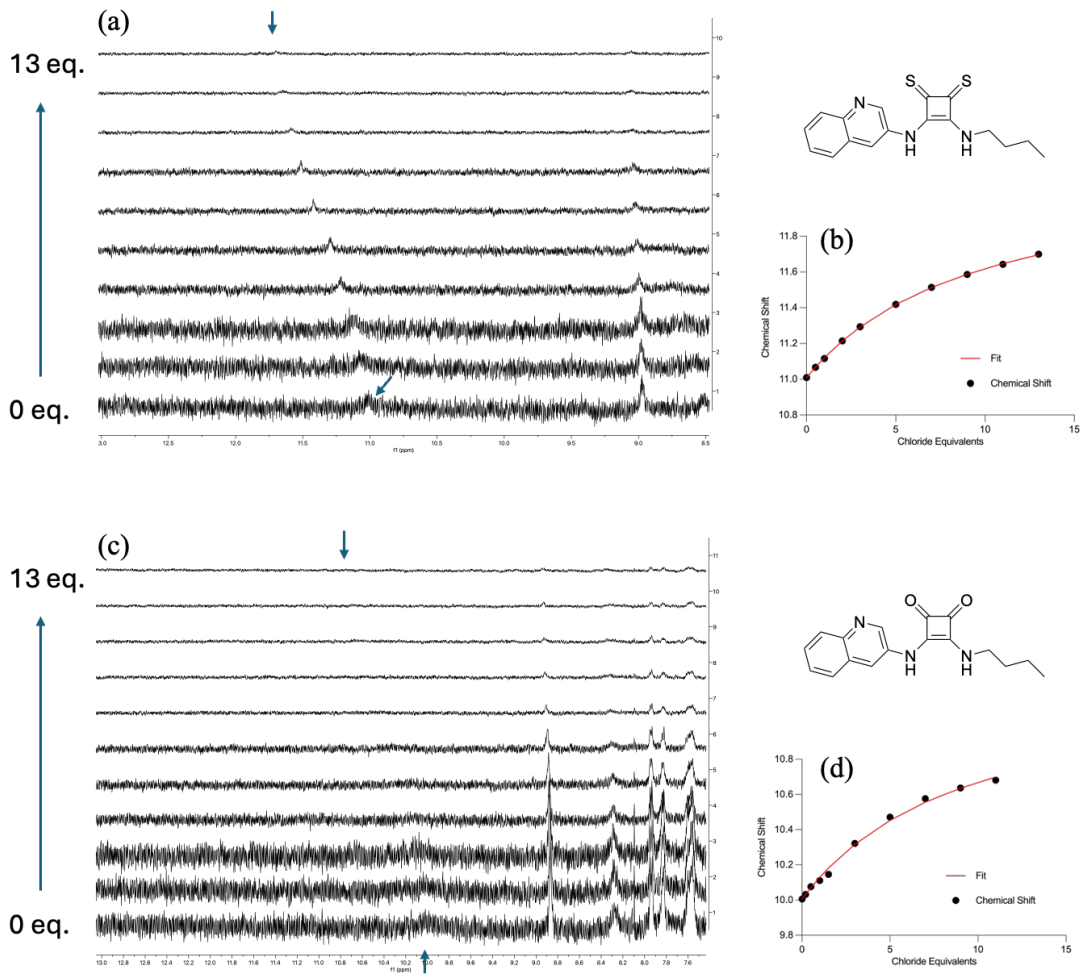

Figure 3.7.2. (a) ^{1}H NMR titration of **3.2** with Cl^- in DMSO-d_6. (b) Fitplot for NH proton at δ = 11.01 ppm. The data were fit to a 1:1 binding model. (c) ^{1}H NMR titration of **3.2B** with Cl^- in DMSO-d_6. (b) Fitplot for NH proton at δ = 10.00 ppm. The data were fit to a 1:1 binding model.

3.8 Zn^{2+} transport studies

As discussed in previous sections, we have shown that quinoline thiosquaramides display strong binding affinity toward both anions and cations. As an essential biological metal ion, Zn^{2+} contributes to the structural stabilisation of many proteins and is critically involved in insulin secretion, neural signaling, and immune regulation.[196,244–247] With the clear ability of quinoline thiosquaramides to bind to Zn^{2+} and exhibit 'switch-on' fluorescent behaviour, we next wished to explore whether they might be capable of Zn^{2+} transport. Again, the FluoZin-3 assay was employed to evaluate the transport performance. Following the method described in Chapter 2, 0.4

mM liposomes containing FluoZin-3 were prepared in 0.01 M PBS solution. Given that the compounds exhibit a fluorescence response upon binding with Zn^{2+}, we first performed several control experiments under the same assay conditions (Excitation 494 nm; Emission 519 nm). As shown in Figure 3.8.1 (a) and (b), we take **3.6** as an example. The individual addition of either Zn^{2+} or receptor to liposomes did not result in any enhancement of fluorescence intensity. To assess the inherent fluorescence of receptors under the assay conditions, both **3.6**(5 μM) and Zn^{2+}(0.1 mM) were introduced to 0.01 M PBS solution without liposomes. The results indicated that the receptor displayed only a minimal fluorescence response (F = 0.68 a.u., at 270 s) under the experimental conditions employed in these assays. In contrast, in the presence of liposomes containing FluoZin-3, the addition of both **3.6** and Zn^{2+} lead to a pronounced fluorescence enhancement, giving F = 30.3 a.u. at 270 s. This corresponds to an approximately 45-fold higher than the control experiment recorded without liposomes. This indicates that, beyond the receptor's inherent fluorescence, the fluorescence of FluoZin-3 encapsulated in liposomes was switched on as well. Subsequently, the experiments were extended to other compounds, and the results revealed that **3.1** - **3.5** displayed properties similar to those of **3.6** (Figure 3.8.1(c)). FluoZin-3 is almost non-fluorescent on its own, but it can exhibit an increase in fluorescence when it binds to Zn^{2+}. The significant enhancement of fluorescence emitted by FluoZin-3 indicated that quinoline thiosquaramide derivatives displayed Zn^{2+} ionophoric activity and switched on FluoZin-3 by transporting Zn^{2+} into liposomes. In the final set of experiments, receptor **3.6** with various concentrations was assessed in detail (Figure 3.8.1(d)). Higher concentrations of **3.6** produced stronger fluorescence responses, owing to more efficient ion transport, which further supported our conclusion that these thiosquaramide-quinoline conjugates are efficient Zn^{2+} ionophores that display typical dose-dependent responses.

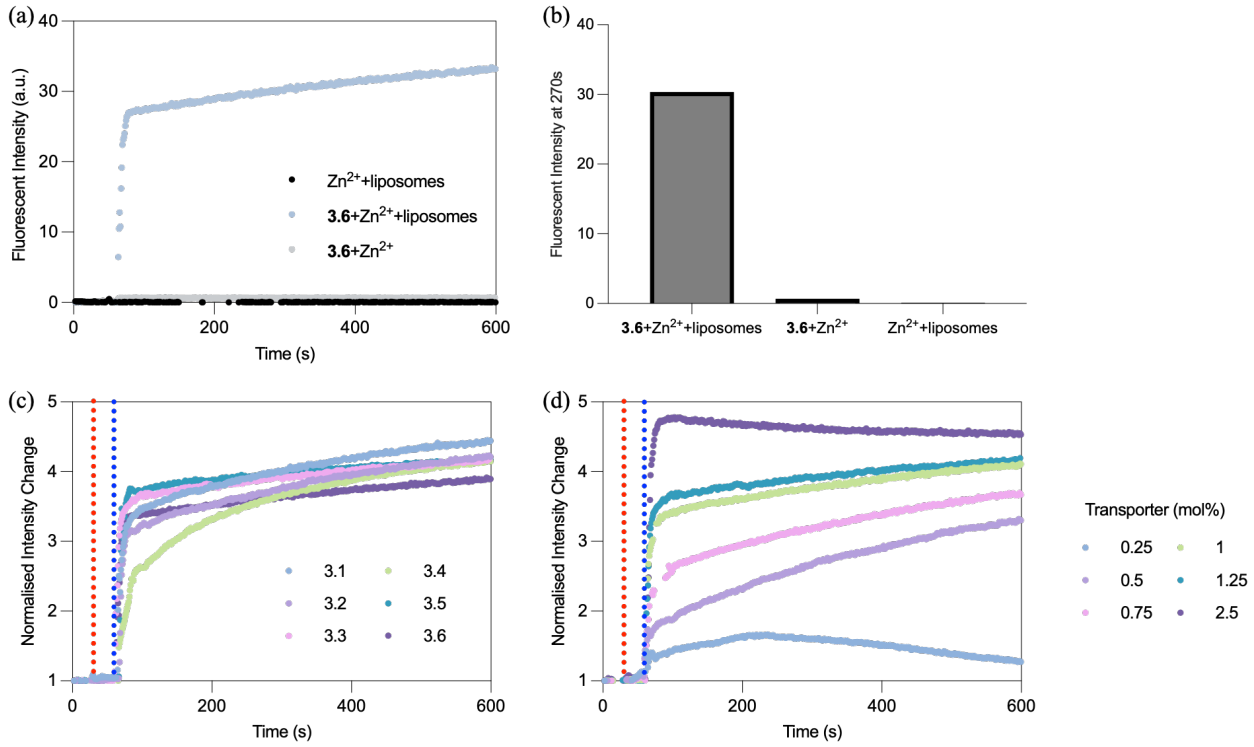

Figure 3.8.1. (a) Control experiments: (1) the addition of 0.1 mM Zn^{2+} to liposomal FluoZin-3 (0.4 mM, in 0.01 M PBS); (2) the addition of **3.6**(5 μM) followed by 0.1 mM Zn^{2+} to liposomal FluoZin-3 (0.4 mM, in 0.01 M PBS); (3) the addition of 0.1 mM Zn^{2+} to **3.6**(5 μM) in 0.01 M PBS solution. (b) Column graph of fluorescent intensity at 270s after the addition. (c) Screen of the addition of **3.1** - **3.6**(5 μM, red line) to liposomal FluoZin-3(0.4 mM, in 0.01 M PBS)followed by 0.1 mM Zn^{2+} (blue line). (d) Normalised intensity changes after the addition of receptor **3.6**(red line) followed by 0.1 mM Zn^{2+}(blue line). Concentration used: 0.25 mol%, 0.5 mol%, 0.75 mol%, 1 mol%, 1.25 mol%, 2.5 mol%.

Given that quinoline thiosquaramides are intrinsically fluorescent, we designed an assay in which, instead of encapsulating Fluozin-3, the vesicles were loaded with $ZnCl_2$. If a fluorescence turn-on were observed, it would indicate that the molecule can traverse the membrane and bind the intravesicular Zn^{2+} directly. Large unilamellar vesicles (LUVs) were prepared as above and loaded with $ZnCl_2$ (25 mM). To avoid interference from chloride in the external phase, PBS was replaced with $NaNO_3$ (225 mM) as the background solution. Compound **3.6** was then added under fluorometric monitoring (Figure 3.8.2). Interestingly, relative to the fluorescence of the molecule-

ion mixture in bulk, the addition of the ionophore to $ZnCl_2$-loaded vesicle suspensions produced no discernible fluorescence increase. While disappointing, this lack of response is plausibly attributable to the compound's low fluorescent intensity, even in the presence of Zn^{2+}, and suggests that any fluorescence response inside the vesicles is too slight to be detected. However, this result does not detract from the earlier results that show the receptors clear ability to function as an ion transporter.

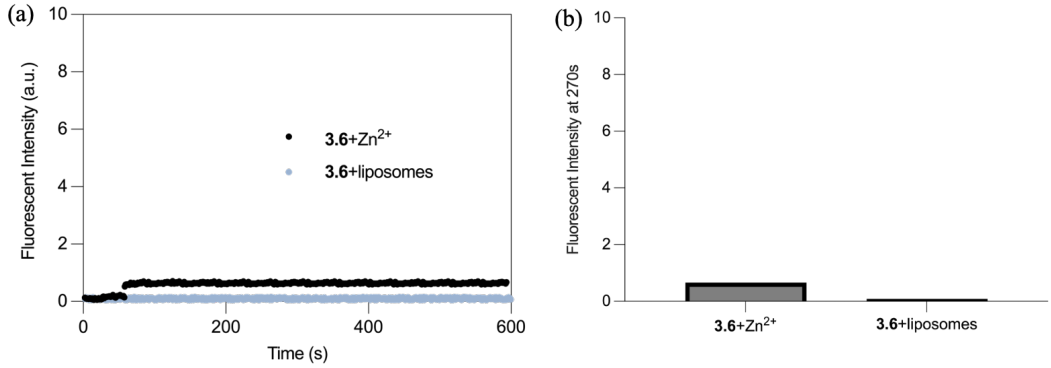

Figure 3.8.2. (1) the addition of 0.1 mM Zn^{2+} to **3.6**(5 μM) (2) the addition of **3.6**(5 μM) to liposomes containing $ZnCl_2$ (25 mM, in 225 mM $NaNO_3$);

3.9 Cl^- transport studies

Finally, we wished to measure anionophoric ability of these receptors. In the previous subsection, we demonstrated that quinoline thiosquaramides are able to form complexes with Cl^-, and in Chapter 2, we established the capability of thiosquaramides for chloride transport. To determine whether quinoline thiosquaramides still retain chloride-transport activity, we again employed the lucigenin assay to evaluate their performance at physiological pH. As an initial screen, we examined compounds **3.1-3.6** at 5 μM. Unless otherwise stated, the excitation and emission for lucigenin assay is set to 430 nm and 505 nm, respectively. Under these conditions (0.4 mM liposomes, 225 mM $NaNO_3$, 7.2 pH), only **3.5** exhibited measurable transport activity after the addition of NaCl pulse (75 μL, 1 M in mM $NaNO_3$)(Figure 3.9.1).

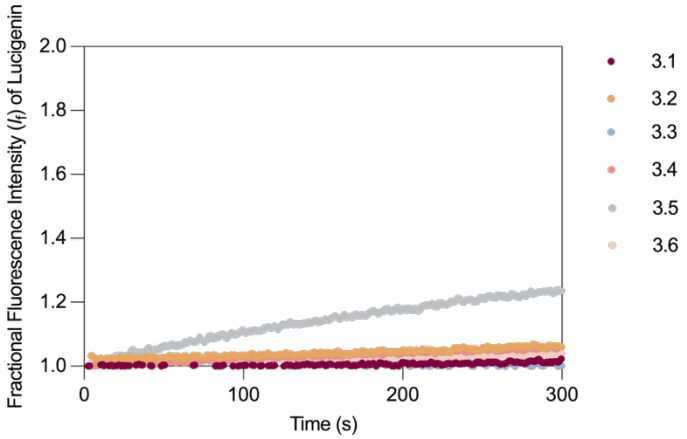

Figure 3.9.1. The change of fractional fluorescent intensity with the addition of **3.1** - **3.6** (5 μM) and NaCl (75 μL, 1 M) to 0.4 mM liposomes containing lucigenin (in 225 mM $NaNO_3$).

As shown in Figure 3.9.2, a detailed titration was conducted for **3.5**. As the transporter concentration increased, the chloride transport rate rose markedly. Hill plot analysis of the titration data afforded an EC_{50} value of 3.0. In comparison with compound **2.3** reported in Chapter 2 (EC_{50}=0.13), the chloride transport rate is substantially lower. Considering the chloride-transport behaviours across both chapters, it appears that for thiosquaramides under physiological pH, scaffolds bearing more acidic NH groups exhibit relatively diminished transport activity, possibly because excessive NH acidity promotes extensive deprotonation and thereby reduces anion affinity.[129,243] Nonetheless, the observed results further confirm the anionophoric ability of 3.5 and provide an interesting preliminary result to suggest there is significant room for design optimisation of these receptors; not just to increase metal transport efficiency, but equally for anion transport efficiency.

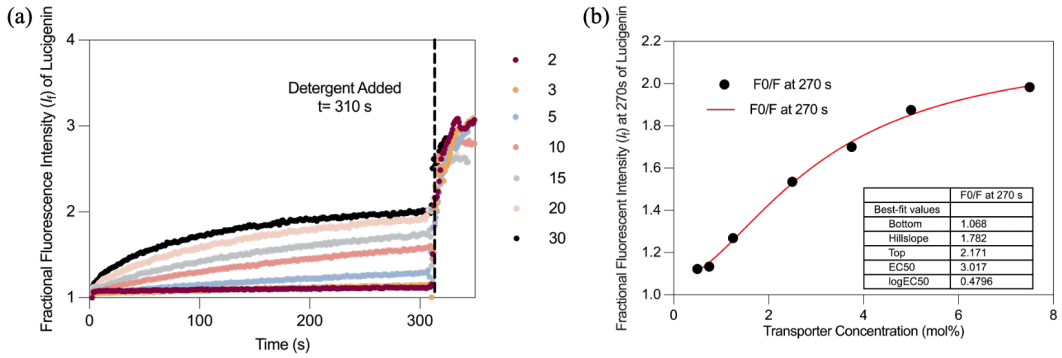

Figure 3.9.2. The change of fractional fluorescent intensity with the addition of **3.5** and NaCl (75 µL, 1 M) to liposomes containing lucigenin (in 225 mM $NaNO_3$) at various transporter concentrations (mol%). (d) Hill plot of the fractional fluorescence intensity with the addition of **3.5** and NaCl (75 µL, 1 M) to liposomes containing lucigenin (in 225 mM $NaNO_3$) at various transporter concentrations (mol%) recorded at 270 s.

3.10 Conclusion and future work

In conclusion, we report the first synthesis of a series of 'switch-on' fluorescent sensors constructed with the thiosquaramide motif. Their ion-binding ability and fluorescence response behaviour have been evaluated by using a range of spectroscopic measurements. With the well-developed method from Chapter 2, the synthesis of quinoline thiosquaramide is evidently not trivial but can be useful to make interesting molecule in acceptable yields. Despite the purification challenges arising from the formation of isomers, the process was streamlined by altering the synthetic pathway to eliminate a purification step. This strategy involved quinoline as a fluorophore being introduced to thiosquarate scaffolds in the 2nd synthetic step, and had the added benefit ofproviding additional ion-binding sites. These novel motifs all show high levels of both anion and cation binding performance (Ag^{+}, Cd^{2+}, Co^{2+}, Cu^{2+}, Ni^{2+}, Pd^{2+}, Zn^{2+} and Cl^{-}), forming 2:1 metal-receptor complexes in MeCN and 1:1 chloride-receptor complexes in DMSO. Notably, the receptors themselves are essentially non-fluorescent, yet their fluorescence could be switched on upon binding with specific metal ions, such as Zn^{2+}. Interestingly, while the receptors were also able to interact with chloride, such interactions failed to induce any fluorescence activation. Using the FluoZin-3 liposome assay, we also evaluated the Zn^{2+} transport performance

of **3.1** – **3.6**, where each of them displays rapid and efficient transport behaviour. In parallel, the lucigenin assay confirmed that compound **3.5** also mediates chloride transport with intermediate kinetics under physiological pH. The present findings establish a basis for the design of more efficient fluorescent metal ion ionophores and have the potential to promote further studies on ion distribution and localisation in biological systems. In Chapter 2, we discussed that although thiosquaramides provide a powerful platform for cation recognition, the parent structure exhibits insufficient ion selectivity. In this chapter, while appending fluorophores to the scaffold, we also attempted to impose preorganization to increase the selectivity by employing quinoline as fluorphore with one more binding site. However, these efforts proved unsuccessful. Prior studies on cation receptors indicate that preorganization effectively enhances cation selectivity, particularly in macrocyclic systems, where cavity size largely decides binding performance. Accordingly, we adopted a new macrocyclic squaramide design: two squaramide units linked by long alkyl chains, with an aromatic ring inserted centrally to increase rigidity and thereby reduce entropic penalties and additional energetic costs upon ion binding. In parallel, naphthalimides or quinoline were attached to the side chains as fluorphores.

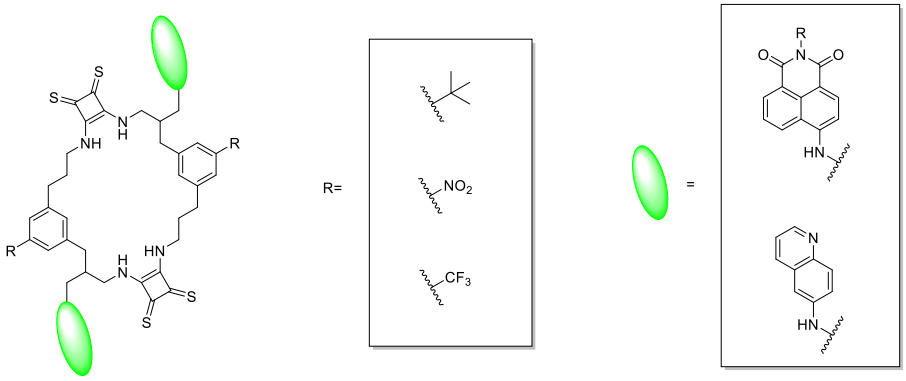

Figure 3.10.1. Potential future direction for the development of thiosquaramide-based fluorescent ion transporter.

Chapter 4: Bipodal squaramide and thiosquaramide ion transporters

4.1 Introduction

Chloride (Cl^-) represents one of the most ubiquitous and functionally indispensable anions in both natural and biological systems.[91,248–250] It serves as a pivotal regulator of osmotic pressure and electrolyte balance in cells and plays a significant role in neuronal signal transmission.[248,251] Beyond these functions, Cl^- is involved in the maintenance of acid–base homeostasis in erythrocytes and in diverse enzymatic catalytic processes.[248,249,252] From an industrial perspective, chloride and its derivatives find extensive applications in water treatment, the manufacture of poly(vinyl chloride) (PVC), and dye fixation.[27,253,254] Given its dual significance in biology and industry, chloride is commonly employed as a model target anion in supramolecular chemistry. Synthetic anion receptors derived from urea[255], thiourea[256], squaramide[184] and thiosquaramide[129] scaffolds have been extensively investigated owing to their selective binding affinity toward chloride.[257] Hossin and co-workers reported two cleft-type receptors based on a meta-xylylene framework,[258] which were functionalized with thiourea and urea, displaying binding affinities for halides and oxoanions. The improved neutral receptor based on a bipodal thiourea framework exhibits stronger binding affinities toward halide anions,[259] and produces pronounced colour changes in the presence of F^-, $H_2PO_4^-$, and CH_3COO^-, demonstrating that thiourea functionalization enhances anion recognition and provides potential for naked-eye detection.

Recently, squaramides and thiosquaramides have been widely employed in the development of ion receptors due to their strong hydrogen-bond-donating ability.

Wang and co-workers reported a class of tripodal receptors centred on a squaramide core for the selective recognition of SO_4^{2-}. Squaramide scaffolds was incorporating to the structure to serve as strong hydrogen bond donors, thereby the receptors are capable of establishing multiple hydrogen-bonding interactions with sulfate in solution, exhibiting remarkable affinity and selectivity toward this anion (Figure 4.1.1).[260] Subsequently, Romanski further refined this class of molecules by introducing cation-binding sites into the side chains of squaramides, enabling the molecules to interact with both sulfate and their corresponding cations, thereby enhancing the binding affinity.[261] It was further demonstrated that such tripodal squaramide receptors are capable of self-assembling into hydrogels at 37 °C under

physiological conditions, primarily facilitated by hydrogen bonding and hydrophobic interactions.[262]

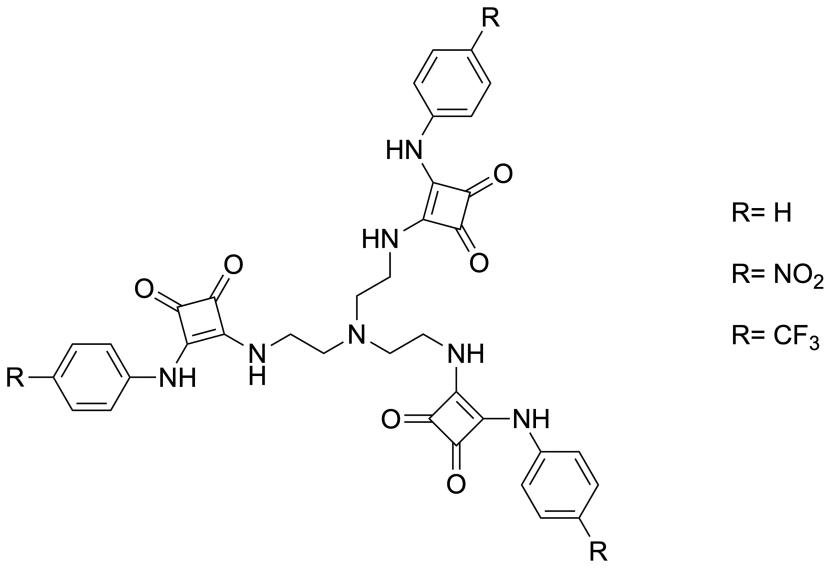

Figure 4.1.1. Molecular structures of tris-(squaramide) receptors reported by Wang and co-workers.[260]

Similarly, a new type of calix[4]arene-based receptor functionalized with dual squaramide units has been reported for colourimetric anion sensing. These kinds of receptors are capable of binding anions via either hydrogen-bonding interactions or acid-base processes. Deprotonation-induced effects give rise to distinct colour changes in the presence of basic anions (*eg.* F^- and AcO^-), allowing for rapid and visual anion detection.[193]

In addition, Soberats and co-workers reported a class of squaramide-based host molecules with Janus-like characteristics, which are capable of interacting with ion pairs and undergoing conformational transformations in the presence of ammonium trimesoate compounds (Figure 4.1.2). The study demonstrates that these hosts not only efficiently bind anions but also exhibit distinctive cooperative recognition behavior when cations are simultaneously present.[263]

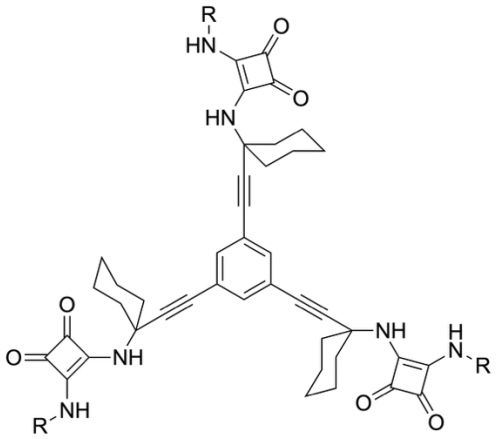

Figure 4.1.2. Structure of squaramide-based tripodal host molecules reported by Soberats.[263]

Zdanowski and co-workers reported a structure based on an L-ornithine scaffold, consisting of two squaramides (anion binding sites) and a crown ether (cation binding site). This molecule are capable of forming stable complex with both cations and anions (Figure 4.1.3 (a))), thereby facilitating the transfer of chloride salts from the aqueous phase into the organic phase.[264] Zalubiniak also introduced a kind of ditopic receptor designed on the basis of a 2,2-bis(aminomethyl)-propionic acid scaffold, which employ multiple hydrogen-bonding sites to achieve cooperative binding of anions and cations, thereby significantly enhancing the efficiency and selectivity of ion-pair recognition (Figure 4.1.3 (b) and (c)).[265]

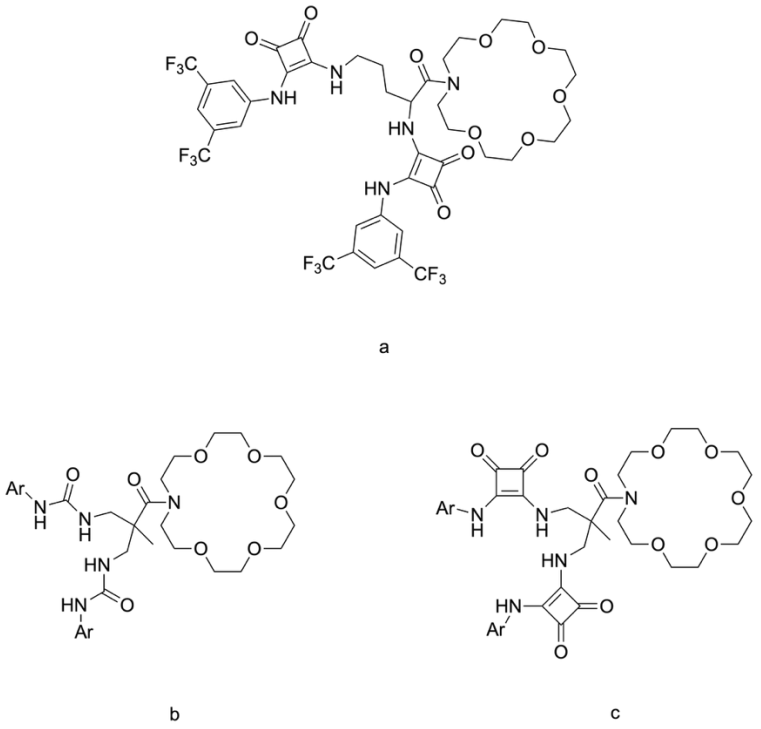

Figure 4.1.3. The structures of compounds reported by Zdanowski and Zalubiniak.[264,265]

Based on the work described in Chapters 2 and 3, we have confirmed that thiosquaramides function as efficient ion receptors with high binding constants toward both anions and cations. Furthermore, these molecules are capable of acting as ionophores to facilitate the transmembrane transport of Cl^-.[243] However, these simple molecular designs lack selectivity for specific ions but show binding to a wide range of both anions and cations. As we know, in order to achieve efficient and selective binding between the receptor and the ion, the pre-organised structure of receptors that match the size of the ion should be employed. Therefore, in this Chapter we would like to design a novel series of squaramide and thiosquaramide-based ion transporter with pre-organised cavities to achieve strong and selective ion recognition.

4.2 Chapter Objectives

This chapter aims to synthesise a series of bipodal oxosquaramides and thiosquaramides. We anticipate that the cavity structure formed by this kind of bipodal

molecule will be capable of recognising ions in a more efficient way and enhancing the selectivity.

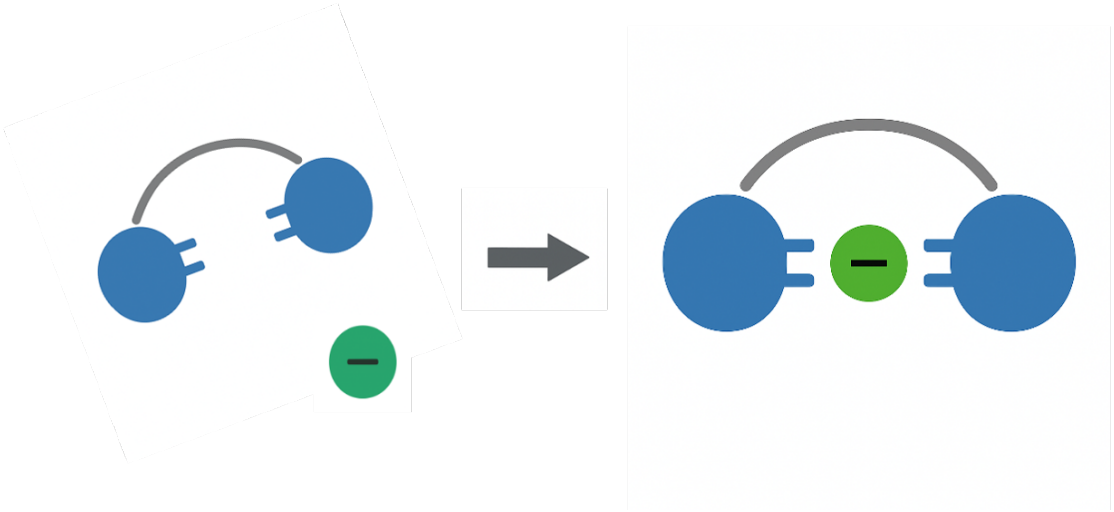

Figure 4.2.2. Illustrative diagram of the anticipated binding model of bipodal squaramides towards ions.

In the beginning, spacer extension was considered to increase the effective ion binding angle, such as Zn^{2+}, and create a more suitable cavity for chelation (Figure 4.2.1). However, increased spacer length is potential to enhance conformational flexibility and leads to complicate membrane behaviour, this chapter prefer to adapt a compact bipodal preorganised design and the systematic spacer-length variation reserved for future optimisation.

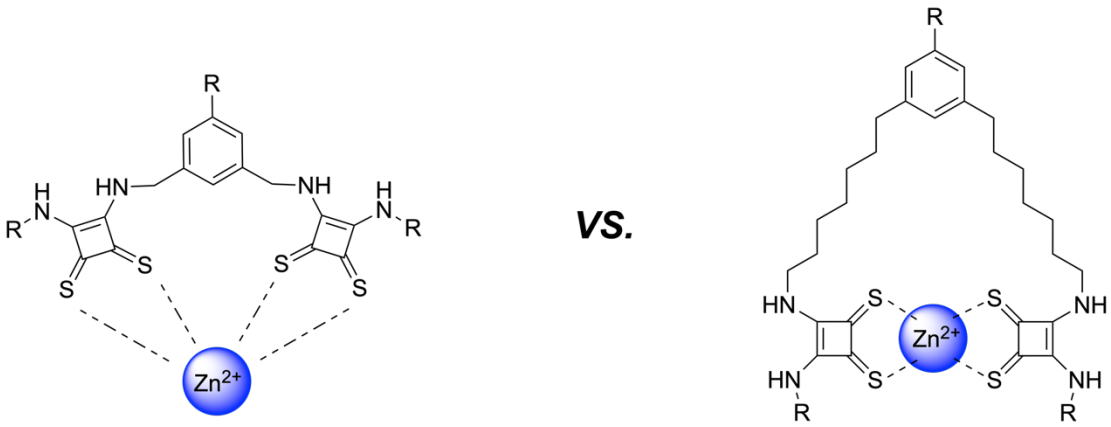

Figure 4.2.1. Potential complex structure of bipodal squaramide with different spacer length.

This class of bipodal receptor will differ in their substitution patterns, in an effort to explore the contributions of different substitutions to their binding capability and ion transport activities, and achieve an optimised ionophore. We envisage these motifs will retain similar ion transport capability as their parent examples. The selection of side chains is based on previous literature examples that contain electron-withdrawing group, *eg.* -CF_3 and -NO_2, that can increase the binding affinity and transport efficacy by enhancing the acidity of the NH group and/or lipophilicity. We firstly designed a family of oxosquaramide containing 1,3-bis(aminomethyl)-5-tert-butylbenzene as the linkage (Scheme 4.2.1). 1,3-bis(aminomethyl)-5-tert-butylbenzene (C1) can be obtained by using a known synthetic method and then reacting with diethyl squarate to generate the squarate monoester intermediate. Subsequently, excess amine could be introduced to obtain the target molecules **4.1**-**4.5**.

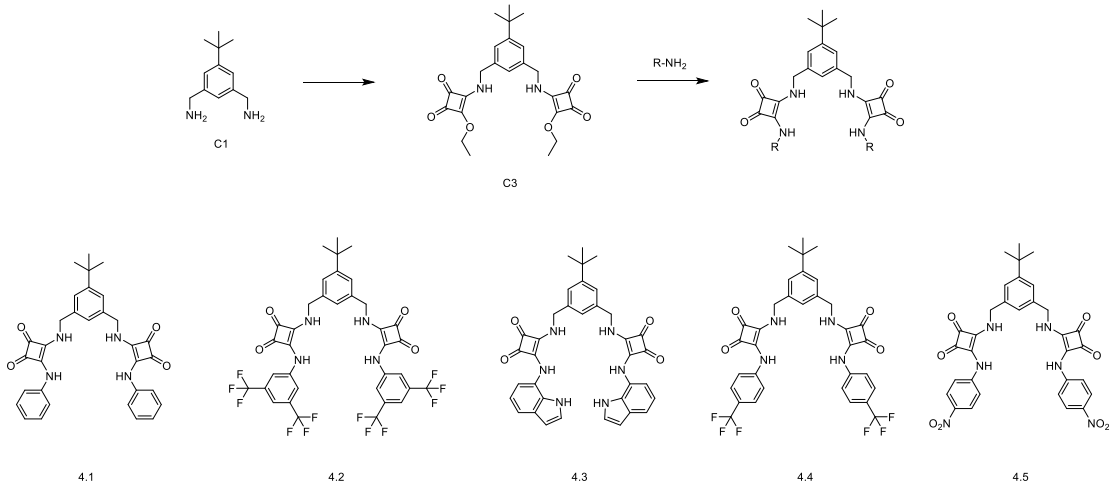

Scheme 4.2.1. Proposed synthetic method of bipodal oxosquaramides **4.1**-**4.5**.

Given that effective operation of the transporter requires a certain level of solubility, we next aimed to use benzoic acid as a linker in a series of molecules to increase the solubility. Following the previously established synthetic route, we anticipate obtaining intermediate C2, which will subsequently be coupled with the squarate and amine to furnish the final products **4.6**-**4.10**.

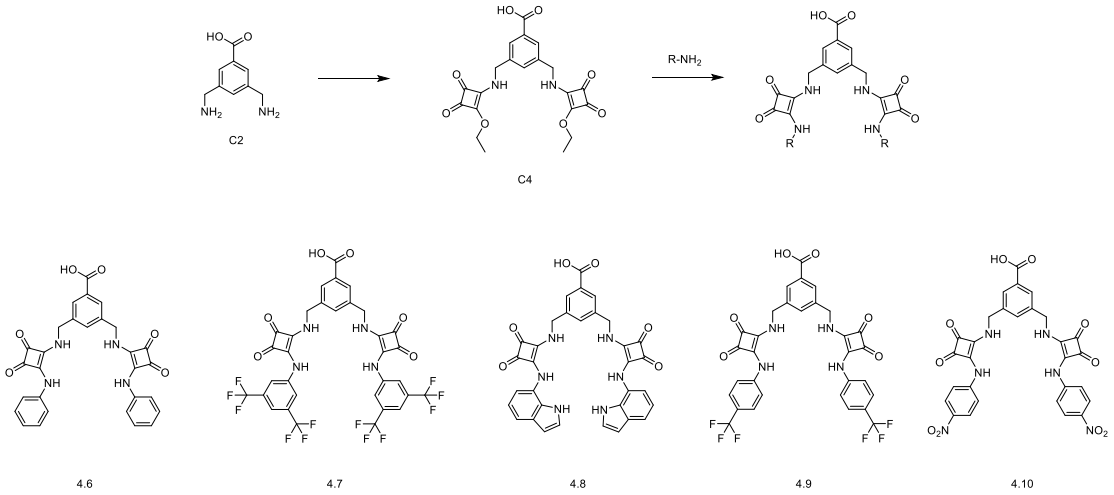

Scheme 4.2.2. Proposed synthetic method of bipodal oxosquaramides **4.6**-**4.10**.

In addition, to evaluate how enhanced lipophilicity influences the transport capability of this class of molecules, we plan to append more lipophilic andantamine groups at the apical position of the scaffold. Using 4.10 as the starting substrate and following previously reported analogous procedures, we anticipate obtaining the target product **4.11** via a two-step substitution sequence (Scheme 4.2.3).

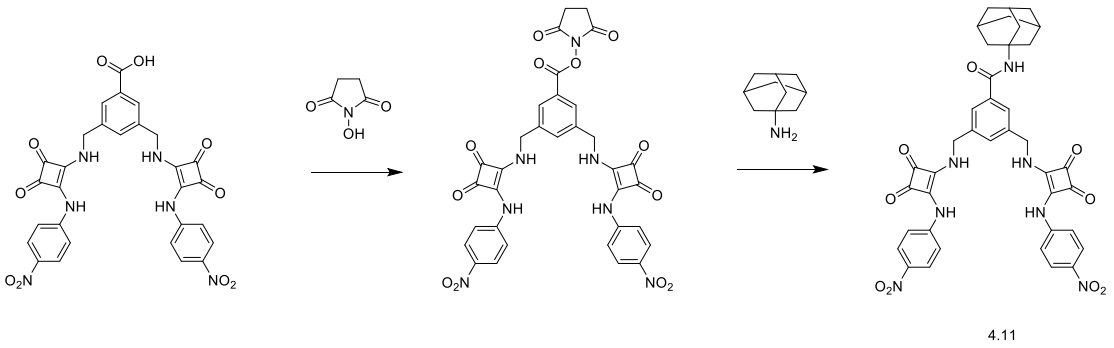

Scheme 4.2.3. Proposed synthetic method of bipodal oxosquaramides **4.11**.

The design of thiosquaramide derivatives is based on the findings presented in Chapter 2 that excessive electron-withdrawing substitution lead to deprotonation, thereby diminishing the transport efficiency of thiosquaramide scaffolds under physiological conditions. The synthesis of the target molecules **4.12**-**4.15** are expected to be readily achieved by coupling C1/C2 with B1/B2 (Scheme 4.2.4) (the synthesis of B1 and B2 is shown in Chapter 3). What follows in this chapter is a detailed description of the

synthesis and analysis of the supramolecular properties of the successfully synthesised bipodal squaramides.

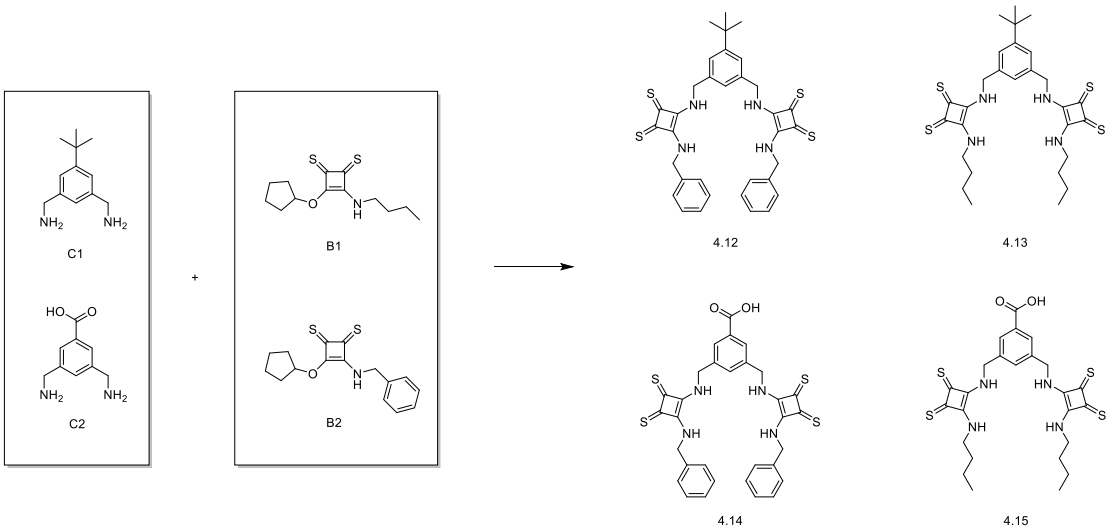

Scheme 4.2.2. Proposed synthetic method of bipodal thiosquaramides **4.12**-**4.15**.

4.3 Synthesis of target molecules

We developed a simple versatile synthetic route to this bipodal squaramide family, allowing us to obtain the desired structure containing two squaramide scaffolds from the initial amine and diethyl squarate. Meanwhile, the bipodal squaramide benzoic acid allows the further development of the analogous by substitution of the OH group to adjust the solubility and hydrophilicity of the structure to meet the requirement of diverse application environment.

Firstly, we synthesized bipodal oxosquaramide family 1 containing **4.1** - **4.5**. The synthesis method can be divided into 3 steps (Scheme 4.3.1). In step 1, diamine **C1** was obtained by modifying the previously reported method.[266,267] In the reported method, CCl_4 was used as the solvent for the first step. For safety and environmental considerations, we replaced CCl_4 with chloroform. The trade-off was a decrease in yield from 90% to 51%, however, we felt this was still acceptable.

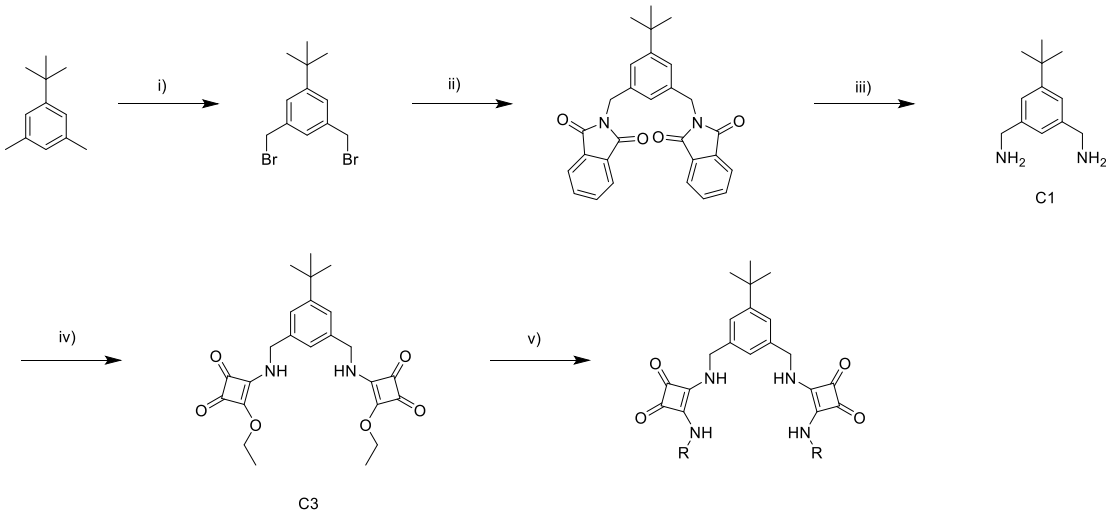

Scheme 4.3.1. Synthetic method towards bipodal oxosquaramide **4.1** - **4.5**. *Reagents and conditions*: (i) chloroform, N-bromosuccinimide, benzoyl peroxide, reflux overnight, 51%; (ii) DMF, potassium pthalimide, 90 °C, 4 h, 47%; (iii) MeOH, hydrazine, rt., 2 h, 53%; (iv) EtOH, triethylamine, stir at room temperature for 24 h, 86%; (v) EtOH, amine, $Zn(OTf)_2$, reflux for 2 days.

As shown in Figure 4.3.1(a), the formation of the significant bipodal squarate monoester **C3** was evident from the ^{1}H NMR spectra with the aromatic protons H2 and H3 display signals at 7.27 ppm and 7.04 ppm, while ethyl protons H4 and H5 appear at 4.67 ppm and 4.46 ppm. The ethyl proton H6 and butyl proton H1 appears in the most downfield position of the spectrum at 1.34 ppm and 1.28 ppm, respectively. Interestingly, the NH appears as two separate peaks at 9.29 ppm and 9.06 ppm. This may be due to the rotation of the CH_2-NH-squaramide bond, which results in the hydrogen bonds on the two sides being inequivalent. Then, this behaviour gives rise to two distinct NH peaks.

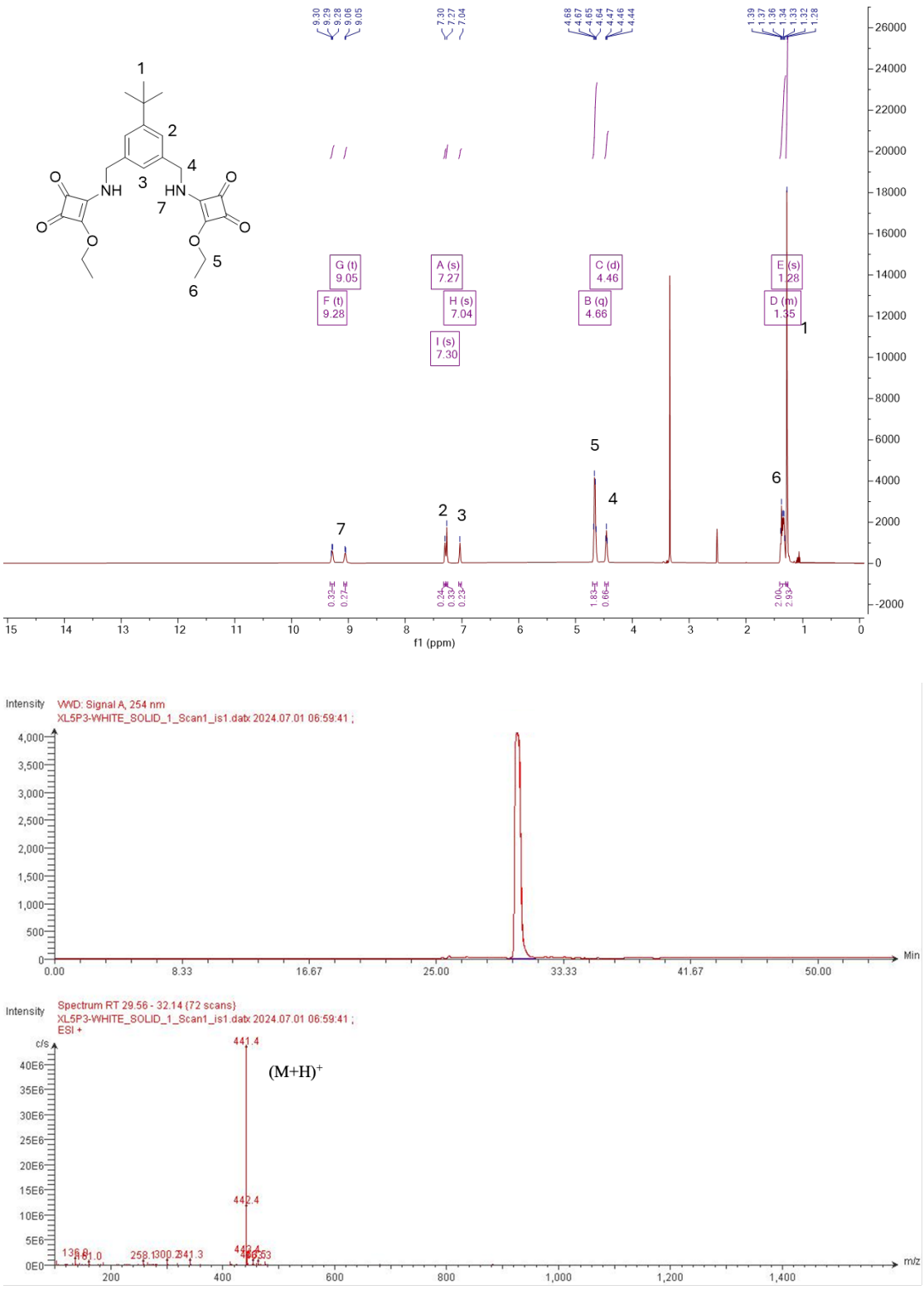

Figure 4.3.1 (a). ^{1}H NMR spectrum and LC-MS spectra of **C3**.

In the COSY spectrum (Figure 4.3.1(b)), the NH resonance H4A shows a cross peak with H7A, while H7B shows a cross peak with H5. Actually, H5 is not expected to

exhibit an NH resonance with H7B. Additionally, in the HSOC spectrum (Figure 4.3.1(c)), H5 exhibits correlations with both Carbon 1 and Carbon 2, indicating that a hydrogen peak of H4B should overlap with H5. These further support our hypothesis above that the rotation leads to two sets of signals of **C3**. The LC-MS spectra display one single peak with $(M+H)^+$= 441.4, which supports the purity of the compound.

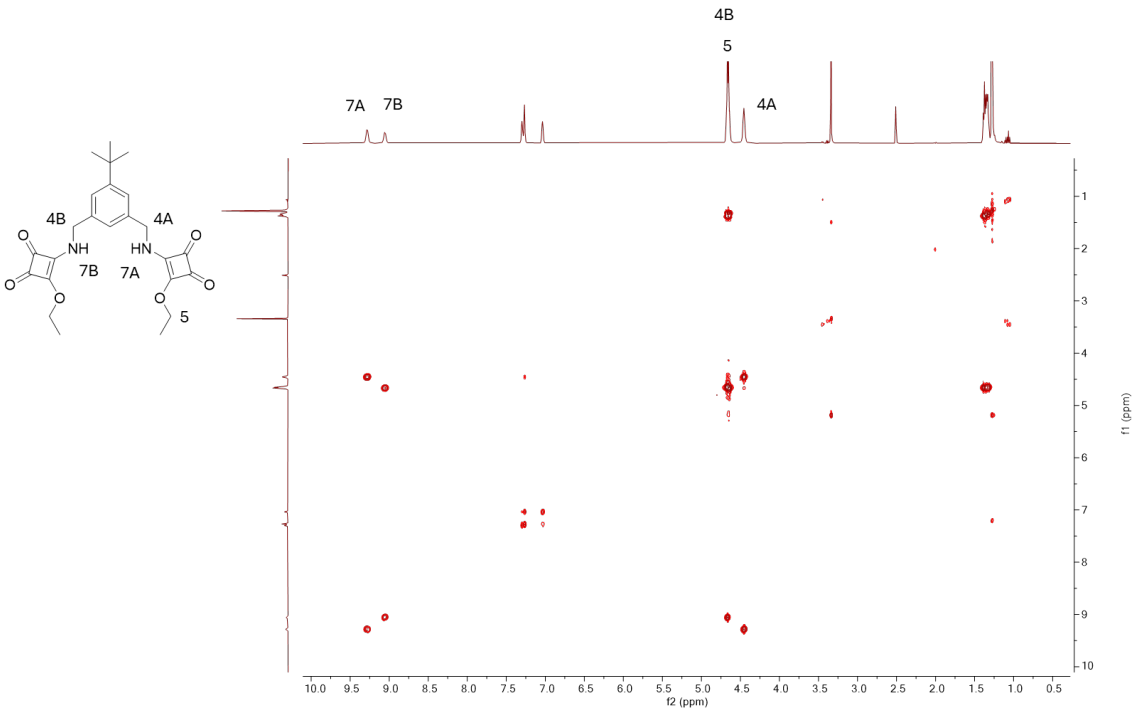

Figure 4.3.1 (b). COSY spectrum of **C3**.

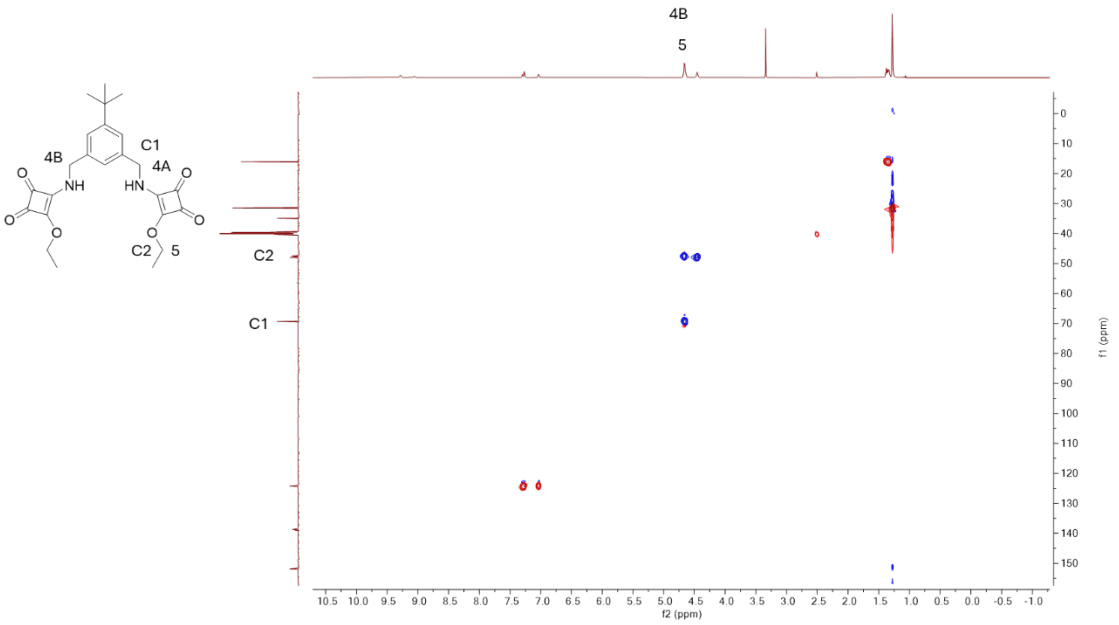

Figure 4.3.1 (c). HSQC spectrum of **C3**.

Then the squarate scaffold was attached to the diamine as the two arms of the molecule to form the bipodal squarate monoester **C3**. Finally, in the presence of $Zn(OTf)_2$, bipodal oxosquaramide **4.1** - **4.5** were synthesised through the reaction of **C3** and primary amine. The yields of each compound are varied from (65% - 78%) based on the steric and electronic effects of amines. Take **4.5** as an example, as shown in Figure 4.3.2(a), the formation of the N-amido linkage was evident from the ^{1}H NMR spectrum with NH signal H5 appearing as a broad singlet at 10.15 ppm. The aromatic protons of benzoate appear at 7.19 ppm and 7.40 ppm, while the aromatic protons of nitroaniline appear at 7.54 ppm and 8.16 ppm. NH signals H4 is located at 8.21 ppm and exhibits partial spectral overlap with aromatic proton H7. Butyl proton H1 appears in the most upfield position of the spectrum at 1.30 ppm. In addition, the carbon 1-4 of squaramide core were clear observed in ^{13}C NMR (Figure 4.3.2(b)).

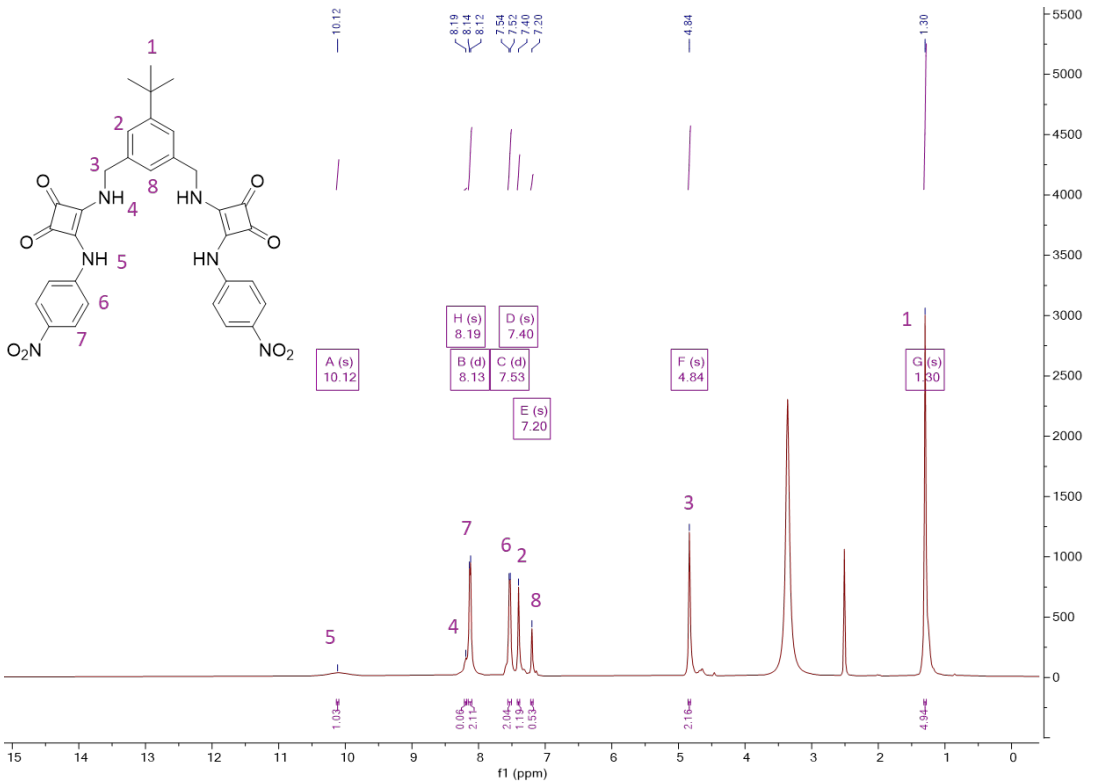

Figure 4.3.2(a). ^{1}H NMR spectrum of **4.5**.

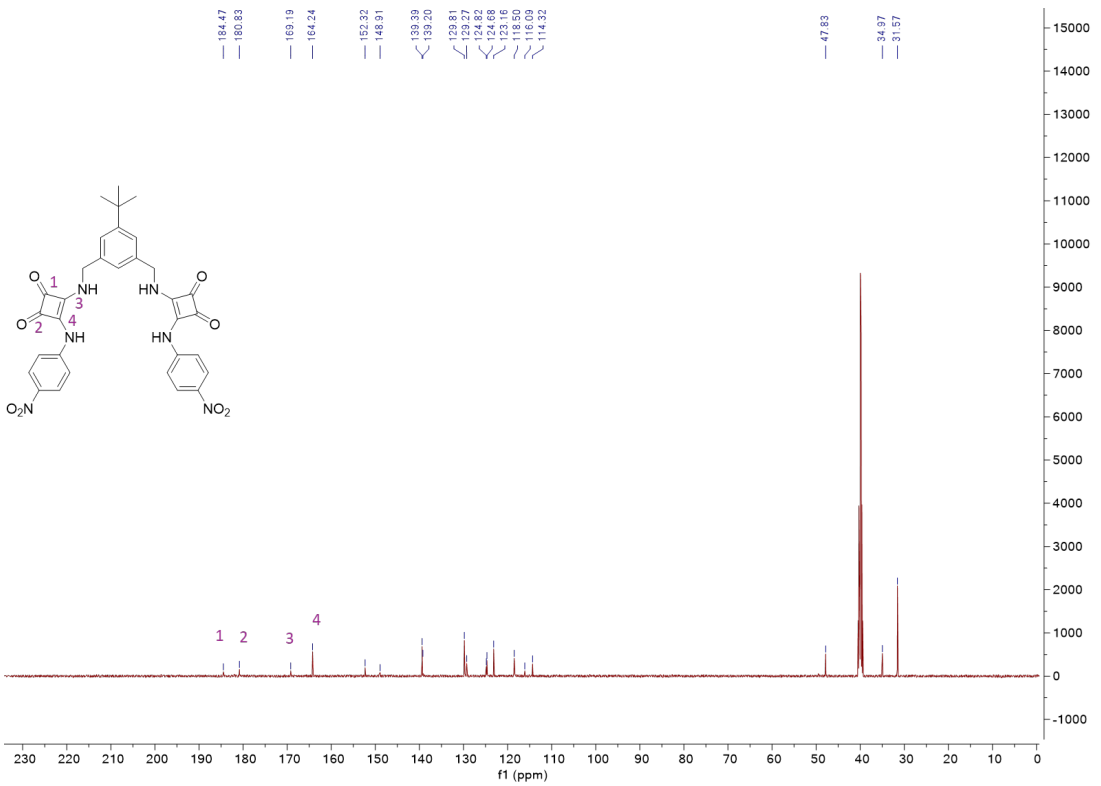

Figure 4.3.2(b). ^{13}C NMR spectrum of **4.5**.

LCMS spectrum revealed a single chromatographic peak at around 33 minutes indicating the purity of compound. However, the mass spectrum did not show the expected molecular mass. Fortunately, HRMS obtained the value of $(M+Na)^+$= 647.1854, confirming the successful formation of the target molecule(Figure 4.3.2(c) and (d)).

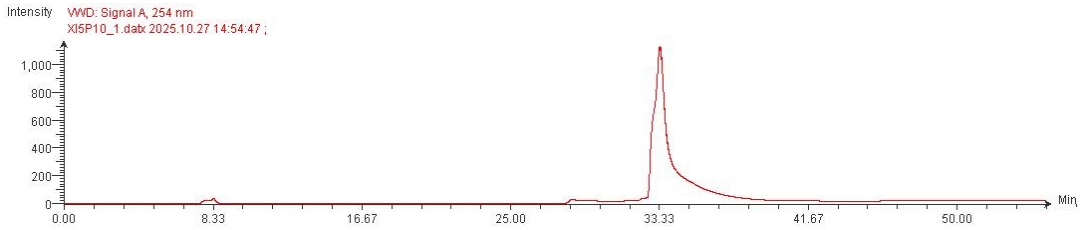

Figure 4.3.2(c). LCMS spectrum of **4.5**.

Figure: Extracted ion chromatogram (EIC) of compound.

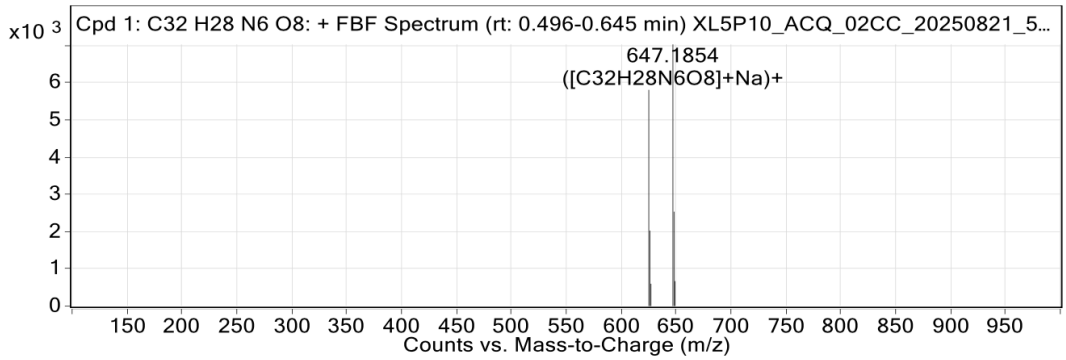

Figure: Full range view of Compound spectra and potential adducts.

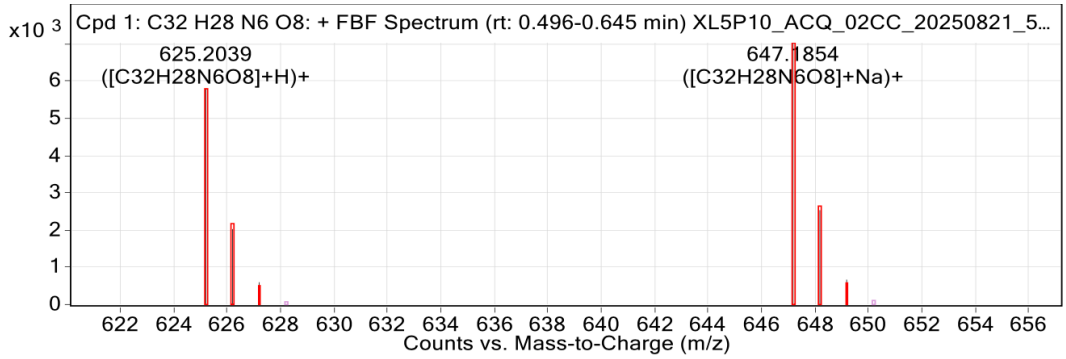

Figure 4.3.2(d). HRMS spectrum of **4.5**.

Next, for the synthesis of the more soluble bipodal oxosquaramide family 2 containing **4.6** - **4.10**, we likewise followed the previously reported procedure to obtained intermediate **C4** and the benzoic acid bipodal oxosquaramide scaffold.(Scheme 4.3.2).[268] Here we used sodium diformylamide in step vii. We did not perform a systematic comparison with a phthalimide-based strategy (Scheme 4.3.1), but this approach was operationally convenient in the synthesis of benzoic acid bipodal oxoxsquaramides because the acidic hydrolysis step (viii) enables the release of the primary amines and the conversion from -COOMe to -COOH in one step.

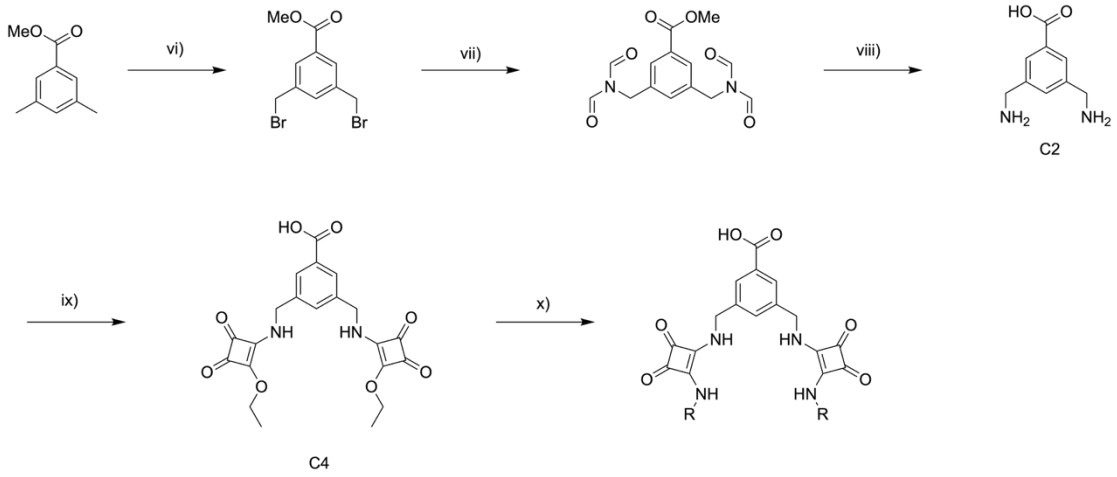

Scheme 4.3.2. Synthetic method towards bipodal oxosquaramide **4.6** - **4.10**. *Reagents and conditions*: (vi) MeCN, N-bromosuccinimide, benzoyl peroxide, reflux overnight, 61%; (vii) anhydrous MeCN, sodium diformylamide, reflux, 4 h, 43%; (viii) 1:1 HCl/1,4-dioxane, 70 °C, 4 h, 84%; (ix) EtOH, triethylamine, stir at room temperature for 24 h, 82%; (x) EtOH, amine, $Zn(OTf)_2$, reflux for 2 days.

As shown in Figure 4.3.3, similar to **C4**, the ^{1}H NMR spectra displays that the NH appearing as two separate broad singlet at 9.33 ppm and 9.11 ppm because of rotation. The aromatic protons H2 and H3 display signals at 7.84 ppm and 7.47 ppm, while ethyl protons H4 and H5 appear at 4.67 ppm and 4.53 ppm. The ethyl proton H6 appears in the most upfield position of the spectrum at 1.34 ppm, while the OH proton H1 appears in the most downfield position at 13.12 ppm. Again, the purity of the product is supported by LCMS that one single peak with $(M+H)^+$=429.0 was observed.

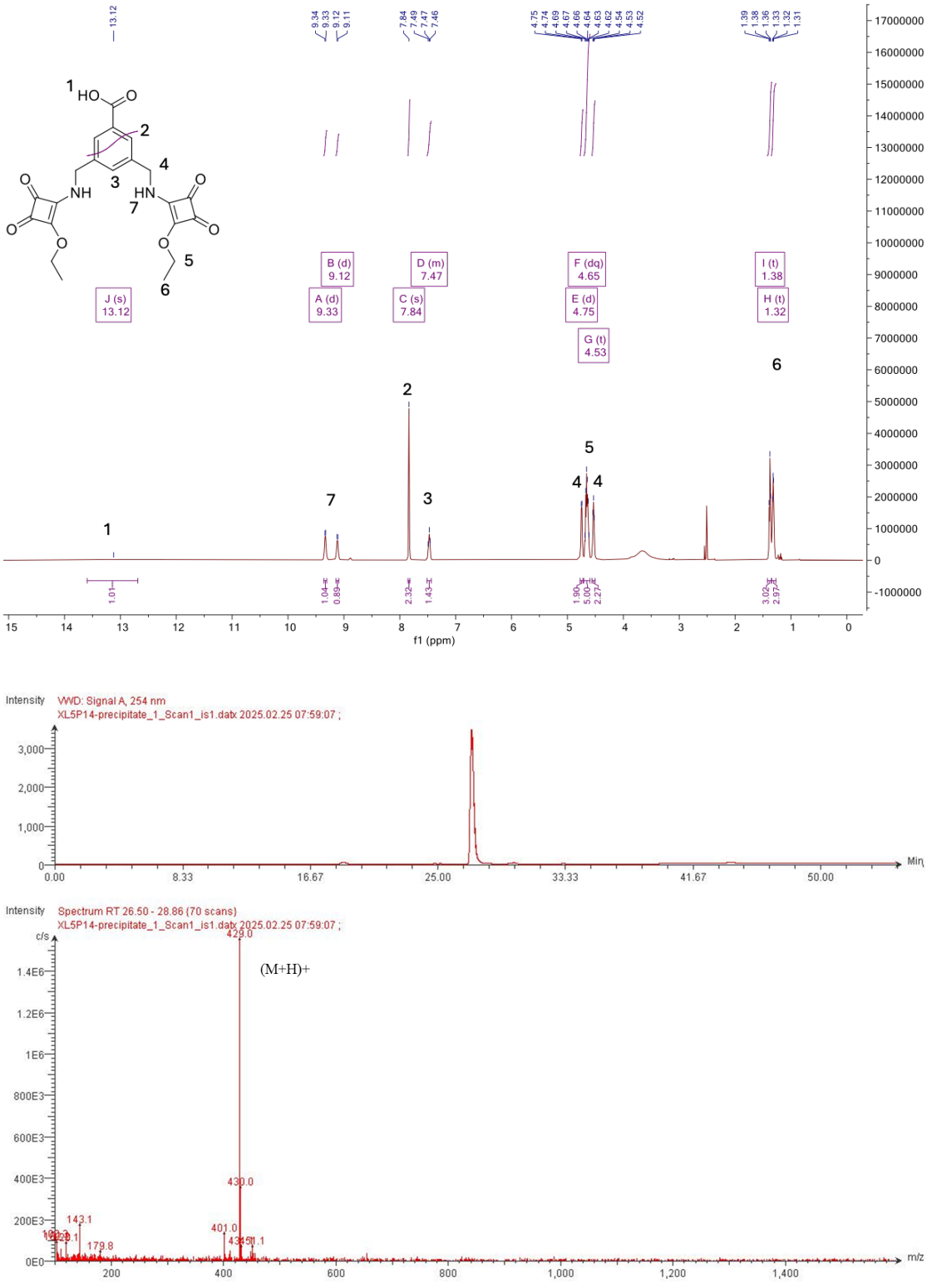

Figure 4.3.3. ^{1}H NMR spectrum and LCMS spectrum of **C4**.

Then, the same procedures as the synthesis of family 1 were employed to obtain **4.6** - **4.10** in the yields from 16% to 68%. Compared to the family 1 derivatives, take **4.4**

and **4.10** as examples, all the peaks of the bipodal benzoic acid squaramide derivatives (family 2) move downfield because of the stronger deshielding effect (Figure 4.3.4). Meanwhile, H1 signal of the OH group is observed at 13.18 ppm as a broad singlet.

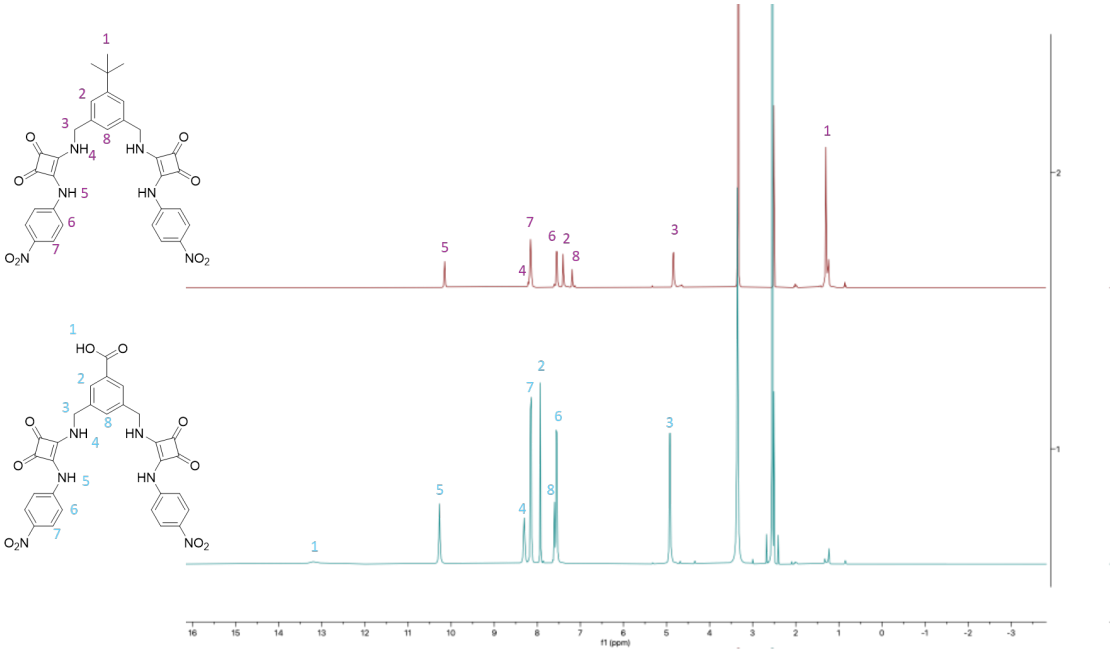

Figure 4.3.4. ^{1}H NMR spectrum of **4.5** (top) and **4.10** (bottom).

Lipophilicity is another important parameter in the the design of ionophores, being closely correlated with the transmembrane transport activity of many known ion carriers.[269,270] With this in mind, we hypothesised that the enhancement of the lipophilicity of the bipodal squaramides may improve their transmembrane transport activity. Accordingly, we modified compound **4.10** by replacing the hydroxyl (-OH) with amantadine to obtain bipodal squaramide **4.11** (Scheme 4.3.2).

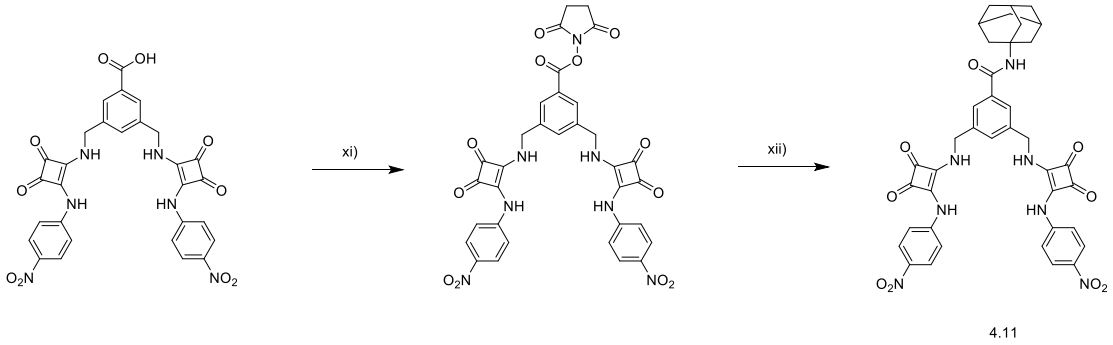

Scheme 4.3.3. Synthetic method towards bipodal oxosquaramide. *Reagents and conditions*: (xi) DMSO, N-hydroxysuccinimide, EDCI, rt., overnight; (xii) DMSO, TEA, andantamine, rt., 24 h, 68%.

Similarly, receptor **4.11**, obtained from **4.10** as the substrate, shows ^{1}H NMR signals that do not differ substantially from those of **4.10** (Figure 4.3.5(a)). The NH signals appear as a sharp singlet at 10.35 ppm and 8.33 ppm. The aromatic protons H2 and H8 appear at 7.56 ppm and 7.47 ppm, while the aromatic protons of nitroaniline appear at 7.73 ppm and 8.15 ppm. Notably, the formatted N-amido linkage H1 displays as a singlet at 7.67 ppm, along with amantadine proton H9 and H10 appear at 2.07 ppm and 1.66 ppm, respectively.

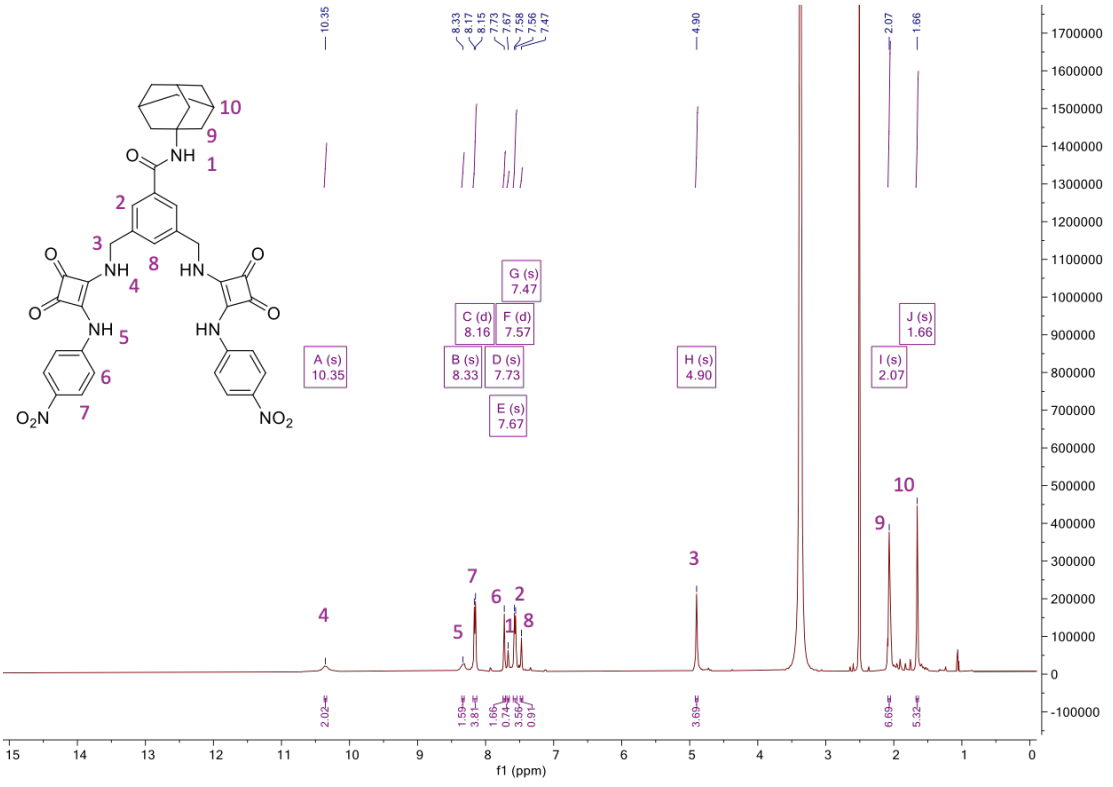

Figure 4.3.5(a). ^{1}H NMR spectrum of **4.11**.

In addition, from the ^{13}C NMR, we confirm the signals carbon 1-4 of the squaramide core appears at 185.6, 180.9, 166.2 and 163.3 ppm. respectively. The carbon 5 of carbonyl group show a peak at 170.4 ppm. Although the mass spectrum gave a good analysis, the HRMS show the $(M+H)^+$= 764.2560. All these data confirm the successful synthesis of compound **4.11** (Figure 4.3.5 (b), (c) and (d)).

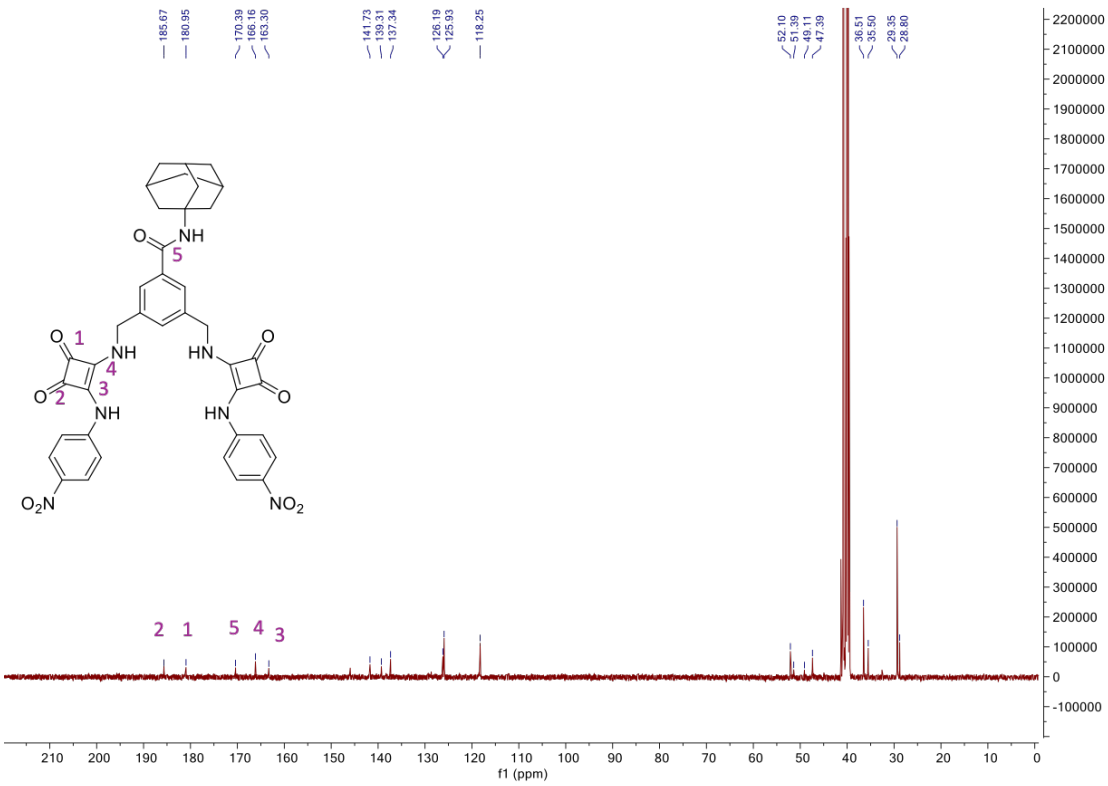

Figure 4.3.5(b). ^{13}C NMR spectrum of **4.11**.

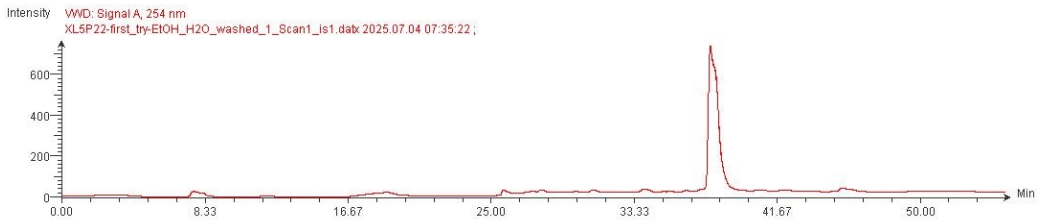

Figure 4.3.5(c). LCMS spectrum of **4.11**.

Figure: Extracted ion chromatogram (EIC) of compound.

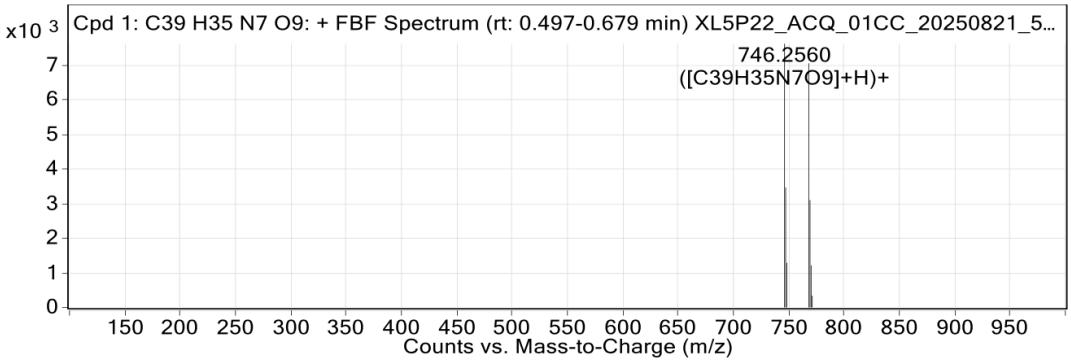

Figure: Full range view of Compound spectra and potential adducts.

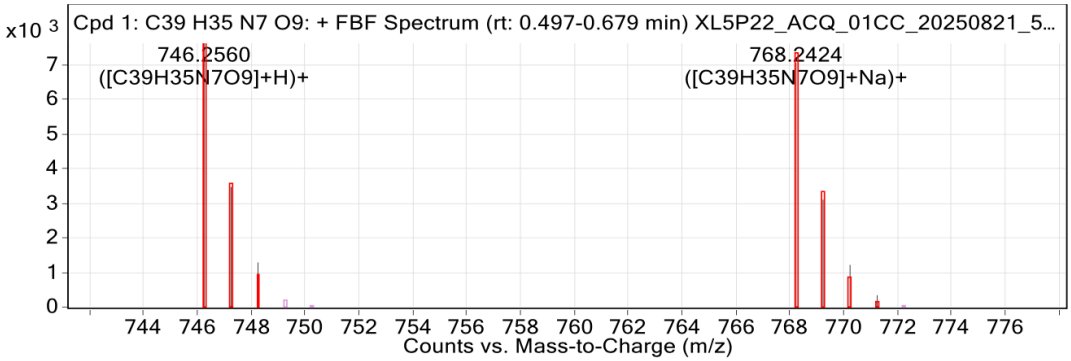

Figure 4.3.5(d). HRMS spectrum of **4.11**.

Finally, to the synthesis of bipodal thiosquaramide derivatives, because of the strong reactivity of dicyclopentyl thiosquarate, the direct addition of the thiosquarate scaffold to diamine lead to the formation of polymer mixtures (even under high dilution conditions), and the crude was unable to be purified. In response, we made several specific adjustments to the synthetic procedure (Scheme 4.3.4). Polymer formation was inhibited by synthesising mono-substituted squarate **B1** and **B2** as an intermediate. The reaction of dicyclopentyl thiosquarate with 0.8 equivalents of amine in anhydrous DCM yielded intermediate **B1** and **B2** in 32% and 38% yield. The detailed synthesis method of thiosquarate **B1** and **B2** was shown in Chapter 3.

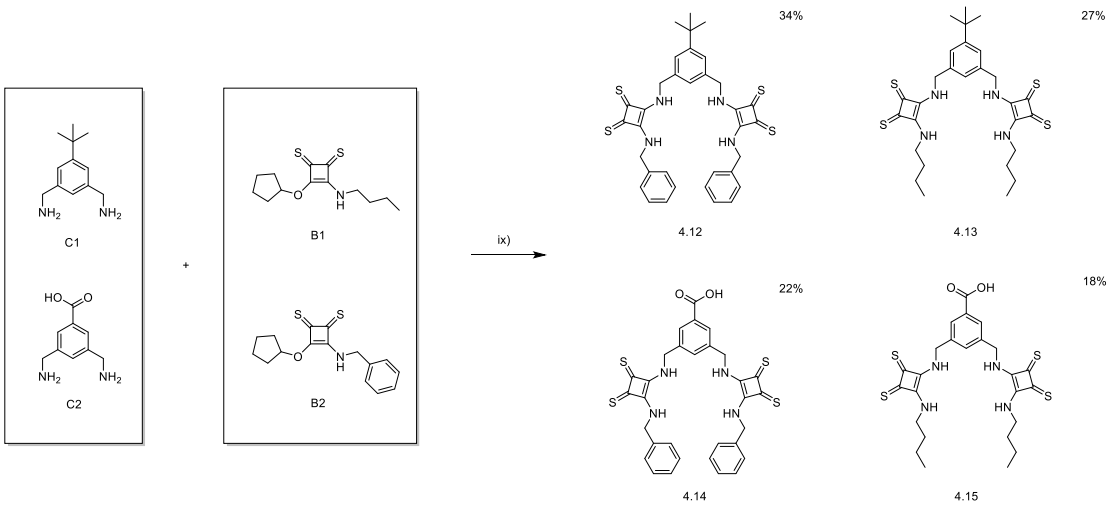

Scheme 4.3.4. Synthetic method towards bipodal thiosquaramide. *Reagents and conditions*: (xiii) anhydrous DCM, anhydrous DCM, stir at room temperature overnight.

Subsequently, the premade thiosquarate units **B1** and **B2** were mixed with diamines **C1** and **C2** in the presence of triethylamine to give bipodal thiosquaramides **4.12** - **4.15** in 28% - 37% yields. As mentioned above, the bipodal structure results in two distinct sets of NMR signals. As thiosquaramide has greater conformational freedom than squaramide derivatives, the effect is more pronounced. Take **4.12** as an example. Compared with oxosquaramide derivatives, the NMR spectrum of thiosquaramide derivatives exhibits a greater number of minor peaks attributable to rotamers. As shown in Figure 4.3.6(a), the compound exists as three rotamers in a ratio of 1:1:5. the NH protons H4 and H5 signals of major rotamer appears at 8.82 ppm, accompanied by two minor rotation-induced signals at 9.40 ppm and 9.63 ppm, respectively. The aromatic region appears as a broad, overlapping peak at 7.17-7.46 ppm, while methyl proton H3 is observed at 5.31 ppm. H1 remains at δ 1.26 ppm. Butyl proton H1 still appear in the most downfield position of the spectrum at 1.26 ppm. Again, combing LCMS and HRMS data, we can confirm that pure compound of target compound **4.12** is obtained.

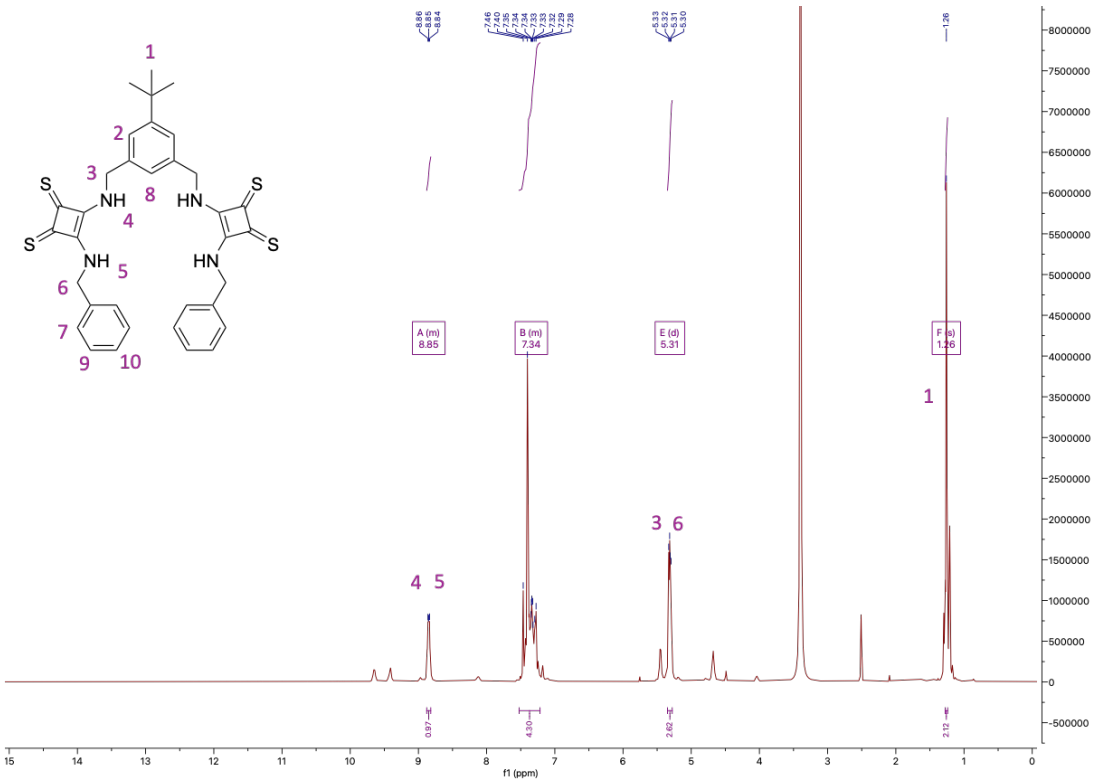

Figure 4.3.6(a). ^{1}H NMR spectrum of **4.12**.

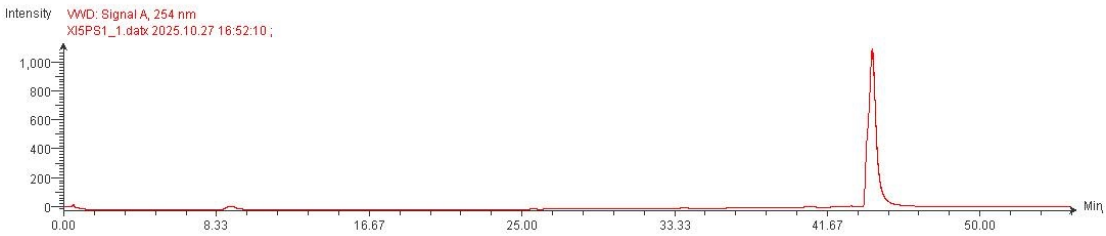

Figure 4.3.6(b). LCMS spectrum of **4.12**.

Figure: Extracted ion chromatogram (EIC) of compound.

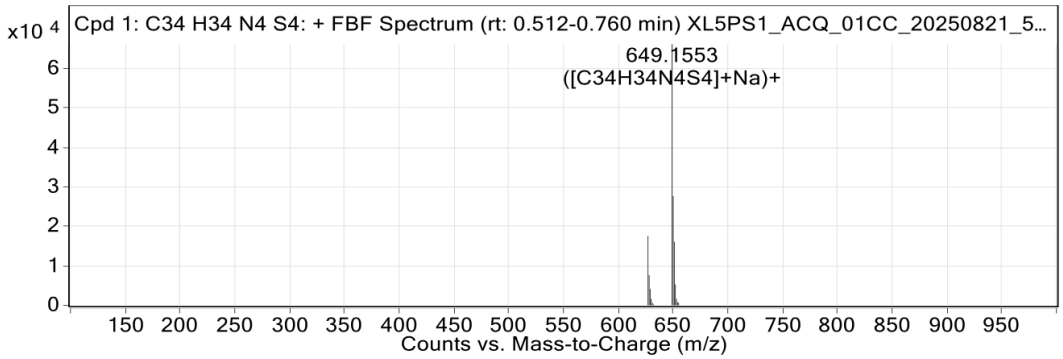

Figure: Full range view of Compound spectra and potential adducts.

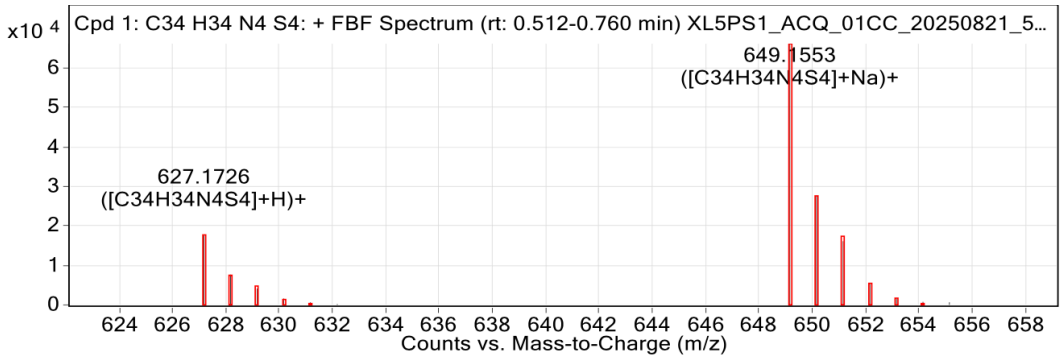

Figure 4.3.6(c). HRMS spectrum of **4.12**.

The synthesis method shown in Scheme 4.3.4 is also suitable for oxosquaramide, but the yield is much lower than that of the first method shown in Scheme 4.3.1 and Scheme 4.3.2 because of the product loss in the purification step. To present our work more clearly, all target molecules synthesised in this chapter are summarised in Figure 4.3.7. ^{1}H NMR, ^{13}C NMR and HRMS confirmed the successful synthesis of target molecule **4.1** - **4.15** and LC-MS confirmed the purity (See appendix).

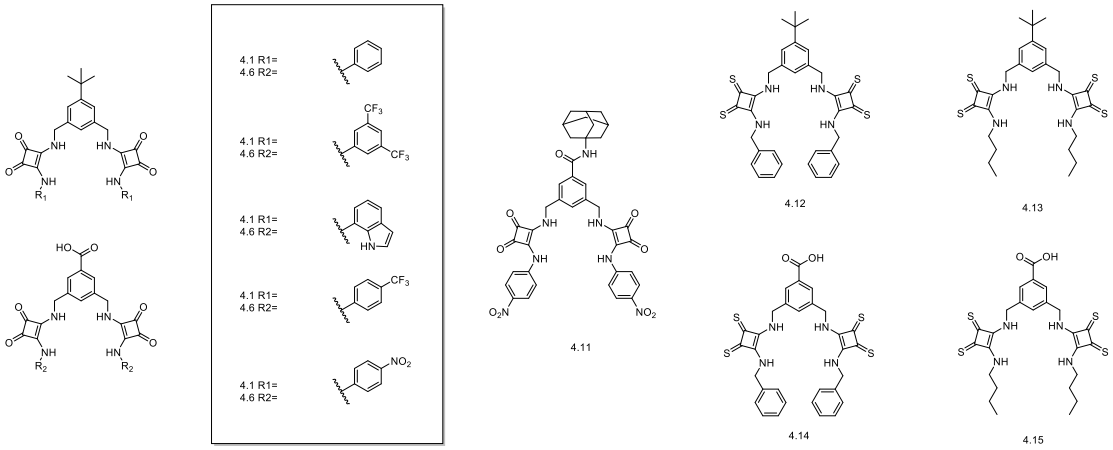

Figure 4.3.7. Summary of the target molecules **4.1**-**4.15**.

4.4 Anion binding studies of bipodal oxosquaramides and thiosquaramides.

To evaluate the anion-binding ability of bipodal squaramides, ^{1}H NMR titrations of each compound were carried out to determine their capability to form host-guest complexes with CH_3COO^- and Cl^- in DMSO-d_6. A 0.4 mM sample solution was prepared for each compound with a 10 mM TBA salt employed as the anion source. We firstly conducted the ^{1}H NMR titration of family 1 containing **4.1**-**4.5** towards Cl^- and AcO^-. Take **4.1** as an example (Figure 4.4.1), a significant downfield shift of the NH signals from 9.65 ppm to 9.99 ppm was observed upon gradual addition of TBA Cl^- (10 eq.), indicating the formation of bipodal squaramide-chloride complexes. The significant deshielding of the NH protons clearly supports the occurrence of host–guest interactions between the receptor and chloride. We initially envisioned that the two arms of bipodal squaramides would cooperatively engage one single anion in a 1:1 binding model, functioning like a tweezer. Unexpectedly, Job's plot suggest that a 1:2 binding model is the better choice to describe the binding behaviour, in which the two arms bind separate anions individually.

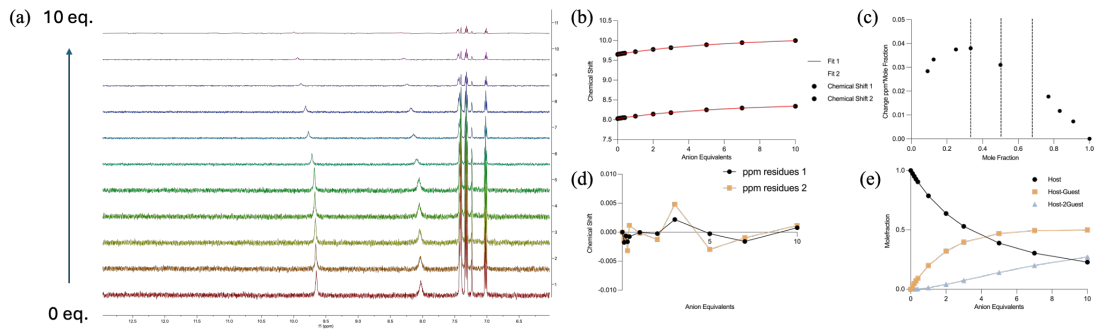

Figure 4.4.1. ^{1}H NMR titration data for **4.1** towards Cl^-. (a) ^{1}H NMR stackplot of **4.1**(0.4 mM in DMSO-d_6) upon addition of increasing molar equivalents of TBACl (0 - 10 eq.). (b) Fitplot of **4.1** towards Cl^- in a 1:2 binding model. (c) Job's plot of Cl^- titration for **4.1**. (d) Residual plot of **4.1**. (e) Mole fraction plot of Host vs. Host-Guest fraction with increasing guest concentration for **4.1**.

A summary of ^{1}H NMR titration results is shown in Table 4.4.1. Unsurprisingly, compound **4.3** with two extra NH binding sites exhibited a relatively higher chloride affinity. Interestingly, the CF_3-substituted molecules **4.2** and **4.4** exhibited a lower binding affinity than **4.1**. To further probe the influence of substituents on binding, we performed the same titration experiments on family 2 (**4.6**-**4.11**) and family 3 (**4.10**-**4.15**), respectively.

Table 4.4.1. A summary of ^{1}H NMR titration results for the binding behaviour of **4.1** - **4.5** towards anions.[a]

	Cl^-	AcO^-
4.1	8.5×10^2	4.3×10^3
4.2	6.9×10^2	-[c]
4.3	1.6×10^3	-[c]
4.4	3.1×10^2	4.5×10^3
4.5	1.1×10^3	-[c]

a All the data were fitted to a 1:2 model; the error of the K_a value is < 10%. b Receptor not sufficiently suitable to allow the accurate calculation of K_a. c Deprotonation prevents the calculation of the binding constant.

Similarly, compound **4.8** with two extra NH binding sites exhibited a relatively higher chloride affinity than other compounds in family 2. The clear interaction between 7-indolyl NHs and anions was observed (Figure 4.4.2). This behaviour is corresponding to the previous reported 7-indolyl squaramides.[271]

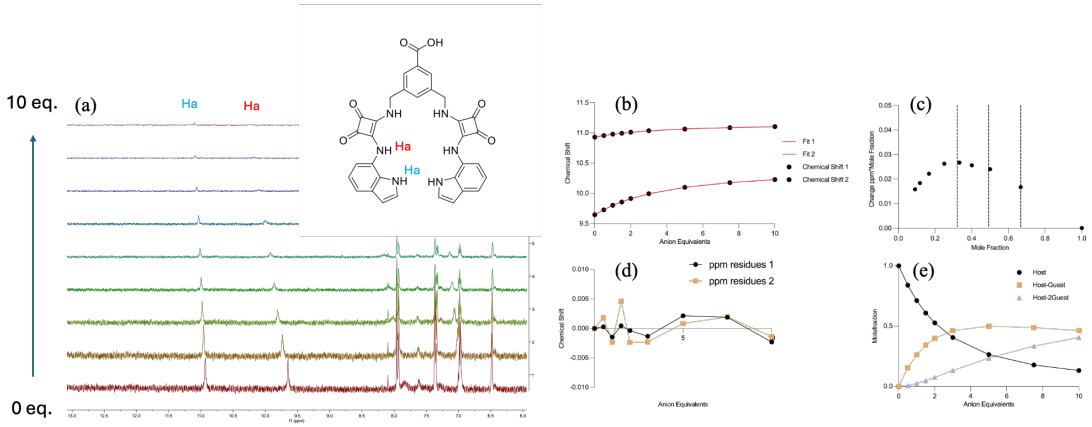

Figure 4.4.2. ^{1}H NMR titration data for **4.8** towards Cl^-. (a) ^{1}H NMR stackplot of **4.1**(0.4 mM in DMSO-d_6) upon addition of increasing molar equivalents of TBACl (0 - 10 eq.). (b) Fitplot of **4.8** towards Cl^- in a 1:2 binding model. (c) Job's plot of Cl^- titration for **4.8**. (d) Residuals plot of **4.8**. (e) Mole fraction plot of Host vs. Host-Guest fraction with increasing guest concentration for **4.8**.

In addition, consistent with our prediction, the CF_3-substituted molecules exhibited higher affinity, attributable to the increased NH acidity (Table 4.4.2). For compound **4.11**, coupling with amdantamine introduces a new NH binding site, such that its interaction with the ion may proceed with a 1:3 stoichiometry (host:guest) or an even more complex speciation, precluding reliable model fitting to extract binding affinities. Compared to the t-butyl group (**4.1** - **4.5**), the introduction of the COOH group (**4.6** - **4.10**) leads to an overall decrease in chloride affinity, suggesting that the substituent effect of COOH diminishes the binding capability of chloride. This may be because the COOH group itself acts as a relatively strong hydrogen bond acceptor, which may promote intermolecular interactions. As a result, part of the hydrogen-bonding sites of squaramide could be "consumed", thereby reducing the overall binding affinity.

Table 4.4.2. A summary of ^{1}H NMR titration results for the binding behaviour of **4.1** - **4.5** towards anions.[a]

	Cl^-	AcO^-
4.6	7.3×10^2	-[c]
4.7	1.0×10^3	-[c]

4.8	1.4×10^3	-[c]
4.9	1.1×10^3	-[c]
4.10	5.6×10^2	-[c]
4.11	-[b]	-[c]

a All the data were fitted to a 1:2 model; the error of the K_a value is < 10%. b Receptor not sufficiently suitable to allow the accurate calculation of K_a. c Deprotonation prevents the calculation of the binding constant.

In addition, the results of thiosquaramide derivatives **4.12**-**4.15** are shown in Table 4.4.3. In this case, bipodal thiosquaramide derivatives exhibited an overall stronger affinity towards Cl^- than bipodal oxosquaramide derivatives, This enhancement can be attributed to the higher acidity of the NH of thiosquaramide scaffolds, which promote more favourable anion binding.[129] Also, -OH substituted compound **4.14** and **4.15** display lower affinity for chloride than t-butyl substituted compound **4.12** and **4.13**. This trend is same to the observation of oxosquaramide derivatives.

Table 4.4.3. A summary of ^{1}H NMR titration results for the binding behaviour of **4.12** - **4.15** towards anions.[a]

	Cl^-	AcO^-
4.12	2.5×10^3	-[c]
4.13	1.7×10^3	-[c]
4.14	9.2×10^2	-[c]
4.15	7.9×10^2	-[c]

a All the data were fitted to a 1:2 model; the error of the K_a value is < 10%. b Receptor not sufficiently suitable to allow the accurate calculation of K_a. c Deprotonation prevents the calculation of the binding constant.

The addition of AcO^- resulted in deprotonation in most receptors and the disappearance of the NH signals, thereby preventing the calculation of binding constants. Fortunately, the NH signals of **4.1** and **4.4** remained clearly observed. The resulting data was fitted to a 1 : 2 binding model by using Bindfit v0.5 again to give the binding affinity (Figure 4.4.2 and ESI). Compared to Cl^-, AcO^- exhibited a

relatively higher binding affinity. This binding trend has been reported to correlate with the basicity of the ions.[272]

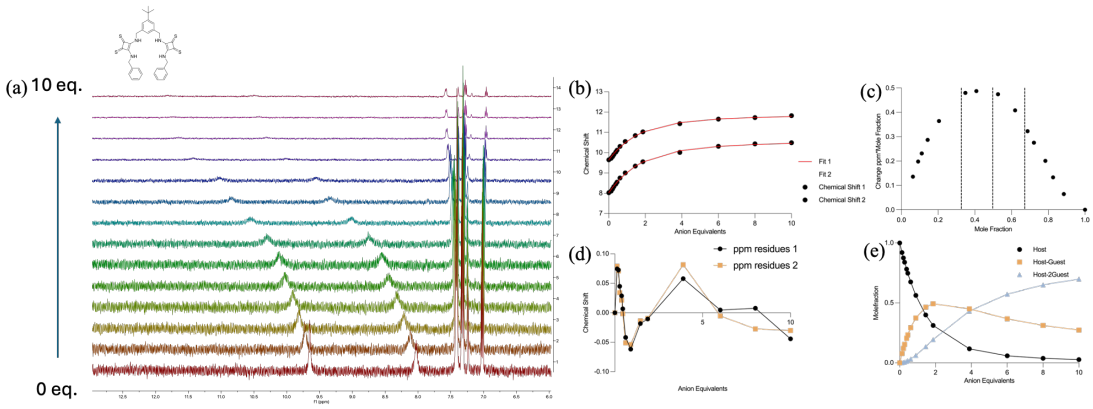

Figure 4.4.2. ^{1}H NMR titration data for **4.1** towards AcO^-. (a) ^{1}H NMR stackplot of **4.1**(0.4 mM in DMSO-d_6) upon addition of increasing molar equivalents of TBA acetate (0 - 10 eq.). (b) Fitplot of **4.1** towards AcO^- in a 1:2 binding model. (c) Job's plot of AcO^- titration for **4.1**. (d) Residuals plot of **4.1**. (e) Mole fraction plot of Host vs. Host-Guest fraction with increasing guest concentration for **4.1**.

4.5 Cation binding studies of bipodal thiosquaramides

Relative to squaramides, thiosquaramides have been demonstrated to possess a markedly enhanced metal ion binding affinity. To further ascertain whether the structurally more complex derivative of thiosquaramide retains the capacity to form host-guest complexes with Zn^{2+} in solution, UV-vis titrations were conducted with **4.12** - **4.15**. Take **4.12** as an example (Figure 4.5.1), the UV-vis absorption spectrum of **4.12** was recorded in DMSO/MeCN mixture solution (1:19) at a concentration of 10 μM. The spectrum exhibits two absorption bands at 388 nm and 274 nm, and a shoulder absorption band was observed at around 353 nm. 0 - 2.3 equivalents of $Zn(ClO_4)_2$ (1 mM) were added sequentially while the spectrum was recorded for each addition. The introduction of Zn^{2+} resulted in a hypochromism at 388 nm with a concomitant blue-shift to 382 nm. Similar behaviour was seen at 274 nm. An increase in absorbance was also observed at 305 nm, and two isosbestic points at 294 nm and 340 nm were obtained. This indicates the strong interaction between the receptor and Zn^{2+}. The changes in absorbance at 388 nm and 311 nm were fitted to a 1:1 model by

using BindFit v0.5 open access software, giving the K_a value of 2.3 × 10^5 (error = 20%). In contrast to thiosquaramide **2.3**, the more complex biopodal thiosquaramide derivative **4.12** binds Zn^{2+} in a 1:1 stoichiometry, arising from its incorporation of two thiosquaramide scaffolds. Due to its multiple binding sites, the molecule iscapable of satisfying the general coordination requirement of 4 - 6 for Zn^{2+}.[273,274] Job's plot analysis shows a peak at 0.5 mole fraction, supporting the choice of the binding model. The same experiments were conducted with **4.13** - **4.15**, which all exhibited strong ion-binding capabilities. A summary of K_a of each receptor towards Zn^{2+} is shown in Table 4.5.1. Similar to the discussion in Chapter 2, the relatively high error may arise from the aggregation of the molecules. However, our objective was to investigate whether bipodal thiosquaramide still displays strong Zn^{2+} binding capability, and the data presented here demonstrates that. Compared to thiosquaramides **2.3**-**2.7**, **4.12**-**4.15** exhibit an order of magnitude higher binding constant K_a, demonstrating the beneficial effect of this bipodal structure on cation binding.

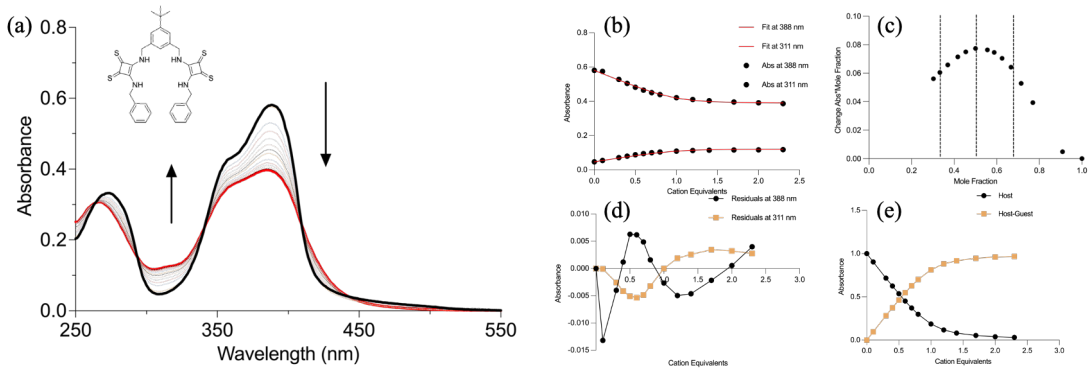

Figure 4.5.1. (a) UV-vis titration of **4.12** (10 μM) against $Zn(ClO_4)_2$ (0 - 2.3 eq., 1 mM) in DMSO/MeCN mixture solution (1:19). (b) Fitplot at 388 nm and 311 nm. (c) Job's plot of Zn^{2+} UV-vis titration for **4.12** in DMSO/MeCN mixture solution (1:19). (d) Residuals plot of **4.12**. (e) Mole fraction plot of Host vs. Host-Guest fraction with increasing guest concentration for **4.12**.

Table 4.5.1. A summary of UV-vis titration results for the binding behaviour of **4.12** – **4.15** towards Zn^{2+}.[a]

	4.12	**4.13**	**4.14**	**4.15**

K_a (M^{-1})	2.4×10^5	-[b]	6.6×10^5	9.4×10^5

a All the data were fitted to a 1:1 model; the error of the K value is < 20%. b Receptor not sufficiently suitable to allow the accurate calculation of K_a.

In addition, the flexible arms of bipodal thiosquaramides may allow the single arm of one molecule to associate with the arm of another molecule to jointly coordinate a Zn^{2+} ion. Although we didn't obtain the crystal structures, the appearance of flocculent precipitates upon the addition of Zn^{2+} to high concentrations of **4.12** (100 mM) indicates that two thiosquaramide molecules may coordinate on single ion through a sandwich-like binding motif, potentially forming polymers (Figure 4.5.2).

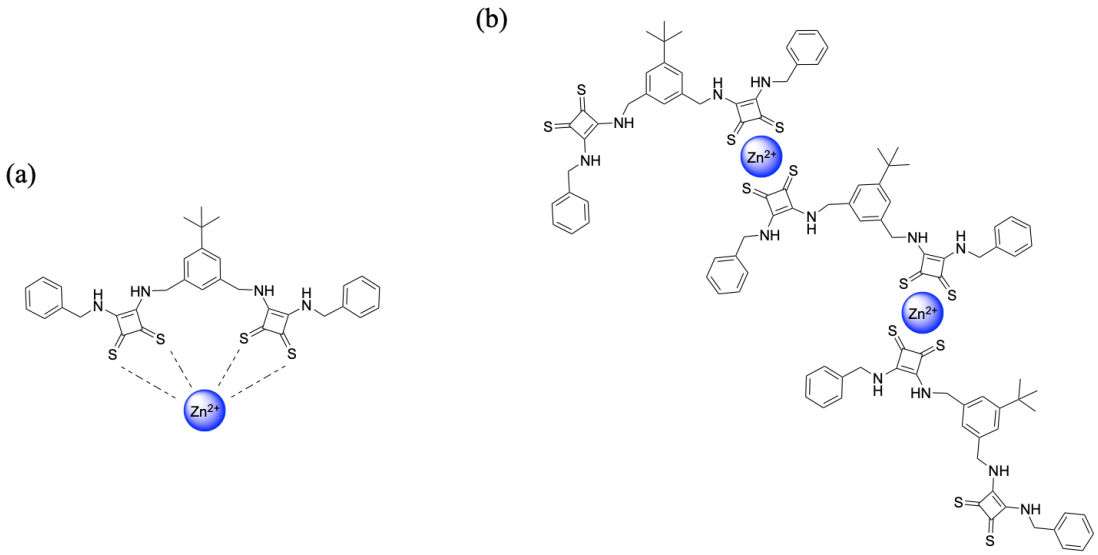

Figure 4.5.2. Schematic illustration of (a) potential binding modes of **4.12** towards Zn^{2+}; (b) Proposed polymer structures.

4.6 Chloride transport studies

In section 4.4, we have demonstrated the ability of bipodal squaramide derivatives to bind Cl^-, so the natural choice was to investigate whether the receptors also exhibit Cl^- transport ability. First, in preliminary experiments, lucigenin assays were carried out again to examine the transport performance of **4.1** - **4.15** (5 μM). We found that NO_2 group affected the fluorescence response of lucigenin, preventing it from accurately reflecting the chloride concentration within the liposomes. Therefore, receptors **4.5**, **4.10** and **4.11** were excluded from the preliminary experiments. As shown in Figure

4.6.1, receptors **4.1** - **4.4** containing t-butyl group exhibited relatively strong transport performance. In contrast, within **4.6** - **4.9**, only **4.7** displayed relatively weak chloride transport behaviour while others displayed almost no transport activities. This phenomenon may arise from the introduction of the COOH group, which decreases the overall lipophilicity of the receptor. As a result, receptors **4.6** - **4.9** are less able to partition into the lipid bilayer, thereby leading to a significant reduction in ion transport activity. Interestingly, in contrast to the case of squaramide derivatives, thiosquaramide derivatives **4.12** and **4.13** containing the t-butyl group exhibited almost no transport behaviour under our experimental conditions, while thiosquaramide derivatives **4.14** and **4.15** containing the carboxylic acid group displayed weak transport behaviour. It has been demonstrated that the introduction of sulfur endows thiosquaramides with stronger acidity and lipophilicity than oxosquaramides.[129,275] A possible explanation is that the tert-butyl substituted thiosquaramide derivative exhibits excessively high lipophilicity, which prevents efficient ion transport. By contrast, introduction of the OH group reduces the molecule's overall lipophilicity and thereby activates its ion transport activity.[129]

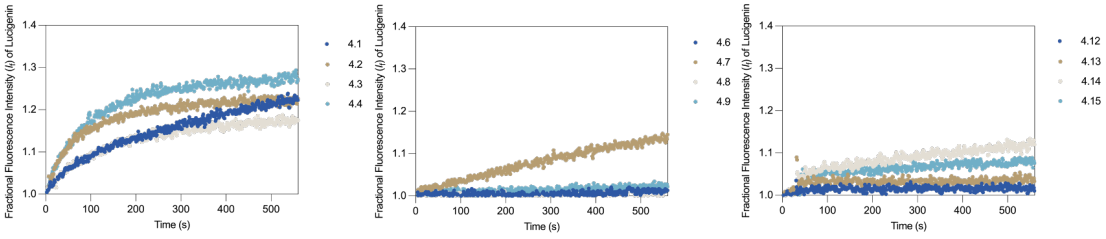

Figure 4.6.1. Lucigenin assay: the change of fractional fluorescent intensity with the addition of **4.1** - **4.15** (5 μM) and NaCl (75 μL, 1 M) to liposomes containing lucigenin (in 225 mM $NaNO_3$).

Subsequently, additional analysis was carried out by Prof. Roberto Quesada from the Departamento de Química at the Universidad de Burgos, Spain. A detailed analysis of bipodal squaramides **4.1** - **4.5** containing the t-butyl group, using an ion-selective electrode exhibited a markedly stronger transport capability . As shown in Figure 4.6.2, with the increasing concentration of **4.1**, the chloride efflux also rises, indicating the transport capability of **4.1** under the experimental conditions. Hill plot analysis gave

an EC_{50} value of 0.075, indicating that **4.1** acted as a chloride ionophore with high efficiency involved in transmembrane ion transport. The EC_{50} (μM) and hill parameter (n) values obtained for compounds **4.1** - **4.5** by using Cl^-/NO_3^- exchange assay are summarised in Table 4.6.1. Notably, in general, an increased degree of fluorination in squaramides can significantly enhance transport activity.[270,276] However, the fluorinated receptors **4.2** and **4.4** did not exhibit higher transport efficiency than the non-fluorinated receptor **4.1**. Additionally, receptor **4.3**, which has relatively high Cl^- affinity, displayed the lowest transport ability. One possible explanation is that a combination of enhanced membrane affinity and strong NH···O hydrogen bonding with phosphate leads to the strong binding of these receptors to the phospholipid head groups at the membrane–water interface. This behaviour can reduce the effective amount of mobile carriers available for transport activity and thereby compete with carrier-mediated chloride transport. Similar competition between anion transport and lipid headgroup binding has been proposed for related squaramide-based anionophores.[277] An alternative explanation is that receptors with higher Cl^- affinity (for example, compound **4.3**) may suffer from slower anion release, which can also reduce transport rates.

Further detailed analysis of the ionophoric behaviour of these compounds is currently underway in Prof. Quesada's lab.

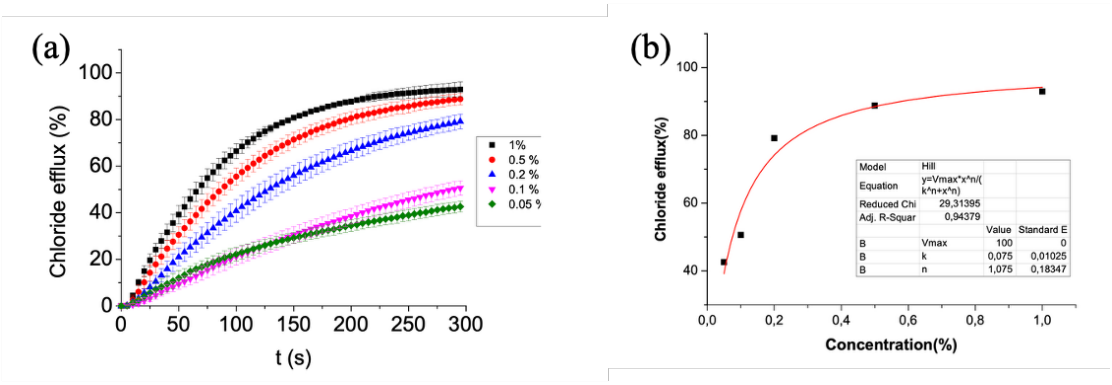

Figure 4.6.2. (a) Chloride efflux promoted by **4.1** compound in unilamellar POPC vesicles. Vesicles were loaded with a 489 mM NaCl solution buffered at pH 7.2 with 5 mM NaH_2PO_4 and dispersed in a 489 mM $NaNO_3$ solution buffered at pH 7.2 with 5 mM NaH_2PO_4. Each trace represents the average of at least three trials, performed with three batches of vesicles. (b) Hill analysis for compound **4.1** (Cl^-/NO_3^- exchange).

Table 4.6.1. EC_{50} (μM) and Hill parameter (n) values obtained for compounds **4.1** - **4.5** by using Cl^-/NO_3^- exchange assay.

Compound	EC_{50} (Cl^-/NO_3^-)	n	EC_{50} (Cl^-/HCO_3^-)	n	EC_{50} (Cl^-/SO_4^{2-})	n
4.1	0.075	1.1	0.30	1.0	0.92	1.4
4.2	0.46	0.68	3.0	0.88	-[a]	-[a]
4.3	-[a]	-[a]	-[a]	-[a]	-[a]	-[a]
4.4	0.27	1.3	0.64	1.1	-[a]	-[a]
4.5	0.063	0.79	0.31	0.90	0.85	1.2

a The low transport activity displayed by the compound prevented the calculation of these values

4.7 Zn^{2+} transport studies

Similar to Chapter 2 and 3, the metal-ion transport studies in this chapter focus on the biologically important Zn^{2+}. To verify if the synthesised bipodal thiosquaramide derivatives retain the ability to transport Zn^{2+}, FluoZin-3 assay was also employed to evaluate the transport performance of **4.12** - **4.15**. The liposomes containing FluoZin-3 were diluted with PBS (0.01 M) to a concentration of 0.4 mM as previously described. The addition of receptors **4.12** - **4.15** (5 μM) individually into liposome suspension (0.4 mM, 3 mL, in 0.01 M PBS) resulted in no changes. Upon further introduction of Zn^{2+} (0.1 mM)(Figure 4.7.1(a)), a significant enhancement of fluorescence was observed in the presence of **4.14** and **4.15**, confirming Zn^{2+} transport behaviour: Zn^{2+} was transported into the liposomes and switched on the FluoZin-3 fluorescence. In contrast, liposome suspension containing receptor **4.12** and **4.13** exhibited no change in fluorescence under the experimental conditions after the addition of Zn^{2+}. A detailed Zn^{2+} titration monitored by a fluorometer at various concentrations of **4.15** was carried out. As shown in Figure 4.7.1 (b) and ESI, high concentrations of **4.15** resulted in enhanced transport efficiency, further supporting our conclusion that bipodal thiosquaramides **4.14** and **4.15** retain the ability to act as Zn^{2+} ionophores.

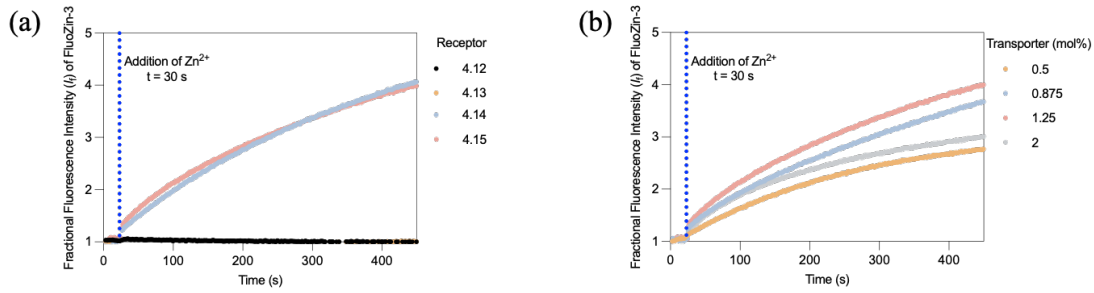

Figure 4.7.1. (a) FluoZin-3 assay: the change of fractional fluorescent intensity with the addition of **4.12** - **4.15** (5 μM) and $Zn(ClO_4)_2$ (0.1 mM) to liposomes containing FluoZin-3 (in 0.01 M PBS, pH 7.4). (b) The dose-dependent change in fluorescence intensity of FluoZin-3 over time of liposomes containing FluoZin-3 in PBS (0.01 M, pH=7.4) upon the addition of **4.15** at a range of increasing concentrations followed by a pulse of $Zn(ClO_4)_2$ (0.1 mM).

4.8 Conclusion and future work

In conclusion, we synthesised a novel family of bipodal squaramide ion receptors, in which two squaramide scaffolds are linked through an aromatic portion. These molecules are obtained through a 5-step synthetic pathway. The yields of the reactions are ranged from 10% - 77%. Novel structures of target molecules are characterised by NMR and HRMS, supported by LCMS.

The binding affinity of receptors towards Cl^- and AcO^- was determined by using ^1H NMR titration, where a 1:2 binding model gave the best fit in all cases. Upon comparison of the binding affinity, bipodal benzoate squaramides displayed relatively stronger binding behaviour than their bipodal benzoic acid squaramide derivatives, indicating the negative effect of the introduction of the carboxylic acid group, thereby revealing the effect of intermolecular interactions on the anion-binding capability. Subsequently, UV-vis titration was employed to evaluate the cation-binding ability of target molecules. As anticipated, the complex thiosquaramide derivatives retained their cation-binding capability. Unlike with anion, bipodal thiosquaramides bind to Zn^{2+} in a 1:1 binding stoichiometry, displaying higher ion affinity than parent thiosquaramides presented in Chapter 2. This demonstrates the favorable influence of the dipodal structure on cation binding. The tert-butyl substituent on the central armotic linker acts as a non-coordinating, hydrophobic ‘baseline’ substituent that

modulates membrane affinity and limits competitive intermolecular hydrogen-bonding. Following this, ion transport assays revealed that the introduction of a COOH group to oxosquaramides not only reduced anion affinity but also inhibited the transmembrane transport process. Although the incorporation of the indole unit as a side-chain substituent significantly increases anion-binding affinity, it proves unfavourable for transport performance. For thiosquaramide derivatives, the opposite trend was observed: incorporation of the COOH group leads to a reduction in anion-binding affinity, but improves the chloride transport efficiency. Moreover, they exhibited the same trend in Zn^{2+} transport. These results reveal the effects of various substituents on both ion affinity and transmembrane transport capability. Overall, although oxosquaramides and thiosquaramides share almost same backbone, the effects of substituent on these two scaffolds diverge substantially. Looking ahead, future work should focus on two aspects: (i) further development of ion transporters based on a bipodal (thio)squaramide framework through rational structural modification. The objective is to fine-tune lipophilicity while preventing self-aggregation. (ii) Like what we did in Chapter 2, leverage biological tools to investigate the application of this class of molecules as antibacterial agents in biological settings.

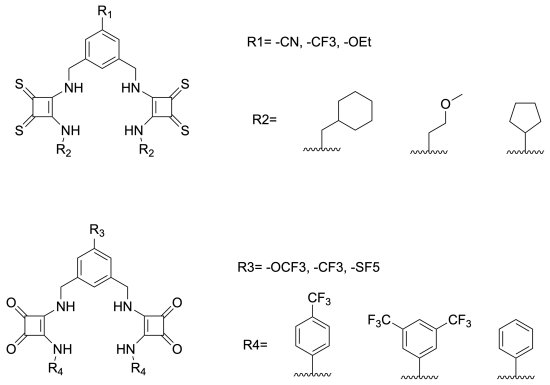

Figure 4.8.1. Potential approaches to the development of (thio)squaramide based bipodal ionophores. Oxosquaramide derivatives modestly increases lipophilicity while retaining the strong electron-withdrawing substituents. Thiosquaramide derivatives slightly modulating lipophilicity. The introduction of the alkyl side chains may suppress self-aggregation and potentially enhance cation-binding affinity.

Chapter 5: Summary of Thesis

5.1 Summary

Synthetic ion transport is emerging as a foundational strategy for building next-generation chemical biology tools and potential drug leads. By enabling the rational exploitation of noncovalent interactions, supramolecular chemistry can selectively recognise and actively translocate biologically relevant ions across membranes. Such controlled perturbation of ion homeostasis carries significant biological implications. For example, restoring epithelial Cl^-/HCO_3^- flux in cystic fibrosis models, modulating autophagy and cell-death pathways by altering organellar pH and membrane potential, and, more recently, eliciting antibacterial effects.

Despite this promise, practical examples of antibacterial ion carriers remain scarce. In this thesis, we take thiosquaramide as a starting point to address its current gap in cation recognition, while further exploring its applications in antibacterial contexts and cellular imaging.

In **Chapter 2**, we synthesised 5 simple thiosquaramide derivatives **2.3**-**2.7**. **2.3** bears a butyl side chain, whereas **2.4**-**2.7** are obtained by extending conjugation between the thiosquaramide central core and distinct aryl rings. Compared to their oxosquaramide derivatives, thiosquaramides exhibit a markedly enhanced affinity for metal ions, with selectivity toward 2+ species such as Cd^{2+}, Pb^{2+}, Hg^{2+}, and Zn^{2+}. Complexation occurs predominantly with a 2:1 (ligand:metal) stoichiometry. This is supported by X-ray crystallography and spectroscopic analyses. Beyond metal coordination, these receptors retain chloride-binding capability. The ion-transport properties of thiosquaramides **2.3**-**2.7** were assessed using liposomes containing FluoZin-3, revealing efficient Zn^{2+} transport behaviour in sharp contrast to oxo-squaramides, which showed no measurable transport under identical conditions. Moreover, in the presence of Zn^{2+}, the chloride transport activity of the thiosquaramides was significantly modulated, consistent with a cotransport mechanism. Importantly, antibacterial assays against *Staphylococcus aureus* demonstrated that the presence of Zn^{2+} substantially potentiated growth inhibition. This pronounced Zn^{2+}-dependent “switch-on” effect indicates that effective cotransport perturbs bacterial ionic homeostasis, thereby supporting the observed antibacterial activity. This conclusion is further supported by confocal microscopy. In summary, these results establish thiosquaramides as a new class of

ion-carrier scaffolds capable of mediating both cation and anion transport while offering tunable bioactivity.

Based on these findings, in **Chapter 3**, we design and synthesise a series of thiosquaramide-based fluorescent sensors **3.1**-**3.6**, which are composed of thiosquaramide units as cation recognition sites and quinoline as fluorophore. These molecules retain metal-binding capability toward various 2+ species such as Ag^{+}, Cd^{2+}, Co^{2+}, Cu^{2+}, Ni^{2+}, Pb^{2+} and Zn^{2+}, forming 2:1 metal-receptor complexes in MeCN. The fluorescence response behaviour of **3.1**-**3.6** was evaluated by using a fluorometer. The results reveal that the addition of metal ions to the MeCN solution of these quinoline thiosquaramide leads to a change from almost no fluorescence to pronounced fluorescence emission. Interestingly, quinoline thiosquaramide is able to form 1:1 complex with Cl^{-} in DMSO solution, but the addition of Cl^{-} to the receptor solution can not 'switch on' the fluorescence. Again, using the FluoZin-3 liposome assay, we evaluated the Zn^{2+} transport performance of **3.1** - **3.6**. The results reveal that quinoline thiosquaramides perform efficient Zn^{2+} transport behaviour. In addition, we further demonstrated that this receptor also exhibits measurable Cl^{-} transport activity by using the lucigenin assay.

In **Chapter 4**, We sought to enhance affinity and selectivity by enforcing preorganization to increase receptor complexity. To this end, we designed a family of bipodal squaramide-based receptor family 1, containing **4.1**-**4.5**. To probe the effects of substituents on ion recognition and transport, we further synthesised receptor family 2 containing **4.6**-**4.10** with improved solubility and **4.11** with increased lipophilicity. In parallel, a family of bipodal thiosquaramide analogues was prepared to assess their performance in cation recognition and transport. Unexpectedly, ^{1}H NMR titrations revealed that the bipodal receptors do not form the anticipated 1:1 chloride complex; instead, the two arms bind Cl^{-} independently and give a 1:2 host-guest complex. Comparison of association constants shows that the thiosquaramide derivatives exhibit the highest affinity towards Cl^{-}, which is owing to their more acidic NH. **4.1**-**4.5** bind Cl^{-} more strongly than **4.6**-**4.10** but less strongly than thiosquaramide derivatives. These findings indicate that -OH substitution improves overall solubility, but it decreases anion affinity. Using the lucigenin assay, we showed that all members of family 1 efficiently mediate chloride transport, whereas within family 2, only **4.7** exhibited discernible transport activity. This finding further

supports that -OH substitution attenuates supramolecular performance. Although all thiosquaramides displayed Cl^- transport behaviour, their efficiencies were generally lower than those of family 1. In addition, we examined the Zn^{2+} transport capability of thiosquaramide derivatives by using the FluoZin-3 assay. Interestingly, in contrast to chloride transport, the results indicate that **4.14** and **4.15** transport Zn^{2+} efficiently, while **4.12** and **4.13** showed no measurable Zn^{2+} transport, which means the introduction of -OH increase the Zn^{2+} transport performance.

In conclusion, we have synthesised a total of 27 squaramide or thiosquaramide candidates and evaluated their supramolecular properties by using various analysis techniques. Building on successful synthesis, we explored the potential of supramolecular structure as ion probes and antibacterial agents. In **Chapter 2**, beginning with five initial compounds, we filled the gap in cation recognition for the thiosquaramide scaffold and established their capacity to exert antibacterial effects via supramolecular mechanisms.. Leveraging this framework, **Chapters 3 and 4** further develop a range of ion transporters and fluorescent probes. Overall, this thesis establishes new supramolecular platforms for antimicrobial and sensing applications, and we anticipate the broad applicability of the methods, assays, and synthetic protocols described herein.

5.2 List of publications

1. L. E. Brennan, **X. Luo**, F. A. Mohammed, K. Kavanagh and R. B. P. Elmes. Uncovering the potent antimicrobial activity of squaramide based anionophores – chloride transport and membrane disruption. *Chem. Sci.*, 2025, **16**, 4075–4084

2. **X. Luo**, L. E. Brennan, C. S. Hawes, T. Krämer, J. Farragher, S. Robinson, K. Kavanagh and R. B. P. Elmes. Thiosquaramides: dual-function ionophores for Zn^{2+} and Cl^- with ion dependent anti-microbial activity. *Org. Biomol. Chem.*, 2025, **23**, 9142–9151.

Chapter 6: Experimental procedures

6.1 Materials and Methods:

Commercial materials were supplied by TCI Europe or Sigma Aldrich and were used without further purification. HPLC grade solvents were used as received. 1H NMR spectra were recorded using a Bruker Avance III 500 at a frequency of 500.13 MHz, and are reported as parts per million (ppm) with CDCl3 (δH 7.26 ppm) or DMSO-d6 (δH 2.50 ppm) as an internal reference. The data are reported as chemical shift (δ), multiplicity (br = broad, s = singlet, d = doublet, t = triplet, m = multiplet), coupling constant (J, Hz) and relative integral. 13C NMR spectra were recorded using a Bruker Avance III 500 at a frequency of 125 MHz and are reported as parts per million (ppm) with CDCl3 (δH 77.1 ppm) or DMSO-d6 (δH 39.5 ppm) as an internal reference. High resolution ESI spectra were recorded on an Agilent Technologies 1200 Series. Analytical TLC was performed using pre-coated silica gel plates (Merck Kieselgel 60 F254). Flash chromatography was performed using silica gel 40-63 μM, 60 Å. FT-IR are reported in wavenumbers (cm-1). 3,4-bis(cyclopentyloxy)cyclobut-3-ene-1,2-dithione and oxosquaramide derivatives were synthesised as previously described.

6.2 pK_a Determination:

The determination of pK_a values was experimentally determined by using the wavelength of maximum difference in absorbance between the UV/Vis spectra of the anionic and the neutral species. Compounds were dissolved in MeCN/H_2O (9:1) containing 0.1 M $TBAPF_6$. An excess of HNO_3 was added to adjust the solution to acidic pH, then, a small aliquot of 0.1 M NaOH solution was titrated slowly to basify the solution. The pH values were adjusted between 2.5 and 14. The difference between absorbance values were plotted against the pH value. The Henderson–Hasselbalch equation was fitted the data to give the pK_a value by Prism 10:

$$Amax + (Amax - Amin)/(1 + 10^{pka-pH})$$

6.3 ^{1}H NMR Chloride Binding Titration:

NMR Binding Studies: NMR titrations were performed by additions of aliquots of the putative anionic guest as the tetrabutylammonium (TBA) salt (200 mM), to

a solution of the receptor (0.4 mM) in either CD_3CN or DMSO-d_6. 0 – 10 equivalents of the respective anion were added to the solution. Both salt and receptor were dried under high vacuum prior to use. ^{1}H NMR spectra were recorded on a Bruker Avance III 500 spectrometer at a frequency of 500.13 MHz and calibrated to the residual protio solvent peak in DMSO-d_6 (δ = 2.50 ppm). Stack plots were made using TopSpin 3.5 and MestReNova. The calculation of association constants (K_a/M^{-1}) was carried out using the open access BindFit software program.

6.4 UV-vis Metal Ion Binding Titration:

UV-vis metal binding studies were performed by additions of aliquots of the putative cationic guest as the perchlorate salt (10 mM) to a solution of the receptor (0.01 mM) in MeCN. Up to 10 equivalents of the respective cation were added to the solution of the receptors. After each addition, the resulting solution was stirred for at least 30 seconds. Both salt and receptor were dried under high vacuum prior to use. The absorbance was monitored before and after the addition of metal ions to the receptor solution by a Varian Cary 50 Scan UV/Vis spectrophotometer. Plots were drawn by using MS Excel/ Prism 10. The data was fitted to a binding model using Bindfit software.

6.5 UV-vis Anion Binding Titration:

Spectroscopic titrations were performed by additions of aliquots of the anion salt solution (as the TBA salt) (10 mM) in MeCN to a solution of the receptor (0.01 mM) in MeCN. After each addition, the resulting solution was stirred for at least 30 seconds and the UV spectrum was recorded. Both salt and receptor were dried under high vacuum prior to use. UV titrations were carried out using a Varian Cary 50 Scan UV/Vis spectrophotometer. Normally, about 5 equivalents of chloride were added to the receptor solution in total. Plots were drawn by using MS Excel. The data was fitted to a binding model using Bindfit software.

6.6 Transport Studies

To prepare large unilamellar liposomes (LUVs), palmitoyl-2-oleoyl-sn-glycero-3-phosphocholine (POPC) in chloroform and cholesterol (7:3) were combined and transferred to a 25 ml round bottom flask.[219] The solvent was evaporated using a rotary evaporator and the formed lipid film was placed under the high vacuum for at least 1h. Either FluoZin-3 (0.5 mL DMSO containing 590.3 μM FluoZin-3 mixed with 3.5 mL 0.01 M PBS (phosphate buffered solution, 0.01 M phosphate buffer containing 0.0027 M KCl and 0.137 M NaCl) or Lucigenin (0.8 mM in 225 mM MNO_3) was added to the film. The mixture was sonicated for 30 s and stirred for 1h to obtain heterogeneous vesicles. Then, multilamellar vesicles were disrupted by 10 freeze-thaw cycles. After that, the vesicle suspension was extruded through a 0.2 mm polycarbonate membrane 29 times to obtain monodisperse large unilamellar vesicles. LUVs were transferred to a size-exclusion column (Seph X-100, eluted with 0.01 M PBS/225 mM MNO_3). The collected vesicles were diluted to 0.4 mM to obtain the liposome solution for the experiment.

For the FluoZin-3 assay (excitation at 494 nm and emission at 519 nm), 3 mL of the liposome suspension was transferred into a cuvette. $Zn(ClO_4)_2$ (0.1 mM) was added to the liposomes (0.4 mM, 3 mL) at 30 s after the start of measurement. The mixture was allowed to equilibrate for 50 s. Then receptors were added to the mixture before the data was collected for at least 600 s.

For the Lucigenin assay (excitation at 430 nm and emission at 505 nm), 3 mL of the liposome suspension was transferred into a cuvette. Receptors were added to the liposomes (0.4 mM, 3 mL) before running, and the mixture was allowed to equilibrate for 3 mins. A pulse of 25 mM MCl (75 μL, 1 M MCl in 225 mM MNO_3) was added to the mixture at 30 s after the start of measurement (for MCl_2 and $M(NO_3)$, the concentration was reduced to 0.5 M MCl_2 and 112.5 $M(NO_3)_2$ to ensure that the concentrations of the anions are the same). The data was collected for at least 600 s, Then Triton X-100 (5% w/w in water) was added to lyse the liposomes, and the recording of data was continued for approx. 2 min.

Double exponential function was employed to analyse data to obtain specific transport rate:

$$\frac{F0}{F} = y - A * e^{-mt} - B * e^{-nt}$$

When t=0, the equation for the initial transport rate:

$$I = Am + Bn$$

The specific initial rate was obtained by dividing the initial transport rate [*I*] by the transporter to lipid concentration.

The data was analysed using the Hill plot to obtain the EC_{50} value. The fractional fluorescence intensity values (F_0/F) at 270 s at different transporter concentrations were measured for Cl^- concentration inside the liposomes. These data were fitted to the Hill equation in Originlab as below:

$$START + (END - START) * x^n/(k^n + x^n)$$

Where *n* is Hill coefficient, *k* presents EC_{50} value (*i.e.*, Concentration of receptors required to achieve the half of max effect).

6.7 DFT Computational Methods

DFT calculation were carried out by Dr. Tobias Kramer.

All calculations presented in this paper have been performed with the ORCA 5.0.3 electronic structure program package.[278] Unconstrained geometry optimizations of receptors 1-4 and subsequent numerical frequency calculations were carried out at the MP2 level, using the def2-TZVP basis set on all atoms.[207] The RI approximation to MP2[208] was invoked as well as the RIJCOSX method[209] in conjunction with appropriate Coulomb def2/J[210] and correlation fitting def2-TZVP/C[279] basis sets. All stationary points were confirmed to be minimal by the absence of imaginary vibrational modes. Vertical transition energies to low-lying excited valence singlet states were computed via time dependent DFT (TDDFT). For these calculations the M06-2X functional[206] with a def-QZVP basis on all atoms was selected.[207] Effects

due to the presence of solvent were included by means of the Conductor-like Polarizable Continuum Model (C-PCM),[280] with parameters corresponding to those of acetonitrile (ε = 36.6; n = 1.344). Non-electrostatic terms to solvation were incorporated through the SMD option.[281] Natural Transition Orbitals (NTO) based on singular value decomposition of the 1-particle Transition density were used to visualize dominant contributions to individual electronic excitations. Geometries and orbitals isosurfaces were visualised using the ChemCraft software tool.[282]

6.8 Biological and imaging experiments:

The following experiments were carried out by Dr. Luke Brennan

6.8.1 Confocal microscopy:

FluoZin-3 doped POPC vesicles were freshly prepared (*vide supra*) the day prior to imaging, where during the experiment vesicles were suspended at 0.1 mM in PBS containing a molar excess of free Zn^{2+} in a live-cell confocal/STED microscopy imaging compatible 96-well plate, making use of central wells to avoid image distortion from the edges of plates. To each well was added either nothing (control), or 10 μM **2.3** - **2.7**. Following a 5 min incubation, images were acquired using a Leica Stellaris 8 confocal microscope.

Confocal images were acquired using a Leica Stellaris 8 fitted with a 3D STED Falcon accessory (objective: Leica HC PL APO CS2 10X/0.40 non-immersion). White light laser was used to excite the fluorophores with a max power of 0.00347 mW close to the focal plane. Images were processed using both LasX, and Image J.

6.8.2 Staphylococcus aureus culture conditions

S. aureus 33591 (ATCC) was cultured at 37 °C in Nutrient Broth (Oxoid) in an orbital shaker at 200 rpm. Stocks were kept on nutrient agar, stored at 4 °C, or as a cell suspension in a 50/50 Glycerol:NB (OD 0.5) mixture at -70 °C.

6.8.3 Toxicity assay

Bacteria were cultured to early stationary phase, in Nutrient Broth at 37 °C, at 200 rpm. Cultures were diluted 1/100, from an overnight culture of OD600 ~ 1.0. Aliquots of culture (100 µL) were added to 100µL serially diluted compounds (to give a final concentration of 200 µM – 0.78 µM) in Nutrient Broth in a 96-well plate (Sarstedt, Germany). Plates were incubated at 37 °C for 24 hr and growth was measured at 600 nm.

6.8.4 Statistical analysis of biological data

All biological experiments were carried out in triplicate, making use of cells of differing origins, on three independent occasions. With experiments concerning the use of 96-well plates, all experiments were carried out as three biological replicates of eight technical replicates. All data is presented as the mean ± SEM of each replicate, unless specified otherwise. All statistical analysis and significance determination was carried out using the Graphpad Prism 8.0.1 software package.

6.9 Synthetic Procedures

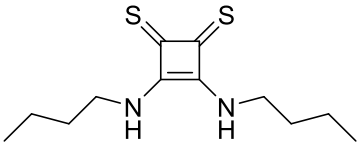

3,4-bis(butylamino)cyclobut-3-ene-1,2-dithione (2.1)

To a solution of 3,4-bis(cyclopentyloxy)cyclobut-3-ene-1,2-dithione (0.141g, 0.5 mmol, 1 equiv) in dry DCM (1 mL) was added butylamine (0.296 mL, 3.0 mmol, 3 equiv.) and stirred for 2 h. The solvent was removed under reduced pressure, and the crude was subjected to flash column chromatography eluting with 6% EtOH in DCM to yield **2.1** as a yellow solid. (40 mg, 0.15 mmol, 31%). ^{1}H NMR (500 MHz, DMSO-d_6)* δ 9.11 (s, 2H), 8.80 (s, 2H), 8.42 (s, 2H), 4.12 (d, J = 6.8 Hz, 4H), 4.04 (d, J = 6.7 Hz, 4H), 3.45 (d, J = 6.7 Hz, 4H), 1.59 (s, 4H), 1.36 (d, J = 7.5 Hz, 4H), 0.92 (s, 6H). ^{13}C NMR (126 MHz, DMSO-d_6): δ= 204.9, 204, 202.8, 172.8, 170.9, 170, 44.3, 42.9, 33.6, 33, 19.4, 13.9. HRMS (ESI) calcd. for $C_{12}H_{21}N_2S_2$ $(M+H)^+$: 257.1141. Found: 257.1150 (+3.5 ppm).

* The ^{1}H and ^{13}C NMR of **2.3** in CD_3CN gave rise to multiple sets of signals. This behaviour is due to the existence of conformations that are interconverting slowly on the NMR timescale. LCMS analysis confirmed the purity of compound **2.3**.

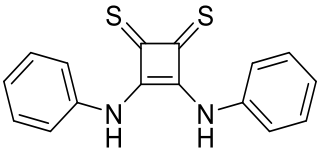

3,4-bis(phenylamino)cyclobut-3-ene-1,2-dithione (2.4)

To a solution of 3,4-bis(cyclopentyloxy)cyclobut-3-ene-1,2-dithione (0.282g, 1.0 mmol, 1 equiv) in dry DCM (3 mL) was added aniline (0.273 mL, 3.0 mmol, 3 equiv). The resulting solution was stirred for 20 h, during which time a yellow precipitate appeared. The precipitate was washed with hexane and yielded product **2.4** as a yellow solid. (210 mg, 0.71 mmol, 71%) ^{1}H NMR (500 MHz, DMSO-d_6): δ= 10.86 (s, 2H), 8.03 – 6.44 (m, 10H). ^{13}C NMR (126 MHz, DMSO-d_6): δ= 208.4, 169.9, 129, 125.8, 122.6. HRMS (ESI) calcd. for $C_{16}H_{13}N_2S_2$ $(M+H)^+$: 297.0525. Found: 297.0523 (-0.67 ppm)

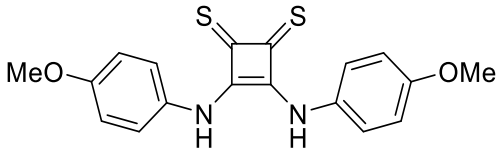

3,4-bis(4-dimethoxyphenyl)amino)cyclobut-3-ene-1,2-dithione (2.5)

To a solution of 3,4-bis(cyclopentyloxy)cyclobut-3-ene-1,2-dithione (141 mg, 0.5 mmol, 1 equiv) in dry DCM (2 mL) was added 4-dimethoxyaniline (130 mg, 1.1 mmol, 2.1 equiv) and stirred overnight. During which time, an orange precipitate formed. Cyclohexane (3 mL) was added, and the suspension was filtered to afford **2.5** as an orange solid. (110 mg, 0.31 mmol, 62%). ^{1}H NMR (500 MHz, CD_3CN): δ= 8.68 (s, 2H), 7.04 (s, 4H), 6.63 (s, 4H), 3.71 (s, 6H). ^{13}C NMR (126 MHz, DMSO-d_6) δ= 207.4, 169.7, 157.5, 131.3, 124.4, 114.2, 55.6. HRMS (ESI) clad. for $C_{18}H_{17}N_2O_2S_2$ $(M+H)^+$: 357.0736. Found: 357.0734 (-0.56 ppm)

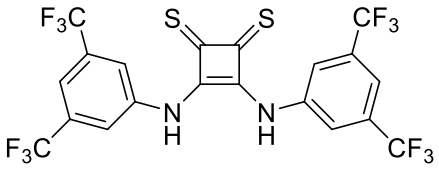

3,4-bis(3,5-bis(trifluoromethyl)phenyl)amino)cyclobut-3-ene-1,2-dithione (2.6)

To a solution of 3,4-bis(cyclopentyloxy)cyclobut-3-ene-1,2-dithione (0.141g, 0.5 mmol, 1 equiv) in dry DCM (1 mL) was added 3,5-bis(trifluoromethyl)aniline (0.25 mL, 2 mmol, 4 equiv) and stirred for 4 days. During which time a yellow precipitate formed. Cyclohexane (2 mL) was added, and the suspension was filtered to afford **2.6** as a yellow solid. (119 mg, 0.21 mmol, 42%). ^{1}H NMR (500 MHz, CD_3CN): δ= 9.21 (s, 2H), 7.71 (s, 4H), 7.65 (s, 2H). ^{13}C NMR (126 MHz, CD_3CN): δ= 212.7, 169.7, 139.3, 132.4 (q, *J* = 34 Hz), 123.4 (q, *J* = 264.6 Hz), 122.7, 122.3, 119.4. HRMS (ESI) clad. for $C_{20}H_9F_{12}N_2S_2$ $(M+H)^+$: 569.0021. Found: 569.0016 (-0.87 ppm)

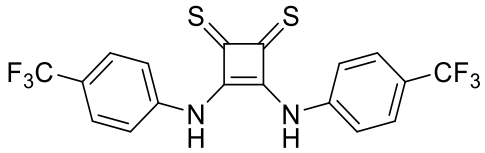

3,4-bis(4-bis(trifluoromethyl)phenyl)amino)cyclobut-3-ene-1,2-dithione (2.7)

To a solution of 3,4-bis(cyclopentyloxy)cyclobut-3-ene-1,2-dithione (0.141g, 0.5 mmol, 1 equiv) in dry DCM (1 mL) was added 4-bis(trifluoromethyl)aniline (0.25 mL, 2 mmol, 4 equiv) and stirred overnight. During which time a yellow precipitate formed. Cyclohexane (3 mL) was added, and the suspension was filtered to afford **2.7** as a yellow solid. (120 mg, 0.27 mmol, 56%). ^{1}H NMR (500 MHz, CD_3CN): δ= 9.09 (s, 2H), 7.39 (d, *J* = 8.3 Hz, 4H), 7.27 (d, *J* = 8.3 Hz, 4H). ^{13}C NMR (126 MHz, CD_3CN): δ= 212.5, 170.7, 142, 128(q, *J* = 32.7 Hz), 127.3, 125.3(q, *J* = 279.7 Hz), 123.7. HRMS (ESI) clad. for $C_{18}H_{11}F_6N_2S_2$ $(M+H)^+$: 433.0273. Found: 433.0272 (-0.23 ppm)

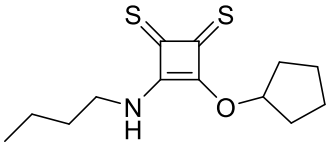

3-(butylamino)-4-(cyclopentyloxy)cyclobut-3-ene-1,2-dithione(B1)

To a solution of 3,4-bis(cyclopentyloxy)cyclobut-3-ene-1,2-dithione (0.141 g, 0.5 mmol, 1 equiv.) in dry DCM (1 mL) was added butylamine (, 0.4 mmol, 0.8 equiv.) at 0 °C and stirred for 2 h. The mixture was loaded directly to the flash column chromatography eluting with DCM to yield **3.1** as a yellow solid. (40 mg, 0.15 mmol, 30%). The compound exists as two rotamers in DMSO-d_6 at room temperature in a ratio of 1:0.55. ^{1}H NMR (500 MHz, DMSO-d_6): δ= 9.76 (t, J = 6.2 Hz, 1H), 9.69 (t, J = 6.2 Hz, 1H), 6.41 (tt, J = 5.2, 2.4 Hz, 1H), 6.32 (tt, J = 5.6, 2.5 Hz, 1H), 3.92 (q, J = 6.8 Hz, 2H), 3.38 (q, J = 6.9 Hz, 2H), 2.03 – 1.91 (m, 4H), 1.78 – 1.70 (m, 4H), 1.70 – 1.62 (m, 4H), 1.60 – 1.52 (m, 2H), 1.34 – 1.26 (m, 2H), 0.89 (td, J = 7.4, 4.8 Hz, 2H). ^{13}C NMR (126 MHz, CD_3CN): δ= 218.5, 218.2, 205.3, 205.2, 183.3, 182.6, 175.4 173.4, 87.6, 87.6, 44.9, 43.2, 34.3, 34.2, 32.8, 32.3, 23.8, 23.6, 19.6, 19.5, 14.0, 13.8.

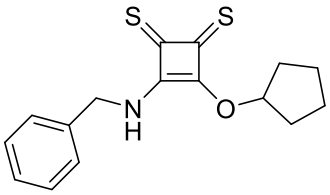

3-(benzylamino)-4-(cyclopentyloxy)cyclobut-3-ene-1,2-dithione(B2)

To a solution of 3,4-bis(cyclopentyloxy)cyclobut-3-ene-1,2-dithione (0.141 g, 0.5 mmol, 1 equiv.) in dry DCM (1 mL) was added benzylamine (86 µL, 0.4 mmol, 0.8 equiv.) at 0 °C and stirred for 2 h. The mixture was filtered, and the precipitate was washed with DCM to yield B1 as an orange solid. (50 mg, 0.16 mmol, 33%). The compound exists as two rotamers in DMSO-d_6 at room temperature in a ratio of 0.89:0.55. ^{1}H NMR (500 MHz, DMSO-d_6) δ= 10.25 (s, 1H), 10.15 (s, 1H), 7.45 – 7.35 (m, 5H), 7.35 – 7.24 (m, 5H), 6.37 (tt, J = 5.1, 2.5 Hz, 1H), 6.32 (tt, J = 2.8, 2.8 Hz, 1H), 5.20 (d, J = 6.4 Hz, 2H), 4.57 (d, J = 6.4 Hz, 2H), 2.03 – 1.95 (m, 4H), 1.95 – 1.85 (m, 4H), 1.77 – 1.72 (m, 4H), 1.69 – 1.57 (m, 4H). ^{13}C NMR (126 MHz,

DMSO-d_6) δ= 218.2, 217.9, 206.0, 183.3, 182.7, 175.6, 173.2, 137.7, 137.7, 129.2, 129.1, 128.4, 128.2, 128.1, 127.9, 87.8, 87.8, 48.4, 46.4, 34.2, 23.5.

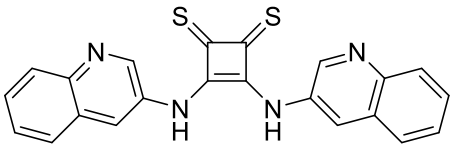

3,4-bis(quinolin-3-ylamino)cyclobut-3-ene-1,2-dithione(3.1)

To a solution of 3,4-bis(cyclopentyloxy)cyclobut-3-ene-1,2-dithione (0.141 g, 0.5 mmol, 1 equiv.) in dry DCM (10 mL) was added 3-aminoquinoline (0.16 g, 1.1 mmol, 2.2 equiv.) and stirred for 2 days. The mixture was filtered, and the precipitate was washed with DCM to yield **3.1** as an orange solid. (168 mg, 0.42 mmol, 85%). ^{1}H NMR (500 MHz, DMSO-d_6) δ= 11.36 (s, 2H), 8.84 (s, 2H), 8.13 (s, 2H), 7.73 – 7.69 (m, 2H), 7.54 (s, 4H), 7.47 – 7.44 (m, 2H). ^{13}C NMR (126 MHz, DMSO-d_6) δ= 209.4, 170.4, 146.4, 145.2, 129.3, 128.6, 128.1, 127.5, 127.2. HRMS (ESI) clad. for $C_{22}H_{14}N_4S_2$ $(M+H)^+$: 399.0740. Found: 399.0783 (-0.0043 ppm).

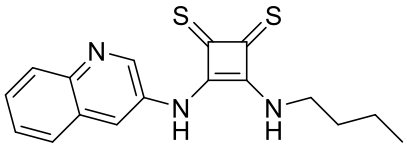

3-(butylamino)-4-(quinolin-3-ylamino)cyclobut-3-ene-1,2-dithione(3.2)

To a solution of **B1** (0.141 g, 0.5 mmol, 1 equiv.) in dry DCM (8 mL) was added 3-aminoquinoline (0.16 g, 1.1 mmol, 2.2 equiv.) and stirred for 1 day. The mixture was filtered, and the precipitate was washed with DCM to yield **3.2** as an orange solid. (123 mg, 0.37 mmol, 75%). The compound exists as two rotamers in DMSO-d_6 at room temperature in a ratio of 0.3:1. Major rotamer ^{1}H NMR (500 MHz, DMSO-d_6) δ= 10.99 (s, 1H), 8.99 (s, 1H), 8.94 (s, 1H), 8.03 (d, J = 8.4 Hz, 1H), 7.95 (d, J = 8.3 Hz, 1H), 7.74 (t, J = 1.5 Hz, 2H), 7.64 (t, J = 1.2 Hz, 1H), 4.09 (q, J = 6.7 Hz, 2H), 1.63 (h, 2H), 1.40 (h, J = 7.4 Hz, 2H), 0.93 (t, J = 7.4 Hz, 3H). ^{13}C NMR (126 MHz, DMSO-d_6) δ= 209.5, 169.6, 146.6, 145.5, 130.3, 129.5, 129.4, 129.1, 128.5, 127.9,

127.7, 127.3, 127.1, 45.1, 43.4, 33.1, 32.4, 19.5, 19.4, 14.0. HRMS (ESI) clad. for $C_{17}H_{17}N_3S_2$ $(M+H)^+$: 328.0948. Found: 328.0943 (-0.0005 ppm).

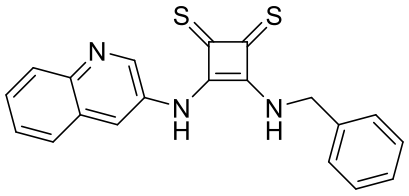

3-(benzylamino)-4-(quinolin-3-ylamino)cyclobut-3-ene-1,2-dithione(3.3)

To a solution of **B2** (0.141 g, 0.5 mmol, 1 equiv.) in dry DCM (10 mL) was added 3-aminoquinoline (0.16 g, 0.55 mmol, 1.1 equiv.) and stirred for 1 day. The mixture was filtered, and the precipitate was washed with DCM to yield **3.3** as an orange solid (125 mg, 0.36 mmol, 72%). The compound exists as two rotamers in DMSO-d_6 at room temperature in a ratio of 1:7. Major rotamer ^{1}H NMR (500 MHz, DMSO-d_6) δ= 8.99 (s, 1H), 8.90 (s, 1H), 8.02 (d, J = 8.4 Hz, 1H), 7.90 (d, J = 8.1 Hz, 1H), 7.73 (d, J = 1.5 Hz, 1H), 7.66 – 7.59 (m, 2H), 7.48 – 7.38 (m, 5H), 5.39 (d, J = 6.0 Hz, 2H). ^{13}C NMR (126 MHz, DMSO-d_6) δ= 209.1, 169.6, 146.6, 145.5, 138.1, 130.3, 129.5, 129.1, 129.14, 128.4, 128.3, 128.1, 127.8, 127.8, 127.1, 46.9. HRMS (ESI) clad. for $C_{20}H_{15}N_3S_2$ $(M+H)^+$: 362.0791. Found: 362.0776 (-0.0015 ppm).

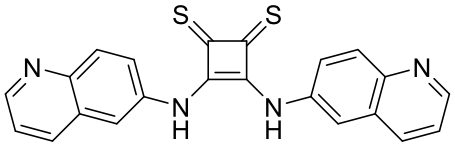

3,4-bis(quinolin-6-ylamino)cyclobut-3-ene-1,2-dithione(3.4)

To a solution of 3,4-bis(cyclopentyloxy)cyclobut-3-ene-1,2-dithione (0.141 g, 0.5 mmol, 1 equiv.) in dry DCM (10 mL) was added 6-aminoquinoline (0.16 g, 1.1 mmol, 2.2 equiv.) and stirred for 2 days. The mixture was filtered, and the precipitate was washed with DCM to yield **3.4** as an orange solid. (163 mg, 0.41 mmol, 81%). ^{1}H NMR (500 MHz, DMSO-d_6) δ= 11.37 (s, 2H), 8.55 (s, 2H), 7.96 (s, 2H), 7.52 (s, 6H), 7.25 (s, 1H). ^{13}C NMR (126 MHz, DMSO-d_6) δ= 209.5, 170.3, 150.0, 145.4,

135.83, 129.7, 127.7, 125.2, 121.9, 120.0. HRMS (ESI) clad. for $C_{22}H_{14}N_4S_2$ $(M+H)^+$: 399.0740. Found: 399.0732 (-0.0008 ppm).

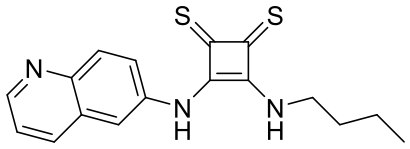

3-(butylamino)-4-(quinolin-6-ylamino)cyclobut-3-ene-1,2-dithione(3.5)

To a solution of **B1** (0.141 g, 0.5 mmol, 1 equiv.) in dry DCM (8 mL) was added 6-aminoquinoline (0.16 g, 1.1 mmol, 2.2 equiv.) and stirred for 1 day. The mixture was filtered, and the precipitate was washed with DCM to yield **3.5** as an orange solid. (124 mg, 0.38 mmol, 76%). The compound exists as two rotamers in DMSO-d_6 at room temperature in a ratio of 1:10. Major rotamer ^{1}H NMR (500 MHz, DMSO-d_6) δ= 10.98 (s, 1H), 8.87 (dd, J = 4.2, 1.6 Hz, 1H), 8.37 (s, 1H), 8.31 (d, J = 8.3 Hz, 1H), 8.03 (d, J = 9.0 Hz, 1H), 7.87 (d, J = 9.2 Hz, 1H), 7.56 (dd, J = 8.3, 4.2 Hz, 2H), 4.09 (q, J = 6.8 Hz, 2H), 1.63 (p, J = 7.1 Hz, 2H), 1.39 (h, J = 7.4 Hz, 2H), 0.93 (t, J = 7.4 Hz, 3H). ^{13}C NMR (126 MHz, DMSO-d_6) δ= 209.2, 169.42, 150.4, 146.0, 136.3, 134.5, 130.3, 128.6, 125.6, 122.6, 122.5, 119.8, 43.5, 33.2, 19.5, 14.1, 13.9. HRMS (ESI) clad. for $C_{17}H_{17}N_3S_2$ $(M+H)^+$: 328.0948. Found: 328.0933 (-0.0015 ppm).

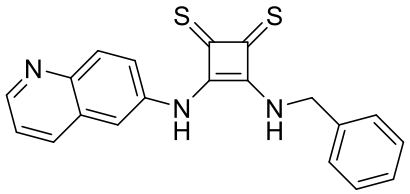

3-(butylamino)-4-(quinolin-6-ylamino)cyclobut-3-ene-1,2-dithione(3.6)

To a solution of **B2** (0.141 g, 0.5 mmol, 1 equiv.) in dry DCM (10 mL) was added 6-aminoquinoline (0.16 g, 0.55 mmol, 1.1 equiv.) and stirred for 1 day. The mixture was filtered, and the precipitate was washed with DCM to yield **3.6** as an orange solid (121 mg, 0.35 mmol, 71%). The compound exists as two rotamers in DMSO-d_6 at room temperature in a ratio of 1:4. Major rotamer ^{1}H NMR (500 MHz, DMSO-d_6)

δ= 11.03 (s, 1H), 8.86 (dd, *J* = 4.2, 1.7 Hz, 1H), 8.79 (s, 1H), 8.25 (d, *J* = 8.3 Hz, 1H), 8.02 (d, *J* = 8.9 Hz, 1H), 7.87 (d, 1H), 7.54 (dd, *J* = 8.3, 4.2 Hz, 2H), 7.48 – 7.38 (m, 5H), 5.39 (d, *J* = 5.9 Hz, 2H). ^{13}C NMR (126 MHz, DMSO-d_6) δ= 208.9, 170.6, 169.4, 150.4, 146.0, 138.2, 136.3, 134.5, 130.2, 129.2, 128.6, 128.3, 128.1, 127.9, 125.7, 122.6, 120.0, 46.9. HRMS (ESI) clad. for $C_{20}H_{15}N_3S_2$ $(M+H)^+$: 362.0791. Found: 362.0775 (-0.0016 ppm).

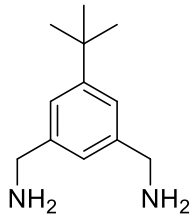

C1

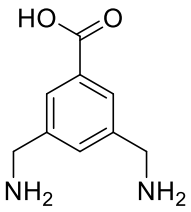

C2

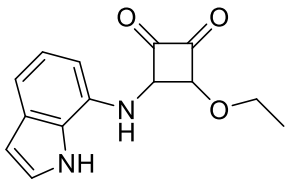

C5

(5-(*tert*-butyl)-1,3-phenylene)dimethanamine (C1) and 3,5-bis(aminomethyl)benzoic acid (C2) was obtained by following the method reported before.[267,283,284]

3-((1*H*-indol-7-yl)amino)-4-ethoxycyclobut-3-ene-1,2-dione (C5) was synthesized by following the method developed by Picci and co-workers.[285,286]

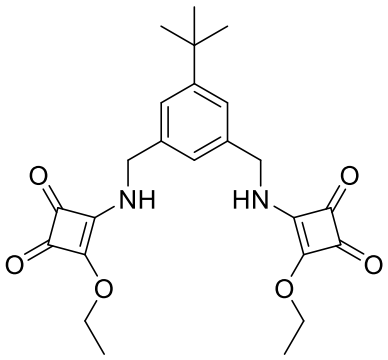

4,4'-(((5-(tert-butyl)-1,3-phenylene)bis(methylene))bis(azanediyl))bis(3-ethoxycyclobut-3-ene-1,2-dione) (C3)

To a solution of diethyl squarate (0.44 mL, 3 mmol, 3 equiv.) in EtOH (40 mL) was slowly added **C1** (0.19 g, 1 mmol, 1 equiv.), followed by 5 eq. triethylamine. The mixture was stirred for 1 day. Diethyl ether was added to crush out the white precipitate. The precipitate was further washed with cold EtOH and diethyl ether to

yield **C3** as a white solid (0.38 g, 0.86 mmol, 86%). ^{1}H NMR (500 MHz, DMSO-d_6) δ= 9.28 (d, J = 6.3 Hz, 1H), 9.05 (d, J = 6.8 Hz, 1H), 7.30 (s, 1H), 7.27 (s, 1H), 7.04 (s, 1H), 4.66 (q, J = 6.9 Hz, 4H), 4.46 (d, J = 6.1 Hz, 4H), 1.41 – 1.30 (m, 6H), 1.28 (s, 9H). ^{13}C NMR (126 MHz, DMSO-d_6) δ= 189.9, 189.6, 182.8, 182.5, 177.7, 177.1, 173.0, 172.4, 151.9, 139.0, 138.7, 124.2, 69.4, 48.0, 47.5, 34.9, 31.5, 16.1.

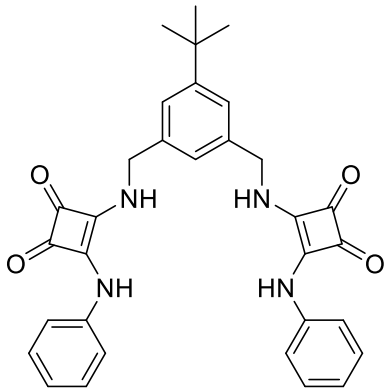

4,4'-(((5-(tert-butyl)-1,3-phenylene)bis(methylene))bis(azanediyl))bis(3-(phenylamino)cyclobut-3-ene-1,2-dione) (4.1)

To a solution of **C3** (0.44 g, 1 mmol, 1 equiv.) in EtOH (40 mL) was added aniline (0.23 mL, 2.5 mmol, 2.5 equiv.). The mixture was refluxed for 2 days. The precipitate was collected and slowly recrystallised from DMSO to yield **4.1** as a white solid (0.42 g, 0.78 mmol, 78%). ^{1}H NMR (500 MHz, DMSO-d_6) δ= 9.63 (s, 2H), 8.01 (s, 2H), 7.43 (s, 2H), 7.41 (s, 4H), 7.32 (t, J = 7.7 Hz, 4H), 7.24 (s, 1H), 7.02 (t, J = 7.4 Hz, 2H), 4.82 (d, J = 5.8 Hz, 4H), 1.29 (s, 9H). ^{13}C NMR (126 MHz, DMSO-d_6) δ= 184.5, 180.8, 169.2, 164.2, 152.3, 139.4, 139.2, 129.8, 129.3, 124.8, 124.7, 123.2, 118.5, 116.1, 114.3, 47.8, 35.0, 31.6. HRMS (ESI) clad. for $C_{32}H_{29}N_4O_4$ $(M+H)^+$: 535.2345. Found: 535.2343 (-0.0002 ppm)

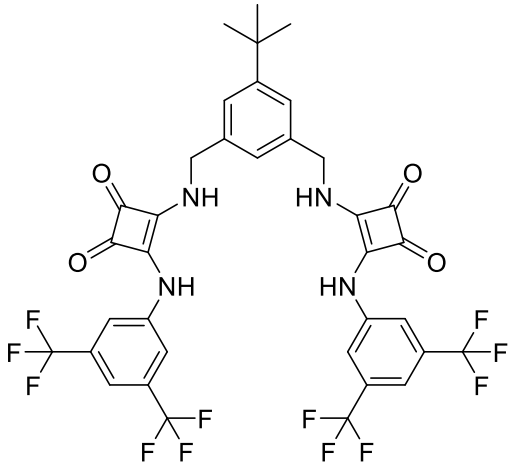

4,4'-(((5-(tert-butyl)-1,3-phenylene)bis(methylene))bis(azanediyl))bis(3-((3,5-bis(trifluoromethyl)phenyl)amino)cyclobut-3-ene-1,2-dione) (4.2)

To a solution of **C3** (0.44 g, 1 mmol, 1 equiv.) in EtOH (40 mL) was added 3,5-bis(trifluoromethyl)aniline (0.34 mL, 2.2 mmol, 2.2 equiv.) The mixture was refluxed for 2 days. The precipitate was collected and recrystallised from hot EtOH to yield **4.2** as a white solid (0.58 g, 0.72 mmol, 72%). ^{1}H NMR (500 MHz, DMSO-d_6) δ= 10.13 (s, 2H), 8.08 (s, 2H), 7.97 (s, 4H), 7.60 (s, 2H), 7.39 (s, 2H), 7.18 (s, 1H), 4.83 (s, 4H), 1.29 (s, 9H). ^{13}C NMR (126 MHz, DMSO-d_6) δ= 185.2, 180.9, 169.8, 163.1, 152.3, 141.5, 139.1, 131.7 (q, J = 33.9 Hz), 124.6, 124.2, 123.5 (q, J = 250.8 Hz), 118.4, 115.1, 79.7, 79.4, 79.2, 47.8, 35.0, 31.5. HRMS (ESI) clad. for $C_{36}H_{26}F_{12}N_4O_4$ $(M+H)^+$: 807.1841. Found: 807.1824 (-0.0017 ppm)

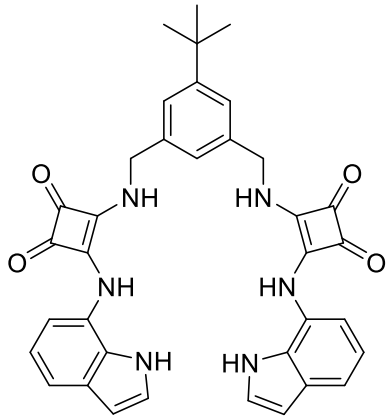

4,4'-(((5-(tert-butyl)-1,3-phenylene)bis(methylene))bis(azanediyl))bis(3-((1H-indol-7-yl)amino)cyclobut-3-ene-1,2-dione) (4.3)

To a solution of **C3** (0.44 g, 1 mmol, 1 equiv.) in EtOH (40 mL) was added 7-aminoindole (0.29 g, 2.2 mmol, 2.2 equiv.). The mixture was refluxed for 2 days. The precipitate was collected and slowly recrystallised from DMSO to yield **4.3** as a cyan solid (0.44 g, 0.72 mmol, 72%). ^{1}H NMR (500 MHz, DMSO-d_6) δ= 10.89 (s, 2H), 9.57 (s, 2H), 7.78 (s, 2H), 7.41 (s, 2H), 7.39 – 7.31 (m, 6H), 7.23 (s, 1H), 6.97 (d, J = 5.4 Hz, 2H), 6.48 (dd, J = 3.1, 1.8 Hz, 2H), 4.81 (s, 4H), 1.31 (s, 9H). ^{13}C NMR (126 MHz, DMSO-d_6) δ= 185.1, 181.8, 169.2, 165.3, 152.2, 139.4, 129.7, 129.0, 126.3, 124.8, 124.5, 123.5, 119.8, 117.1, 113.9, 102.5, 47.8, 35.0, 31.6. HRMS (ESI) calcd. for $C_{36}H_{33}N_6O_4$ $(M+H)^+$: 613.2563. Found: 613.2546 (-2.77 ppm)

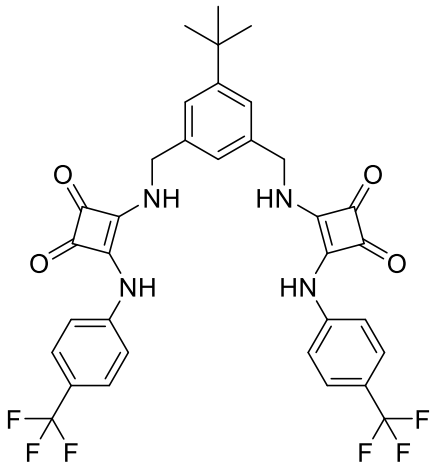

4,4'-(((5-(tert-butyl)-1,3-phenylene)bis(methylene))bis(azanediyl))bis(3-((4-(trifluoromethyl)phenyl)amino)cyclobut-3-ene-1,2-dione) (4.4)

To a solution of **C3** (0.44 g, 1 mmol, 1 equiv.) in EtOH (40 mL) was added 4-(trifluoromethyl)aniline (0.28 mL, 2.2 mmol, 2.2 equiv.). The mixture was refluxed for 2 days. The precipitate was collected and slowly recrystallised from DMSO to yield **4.4** as a white solid (0.44 g, 0.65 mmol, 65%). ^{1}H NMR (500 MHz, DMSO-d_6) δ= 9.91 (s, 2H), 8.10 (s, 2H), 7.63 (d, J = 8.4 Hz, 4H), 7.56 (d, J = 8.4 Hz, 4H), 7.41 (s, 2H), 7.22 (s, 1H), 4.83 (d, J = 6.2 Hz, 4H), 1.29 (s, 9H). ^{13}C NMR (126 MHz, DMSO-d_6) δ= 185.2, 180.7, 169.7, 163.6, 152.3, 143.0, 139.1, 127.0, 125.4 (q, J = 272.2 Hz), 124.6, 124.5, 123.0, 122.7, 118.4, 47.9, 35.0, 31.5. HRMS (ESI) clad. for $C_{34}H_{28}F_6N_4O_4$ $(M+H)^+$: 671.2093. Found: 671.2076 (-0.0017 ppm)

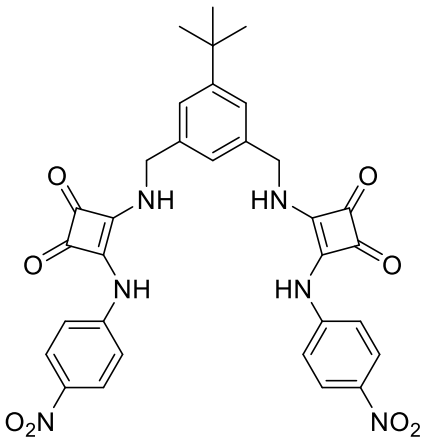

4,4'-(((5-(tert-butyl)-1,3-phenylene)bis(methylene))bis(azanediyl))bis(3-((4-nitrophenyl)amino)cyclobut-3-ene-1,2-dione) (4.5)

To a solution of **C3** (0.44 g, 1 mmol, 1 equiv.) in EtOH (40 mL) was added 4-nitroaniline (0.31 g, 2.2 mmol, 2.2 equiv.). The mixture was refluxed for 2 days. The precipitate was collected and slowly recrystallised from DMSO to yield **4.5** as an orange solid (0.43 g, 0.69 mmol, 69%). ^{1}H NMR (500 MHz, DMSO-d_6) δ= 10.12 (s, 2H), 8.19 (s, 2H), 8.13 (d, J = 8.7 Hz, 4H), 7.53 (d, J = 8.7 Hz, 4H), 7.40 (s, 2H), 7.20 (s, 1H), 4.84 (s, 4H), 1.30 (s, 9H). ^{13}C NMR (126 MHz, DMSO-d_6) δ= 185.7, 180.7, 170.2, 163.0, 152.3, 145.7, 141.8, 139.0, 125.9, 124.6, 124.3, 118.1, 47.9, 35.0, 31.6. HRMS (ESI) clad. for $C_{32}H_{28}N_6O_8$ $(M+H)^+$: 625.2047. Found: 625.2039 (-0.0008 ppm)

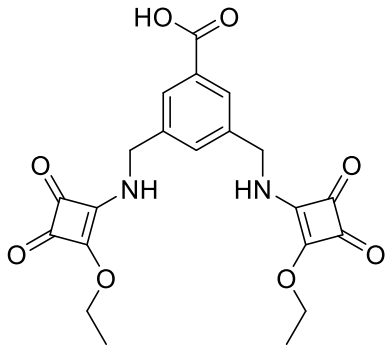

3,5-bis(((2-ethoxy-3,4-dioxocyclobut-1-en-1-yl)amino)methyl)benzoic acid (C4)

To a solution of diethyl squarate (0.44 mL, 3 mmol, 3 equiv.) in EtOH (40 mL) was added **C2** (0.25 g, 1 mmol, 1 equiv.), followed by 5 eq. triethylamine. The mixture was stirred for 1 day. The solvent was removed under reduced pressure, and the

residue was suspended in 2 M HCl overnight. The precipitate was filtered and further washed with H_2O to yield C4 as a white solid (0.35 g, 0.82 mmol, 82%). ^{1}H NMR (500 MHz, DMSO-d_6) δ= 13.12 (s, 1H), 9.33 (d, J = 5.7 Hz, 1H), 9.12 (d, J = 6.3 Hz, 1H), 7.84 (s, 2H), 7.51 – 7.44 (m, 1H), 4.75 (d, J = 6.4 Hz, 2H), 4.65 (dq, J = 14.3, 7.1 Hz, 4H), 4.53 (t, J = 5.2 Hz, 2H), 1.38 (t, J = 7.1 Hz, 3H), 1.32 (t, J = 3.7 Hz, 3H). ^{13}C NMR (126 MHz, DMSO-d_6) δ= 189.8, 189.5, 182.9, 182.6, 177.9, 177.3, 173.2, 172.4, 167.3, 139.9, 139.7, 131.9, 131.3, 128.1, 69.5, 47.3, 46.8, 16.0, 16.0.

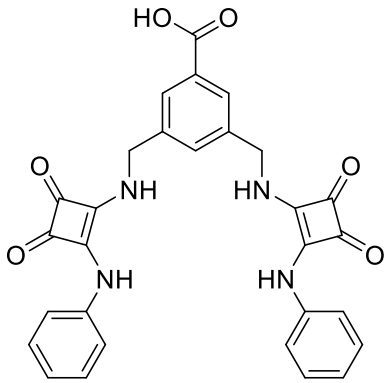

3,5-bis(((3,4-dioxo-2-(phenylamino)cyclobut-1-en-1-yl)amino)methyl)benzoic acid (4.6)

To a solution of **C4** (0.42 g, 1 mmol, 1 equiv.) and $Zn(OTf)_2$ (0.14 g, 0.4 mmol, 0.4 equiv.) in DMF (10 mL) was added aniline (0.36 mL, 4 mmol, 4 equiv.). The mixture was heated at 70 °C for 3 days. The precipitate was collected by filtration and further washed with EtOH and Diethyl ether. Then the crude was slowly recrystallised from DMF to yield **4.6** as a grey solid (0.2 g, 0.38 mmol, 38%).^{1}H NMR (500 MHz, DMSO-d_6) δ= 9.77 (s, 2H), 8.18 (s, 2H), 7.93 (s, 2H), 7.50 (s, 1H), 7.42 (d, J = 7.9 Hz, 4H), 7.31 (t, J = 7.8 Hz, 4H), 7.01 (t, J = 7.4 Hz, 2H), 4.88 (s, 4H). ^{13}C NMR (126 MHz, DMSO-d_6) δ= 184.5, 180.9, 169.2, 164.3, 139.4, 129.8, 128.4, 123.2, 118.6, 47.4. HRMS (ESI) clad. for $C_{29}H_{22}N_4O_6$ $(M+H)^+$: 523.1618. Found: 523.1604 (-0.0014 ppm).

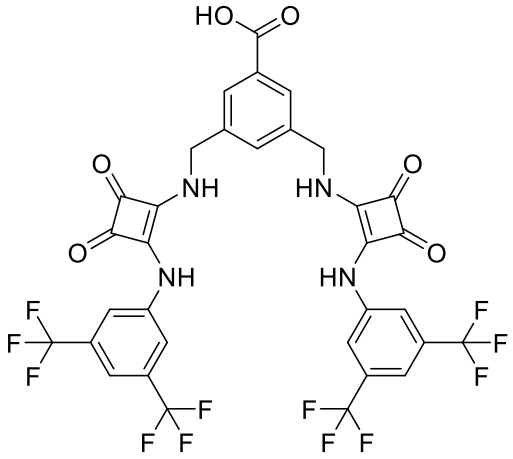

3,5-bis(((2-((3,5-bis(trifluoromethyl)phenyl)amino)-3,4-dioxocyclobut-1-en-1-yl)amino)methyl)benzoic acid (4.7)

To a solution of **C4** (0.42 g, 1 mmol, 1 equiv.) and $Zn(OTf)_2$ (0.14 g, 0.4 mmol, 0.4 equiv.) in DMF (10 mL) was added 3,5-bis(trifluoromethyl)aniline (0.62 mL, 4 mmol, 4 equiv.). The mixture was heated at 70 °C for 3 days. The precipitate was collected by filtration and further washed with EtOH and Diethyl ether to yield **4.7** as a white solid (0.25 g, 0.32 mmol, 32%).^{1}H NMR (500 MHz, DMSO-d_6) δ= 13.17 (s, 1H), 10.20 (s, 2H), 8.15 (s, 2H), 7.98 (s, 4H), 7.93 (d, J = 1.7 Hz, 2H), 7.61 (s, 1H), 7.60 (s, 2H), 4.92 (d, J = 6.3 Hz, 4H). ^{13}C NMR (126 MHz, DMSO-d_6) δ= 185.3, 181.1, 169.9, 167.4, 163.3, 141.4, 140.1, 131.7 (q, J = 33.4 Hz), 131.2, 128.0, 123.6 (q, J = 272.7 Hz), 118.5, 115.2, 47.2. HRMS (ESI) clad. for $C_{33}H_{18}F_{12}N_4O_6$ $(M+H)^+$: 795.1113. Found: 795.1103 (-0.0010 ppm).

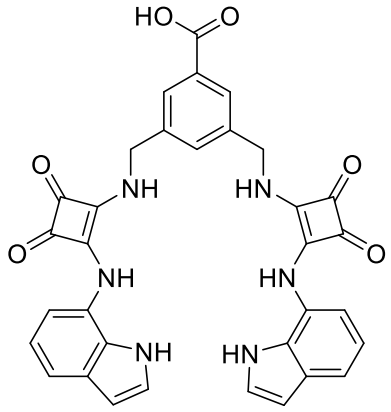

3,5-bis(((2-((1H-indol-7-yl)amino)-3,4-dioxocyclobut-1-en-1-yl)amino)methyl)benzoic acid (4.8)

To a solution of **C2** (0.25 g, 1 mmol, 1 equiv.) in EtOH was added C5 (0.64 g, 2.5 mmol, 2.5 equiv.), followed by TEA (0.83 mL, 6 mmol, 6 equiv.). The mixture was stirred for 1 day. The precipitate was collected and suspended in 1M HCl, stirred for 30 minutes and then filtered and washed with 1M HCl and EtOH. The crude was slowly recrystallised from DMF to yield **4.8** as a cyan solid (100 mg, 0.16 mmol, 16%). ^{1}H NMR (500 MHz, DMSO-d_6) δ= 13.08 (s, 1H), 10.86 (s, 2H), 9.59 (s, 2H), 7.86 (s, 2H), 7.78 (s, 2H), 7.54 (s, 1H), 7.32 – 7.24 (m, 6H), 6.90 (d, J = 6.6 Hz, 2H), 6.41 (dd, J = 3.1, 1.9 Hz, 2H), 4.81 (s, 4H). ^{13}C NMR (126 MHz, DMSO-d_6) δ= 185.7, 180.7, 170.2, 163.1, 145.6, 141.9, 139.9, 128.1, 126.0, 118.2, 47.3. HRMS (ESI) clad. for $C_{33}H_{24}N_6O_6$ $(M+H)^+$: 601.1836. Found: 601.1826 (-0.0010 ppm).

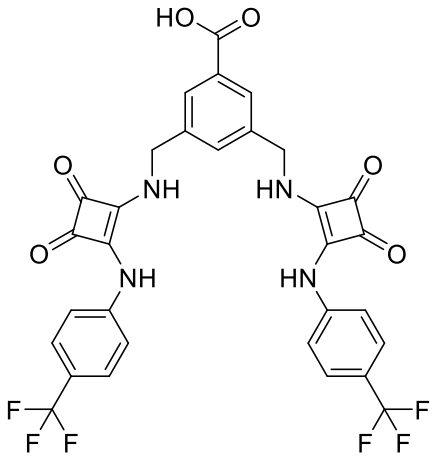

3,5-bis(((3,4-dioxo-2-((4-(trifluoromethyl)phenyl)amino)cyclobut-1-en-1-yl)amino)methyl)benzoic acid (4.9)

To a solution of **C4** (0.42 g, 1 mmol, 1 equiv.) and $Zn(OTf)_2$ (0.14 g, 0.4 mmol, 0.4 equiv.) in EtOH (100 mL) was added 4-(trifluoromethyl)aniline (0.5 mL, 4 mmol, 4 equiv.). The mixture was heated at 70 °C for 3 days. The precipitate was collected by filtration and further washed with EtOH and Diethyl ether. Then the crude was slowly recrystallised from DMF to yield **4.9** as a white solid (0.23 mg, 0.35 mmol, 35%). ^{1}H NMR (500 MHz, DMSO-d_6) δ= 13.18 (s, 1H), 9.98 (s, 2H), 8.16 (s, 2H), 7.93 (s, 2H), 7.65 (d, J = 8.1 Hz, 4H), 7.56 (d, J = 8.4 Hz, 4H), 4.92 (d, J = 6.4 Hz, 4H). ^{13}C NMR (126 MHz, DMSO-d_6) δ= 185.2, 180.9, 169.8, 167.4, 163.8, 142.9, 140.1, 132.1, 131.4, 128.0, 127.0, 124.9 (d, J = 271.1 Hz), 122.9 (q, J = 32.1 Hz),

118.5, 47.2. HRMS (ESI) clad. for $C_{31}H_{20}F_6N_4O_6$ $(M+H)^+$: 659.1365. Found: 659.1356 (-0.0009 ppm).

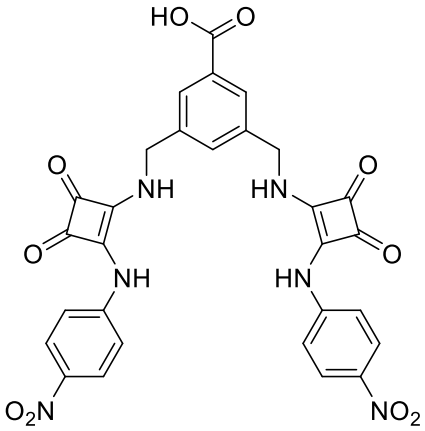

3,5-bis(((2-((4-nitrophenyl)amino)-3,4-dioxocyclobut-1-en-1 yl)amino)methyl)benzoic acid (4.10)

To a solution of **C4** (0.42 g, 1 mmol, 1 equiv.) and $Zn(OTf)_2$ (0.14 g, 0.4 mmol, 0.4 equiv.) in DMF (10 mL) was added 4-nitroaniline (0.49 g, 4 mmol, 4 equiv.). The mixture was heated at 70 °C for 3 days. Diethyl ether was added to crush out the orange precipitate. The precipitate was collected and further washed with EtOH and Diethyl ether. Then the crude was slowly recrystallised from DMF to yield **4.10** as an orange solid (0.39 g, 0.63 mmol, 63%). ^{1}H NMR (500 MHz, DMSO-d_6) δ= 13.18 (s, 1H), 10.27 (s, 2H), 8.30 (s, 2H), 8.15 (d, J = 8.7 Hz, 4H), 7.95 – 7.91 (m, 2H), 7.60 (s, 1H), 7.55 (d, J = 8.7 Hz, 4H), 4.92 (d, J = 6.2 Hz, 4H). ^{13}C NMR (126 MHz, DMSO-d_6) δ= 185.70, 180.73, 170.24, 163.05, 145.61, 141.87, 139.89, 128.10, 125.97, 118.17, 47.27. HRMS (ESI) clad. for $C_{29}H_{20}N_6O_{10}$ $(M+H)^+$: 613.1319. Found: 613.1308 (-0.0011 ppm).

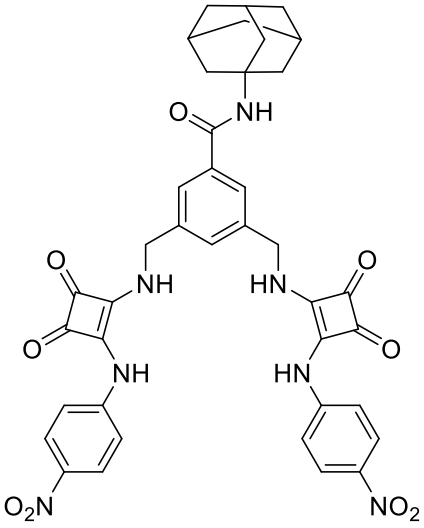

_N_-(adamantan-1-yl)-3,5-bis(((2-((4-nitrophenyl)amino)-3,4-dioxocyclobut-1-en-1-yl)amino)methyl)benzamide (4.11)

To a solution of **3.10** (100 mg, 0.16 mmol, 1 equiv.) in DMF (5 mL) was added N-hydroxysuccinimide (36 mg, 0.32 mmol, 2 equiv.) followed by EDCI (60 mg, 0.32 mmol, 2 equiv.). The mixture was stirred overnight, and then the solvent was removed under. The crude was washed with water and DCM to form the intermediate. Next, the intermediate was dissolved in DMSO (5 mL) followed by 1-adamantylamine (75 mg, 0.22 mmol) and TEA (60 µL, 0.44 mmol). The mixture was allowed to stir for 24 hours at room temperature. Then, DMSO was removed by freeze dryer to obtain a purple solid. The solid was washed with water and EtOH to yield **4.11** as an orange solid (86 mg, 0.11 mmol, 68%). ^{1}H NMR (500 MHz, DMSO-d_6) δ= 10.35 (s, 2H), 8.33 (s, 2H), 8.16 (d, J = 8.8 Hz, 4H), 7.73 (s, 2H), 7.67 (s, 1H), 7.57 (d, J = 8.7 Hz, 4H), 7.47 (s, 1H), 4.90 (s, 4H), 2.07 (s, 12H), 1.66 (s, 3H). ^{13}C NMR (126 MHz, DMSO-d_6) δ= 185.7, 180.9, 170.4, 166.2, 163.3, 141.7, 139.3, 137.3, 126.2, 125.9, 118.3, 52.1, 49.1, 47.4, 36.5, 35.5, 29.4, 28.8. HRMS (ESI) clad. for $C_{39}H_{35}N_7O_9$ $(M+H)^+$: 746.2575. Found: 746.2560 (-0.0015 ppm).

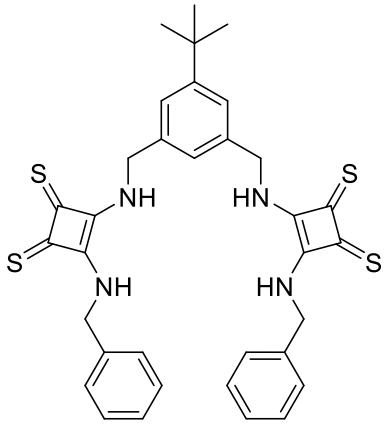

4,4'-(((5-(*tert*-butyl)-1,3-phenylene)bis(methylene))bis(azanediyl))bis(3-(benzylamino)cyclobut-3-ene-1,2-dithione) (4.12)

To a solution of **C1** (57 mg, 0.3 mmol, 1 equiv.) in dry DCM (8 mL) was slowly added 5 mL DCM solution of **B2** (200 mg, 0.66 mmol, 2.2 equiv.) and stirred for 1 day. The mixture was filtered, and the precipitate was washed with DCM to yield **4.12** as an orange solid. (62 mg, 0.1 mmol, 34%). ^{1}H NMR (500 MHz, DMSO-d_6) δ= 8.88 – 8.82 (m, 4H), 7.52 – 7.22 (m, 13H), 5.31 (d, J = 6.5 Hz, 8H), 1.26 (s, 9H). ^{13}C NMR (126 MHz, DMSO-d_6) δ= 204.5, 204.5, 170.5, 170.4, 152.4, 138.2, 137.9, 129.3, 129.1, 129.0, 128.4, 128.3, 127.9, 125.4, 125.2, 46.6, 46.5, 35.1, 31.5, 31.5. HRMS (ESI) clad. for $C_{34}H_{34}N_4S_4$ $(M+H)^+$: 627.1750. Found: 627.1726 (-0.0024 ppm).

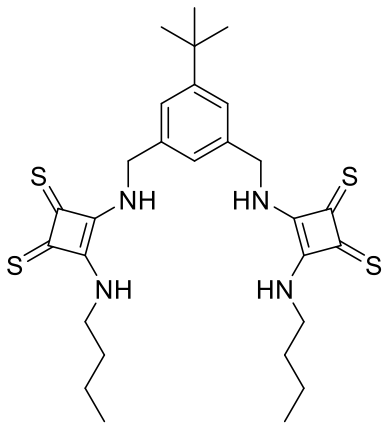

4,4'-(((5-(*tert*-butyl)-1,3-phenylene)bis(methylene))bis(azanediyl))bis(3-(butylamino)cyclobut-3-ene-1,2-dithione) (4.13)

To a solution of **C1** (57 mg, 0.3 mmol, 1 equiv.) in dry DCM (8 mL) was slowly added 5 mL DCM solution of **B1** (178 mg, 0.66 mmol, 2.2 equiv.) and stirred for 1 day. The mixture was filtered, and the precipitate was washed with DCM to yield **4.13** as an orange solid. (45 mg, 0.081 mmol, 27%). The compound exists as three rotamers in DMSO-d_6 at room temperature in a ratio of 1:1:7. Major rotamer ^{1}H NMR (500 MHz, DMSO-d_6) δ= 8.80 (t, J = 6.4 Hz, 2H), 8.40 (t, J = 6.6 Hz, 2H), 7.49 – 7.41 (m, 2H), 7.36 (s, 1H), 5.31 (d, J = 6.2 Hz, 4H), 4.04 (d, J = 6.7 Hz, 4H), 1.63 – 1.48 (m, 4H), 1.34 (q, J = 7.3 Hz, 4H), 1.31 – 1.19 (m, 9H), 0.96 – 0.82 (m, 6H). ^{13}C NMR (126 MHz, DMSO-d_6) δ= 204.8, 203.9, 170.9, 170.5, 169.9, 152.4, 138.3, 125.4, 125.2, 125.1, 46.5, 44.5, 43.0, 35.1, 35.0, 32.9, 31.6, 31.6, 31.5, 19.4, 14.1, 14.0. HRMS (ESI) clad. for $C_{28}H_{38}N_4S_4$ $(M+H)^+$: 559.2063. Found: 559.2046 (-0.0017 ppm).

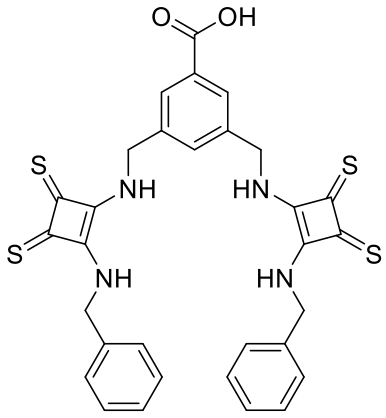

3,5-bis(((2-(benzylamino)-3,4-dithioxocyclobut-1-en-1-yl)amino)methyl)benzoic acid (4.14)

To a solution of **C2** (75 mg, 0.3 mmol, 1 equiv.) in dry DCM (8 mL) was slowly added 5 mL DCM solution of **B2** (200 mg, 0.66 mmol, 2.2 equiv.) and stirred for 1 day. The mixture was filtered, and the precipitate was washed with DCM. Then the solid was suspended in 1M HCl, stirred for 30 minutes. Next, the solid was collected by filtration and suspended in 10 mL of water. During which time the pH was adjusted to 10-11 with 1M NaOH, and the mixture was stirred for 10 minutes. Subsequently, 20 mL of 1M HCl was added, and a precipitate formed. The precipitate was filtered and washed with 1M HCl. This treatment with NaOH and HCl was repeated 2-4 times to yield **4.14** as an orange solid. (40 mg, 0.066 mmol,

22%). ^{1}H NMR (500 MHz, DMSO-d_6) δ= 13.16 (s, 1H), 9.04 (dt, J = 6.7, 3.4 Hz, 4H), 7.94 (d, J = 1.7 Hz, 2H), 7.69 (s, 1H), 7.44 – 7.26 (m, 9H), 5.41 (d, J = 6.5 Hz, 4H), 5.32 (d, J = 6.5 Hz, 4H). ^{13}C NMR (126 MHz, DMSO-d_6) δ= 204.7, 204.3, 170.6, 170.4, 167.2, 139.2, 137.9, 132.3, 132.1, 129.3, 129.3, 129.1, 129.0, 128.5, 128.4, 128.2, 128.1, 128.0, 46.5, 45.9. HRMS (ESI) clad. for $C_{31}H_{26}N_4O_2S_4$ $(M+H)^+$: 615.1022. Found: 615.1002 (-0.0020 ppm).

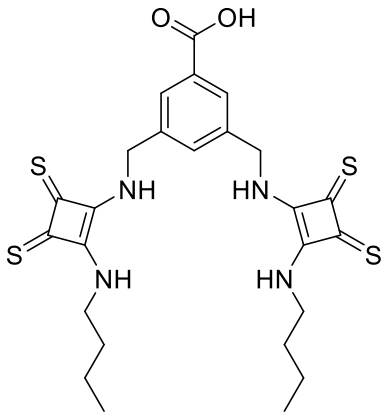

3,5-bis(((2-(butylamino)-3,4-dithioxocyclobut-1-en-1-yl)amino)methyl)benzoic acid (4.15)

To a solution of **C2** (75 mg, 0.3 mmol, 1 equiv.) in dry DCM (8 mL) was slowly added 5 mL DCM solution of **B1** (178 mg, 0.66 mmol, 2.2 equiv.) and stirred for 1 day. The mixture was filtered, and the precipitate was washed with DCM. Then the solid was suspended in 1M HCl, stirred for 30 minutes. Next, the solid was collected by filtration and suspended in 10 mL of water. During which time the pH was adjusted to 10-11 with 1M NaOH, and the mixture was stirred for 10 minutes. Subsequently, 20 mL of 1M HCl was added, and a precipitate formed. The precipitate was filtered and washed with 1M HCl. This treatment with NaOH and HCl was repeated 2-4 times to yield **4.15** as an orange solid. (29 mg, 0.054 mmol, 18%). ^{1}H NMR (500 MHz, DMSO-d_6) δ= 13.17 (s, 1H), 8.94 (t, J = 6.6 Hz, 2H), 8.56 (d, J = 6.3 Hz, 2H), 7.95 (d, J = 1.7 Hz, 2H), 7.70 (s, 1H), 5.42 (d, J = 6.5 Hz, 4H), 4.05 (d, J = 6.7 Hz, 4H), 1.59 (p, 4H), 1.35 (h, 4H), 0.91 (t, J = 7.4 Hz, 6H). ^{13}C NMR (126 MHz, DMSO-d_6) δ= 205.1, 203.6, 170.8, 170.7, 170.0, 167.2, 139.3, 132.3, 132.1, 128.5, 45.9, 44.6, 43.0, 33.5, 32.9, 32.8, 19.5, 14.1, 14.0. HRMS (ESI) clad. for $C_{25}H_{30}N_4O_2S_4$ $(M+H)^+$: 547.1335. Found: 547.1316 (-0.0019 ppm).

Chapter 7: Bibiography

1. Pedersen, C. J. Cyclic polyethers and their complexes with metal salts. *J. Am. Chem. Soc.* **89**, 7017–7036 (1967).
2. Anion Coordination Chemistry and the Recognition of Anionic Substrates. in *Supramolecular Chemistry* 31–35 (John Wiley & Sons, Ltd, 1995). doi:https://doi.org/10.1002/3527607439.ch3.
3. From Molecular to Supramolecular Chemistry. in *Supramolecular Chemistry* 1–9 (John Wiley & Sons, Ltd, 1995). doi:https://doi.org/10.1002/3527607439.ch1.
4. Molecular Recognition. in *Supramolecular Chemistry* 11–30 (John Wiley & Sons, Ltd, 1995). doi:https://doi.org/10.1002/3527607439.ch2.
5. Whitesides, G. M. & Grzybowski, B. Self-Assembly at All Scales. *Science* **295**, 2418–2421 (2002).
6. A. Gale, P., Busschaert, N., E. Haynes, C. J., E. Karagiannidis, L. & L. Kirby, I. Anion receptor chemistry: highlights from 2011 and 2012. *Chem. Soc. Rev.* **43**, 205–241 (2014).
7. Kubik, S. Anion recognition in water. *Chem. Soc. Rev.* **39**, 3648–3663 (2010).
8. Wang, H.-B., Wisner, J. A. & Jennings, M. C. Anion receptors containing thiazine-1,1-dioxide heterocycles as hydrogen bond donors. *Beilstein J. Org. Chem.* **6**, 50 (2010).
9. Che, M., Flood, A. H. & Raghavachari, K. Anion Binding by Macrocyclic Receptors: Computational Landscape of 1:1 and 2:1 Stoichiometries. *J. Comput. Chem.* **46**, e70270 (2025).
10. Liu, Y., Sengupta, A., Raghavachari, K. & Flood, A. H. Anion Binding in Solution: Beyond the Electrostatic Regime. *Chem* **3**, 411–427 (2017).
11. Schottel, B. L., Chifotides, H. T. & Dunbar, K. R. Anion–π interactions. *Chem. Soc. Rev.* **37**, 68–83 (2007).
12. Giese, M., Albrecht, M. & Rissanen, K. Experimental investigation of anion–π interactions – applications and biochemical relevance. *Chem. Commun.* **52**, 1778–1795 (2016).
13. Sommer, F., Marcus, Y. & Kubik, S. Effects of Solvent Properties on the Anion Binding of Neutral Water-Soluble Bis(cyclopeptides) in Water and Aqueous Solvent Mixtures. *ACS Omega* **2**, 3669–3680 (2017).
14. Lindman, B., Medronho, B., Alves, L., Norgren, M. & Nordenskiöld, L. Hydrophobic interactions control the self-assembly of DNA and cellulose. *Q. Rev. Biophys.* **54**, e3 (2021).
15. Almeida, F. C. L., Sanches, K., Pinheiro-Aguiar, R., Almeida, V. S. & Caruso, I. P. Protein Surface Interactions—Theoretical and Experimental Studies. *Front. Mol. Biosci.* **8**, (2021).
16. Nick Pace, C., Scholtz, J. M. & Grimsley, G. R. Forces stabilizing proteins. *FEBS Lett.* **588**, 2177–2184 (2014).

17. Pace, C. N. *et al.* Contribution of hydrogen bonds to protein stability. *Protein Sci. Publ. Protein Soc.* **23**, 652–661 (2014).
18. Gong, Q. *et al.* Application of cation-π interactions in enzyme-substrate binding: Design, synthesis, biological evaluation, and molecular dynamics insights of novel hydrophilic substrates for NQO1. *Eur. J. Med. Chem.* **221**, 113515 (2021).
19. Waldner, B. J. *et al.* Electrostatic recognition in substrate binding to serine proteases. *J. Mol. Recognit.* **31**, e2727 (2018).
20. Kim, S. K. & Sessler, J. L. Ion pair receptors. *Chem. Soc. Rev.* **39**, 3784–3809 (2010).
21. Picci, G., Montis, R., Lippolis, V. & Caltagirone, C. Squaramide-based receptors in anion supramolecular chemistry: insights into anion binding, sensing, transport and extraction. *Chem. Soc. Rev.* **53**, 3952–3975 (2024).
22. Liu, Y., Sengupta, A., Raghavachari, K. & Flood, A. H. Anion Binding in Solution: Beyond the Electrostatic Regime. *Chem* **3**, 411–427 (2017).
23. Patrick, S. C., Beer, P. D. & Davis, J. J. Solvent effects in anion recognition. *Nat. Rev. Chem.* **8**, 256–276 (2024).
24. I. Assaf, K. & M. Nau, W. Large anion binding in water. *Org. Biomol. Chem.* **21**, 6636–6651 (2023).
25. Zhang, X. X., Izatt, R. M., Bradshaw, J. S. & Krakowiak, K. E. Approaches to improvement of metal ion selectivity by cryptands. *Coord. Chem. Rev.* **174**, 179–189 (1998).
26. Kim, S. K. & Sessler, J. L. Ion pair receptors. *Chem. Soc. Rev.* **39**, 3784–3809 (2010).
27. Li, Y. *et al.* Removal of chloride from water and wastewater: Removal mechanisms and recent trends. *Sci. Total Environ.* **821**, 153174 (2022).
28. Adams, H. K., Kadarauch, M., Hodson, N. J., Lit, A. R. & Phipps, R. J. Design Approaches That Utilize Ionic Interactions to Control Selectivity in Transition Metal Catalysis. *Chem. Rev.* **125**, 2846–2907 (2025).
29. Martinez, A. H. & Mohiuddin, S. S. Biochemistry, Chloride Channels. in *StatPearls* (StatPearls Publishing, Treasure Island (FL), 2025).
30. Marchetti, L. A., Kumawat, L. K., Mao, N., Stephens, J. C. & Elmes, R. B. P. The Versatility of Squaramides: From Supramolecular Chemistry to Chemical Biology. *Chem* **5**, 1398–1485 (2019).
31. A. Marchetti, L., Krämer, T. & P. Elmes, R. B. Amidosquaramides – a new anion binding motif with pH sensitive anion transport properties. *Org. Biomol. Chem.* **20**, 7056–7066 (2022).

32. Mogashane, T. M., Mapazi, O., Motlatle, M. A., Mokoena, L. & Tshilongo, J. A Review of Recent Developments in Analytical Methods for Determination of Phosphorus from Environmental Samples. *Molecules* **30**, 1001 (2025).
33. Xiao, H., Li, X. & Fu, Y. Advances in Anion Chemistry in the Electrolyte Design for Better Lithium Batteries. *Nano-Micro Lett.* **17**, 149 (2025).
34. Pham, T. C. *et al.* Visual Simultaneous Detection and Real-Time Monitoring of Cadmium Ions Based on Conjugated Polydiacetylenes. *ACS Omega* **5**, 31254–31261 (2020).
35. Doulache, M., Bakirhan, N. K., Saidat, B., Trari, M. & Ozkan, S. A. Electrochemical sensing of nitrite in drinking water using multi-walled carbon nanotubes modified platinum electrode. *Explor. Foods Foodomics* **2**, 659–671 (2024).
36. Borah, J., Hazarika, U. N. & Khakhlary, P. Extending the Chemistry of Reaction between BODIPY and Cyanide Ions: An Application in Selective Sensing of Fluoride and Cyanide Ions. *ACS Omega* **7**, 46234–46240 (2022).
37. McNaughton, D. A. *et al.* New insights and discoveries in anion receptor chemistry. *Chem* **9**, 3045–3112 (2023).
38. Cram, D. J. Preorganization—From Solvents to Spherands. *Angew. Chem.* **25**, 1039–1057 (1986).
39. Cram, D. J. *et al.* Host-guest complexation. 35. Spherands, the first completely preorganized ligand systems. *J. Am. Chem. Soc.* **107**, 3645–3657 (1985).
40. Esteves, C. V. *et al.* Phosphate and polyphosphate anion recognition by a dinuclear copper(II) complex of an unsymmetrical squaramide. *Dalton Trans.* **48**, 10104–10115 (2019).
41. Cram, D. J. THE DESIGN OF MOLECULAR HOSTS, GUESTS, AND THEIR COMPLEXES.
42. Parks, F. C. *et al.* Revealing the Hidden Costs of Organization in Host–Guest Chemistry Using Chloride-Binding Foldamers and Their Solvent Dependence. *J. Am. Chem. Soc.* **144**, 1274–1287 (2022).
43. Langton, M. J., Serpell, C. J. & Beer, P. D. Anion Recognition in Water: Recent Advances from a Supramolecular and Macromolecular Perspective. *Angew. Chem. Int. Ed Engl.* **55**, 1974–1987 (2016).
44. Amendola, V., Bergamaschi, G., Boiocchi, M., Fabbrizzi, L. & Milani, M. The Squaramide versus Urea Contest for Anion Recognition. *Chem. – Eur. J.* **16**, 4368–4380 (2010).
45. Gholiee, Y. What drives enhanced chloride recognition of squaramide-based receptors over urea and thiourea? A computational exploration in the gas-phase and various solvents. *Comput. Theor. Chem.* **1248**, 115191 (2025).

46. Lee, A. *et al.* Cyclo[2]carbazole[2]pyrrole: a preorganized calix[4]pyrrole analogue. *Chem. Sci.* **14**, 1218–1226 (2023).
47. Lee, A. *et al.* Cyclo[2]carbazole[2]pyrrole: a preorganized calix[4]pyrrole analogue. *Chem. Sci.* **14**, 1218–1226 (2023).
48. Mohammed, F. A., Xiao, T., Wang, L. & Elmes, R. B. P. Macrocyclic receptors for anion recognition. *Chem. Commun.* **60**, 11812–11836 (2024).
49. Qin, L., Hartley, A., Turner, P., P. Elmes, R. B. & A. Jolliffe, K. Macrocyclic squaramides: anion receptors with high sulfate binding affinity and selectivity in aqueous media. *Chem. Sci.* **7**, 4563–4572 (2016).
50. Moustakas, M. The Role of Metal Ions in Biology, Biochemistry and Medicine. *Materials* **14**, 549 (2021).
51. Chen, I. & Lui, F. Neuroanatomy, Neuron Action Potential. in *StatPearls* (StatPearls Publishing, Treasure Island (FL), 2025).
52. Pirahanchi, Y., Jessu, R. & Aeddula, N. R. Physiology, Sodium Potassium Pump. in *StatPearls* (StatPearls Publishing, Treasure Island (FL), 2025).
53. Bagur, R. & Hajnóczky, G. Intracellular Ca2+ sensing: role in calcium homeostasis and signaling. *Mol. Cell* **66**, 780–788 (2017).
54. Pinton, P., Giorgi, C., Siviero, R., Zecchini, E. & Rizzuto, R. Calcium and apoptosis: ER-mitochondria Ca2+ transfer in the control of apoptosis. *Oncogene* **27**, 6407–6418 (2008).
55. Leonarski, F., D'Ascenzo, L. & Auffinger, P. Mg2+ ions: do they bind to nucleobase nitrogens? *Nucleic Acids Res.* **45**, 987–1004 (2017).
56. Cowan, J. A. Understanding the Thermodynamics of Magnesium Binding to RNA Structural Motifs. *Life* **14**, 765 (2024).
57. Ruiz, L. M., Libedinsky, A. & Elorza, A. A. Role of Copper on Mitochondrial Function and Metabolism. *Front. Mol. Biosci.* **8**, 711227 (2021).
58. McCall, K. A., Huang, C. & Fierke, C. A. Function and Mechanism of Zinc Metalloenzymes. *J. Nutr.* **130**, 1437S-1446S (2000).
59. Chakraborty, S., Das, K. & Halder, S. A review on chemo sensors and fluro sensors of mercury ions. *Inorganica Chim. Acta* **566**, 122026 (2024).
60. Zhang, H. *et al.* Recent progress in macrocyclic chemosensors for lead, cadmium and mercury heavy metal ions. *Dyes Pigments* **216**, 111380 (2023).
61. van Dun, S., Ottmann, C., Milroy, L.-G. & Brunsveld, L. Supramolecular Chemistry Targeting Proteins. *J. Am. Chem. Soc.* **139**, 13960–13968 (2017).

62. Pearson, R. G. Hard and soft acids and bases, HSAB, part 1: Fundamental principles. *J. Chem. Educ.* **45**, 581 (1968).
63. Bonnin, M. A. & Feldmann, C. Insights of the Structure and Luminescence of Mn2+/Sn2+-Containing Crown-Ether Coordination Compounds. *Inorg. Chem.* **60**, 14645–14654 (2021).
64. Shepodd, T. J., Petti, M. A. & Dougherty, D. A. Molecular recognition in aqueous media: donor-acceptor and ion-dipole interactions produce tight binding for highly soluble guests. *J. Am. Chem. Soc.* **110**, 1983–1985 (1988).
65. Liu, Z. *et al.* Unraveling cooperative interactions between complexed ions in dual-host strategy for cesium salt separation. *Beilstein J. Org. Chem.* **21**, 845–853 (2025).
66. Roelens, S., Vacca, A., Francesconi, O. & Venturi, C. Ion-pair binding: is binding both binding better? *Chem. Weinh. Bergstr. Ger.* **15**, 8296–8302 (2009).
67. McConnell, A. J. & Beer, P. D. Heteroditopic receptors for ion-pair recognition. *Angew. Chem. Int. Ed Engl.* **51**, 5052–5061 (2012).
68. Marcus, Y. & Hefter, G. Ion Pairing. *Chem. Rev.* **106**, 4585–4621 (2006).
69. Dougherty, D. A. Cation-π Interactions Involving Aromatic Amino Acids1234. *J. Nutr.* **137**, 1504S-1508S (2007).
70. Dougherty, D. A. The Cation—π Interaction in Chemistry and Biology. *Chem. Rev.* **125**, 2793–2808 (2025).
71. Ahern, C. A., Eastwood, A. L., Lester, H. A., Dougherty, D. A. & Horn, R. A cation-pi interaction between extracellular TEA and an aromatic residue in potassium channels. *J. Gen. Physiol.* **128**, 649–657 (2006).
72. Ahern, C. A., Eastwood, A. L., Lester, H. A., Dougherty, D. A. & Horn, R. A Cation–π Interaction between Extracellular TEA and an Aromatic Residue in Potassium Channels. *J. Gen. Physiol.* **128**, 649–657 (2006).
73. Reek, J. N. H. *et al.* Transition Metal Catalysis Controlled by Hydrogen Bonding in the Second Coordination Sphere. *Chem. Rev.* **122**, 12308–12369 (2022).
74. Beauchamp, D. A. & Loeb, S. J. Hydrogen-Bonded Networks through Second-Sphere Coordination. *Chem. – Eur. J.* **8**, 5084–5088 (2002).
75. Beauchamp, D. A. & Loeb, S. J. Hydrogen-Bonded Networks through Second-Sphere Coordination. *Chem. – Eur. J.* **8**, 5084–5088 (2002).
76. Varner, C. T., Rosen, T., Martin, J. T. & Kane, R. S. Recent Advances in Engineering Polyvalent Biological Interactions. *Biomacromolecules* **16**, 43–55 (2015).

77. Mammen, M., Choi, S.-K. & Whitesides, G. M. Polyvalent Interactions in Biological Systems: Implications for Design and Use of Multivalent Ligands and Inhibitors. *Angew. Chem. Int. Ed.* **37**, 2754–2794 (1998).
78. Haymore, B. L., Lamb, J. D., Izatt, R. M. & Christensen, J. J. Thermodynamic origin of the macrocyclic effect in crown ether complexes of sodium(1+), potassium(1+), and barium(2+). *Inorg. Chem.* **21**, 1598–1602 (1982).
79. Bradshaw, J. S. & Izatt, R. M. Crown Ethers: The Search for Selective Ion Ligating Agents. *Acc. Chem. Res.* **30**, 338–345 (1997).
80. Jamali, S. H. *et al.* Thermodynamic and Transport Properties of Crown-Ethers: Force Field Development and Molecular Simulations. *J. Phys. Chem. B* **121**, 8367–8376 (2017).
81. Inokuchi, Y. *et al.* Ion Selectivity of Crown Ethers Investigated by UV and IR Spectroscopy in a Cold Ion Trap. *J. Phys. Chem. A* **116**, 4057–4068 (2012).
82. Meadows, E. S., De Wall, S. L., Barbour, L. J. & Gokel, G. W. Alkali Metal Cation–π Interactions Observed by Using a Lariat Ether Model System. *J. Am. Chem. Soc.* **123**, 3092–3107 (2001).
83. Shinka, S., Minami, T., Kusano, Y. & Manabe, O. A new "switched-on" crown ether which exhibits a reversible all-or-none ion-binding ability. *Tetrahedron Lett.* **23**, 2581–2584 (1982).
84. Shinkai, S. *et al.* Photoresponsive Crown Ethers. 9. Cylindrical and Phane Crown Ethers with Azobenzene Segments as a Light-switch Functional Group. *Bull. Chem. Soc. Jpn.* **56**, 1700–1704 (1983).
85. Español, E. S. & Villamil, M. M. Calixarenes: Generalities and Their Role in Improving the Solubility, Biocompatibility, Stability, Bioavailability, Detection, and Transport of Biomolecules. *Biomolecules* **9**, 90 (2019).
86. Remigante, A., Gavazzo, P., Morabito, R. & Dossena, S. Editorial: Ion transporters and channels in cellular pathophysiology. *Front. Cell Dev. Biol.* **10**, 1049433 (2022).
87. Bertomeu, J. B. *et al.* The Role of Ion-Transporting Proteins on Crosstalk Between the Skeletal Muscle and Central Nervous Systems Elicited by Physical Exercise. *Mol. Neurobiol.* **62**, 5546–5565 (2025).
88. Kress, G. J. & Mennerick, S. Action potential initiation and propagation: upstream influences on neurotransmission. *Neuroscience* **158**, 211–222 (2009).
89. Südhof, T. C. Calcium Control of Neurotransmitter Release. *Cold Spring Harb. Perspect. Biol.* **4**, a011353 (2012).

90. Osei-Owusu, J., Yang, J., del Carmen Vitery, M. & Qiu, Z. Molecular Biology and Physiology of Volume-Regulated Anion Channel (VRAC). *Curr. Top. Membr.* **81**, 177–203 (2018).
91. Raut, S. K. *et al.* Chloride ions in health and disease. *Biosci. Rep.* **44**, BSR20240029 (2024).
92. Vinothkumar, K. R. & Henderson, R. Structures of membrane proteins. *Q. Rev. Biophys.* **43**, 65–158 (2010).
93. Doyle, D. A. *et al.* The Structure of the Potassium Channel: Molecular Basis of K^+ Conduction and Selectivity. *Science* **280**, 69–77 (1998).
94. Luo, Y., Zhu, C., Zhang, T., Yan, T. & Liu, J. Self-assembled Supramolecular Artificial Transmembrane Ion Channels: Recent Progress and Application. *Chem. Res. Chin. Univ.* **39**, 3–12 (2023).
95. Cockrell, R. S., Harris, E. J. & Pressman, B. C. Energetics of Potassium Transport in Mitochondria Induced by Valinomycin*. *Biochemistry* **5**, 2326–2335 (1966).
96. Hladky, S. B. & Haydon, D. A. Ion transfer across lipid membranes in the presence of gramicidin A: I. Studies of the unit conductance channel. *Biochim. Biophys. Acta BBA - Biomembr.* **274**, 294–312 (1972).
97. Pedersen, C. J. Cyclic polyethers and their complexes with metal salts. *J. Am. Chem. Soc.* **89**, 2495–2496 (1967).
98. Gokel, G. W. & Negin, S. Synthetic Ion Channels: From Pores to Biological Applications. *Acc. Chem. Res.* **46**, 2824–2833 (2013).
99. Finkelstein, A. & Andersen, O. S. The gramicidin a channel: A review of its permeability characteristics with special reference to the single-file aspect of transport. *J. Membr. Biol.* **59**, 155–171 (1981).
100. Negin, S., Smith, B. A., Unger, A., Leevy, W. M. & Gokel, G. W. Hydraphiles: A Rigorously Studied Class of Synthetic Channel Compounds with In Vivo Activity. *Int. J. Biomed. Imaging* **2013**, 803579 (2013).
101. McNALLY, B. A., LEEVY, W. M. & SMITH, B. D. Recent Advances in Synthetic Membrane Transporters. *Supramol. Chem.* **19**, 29–37 (2007).
102. Stolwijk, T. B., Sudhoelter, E. J. R. & Reinhoudt, D. N. Crown ether mediated transport: a kinetic study of potassium perchlorate transport through a supported liquid membrane containing dibenzo-18-crown-6. *J. Am. Chem. Soc.* **109**, 7042–7047 (1987).
103. Yang, J. *et al.* Artificial transmembrane ion transporters as potential therapeutics. *Chem* **7**, 3256–3291 (2021).

104. A. Gale, P., T. Davis, J. & Quesada, R. Anion transport and supramolecular medicinal chemistry. *Chem. Soc. Rev.* **46**, 2497–2519 (2017).
105. Weber, M. E., Elliott, E. K. & Gokel, G. W. Activity of synthetic ion channels is influenced by cation–π interactions with phospholipid headgroups. *Org. Biomol. Chem.* **4**, 83–89 (2006).
106. Leevy, W. M. *et al.* Correlation of bilayer membrane cation transport and biological activity in alkyl-substituted lariat ethers. *Org. Biomol. Chem.* **3**, 1647–1652 (2005).
107. Chen, S. *et al.* An Artificial Molecular Shuttle Operates in Lipid Bilayers for Ion Transport. *J. Am. Chem. Soc.* **140**, 17992–17998 (2018).
108. Hoser, J., Dabrowska, A., Zajac, M. & Bednarczyk, P. Changes in Ion Transport across Biological Membranes Exposed to Particulate Matter. *Membranes* **13**, 763 (2023).
109. Pressey, J. C., de Saint-Rome, M., Raveendran, V. A. & Woodin, M. A. Chloride transporters controlling neuronal excitability. *Physiol. Rev.* **103**, 1095–1135 (2023).
110. Dunn, J. & Grider, M. H. Physiology, Adenosine Triphosphate. in *StatPearls* (StatPearls Publishing, Treasure Island (FL), 2025).
111. Dutzler, R. Structural basis for ion conduction and gating in ClC chloride channels. *FEBS Lett.* **564**, 229–233 (2004).
112. Hanssens, L. S., Duchateau, J. & Casimir, G. J. CFTR Protein: Not Just a Chloride Channel? *Cells* **10**, 2844 (2021).
113. Harwood, K. H., McQuade, R. M., Jarnicki, A. & Schneider-Futschik, E. K. Anti-Inflammatory Influences of Cystic Fibrosis Transmembrane Conductance Regulator Drugs on Lung Inflammation in Cystic Fibrosis. *Int. J. Mol. Sci.* **22**, 7606 (2021).
114. Davis, A. P., Sheppard, D. N. & Smith, B. D. Development of synthetic membrane transporters for anions. *Chem. Soc. Rev.* **36**, 348–357 (2007).
115. Gale, P. A., Davis, J. T. & Quesada, R. Anion transport and supramolecular medicinal chemistry. *Chem. Soc. Rev.* **46**, 2497–2519 (2017).
116. de Jong, J., Bos, J. E. & Wezenberg, S. J. Stimulus-Controlled Anion Binding and Transport by Synthetic Receptors. *Chem. Rev.* **123**, 8530–8574 (2023).
117. Busschaert, N. *et al.* Structure–Activity Relationships in Tripodal Transmembrane Anion Transporters: The Effect of Fluorination. *J. Am. Chem. Soc.* **133**, 14136–14148 (2011).
118. Gomez, D. T., Pratt, L. R., Asthagiri, D. N. & Rempe, S. B. Hydrated Anions: From Clusters to Bulk Solution with Quasi-Chemical Theory. *Acc. Chem. Res.* **55**, 2201–2212 (2022).

119. Fossat, M. J., Zeng, X. & Pappu, R. V. Uncovering Differences in Hydration Free Energies and Structures for Model Compound Mimics of Charged Side Chains of Amino Acids. *J. Phys. Chem. B* **125**, 4148–4161 (2021).
120. Ren, B., Sun, Y. & Xin, P. Recent Advances in Artificial Anion Channels and Their Selectivity. *ChemPlusChem* **89**, e202400466 (2024).
121. Montenegro, J., Ghadiri, M. R. & Granja, J. R. Ion Channel Models Based on Self-Assembling Cyclic Peptide Nanotubes. *Acc. Chem. Res.* **46**, 2955–2965 (2013).
122. Reddy, G. L., Iwamoto, T., Tomich, J. M. & Montal, M. Synthetic peptides and four-helix bundle proteins as model systems for the pore-forming structure of channel proteins. II. Transmembrane segment M2 of the brain glycine receptor is a plausible candidate for the pore-lining structure. *J. Biol. Chem.* **268**, 14608–14615 (1993).
123. Wallace, D. P. *et al.* A synthetic peptide derived from glycine-gated Cl- channel induces transepithelial Cl- and fluid secretion. *Am. J. Physiol.-Cell Physiol.* **272**, C1672–C1679 (1997).
124. Judd, L. W. & Davis, A. P. From cholapod to cholaphane transmembrane anion carriers: accelerated transport through binding site enclosure. *Chem. Commun.* **46**, 2227–2229 (2010).
125. Gale, P. A. From Anion Receptors to Transporters. *Acc. Chem. Res.* **44**, 216–226 (2011).
126. Andrews, N. J. *et al.* Structurally simple lipid bilayer transport agents for chloride and bicarbonate. *Chem. Sci.* **2**, 256–260 (2011).
127. Ren, B., Sun, Y. & Xin, P. Recent Advances in Artificial Anion Channels and Their Selectivity. *ChemPlusChem* **89**, e202400466 (2024).
128. Muraoka, T. *et al.* A synthetic ion channel with anisotropic ligand response. *Nat. Commun.* **11**, 2924 (2020).
129. Busschaert, N. *et al.* Thiosquaramides: pH switchable anion transporters. *Chem. Sci.* **5**, 3617–3626 (2014).
130. Li, X. *et al.* Supramolecular Antibacterial Materials for Combatting Antibiotic Resistance. *Adv. Mater.* **31**, 1805092 (2019).
131. Gale, P. A., Davis, J. T. & Quesada, R. Anion transport and supramolecular medicinal chemistry. *Chem. Soc. Rev.* **46**, 2497–2519 (2017).
132. Davis, J. T., Gale, P. A. & Quesada, R. Advances in anion transport and supramolecular medicinal chemistry. *Chem. Soc. Rev.* **49**, 6056–6086 (2020).

133. Cooper, G. M. Cell Membranes. in *The Cell: A Molecular Approach. 2nd edition* (Sinauer Associates, 2000).
134. Davis, A. P., Sheppard, D. N. & Smith, B. D. Development of synthetic membrane transporters for anions. *Chem. Soc. Rev.* **36**, 348–357 (2007).
135. Busschaert, N. *et al.* A synthetic ion transporter that disrupts autophagy and induces apoptosis by perturbing cellular chloride concentrations. *Nat. Chem.* **9**, 667–675 (2017).
136. Barba-Bon, A., Nilam, M. & Hennig, A. Supramolecular Chemistry in the Biomembrane. *ChemBioChem* **21**, 886–910 (2020).
137. Martínez-Crespo, L. & Valkenier, H. Transmembrane Transport of Bicarbonate by Anion Receptors. *Chempluschem* **87**, e202200266 (2022).
138. Saji, V. S. Supramolecular organic nanotubes for drug delivery. *Mater. Today Adv.* **14**, 100239 (2022).
139. Liu, Y., Wu, Y., Luo, Z. & Li, M. Designing supramolecular self-assembly nanomaterials as stimuli-responsive drug delivery platforms for cancer therapy. *iScience* **26**, 106279 (2023).
140. Muheyati, M., Wu, G., Li, Y., Pan, Z. & Chen, Y. Supramolecular nanotherapeutics based on cucurbiturils. *J. Nanobiotechnology* **22**, 790 (2024).
141. Zyryanov, G. V. *et al.* Pillararenes as Promising Carriers for Drug Delivery. *Int. J. Mol. Sci.* **24**, 5167 (2023).
142. Hu, Q.-D., Tang, G.-P. & Chu, P. K. Cyclodextrin-Based Host–Guest Supramolecular Nanoparticles for Delivery: From Design to Applications. *Acc. Chem. Res.* **47**, 2017–2025 (2014).
143. Wankar, J. *et al.* Recent Advances in Host–Guest Self-Assembled Cyclodextrin Carriers: Implications for Responsive Drug Delivery and Biomedical Engineering. *Adv. Funct. Mater.* **30**, 1909049 (2020).
144. Hong, W. *et al.* A Novel Folic Acid Receptor-Targeted Drug Delivery System Based on Curcumin-Loaded β-Cyclodextrin Nanoparticles for Cancer Treatment. *Drug Des. Devel. Ther.* **15**, 2843–2855 (2021).
145. Zhou, Q. *et al.* Target-Specific Cellular Uptake of Folate-Decorated Biodegradable Polymer Micelles. *J. Phys. Chem. B* **115**, 12662–12670 (2011).
146. Bayle, E. A., Ilhami, F. B., Chen, J.-K. & Cheng, C.-C. Potential of a CO2-Responsive supramolecular drug-carrier system as a safer and more effective treatment for cancer. *Mater. Today Bio* **29**, 101319 (2024).
147. Olivieri, F., Castaldo, R., Cocca, M., Gentile, G. & Lavorgna, M. Innovative Silver-Based Capping System for Mesoporous Silica Nanocarriers Able to Exploit a Twofold Anticorrosive Mechanism

in Composite Polymer Coatings: Tailoring Benzotriazole Release and Capturing Chloride Ions. *ACS Appl. Mater. Interfaces* **13**, 48141–48152 (2021).
148. Singh, N. *et al.* Bioresponsive Mesoporous Silica Nanoparticles for Triggered Drug Release. *J. Am. Chem. Soc.* **133**, 19582–19585 (2011).
149. Bischof, H. *et al.* Live-Cell Imaging of Physiologically Relevant Metal Ions Using Genetically Encoded FRET-Based Probes. *Cells* **8**, 492 (2019).
150. Picci, G., Montis, R., Lippolis, V. & Caltagirone, C. Squaramide-based receptors in anion supramolecular chemistry: insights into anion binding, sensing, transport and extraction. *Chem. Soc. Rev.* **53**, 3952–3975 (2024).
151. Jiao, Y., Zhu, B., Chen, J. & Duan, X. Fluorescent Sensing of Fluoride in Cellular System. *Theranostics* **5**, 173–187 (2015).
152. Lasitha, P., Dasgupta, S. & Naresh Patwari, G. Unraveling the Origin of Differentiable 'Turn-On' Fluorescence Sensing of Zn2+ and Cd2+ Ions with Squaramides. *ChemPhysChem* **21**, 1564–1570 (2020).
153. Snitsarev, V. *et al.* Fluorescent detection of Zn(2+)-rich vesicles with Zinquin: mechanism of action in lipid environments. *Biophys. J.* **80**, 1538–1546 (2001).
154. Pratt, E. P. S., Damon, L. J., Anson, K. J. & Palmer, A. E. Tools and techniques for illuminating the cell biology of zinc. *Biochim. Biophys. Acta Mol. Cell Res.* **1868**, 118865 (2021).
155. Yang, J. *et al.* Artificial transmembrane ion transporters as potential therapeutics. *Chem* **7**, 3256–3291 (2021).
156. Feo, E. & Gale, P. A. Therapeutic synthetic anion transporters. *Curr. Opin. Chem. Biol.* **83**, 102535 (2024).
157. Brennan, L. E., Luo, X., Mohammed, F. A., Kavanagh, K. & Elmes, R. B. P. Uncovering the potent antimicrobial activity of squaramide based anionophores – chloride transport and membrane disruption. *Chem. Sci.* **16**, 4075–4084 (2025).
158. Brennan, L. E. *et al.* Potent antimicrobial effect induced by disruption of chloride homeostasis. *Chem* **9**, 3138–3158 (2023).
159. Share, A. I. *et al.* Chloride anion transporters inhibit growth of methicillin-resistant Staphylococcus aureus (MRSA) in vitro. *Chem. Commun. Camb. Engl.* **52**, 7560–7563 (2016).
160. Kevin II, D. A., Meujo, D. A. & Hamann, M. T. Polyether ionophores: broad-spectrum and promising biologically active molecules for the control of drug-resistant bacteria and parasites. *Expert Opin. Drug Discov.* **4**, 109–146 (2009).

161. Fong, P.-M. *et al.* Synthetic Cation Transporters Eradicate Drug-Resistant Staphylococcus aureus, Persisters, and Biofilms. *JACS Au* **5**, 1328–1339 (2025).
162. Benfield, A. H. & Henriques, S. T. Mode-of-Action of Antimicrobial Peptides: Membrane Disruption vs. Intracellular Mechanisms. *Front. Med. Technol.* **2**, (2020).
163. Hou, C., Chang, Y.-F. & Yao, X. Supramolecular Adhesive Materials with Antimicrobial Activity for Emerging Biomedical Applications. *Pharmaceutics* **14**, 1616 (2022).
164. Riga, E. K., Vöhringer, M., Widyaya, V. T. & Lienkamp, K. Polymer-Based Surfaces Designed to Reduce Biofilm Formation: From Antimicrobial Polymers to Strategies for Long-Term Applications. *Macromol. Rapid Commun.* **38**, 1700216 (2017).
165. Zhang, W. *et al.* Recent Advances of Silver-Based Coordination Polymers on Antibacterial Applications. *Molecules* **27**, 7166 (2022).
166. Mette, M. *et al.* Silver Carboxylate as an Antibiotic-Independent Antimicrobial: A Review of Current Formulations, in vitro Efficacy, and Clinical Relevance. *Med. Res. Arch.* **10**, (2022).
167. Lu, X. & Masson, E. Formation and Stabilization of Silver Nanoparticles with Cucurbit[n]urils (n = 5–8) and Cucurbituril-Based Pseudorotaxanes in Aqueous Medium. *Langmuir* **27**, 3051–3058 (2011).
168. Storer, R. I., Aciro, C. & Jones, L. H. Squaramides: physical properties, synthesis and applications. *Chem. Soc. Rev.* **40**, 2330–2346 (2011).
169. Amendola, V., Bergamaschi, G., Boiocchi, M., Fabbrizzi, L. & Milani, M. The Squaramide versus Urea Contest for Anion Recognition. *Chem. – Eur. J.* **16**, 4368–4380 (2010).
170. Amendola, V., Fabbrizzi, L., Mosca, L. & Schmidtchen, F.-P. Urea-, Squaramide-, and Sulfonamide-Based Anion Receptors: A Thermodynamic Study. *Chem. – Eur. J.* **17**, 5972–5981 (2011).
171. Mert, S. & Erdebil, Ö. Anion-Binding Properties of Aliphatic Symmetric Squaramide Receptors. *ACS Omega* **9**, 8333–8342 (2024).
172. Picci, G., Montis, R., Lippolis, V. & Caltagirone, C. Squaramide-based receptors in anion supramolecular chemistry: insights into anion binding, sensing, transport and extraction. *Chem. Soc. Rev.* **53**, 3952–3975 (2024).
173. Lane, J. D. E., Shiels, G., Ramamurthi, P., Müllner, M. & Jolliffe, K. A. Water-Soluble Squaramide-Functionalized Copolymers for Anion Recognition. *Macromol. Rapid Commun.* **n/a**, 2300406.

174. Rostami, A. *et al.* N,N′-Diarylsquaramides: General, High-Yielding Synthesis and Applications in Colorimetric Anion Sensing. *J. Org. Chem.* **75**, 3983–3992 (2010).
175. Lane, J. D. E., Shiels, G., Ramamurthi, P., Müllner, M. & Jolliffe, K. A. Water-Soluble Squaramide-Functionalized Copolymers for Anion Recognition. *Macromol. Rapid Commun.* **46**, 2300406 (2025).
176. Mommer, S. & Wezenberg, S. J. Anion-Induced Reversible Actuation of Squaramide-Crosslinked Polymer Gels. *ACS Appl. Mater. Interfaces* **14**, 43711–43718 (2022).
177. Zaleskaya-Hernik, M., Megiel, E. & Romański, J. Utilizing a polymer containing squaramide-based ion pair receptors for salt extraction. *J. Mol. Liq.* **361**, 119600 (2022).
178. Prohens, R. *et al.* Squaramido-based receptors: Molecular recognition of carboxylate anions in highly competitive media. *Tetrahedron Lett.* **39**, 1063–1066 (1998).
179. Busschaert, N. *et al.* Squaramides as Potent Transmembrane Anion Transporters. *Angew. Chem. Int. Ed.* **51**, 4426–4430 (2012).
180. Bao, X. *et al.* Fluorescent squaramides as anion receptors and transmembrane anion transporters. *Chem. Commun.* **54**, 1363–1366 (2018).
181. Abogunrin, A. A., Healy, S. A., Fenelon, O. & Elmes, R. B. P. Head vs. Tail Squaramide–Naphthalimide Conjugates: Self-Assembly and Anion Binding Behaviour. *Chemistry* **4**, 1288–1299 (2022).
182. Qin, L., Hartley, A., Turner, P., P. Elmes, R. B. & A. Jolliffe, K. Macrocyclic squaramides: anion receptors with high sulfate binding affinity and selectivity in aqueous media. *Chem. Sci.* **7**, 4563–4572 (2016).
183. Spiaggia, F. *et al.* A Squaramide-Based Organocatalyst as a Novel Versatile Chiral Solvating Agent for Carboxylic Acids. *Molecules* **29**, 2389 (2024).
184. Marchetti, L. A., Kumawat, L. K., Mao, N., Stephens, J. C. & Elmes, R. B. P. The Versatility of Squaramides: From Supramolecular Chemistry to Chemical Biology. *Chem* **5**, 1398–1485 (2019).
185. Malerich, J. P., Hagihara, K. & Rawal, V. H. Chiral Squaramide Derivatives are Excellent Hydrogen Bond Donor Catalysts. *J. Am. Chem. Soc.* **130**, 14416–14417 (2008).
186. Agnew-Francis, K. A. & Williams, C. M. Squaramides as Bioisosteres in Contemporary Drug Design. *Chem. Rev.* **120**, 11616–11650 (2020).

187. Singh, A. *et al.* Calix[6]arenes with halogen bond donor groups as selective and efficient anion transporters. *Chem. Commun.* **58**, 6255–6258 (2022).
188. Yang, J. H. & Kim, S. K. A squaramide cage capable of binding and extracting H2PO4− and HP2O73− in highly polar protic media. *Chem. Commun.* **59**, 9988–9991 (2023).
189. Yu, M. *et al.* Antibacterial Activity of Squaric Amide Derivative SA2 against Methicillin-Resistant Staphylococcus aureus. *Antibiotics* **11**, 1497 (2022).
190. Quintana, M., Alegre-Requena, J. V., Marqués-López, E., Herrera, R. P. & Triola, G. Squaramides with cytotoxic activity against human gastric carcinoma cells HGC-27: synthesis and mechanism of action. *MedChemComm* **7**, 550–561 (2016).
191. Berney, M. *et al.* Synthesis and evaluation of squaramide and thiosquaramide inhibitors of the DNA repair enzyme SNM1A. *Bioorg. Med. Chem.* **46**, 116369 (2021).
192. Arun, A., Docker, A., Tay, H. M. & Beer, P. D. Squaramide-based Heteroditopic [2]Rotaxanes for Sodium Halide Ion-pair Recognition. *Chem. – Eur. J.* **n/a**, e202301446.
193. Jin, C. *et al.* Novel calix[4]arene-based receptors with bis-squaramide moieties for colorimetric sensing of anions via two different interaction modes. *Tetrahedron Lett.* **54**, 796–801 (2013).
194. Daniele, R. P. & Holian, S. K. A potassium ionophore (valinomycin) inhibits lymphocyte proliferation by its effects on the cell membrane. *Proc. Natl. Acad. Sci. U. S. A.* **73**, 3599–3602 (1976).
195. Łowicki, D. & Huczyński, A. Structure and Antimicrobial Properties of Monensin A and Its Derivatives: Summary of the Achievements. *BioMed Res. Int.* **2013**, 742149 (2013).
196. Bonaventura, P., Benedetti, G., Albarède, F. & Miossec, P. Zinc and its role in immunity and inflammation. *Autoimmun. Rev.* **14**, 277–285 (2015).
197. Harbison-Price, N. *et al.* Multiple Bactericidal Mechanisms of the Zinc Ionophore PBT2. *mSphere* **5**, 10.1128/msphere.00157-20 (2020).
198. Bohlmann, L. *et al.* Chemical Synergy between Ionophore PBT2 and Zinc Reverses Antibiotic Resistance. *mBio* **9**, e02391-18 (2018).
199. Wu, Y.-L. & Wright, A. I. Why does thionating a carbonyl molecule make it a better electron acceptor? *Phys. Chem. Chem. Phys.* **25**, 1342–1348 (2023).
200. Rostami, A. *et al.* N,N′-Diarylsquaramides: General, High-Yielding Synthesis and Applications in Colorimetric Anion Sensing. *J. Org. Chem.* **75**, 3983–3992 (2010).

201. Rombola, M. & Rawal, V. H. Dicyclopentyl Dithiosquarate as an Intermediate for the Synthesis of Thiosquaramides. *Org. Lett.* **20**, 514–517 (2018).
202. Bergman, J., Pettersson, B., Hasimbegovic, V. & Svensson, P. H. Thionations Using a P4S10−Pyridine Complex in Solvents Such as Acetonitrile and Dimethyl Sulfone. *J. Org. Chem.* **76**, 1546–1553 (2011).
203. Martincigh, B. S., Mhike, M., Morakinyo, K., Adigun, R. A. & Simoyi, R. H. Oxyhalogen–Sulfur Chemistry: Oxidation of a Thiourea Dimer, Formamidine Disulfide, by Chlorine Dioxide. *Aust. J. Chem.* **66**, 362–369 (2013).
204. Chakrabarty, R., Bora, S. J. & Das, B. K. Synthesis, Structure, Spectral and Electrochemical Properties, and Catalytic Use of Cobalt(III)−Oxo Cubane Clusters. *Inorg. Chem.* **46**, 9450–9462 (2007).
205. Wiberg, K. B. & Wang, Y. A comparison of some properties of C=O and C=S bonds. *Arkivoc* **2011**, 45–56 (2010).
206. Zhao, Y. & Truhlar, D. G. The M06 suite of density functionals for main group thermochemistry, thermochemical kinetics, noncovalent interactions, excited states, and transition elements: two new functionals and systematic testing of four M06-class functionals and 12 other functionals. *Theor. Chem. Acc.* **120**, 215–241 (2008).
207. Weigend, F. & Ahlrichs, R. Balanced basis sets of split valence, triple zeta valence and quadruple zeta valence quality for H to Rn: Design and assessment of accuracy. *Phys. Chem. Chem. Phys.* **7**, 3297–3305 (2005).
208. Feyereisen, M., Fitzgerald, G. & Komornicki, A. Use of approximate integrals in ab initio theory. An application in MP2 energy calculations. *Chem. Phys. Lett.* **208**, 359–363 (1993).
209. Helmich-Paris, B., de Souza, B., Neese, F. & Izsák, R. An improved chain of spheres for exchange algorithm. *J. Chem. Phys.* **155**, 104109 (2021).
210. Weigend, F. Accurate Coulomb-fitting basis sets for H to Rn. *Phys. Chem. Chem. Phys.* **8**, 1057–1065 (2006).
211. Thordarson, P. Determining association constants from titration experiments in supramolecular chemistry. *Chem. Soc. Rev.* **40**, 1305–1323 (2011).
212. Hibbert, D. B. & Thordarson, P. The death of the Job plot, transparency, open science and online tools, uncertainty estimation methods and other developments in supramolecular chemistry data analysis. *Chem. Commun.* **52**, 12792–12805 (2016).

213. Frazzini, V. *et al.* The pharmacological perturbation of brain zinc impairs BDNF-related signaling and the cognitive performances of young mice. *Sci. Rep.* **8**, 9768 (2018).
214. Chinigo, G. M. *et al.* Early Process Development of PF-07054894, a Squaramide-Based Antagonist of C-C Chemokine Receptor Type 6 (CCR6). *Org. Process Res. Dev.* https://doi.org/10.1021/acs.oprd.3c00451 (2024) doi:10.1021/acs.oprd.3c00451.
215. Bujosa, S., Rubert, L., Rotger, C. & Soberats, B. Modulating self-assembly and polymorph transitions in bisdendronized squaramides. *Commun. Chem.* **7**, 296 (2024).
216. Role of Zinc and Zinc Ionophores in Brain Health and Depression Especially during the COVID-19 Pandemic | IntechOpen. https://www.intechopen.com/chapters/80582.
217. Yoshino, S. *et al.* Effect of quercetin and glucuronide metabolites on the monoamine oxidase-A reaction in mouse brain mitochondria. *Nutrition* **27**, 847–852 (2011).
218. Clergeaud, G., Dabbagh-Bazarbachi, H., Ortiz, M., Fernández-Larrea, J. B. & O'Sullivan, C. K. A simple liposome assay for the screening of zinc ionophore activity of polyphenols. *Food Chem.* **197**, 916–923 (2016).
219. Chvojka, M. *et al.* The Lucigenin Assay: Measuring Anion Transport in Lipid Vesicles**. *Anal. Sens.* **n/a**, e202300044.
220. Hickey, E. E., Page, S. W. & Trott, D. J. In vitro efficacy and pharmacodynamic profiles of four polyether ionophores against methicillin-resistant Staphylococcus spp. *J. Vet. Pharmacol. Ther.* **43**, 499–507 (2020).
221. Klinman, J. P. & Brenner, M. Role of copper and catalytic mechanism in the copper monooxygenase, dopamine beta-hydroxylase (D beta H). *Prog. Clin. Biol. Res.* **274**, 227–248 (1988).
222. Klinman, J. P., Krueger, M., Brenner, M. & Edmondson, D. E. Evidence for two copper atoms/subunit in dopamine beta-monooxygenase catalysis. *J. Biol. Chem.* **259**, 3399–3402 (1984).
223. Zhu, Z. *et al.* Copper homeostasis and cuproptosis in central nervous system diseases. *Cell Death Dis.* **15**, 850 (2024).
224. Scolari Grotto, F. & Glaser, V. Are high copper levels related to Alzheimer's and Parkinson's diseases? A systematic review and meta-analysis of articles published between 2011 and 2022. *BioMetals* **37**, 3–22 (2024).
225. Wessels, I., Maywald, M. & Rink, L. Zinc as a Gatekeeper of Immune Function. *Nutrients* **9**, 1286 (2017).
226. Wessels, I., Fischer, H. J. & Rink, L. Dietary and Physiological Effects of Zinc on the Immune System. *Annu. Rev. Nutr.* **41**, 133–175 (2021).

227. Duncan, F. E. *et al.* The zinc spark is an inorganic signature of human egg activation. *Sci. Rep.* **6**, 24737 (2016).
228. Marchetti, L. A., Kumawat, L. K., Mao, N., Stephens, J. C. & Elmes, R. B. P. The Versatility of Squaramides: From Supramolecular Chemistry to Chemical Biology. *Chem* **5**, 1398–1485 (2019).
229. Bao, X. *et al.* Fluorescent squaramides as anion receptors and transmembrane anion transporters. *Chem. Commun.* **54**, 1363–1366 (2018).
230. Kumawat, L. K. *et al.* Squaramide—Naphthalimide Conjugates as "Turn-On" Fluorescent Sensors for Bromide Through an Aggregation-Disaggregation Approach. *Front. Chem.* **7**, (2019).
231. Tomàs, S. *et al.* Squaramido-Based Receptors: Design, Synthesis, and Application to the Recognition of Tetraalkylammonium Compounds. *J. Org. Chem.* **61**, 9394–9401 (1996).
232. Li, Y., Wang, H., Tao, Q. & Wang, B. Two Squaramide-Based Fluorescent Probes for Cu2+ and Cd2+. *J. Fluoresc.* https://doi.org/10.1007/s10895-024-03956-7 (2024) doi:10.1007/s10895-024-03956-7.
233. Jagleniec, D., Dobrzycki, Ł. & Romański, J. Modulating fluorescent sensing of the pyrene-based ion pair receptor by docking on graphene quantum dots. *J. Mol. Liq.* **399**, 124410 (2024).
234. Zaleskaya-Hernik, M., Wilczek, M., Dobrzycki, Ł. & Romański, J. Zwitterion detection with a fluorescent squaramide cryptand: a study on size-dependent salt recognition and sensing. *Org. Chem. Front.* **11**, 4820–4828 (2024).
235. Zaleskaya, M., Jagleniec, D. & Romański, J. Macrocyclic squaramides as ion pair receptors and fluorescent sensors selective towards sulfates. *Dalton Trans.* **50**, 3904–3915 (2021).
236. Berry, S. N. *et al.* Fluorescent transmembrane anion transporters: shedding light on anionophoric activity in cells †Electronic supplementary information (ESI) available: Experimental synthesis details and characterisation of all compounds; 1H NMR titration binding studies, stacked spectra and fitted binding isotherms; UV-Vis and fluorescence spectroscopy studies data; various vesicle assays methods and Hill plots for ISE transport studies; details of MTT assay and annexin V assay, dose–response curves and IC50 values for cell viability studies; additional fluorescence microscopy images and co-staining experiments. CCDC 1424345. For ESI and crystallographic data in CIF or other electronic format see DOI: 10.1039/c6sc01643j ‡The data underlying this paper has been made available online at http://dx.doi.org/10.5258/SOTON/392749 to

comply with the EPSRC open data policy. *Chem. Sci.* **7**, 5069–5077 (2016).
237. E. Bickerton, L., G. Johnson, T., Kerckhoffs, A. & J. Langton, M. Supramolecular chemistry in lipid bilayer membranes. *Chem. Sci.* **12**, 11252–11274 (2021).
238. Meeusen, J. W., Tomasiewicz, H., Nowakowski, A. & Petering, D. H. TSQ (6-Methoxy-8-p-Toluenesulfonamido-Quinoline), a Common Fluorescent Sensor for Cellular Zinc, Images Zinc Proteins. *Inorg. Chem.* **50**, 7563–7573 (2011).
239. Bronson, R. T. *et al.* Origins of 'on-off' fluorescent behavior of 8-hydroxyquinoline containing chemosensors. *Tetrahedron* **60**, 11139–11144 (2004).
240. Albrecht, M., Witt, K., Fröhlich, R. & Kataeva, O. Inter- and intramolecular hydrogen bonding in amide- and urea-substituted 8-hydroxyquinoline derivatives. *Tetrahedron* **58**, 561–567 (2002).
241. Lane, J. D. E. & Jolliffe, K. A. Squaramides for colorimetric and fluorescent anion sensing. *Org. Biomol. Chem.* **21**, 3226–3234 (2023).
242. Elmes, R. B. P., Busschaert, N., Czech, D. D., Gale, P. A. & Jolliffe, K. A. pH switchable anion transport by an oxothiosquaramide. *Chem. Commun.* **51**, 10107–10110 (2015).
243. Elmes, R. B. P. *et al.* Thiosquaramides: Dual-Function Ionophores for Zn^{2+} and Cl^- with Ion Dependent Anti-Microbial Activity. *Org. Biomol. Chem.* https://doi.org/10.1039/D5OB01166C (2025) doi:10.1039/D5OB01166C.
244. Krall, R. F., Tzounopoulos, T. & Aizenman, E. The Function and Regulation of Zinc in the Brain. *Neuroscience* **457**, 235–258 (2021).
245. Lemaire, K. *et al.* Insulin crystallization depends on zinc transporter ZnT8 expression, but is not required for normal glucose homeostasis in mice. *Proc. Natl. Acad. Sci.* **106**, 14872–14877 (2009).
246. Zhang, Y. & Gladyshev, V. N. Comparative Genomics of Trace Element Dependence in Biology *. *J. Biol. Chem.* **286**, 23623–23629 (2011).
247. Andreini, C., Banci, L., Bertini, I. & Rosato, A. Counting the Zinc-Proteins Encoded in the Human Genome. *J. Proteome Res.* **5**, 196–201 (2006).
248. Marunaka, Y. Physiological roles of chloride ions in bodily and cellular functions. *J. Physiol. Sci.* **73**, 31 (2023).
249. Berend, K., Hulsteijn, L. H. van & Gans, R. O. B. Chloride: The queen of electrolytes? *Eur. J. Intern. Med.* **23**, 203–211 (2012).

250. Jentsch, T. J., Stein, V., Weinreich, F. & Zdebik, A. A. Molecular Structure and Physiological Function of Chloride Channels. *Physiol. Rev.* **82**, 503–568 (2002).
251. Kaila, K., Price, T. J., Payne, J. A., Puskarjov, M. & Voipio, J. Cation-chloride cotransporters in neuronal development, plasticity and disease. *Nat. Rev. Neurosci.* **15**, 637–654 (2014).
252. Westen, E. A. & Prange, H. D. A Reexamination of the Mechanisms Underlying the Arteriovenous Chloride Shift. *Physiol. Biochem. Zool.* **76**, 603–614 (2003).
253. Edo, G. I. *et al.* Poly(vinyl chloride) (PVC): an updated review of its properties, polymerization, modification, recycling, and applications. *J. Mater. Sci.* **59**, 21605–21648 (2024).
254. Gregory, P. Functional Dyes. in *Industrial Dyes* 543–584 (John Wiley & Sons, Ltd, 2002). doi:https://doi.org/10.1002/3527602011.ch6.
255. Kundu, S., Egboluche, T. K. & Hossain, Md. A. Urea- and Thiourea-Based Receptors for Anion Binding. *Acc. Chem. Res.* **56**, 1320–1329 (2023).
256. Li, A.-F., Wang, J.-H., Wang, F. & Jiang, Y.-B. Anion complexation and sensing using modified urea and thiourea-based receptors. *Chem. Soc. Rev.* **39**, 3729–3745 (2010).
257. Gale, P. A. Anion receptor chemistry. *Chem. Commun.* **47**, 82–86 (2010).
258. Manna, U., Portis, B., Egboluche, T. K., Nafis, M. & Hossain, M. A. Anion Binding Studies of Urea and Thiourea Functionalized Molecular Clefts. *Front. Chem.* **8**, (2021).
259. Emami Khansari, M., Wallace, K. D. & Hossain, Md. A. Synthesis and anion recognition studies of a dipodal thiourea-based sensor for anions. *Tetrahedron Lett.* **55**, 438–440 (2014).
260. Jin, C. *et al.* Squaramide-based tripodal receptors for selective recognition of sulfate anion. *Chem. Commun.* **49**, 2025–2027 (2013).
261. Jagleniec, D., Wilczek, M. & Romański, J. Tripodal, Squaramide-Based Ion Pair Receptor for Effective Extraction of Sulfate Salt. *Molecules* **26**, 2751 (2021).
262. Tong, C. *et al.* Squaramide-Based Supramolecular Materials for Three-Dimensional Cell Culture of Human Induced Pluripotent Stem Cells and Their Derivatives. *Biomacromolecules* **19**, 1091–1099 (2018).
263. Soberats, B. *et al.* Janus-Like Squaramide-Based Hosts: Dual Mode of Binding and Conformational Transitions Driven by Ion-Pair Recognition. *Chem. – Eur. J.* **18**, 7533–7542 (2012).

264. Zdanowski, S., Piątek, P. & Romański, J. An ion pair receptor facilitating the extraction of chloride salt from the aqueous to the organic phase. *New J. Chem.* **40**, 7190–7196 (2016).
265. Załubiniak, D., Zakrzewski, M. & Piątek, P. Highly effective ion-pair receptors based on 2,2-bis(aminomethyl)-propionic acid. *Dalton Trans.* **45**, 15557–15564 (2016).
266. Gabutti, S. *et al.* A rigid sublimable naphthalenediimide cyclophane as model compound for UHV STM experiments. *Chem. Commun.* 2370–2372 (2008) doi:10.1039/B719796A.
267. Hoeg-Jensen, T. *et al.* Glucose Sensitive Insulin Derivatives. (2020).
268. Maeda, D. Y., Mahajan, S. S., Atkins, W. M. & Zebala, J. A. Bivalent inhibitors of glutathione *S*-transferase: The effect of spacer length on isozyme selectivity. *Bioorg. Med. Chem. Lett.* **16**, 3780–3783 (2006).
269. Saggiomo, V. *et al.* The role of lipophilicity in transmembrane anion transport. *Chem. Commun.* **48**, 5274–5276 (2012).
270. Busschaert, N. *et al.* Squaramides as Potent Transmembrane Anion Transporters. *Angew. Chem. Int. Ed.* **51**, 4426–4430 (2012).
271. Picci, G. *et al.* The role of indolyl substituents in squaramide-based anionophores. *Org. Biomol. Chem.* **20**, 7981–7986 (2022).
272. Zwicker, V. E. *et al.* Deltamides and Croconamides: Expanding the Range of Dual H-bond Donors for Selective Anion Recognition. *Chem. – Eur. J.* **24**, 1140–1150 (2018).
273. Ataie, N. J. *et al.* Zinc Coordination Geometry and Ligand Binding Affinity: The Structural and Kinetic Analysis of the Second-Shell Serine 228 Residue and the Methionine 180 Residue of the Aminopeptidase from Vibrio proteolyticus. *Biochemistry* **47**, 7673–7683 (2008).
274. Krężel, A. & Maret, W. The biological inorganic chemistry of zinc ions. *Arch. Biochem. Biophys.* **611**, 3–19 (2016).
275. Saez Talens, V. *et al.* Thiosquaramide-Based Supramolecular Polymers: Aromaticity Gain in a Switched Mode of Self-Assembly. *J. Am. Chem. Soc.* **142**, 19907–19916 (2020).
276. Bernús, M. *et al.* Impact of Fluorine Pattern on Lipophilicity and Acid–Base Properties of 2-(Thiofluoroalkyl)pyridines: Insights from Experiments and Statistical Modeling. *J. Med. Chem.* **68**, 4787–4800 (2025).
277. Marques, I. *et al.* Full elucidation of the transmembrane anion transport mechanism of squaramides using in silico investigations. *Phys. Chem. Chem. Phys.* **20**, 20796–20811 (2018).
278. Neese, F. Software update: The ORCA program system—Version 5.0. *WIREs Comput. Mol. Sci.* **12**, e1606 (2022).

279. Hellweg, A., Hättig, C., Höfener, S. & Klopper, W. Optimized accurate auxiliary basis sets for RI-MP2 and RI-CC2 calculations for the atoms Rb to Rn. *Theor. Chem. Acc.* **117**, 587–597 (2007).
280. Ota, N., Nakada, T., Shintani, T., Kamitori, Y. & Okada, E. Computational Study for the Aromatic Nucleophilic Substitution Reaction on 1-Dimethylamino-2,4-bis(trifluoroacetyl)-naphthalene with Amines. *Int. J. Org. Chem.* **8**, 273–281 (2018).
281. Marenich, A. V., Cramer, C. J. & Truhlar, D. G. Universal Solvation Model Based on Solute Electron Density and on a Continuum Model of the Solvent Defined by the Bulk Dielectric Constant and Atomic Surface Tensions. *J. Phys. Chem. B* **113**, 6378–6396 (2009).
282. Bine, F. K., Tasheh, N. S. & Ghogomu, J. N. A Quantum Chemical Screening of Two Imidazole-Chalcone Hybrid Ligands and Their Pd, Pt and Zn Complexes for Charge Transport and Nonlinear Optical (NLO) Properties: A DFT Study. *Comput. Chem.* **9**, 215–237 (2021).
283. Tobe, Y., Sasaki, S., Mizuno, M., Hirose, K. & Naemura, K. Novel Self-Assembly of m-Xylylene Type Dithioureas by Head-to-Tail Hydrogen Bonding. *J. Org. Chem.* **63**, 7481–7489 (1998).
284. Gabutti, S. *et al.* A rigid sublimable naphthalenediimide cyclophane as model compound for UHV STM experiments. *Chem. Commun.* 2370–2372 (2008) doi:10.1039/B719796A.
285. Picci, G. *et al.* The role of indolyl substituents in squaramide-based anionophores. *Org. Biomol. Chem.* **20**, 7981–7986 (2022).
286. Picci, G. *et al.* Fluorescent sensing of non-steroidal anti-inflammatory drugs naproxen and ketoprofen by dansylated squaramide-based receptors. *Org. Biomol. Chem.* **21**, 2968–2975 (2023).

Appendix

Supporting information for Chapter 2

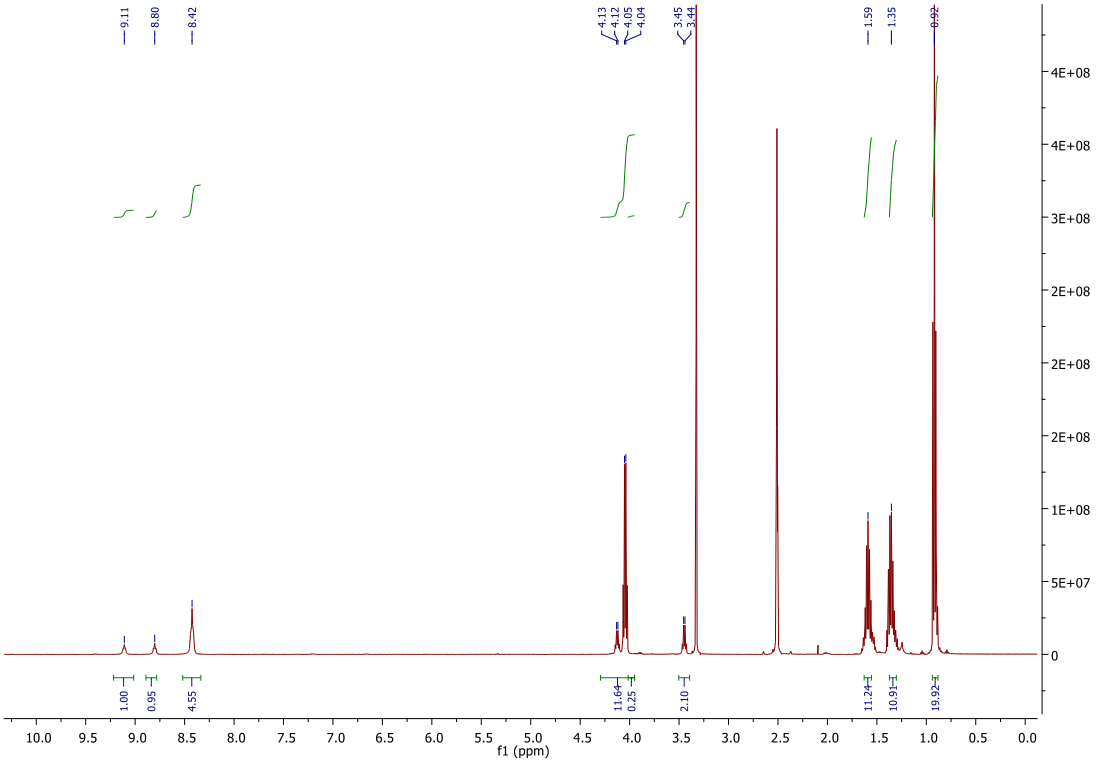

Figure SA1. ^{1}H NMR (DMSO-d_6, 500MHz) spectrum of **2.3**

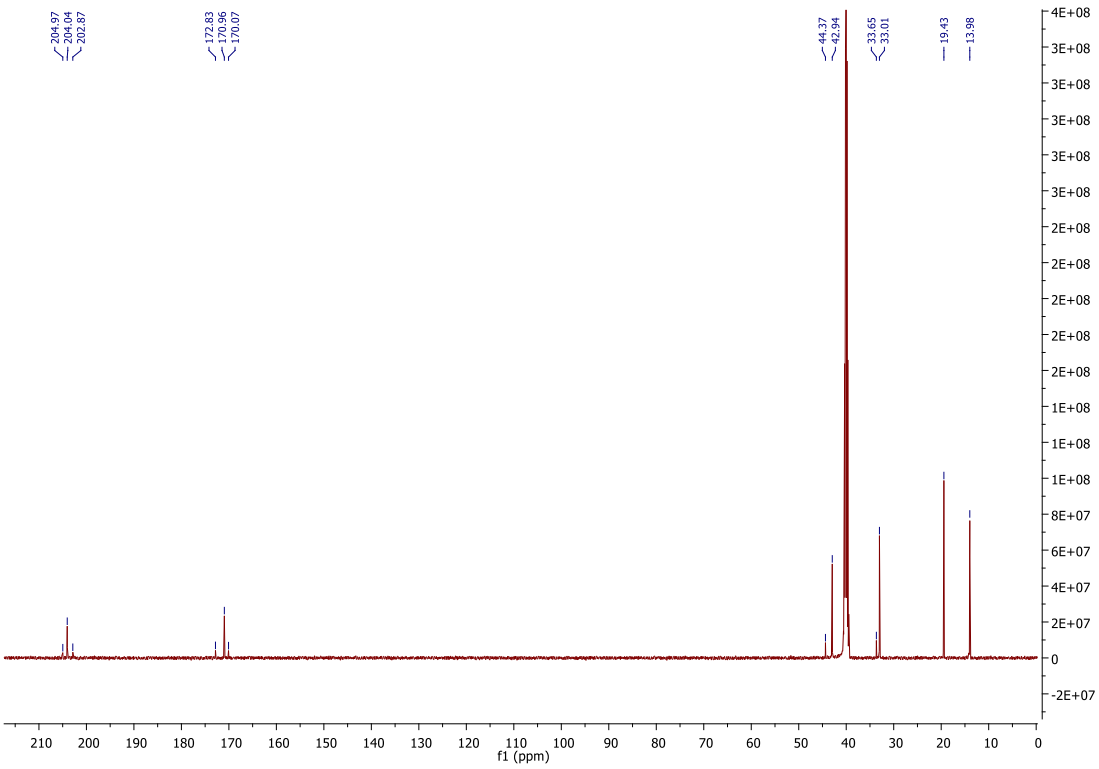

Figure SA2. ^{13}C NMR (DMSO-d_6, 126MHz) spectrum of **2.3**

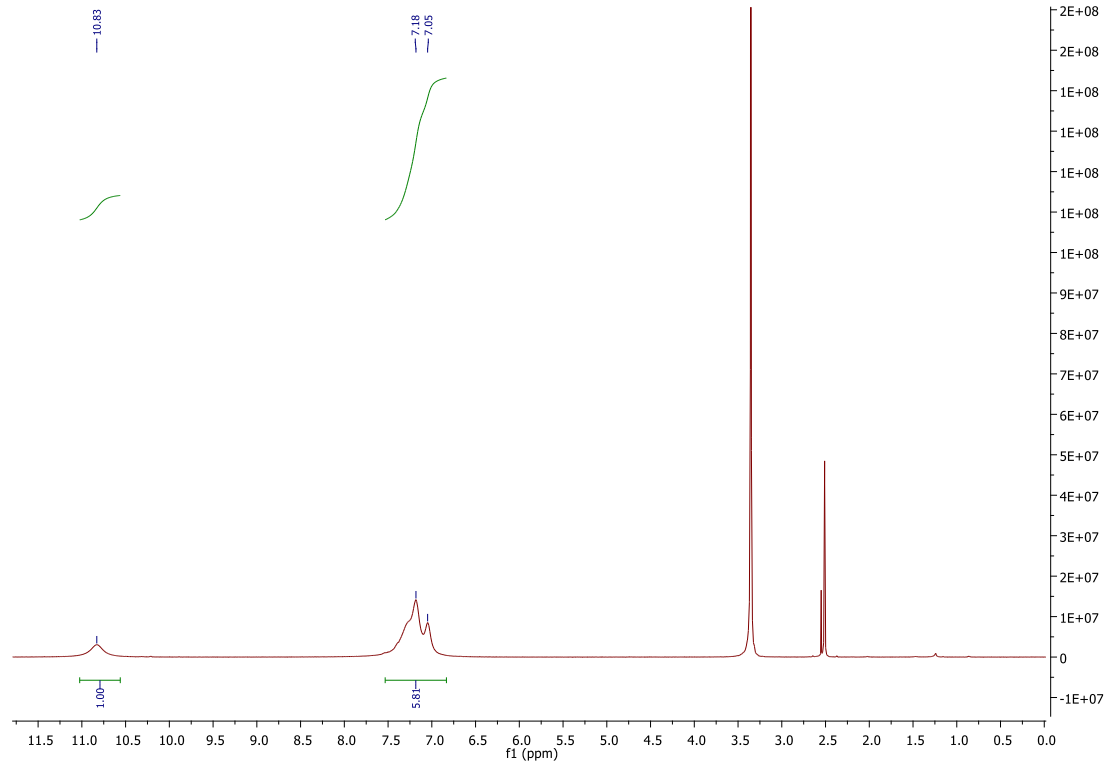

Figure SA3. ^{1}H NMR (DMSO-d_6, 500MHz) spectrum of **2.4**

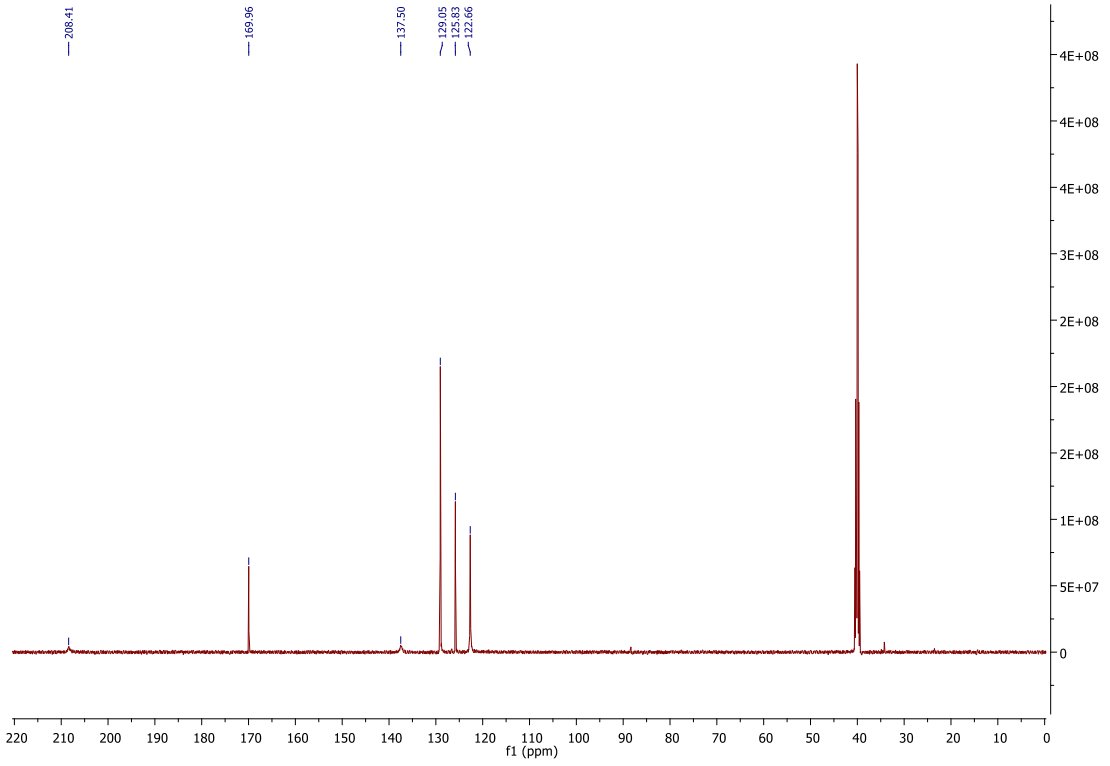

Figure SA4. ^{13}C NMR (DMSO-d_6, 126MHz) spectrum of **2.4**

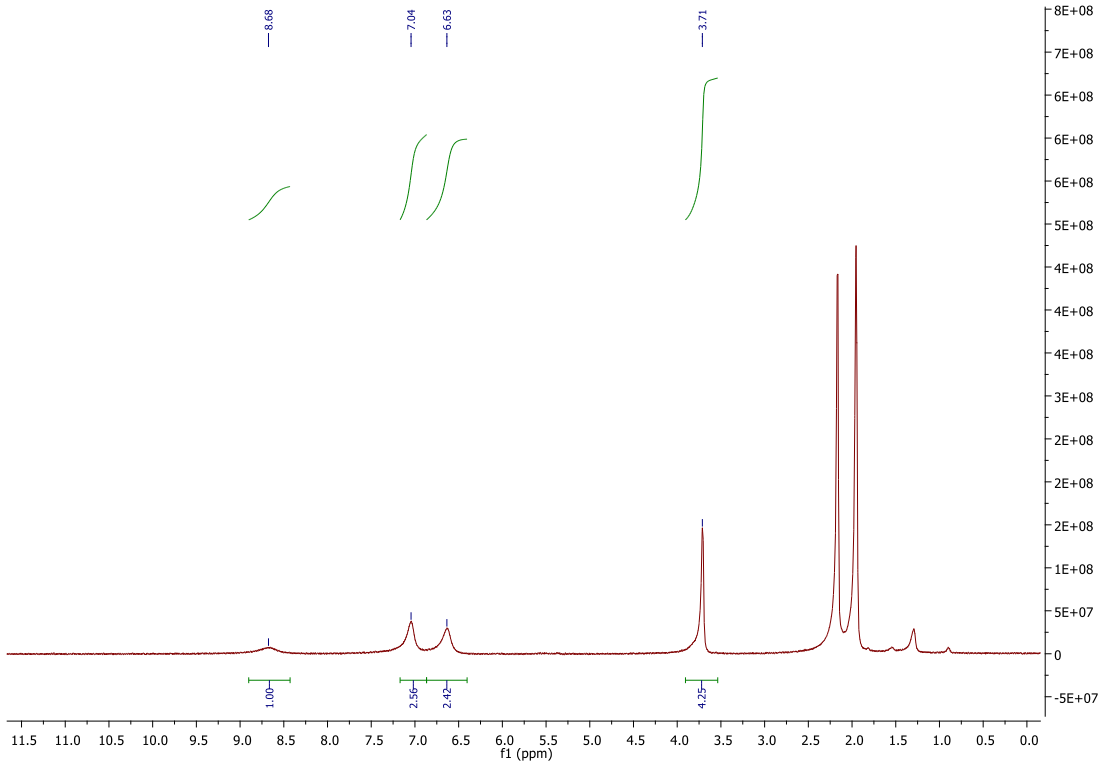

Figure SA5. ^{1}H NMR (CD_3CN, 500MHz) spectrum of **2.5**

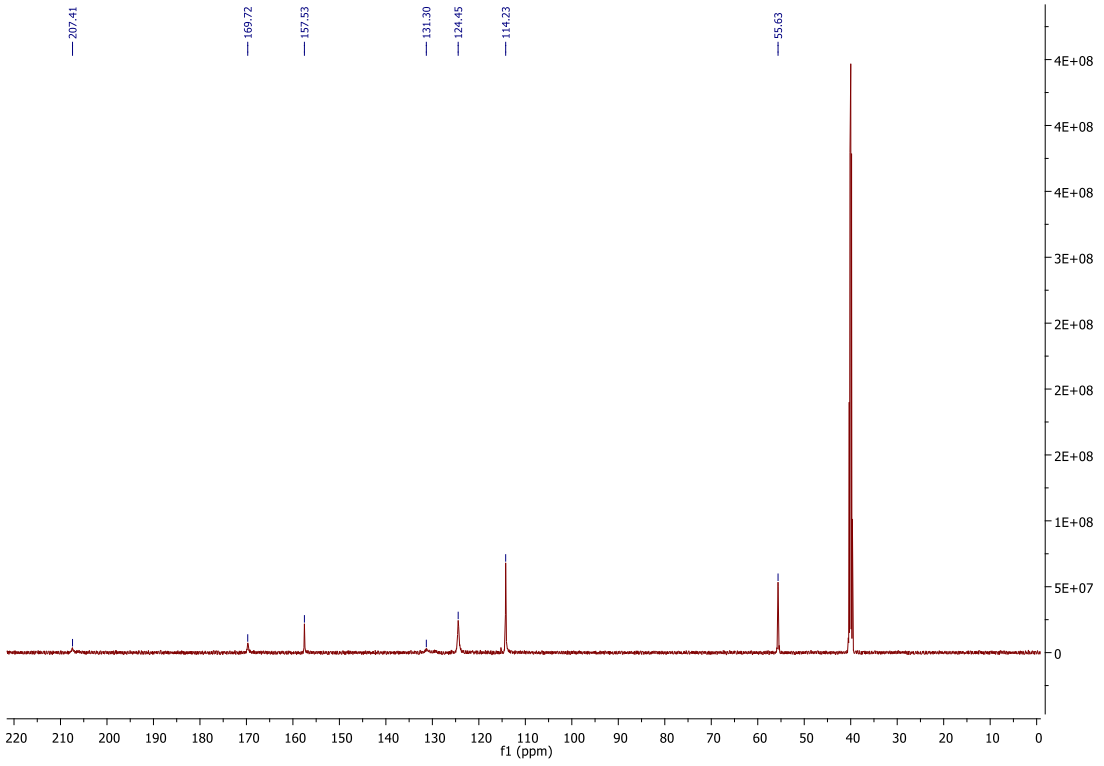

Figure SA6. ^{13}C NMR (DMSO-d_6, 126MHz) spectrum of **2.5**

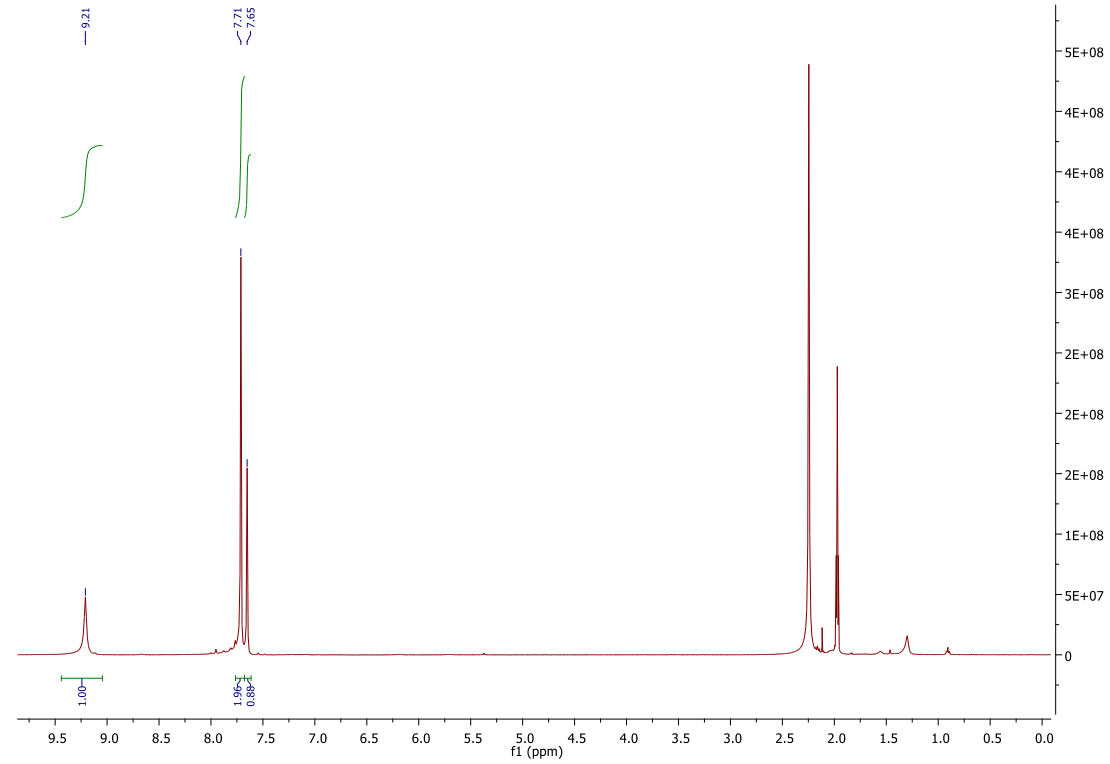

Figure SA7. ^{1}H NMR (CD_3CN, 500MHz) spectrum of **2.6**

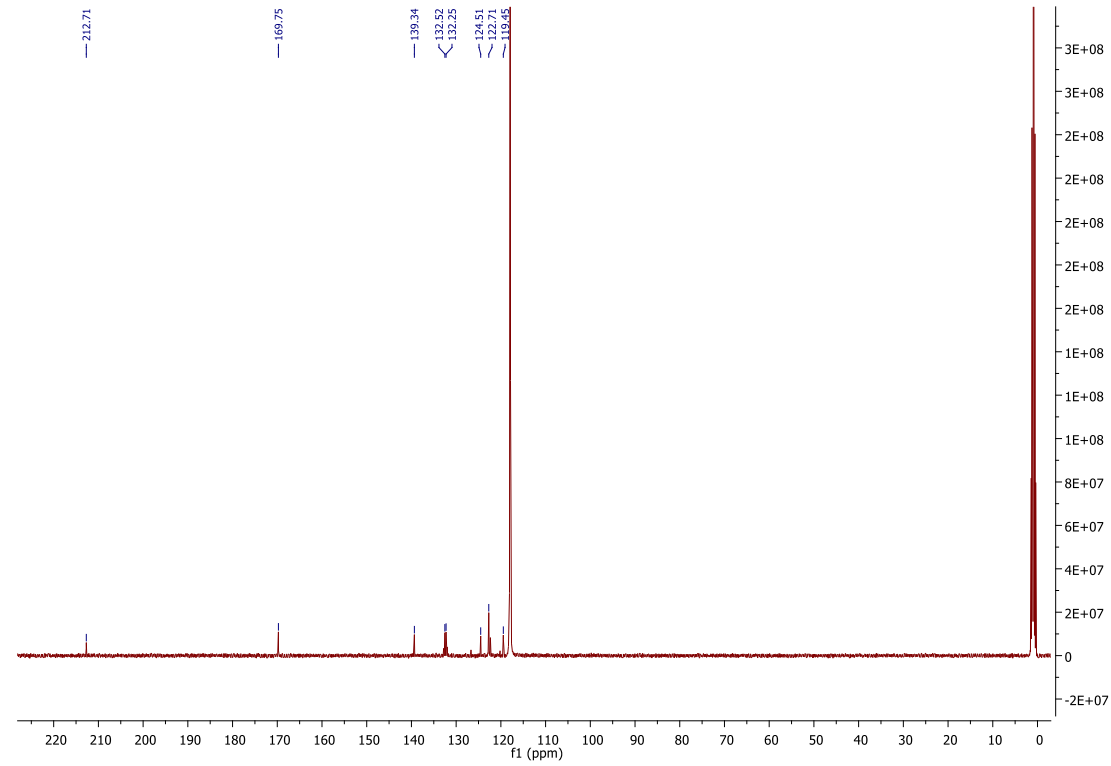

Figure SA8. ^{13}C NMR (CD_3CN, 126MHz) spectrum of **2.6**

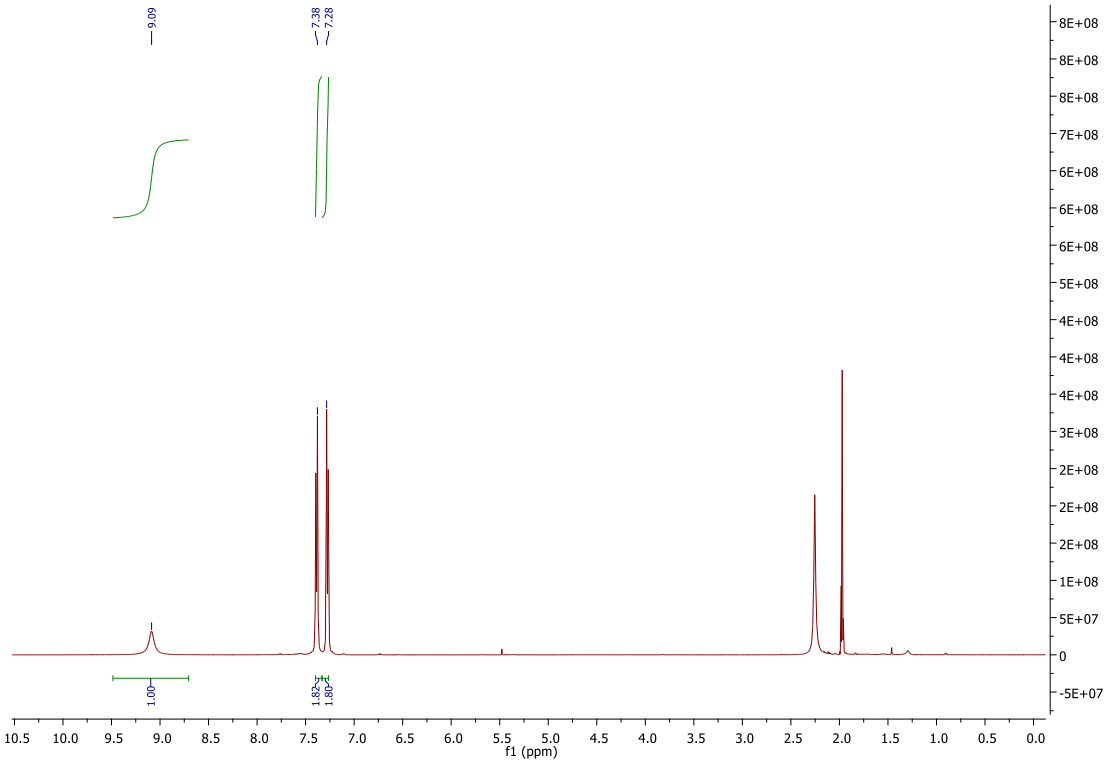

Figure SA9. ^{1}H NMR (CD_3CN, 500MHz) spectrum of **2.7**

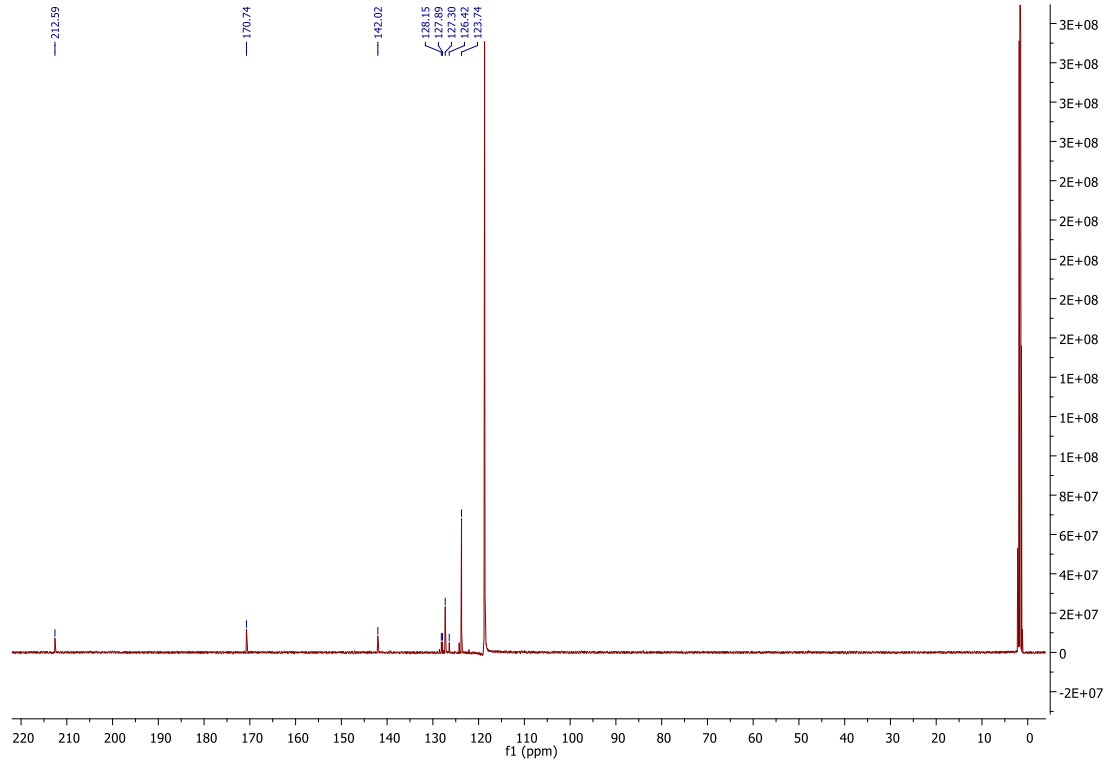

Figure SA10. ^{13}C NMR (CD_3CN, 126MHz) spectrum of **2.7**

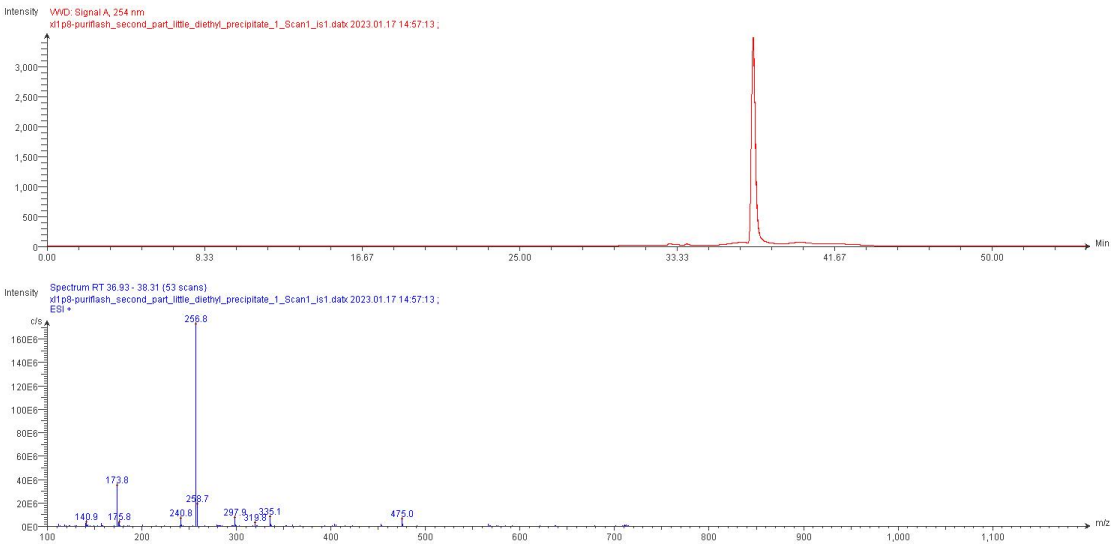

Figure SA11. Analytical LCMS trace of **2.3**, $(M+H)^+$: 257

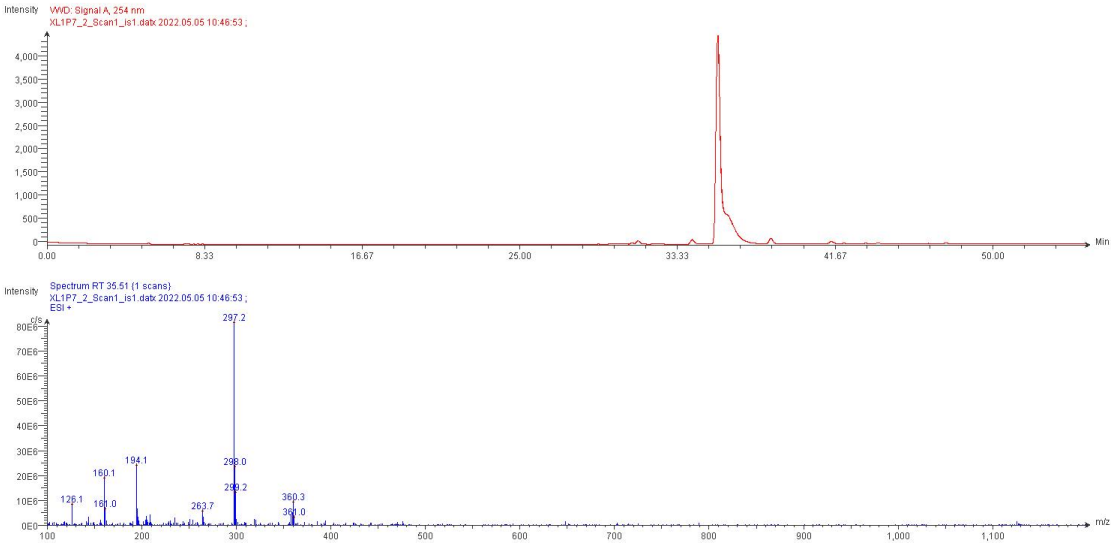

Figure SA12. Analytical LCMS trace of **2.4**, $(M+H)^+$: 297

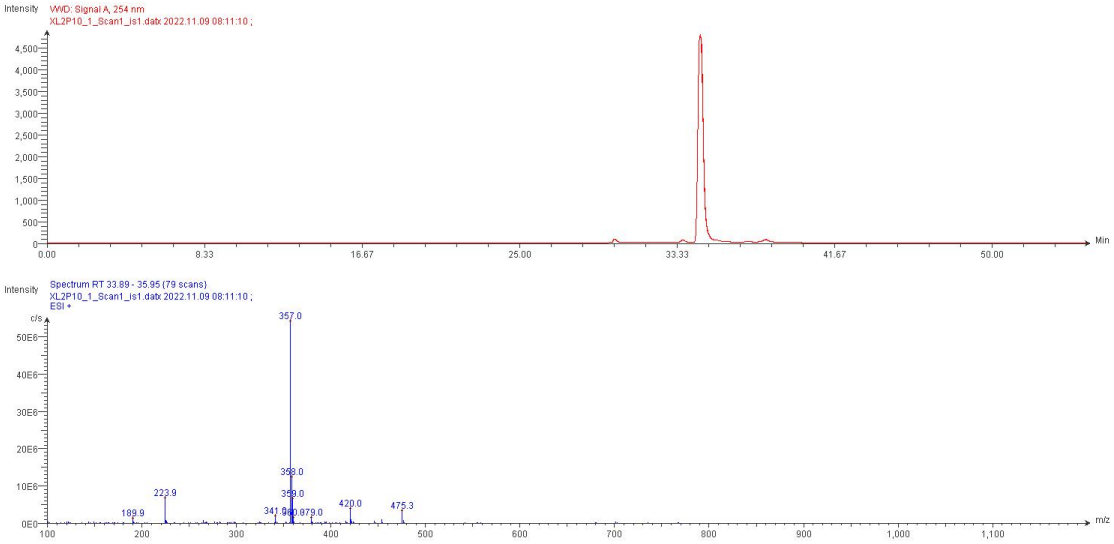

Figure SA13. Analytical LCMS trace of **2.5**, $(M+H)^+$: 357

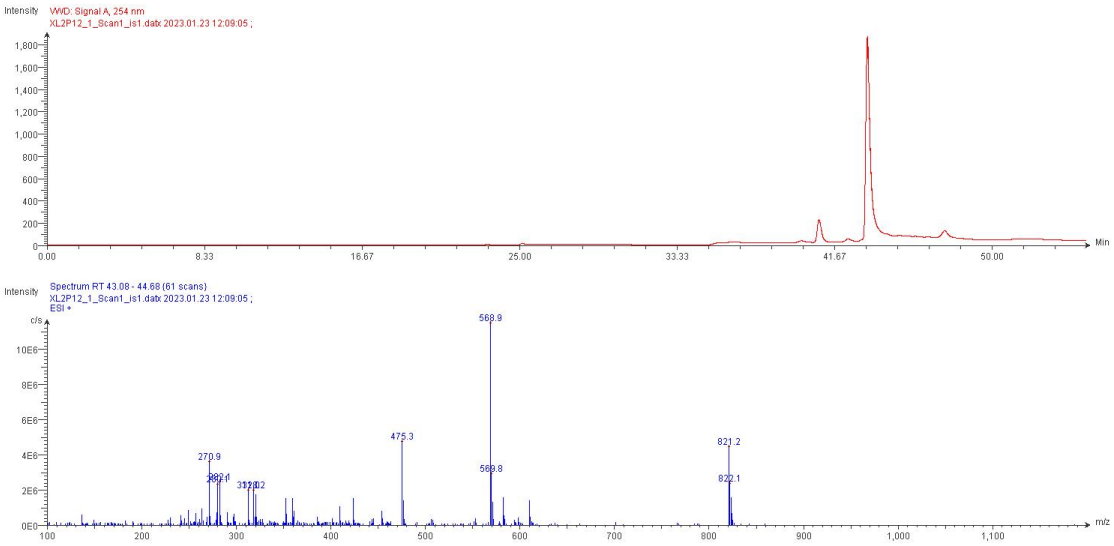

Figure SA14. Analytical LCMS trace of **2.6**, $(M+H)^+$: 569

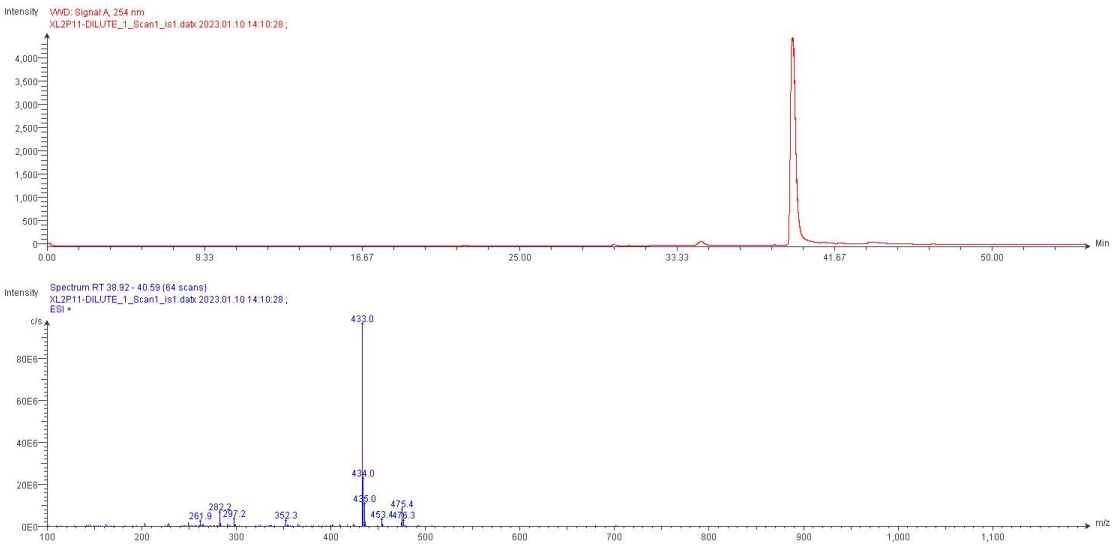

Figure SA15. Analytical LCMS trace of **2.7**, $(M+H)^+$: 433

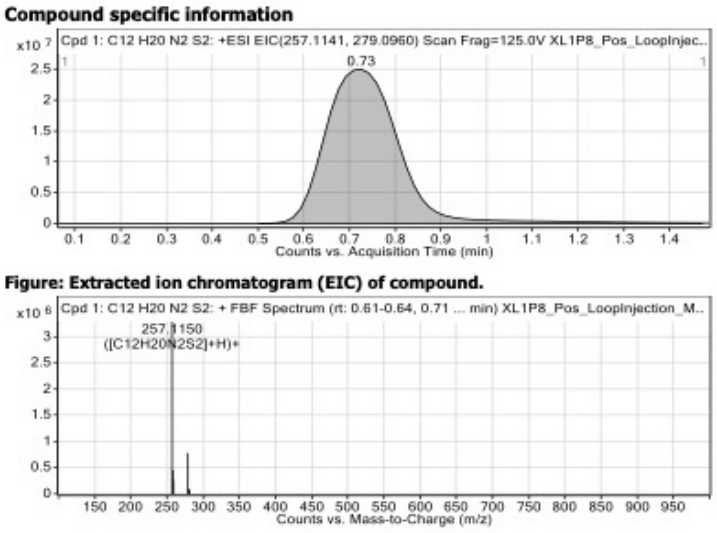

Figure SA16. Analytical HRMS trace of **2.3**

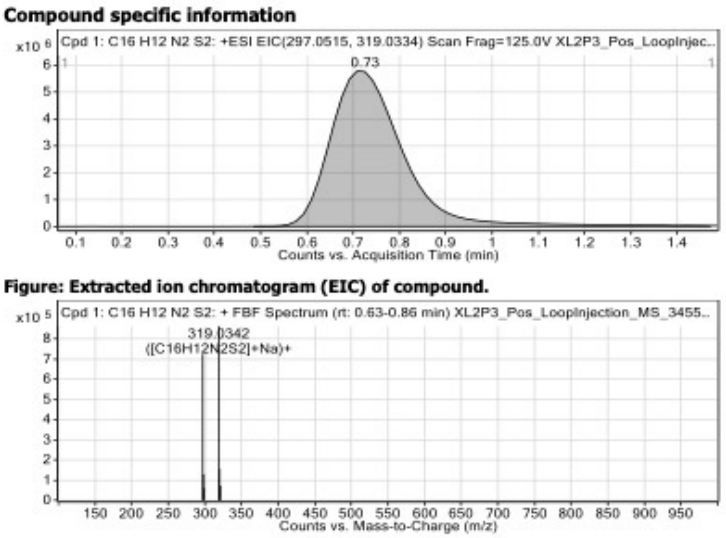

Figure SA17. Analytical HRMS trace of **2.4**

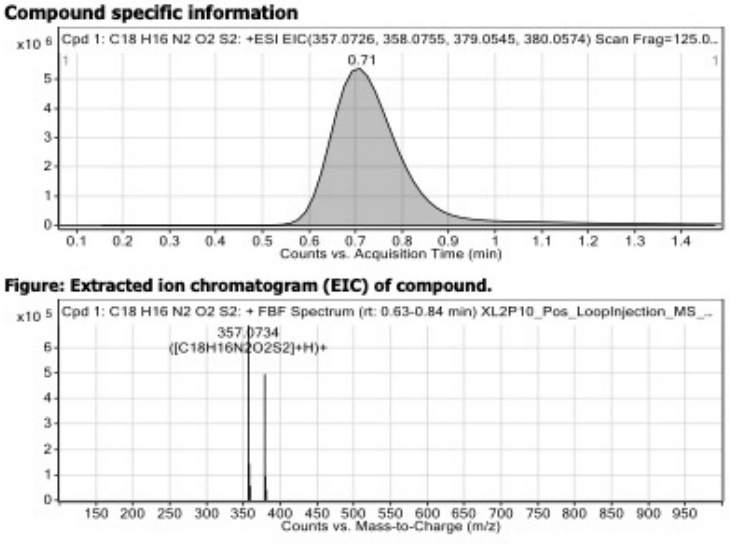

Figure SA18. Analytical HRMS trace of **2.5**

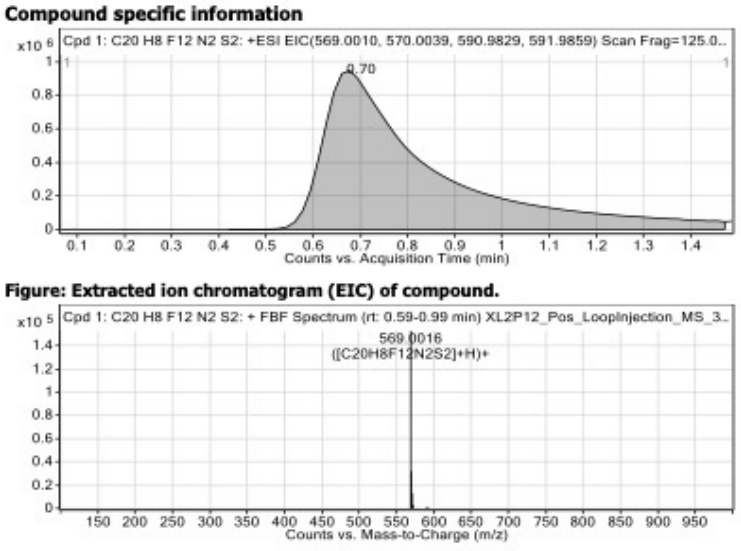

Figure SA19. Analytical HRMS trace of **2.6**

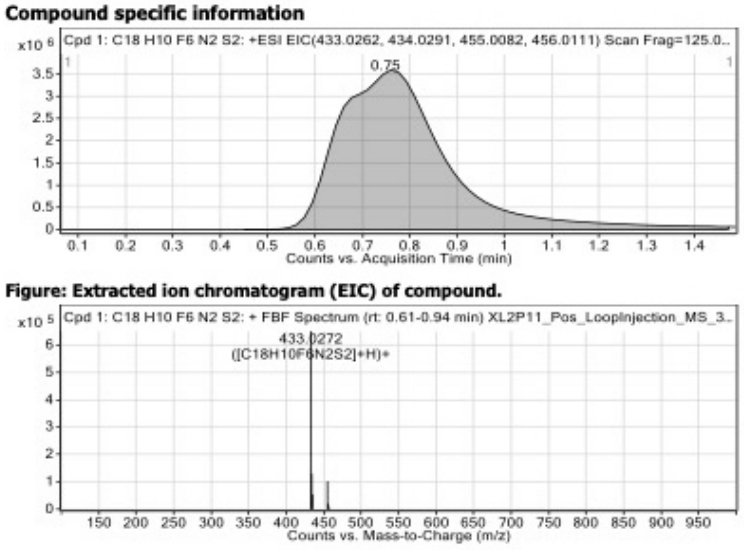

Figure SA20. Analytical HRMS trace of **2.7**

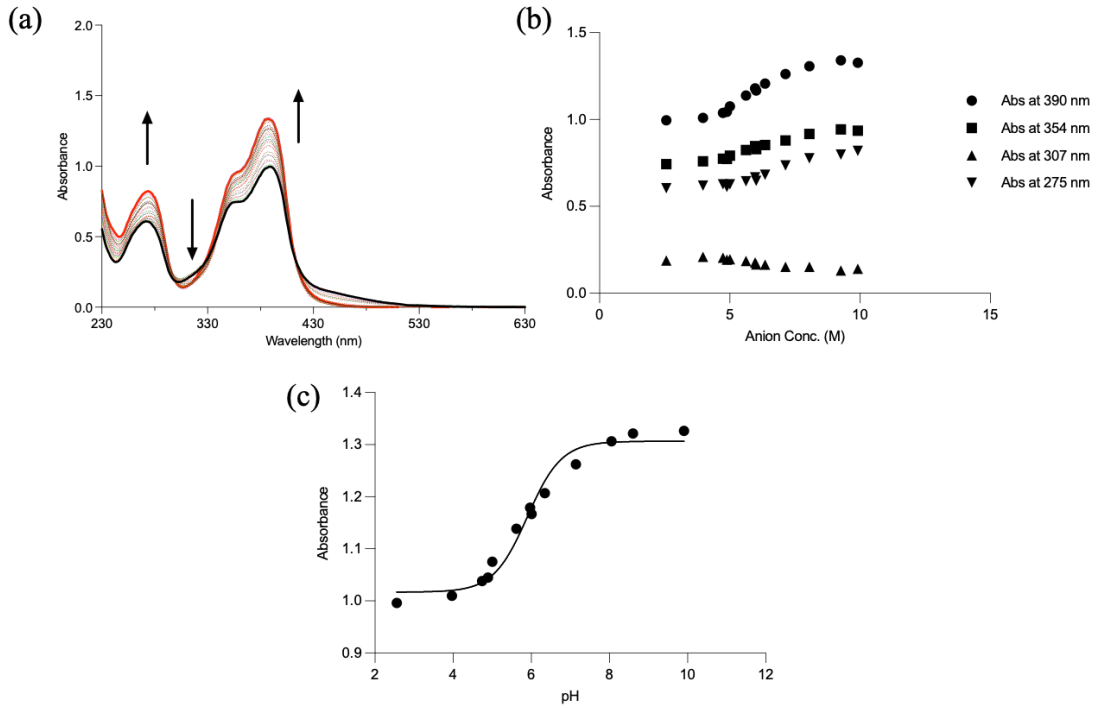

Figure SA21. (a) Absorption spectra of a pH-spectrophotometric titration of **2.3** (4×10^{-5} M) in an MeCN/H_2O mixture (9/1 v/v; 0.1 M in $TBAPF_6$). (b) Comparison plots of absorbance at 390 nm, 354 nm, 307 nm and 275 nm vs. pH. (c) The data was fitted to give the pK_a value of 5.9.

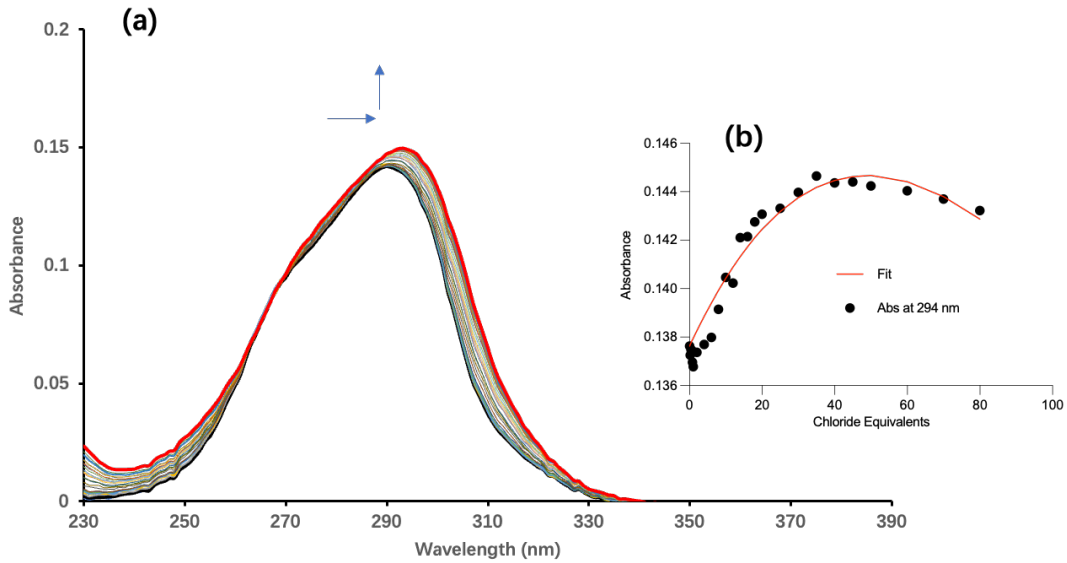

Figure SA22. (a) Absorption spectra of Cl^- titration of **2.1** in MeCN. (b) Fitplot for absorbance at 294 nm. The data was fitted to a 2:1 binding model.

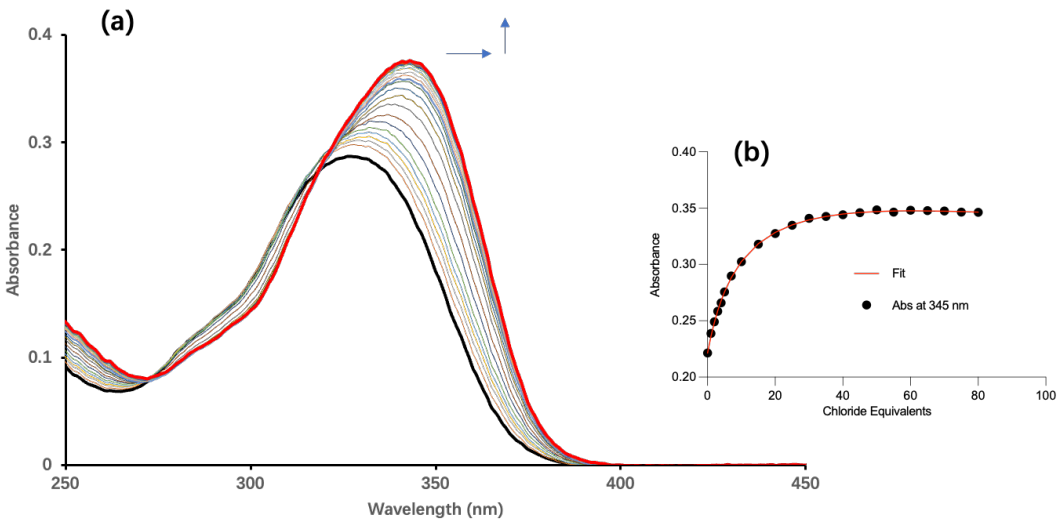

Figure SA23. (a) Absorption spectra of Cl^- titration of **2.2** in MeCN. (b) Fitplot for absorbance at 345 nm. The data was fitted to a 2:1 binding model.

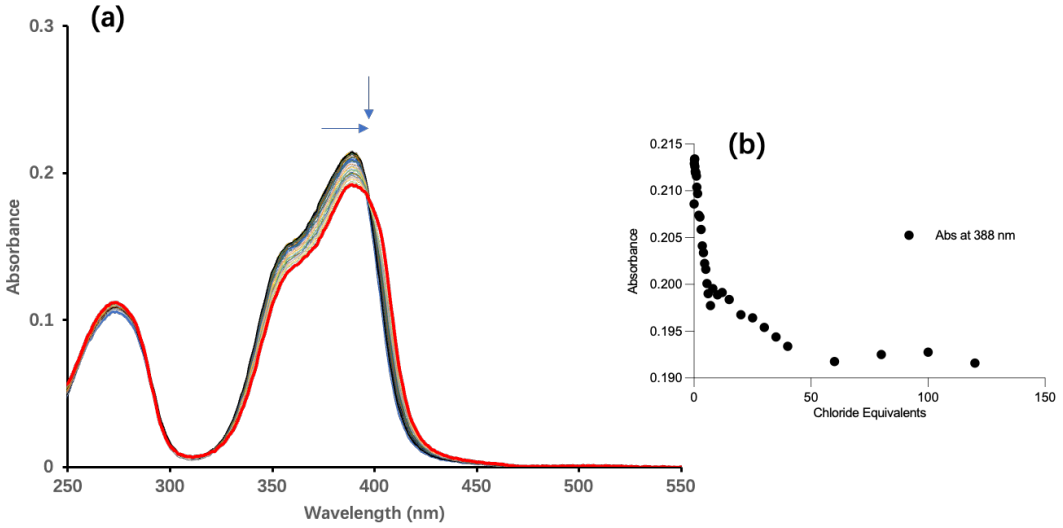

Figure SA24. (a) Absorption spectra of Cl^- titration of **2.3** in MeCN. (b) Fitplot for absorbance at 388 nm. The data was fitted to a 2:1 binding model.

* The large error is likely due to the self-assembly of **2.3** in solution as supported by single crystal X-ray diffraction and ^{1}H NMR variable concentration experiments.

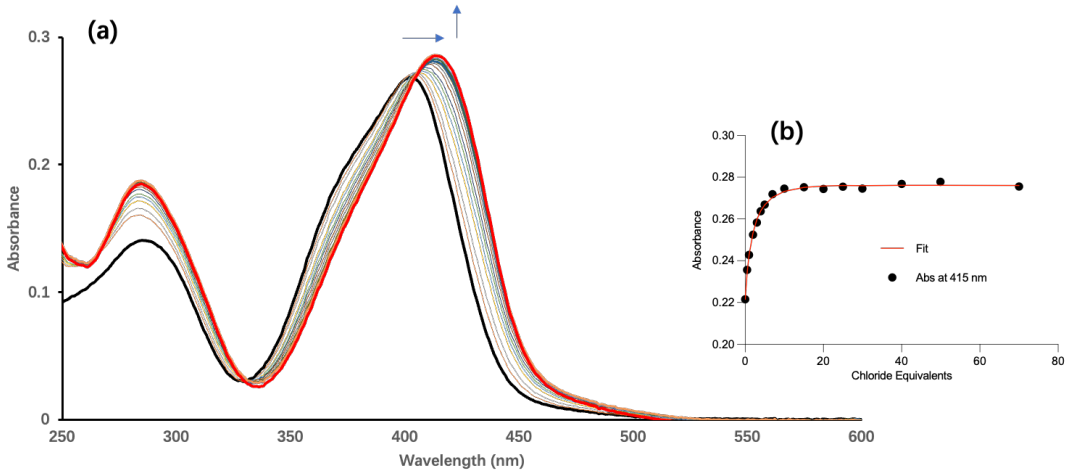

Figure SA25. (a) Absorption spectra of Cl^- titration of **2.4** in MeCN. (b) Fitplot for absorbance at 415 nm. The data was fitted to a 2:1 binding model.

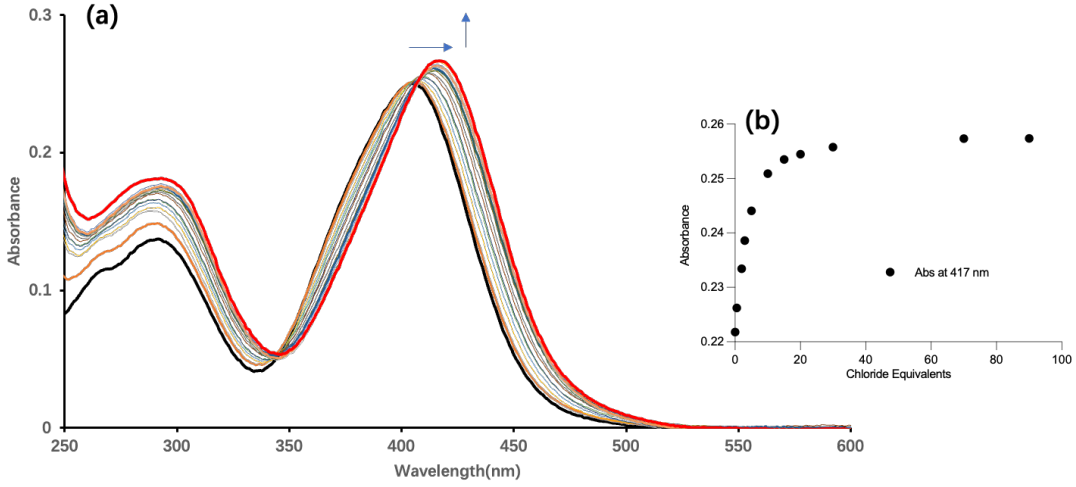

Figure SA26. (a) Absorption spectra of Cl^- titration of **2.5** in MeCN. (b) Fitplot for absorbance at 417 nm.

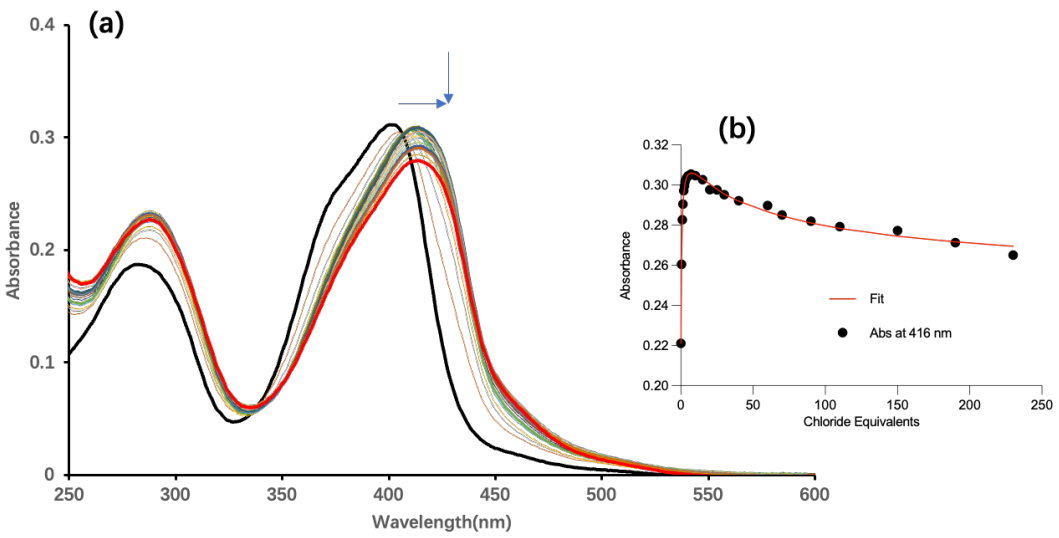

Figure SA27. (a) Absorption spectra of Cl^- titration of **2.6** in MeCN. (b) Fitplot for absorbance at 416 nm. The data was fitted to a 2:1 binding model.

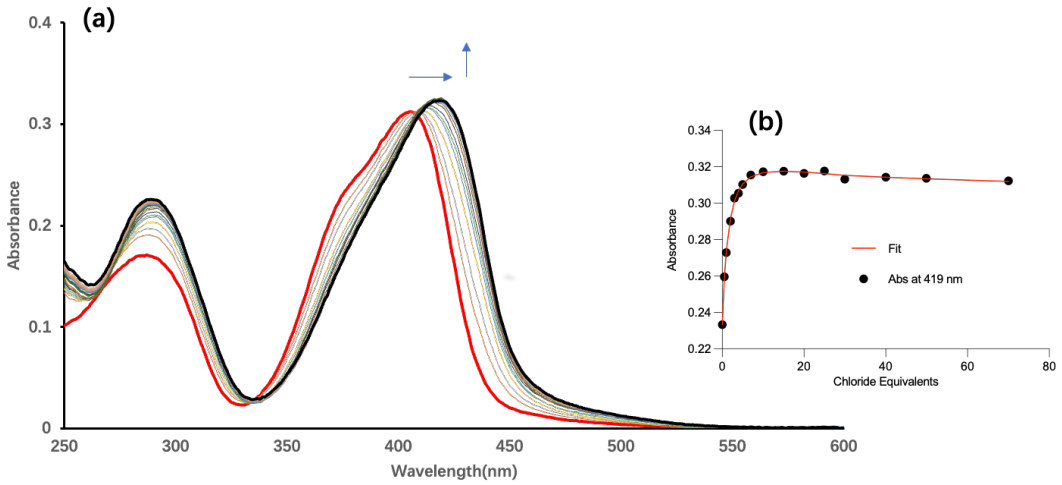

Figure SA28. (a) Absorption spectra of Cl^- titration of **2.7** in MeCN. (b) Fitplot for absorbance at 419 nm. The data was fitted to a 2:1 binding model.

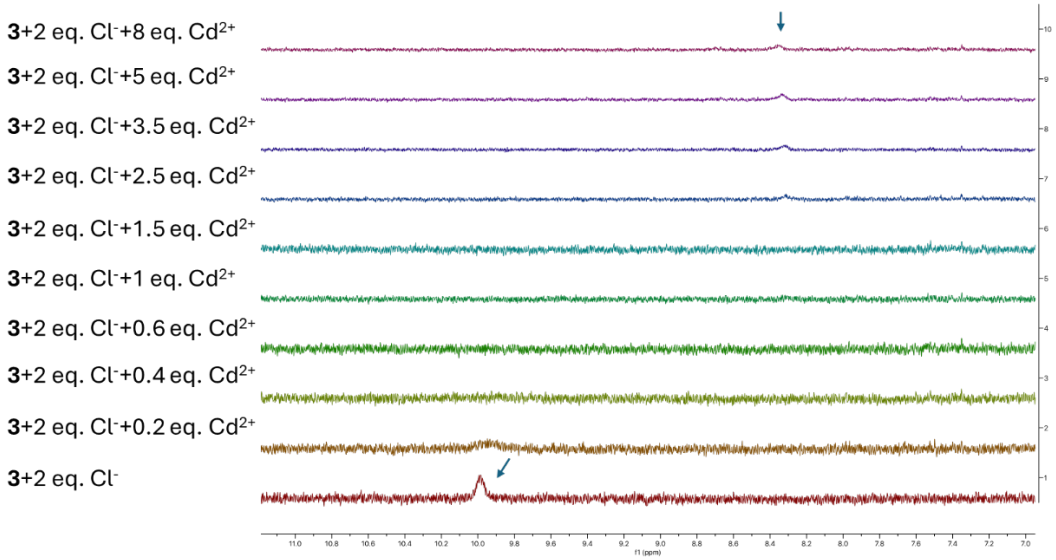

Figure SA29. Cd^{2+} titration of **2.3** in CD_3CN containing 2 eq. chloride.

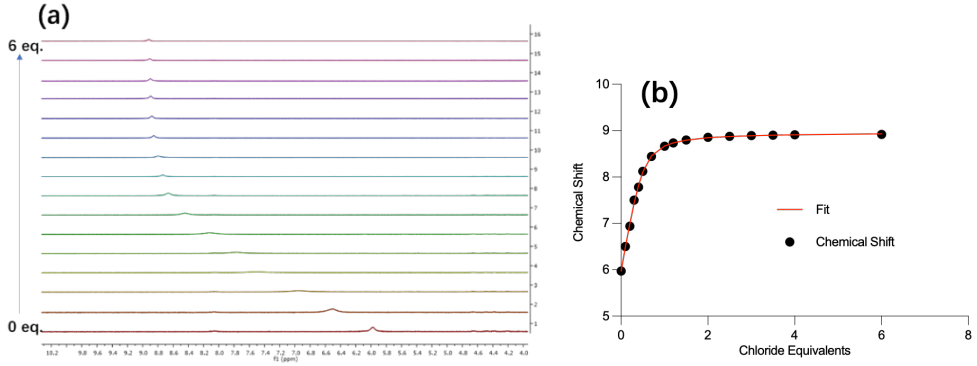

Figure SA30. (a) ^1H NMR stackplot of **2.1** with TBACl in CD_3CN. (b) Fitplot for NH proton at δ = 5.97 ppm. The data was fitted to a 2:1 binding model, giving a K_{11} value of 3.5×10^2 M^{-1} (7.7% error) and a K_{21} value of 9.4×10^2 M^{-1} (9.1% error)

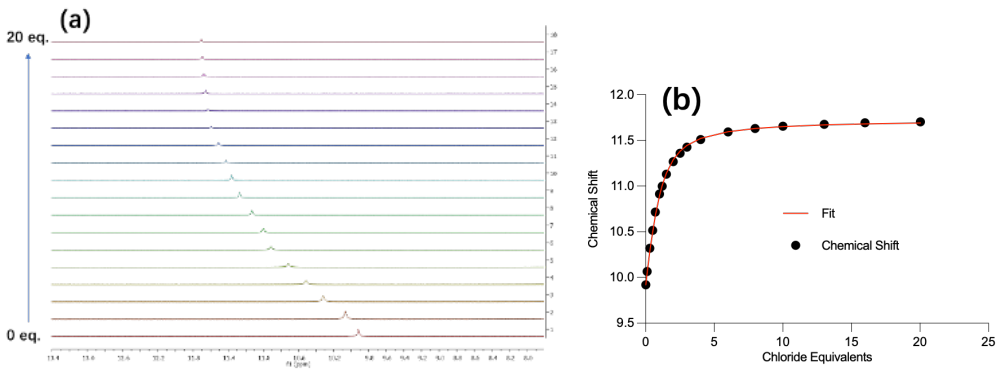

Figure SA31. (a) ^{1}H NMR stackplot of **2.2** with TBACl in DMSO-d_6. (b) Fitplot for NH proton at δ = 9.92 ppm. The data was fitted to a 1:1 binding model and gave a K_a value of 5.0 × 10^2 M^{-1} (5.0% error)

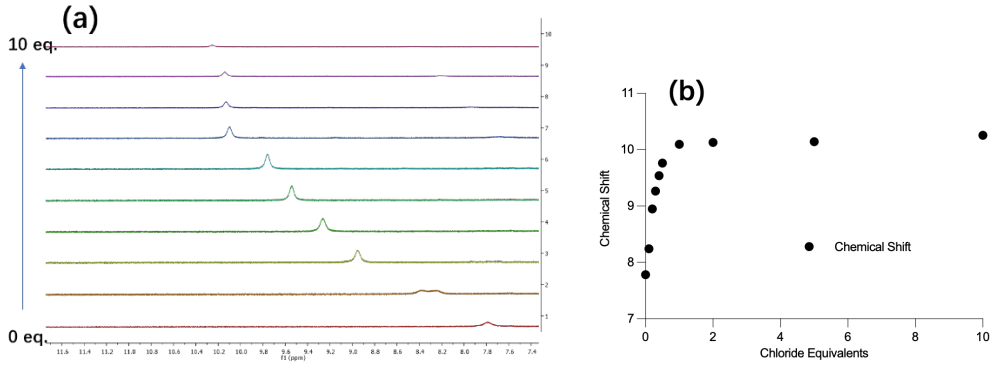

Figure SA32. (a) ^{1}H NMR stackplot of **2.3** with TBACl in CD_3CN. (b) Plot for NH proton at δ = 7.79 ppm. Complex binding behaviour prevents fitting, the large error is likely due to the self-assembly of **2.3** in solution as supported by single crystal X-ray diffraction.

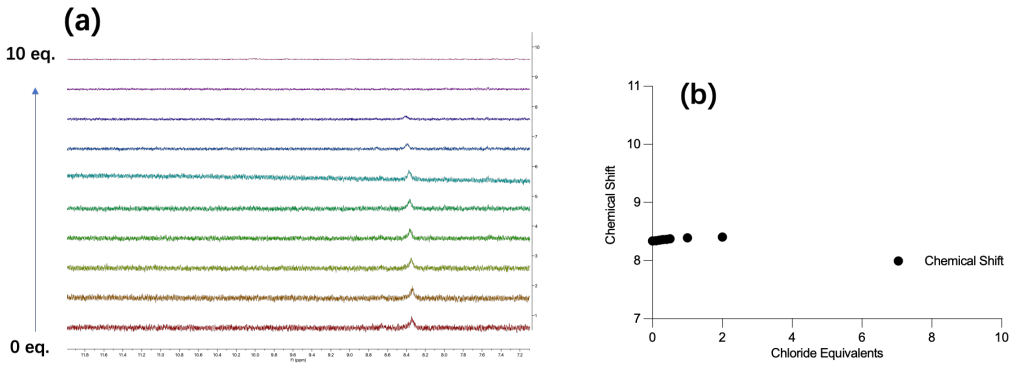

Figure SA33. (a) ^{1}H NMR stackplot: Cl^- titration of **2.3** in CD_3CN containing 8 eq. Cd^{2+}. (b) Plot for NH proton at δ = 8.33 ppm.

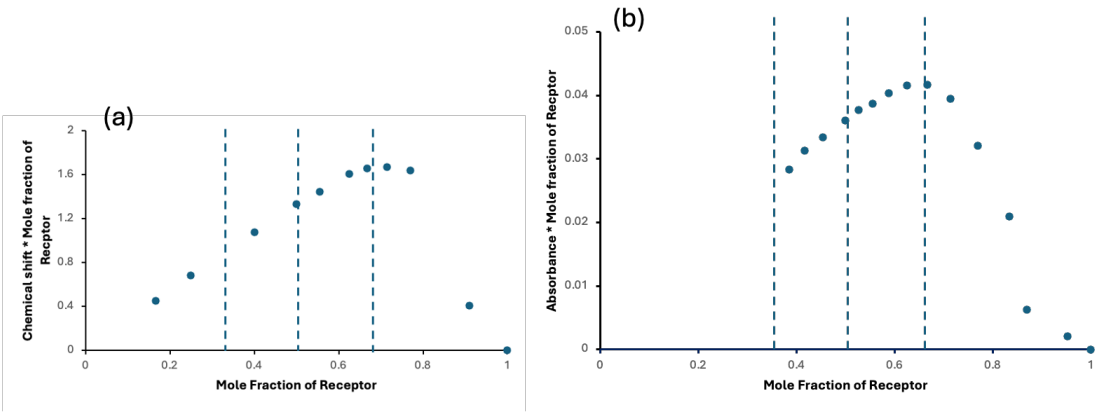

Figure SA34. (a) ^{1}H NMR Job's Plot of **2.4** with TBACl in CD_3CN/DMSO-d_6 (49:1) evaluated by the chemical shift changes of the squaramide NH protons. (b) UV/Vis Job's Plot of **2.3** with Zn^{2+} evaluated by changes in the absorption spectrum.

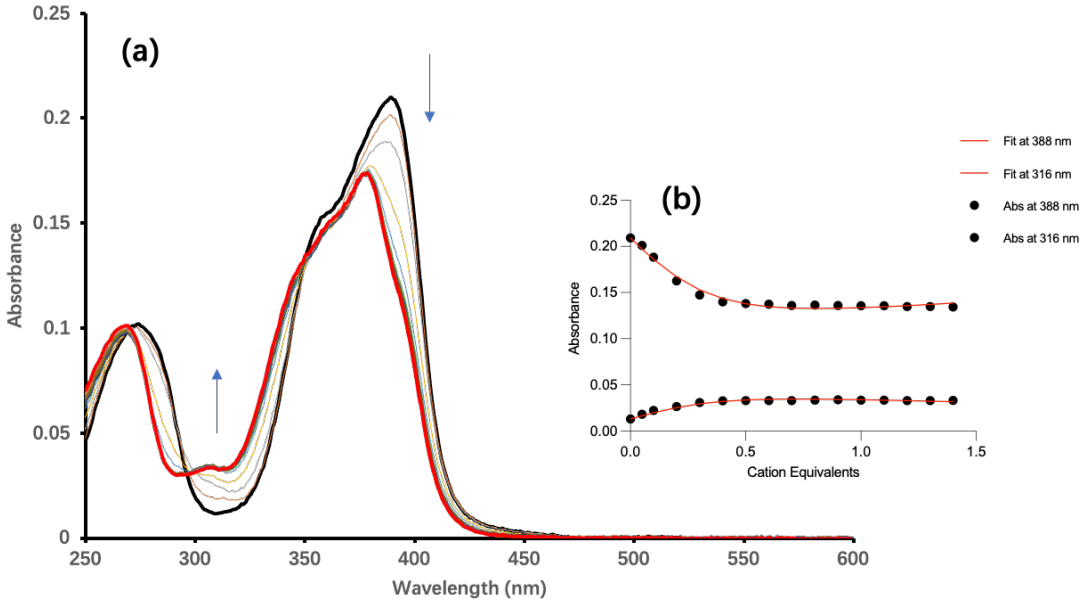

Figure SA35. (a) Absorption spectra of Cd^{2+} titration of **2.3** in MeCN. (b) Fitplot for absorbance at 388 and 316 nm. The data was fitted to a 2.1 binding model.

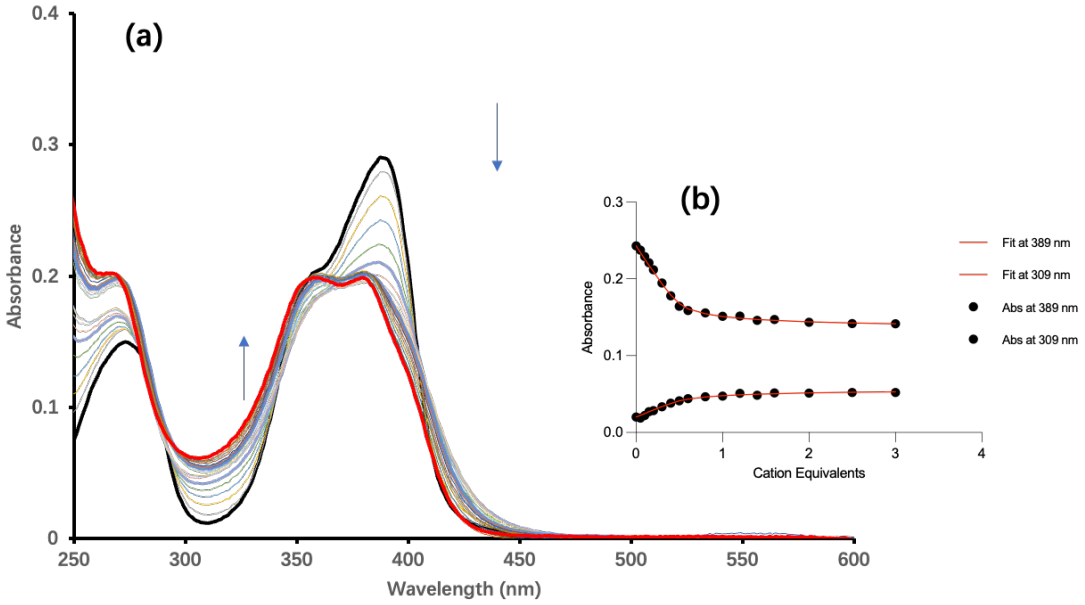

Figure SA36. (a) Absorption spectra of Pb^{2+} titration of **2.3** in MeCN. (b) Fitplot for absorbance at 388 and 309 nm. The data was fitted to a 2.1 binding model.

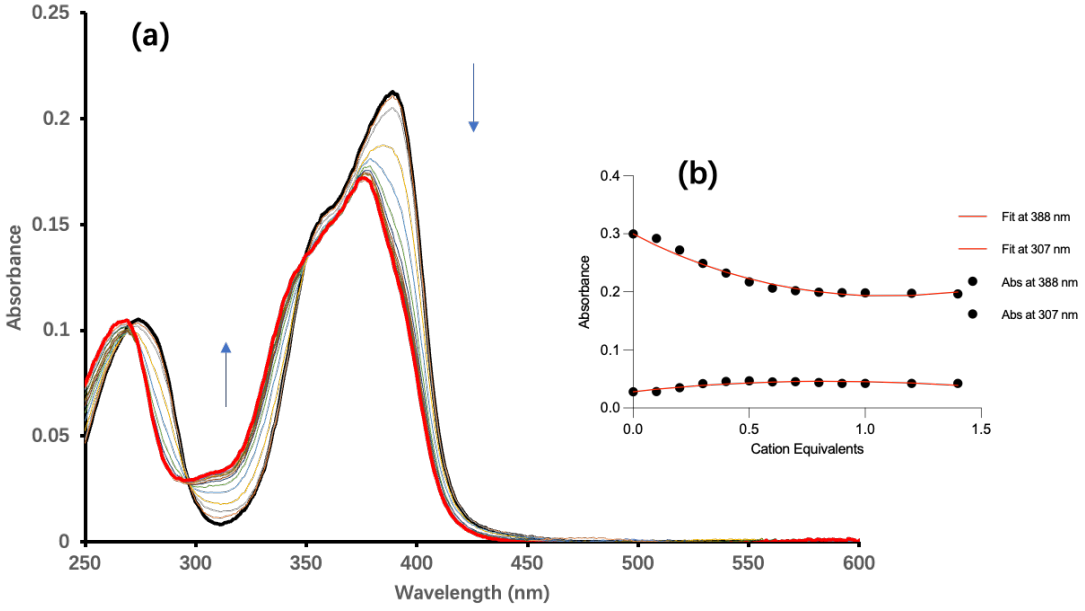

Figure SA37. (a) Absorption spectra of Zn^{2+} titration of **2.3** in MeCN. (b) Fitplot for absorbance at 388 and 307 nm. The data was fitted to a 2:1 binding model.

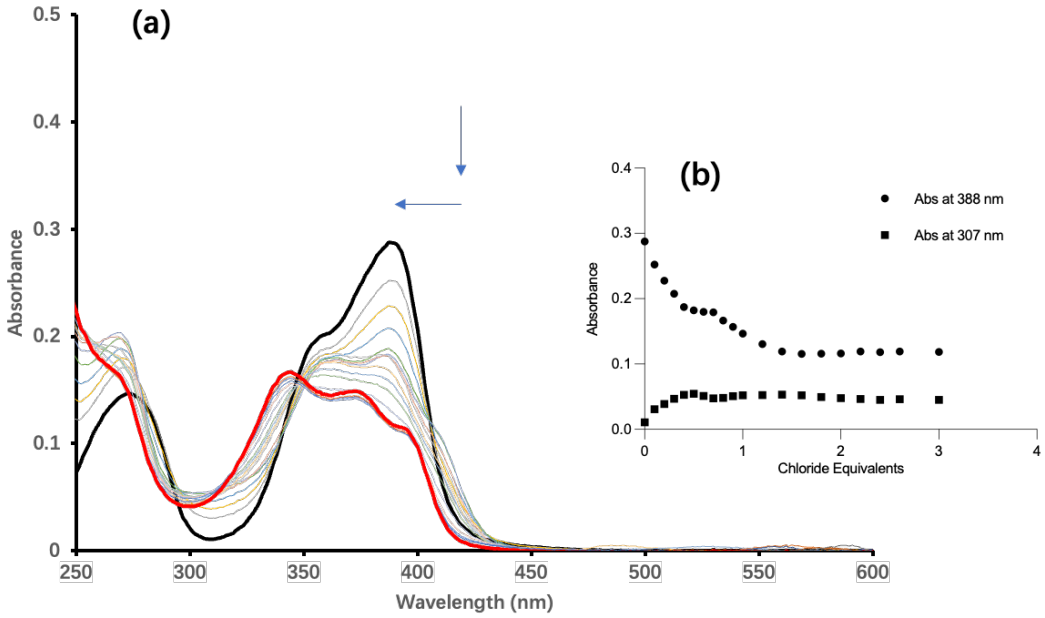

Figure SA38. (a) Absorption spectra of Hg^{2+} titration of **2.3** in MeCN. (b) Absorbance at 388 nm and 307 nm (Changes could not be fit reliably to a binding model).

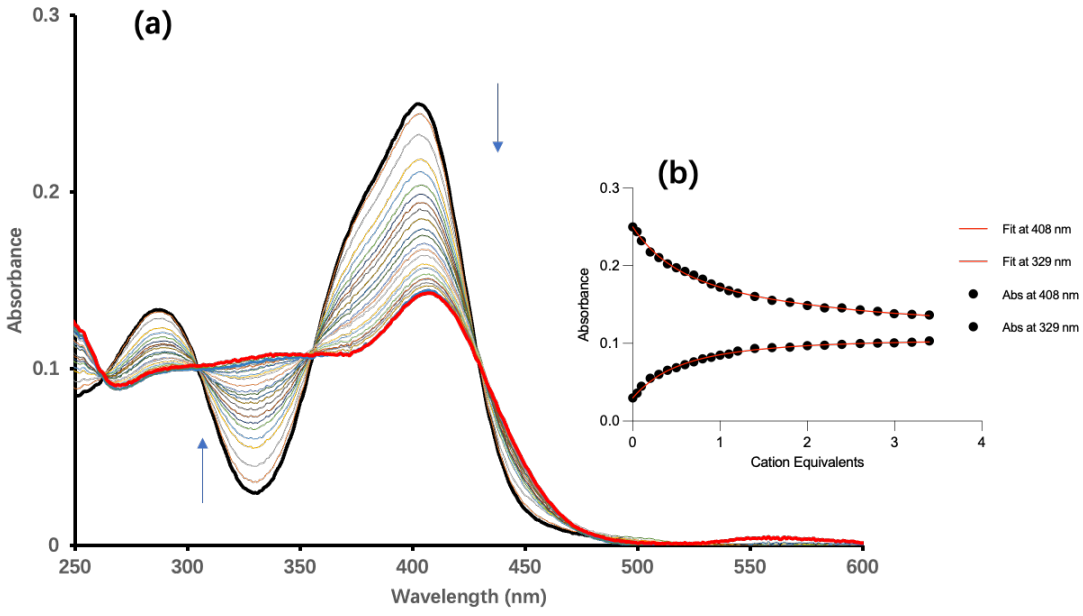

Figure SA39. (a) Absorption spectra of Zn^{2+} titration of **2.4** in MeCN. (b) Fitplot for absorbance at 408 and 329 nm. The data was fitted to a 2:1 binding model.

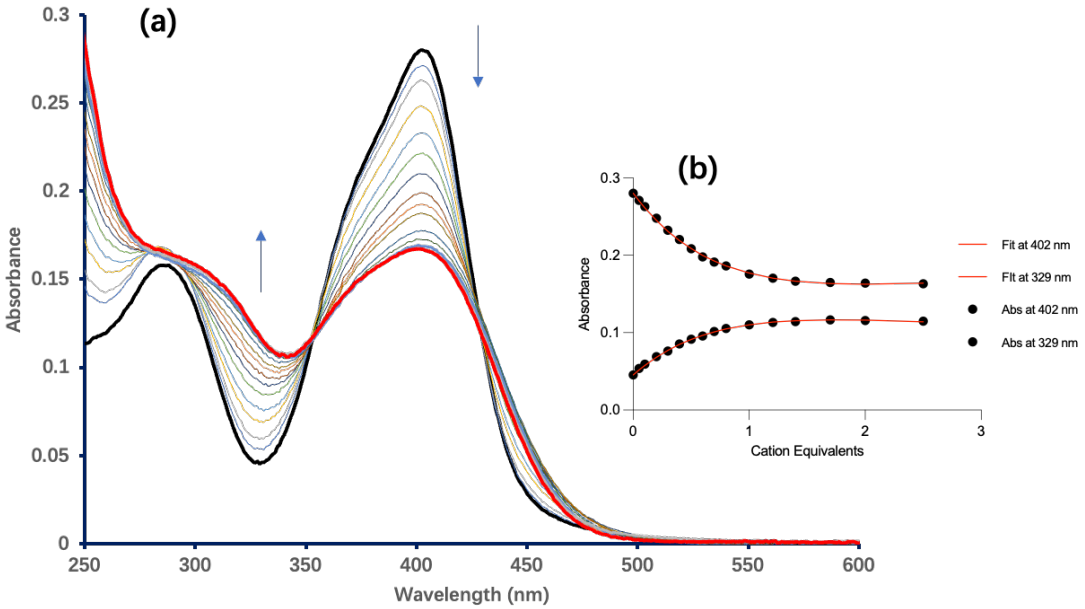

Figure SA40. (a) Absorption spectra of Pb^{2+} titration of **2.4** in MeCN. (b) Fitplot for absorbance at 402 and 329 nm. The data was fitted to a 2:1 binding model.

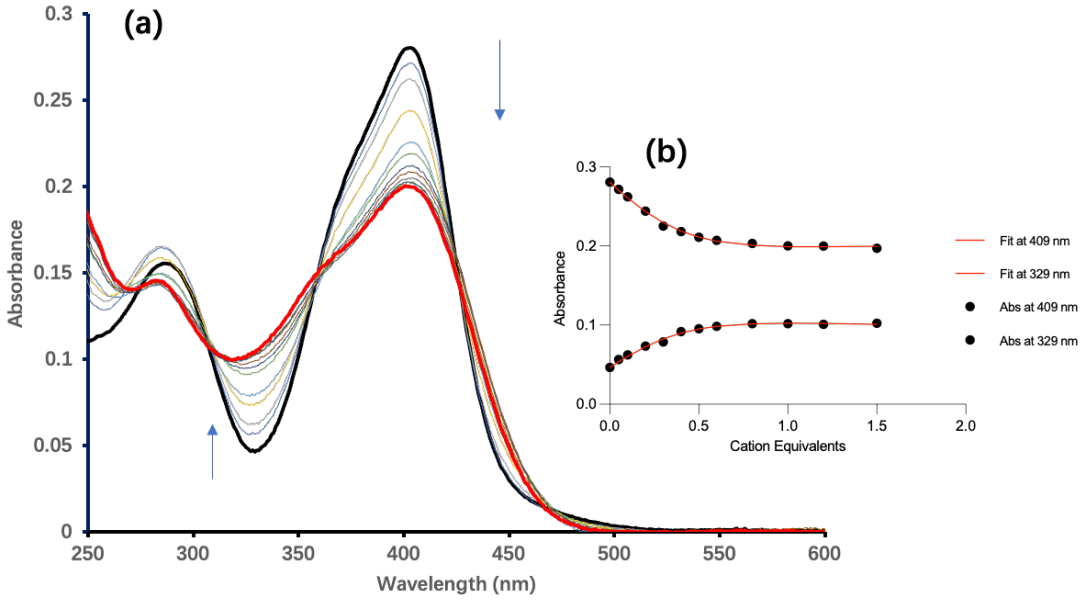

Figure SA41. (a) Absorption spectra of Cd^{2+} titration of **2.4** in MeCN. (b) Fitplot for absorbance at 409 and 329 nm. The data was fitted to a 2:1 binding model.

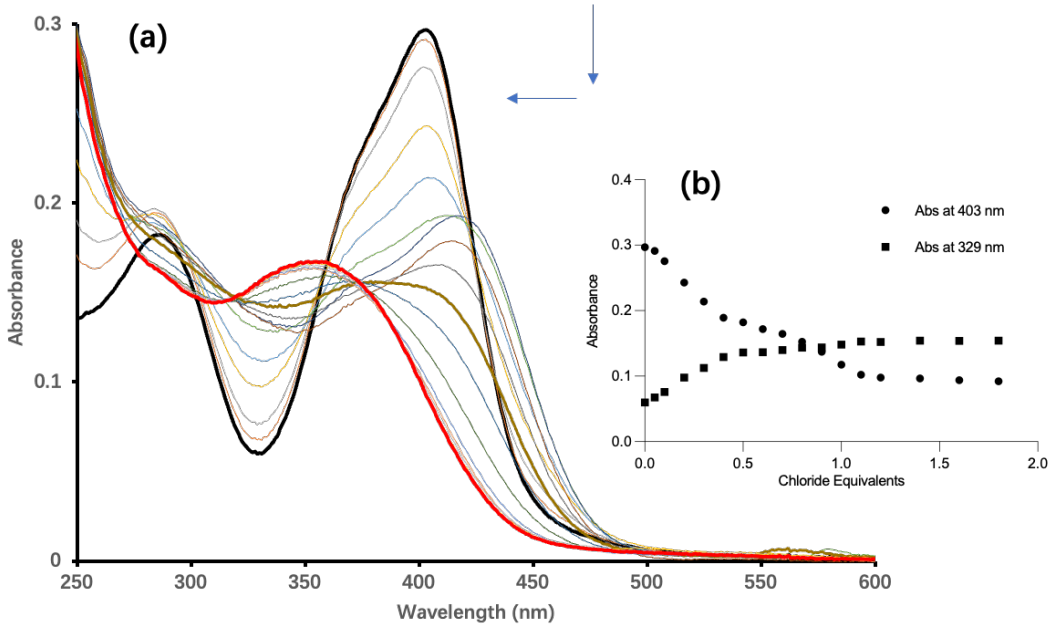

Figure SA42. (a) Absorption spectra of Hg^{2+} titration of **2.4** in MeCN. (b) Absorbance at 403 nm and 329 nm. (Changes could not be fit reliably to a binding model).

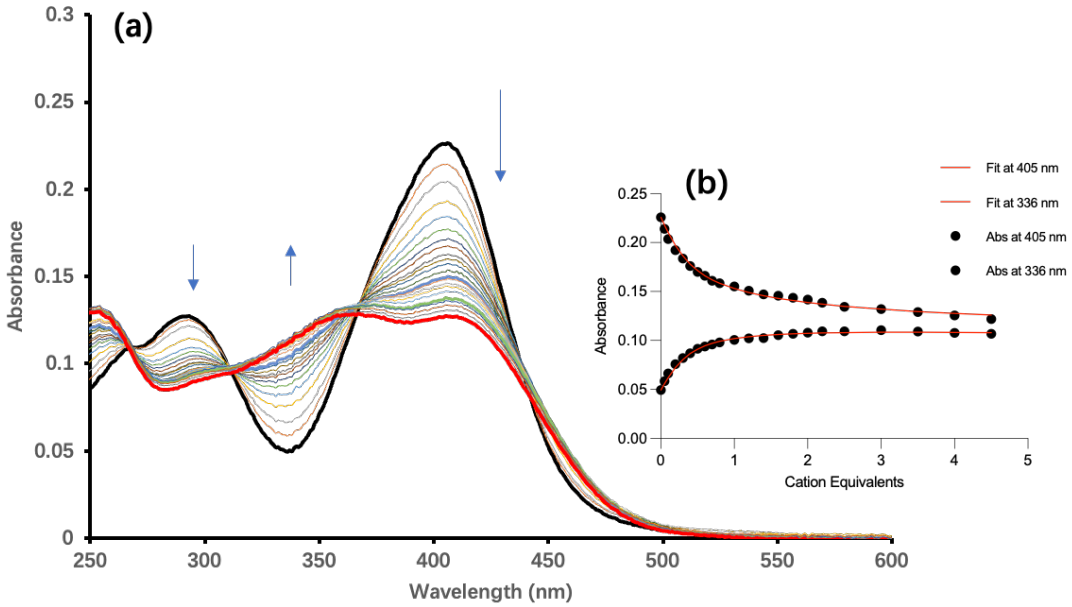

Figure SA43. (a) Absorption spectra of Zn^{2+} titration of **2.5** in MeCN. (b) Fitplot for absorbance at 405 and 336 nm. The data was fitted to a 2:1 binding model.

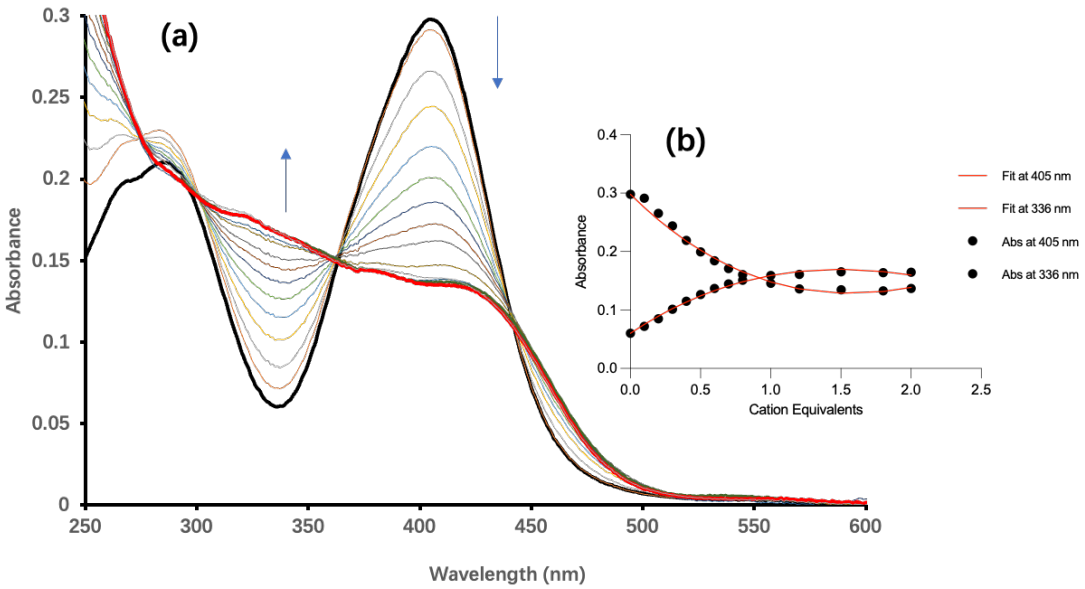

Figure SA44. (a) Absorption spectra of Pb^{2+} titration of **2.5** in MeCN. (b) Fitplot for absorbance at 405 and 336 nm. The data was fitted to a 2:1 binding model.

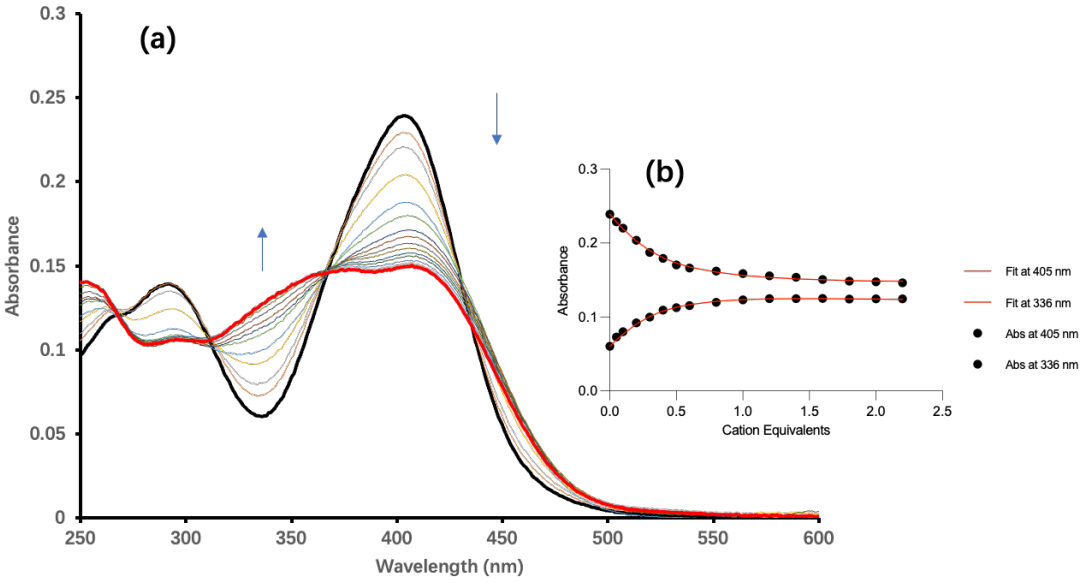

Figure SA45. (a) Absorption spectra of Cd^{2+} titration of **2.5** in MeCN. (b) Fitplot for absorbance at 405 and 336 nm. The data was fitted to a 2:1 binding model.

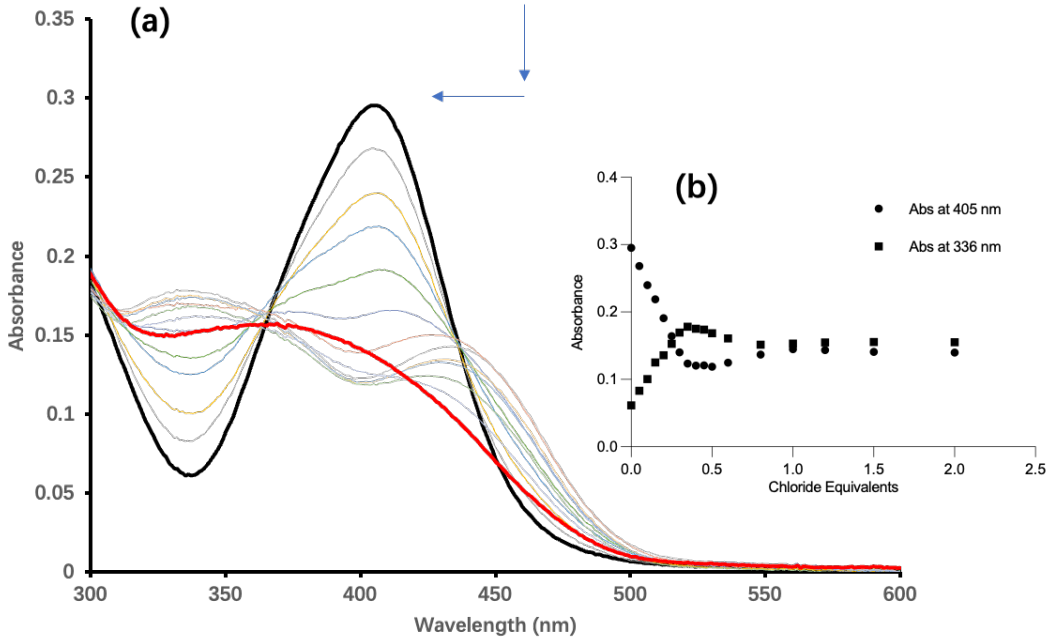

Figure SA46. (a) Absorption spectra of Hg^{2+} titration of **2.5** in MeCN. (b) Absorbance at 405 nm and 336 nm. (Changes could not be fit reliably to a binding model).

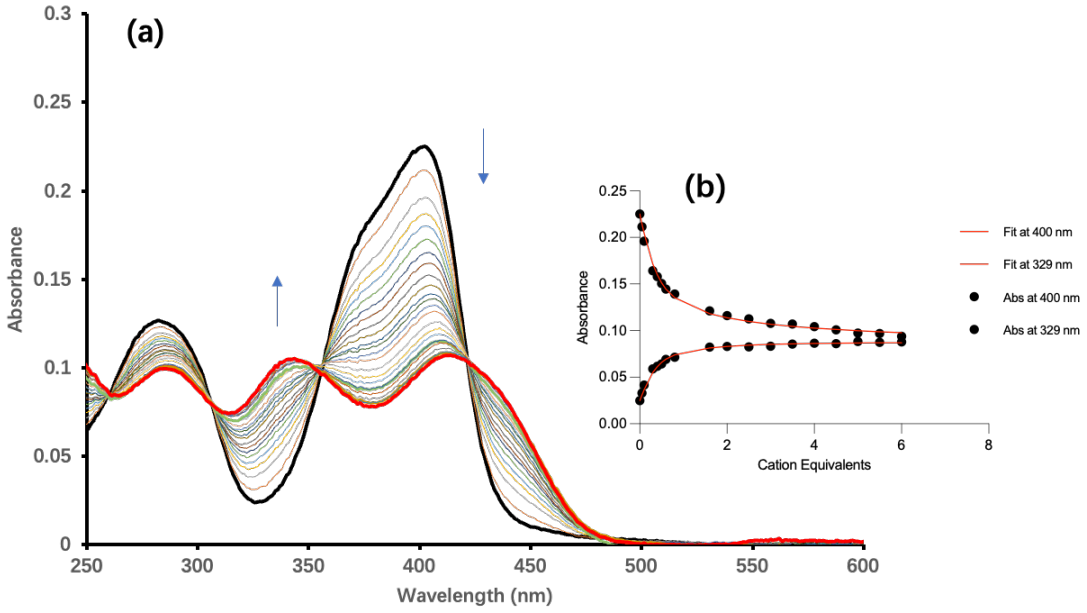

Figure SA47. (a) Absorption spectra of Zn^{2+} titration of **2.6** in MeCN. (b) Fitplot for absorbance at 400 and 329 nm. The data was fitted to a 2:1 binding model.

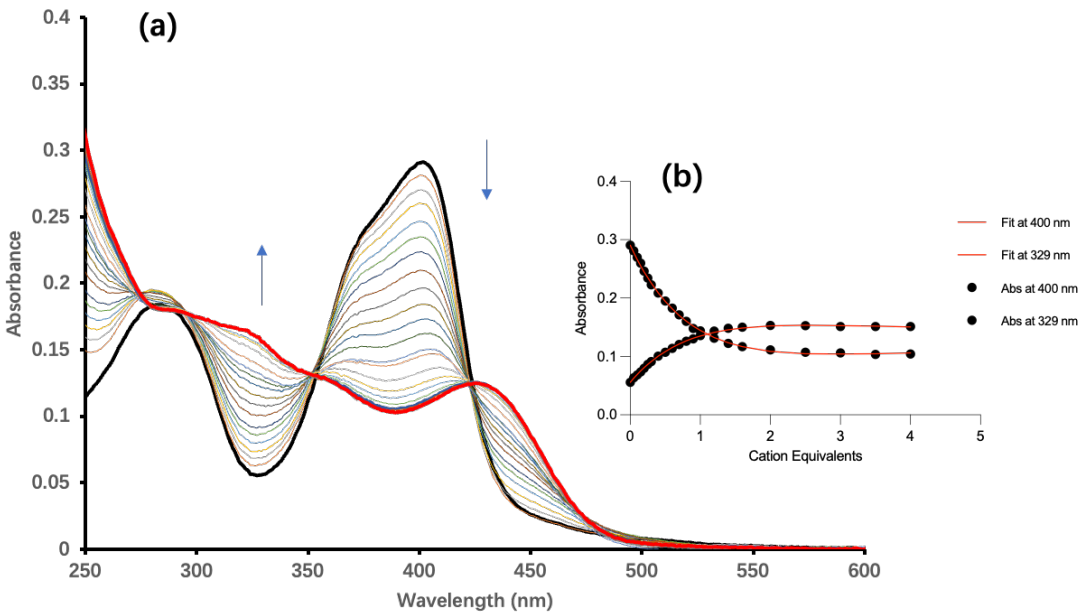

Figure SA48. (a) Absorption spectra of Pb^{2+} titration of **2.6** in MeCN. (b) Fitplot for absorbance at 400 and 329 nm. The data was fitted to a 2:1 binding model.

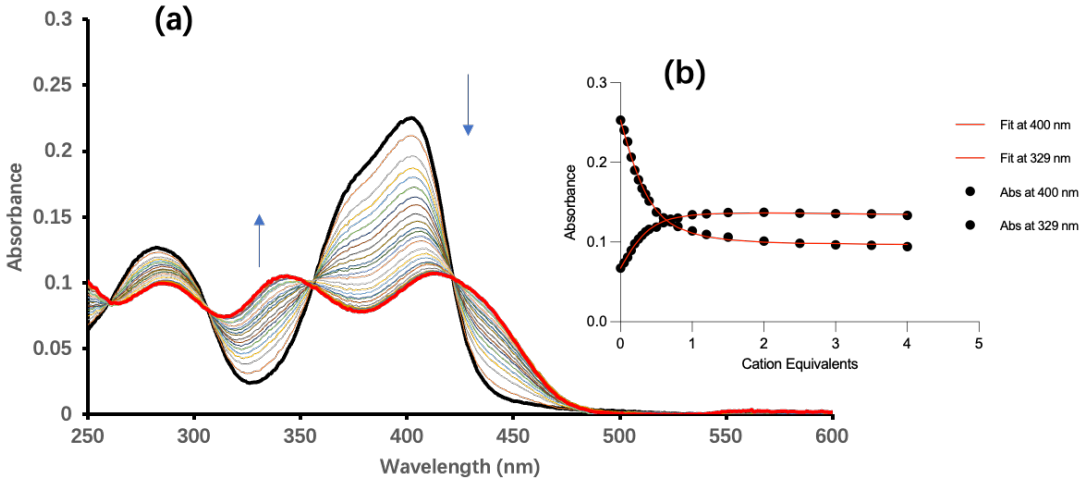

Figure SA49. (a) Absorption spectra of Cd^{2+} titration of **2.6** in MeCN. (b) Fitplot for absorbance at 400 and 329 nm. The data was fitted to a 2:1 binding model.

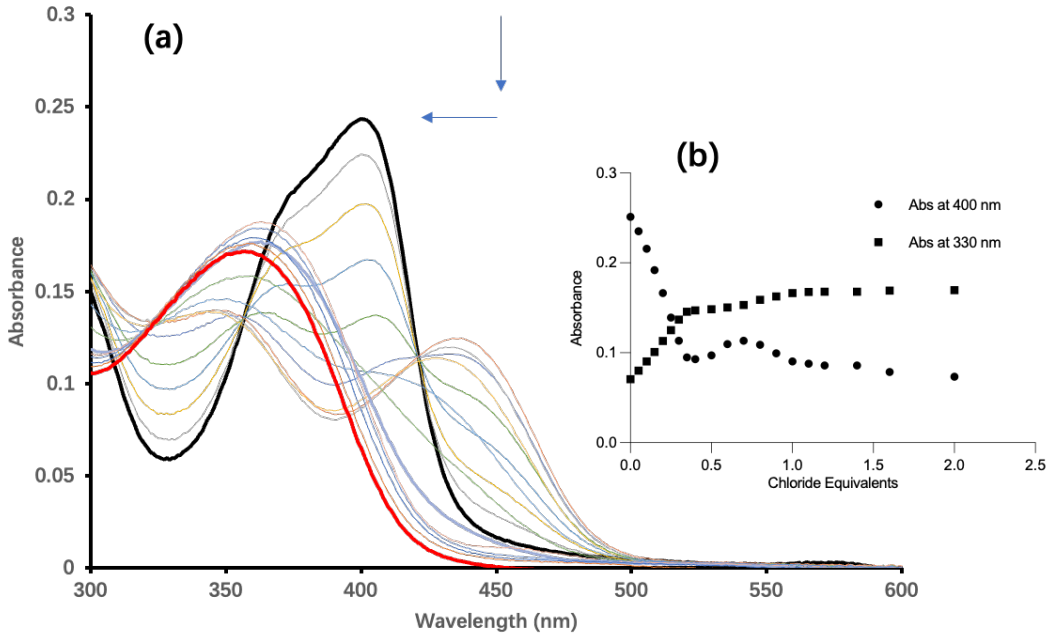

Figure SA50. (a) Absorption spectra of Hg^{2+} titration of **2.6** in MeCN. (b) Absorbance at 400 nm and 330 nm (Changes could not be fit reliably to a binding model).

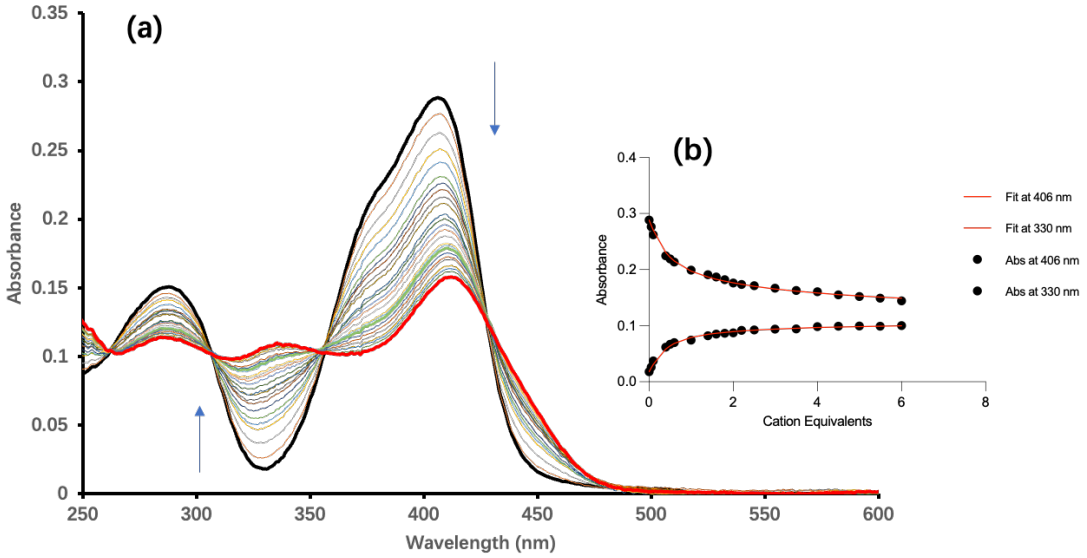

Figure SA51. (a) Absorption spectra of Zn^{2+} titration of **2.7** in MeCN. (b) Fitplot for absorbance at 406 and 330 nm. The data was fitted to a 2:1 binding model.

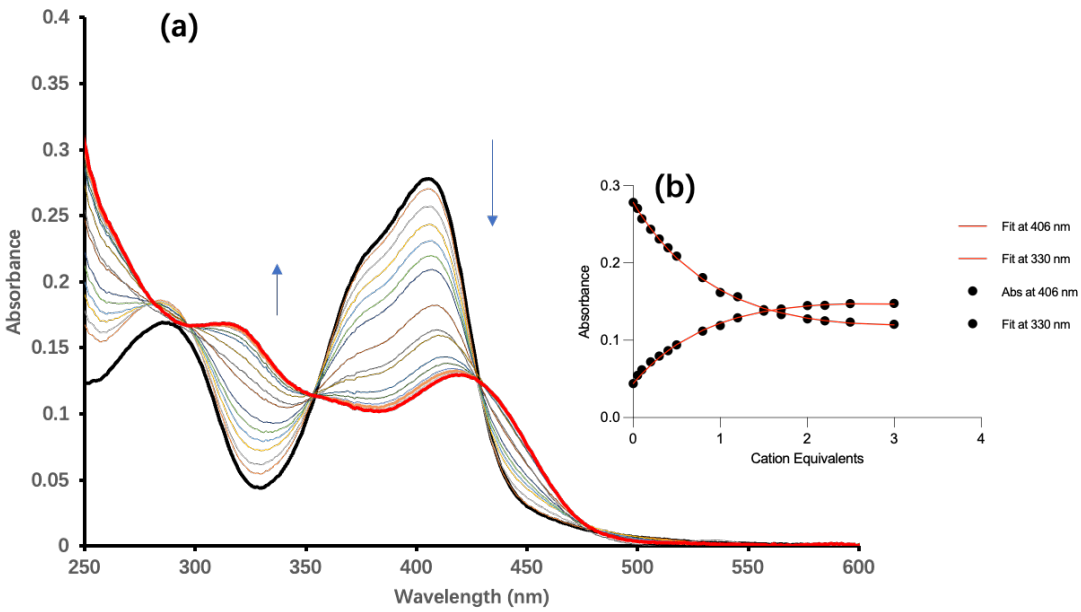

Figure SA52. (a) Absorption spectra of Pb^{2+} titration of **2.7** in MeCN. (b) Fitplot for absorbance at 406 and 330 nm. The data was fitted to a 2:1 binding model.

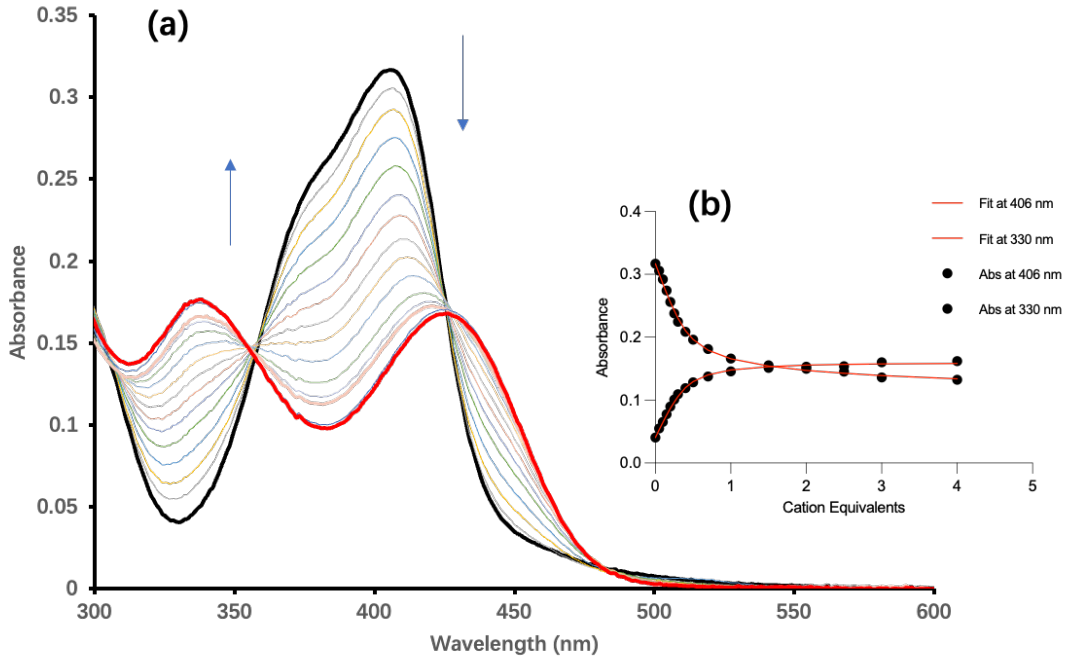

Figure SA53. (a) Absorption spectra of Cd^{2+} titration of **2.7** in MeCN. (b) Fitplot for absorbance at 406 and 330 nm. The data was fitted to a 2:1 binding model.

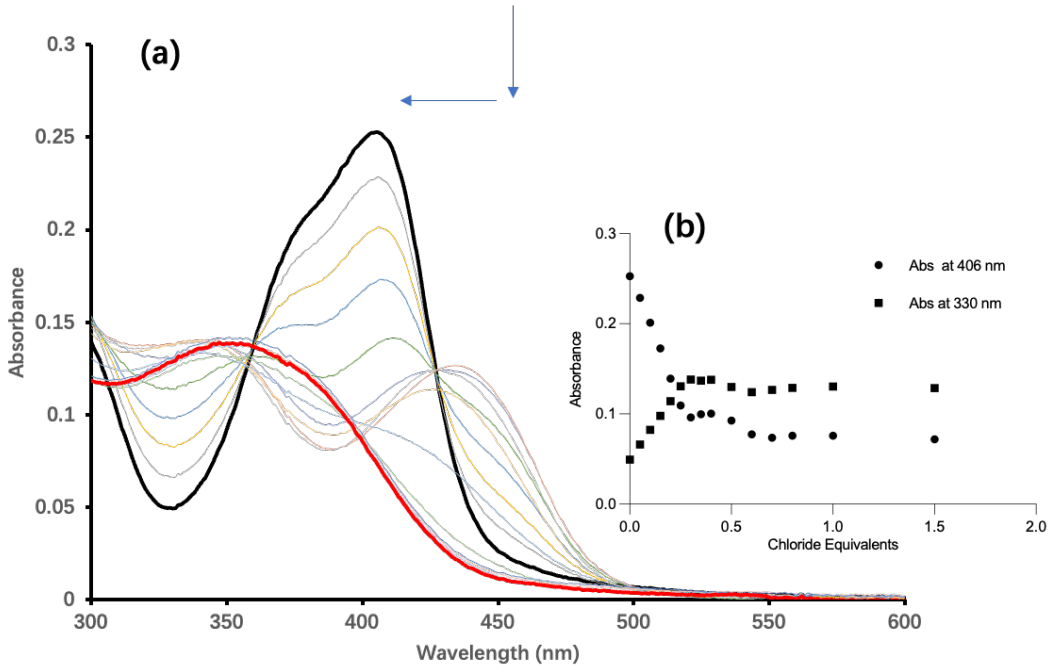

Figure SA54. (a) Absorption spectra of Hg^{2+} titration of **2.7** in MeCN. (b) Absorbance at 406 nm and 330 nm (Changes could not be fit reliably to a binding model).

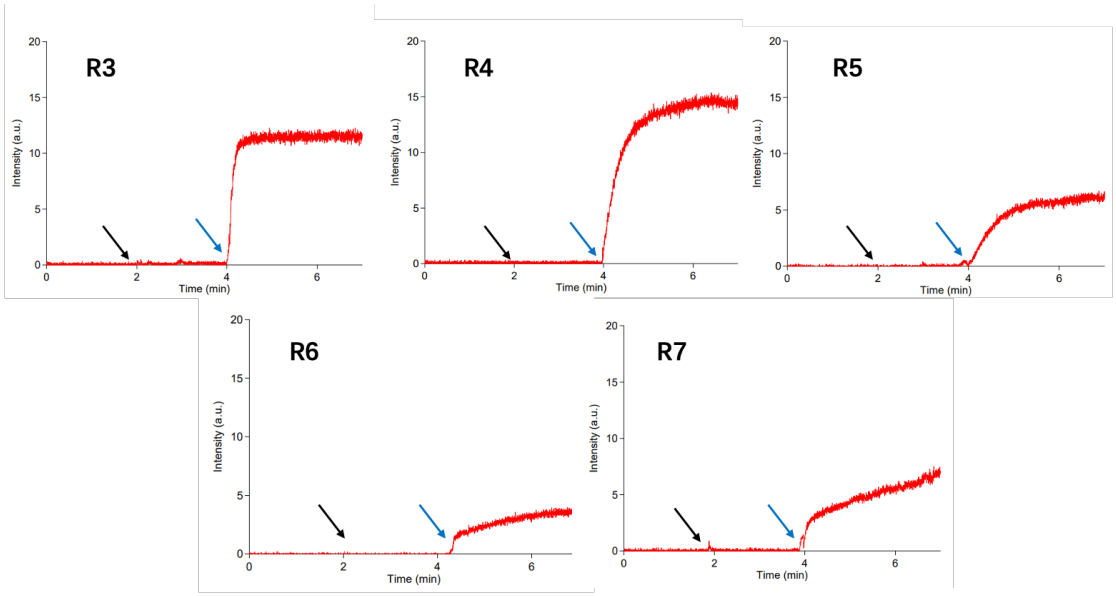

Figure SA55. FluoZin-3 assay control experiment: The fluorescence intensity of liposomes containing FluoZin-3 in PBS (0.4 mM in 0.01 M PBS, pH=7.4) after the addition of the receptor (0.01 mol%, black arrow) followed by the addition of Zn^{2+}(0.1 mM, blue arrow)

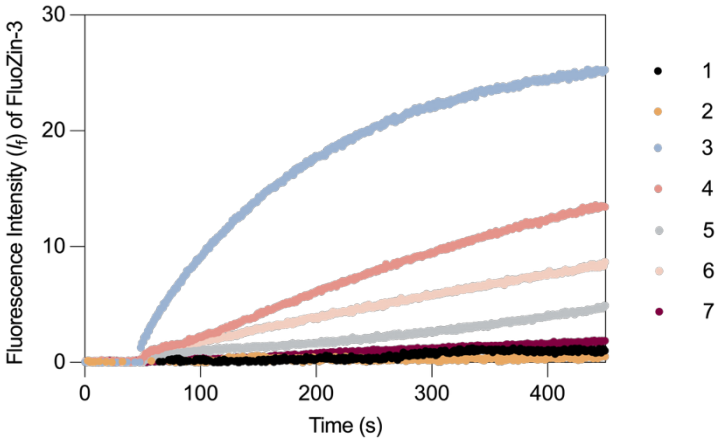

Figure SA56. Fluorescence intensity of liposomes containing FluoZin-3 in PBS (0.4 mM in 0.01 M PBS, pH=7.4) after the addition of Zn^{2+}(0.1 mM) followed by **2.1**-**2.7** (0.01 mol%).

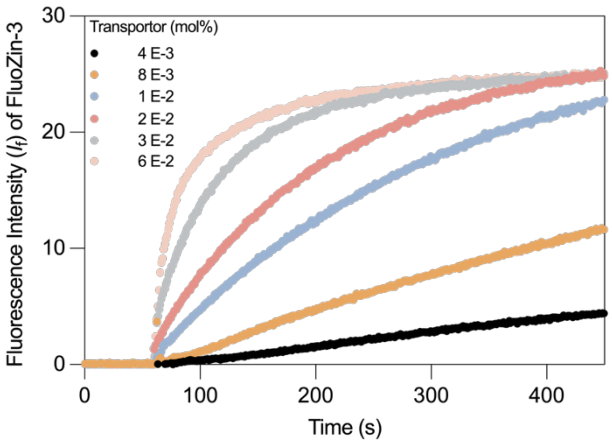

Figure SA57. Fluorescence intensity of liposomes containing FluoZin-3 in PBS (0.4 mM in 0.01 M PBS, pH=7.4) before and after adding Zn^{2+}(0.1 mM) and **2.3** at different concentrations.

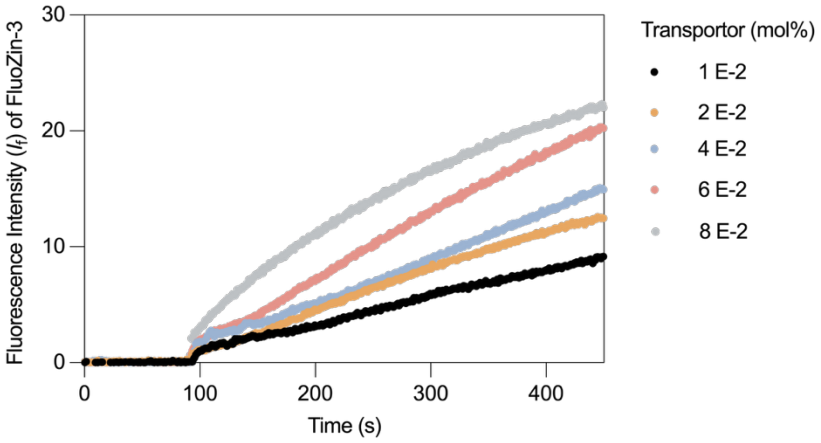

Figure SA58. Fluorescence intensity of liposomes containing FluoZin-3 in PBS (0.4 mM in 0.01 M PBS, pH=7.4) before and after adding Zn^{2+}(0.1 mM) and **2.4** at different concentrations.

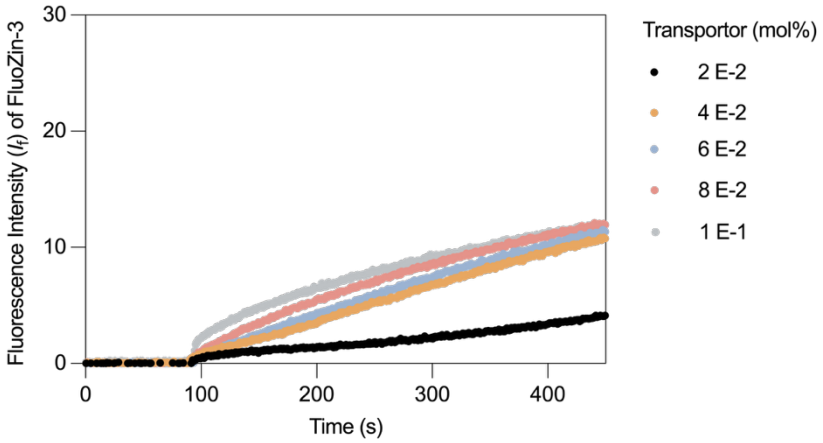

Figure SA59. Fluorescence intensity of liposomes containing FluoZin-3 in PBS (0.4 mM in 0.01 M PBS, pH=7.4) before and after adding Zn^{2+}(0.1 mM) and **2.5** at different concentrations.

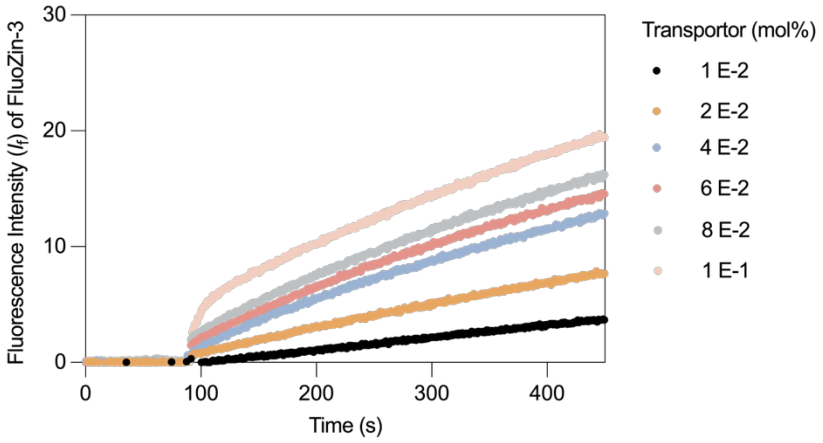

Figure SA60. Fluorescence intensity of liposomes containing FluoZin-3 in PBS (0.4 mM in 0.01 M PBS, pH=7.4) before and after adding Zn^{2+}(0.1 mM) and **2.6** at different concentrations.

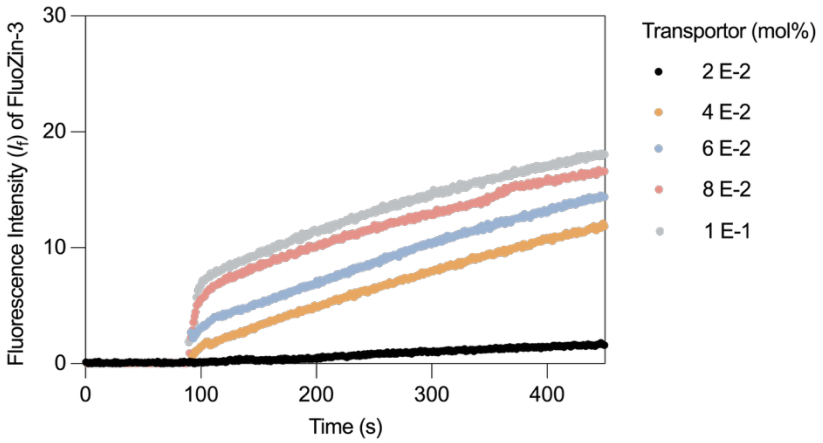

Figure SA61. Fluorescence intensity of liposomes containing FluoZin-3 in PBS (0.4 mM in 0.01 M PBS, pH=7.4) before and after adding Zn^{2+}(0.1 mM) and **2.7** at different concentrations.

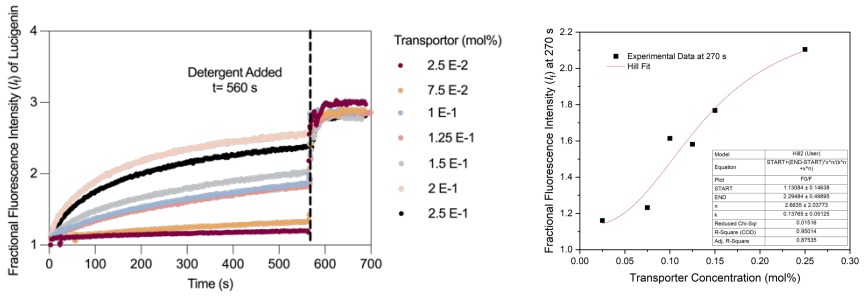

Figure SA62. (a) The change of fractional fluorescent intensity with the addition of **2.3** and NaCl (75 µL, 1 M) to the liposomes containing lucigenin (225 mM $NaNO_3$, pH 7.2) at various transporter concentrations (mol%). (b) Hill plot of the fractional fluorescence intensity of lucigenin recorded at 270 s for each experiment carried out at various transporter concentrations.

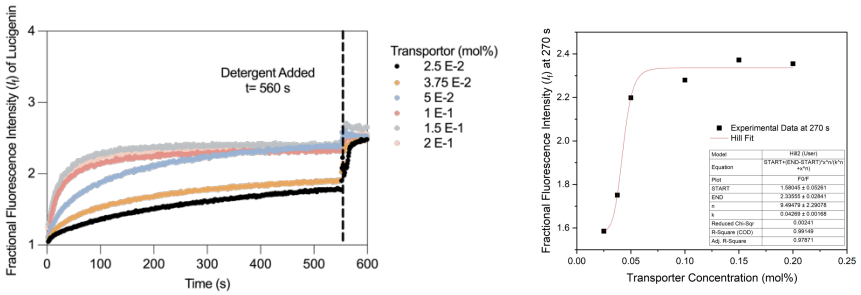

Figure SA63. (a) The change of fractional fluorescent intensity with the addition of **2.3** and $ZnCl_2$ (75 µL, 0.5 M) to the liposomes containing lucigenin (225 mM $NaNO_3$, pH 7.2) at various transporter concentrations (mol%). (b) Hill plot of the fractional fluorescence intensity of lucigenin recorded at 270 s for each experiment carried out at various transporter concentrations.

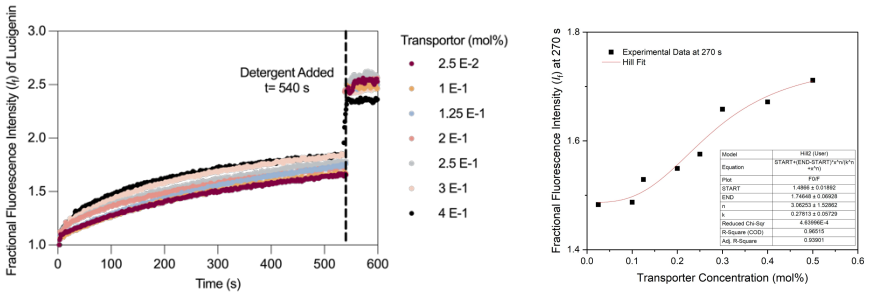

Figure SA64. (a) The change of fractional fluorescent intensity with the addition of **2.3** and $CuCl_2$ (75 µL, 0.5 M) to the liposomes containing lucigenin (112.5 mM $Cu(NO_3)_2$) at various transporter concentrations (mol%). (b) Hill plot of the fractional fluorescence intensity of lucigenin recorded at 270 s for each experiment carried out at various transporter concentrations.

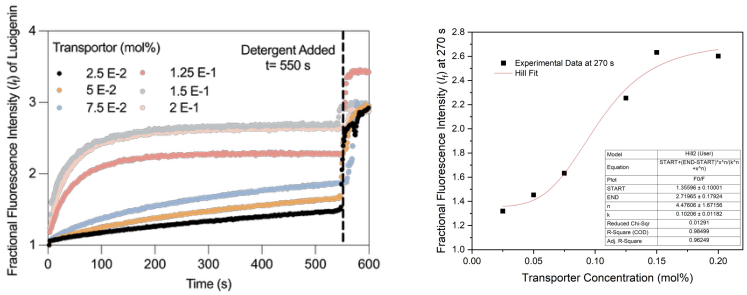

Figure SA65. (a) The change of fractional fluorescent intensity with the addition of **2.3** and $ZnCl_2$ (75 µL, 0.5 M) to the liposomes containing lucigenin (112.5 mM $Zn(NO_3)_2$) at various transporter concentrations (mol%). (b) Hill plot of the fractional fluorescence intensity of lucigenin recorded at 270 s for each experiment carried out at various transporter concentrations.

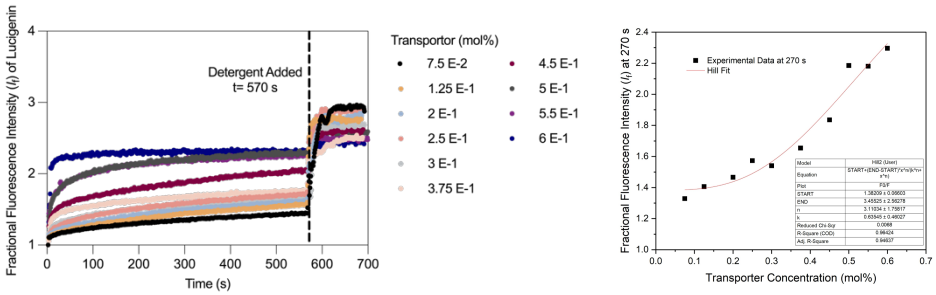

Figure SA66. (a) The change of fractional fluorescent intensity with the addition of **2.3** and $NiCl_2$ (75 µL, 0.5 M) to the liposomes containing lucigenin (112.5 mM $Ni(NO_3)_2$) at various transporter concentrations (mol%). (b) Hill plot of the fractional fluorescence intensity of lucigenin recorded at 270 s for each experiment carried out at various transporter concentrations.

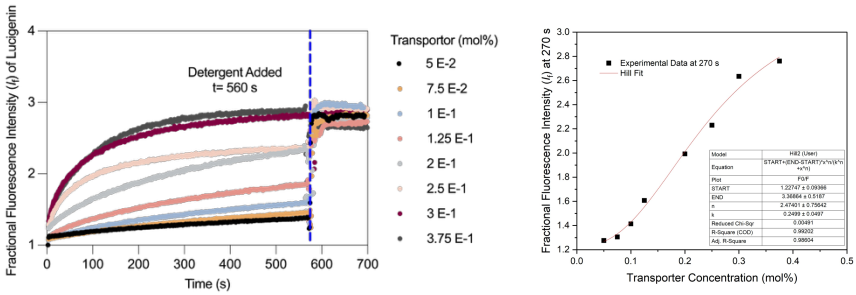

Figure SA67. (a) The change of fractional fluorescent intensity with the addition of **2.3** and KCl (75 µL, 1 M) to the liposomes containing lucigenin (225 mM KNO_3) at various transporter concentrations (mol%). (b) Hill plot of the fractional fluorescence intensity of lucigenin recorded at 270 s for each experiment carried out at various transporter concentrations.

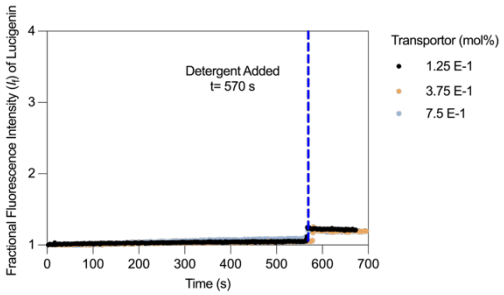

Figure SA68. The change of fractional fluorescent intensity with the addition of **2.3** and $CdCl_2$ (75 μL, 0.5 M) to the liposomes containing lucigenin (112.5 mM $Cd(NO_3)_2$) at various transporter concentrations (mol%).

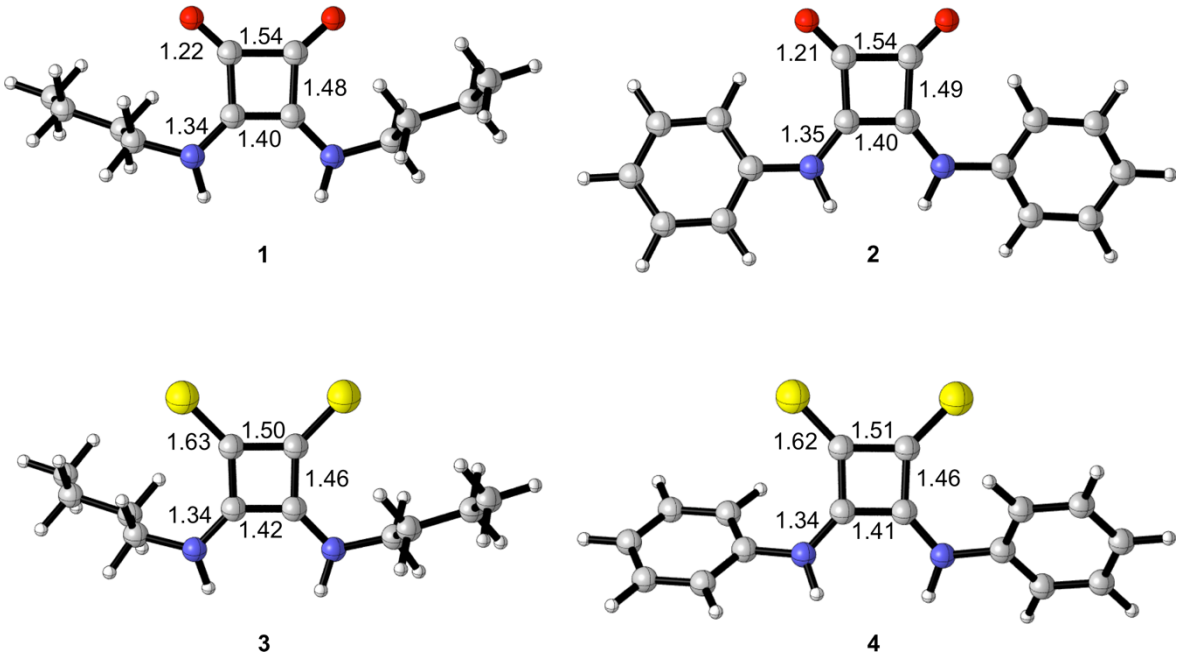

Figure SA69. Optimised geometries [RI-MP2/def2-TZVP] of receptors **2.1**-**2.4**, including key bond distances (in Å).

Table SA1. Calculated force constants and bond distances of C=X (X = O, S) bonds for receptors **2.1**-**2.4** [RI-MP2/def2-TZVP].

	***k* / mdyne Å^{-1}**	***r*(C=X) / Å**
2.1	10.74 / 10.77	1.216
2.2	10.91 / 10.92	1.211
2.3	5.54 / 5.55	1.626
2.4	5.69 / 5.68	1.619

Table SA2. Calculated excited state energies, oscillator strengths and largest coefficients of the CI expansion [SMD-CPCM(AcCN)/M06-2X/def2-QZVP].

Receptor	State	Excitation energy (λ_{max})	Oscillator strength	CI coefficient
2.1	S_7	251.5 nm	f = 0.3776	60 → 61 0.1384 60 → 62 –0.6751
	S_8	250.7 nm	f = 0.7348	60 → 61 0.6742 60 → 62 0.1384
2.2	S_5	302.6 nm	f = 1.3317	68 → 69 –0.6872
	S_{11}	284.7 nm	f = 0.2442	66 → 69 –0.1831 68 → 70 –0.6428
	S_{16}	248.9 nm	f = 0.0540	64 → 70 0.1264 65 → 69 0.1836 67 → 71 0.2585 68 → 72 –0.5632
2.3	S_7	333.2 nm	f = 0.6223	68 → 69 0.6866
	S_8	326.9 nm	f = 0.4048	68 → 70 –0.6752

	S_{12}	305.1 nm	f = 0.0240	66 → 70 67 → 69 68 → 70	–0.6094 0.3132 –0.1233
	S_{17}	228.1 nm	f = 0.3726	65 → 69 65 → 70 68 → 71	–0.2520 0.6226 0.1152
2.4	S_7	358.1 nm	f = 0.3057	74 → 78 75 → 77 76 → 78	–0.1768 0.2234 –0.6285
	S_8	354.2 nm	f = 0.9821	75 → 78 76 → 77	0.1458 –0.6725
	S_{12}	316.0 nm	f = 0.1183	74 → 78 75 → 77 76 → 78	0.5583 –0.3031 –0.2600
	S_{22}	251.7 nm	f = 0.7316	69 → 78 70 → 77 72 → 78 73 → 78 76 → 79 76 → 81	0.1328 –0.1163 –0.1581 0.5667 –0.2406 0.1105

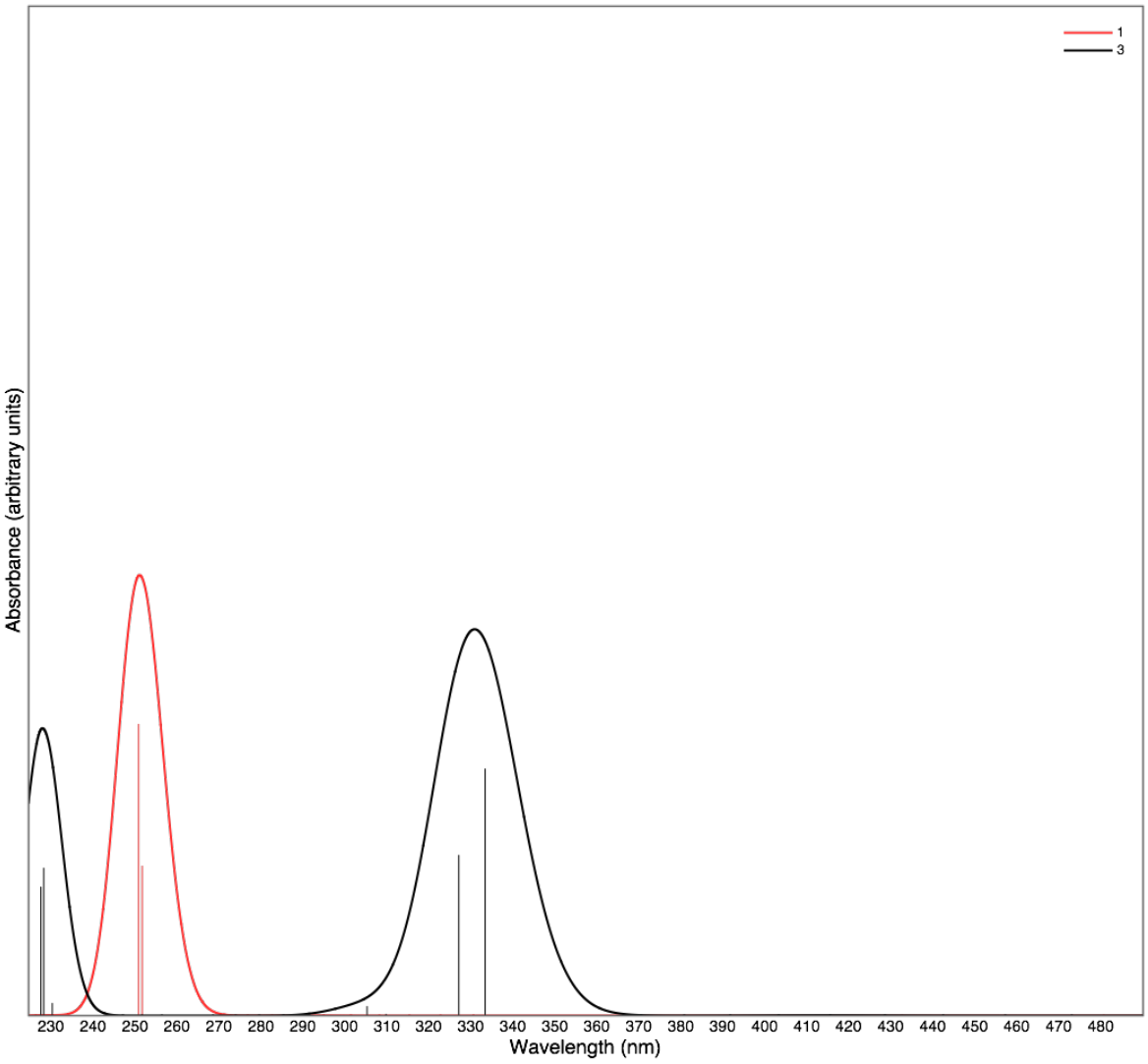

Figure SA70. TD-DFT calculated absorption spectra for receptors **2.1** and **2.3** [SMD-CPCM(AcCN)/M06-2X/def2-QZVP].

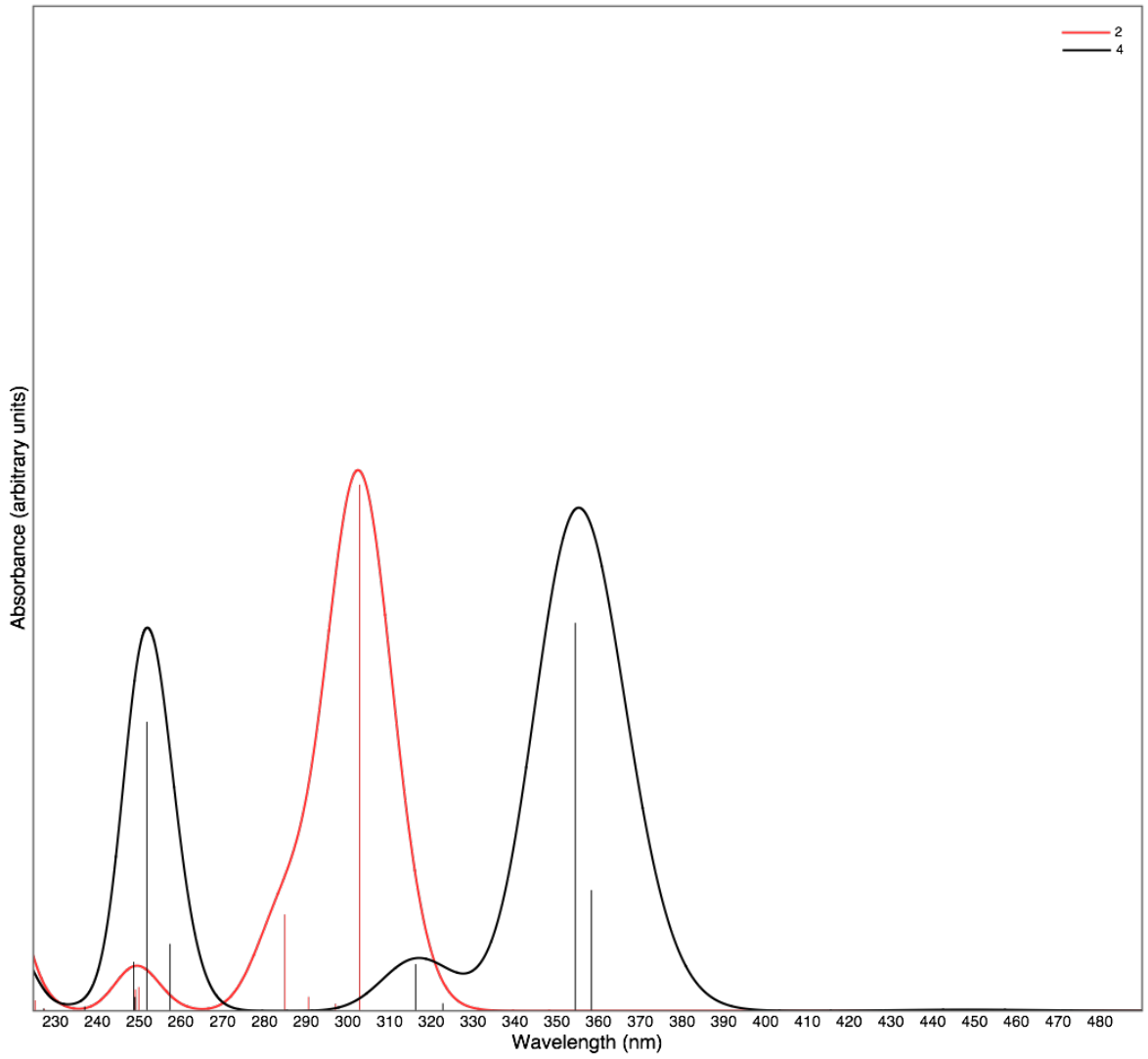

Figure SA71. TD-DFT calculated absorption spectra for receptors **2.2** and **2.4** [SMD-CPCM(AcCN)/M06-2X/def2-QZVP].

For instance, the spectrum of **2.1** shows a peak centred around 251 nm with dominant contributions from two nearly coalescing HOMO→LUMO (250.7 nm) and HOMO→LUMO+1 (251.5 nm) transitions (Figure SA72). In contrast, peaks in **2.3** are more separated, splitting into transitions that appear at 333.2 and 326.9 nm, with a smaller shoulder around 305 nm corresponding to a HOMO–1→LUMO+1 transition with n→π^* character (Figure SA73). This behaviour aligns with the general observation that the absorption band shifts into the visible spectral region for thiocarbonyl compounds compared to the corresponding carbonyl derivatives. Similar behaviour is observed for receptors **2.2** and **2.4**, with additional peaks emerging at 230

and 250 nm in these cases, respectively, due to transitions from the C=S π-orbital into the LUMO (Figure SA74 and SA75). The red shift of the absorptions in **2.3** and **2.4** can be attributed to the energy lowering of the LUMO and LUMO+1 in these thiocarbonyl derivatives, leading to an overall narrowing of the energy gap in the frontier orbital region (Figure SA76 and SA77). Given the lengthier C=S bond and the disparity in sizes of the 2p and 3p orbitals, this phenomenon can be explained by the less effective overlap between the C(2p) and S(3p) orbitals compared to the interactions in the carbonyl's C(2p)/O(2p) orbitals. Moreover, this effect corresponds with the lower relative bond strengths of the thiocarbonyl group versus the carbonyl group, as evidenced by their respective stretching force constants outlined in Table SA3.

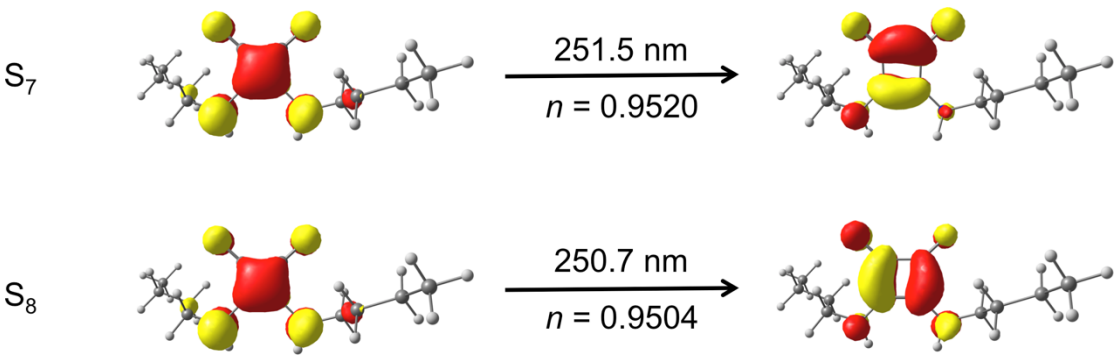

Figure SA72. Plots (isovalue = 0.05) of Natural Transition Orbital (NTO) pairs for key electronic transitions in receptor **2.1**. Excitation energies are given along with natural occupation numbers for each NTO pain [SMD-CPCM(AcCN)/M06-2X/def2-QZVP].

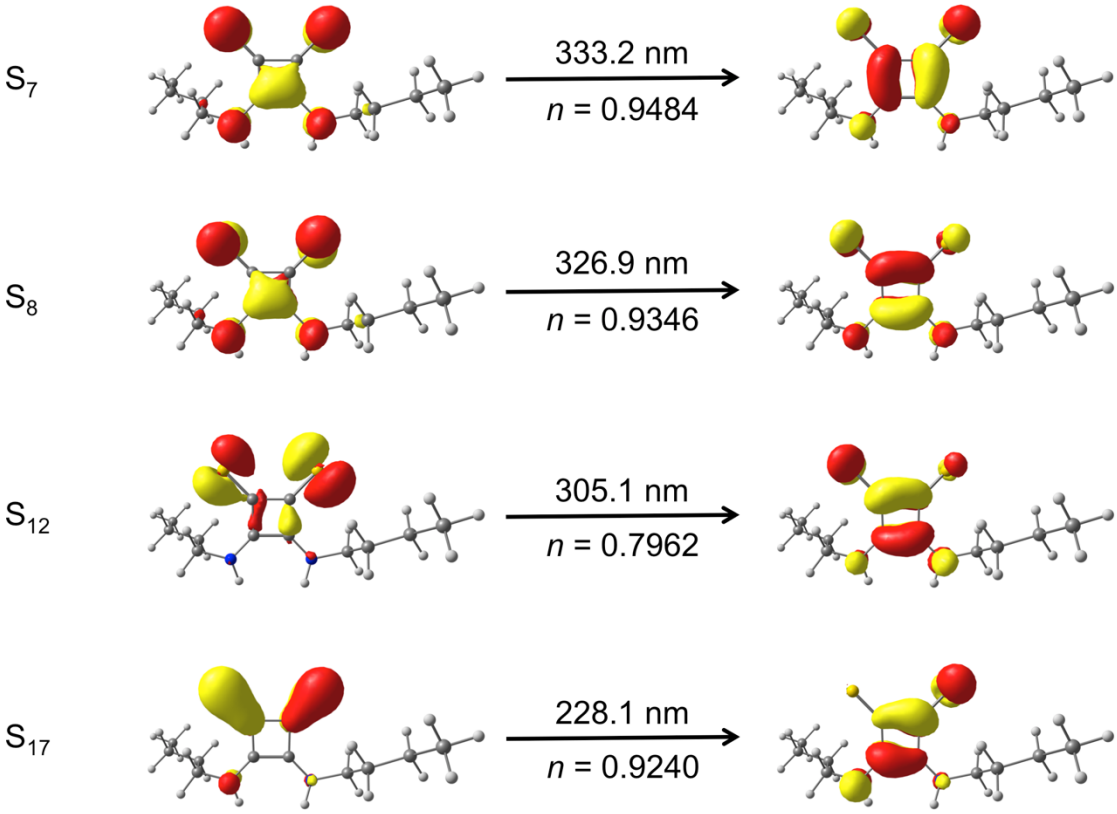

Figure SA73. Plots (isovalue = 0.05) of Natural Transition Orbital (NTO) pairs for key electronic transitions in receptor **2.3**. Excitation energies are given along with natural occupation numbers for each NTO pain [SMD-CPCM(AcCN)/M06-2X/def2-QZVP].

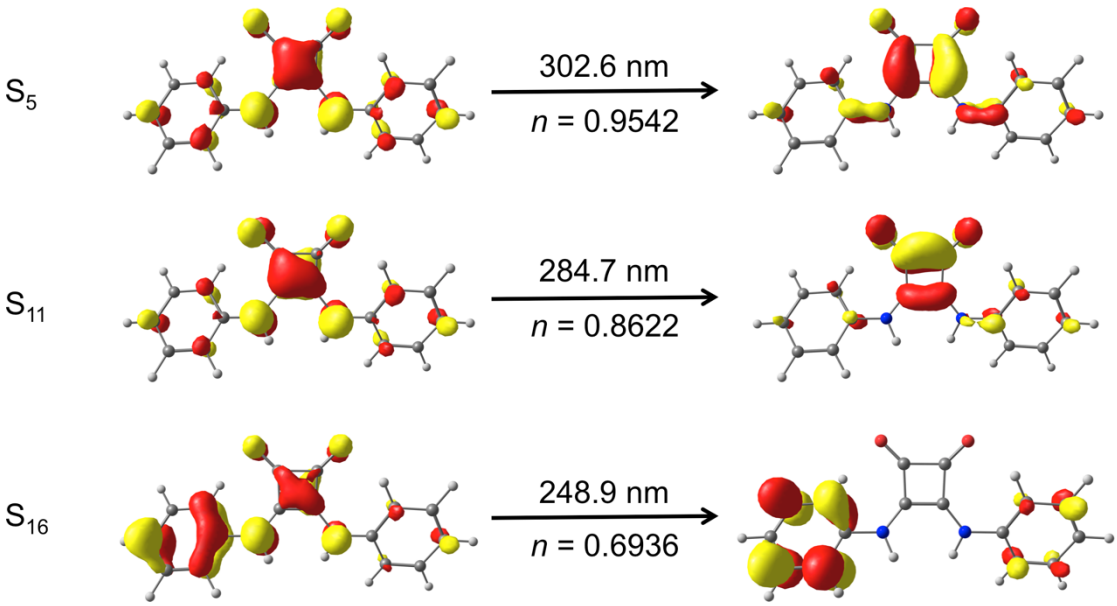

Figure SA74. Plots (isovalue = 0.05) of Natural Transition Orbital (NTO) pairs for key electronic transitions in receptor **2.2**. Excitation energies are given along with natural occupation numbers for each NTO pain [SMD-CPCM(AcCN)/M06-2X/def2-QZVP].

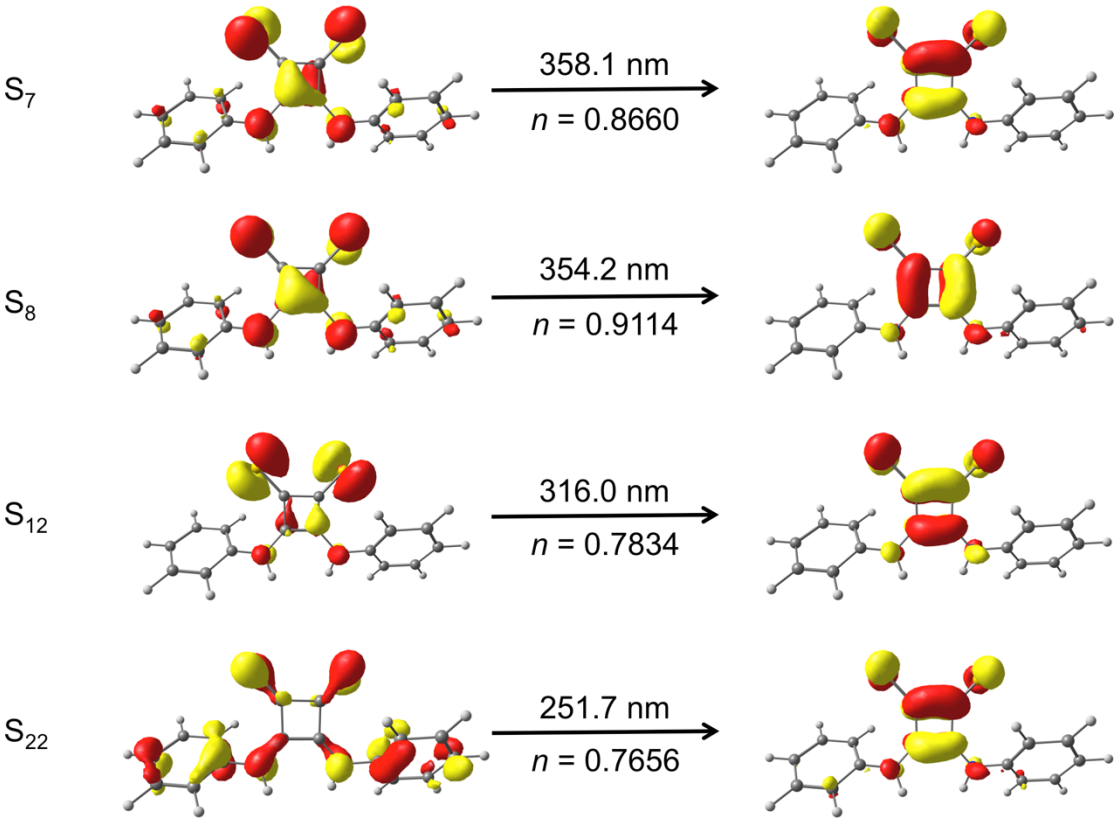

Figure SA75. Plots (isovalue = 0.05) of Natural Transition Orbital (NTO) pairs for key electronic transitions in receptor **2.4**. Excitation energies are given along with natural occupation numbers for each NTO pain [SMD-CPCM(AcCN)/M06-2X/def2-QZVP].

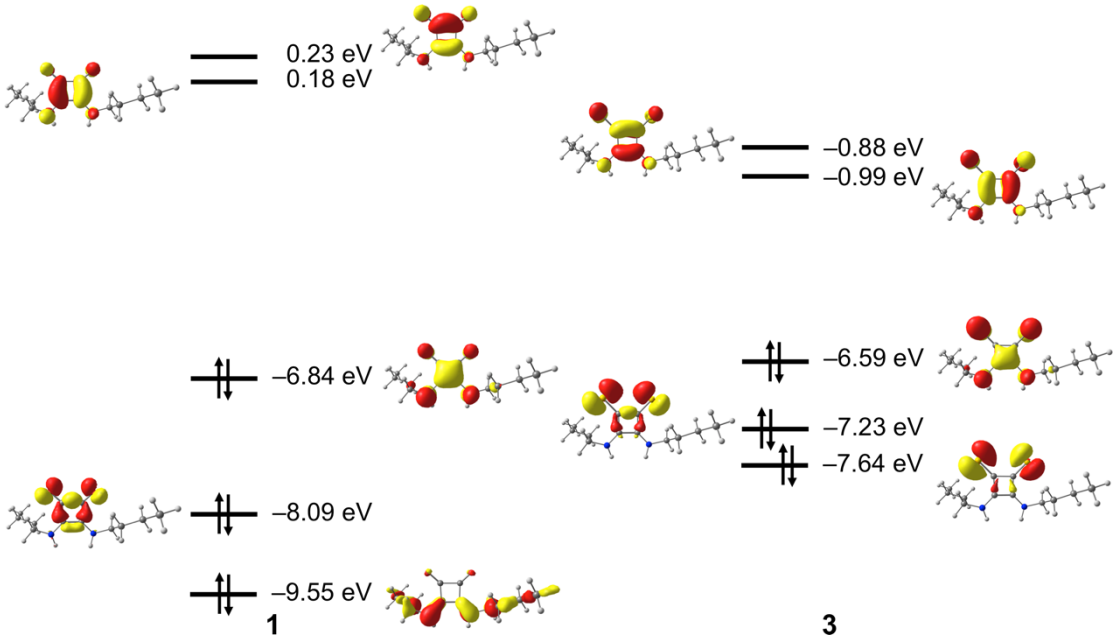

Figure SA76. Schematic diagram of the canonical Kohn-Sham frontier molecular orbitals in **2.1** and **2.3** (isovalue = 0.05 au) [SMD-CPCM(AcCN)/M06-2X/def2-QZVP].

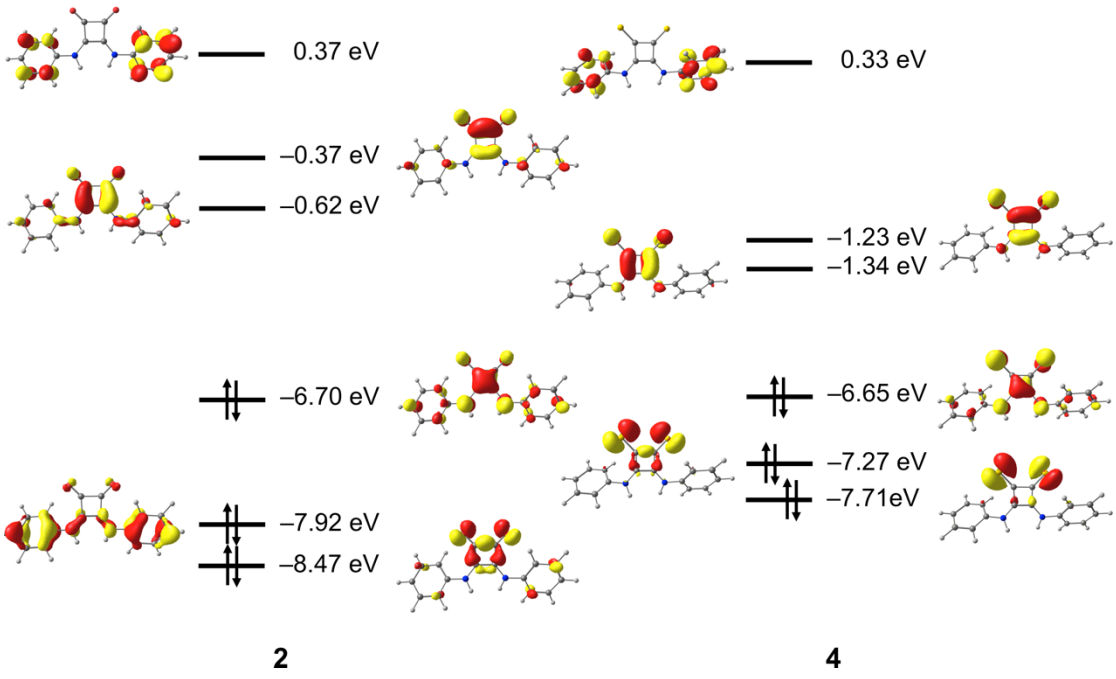

Figure SA77. Schematic diagram of the canonical Kohn-Sham frontier molecular orbitals in **2.2** and **2.4** (isovalue = 0.05 au) [SMD-CPCM(AcCN)/M06-2X/def2-QZVP].

Table SA3 Structural and Refinement Information for all X-ray structures

Identification code	3	3_BuNH3_SO4	4-Pb
Empirical formula	$C_{12}H_{20}N_2S_2$	$C_{96}H_{192}N_{18}O_{12}S_{15}$	$C_{32}H_{24}Cl_2N_4O_8PbS_4$
Formula weight	256.42	2271.56	998.88
Temperature/K	150	150	150
Crystal system	monoclinic	trigonal	monoclinic
Space group	*C*2/*m*	*R*-3	$P2_1/c$
a/Å	8.4881(12)	17.4462(5)	17.8074(18)
b/Å	6.8098(9)	17.4462(5)	19.4115(17)
c/Å	12.4405(17)	40.0341(19)	21.364(2)
α/°	90	90	90
β/°	103.668(4)	90	107.795(3)
γ/°	90	120	90
Volume/Å^3	698.73(17)	10552.7(8)	7031.4(12)
Z	2	3	8
ρ_{calc}g/cm^3	1.219	1.072	1.887
μ/mm^{-1}	0.359	0.283	5.246
F(000)	276	3690	3904
Crystal size/mm^3	0.2 × 0.11 × 0.04	0.2 × 0.12 × 0.08	0.15 × 0.03 × 0.01
Radiation	MoKα (λ = 0.71073)	MoKα (λ = 0.71073)	MoKα (λ = 0.71073)
2Θ range for data collection/°	6.742 to 52.654	4.882 to 54.26	4.804 to 50.824

Index ranges	$-10 \le h \le 10$, $-8 \le k \le 8$, $-15 \le l \le 15$	$-21 \le h \le 22$, $-22 \le k \le 22$, $-51 \le l \le 51$	$-21 \le h \le 20$, $-23 \le k \le 19$, $-25 \le l \le 25$
Reflections collected	6198	57599	77976
Independent reflections	778 [R_{int} = 0.0735, R_{sigma} = 0.0476]	5197 [R_{int} = 0.1262, R_{sigma} = 0.0732]	12890 [R_{int} = 0.1719, R_{sigma} = 0.1386]
Data/restraints/parameters	778/1/71	5197/12/237	12890/317/985
Goodness-of-fit on F^2	1.093	1.036	1.016
Final R indexes [I>=2σ (I)]	R_1 = 0.0506, wR_2 = 0.0822	R_1 = 0.0624, wR_2 = 0.1290	R_1 = 0.0581, wR_2 = 0.0981
Final R indexes [all data]	R_1 = 0.0723, wR_2 = 0.0879	R_1 = 0.1136, wR_2 = 0.1493	R_1 = 0.1409, wR_2 = 0.1207
Largest diff. peak/hole / e $Å^{-3}$	0.23/-0.25	0.71/-0.31	0.96/-1.27
CCDC No.	2324085	2324086	2324087

Crystal and refinement parameters are given in Table SA3. All data were collected on a Bruker D8 Quest ECO diffractometer using graphite-monochromated Mo Kα radiation (λ = 0.71073 Å) and a Photon II-C14 CPAD detector. Crystals were mounted on Mitegen micromounts in NVH immersion oil, and all collections were carried out at 150 K using an Oxford cryostream. Data collections were carried out using φ and ω scans, with collections and data reductions carried out in the Bruker APEX-3 suite of programs.[1] Multi-scan absorption corrections were applied for all datasets using SADABS.[2] The data were solved with the intrinsic phasing routine in SHELXT,[3] and all data were refined on F^2 with full-matrix least squares procedures in SHELXL,[8] operating within the OLEX-2 GUI.[4] All non-hydrogen atoms were refined with anisotropic displacement parameters. Carbon-bound hydrogen atoms were placed in

riding positions and refined with isotropic displacement parameters equal to 1.2 or 1.5 times the isotropic equivalent of their carrier atom. CCDC 2324085-2324087.

Compound **2.3** forms one-dimensional hydrogen bonded chains which show no longer range directionality, such that the best crystallographic model was to treat these as fully disordered across the +*b*/-*b* directions in the C2/m space group, as this allowed for the most reasonable model of the heavy atom positions (the sulfur and nitrogen positions are shared across both orientations) without the need for restraints. We observed no interstitial reflections consistent with any further ordering of these chains, and attempts to model lower symmetry settings of this structure led to unreasonable correlation elements and worsened refinement statistics.

The structure model for **2.3**_$BuNH_3$_SO_4 was obtained from a minor decomposition product and could not be prepared on sufficient scale for bulk phase characterisation. As such, while the contribution to the measured structure factors from two small, disordered solvent regions coincident with the threefold axis were addressed with the solvent masking routine in OLEX2 and allocated as 5 water molecules per formula unit, the exact solvation cannot be unambiguously confirmed (*e.g.*, water *versus* acetonitrile).[5]

The crystals for **2.4-Pb** exhibited relatively poor diffraction characteristics, including rapid dropoff in intensity beyond 1 Å. Disorder was evident on phenyl ring C11-C16 and perchlorates Cl1 and Cl4 which were modelled with DFIX and RIGU restraints to maintain sensible geometries, and the anions with higher mobilities unavoidably (and expectedly) display larger ADPs than the more tightly bound species.

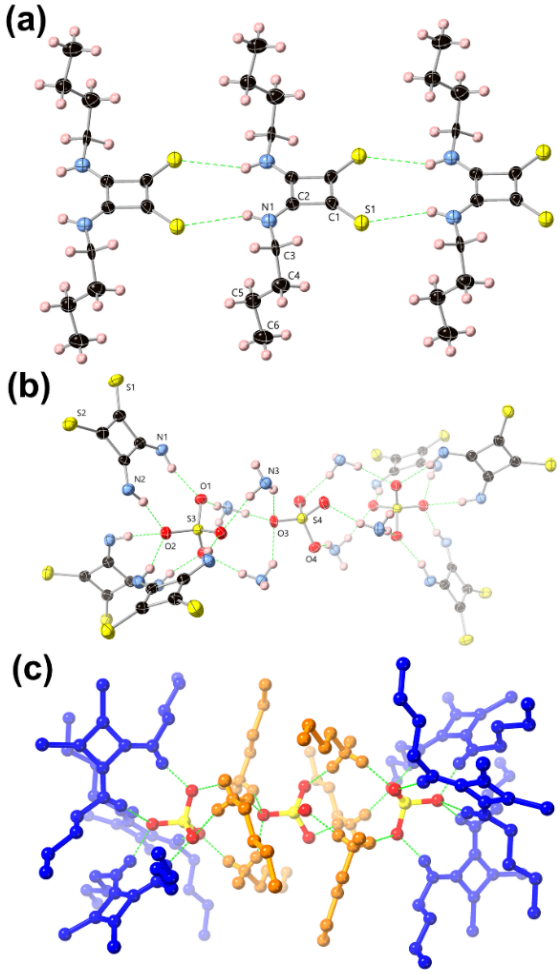

Figure SA82. (a) Structure of **2.3** with labels for unique heteroatoms. Disorder is omitted for clarity. (b) The core hydrogen bonding structure in the butylammonium sulfate adduct $(BuNH_3)_6$(**2.3**)$_6(SO_4)_3$, with labels for unique heteroatoms and all butyl chains omitted for clarity. ADPs are rendered at the 50% probability level. (c) Complete structure of $(BuNH_3)_6$(**2.3**)$_6(SO_4)_3$ with thiosquaramide molecules coloured blue and butylammonium species coloured orange, selected hydrogen atoms and disorder in the central sulfate are omitted for clarity.

Reference

(1) G. A. Zhurko; Chemcraft – Graphical Program for Visualization of Quantum Chemistry Computations, Version 1.8 (build 536a); Ivanovo, 2005.
(2) *Bruker APEX-3*, Bruker-AXS Inc., Madison, WI, 2016.
(3) *SADABS*, Bruker-AXS Inc., Madison, WI, 2016.
(4) G. M. Sheldrick, *Acta Crystallogr., Sect. A: Found. Adv.*, 2015, **71**, 3–8.
(5) G. M. Sheldrick, *Acta Crystallogr., Sect. C: Struct. Chem.*, 2015, **71**, 3–8.

Supporting information for Chapter 3

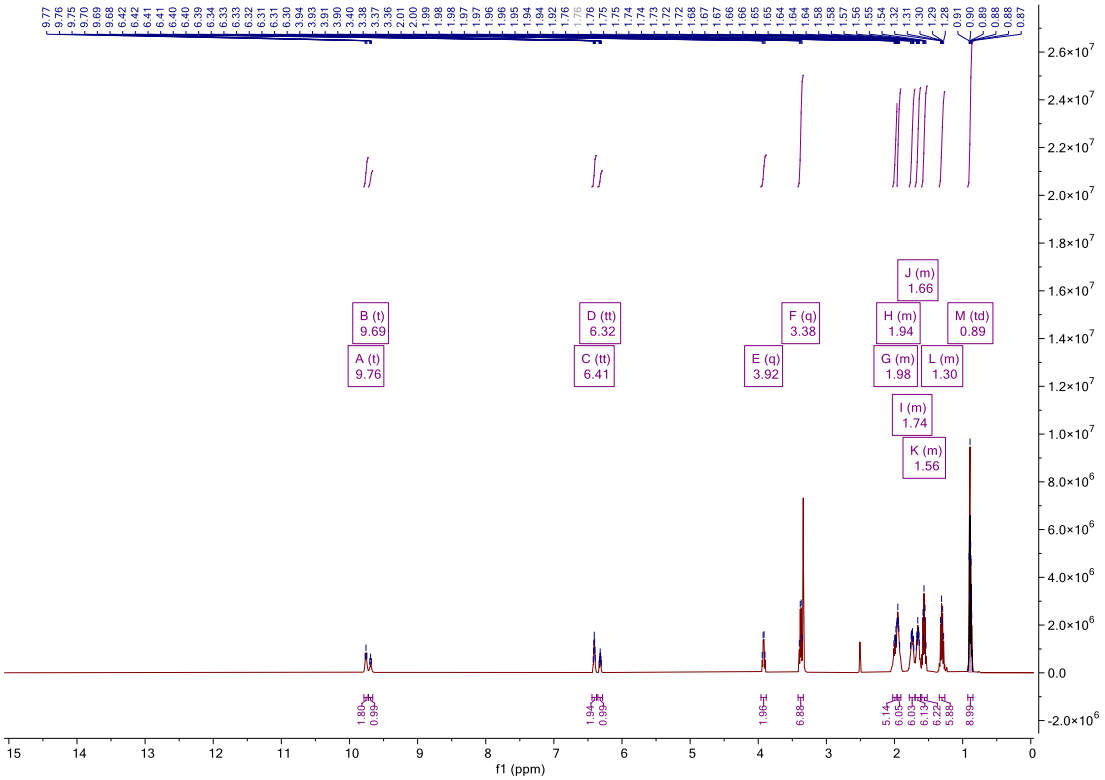

Figure SB1. ^{1}H NMR (DMSO-d_6, 500MHz) spectrum of **B1**.

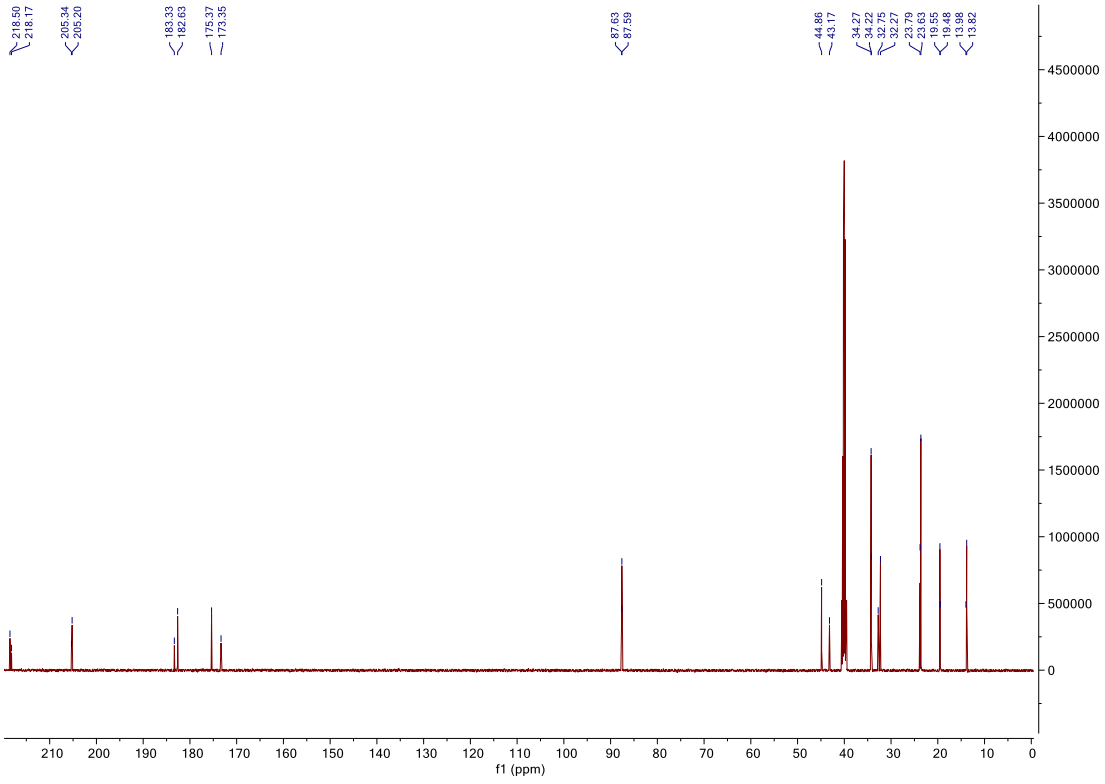

Figure SB2. ^{13}C NMR (DMSO-d_6, 126MHz) spectrum of **B1**.

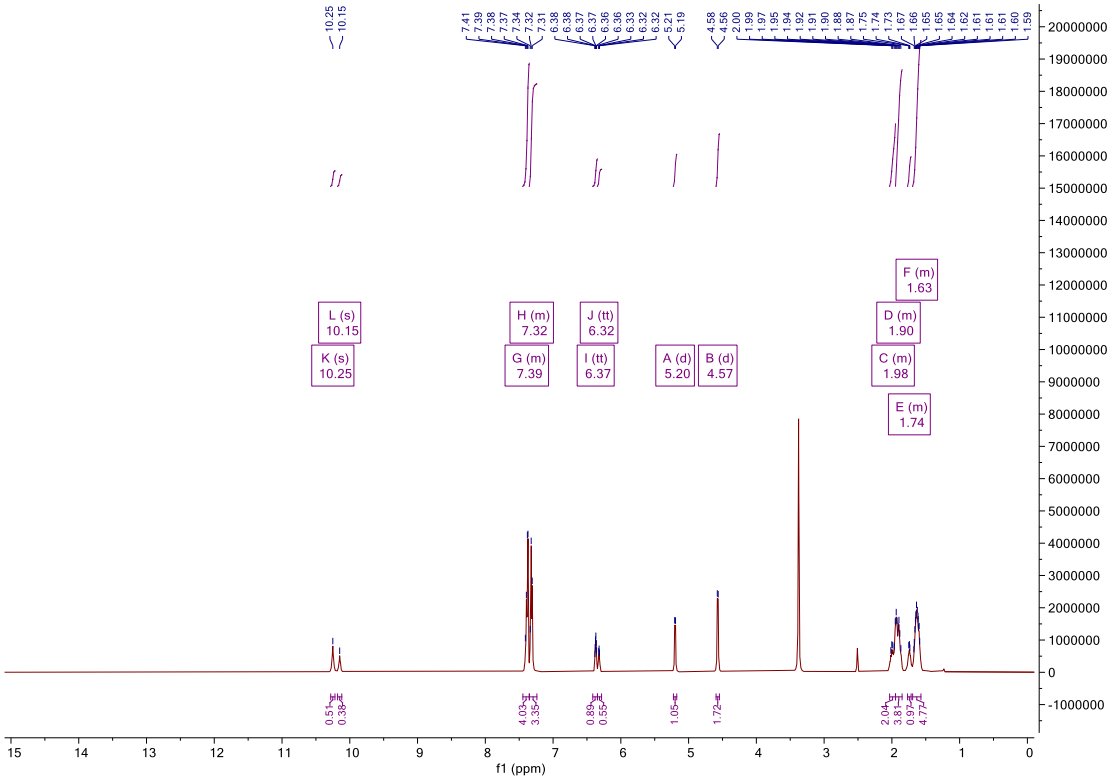

Figure SB3. ^{1}H NMR (DMSO-d_6, 500MHz) spectrum of **B2**.

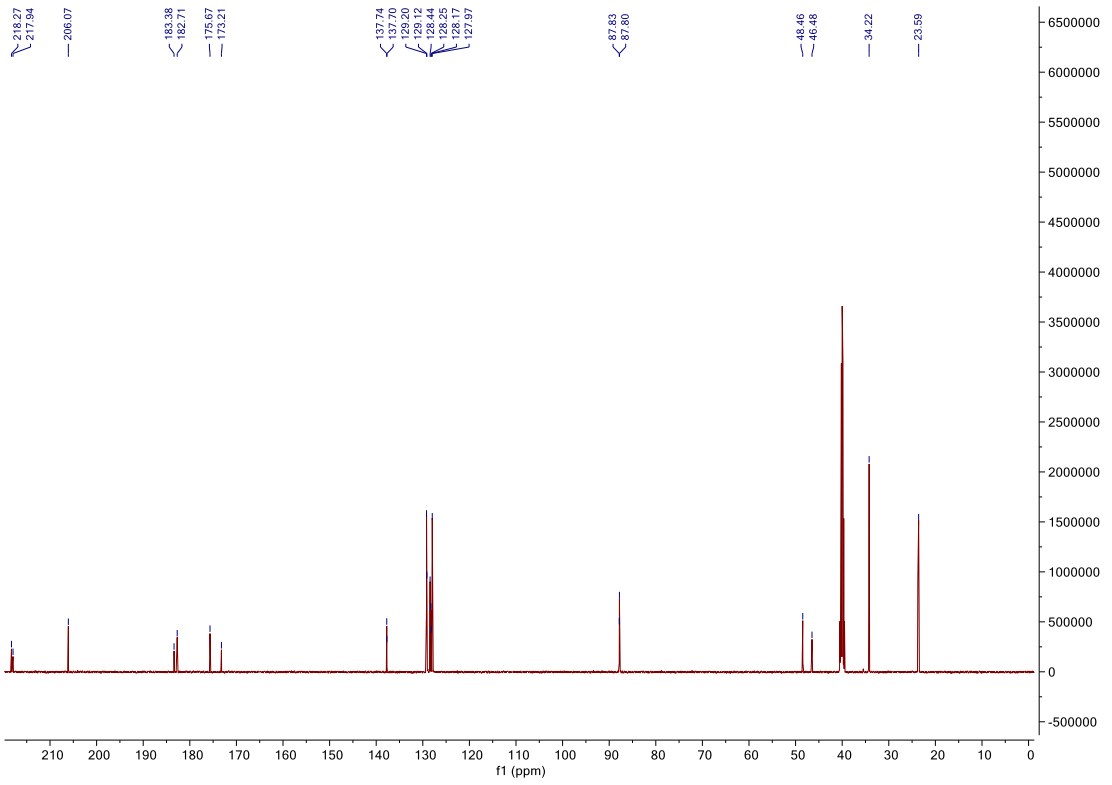

Figure SB4. ^{13}C NMR (DMSO-d_6, 126MHz) spectrum of **B2**.

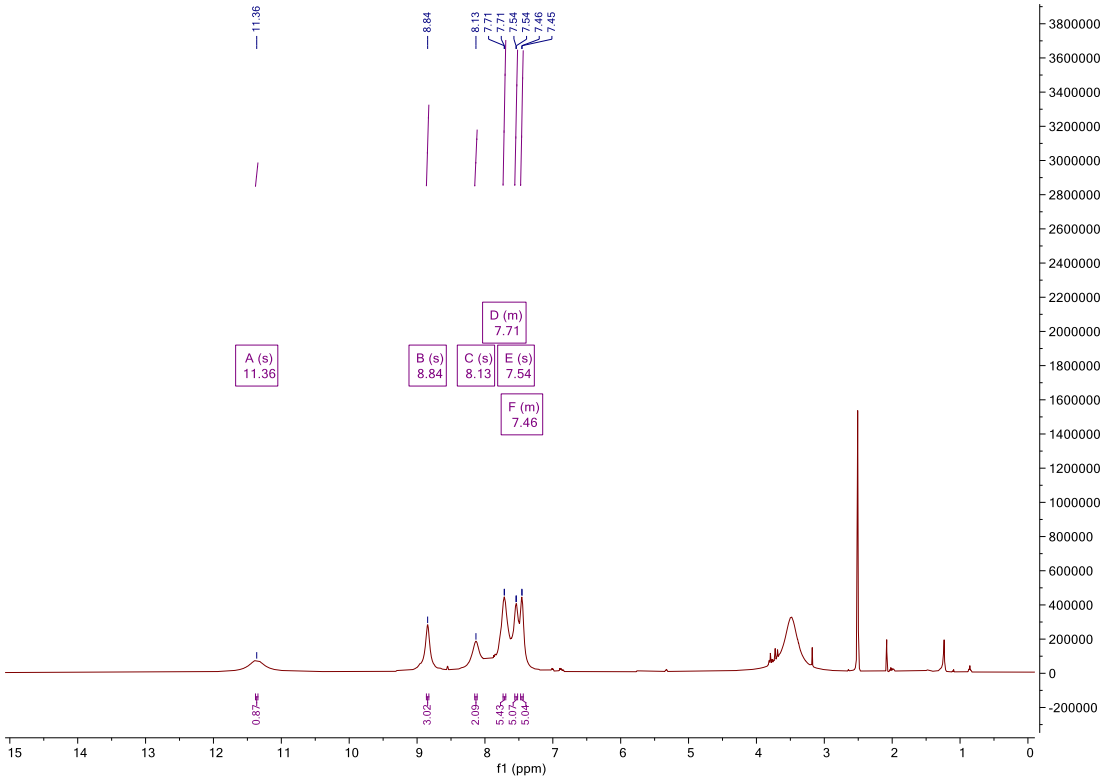

Figure SB5. ^{1}H NMR (DMSO-d_6, 500MHz) spectrum of **3.1**.

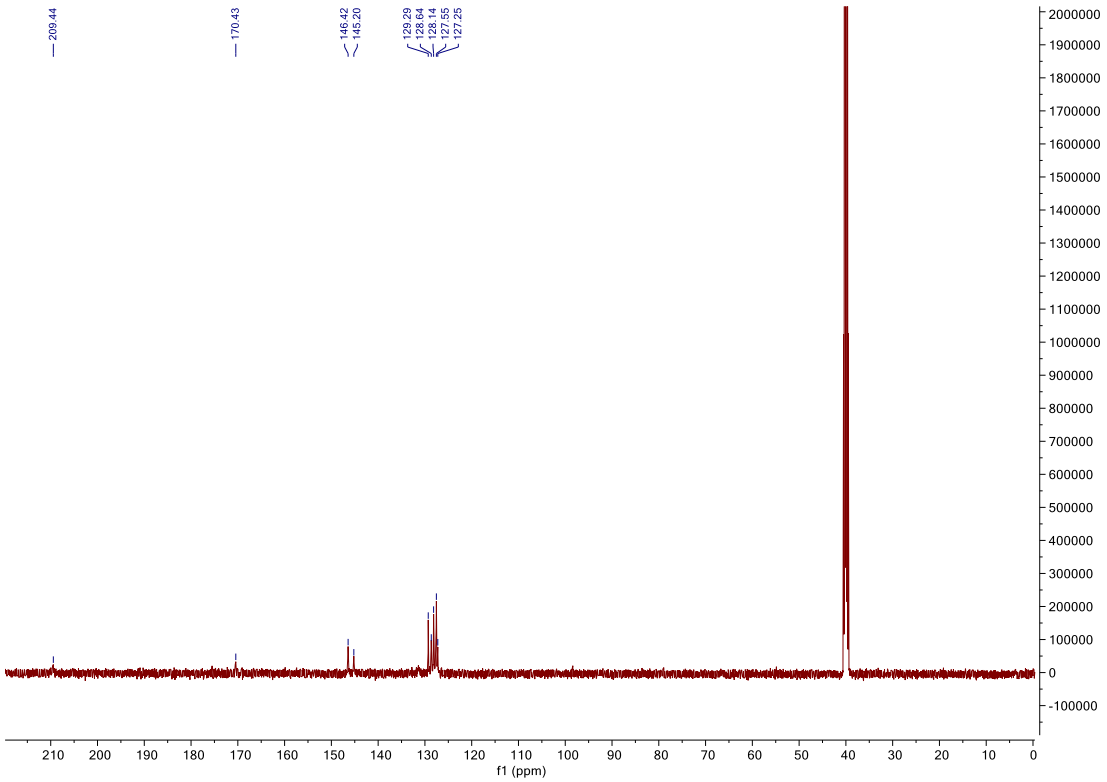

Figure SB6. ^{13}C NMR (DMSO-d_6, 126MHz) spectrum of **3.1**.

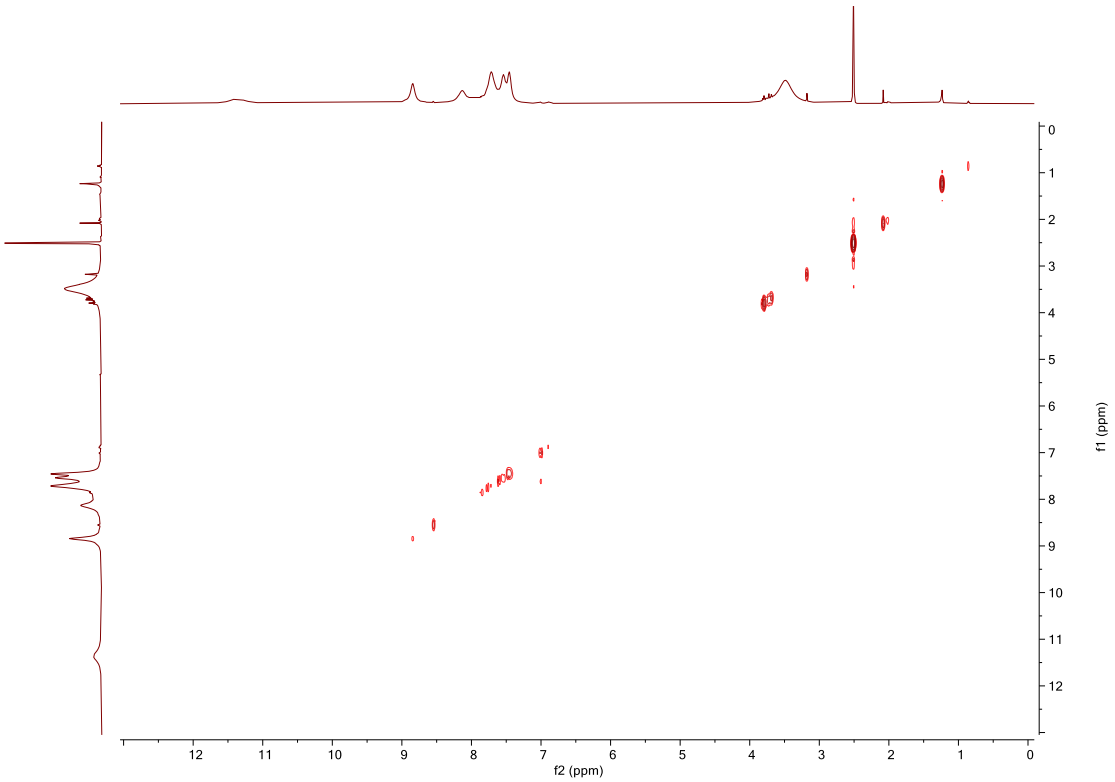

Figure SB7. COSY NMR (DMSO-d_6) spectrum of **3.1**.

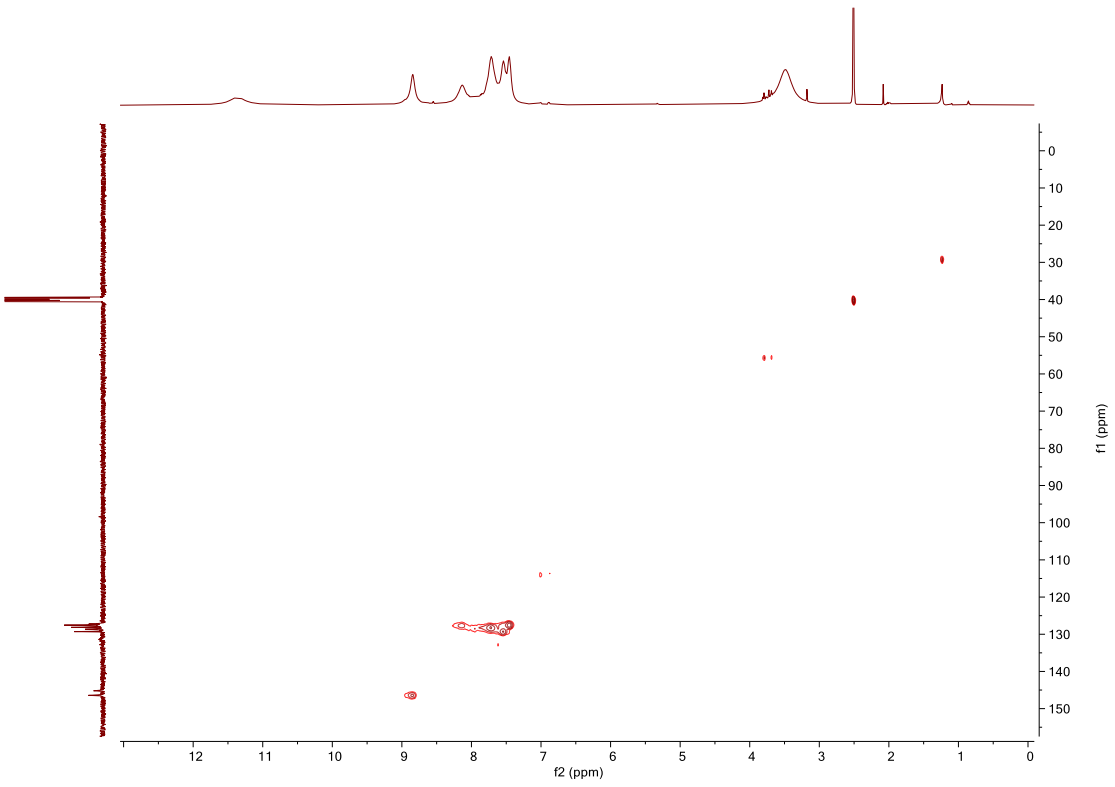

Figure SB8. HSQC NMR (DMSO-d_6) spectrum of **3.1**.

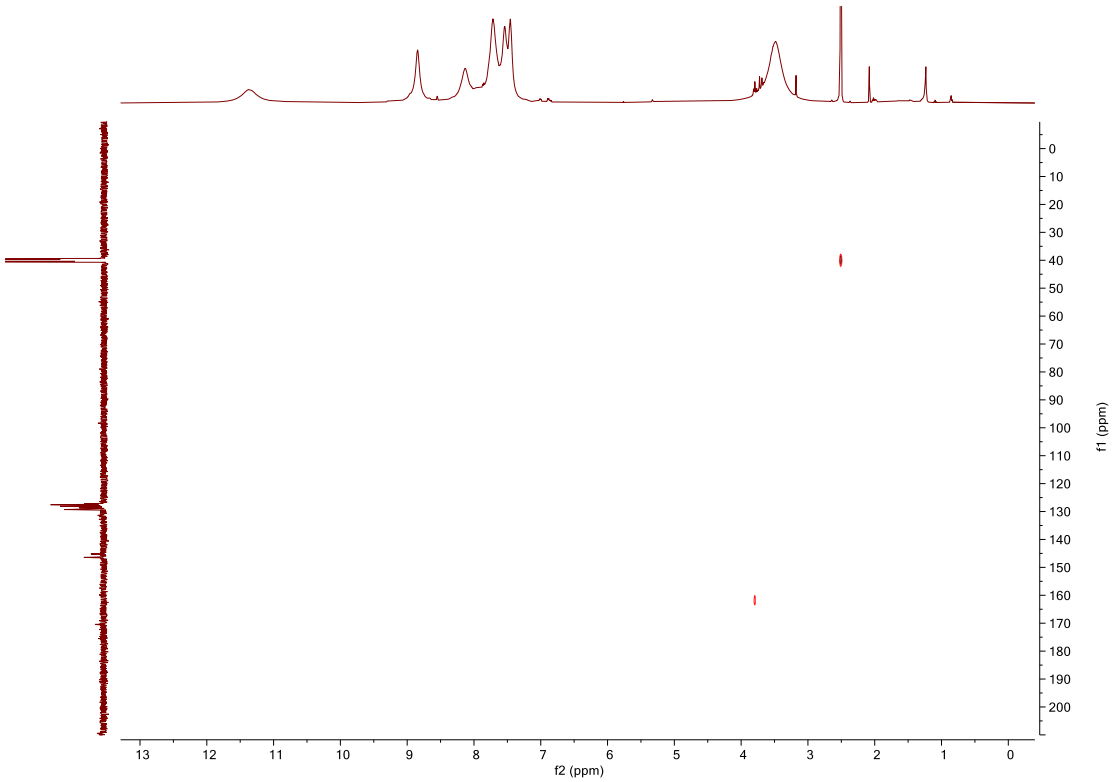

Figure SB9. HMBC NMR (DMSO-d_6) spectrum of **3.1**.

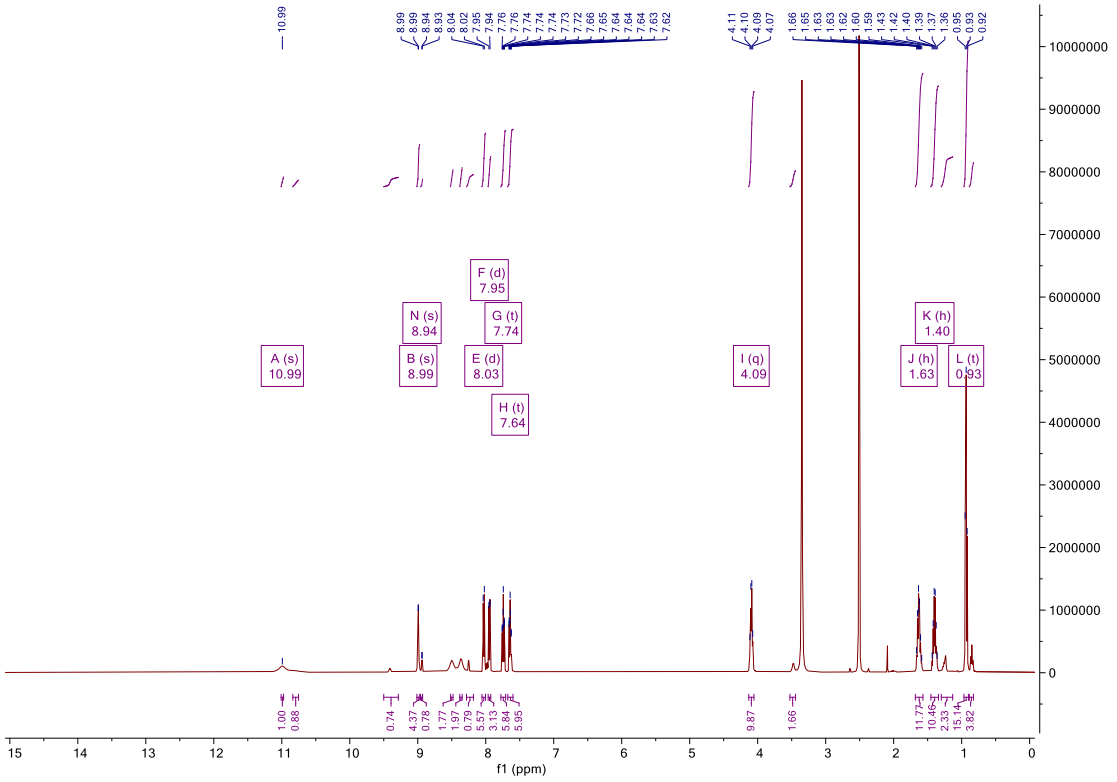

Figure SB10. ^{1}H NMR (DMSO-d_6, 500MHz) spectrum of **3.2**.

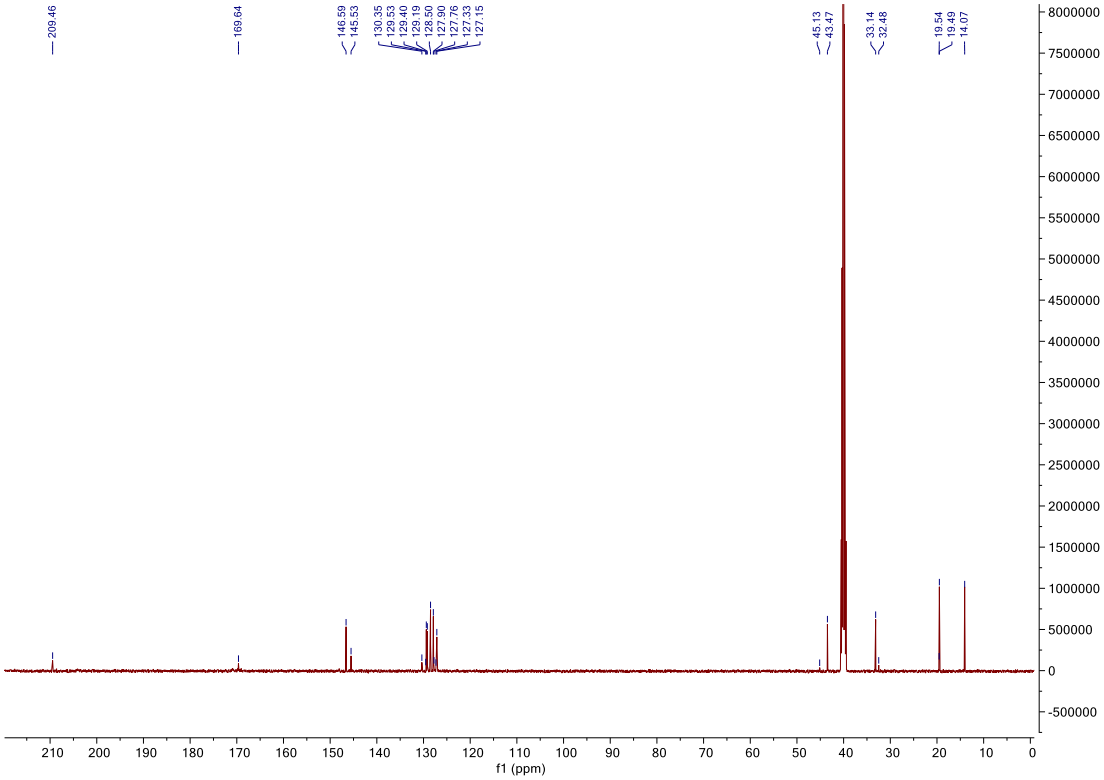

Figure SB11. ^{13}C NMR (DMSO-d_6, 126MHz) spectrum of **3.2**.

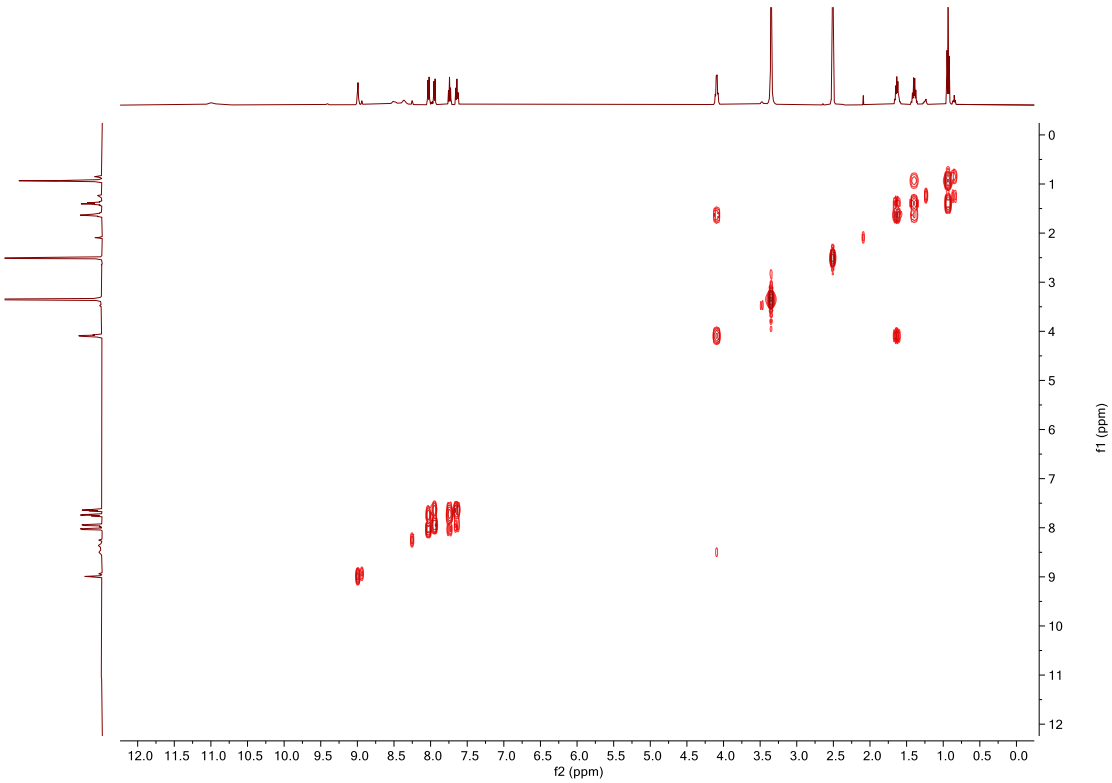

Figure SB11. COSY NMR (DMSO-d_6) spectrum of **3.2**.

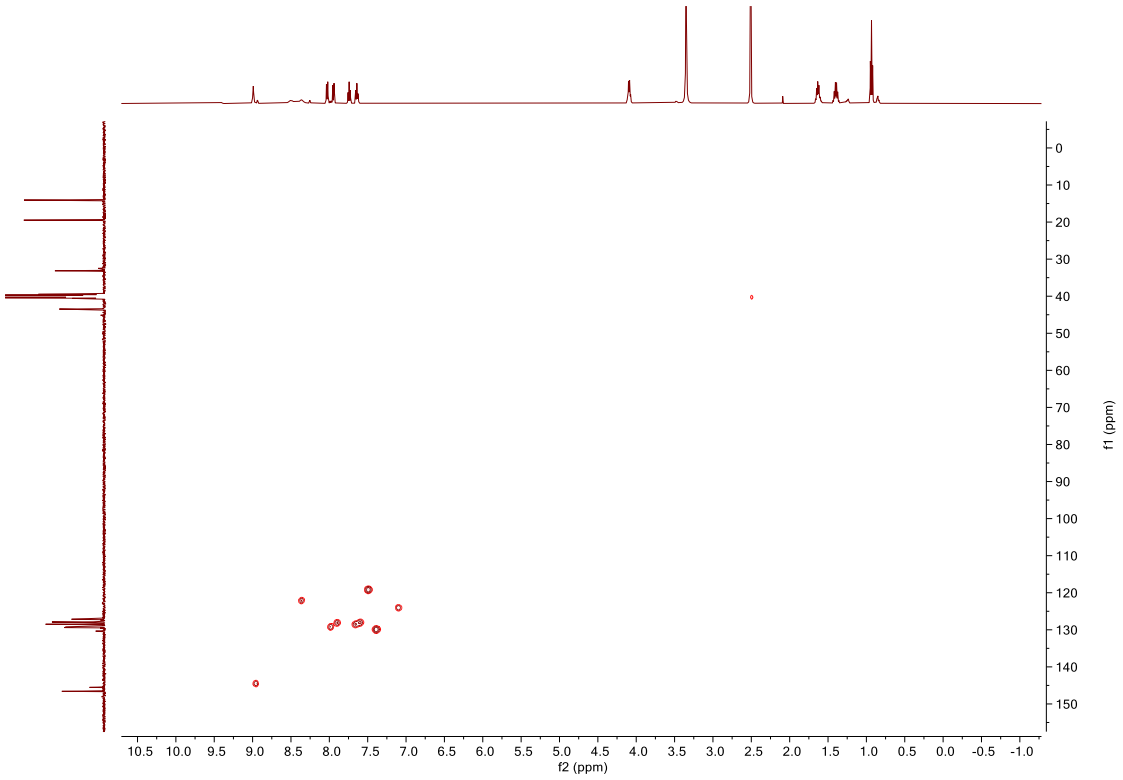

Figure SB12. HSQC NMR (DMSO-d_6) spectrum of **3.2**.

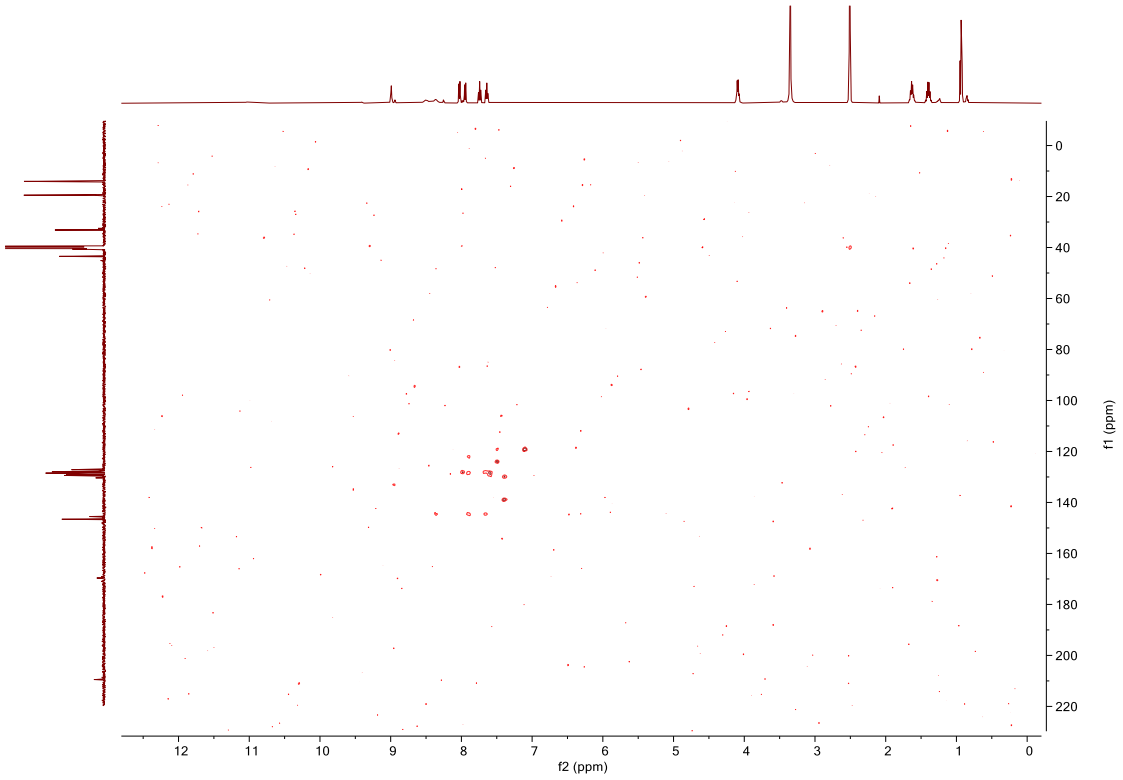

Figure SB13. HMBC NMR (DMSO-d_6) spectrum of **3.2**.

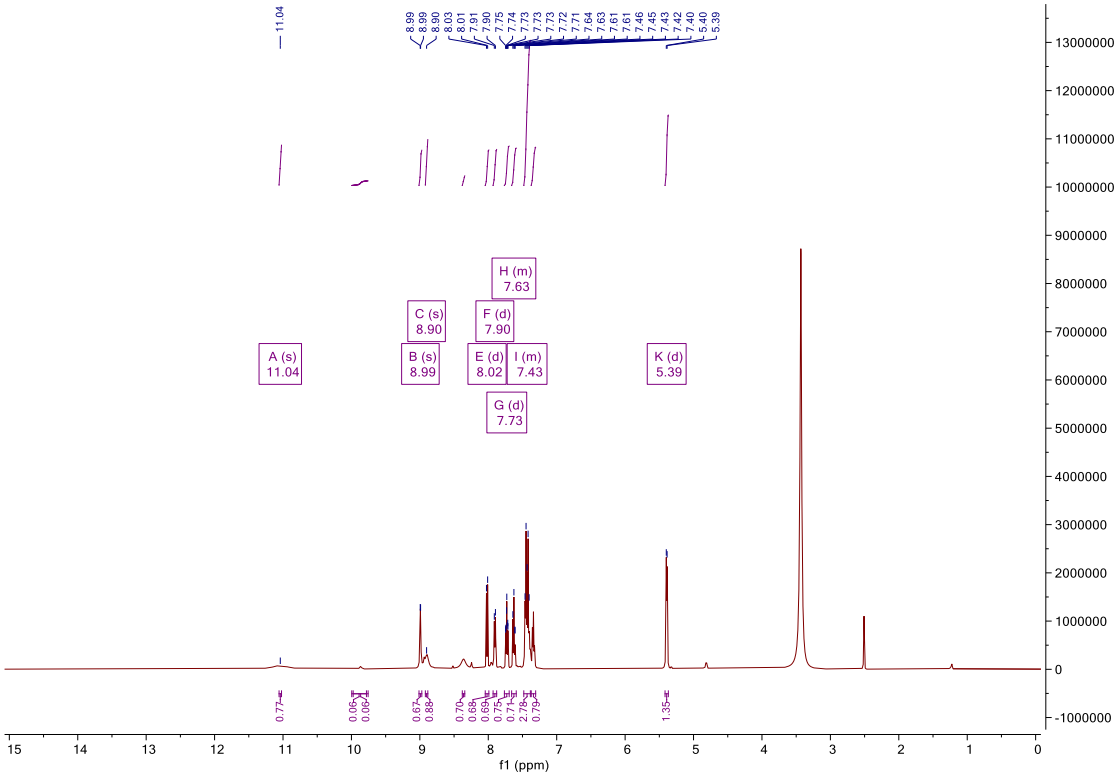

Figure SB14. ^{1}H NMR (DMSO-d_6, 500MHz) spectrum of **3.3**.

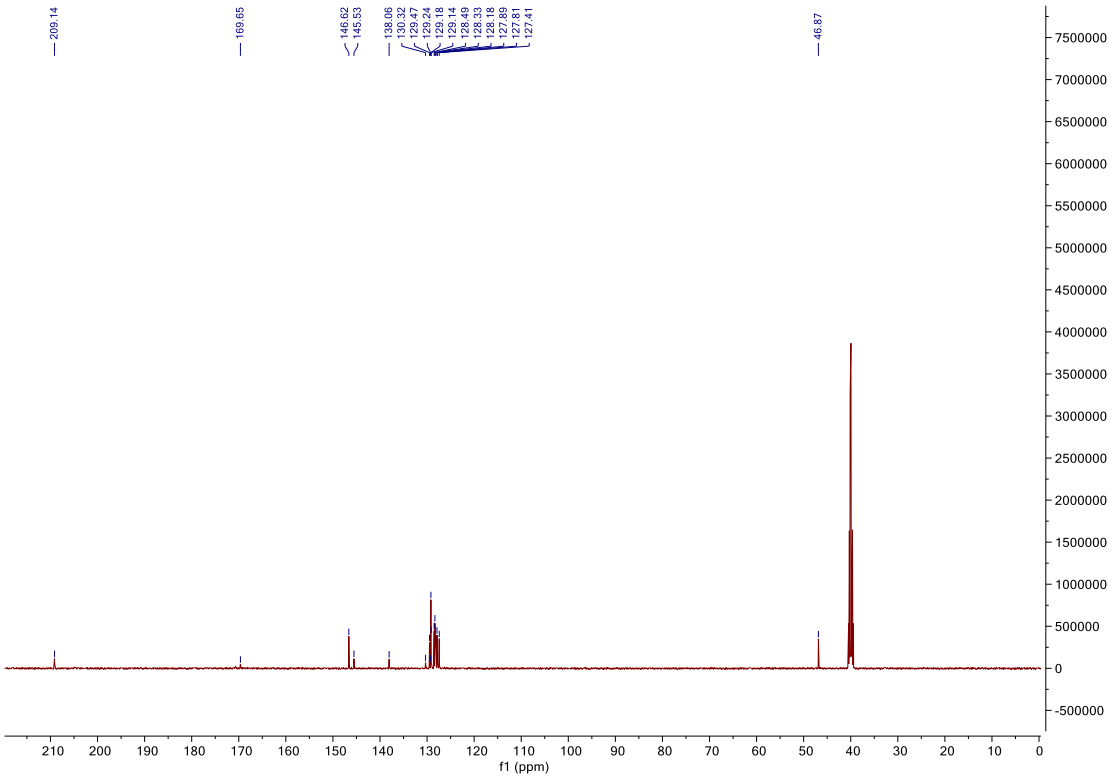

Figure SB14. ^{13}C NMR (DMSO-d_6, 126MHz) spectrum of **3.3**.

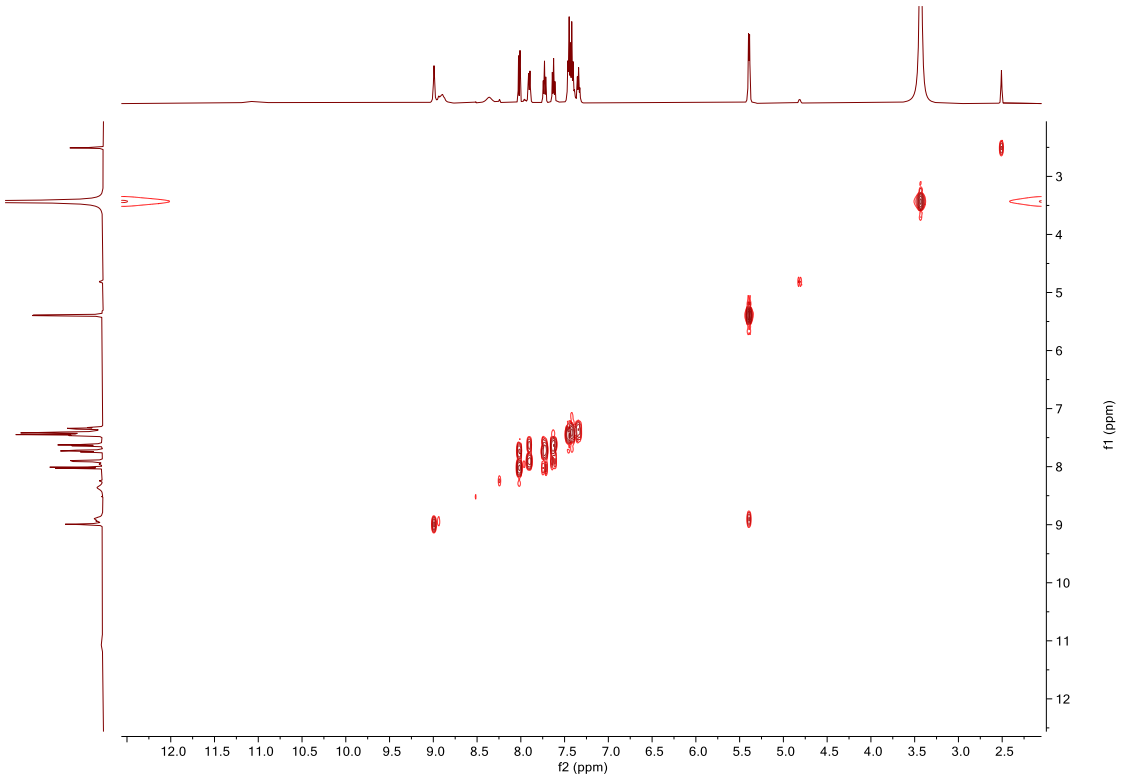

Figure SB15. COSY NMR (DMSO-d_6) spectrum of **3.3**.

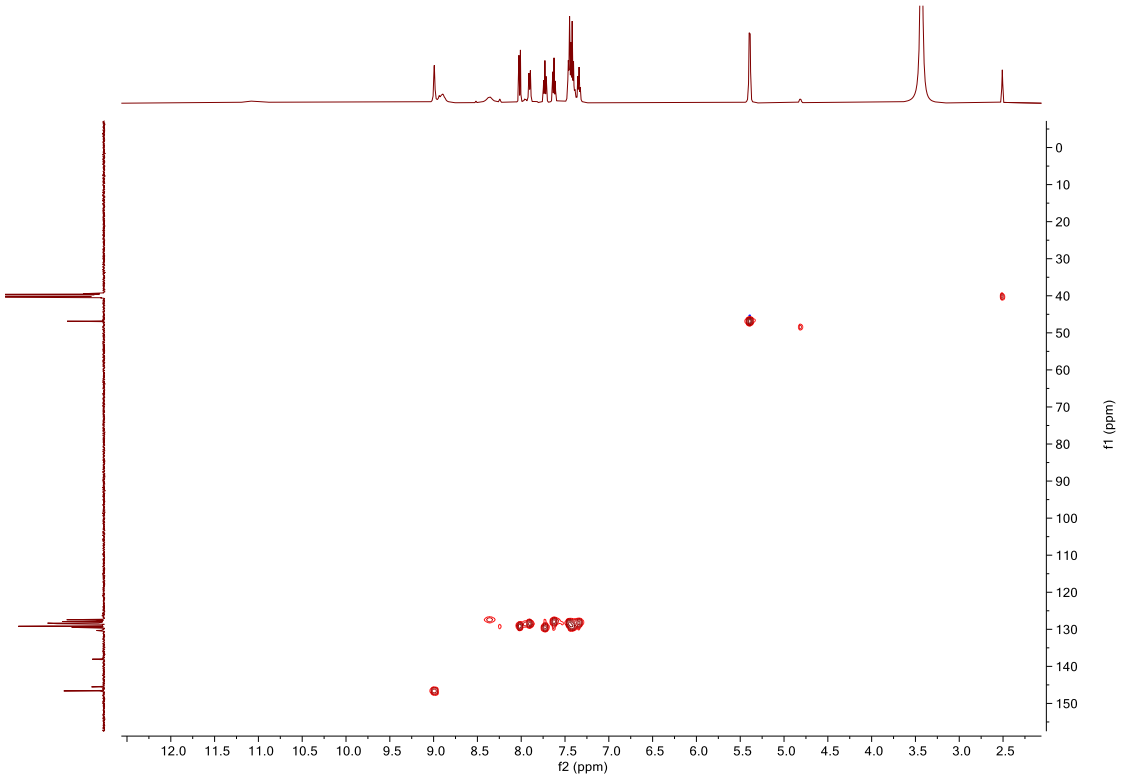

Figure SB16. HSQC NMR (DMSO-d_6) spectrum of **3.3**.

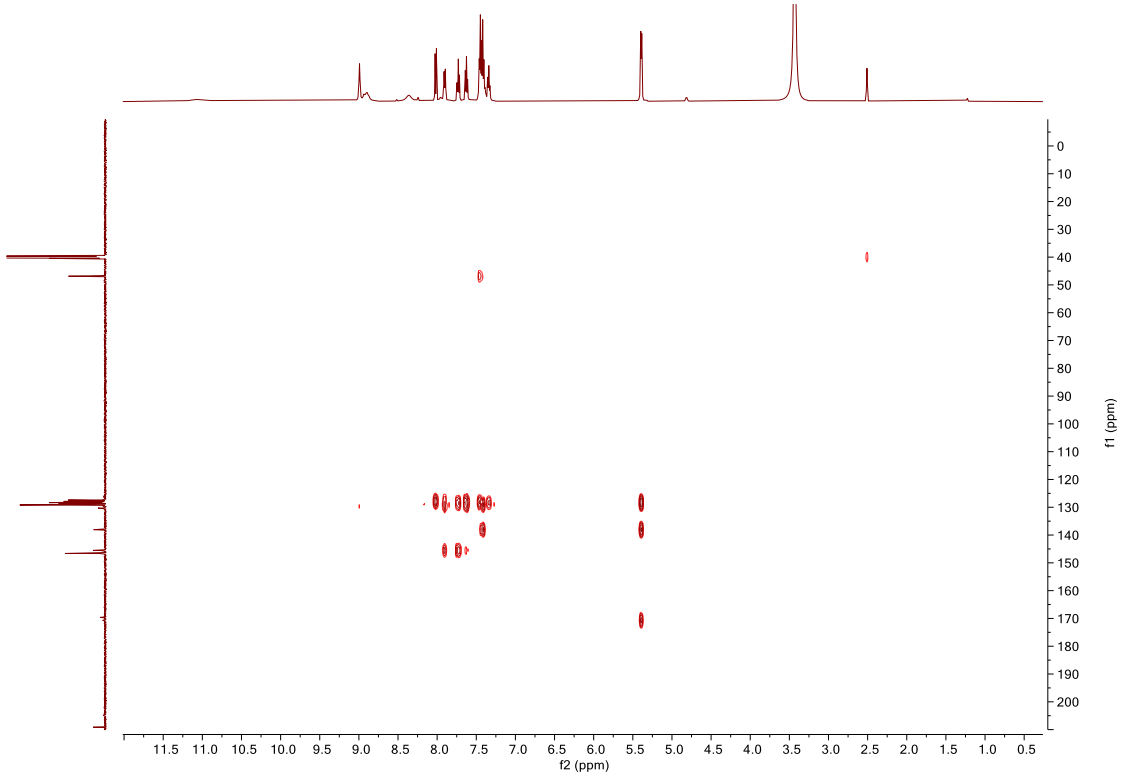

Figure SB17. HMBC NMR (DMSO-d_6) spectrum of **3.3**.

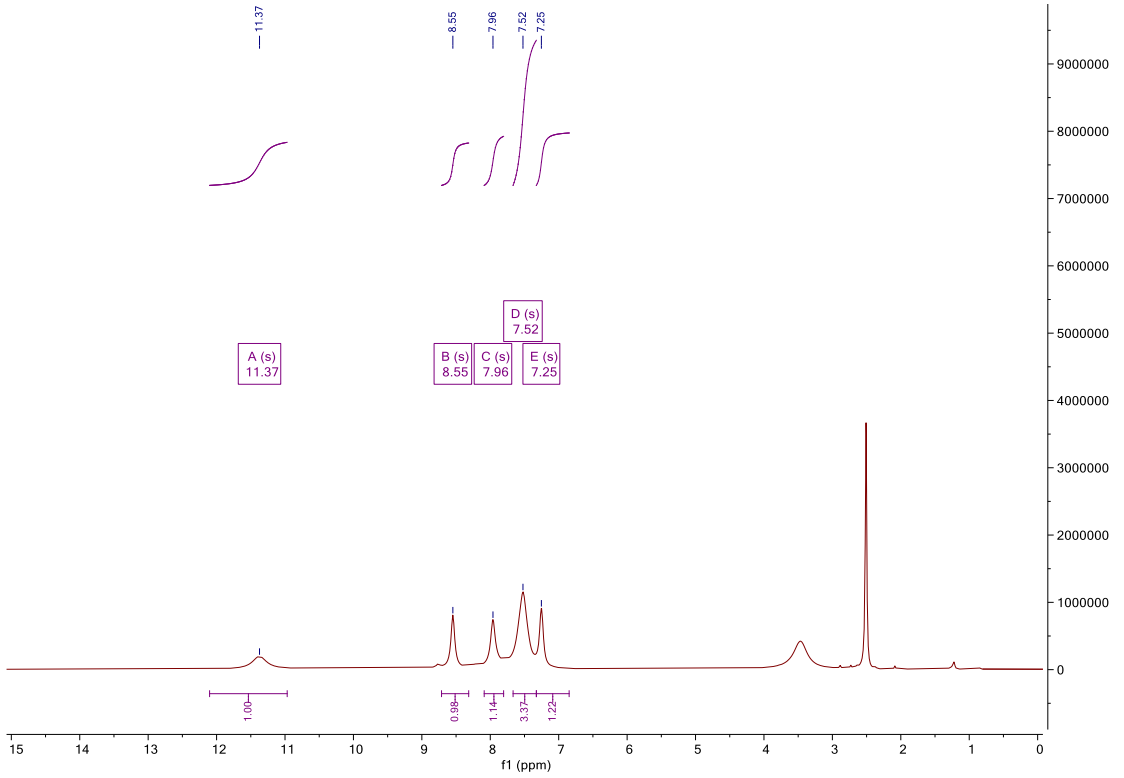

Figure SB18. ^{1}H NMR (DMSO-d_6, 500MHz) spectrum of **3.4**.

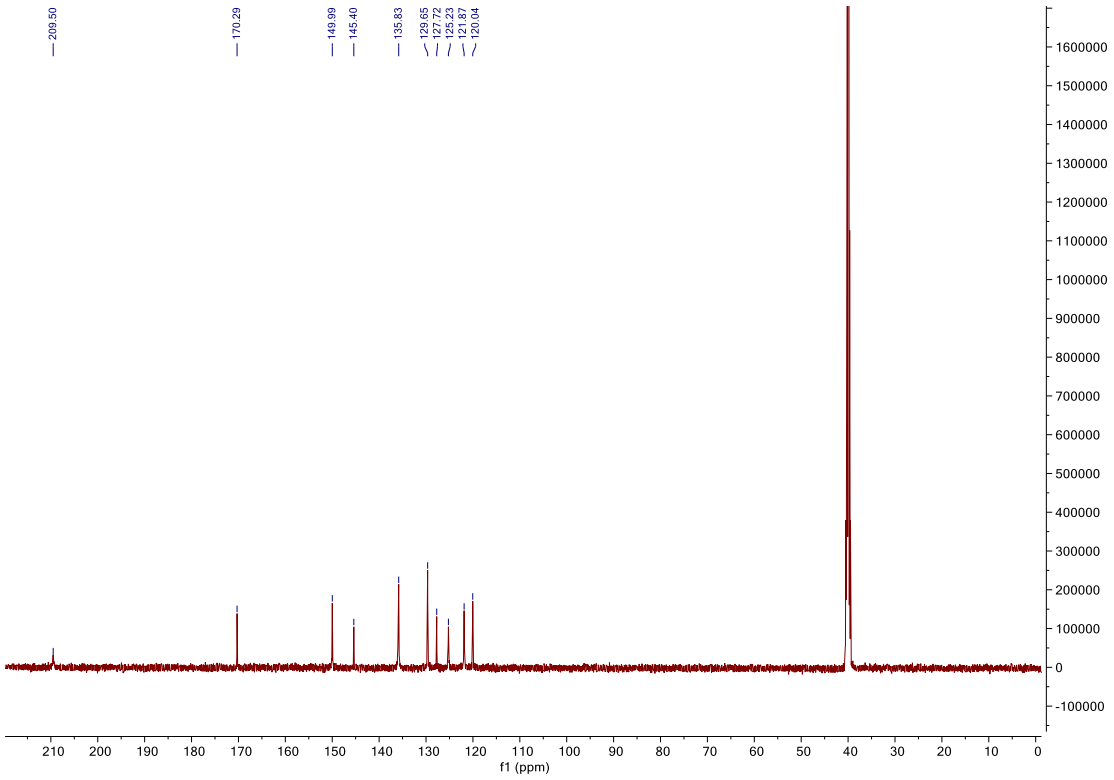

Figure SB19. ^{13}C NMR (DMSO-d_6, 126MHz) spectrum of **3.4**.

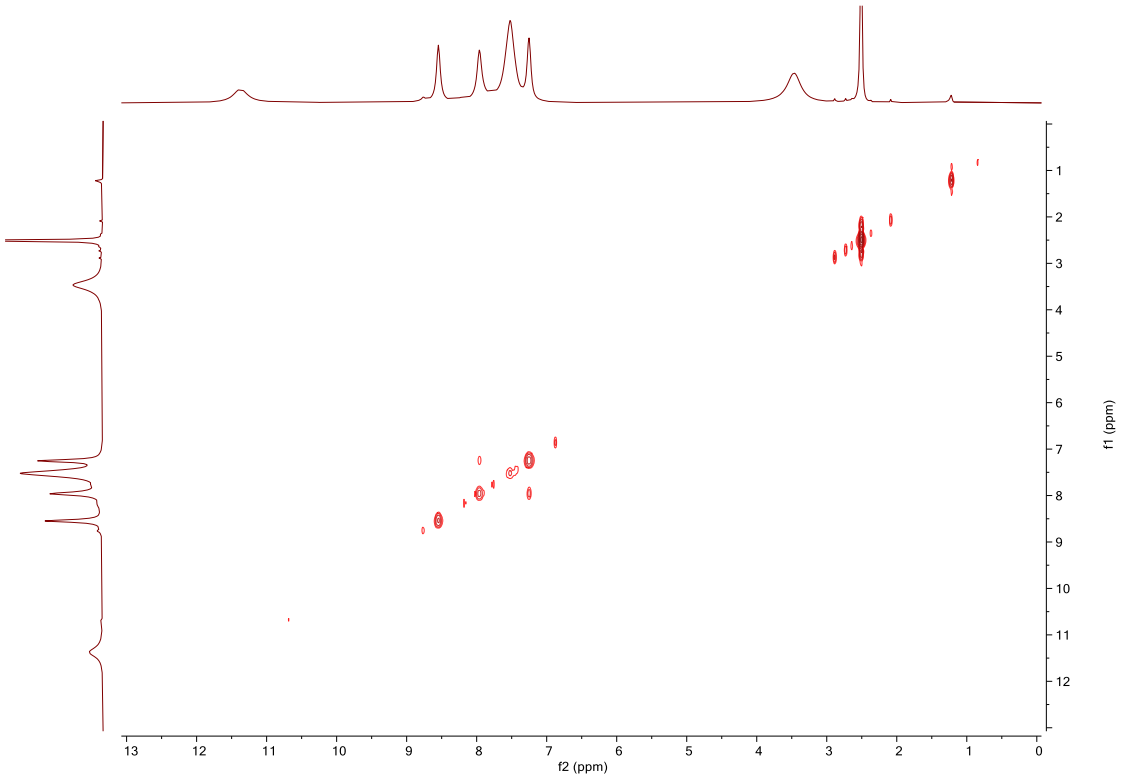

Figure SB20. COSY NMR (DMSO-d_6) spectrum of **3.3**.

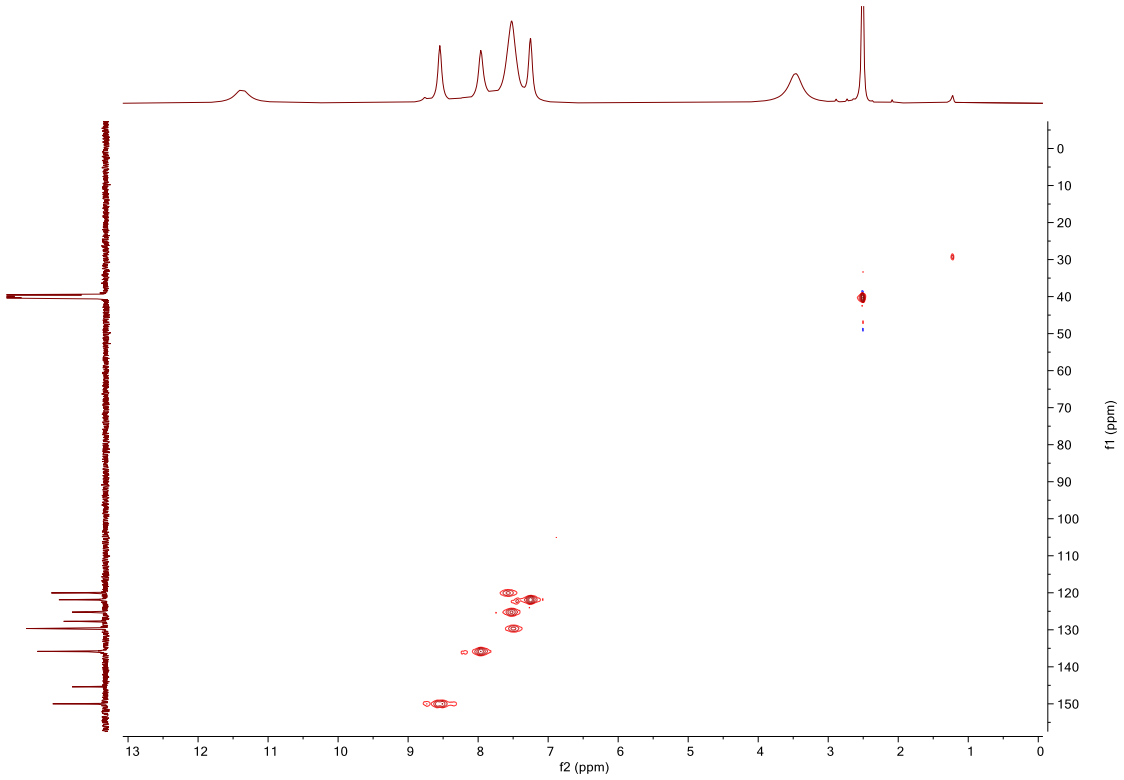

Figure SB21. HSQC NMR (DMSO-d_6) spectrum of **3.4**.

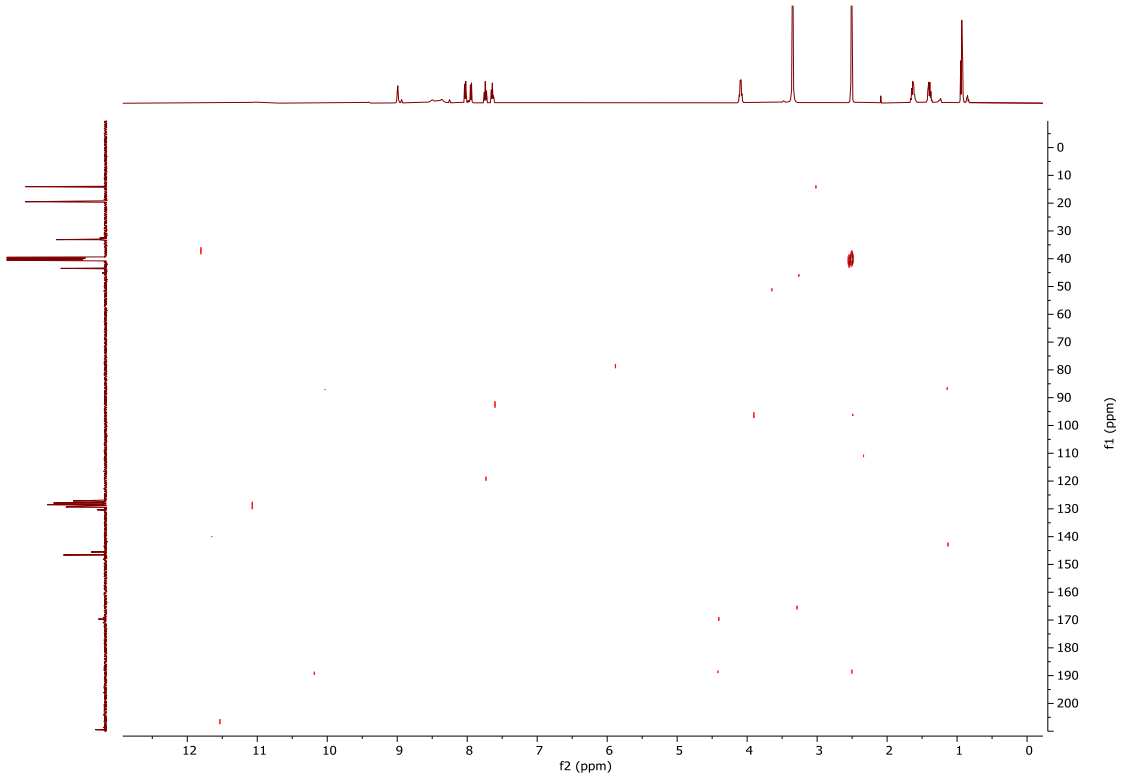

Figure SB22. HMBC NMR (DMSO-d_6) spectrum of **3.4**.

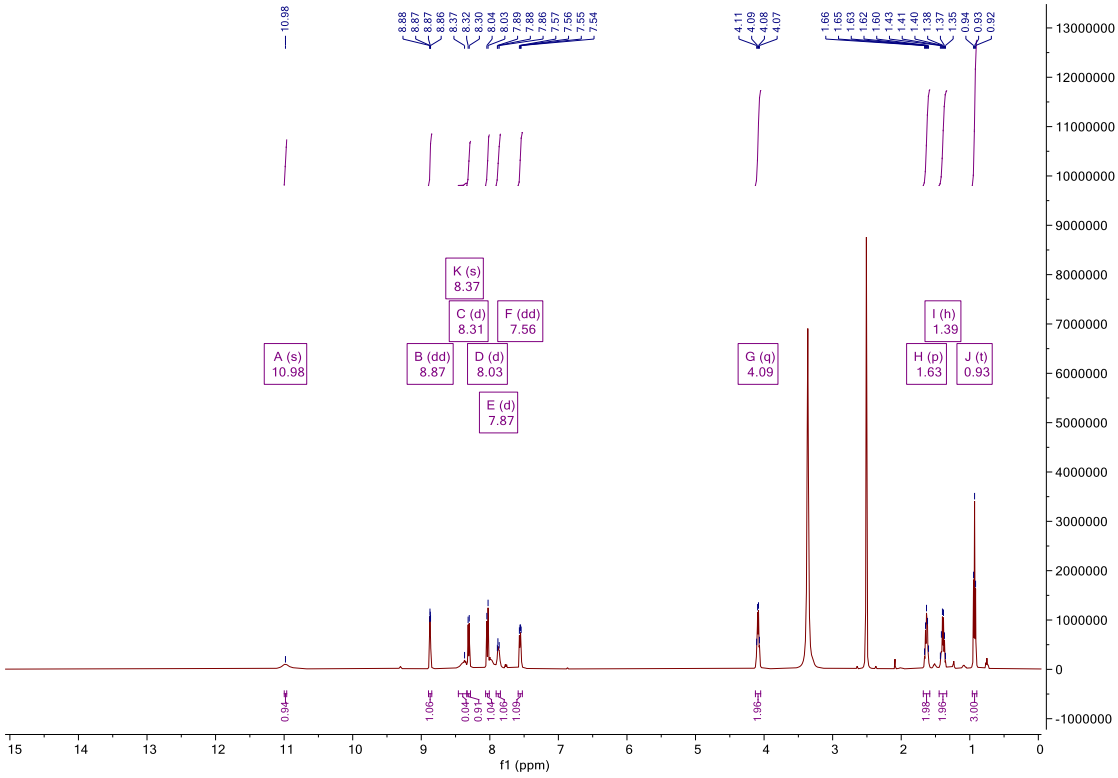

Figure SB22. ^{1}H NMR (DMSO-d_6, 500MHz) spectrum of **3.5**.

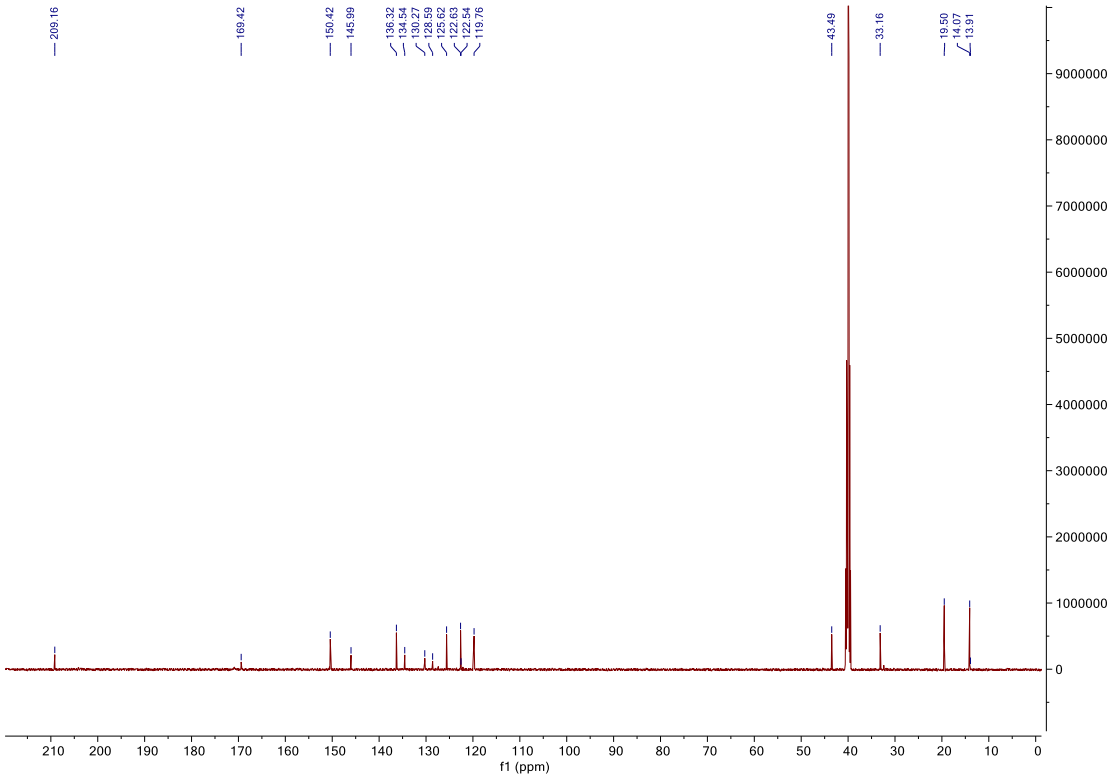

Figure SB23. ^{13}C NMR (DMSO-d_6, 126MHz) spectrum of **3.5**.

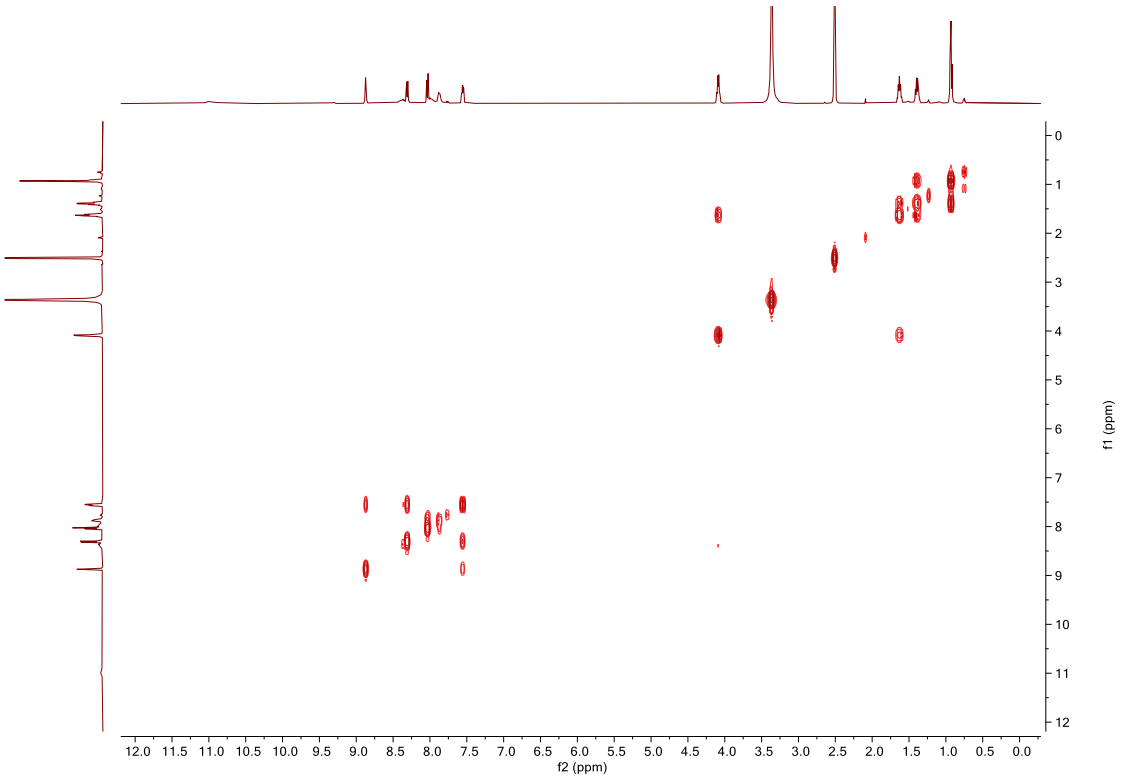

Figure SB24. COSY NMR (DMSO-d_6) spectrum of **3.5**.

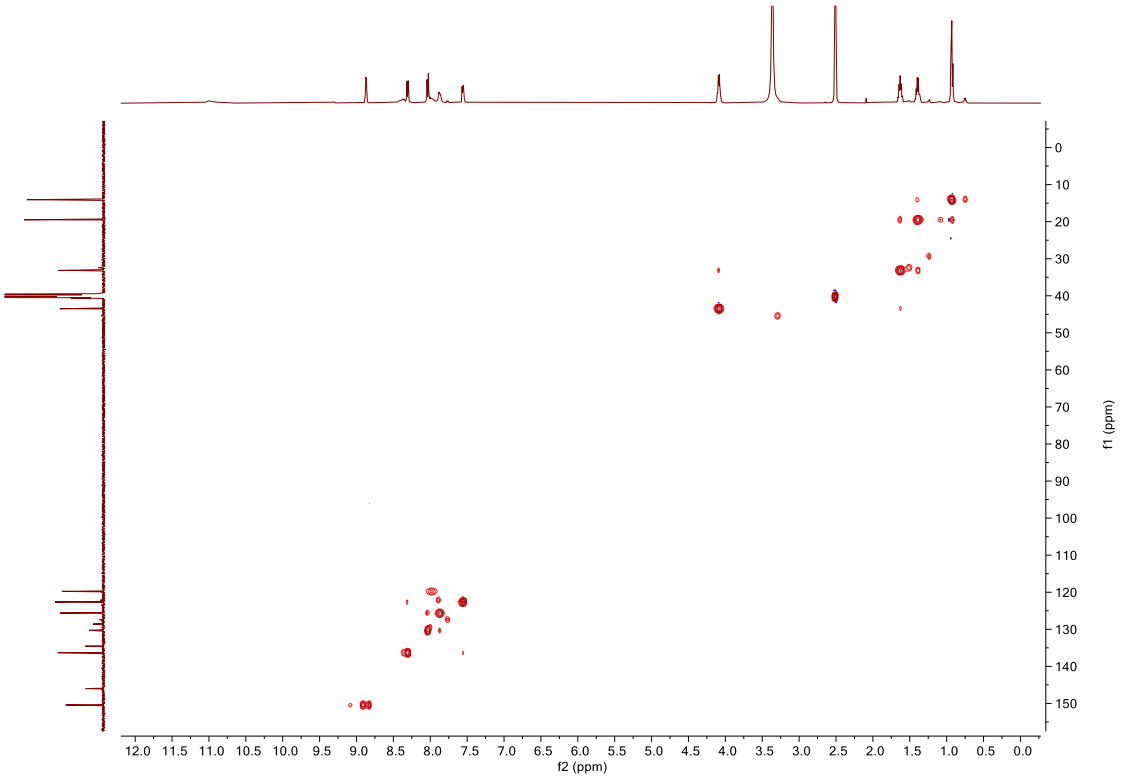

Figure SB25. HSQC NMR (DMSO-d_6) spectrum of **3.5**.

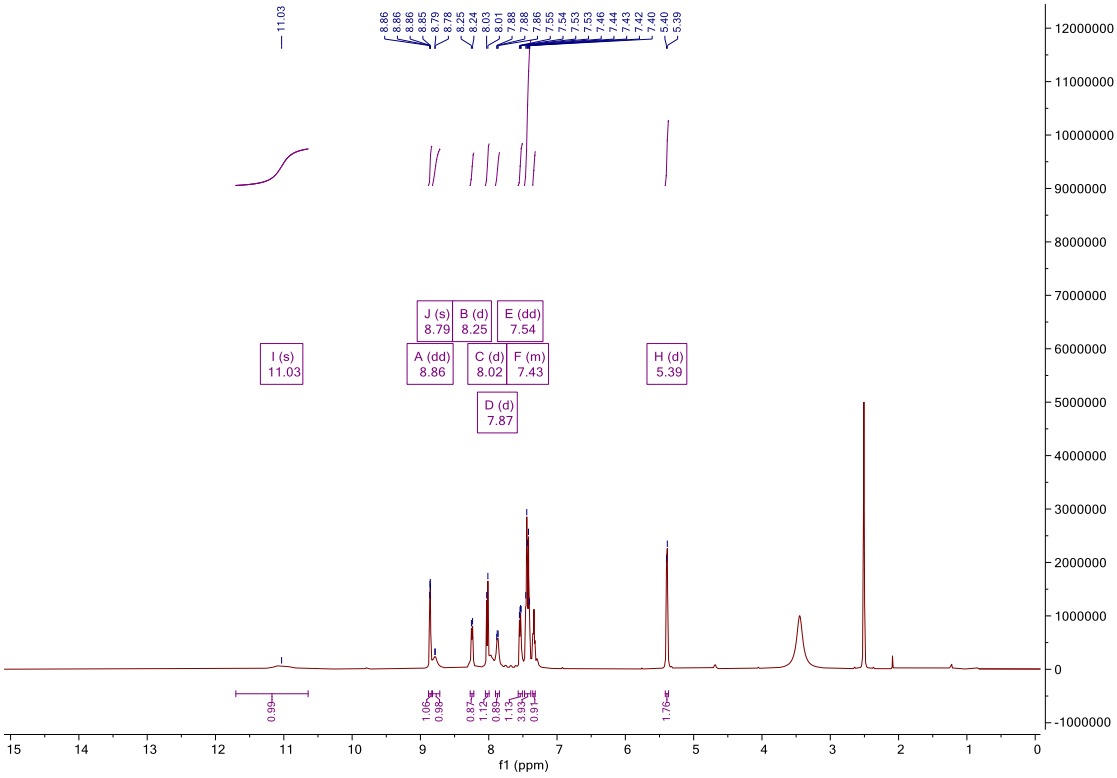

Figure SB26. ^{1}H NMR (DMSO-d_6, 500MHz) spectrum of **3.6**.

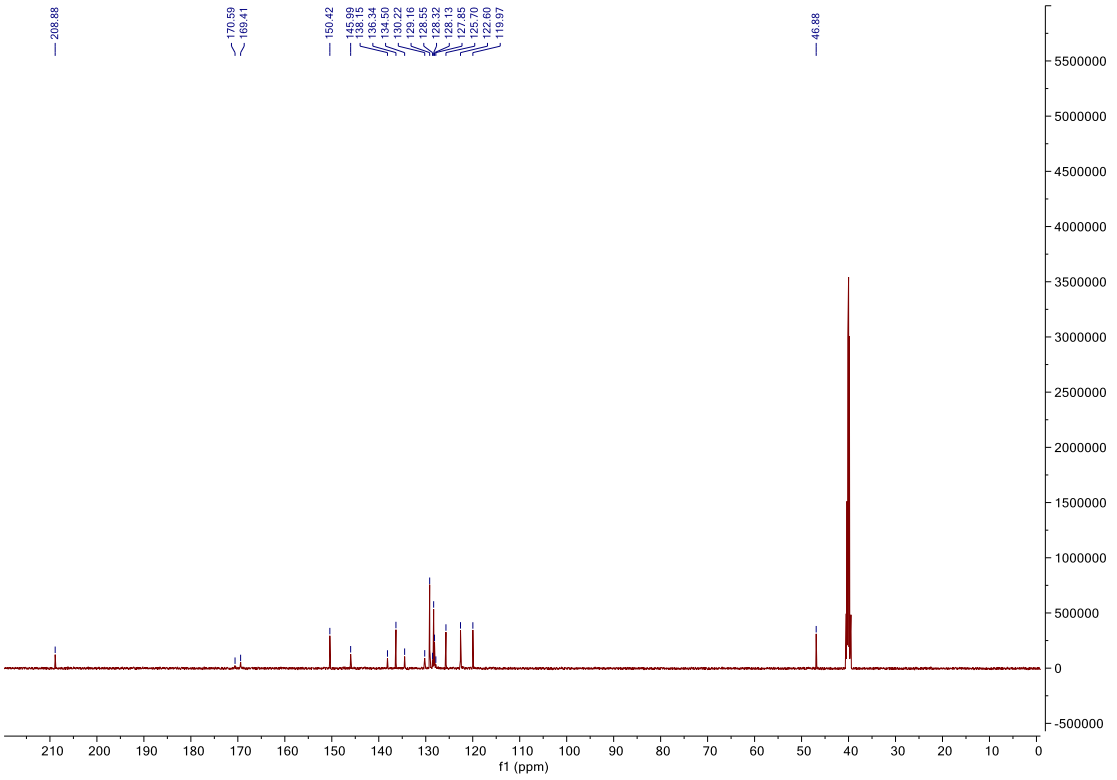

Figure SB27. ^{13}C NMR (DMSO-d_6, 126MHz) spectrum of **3.6**.

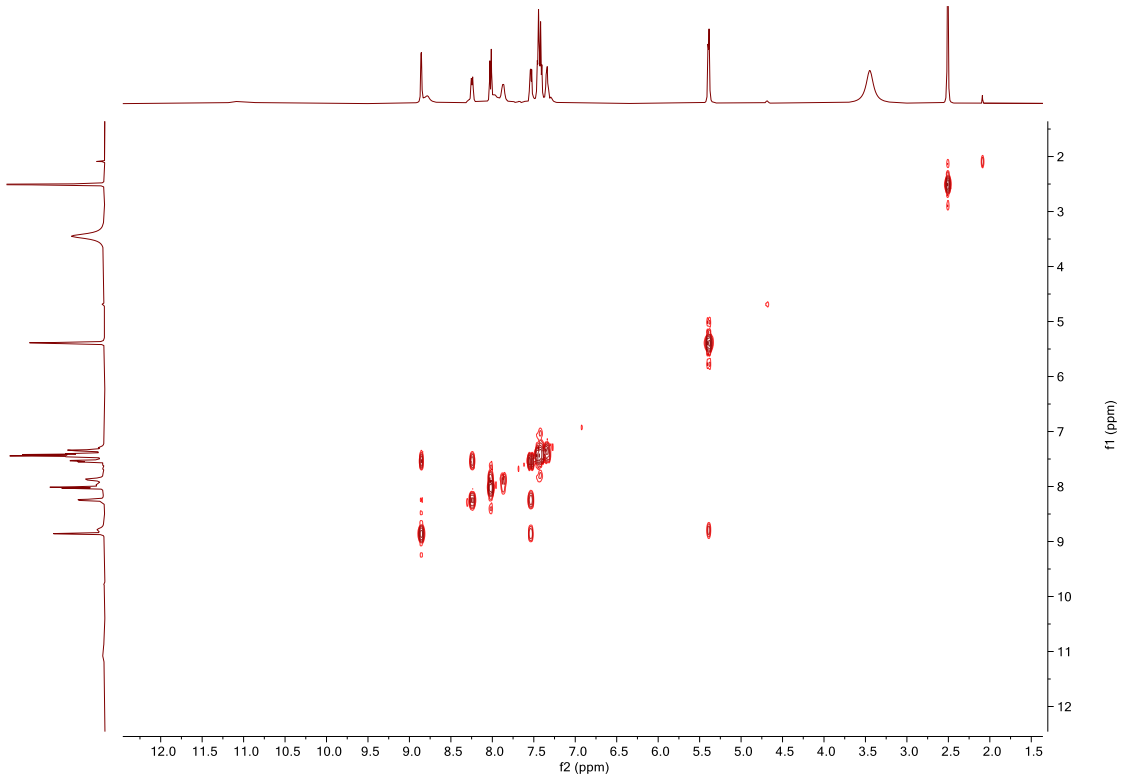

Figure SB28. COSY NMR (DMSO-d_6) spectrum of **3.6**.

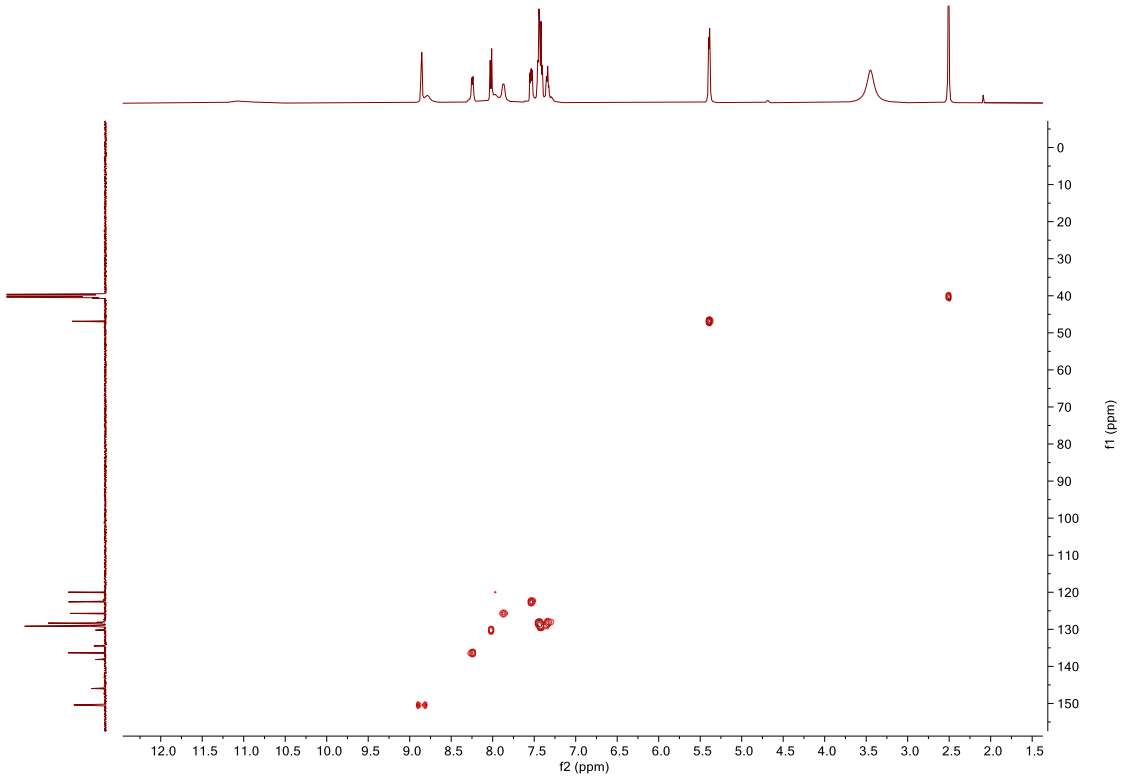

Figure SB29. HSQC NMR (DMSO-d_6) spectrum of **3.6**.

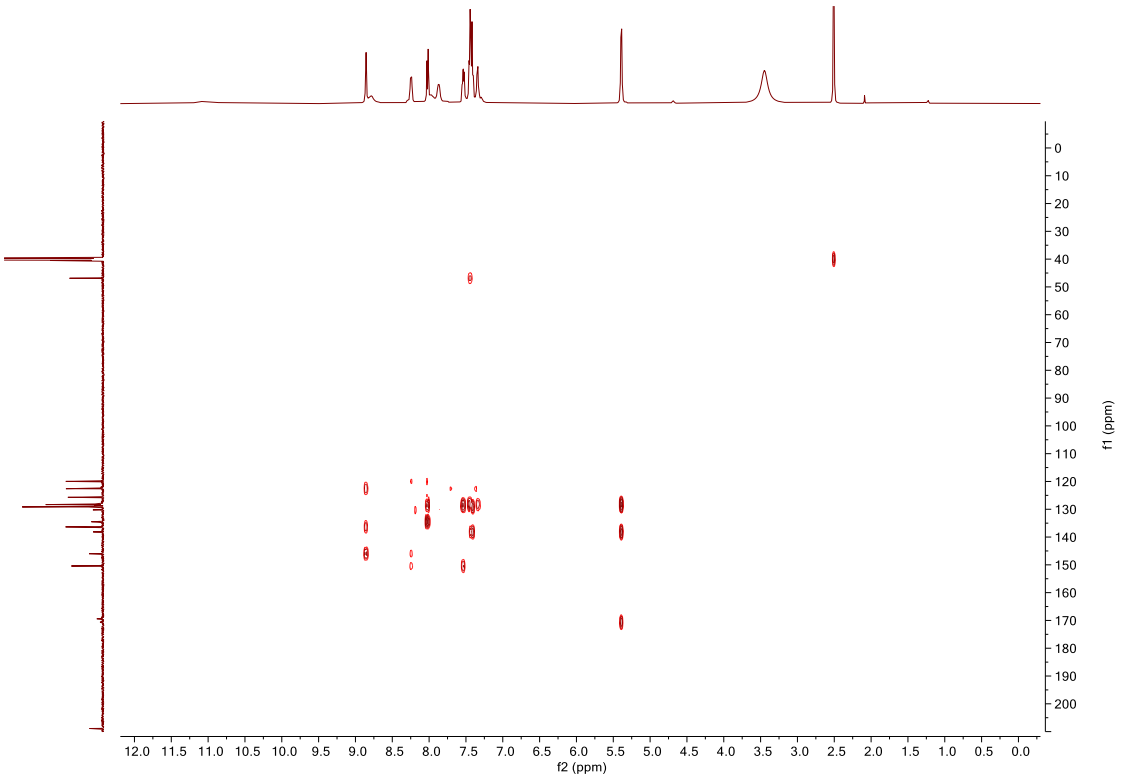

Figure SB30. HMBC NMR (DMSO-d_6) spectrum of **3.6**.

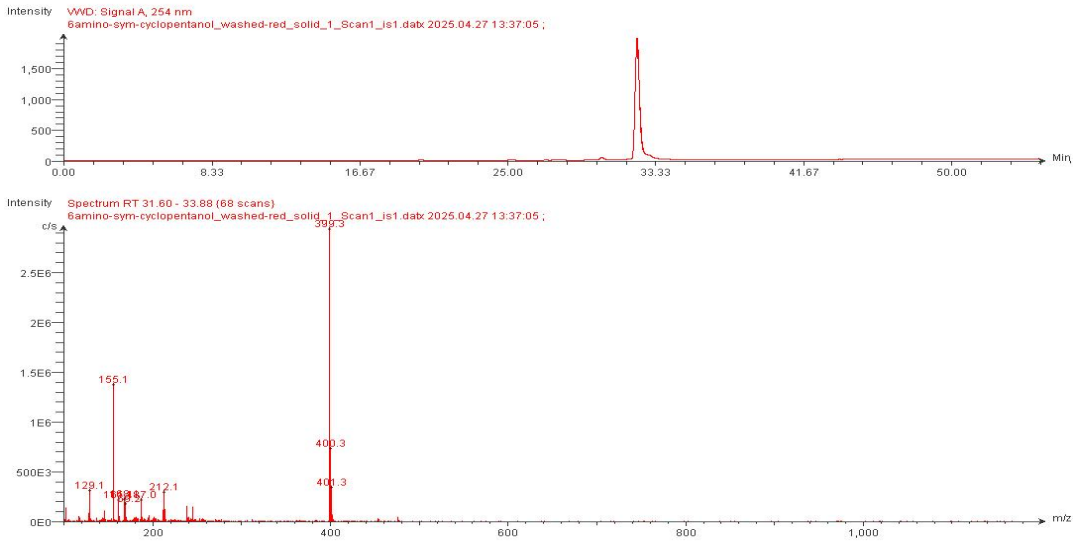

Figure SB31. Analytical LC-MS trace of **3.1**, $(M+H)^+$: 399.

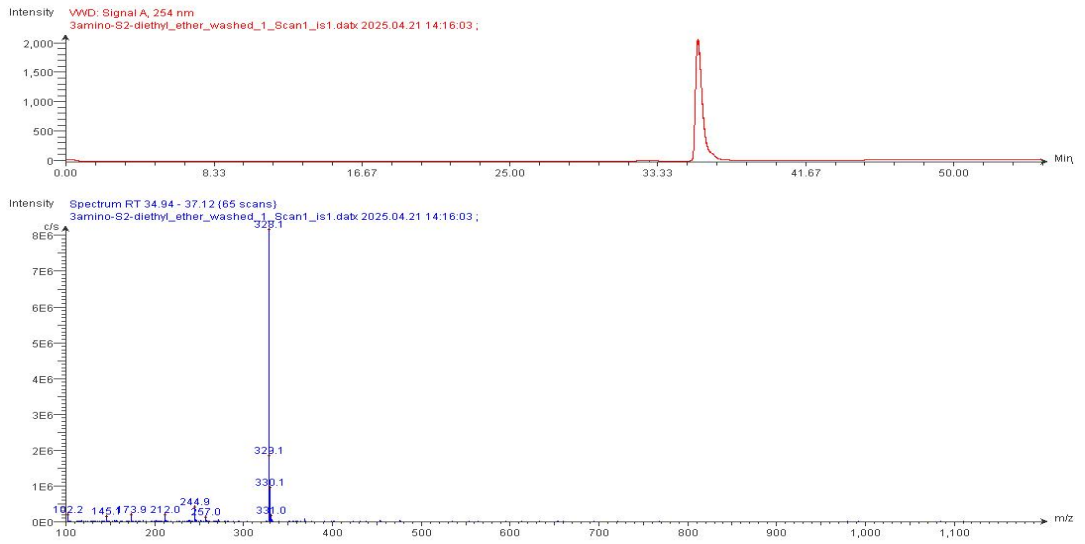

Figure SB32. Analytical LC-MS trace of **3.2**, $(M+H)^+$: 328.

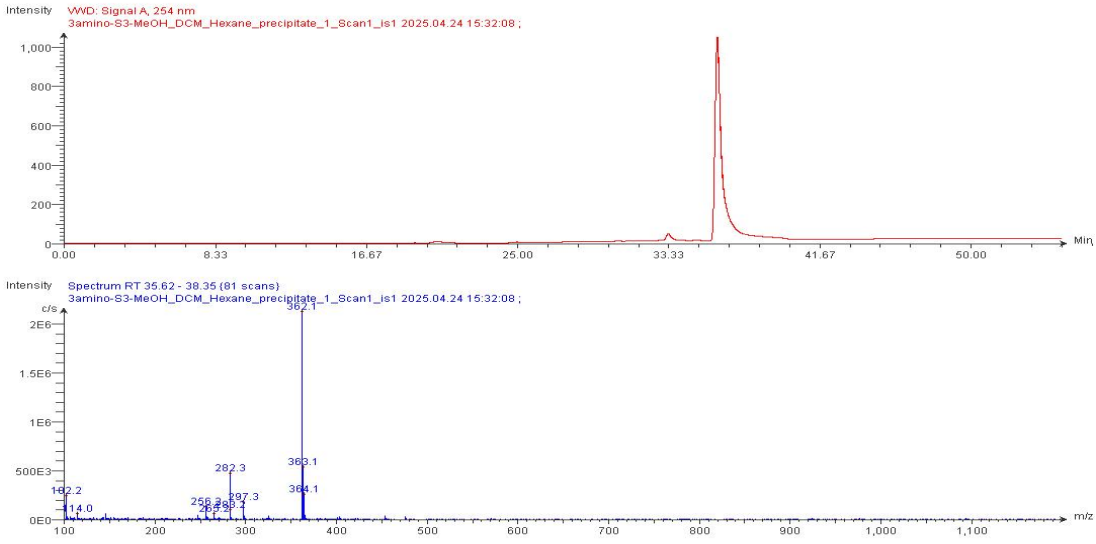

Figure SB33. Analytical LC-MS trace of **3.3**, $(M+H)^+$: 362.

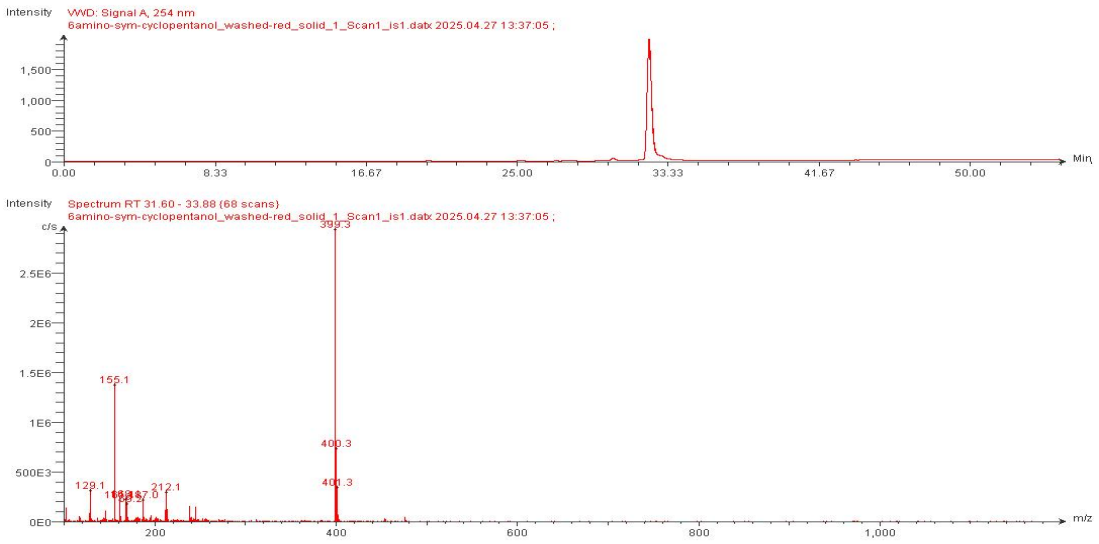

Figure SB34. Analytical LC-MS trace of **3.4**, $(M+H)^+$: 399.

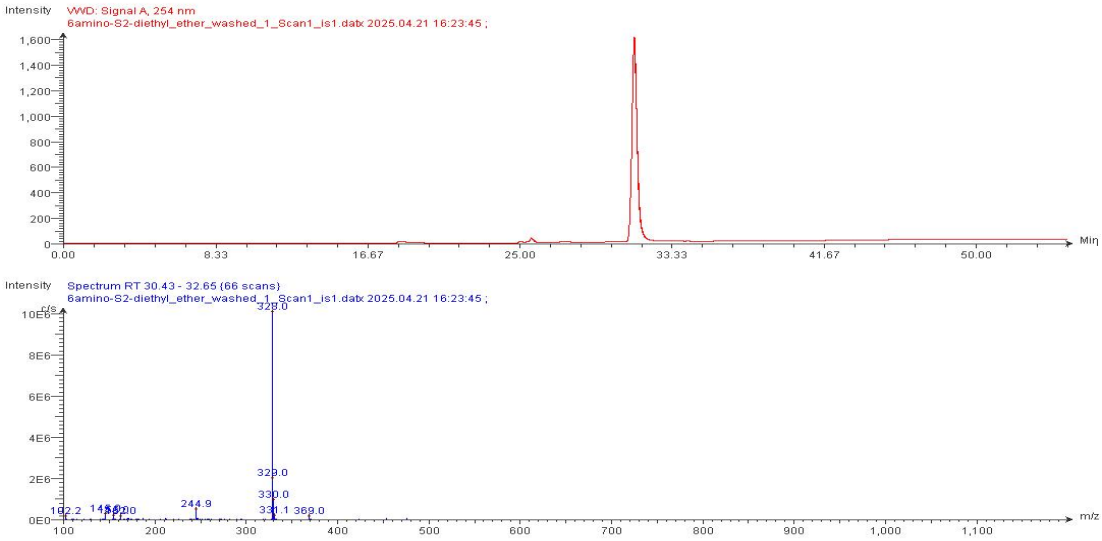

Figure SB35. Analytical LC-MS trace of **3.5**, $(M+H)^+$: 328.

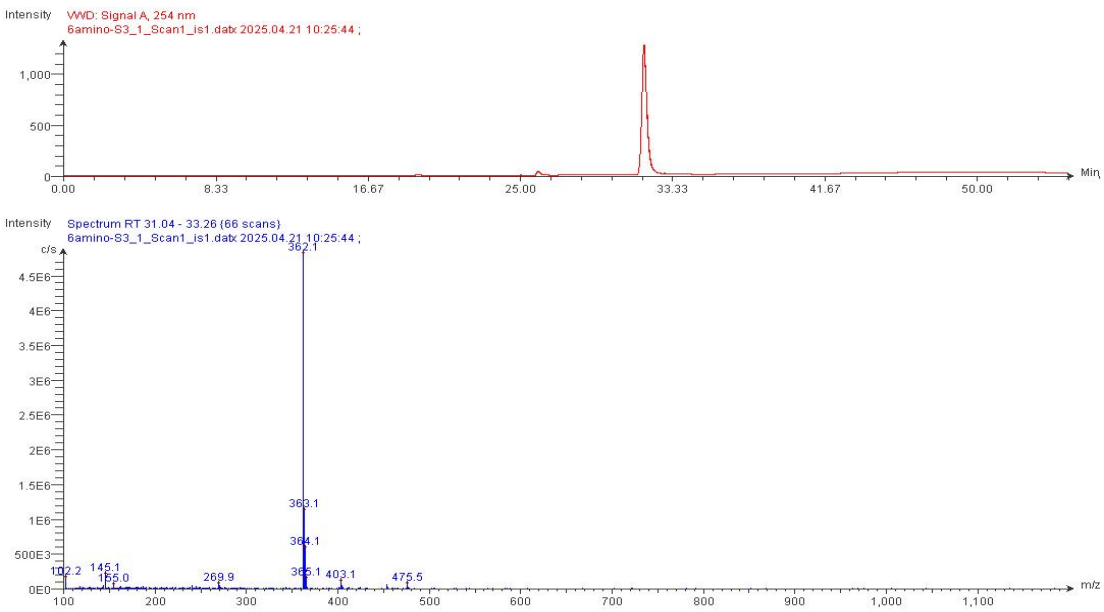

Figure SB36. Analytical LC-MS trace of **3.6**, $(M+H)^+$: 362.

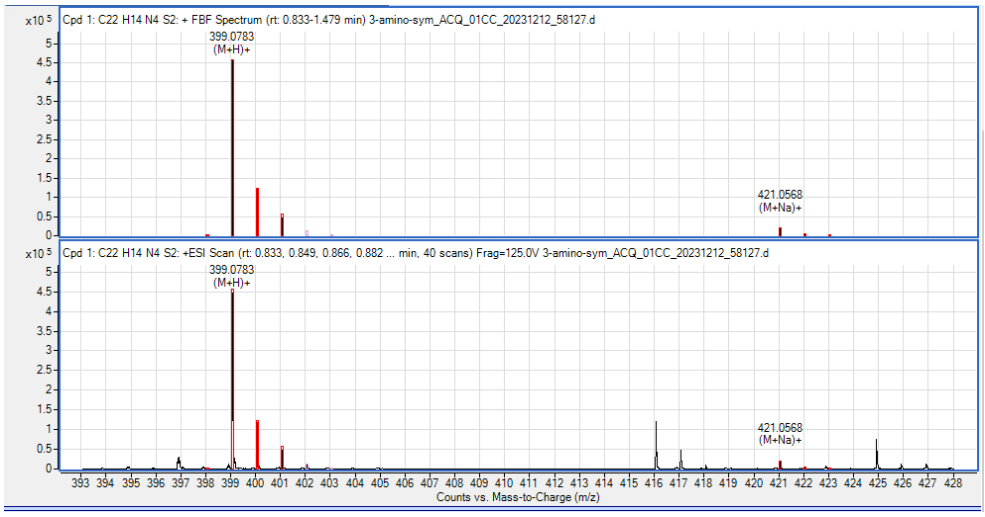

Figure SB37. Analytical HRMS trace of **3.1**.

Figure: Extracted ion chromatogram (EIC) of compound.

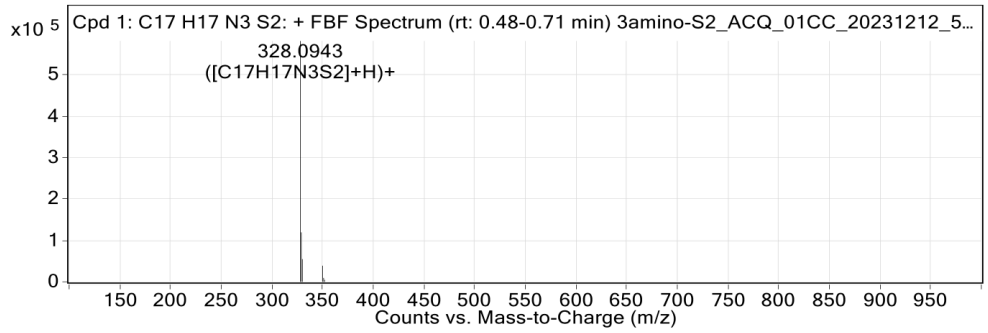

Figure: Full range view of Compound spectra and potential adducts.

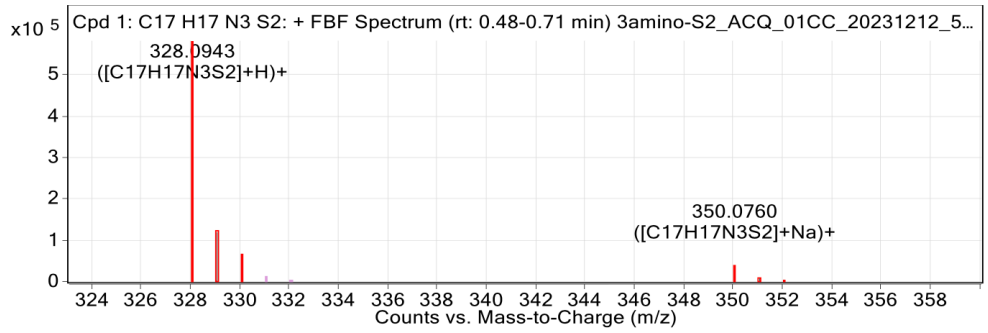

Figure SB38. Analytical HRMS trace of **3.2**.

Figure: Extracted ion chromatogram (EIC) of compound.

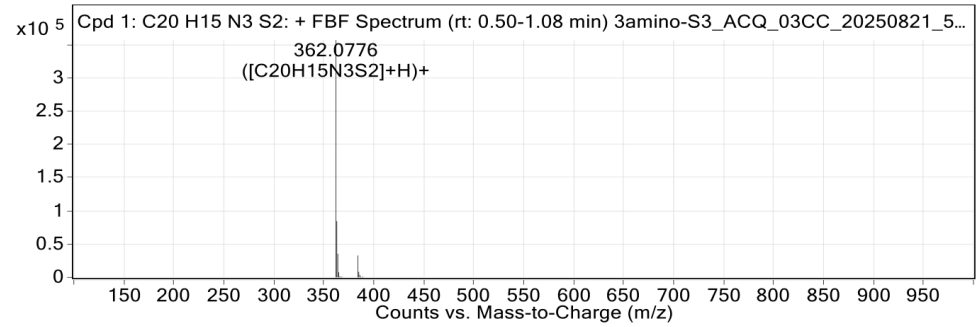

Figure: Full range view of Compound spectra and potential adducts.

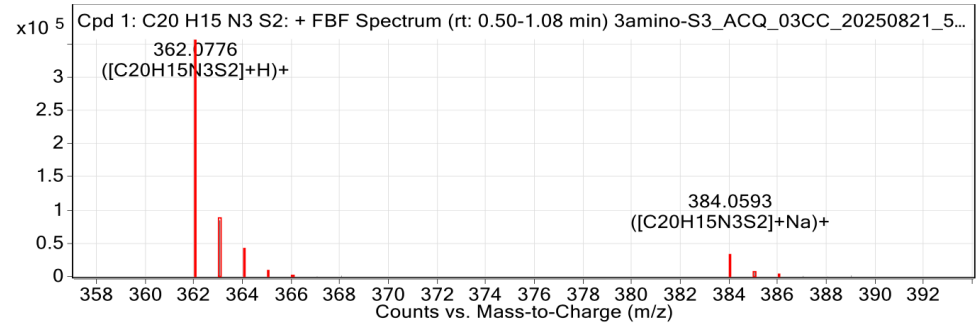

Figure SB39. Analytical HRMS trace of **3.3**.

Figure: Extracted ion chromatogram (EIC) of compound.

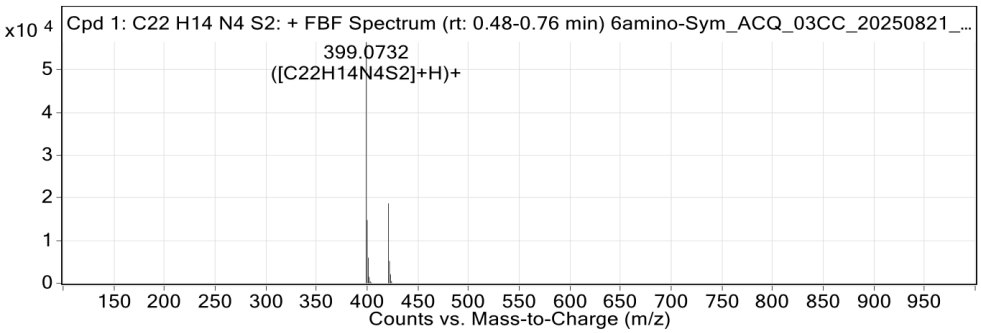

Figure: Full range view of Compound spectra and potential adducts.

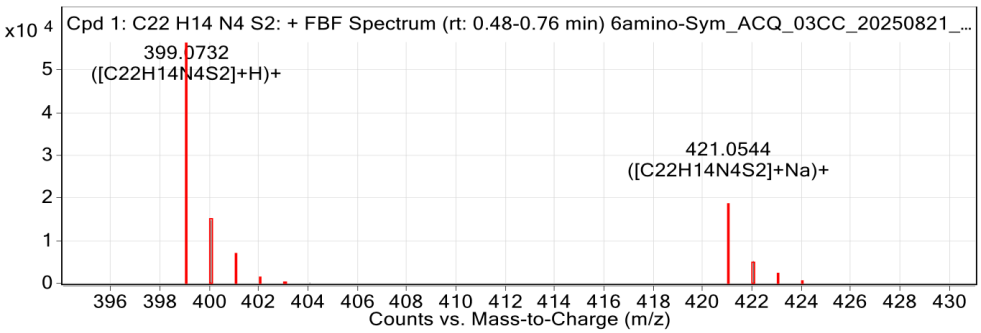

Figure SB40. Analytical HRMS trace of **3.4**.

Figure: Extracted ion chromatogram (EIC) of compound.

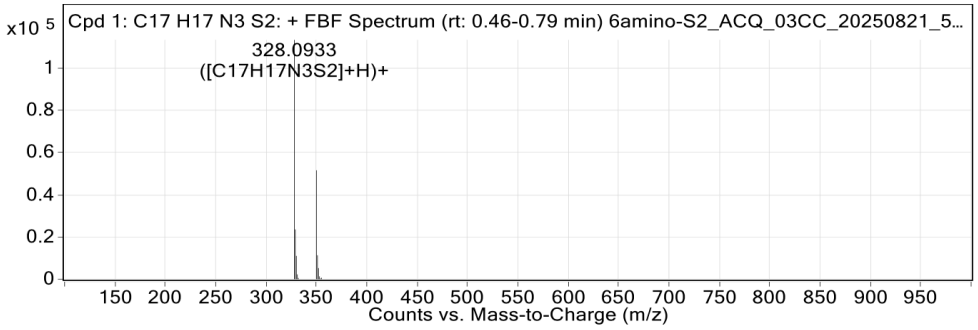

Figure: Full range view of Compound spectra and potential adducts.

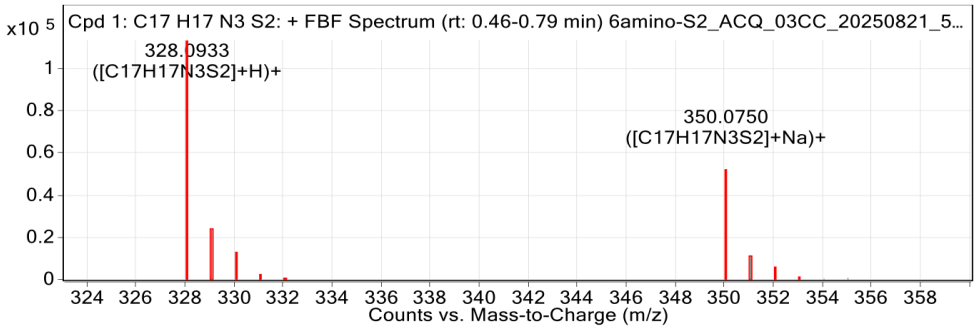

Figure SB41. Analytical HRMS trace of **3.5**.

Figure: Extracted ion chromatogram (EIC) of compound.

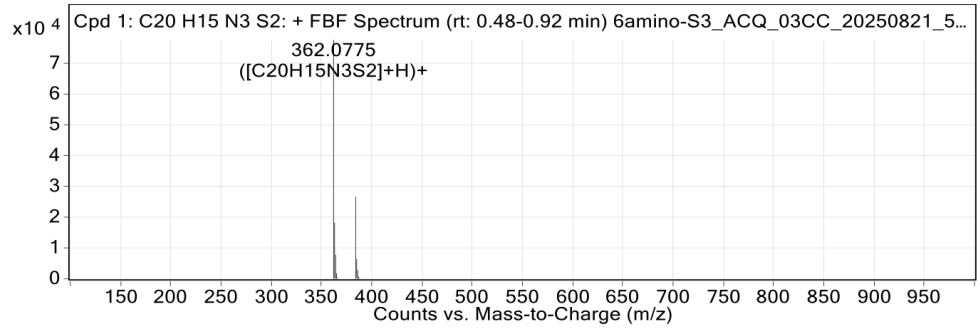

Figure: Full range view of Compound spectra and potential adducts.

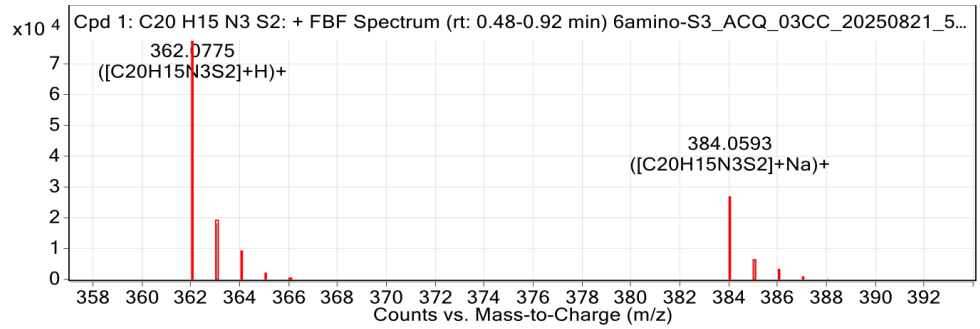

Figure SB42. Analytical HRMS trace of **3.6**.

Table SB1. A summary of UV-vis titration results for the binding behaviour of **3.1** towards various metal ions.[a]

Metal ions	K_{11} (M^{-1})	K_{12} (M^{-1})	Binding mode
Ag^{+}	-[b]	-[b]	2:1
Cd^{2+}	-[b]	-[b]	2:1
Co^{2+}	3.6×10^4	8.6×10^5	2:1
Cu^{2+}	1.1×10^4	9.9×10^4	2:1
Ni^{2+}	-[b]	-[b]	2:1
Pd^{2+}	2.9×10^4	1.2×10^4	2:1
Zn^{2+}	1.0×10^5	9.2×10^5	2:1

a The errors of the K_a value shown in the table are < 25%. b High errors result in unreliable K_a value.

Table SB2. A summary of UV-vis titration results for the binding behaviour of **3.2** towards various metal ions.[a]

Metal ions	K_{11} (M^{-1})	K_{12} (M^{-1})	Binding mode
Ag^{+}	-[b]	-[b]	2:1
Cd^{2+}	4.8×10^4	9.6×10^5	2:1
Co^{2+}	6.0×10^4	3.8×10^5	2:1
Cu^{2+}	2.3×10^4	8.1×10^5	2:1
Ni^{2+}	2.9×10^4	5.8×10^5	2:1
Pd^{2+}	1.6×10^4	7.1×10^4	2:1
Zn^{2+}	-[b]	-[b]	2:1

a The errors of the K_a value shown in the table are < 25%. b High errors result in unreliable K_a value.

Table SB3. A summary of UV-vis titration results for the binding behaviour of **3.3** towards various metal ions.[a]

Metal ions	K_{11} (M^{-1})	K_{12} (M^{-1})	Binding mode
Ag^{+}	4.7×10^4	2.3×10^4	2:1
Cd^{2+}	3.5×10^4	1.0×10^4	2:1
Co^{2+}	-[b]	-[b]	2:1
Cu^{2+}	2.3×10^4	1.4×10^4	2:1
Ni^{2+}	-[b]	-[b]	2:1
Pd^{2+}	2.5×10^4	1.0×10^5	2:1
Zn^{2+}	1.4×10^5	3.6×10^5	2:1

a The errors of the K_a value shown in the table are < 25%. b High errors result in unreliable K_a value.

Table SB4. A summary of UV-vis titration results for the binding behaviour of **3.4** towards various metal ions.[a]

Metal ions	K_{11} (M^{-1})	K_{12} (M^{-1})	Binding mode
Ag^{+}	-[b]	-[b]	2:1
Cd^{2+}	4.5×10^5	8.6×10^5	2:1
Co^{2+}	-[b]	-[b]	2:1
Cu^{2+}	-[b]	-[b]	2:1
Ni^{2+}	-[b]	-[b]	2:1
Pd^{2+}	5.8×10^5	3.0×10^5	2:1
Zn^{2+}	8.0×10^4	3.3×10^5	2:1

a The errors of the K_a value shown in the table are < 25%. b High errors result in unreliable K_a value.

Table SB5. A summary of UV-vis titration results for the binding behaviour of **3.5** towards various metal ions.[a]

Metal ions	K_{11} (M^{-1})	K_{12} (M^{-1})	Binding mode
Ag^{+}	-[b]	-[b]	2:1
Cd^{2+}	-[b]	-[b]	2:1
Co^{2+}	1.8×10^5	1.9×10^4	2:1
Cu^{2+}	-[b]	-[b]	2:1
Ni^{2+}	5.5×10^4	3.8×10^5	2:1
Pd^{2+}	-[b]	-[b]	2:1
Zn^{2+}	-[b]	-[b]	2:1

a The errors of the K_a value shown in the table are < 25%. b High errors result in unreliable K_a value.

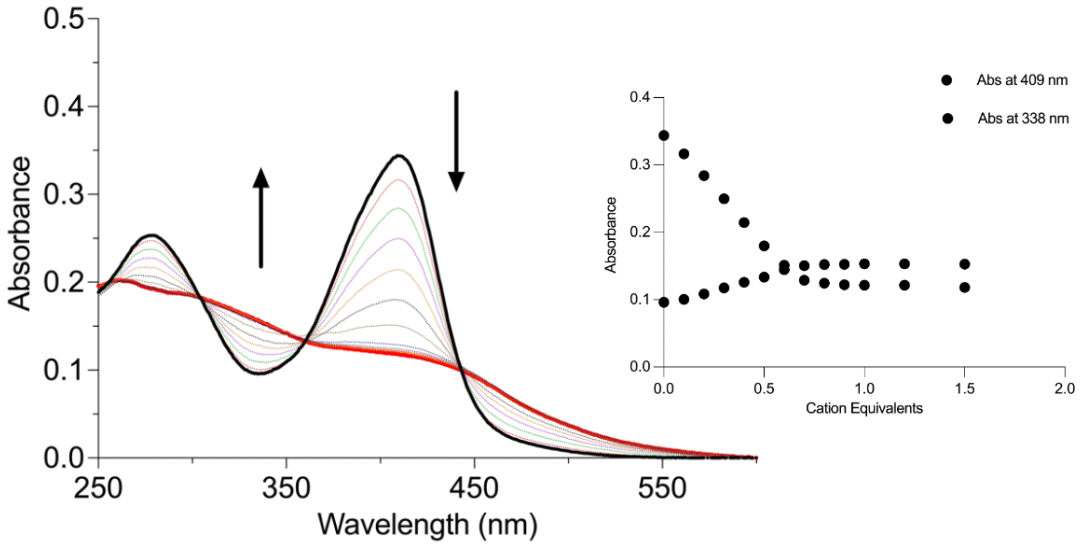

Figure SB43. Absorption spectra of Ag^+ titration of **3.1** (10 μM) in MeCN. {insert} Fitplot for absorbance at 409 and 338 nm.

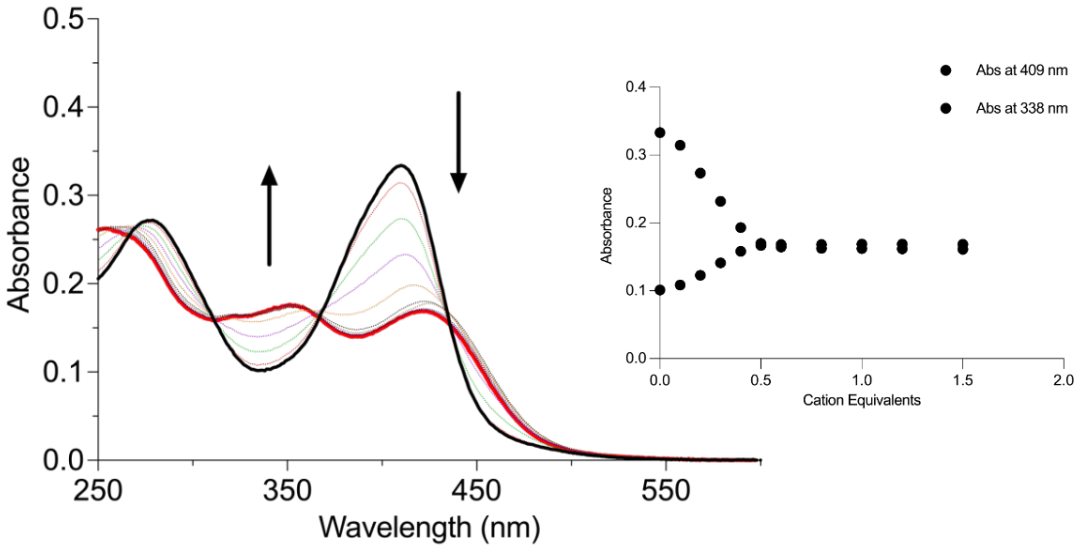

Figure SB44. Absorption spectra of Cd^{2+} titration of **3.1** (10 μM) in MeCN. {insert} Fitplot for absorbance at 409 and 338 nm.

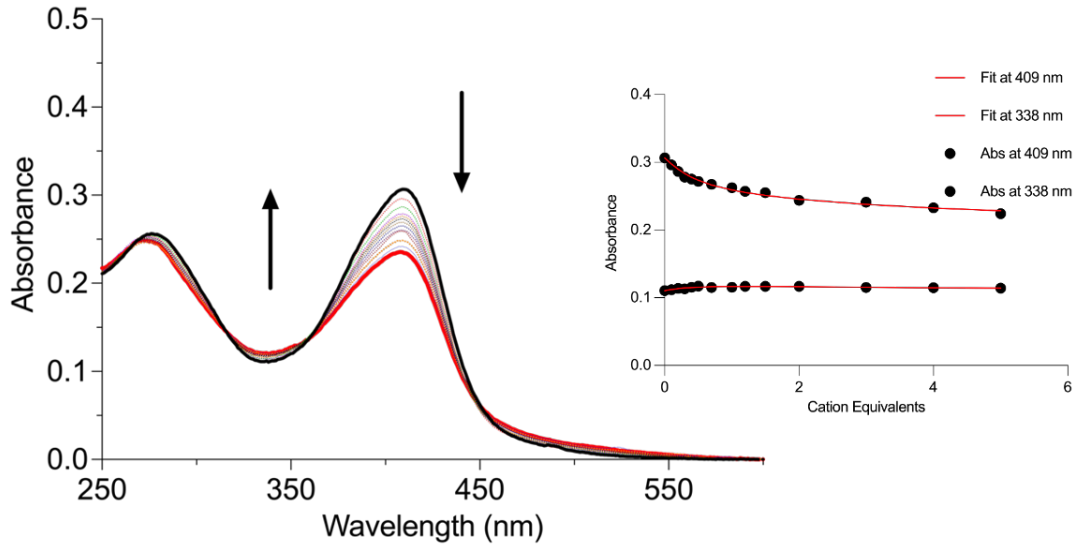

Figure SB45. Absorption spectra of Co^{2+} titration of **3.1** (10 μM) in MeCN. {insert} Fitplot for absorbance at 409 and 338 nm. The data were fitted to a 2:1 binding model.

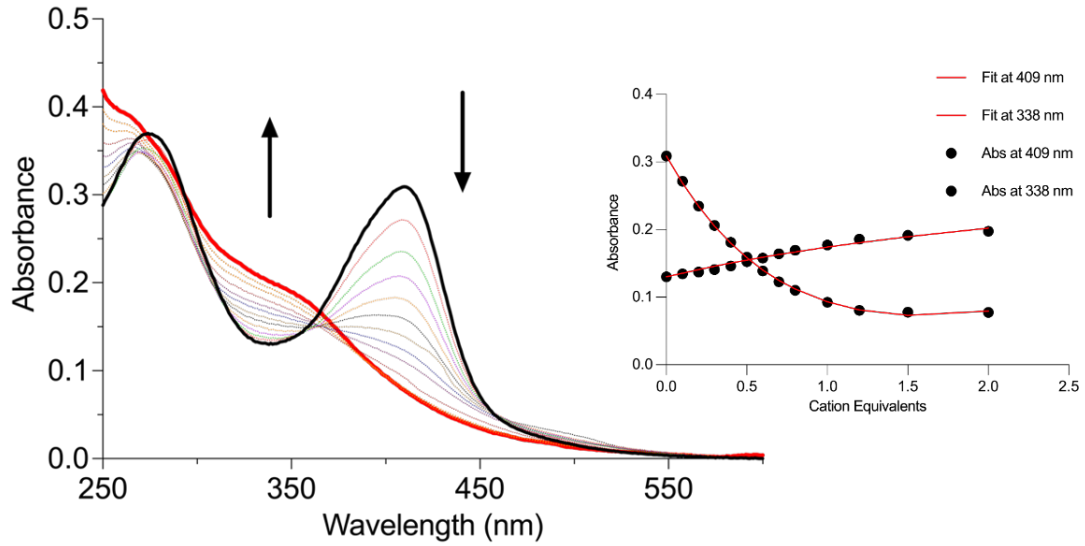

Figure SB46. Absorption spectra of Cu^{2+} titration of **3.1** (10 μM) in MeCN. {insert} Fitplot for absorbance at 409 and 338 nm. The data were fitted to a 2:1 binding model.

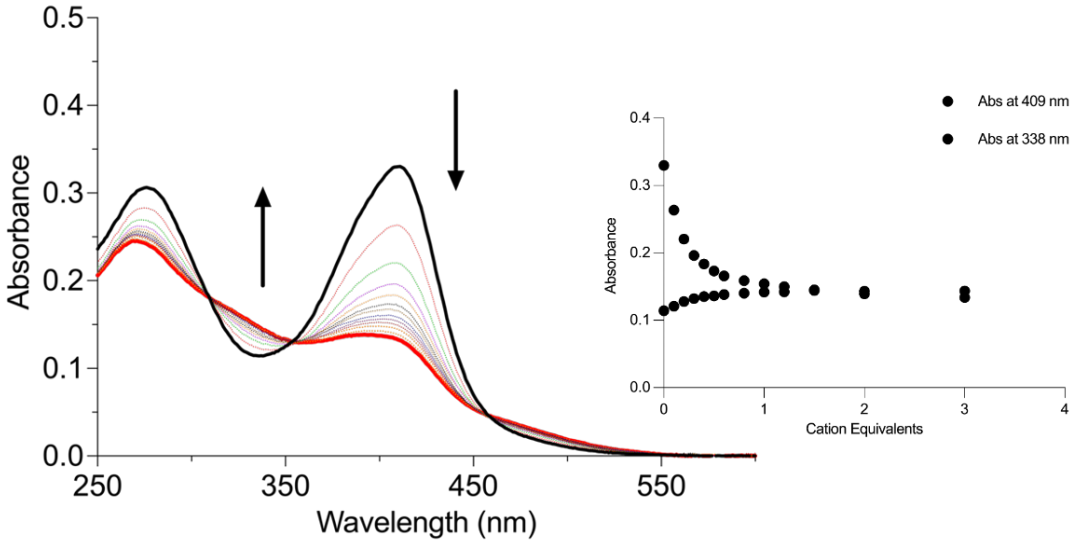

Figure SB47. Absorption spectra of Ni^{2+} titration of **3.1** (10 μM) in MeCN. {insert} Fitplot for absorbance at 409 and 338 nm.

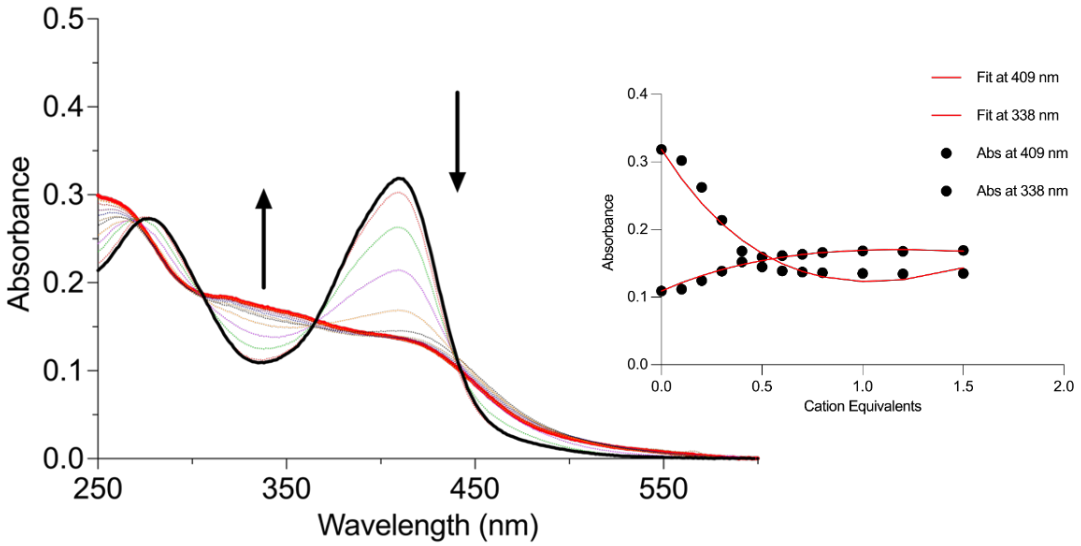

Figure SB48. Absorption spectra of Pb^{2+} titration of **3.1** (10 μM) in MeCN. {insert} Fitplot for absorbance at 409 and 338 nm. The data were fitted to a 2:1 binding model.

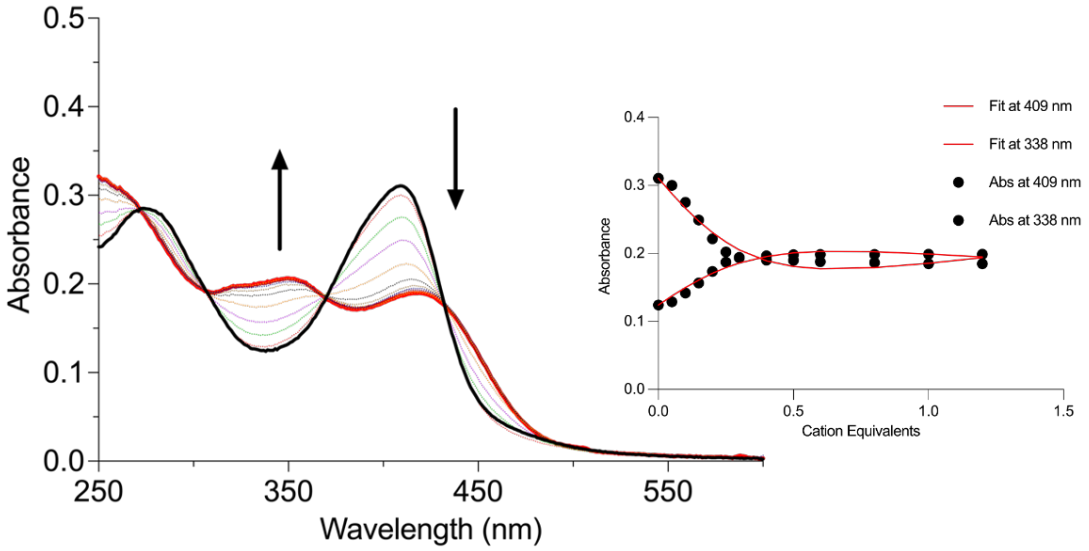

Figure SB49. Absorption spectra of Zn^{2+} titration of **3.1** (10 μM) in MeCN. {insert} Fitplot for absorbance at 409 and 338 nm. The data were fitted to a 2:1 binding model.

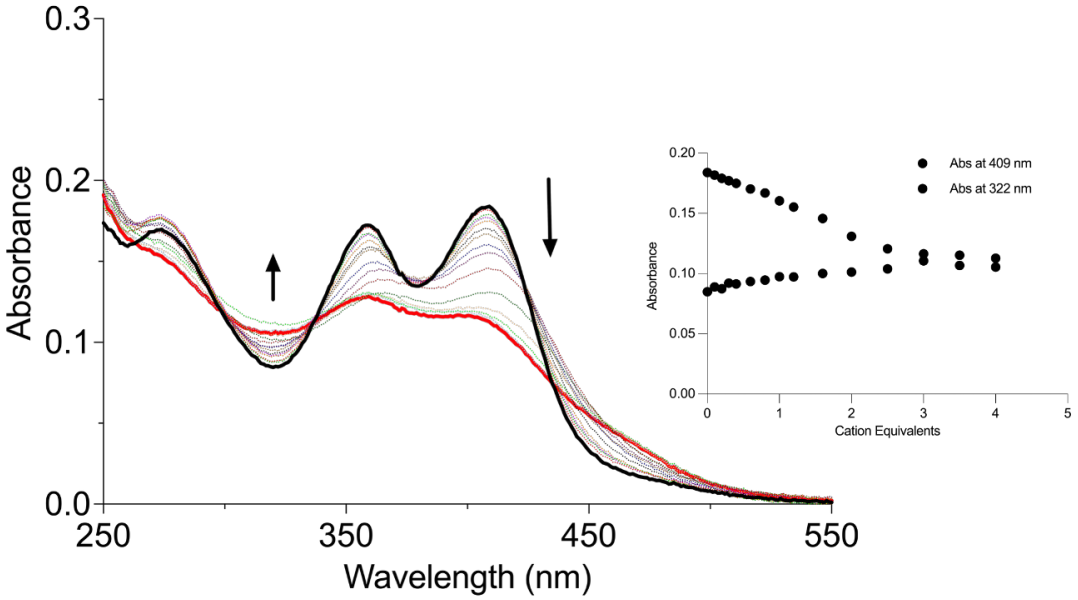

Figure SB50. Absorption spectra of Ag^{+} titration of **3.2** (10 μM) in MeCN. {insert} Fitplot for absorbance at 409 and 322 nm.

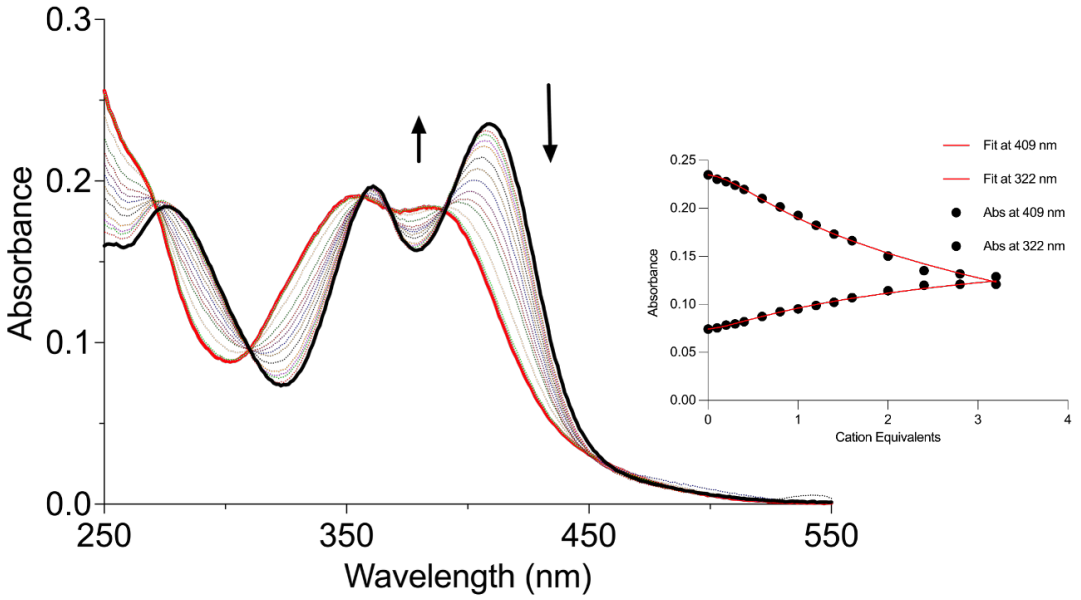

Figure SB51. Absorption spectra of Cd^{2+} titration of **3.2** (10 μM) in MeCN. {insert} Fitplot for absorbance at 409 and 322 nm. The data were fitted to a 2:1 binding model.

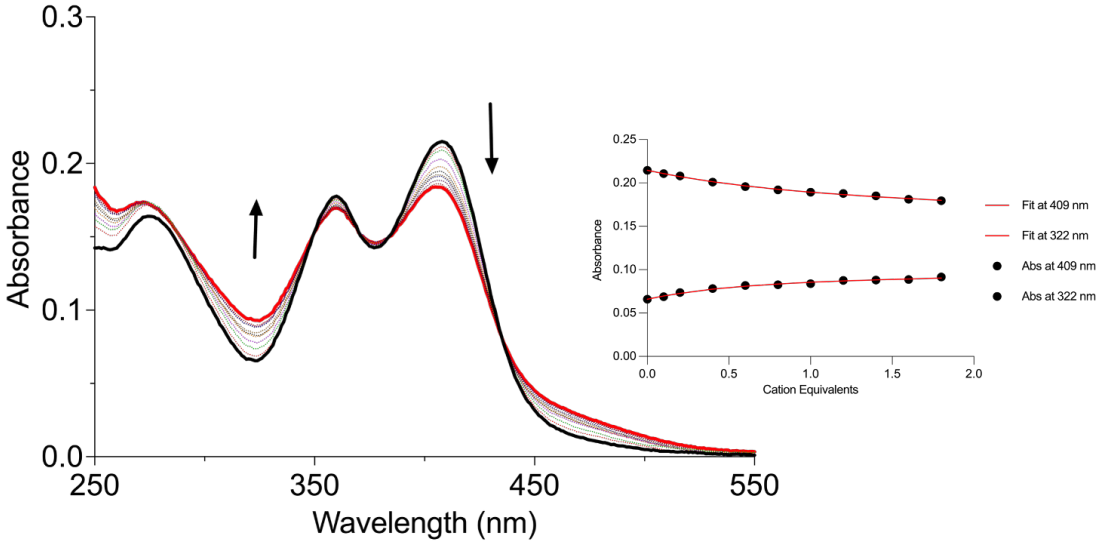

Figure SB52. Absorption spectra of Co^{2+} titration of **3.2** (10 μM) in MeCN. {insert} Fitplot for absorbance at 409 and 322 nm. The data were fitted to a 2:1 binding model.

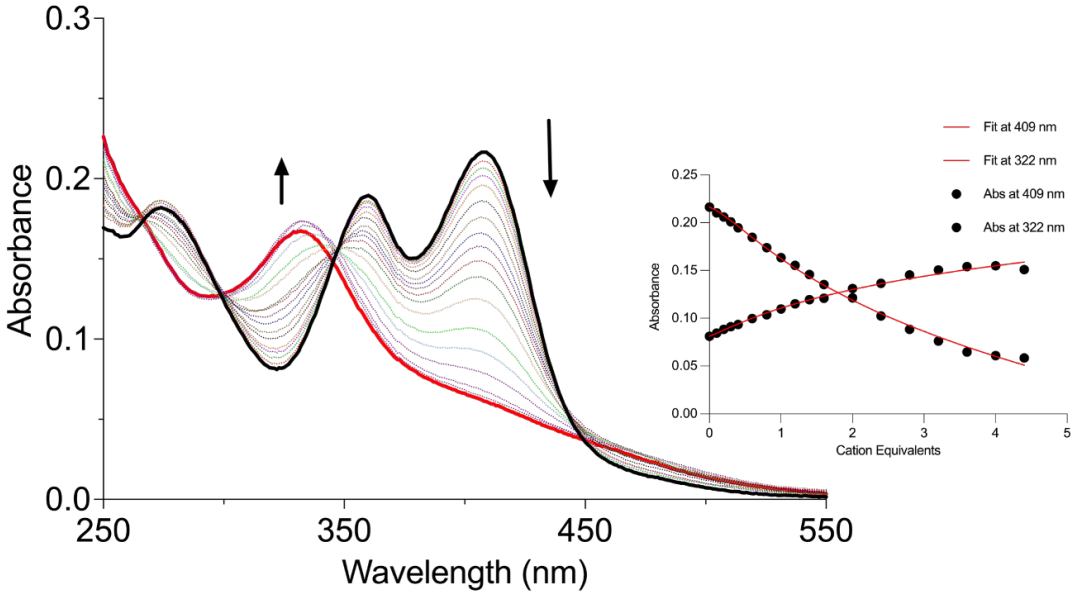

Figure SB53. Absorption spectra of Cu^{2+} titration of **3.2** (10 μM) in MeCN. {insert} Fitplot for absorbance at 409 and 322 nm. The data were fitted to a 2:1 binding model.

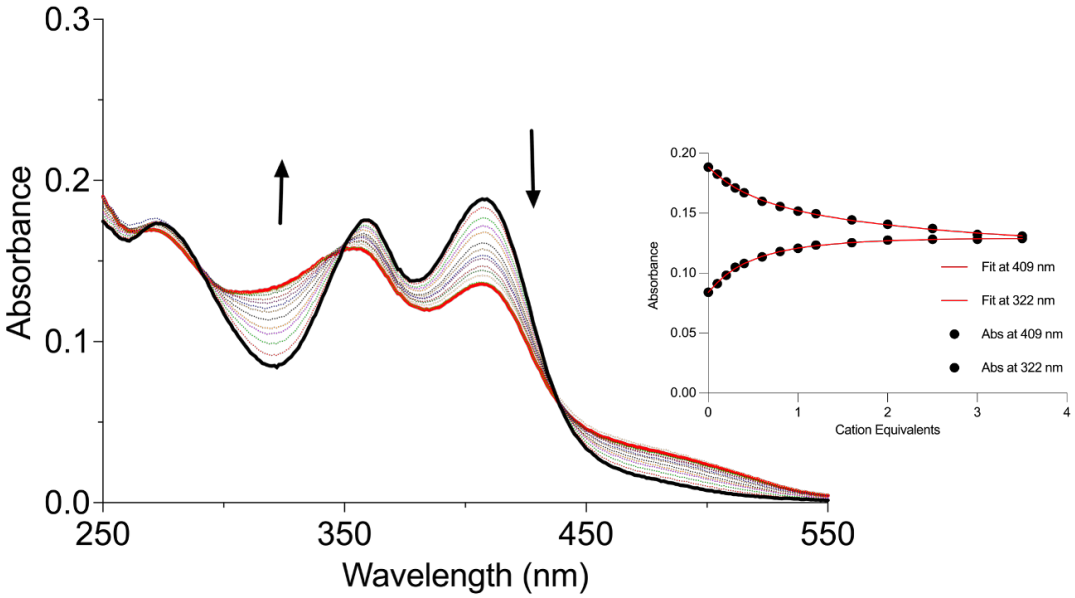

Figure SB54. Absorption spectra of Ni^{2+} titration of **3.2** (10 μM) in MeCN. {insert} Fitplot for absorbance at 409 and 322 nm. The data were fitted to a 2:1 binding model.

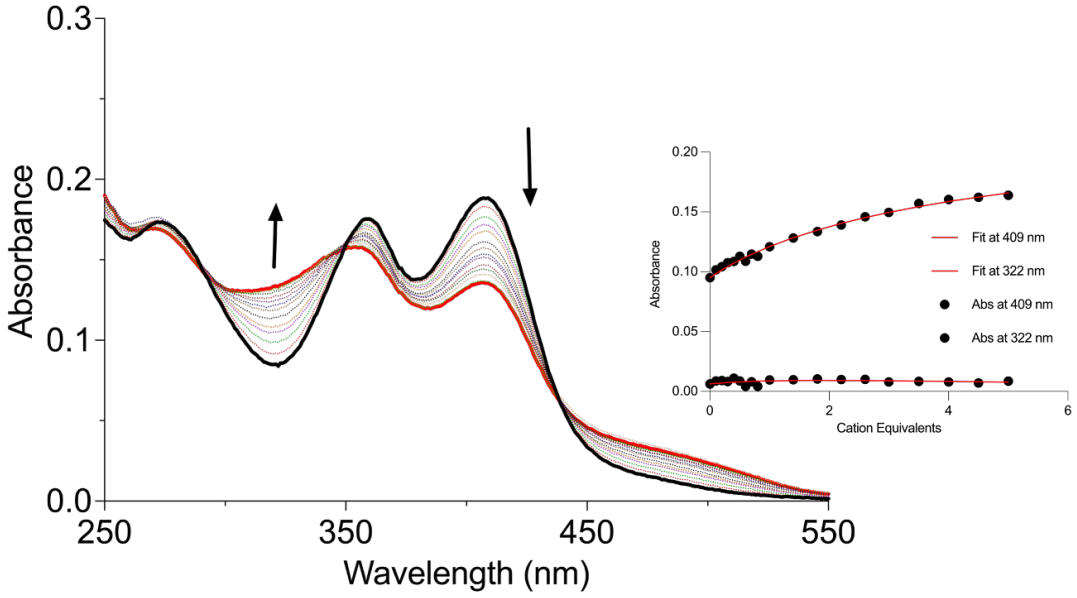

Figure SB55. Absorption spectra of Pb^{2+} titration of **3.2** (10 μM) in MeCN. {insert} Fitplot for absorbance at 409 and 322 nm. The data were fitted to a 2:1 binding model.

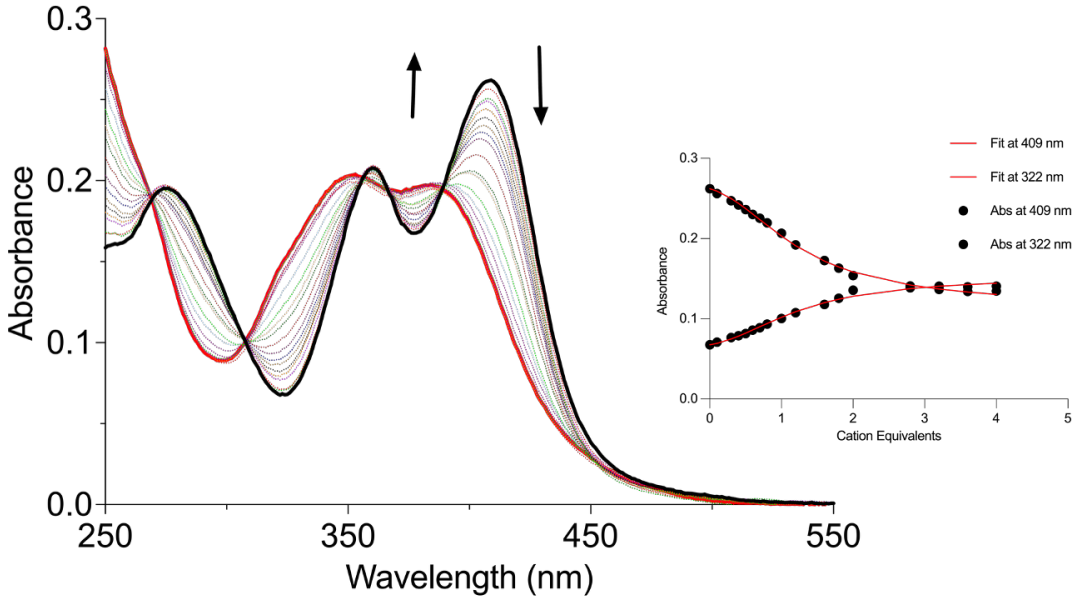

Figure SB56. Absorption spectra of Zn^{2+} titration of **3.2** (10 μM) in MeCN. {insert} Fitplot for absorbance at 409 and 322 nm. The data were fitted to a 2:1 binding model.

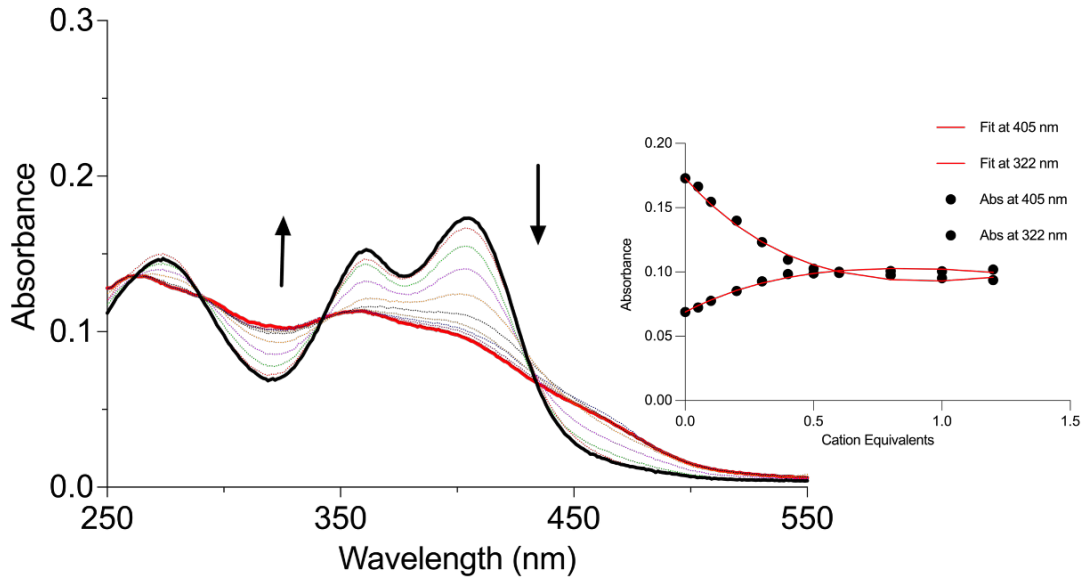

Figure SB57. Absorption spectra of Ag^{+} titration of **3.3** (10 μM) in MeCN. {insert} Fitplot for absorbance at 405 and 322 nm. The data were fitted to a 2:1 binding model.

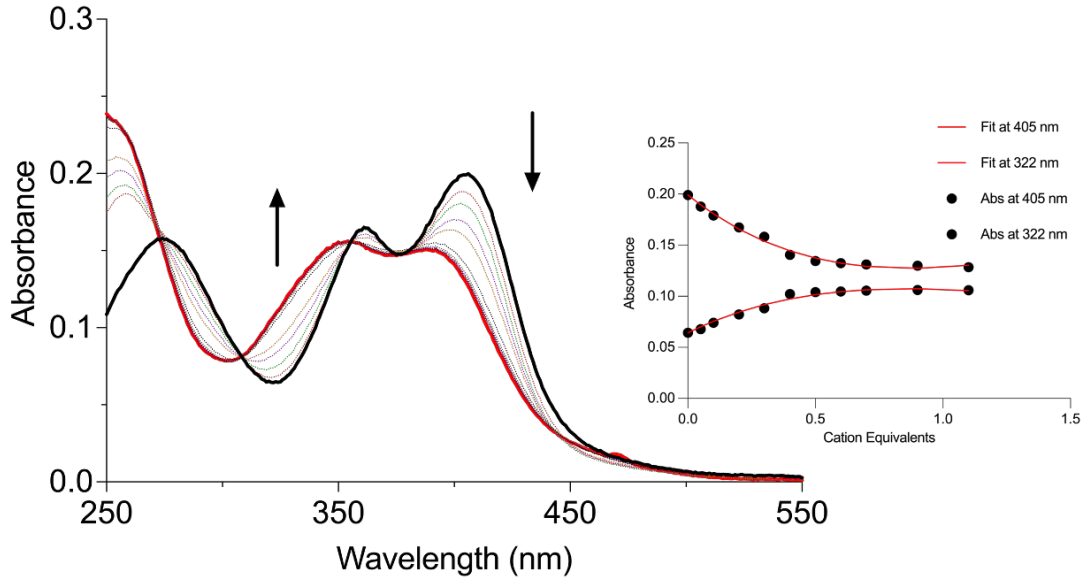

Figure SB58. Absorption spectra of Cd^{2+} titration of **3.3** (10 μM) in MeCN. {insert} Fitplot for absorbance at 405 and 322 nm. The data were fitted to a 2:1 binding model.

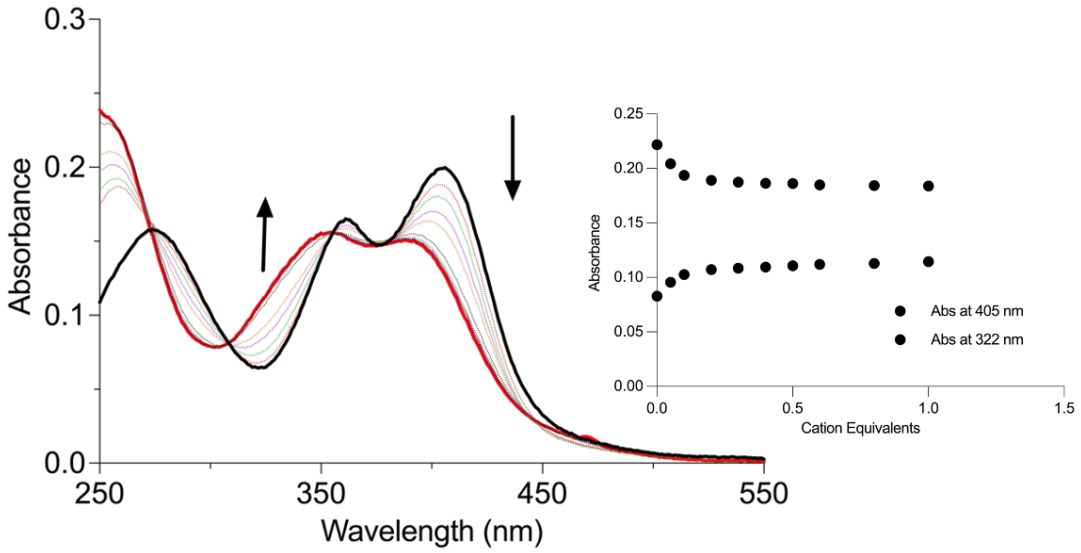

Figure SB59. Absorption spectra of Co^{2+} titration of **3.3** (10 μM) in MeCN. {insert} Fitplot for absorbance at 405 and 322 nm.

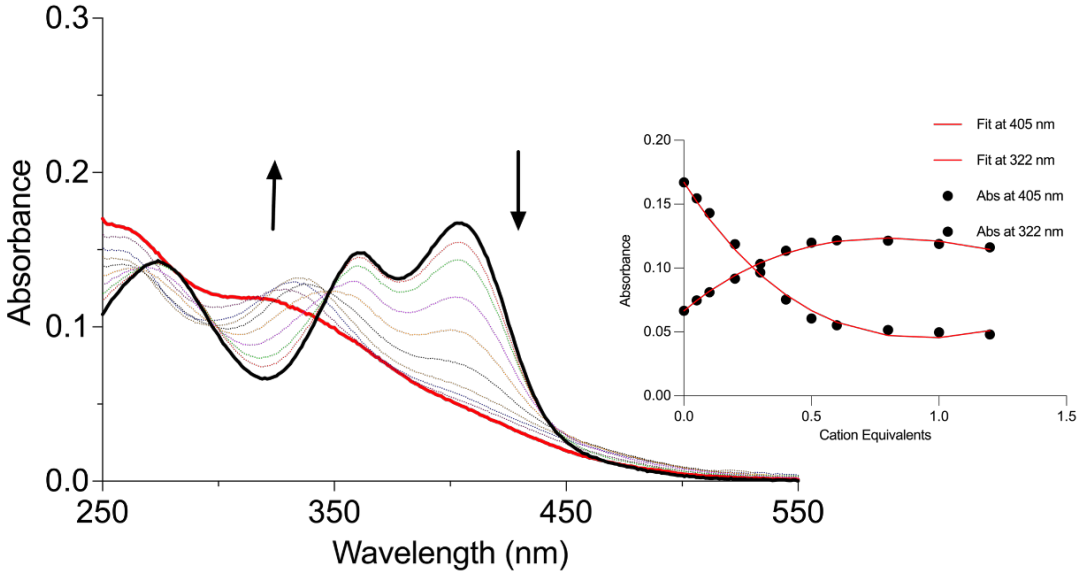

Figure SB60. Absorption spectra of Cu^{2+} titration of **3.3** (10 μM) in MeCN. {insert} Fitplot for absorbance at 405 and 322 nm. The data were fitted to a 2:1 binding model.

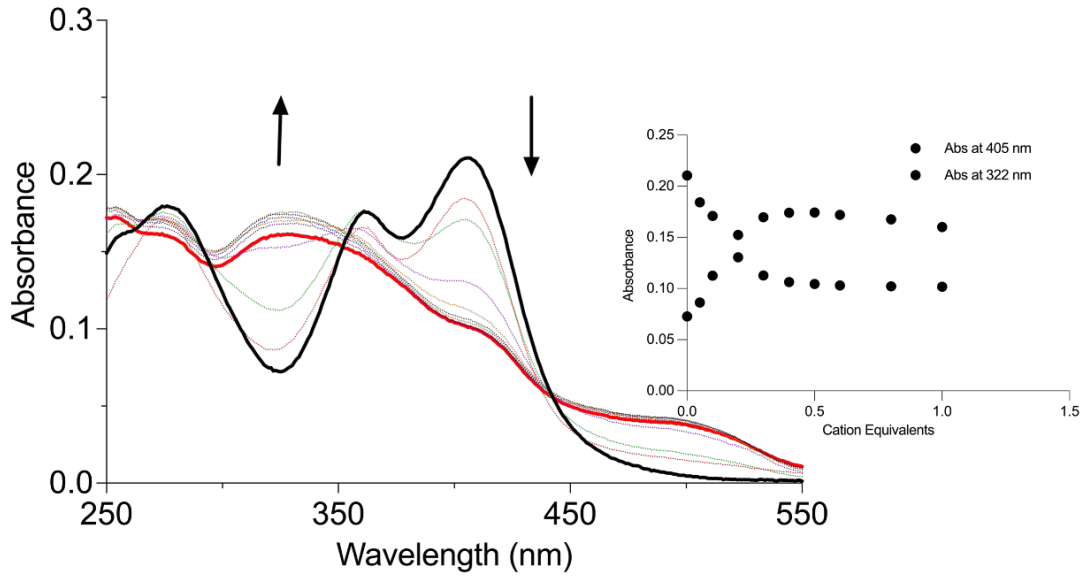

Figure SB61. Absorption spectra of Ni^{2+} titration of **3.3** (10 μM) in MeCN. {insert} Fitplot for absorbance at 405 and 322 nm.

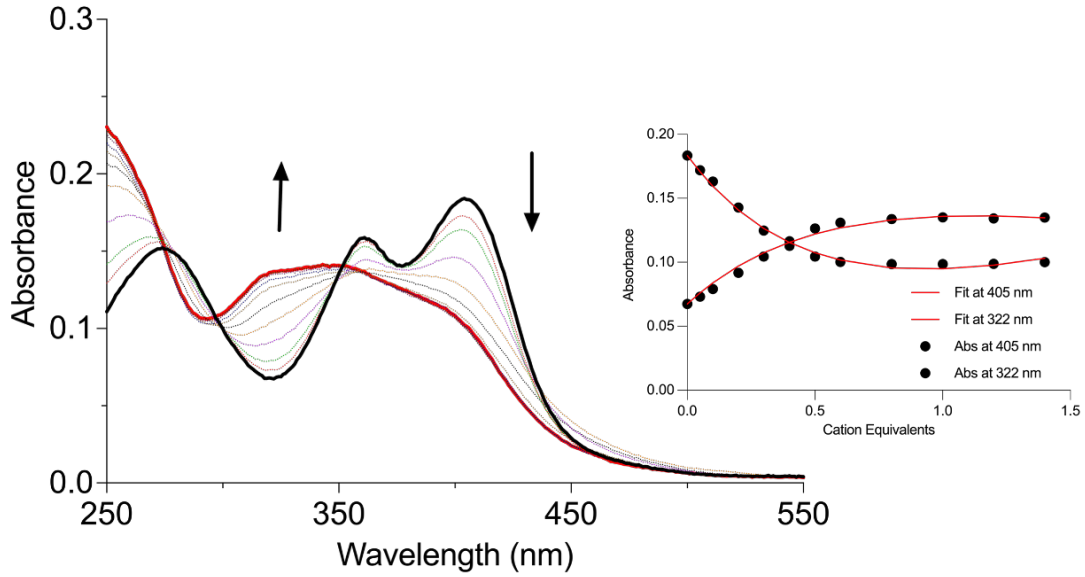

Figure SB62. Absorption spectra of Pb^{2+} titration of **3.3** (10 μM) in MeCN. {insert} Fitplot for absorbance at 405 and 322 nm. The data were fitted to a 2:1 binding model.

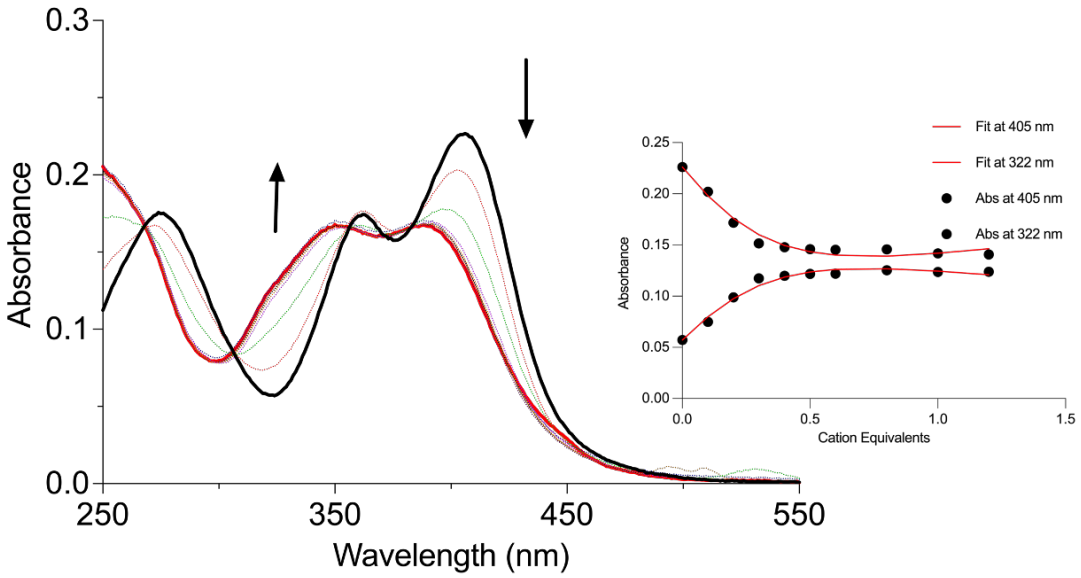

Figure SB63. Absorption spectra of Zn^{2+} titration of **3.3** (10 μM) in MeCN. {insert} Fitplot for absorbance at 405 and 322 nm. The data were fitted to a 2:1 binding model.

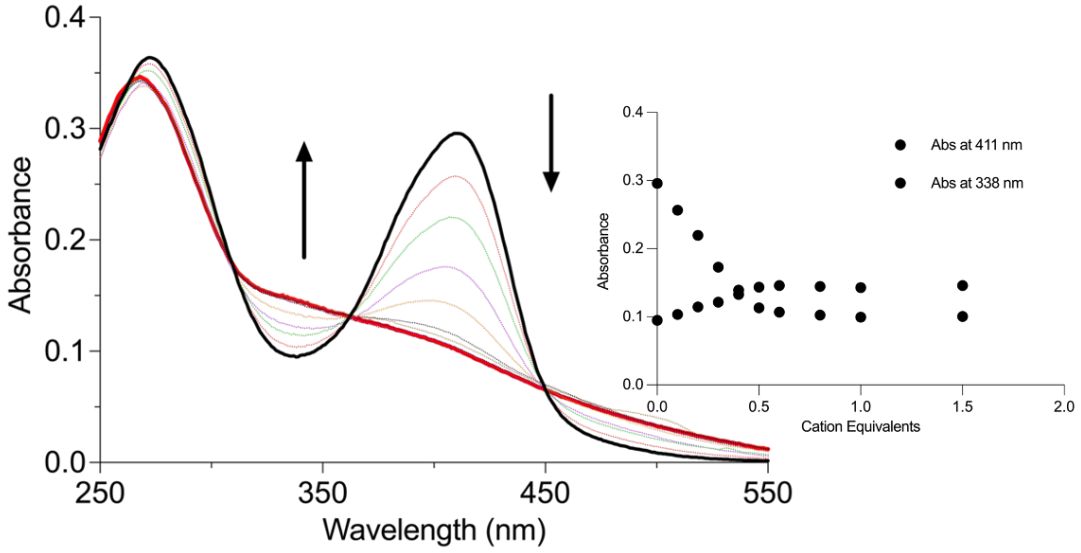

Figure SB64. Absorption spectra of Ag^{+} titration of **3.4** (10 μM) in MeCN. {insert} Fitplot for absorbance at 411 and 338 nm.

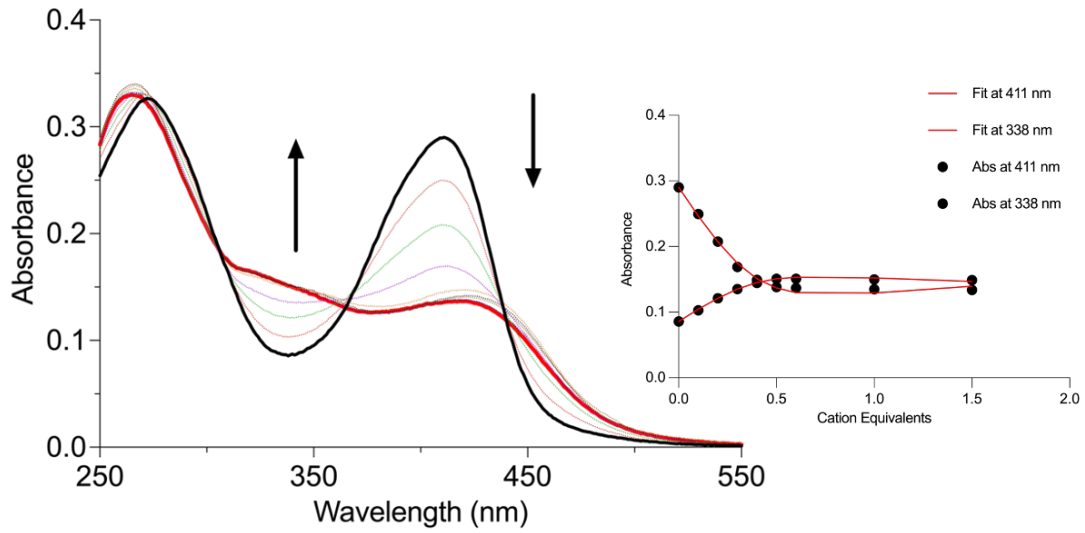

Figure SB65. Absorption spectra of Cd^{2+} titration of **3.4** (10 μM) in MeCN. {insert} Fitplot for absorbance at 411 and 338 nm. The data were fitted to a 2:1 binding model.

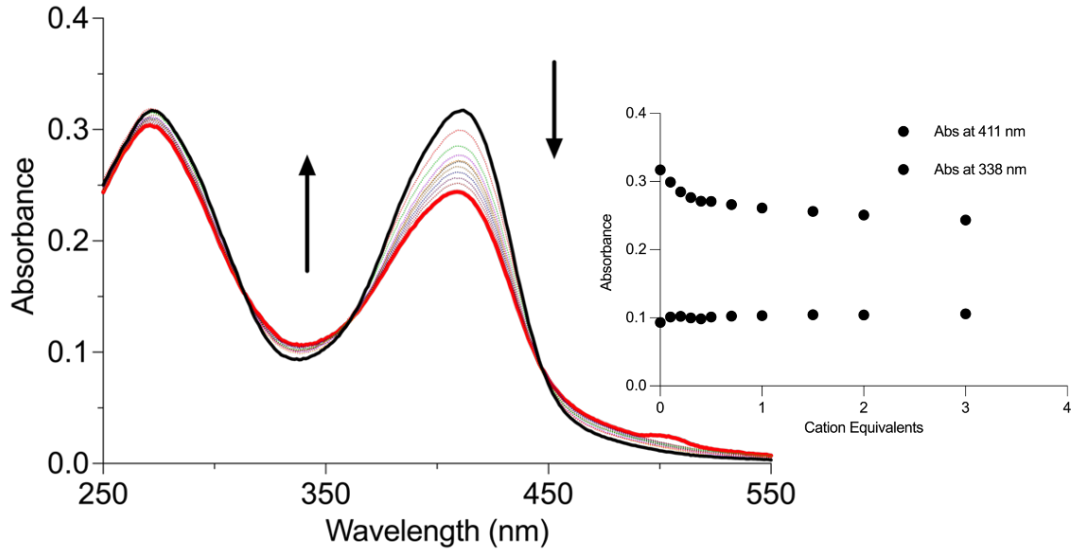

Figure SB66. Absorption spectra of Co^{2+} titration of **3.4** (10 μM) in MeCN. {insert} Fitplot for absorbance at 411 and 338 nm.

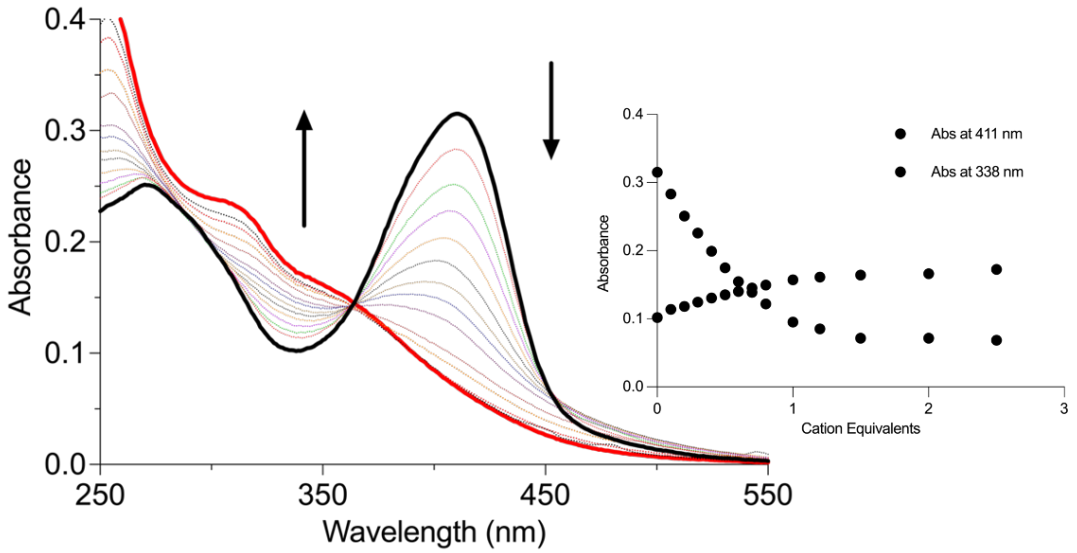

Figure SB67. Absorption spectra of Cu^{2+} titration of **3.4** (10 μM) in MeCN. {insert} Fitplot for absorbance at 411 and 338 nm.

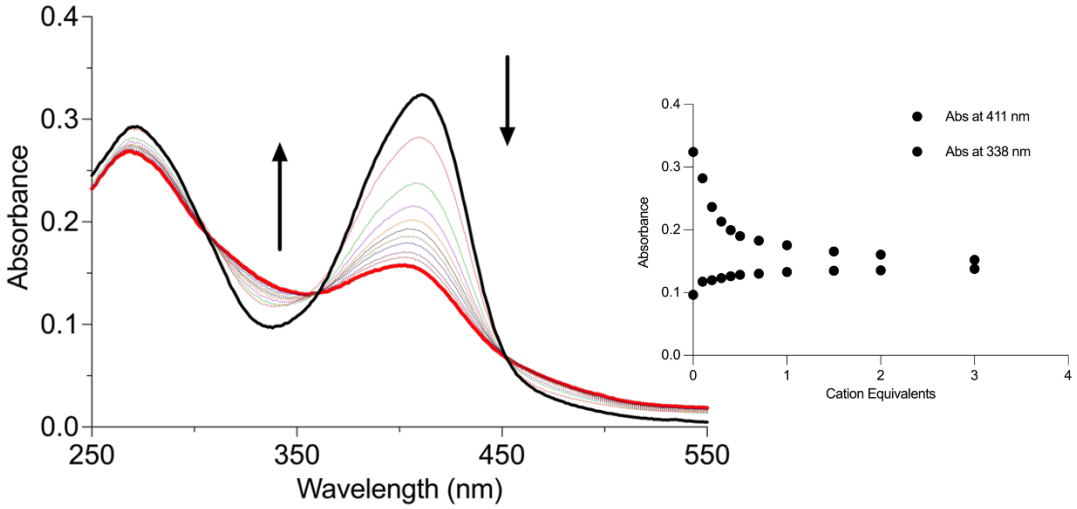

Figure SB68. Absorption spectra of Ni^{2+} titration of **3.4** (10 μM) in MeCN. {insert} Fitplot for absorbance at 411 and 338 nm.

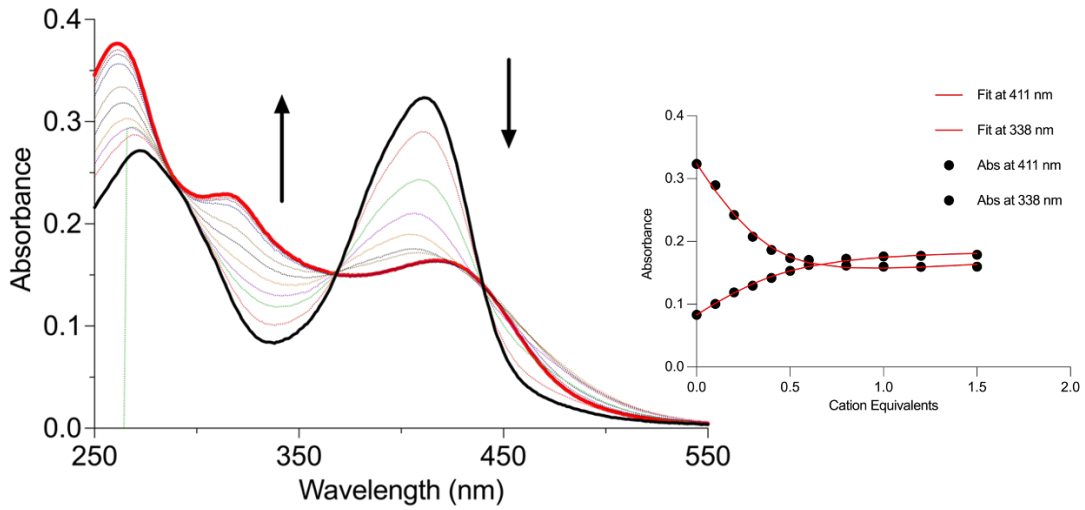

Figure SB69. Absorption spectra of Pb^{2+} titration of **3.4** (10 μM) in MeCN. {insert} Fitplot for absorbance at 411 and 338 nm. The data were fitted to a 2:1 binding model.

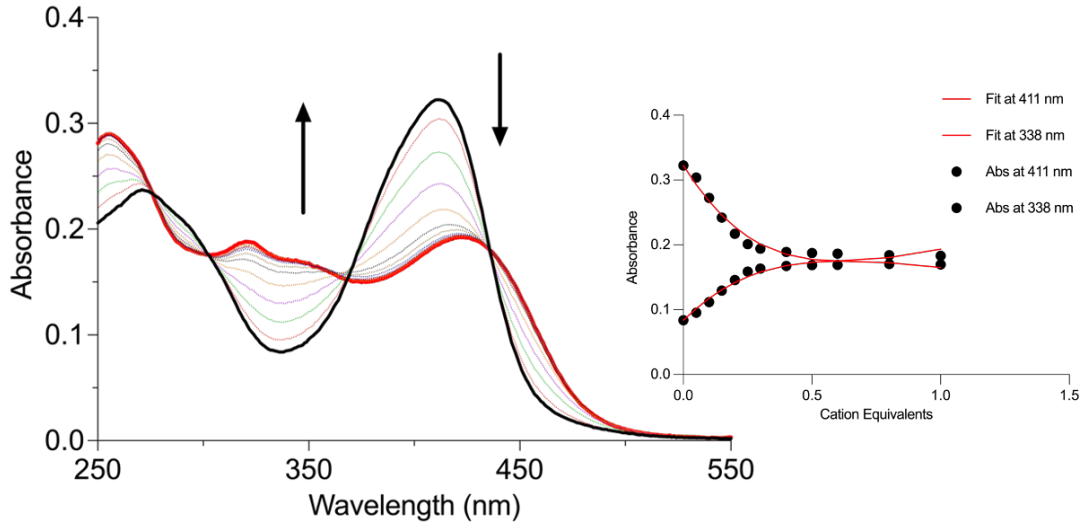

Figure SB70. Absorption spectra of Zn^{2+} titration of **3.4** (10 μM) in MeCN. {insert} Fitplot for absorbance at 411 and 338 nm. The data were fitted to a 2:1 binding model.

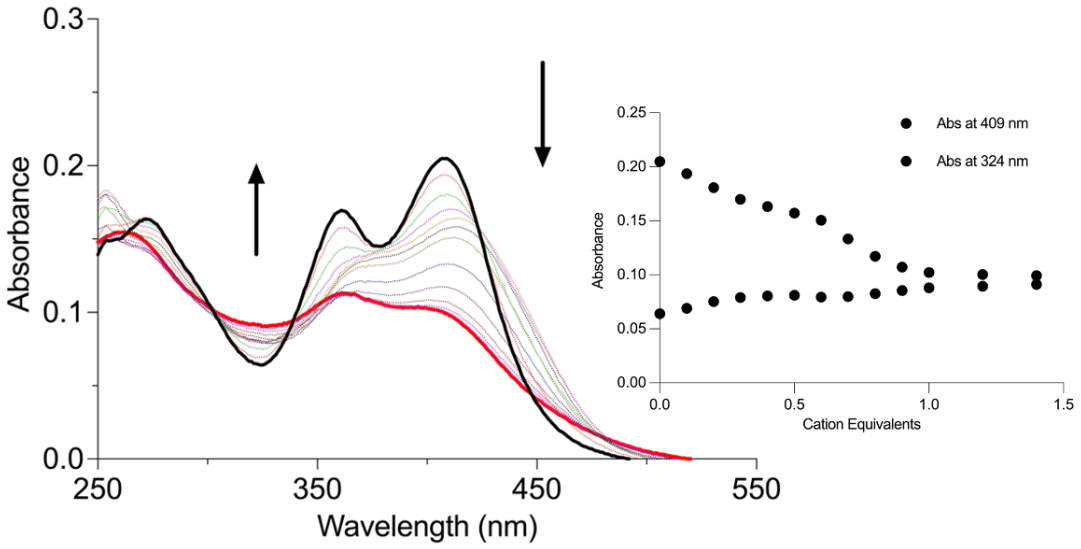

Figure SB71. Absorption spectra of Ag^{+} titration of **3.5** (10 μM) in MeCN. {insert} Fitplot for absorbance at 409 and 324 nm.

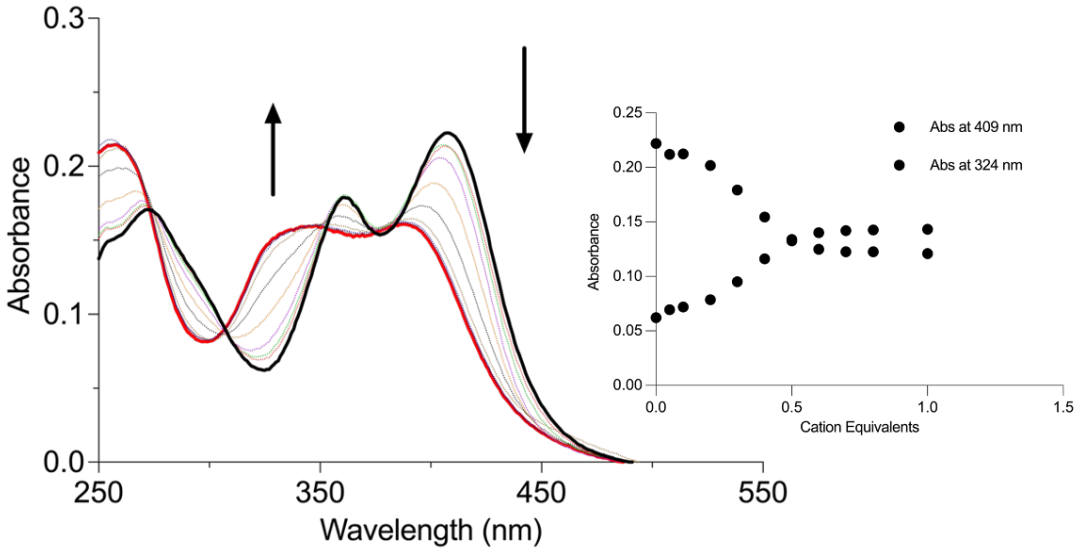

Figure SB72. Absorption spectra of Cd^{2+} titration of **3.5** (10 μM) in MeCN. {insert} Fitplot for absorbance at 409 and 324 nm.

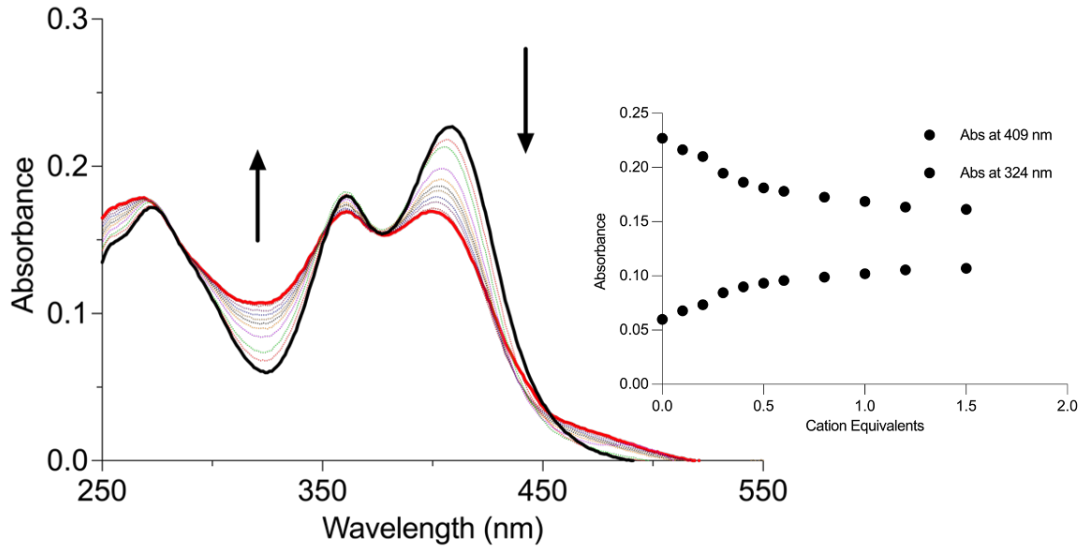

Figure SB73. Absorption spectra of Co^{2+} titration of **3.5** (10 μM) in MeCN. {insert} Fitplot for absorbance at 409 and 324 nm.

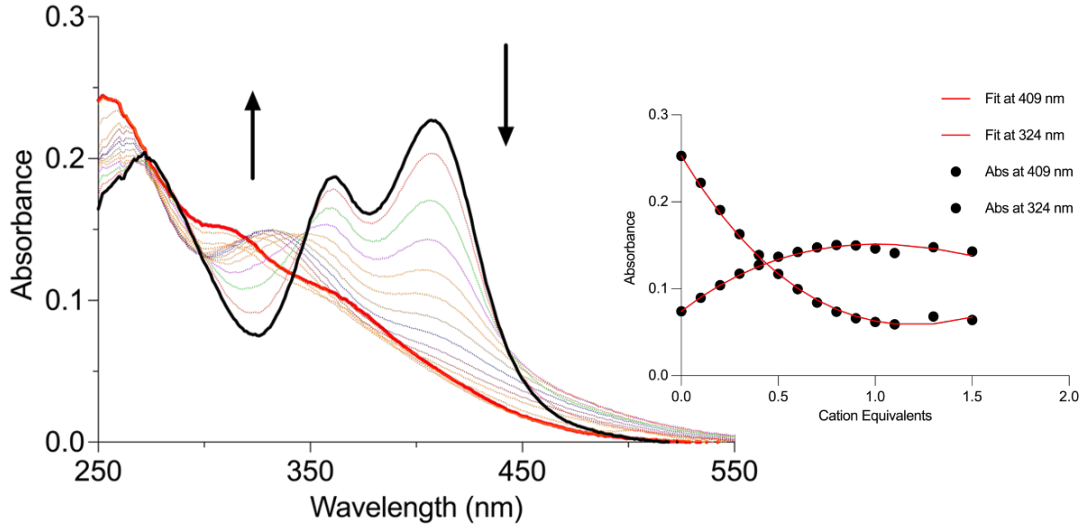

Figure SB74. Absorption spectra of Cu^{2+} titration of **3.5** (10 μM) in MeCN. {insert} Fitplot for absorbance at 409 and 324 nm. The data were fitted to a 2:1 binding model.

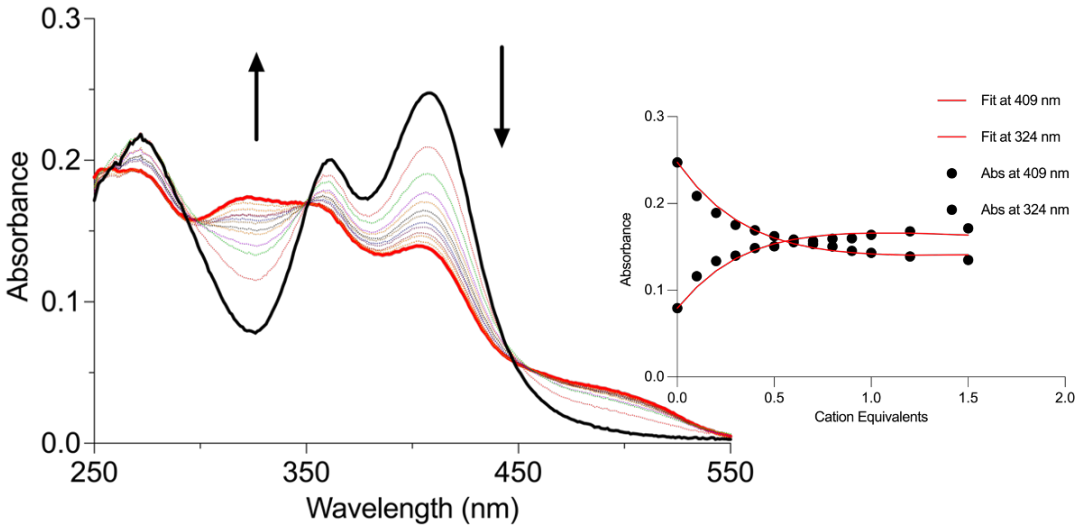

Figure SB75. Absorption spectra of Ni^{2+} titration of **3.5** (10 μM) in MeCN. {insert} Fitplot for absorbance at 409 and 324 nm. The data were fitted to a 2:1 binding model.

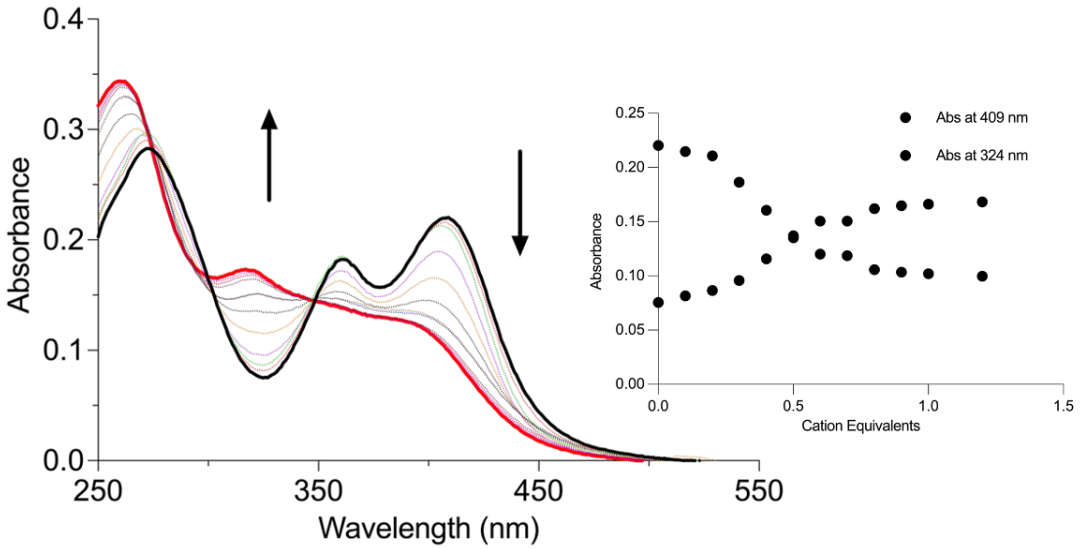

Figure SB76. Absorption spectra of Pb^{2+} titration of **3.5** (10 μM) in MeCN. {insert} Fitplot for absorbance at 409 and 324 nm.

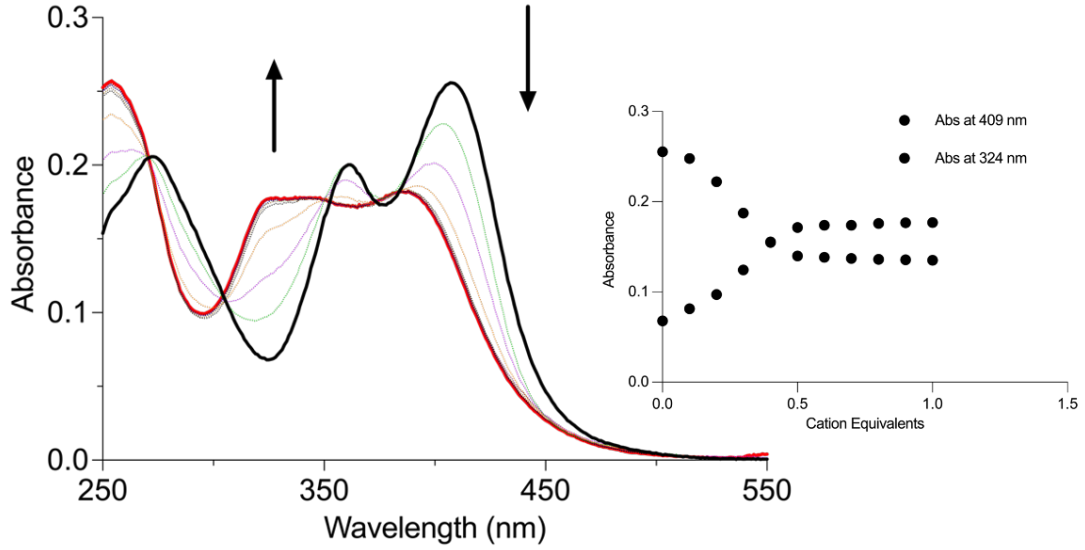

Figure SB77. Absorption spectra of Zn^{2+} titration of **3.5** (10 μM) in MeCN. {insert} Fitplot for absorbance at 409 and 324 nm.

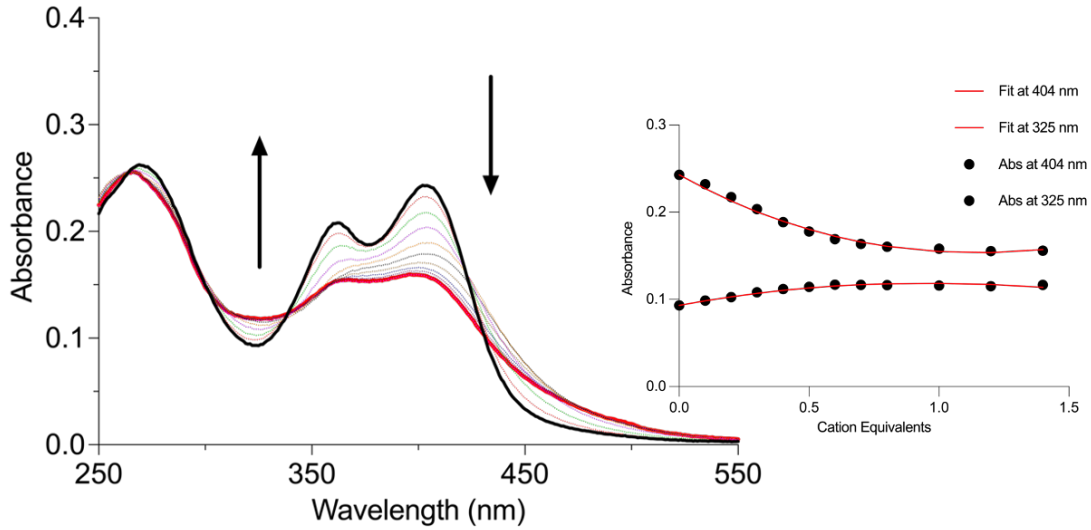

Figure SB78. Absorption spectra of Ag^{+} titration of **3.6** (10 μM) in MeCN. {insert} Fitplot for absorbance at 404 and 325 nm. The data were fitted to a 2:1 binding model.

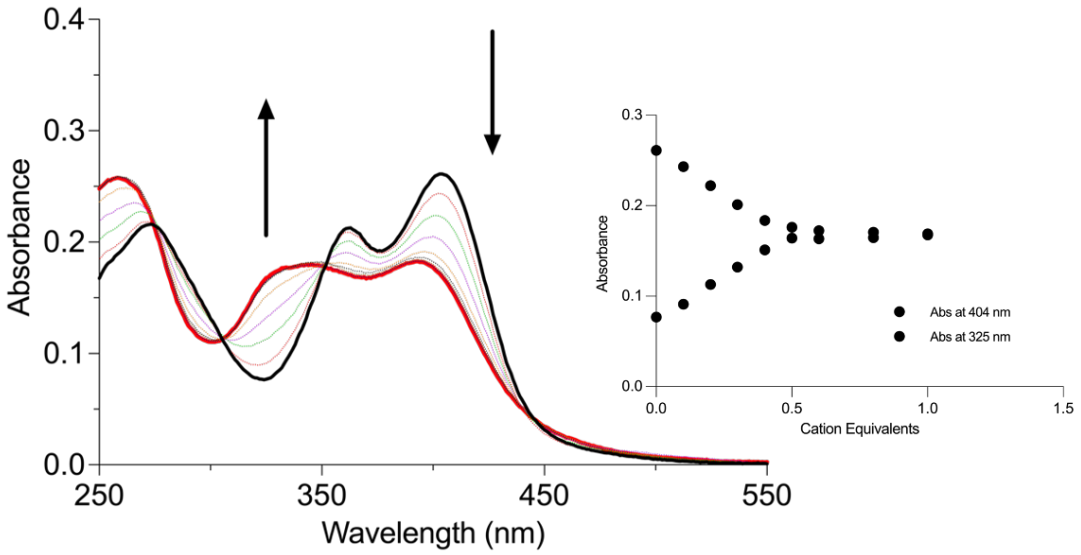

Figure SB79. Absorption spectra of Cd^{2+} titration of **3.6** (10 μM) in MeCN. {insert} Fitplot for absorbance at 404 and 325 nm.

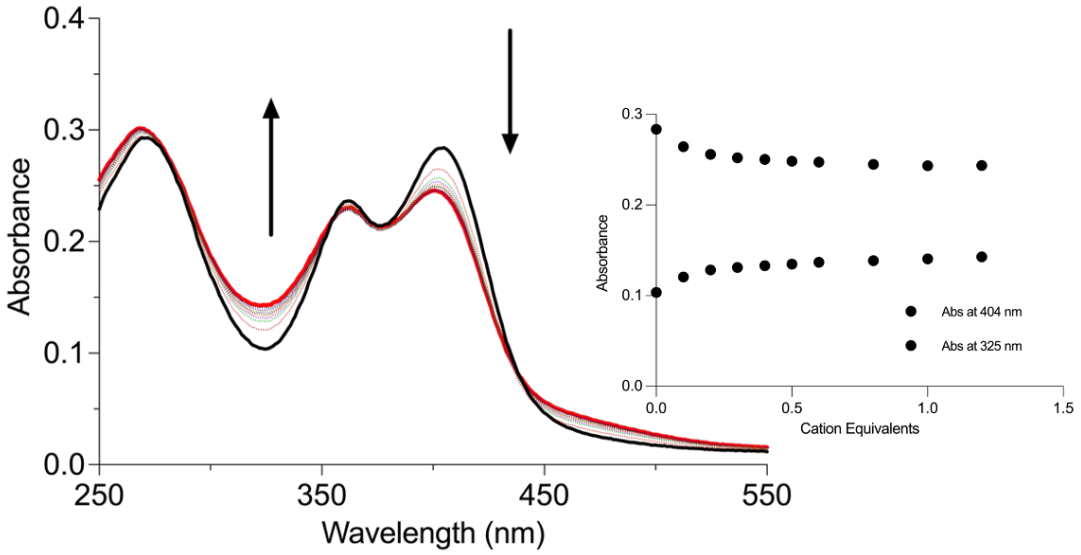

Figure SB80. Absorption spectra of Co^{2+} titration of **3.6** (10 μM) in MeCN. {insert} Fitplot for absorbance at 404 and 325 nm.

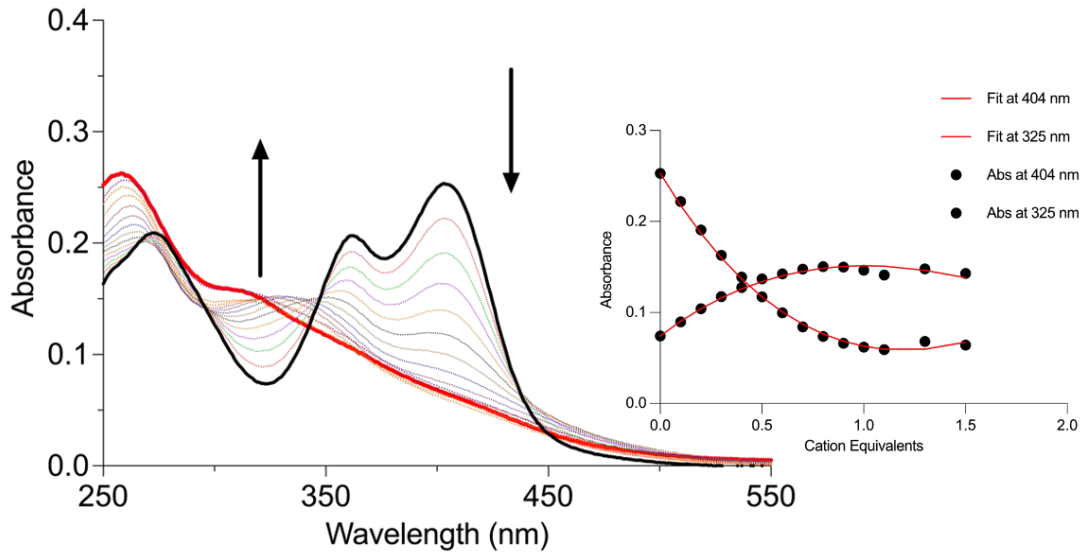

Figure SB81. Absorption spectra of Cu^{2+} titration of **3.6** (10 μM) in MeCN. {insert} Fitplot for absorbance at 404 and 325 nm. The data were fitted to a 2:1 binding model.

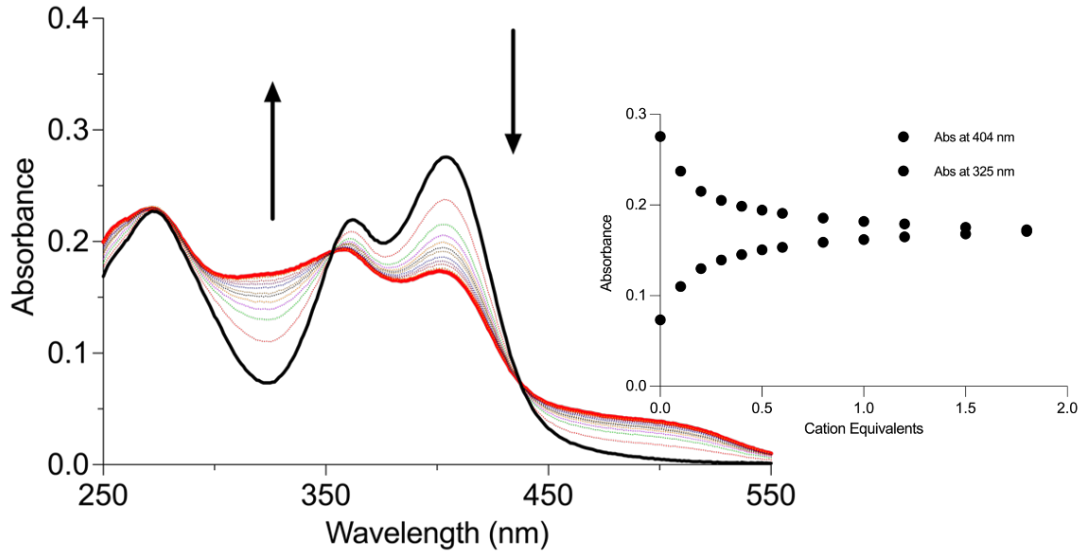

Figure SB82. Absorption spectra of Ni^{2+} titration of **3.6** (10 μM) in MeCN. {insert} Fitplot for absorbance at 404 and 325 nm.

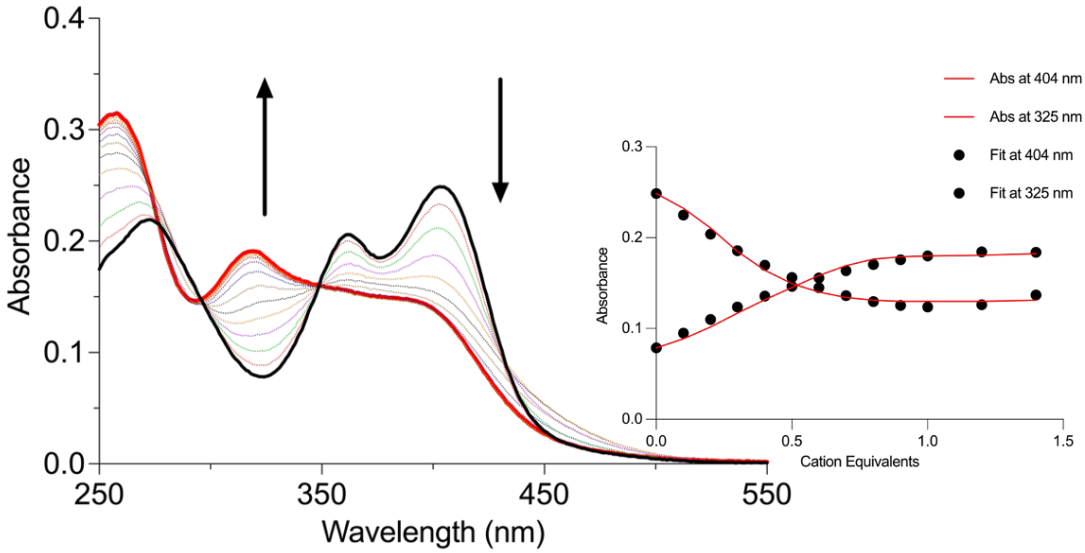

Figure SB83. Absorption spectra of Pb^{2+} titration of **3.6** (10 μM) in MeCN. {insert} Fitplot for absorbance at 404 and 325 nm. The data were fitted to a 2:1 binding model.

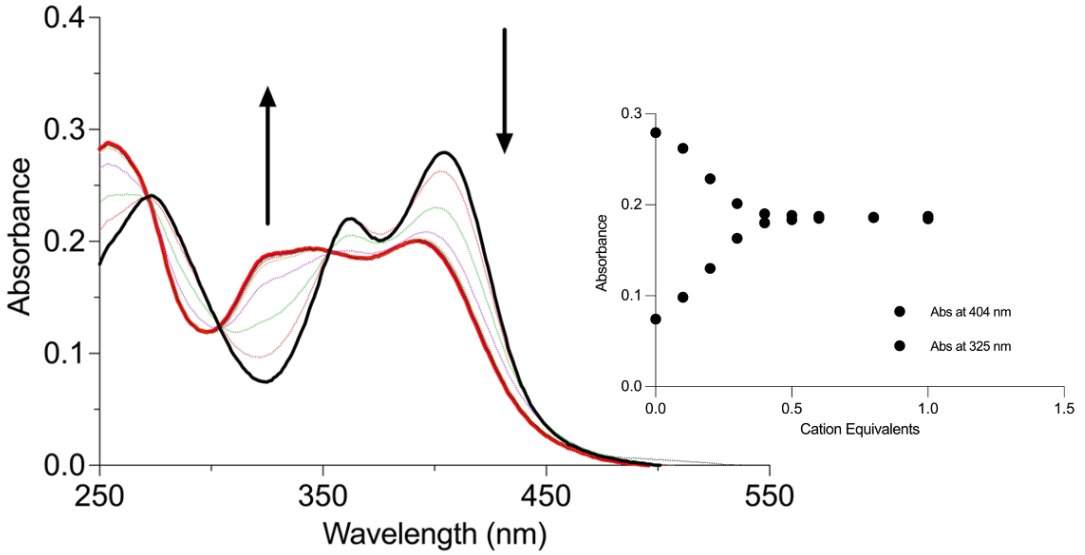

Figure S84. Absorption spectra of Zn^{2+} titration of **3.6** (10 μM) in MeCN. {insert} Fitplot for absorbance at 404 and 325 nm.

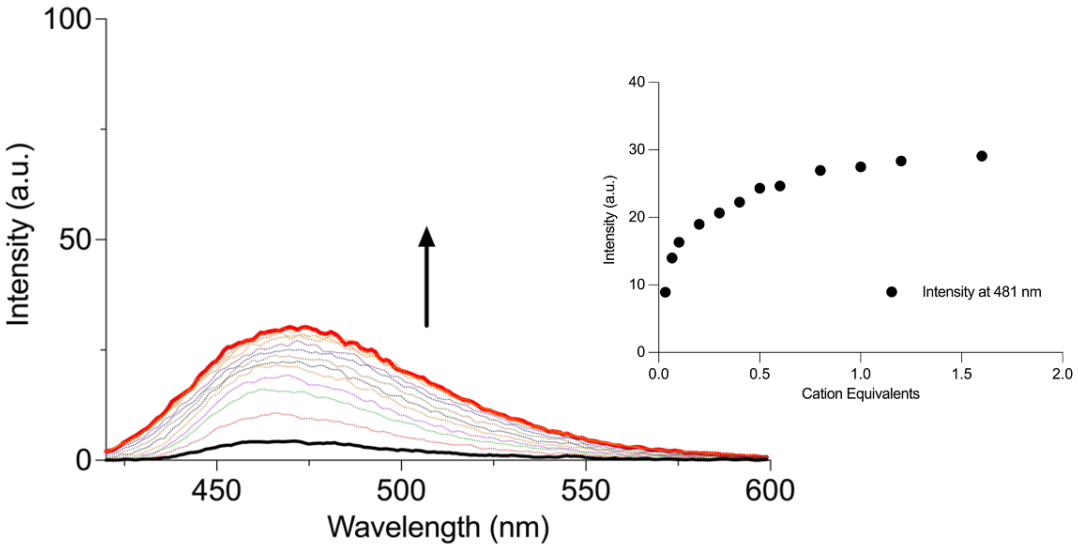

Figure SB85. Fluorescent spectra of Ag^{+} titration of **3.1** (1 mM) in MeCN. {insert} Fitplot for fluorescence intensity at 481 nm.

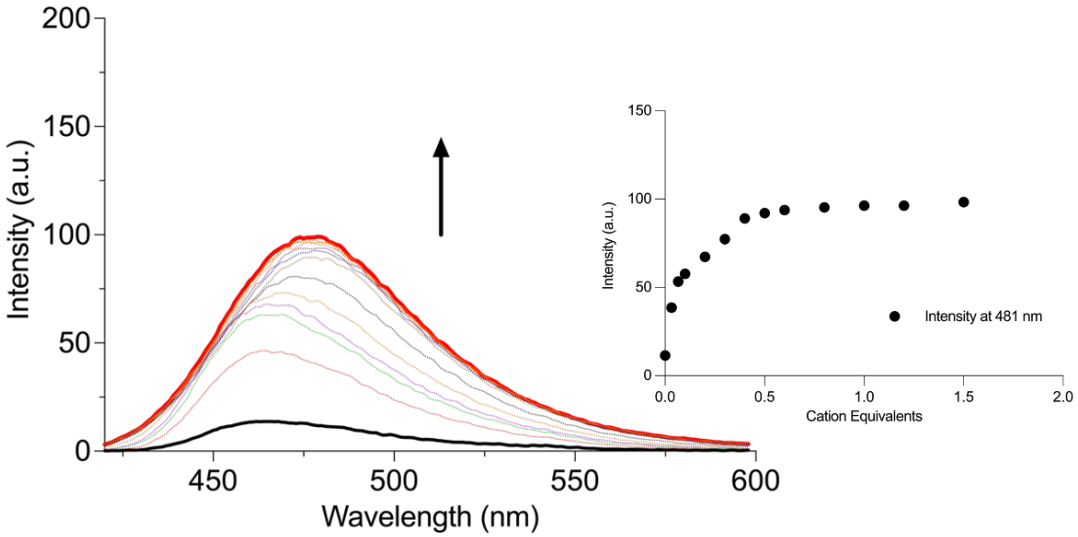

Figure SB86. Fluorescent spectra of Cd^{2+} titration of **3.1** (1 mM) in MeCN. {insert} Fitplot for fluorescence intensity at 481 nm.

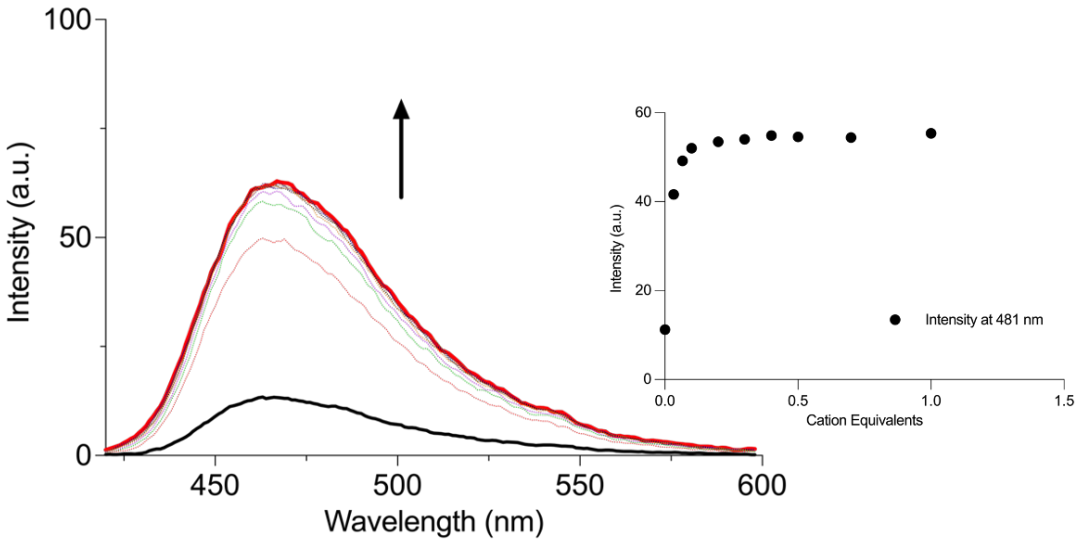

Figure SB87. Fluorescent spectra of Co^{2+} titration of **3.1** (1 mM) in MeCN. {insert} Fitplot for fluorescence intensity at 481 nm.

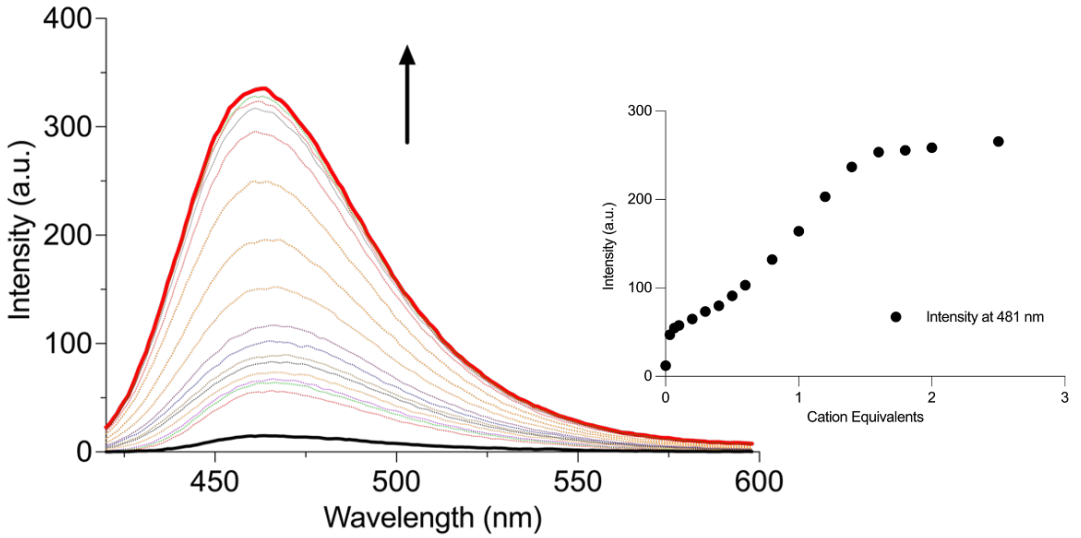

Figure SB88. Fluorescent spectra of Cu^{2+} titration of **3.1** (1 mM) in MeCN. {insert} Fitplot for fluorescence intensity at 481 nm.

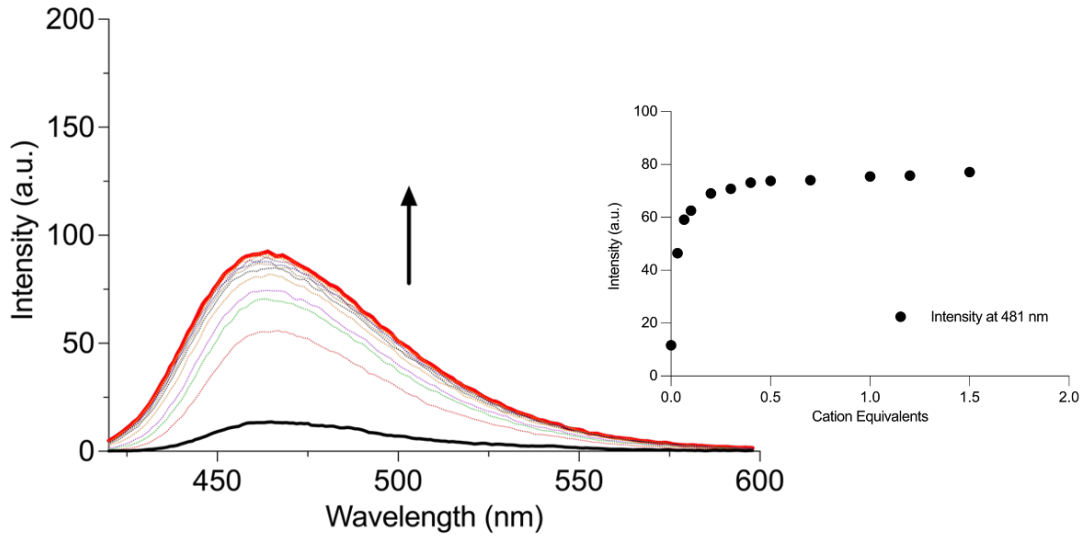

Figure SB89. Fluorescent spectra of Ni^{2+} titration of **3.1** (1 mM) in MeCN. {insert} Fitplot for fluorescence intensity at 481 nm.

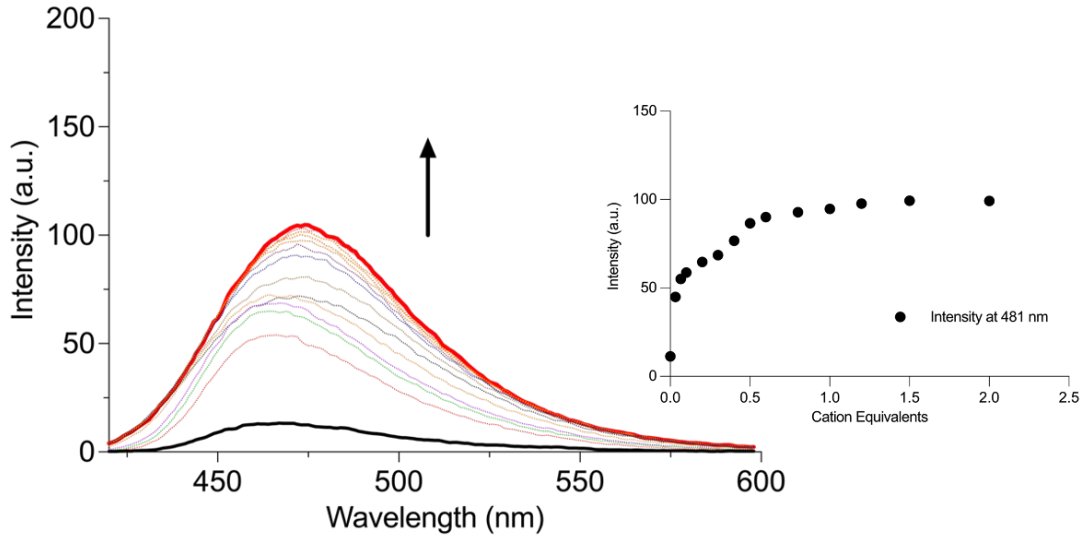

Figure SB90. Fluorescent spectra of Pb^{2+} titration of **3.1** (1 mM) in MeCN. {insert} Fitplot for fluorescence intensity at 481 nm.

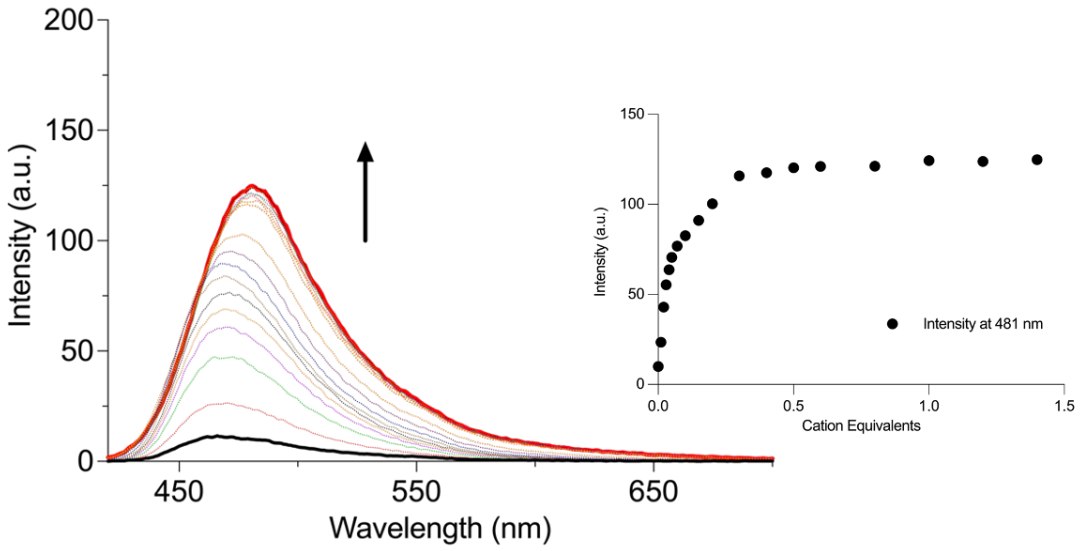

Figure SB91. Fluorescent spectra of Zn^{2+} titration of **3.1** (1 mM) in MeCN. {insert} Fitplot for fluorescence intensity at 481 nm.

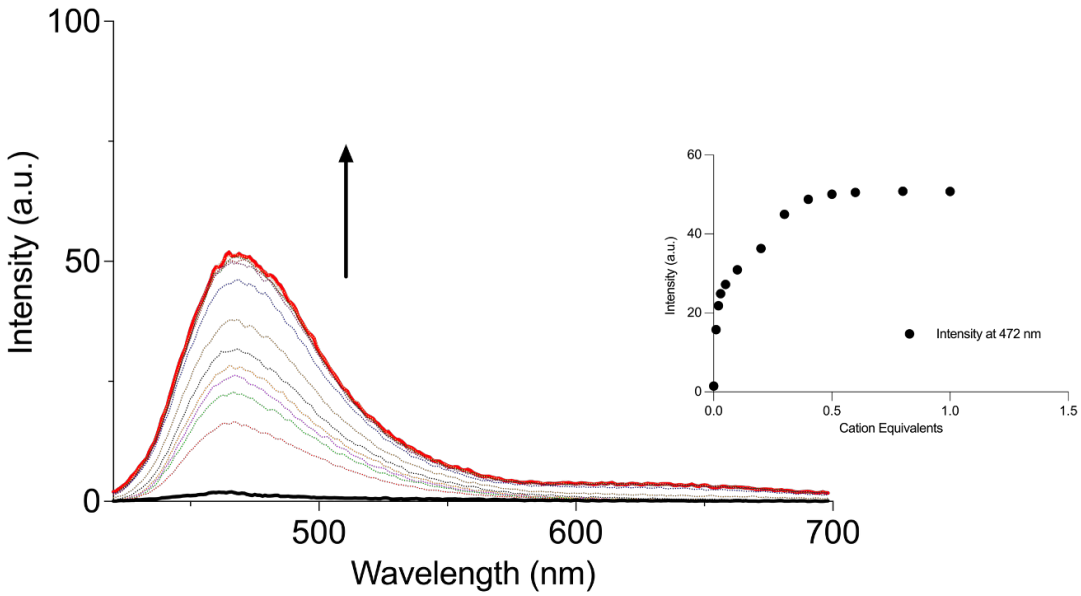

Figure SB92. Fluorescent spectra of Zn^{2+} titration of **3.2** (1 mM) in MeCN. {insert} Fitplot for fluorescence intensity at 472 nm.

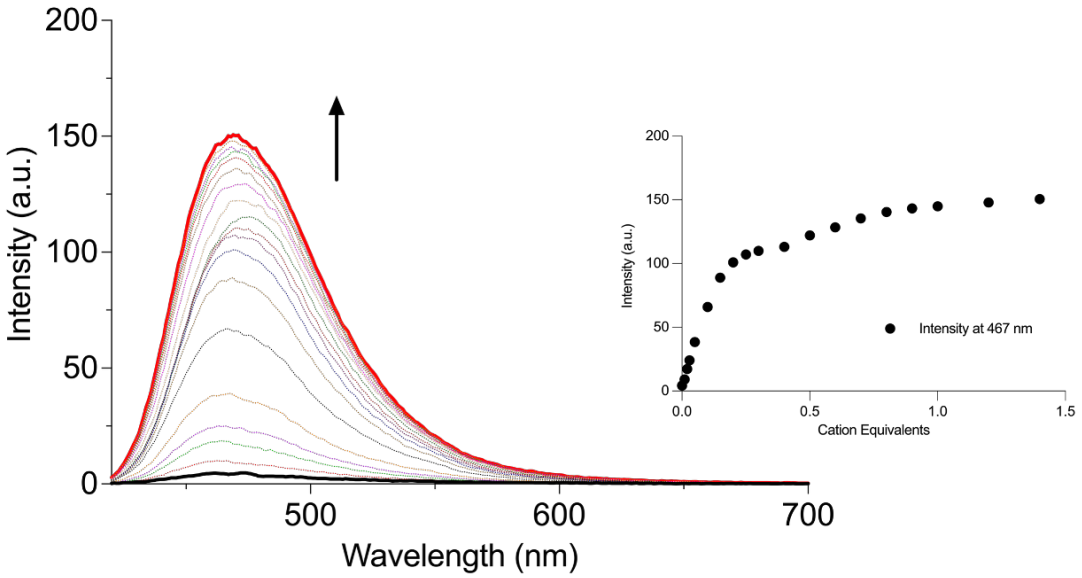

Figure SB93. Fluorescent spectra of Ag^{+} titration of **3.3** (1 mM) in MeCN. {insert} Fitplot for fluorescence intensity at 467 nm.

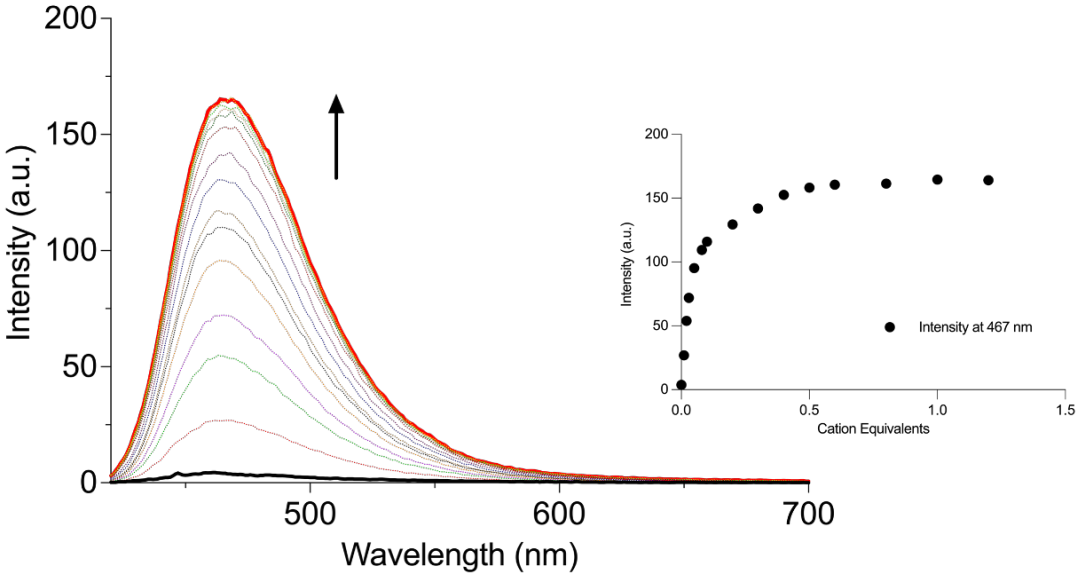

Figure SB94. Fluorescent spectra of Cd^{2+} titration of **3.3** (1 mM) in MeCN. {insert} Fitplot for fluorescence intensity at 467 nm.

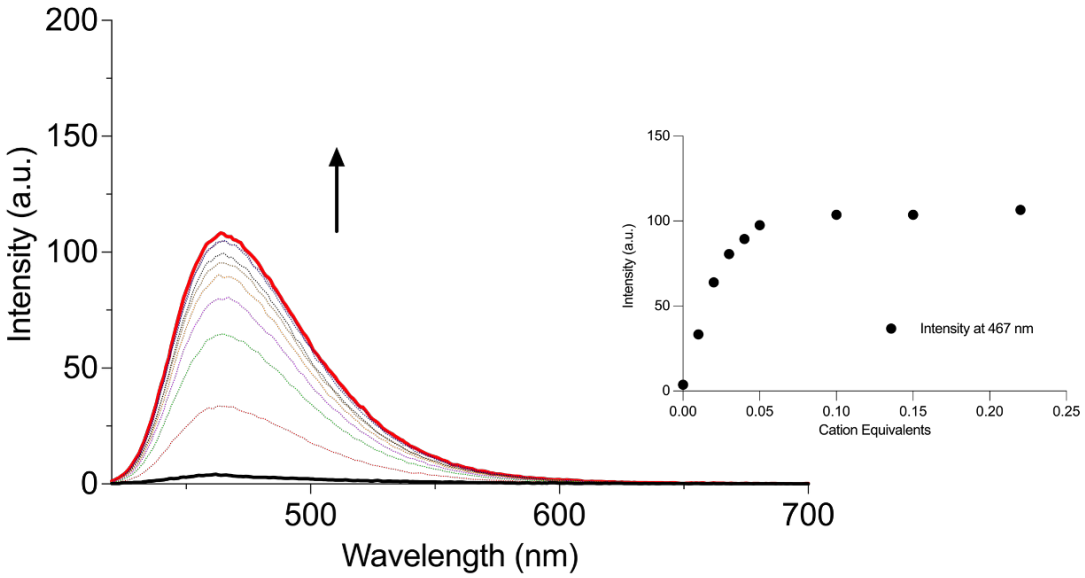

Figure SB95. Fluorescent spectra of Co^{2+} titration of **3.3** (1 mM) in MeCN. {insert} Fitplot for fluorescence intensity at 467 nm.

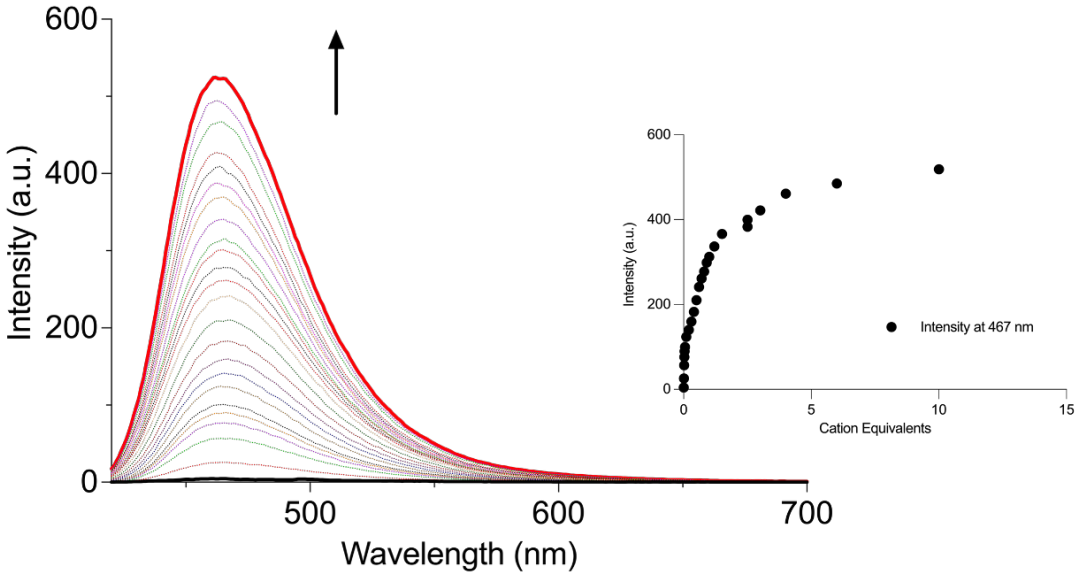

Figure SB96. Fluorescent spectra of Cu^{2+} titration of **3.3** (1 mM) in MeCN. {insert} Fitplot for fluorescence intensity at 467 nm.

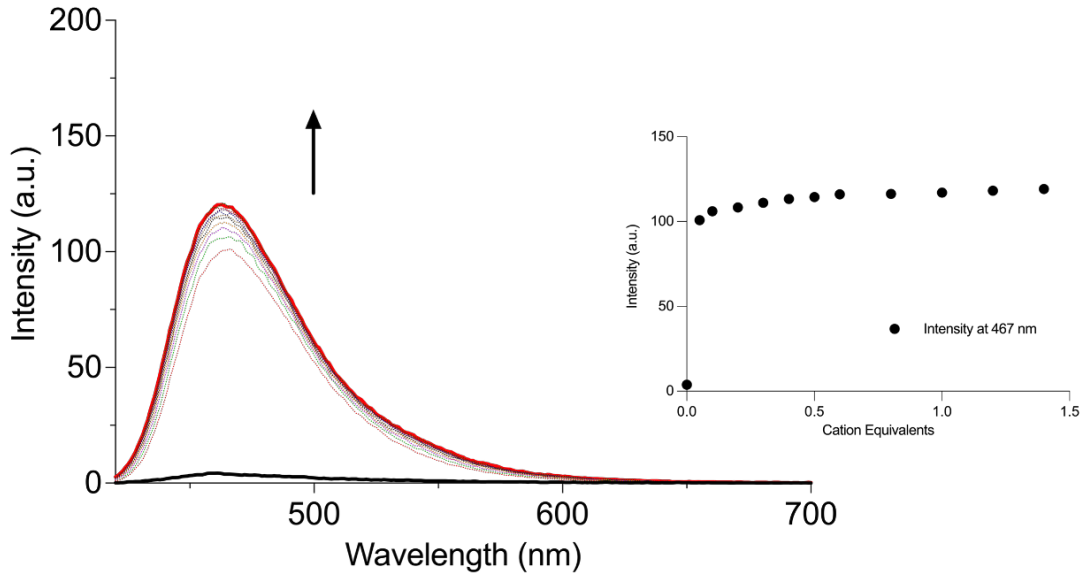

Figure SB97. Fluorescent spectra of Ni^{2+} titration of **3.3** (1 mM) in MeCN. {insert} Fitplot for fluorescence intensity at 467 nm.

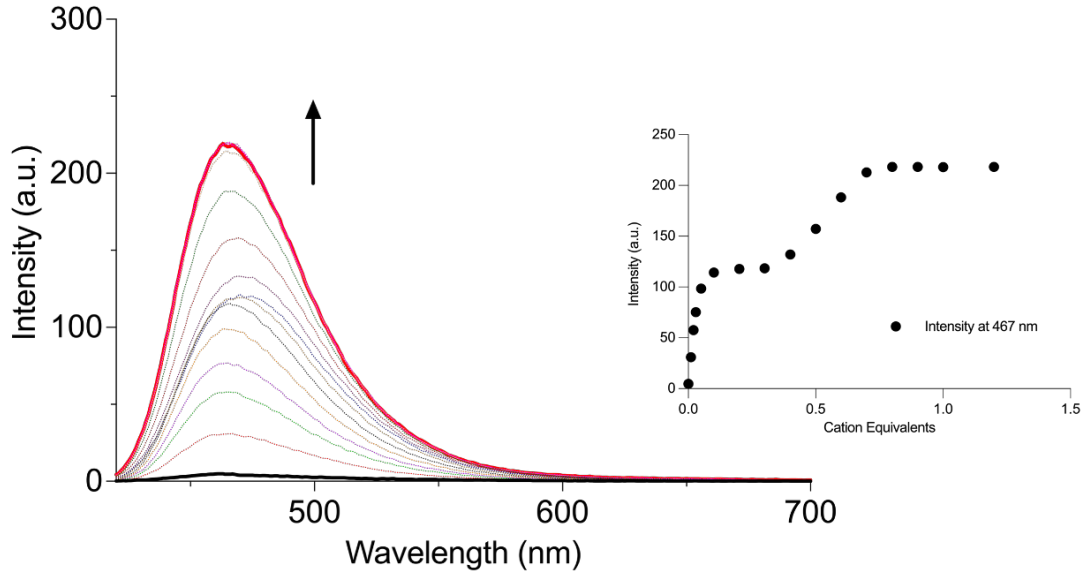

Figure SB98. Fluorescent spectra of Pb^{2+} titration of **3.3** (1 mM) in MeCN. {insert} Fitplot for fluorescence intensity at 467 nm.

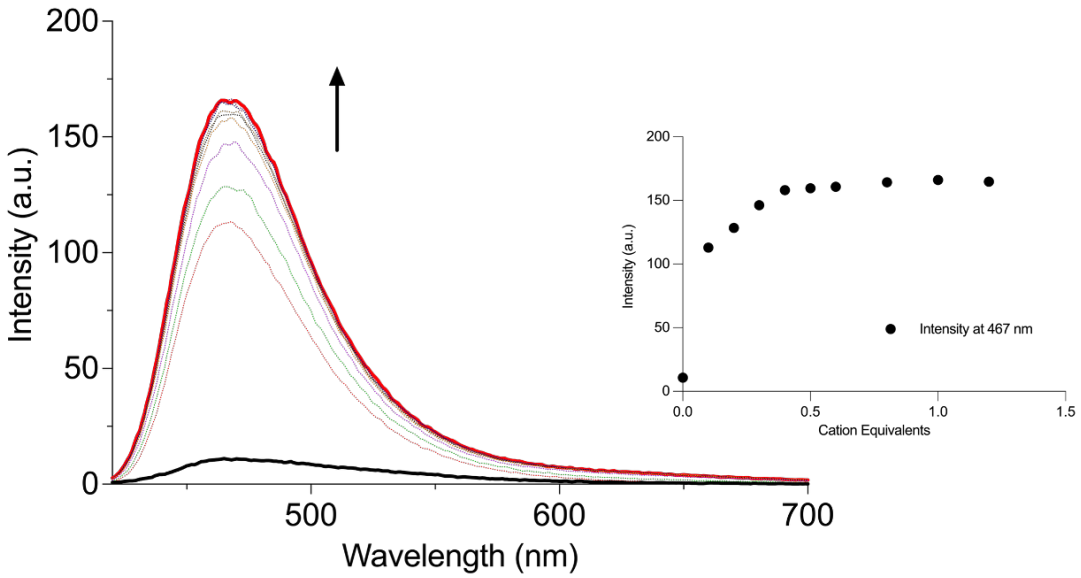

Figure SB99. Fluorescent spectra of Zn^{2+} titration of **3.3** (1 mM) in MeCN. {insert} Fitplot for fluorescence intensity at 467 nm.

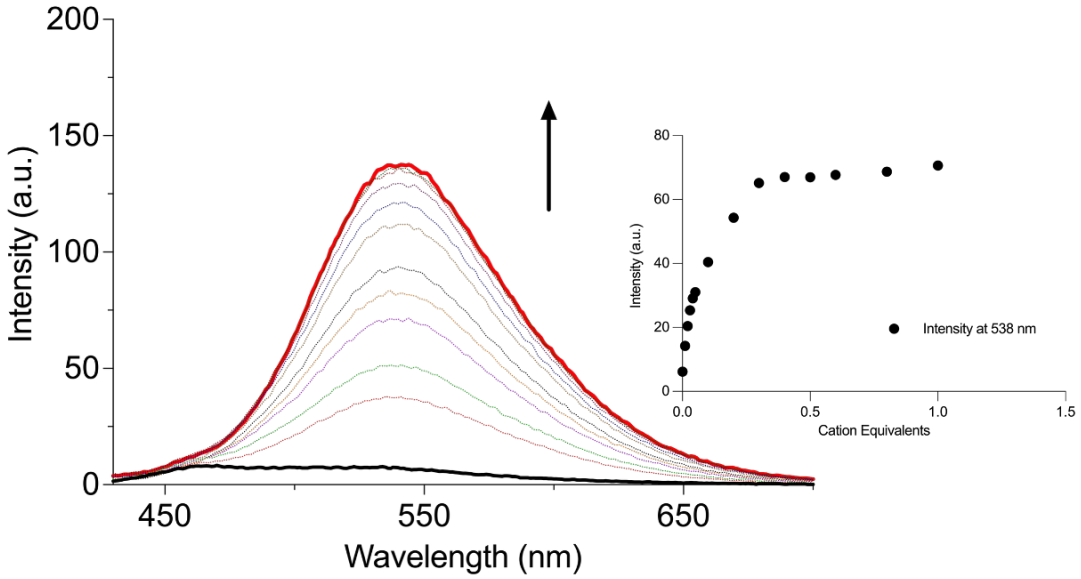

Figure SB100. Fluorescent spectra of Ag^{+} titration of **3.4** (1 mM) in MeCN. {insert} Fitplot for fluorescence intensity at 538 nm.

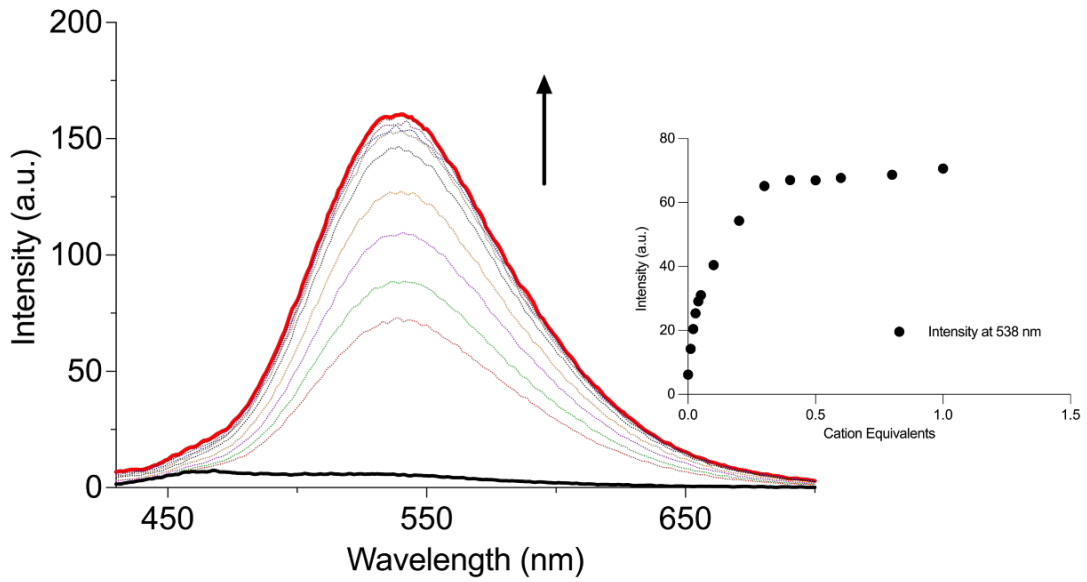

Figure SB101. Fluorescent spectra of Cd^{2+} titration of **3.4** (1 mM) in MeCN. {insert} Fitplot for fluorescence intensity at 538 nm.

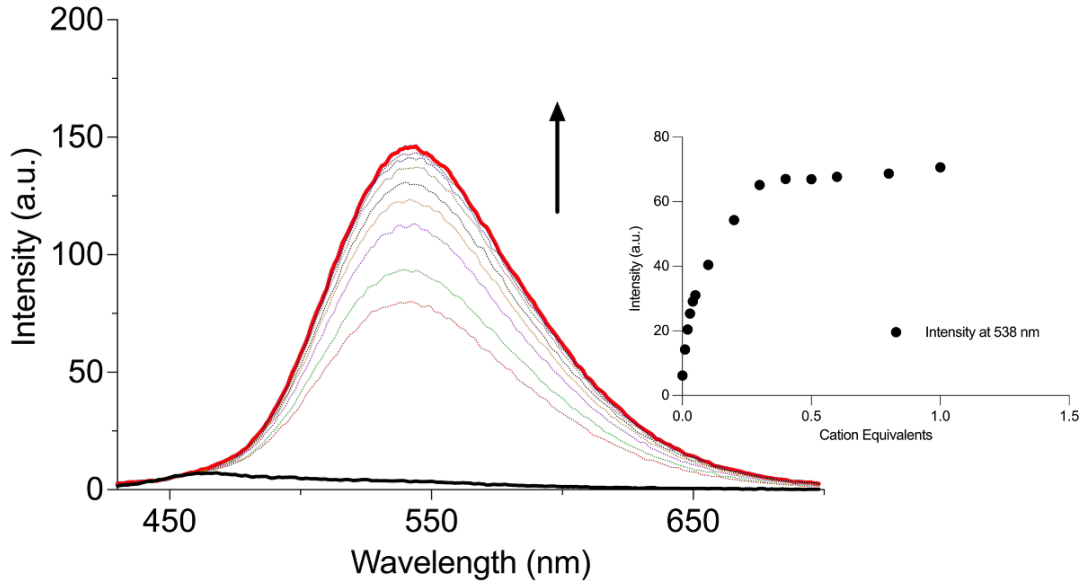

Figure SB102. Fluorescent spectra of Co^{2+} titration of **3.4** (1 mM) in MeCN. {insert} Fitplot for fluorescence intensity at 538 nm.

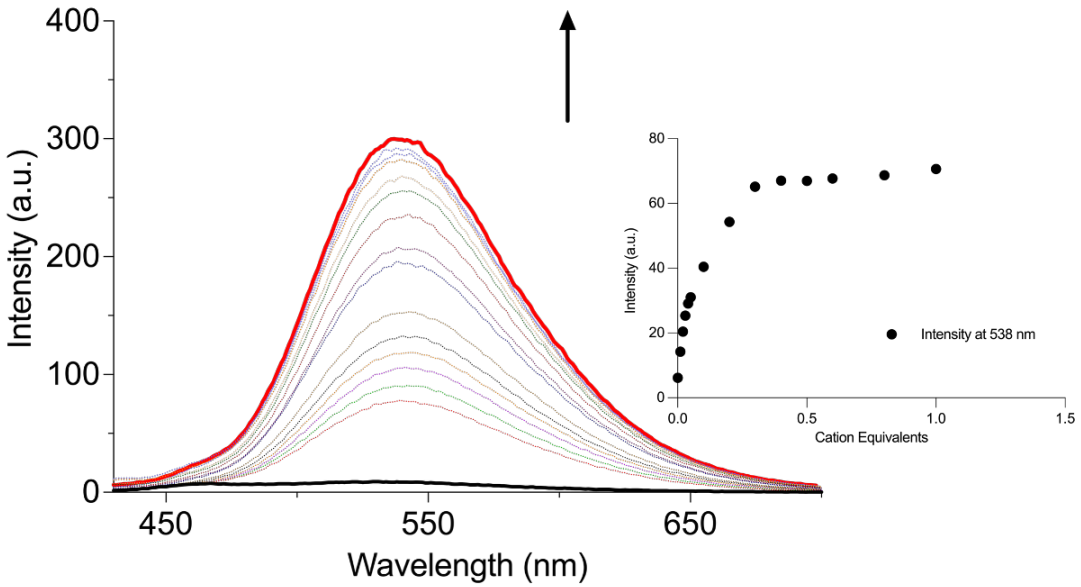

Figure SB103. Fluorescent spectra of Cu^{2+} titration of **3.4** (1 mM) in MeCN. {insert} Fitplot for fluorescence intensity at 538 nm.

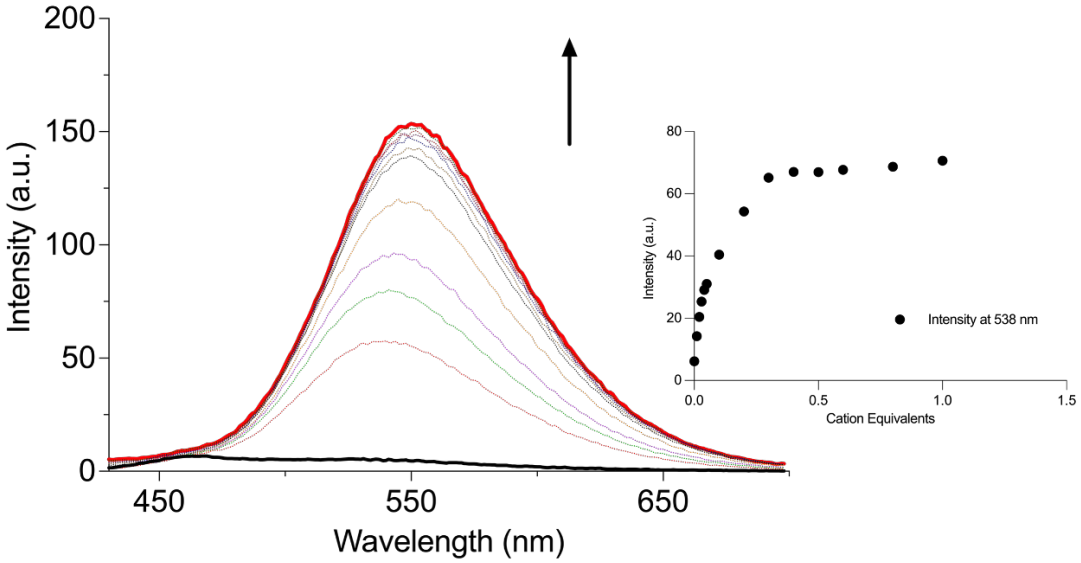

Figure SB104. Fluorescent spectra of Ni^{2+} titration of **3.4** (1 mM) in MeCN. {insert} Fitplot for fluorescence intensity at 538 nm.

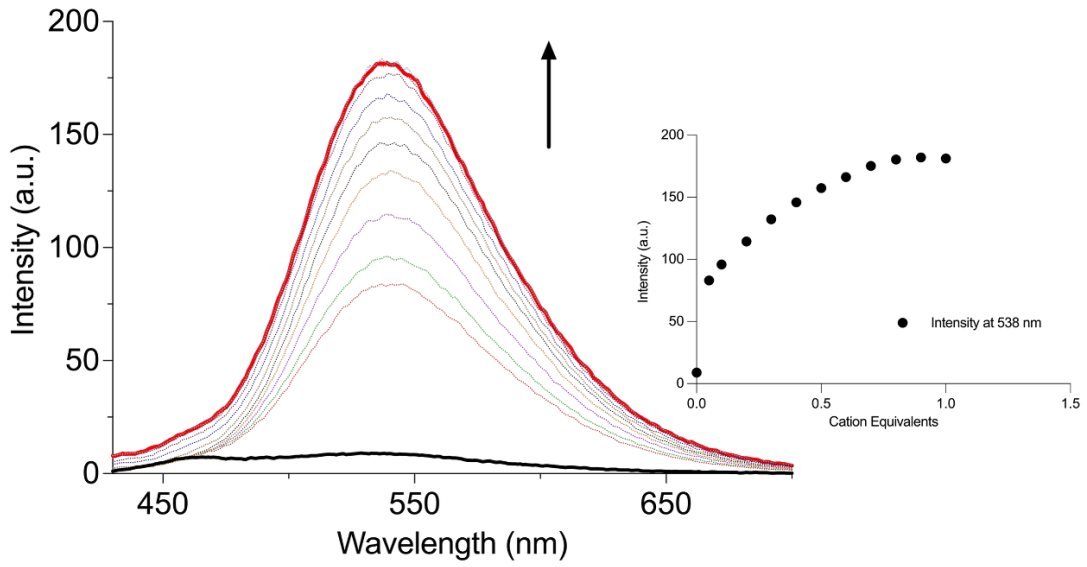

Figure SB105. Fluorescent spectra of Pb^{2+} titration of **3.4** (1 mM) in MeCN. {insert} Fitplot for fluorescence intensity at 538 nm.

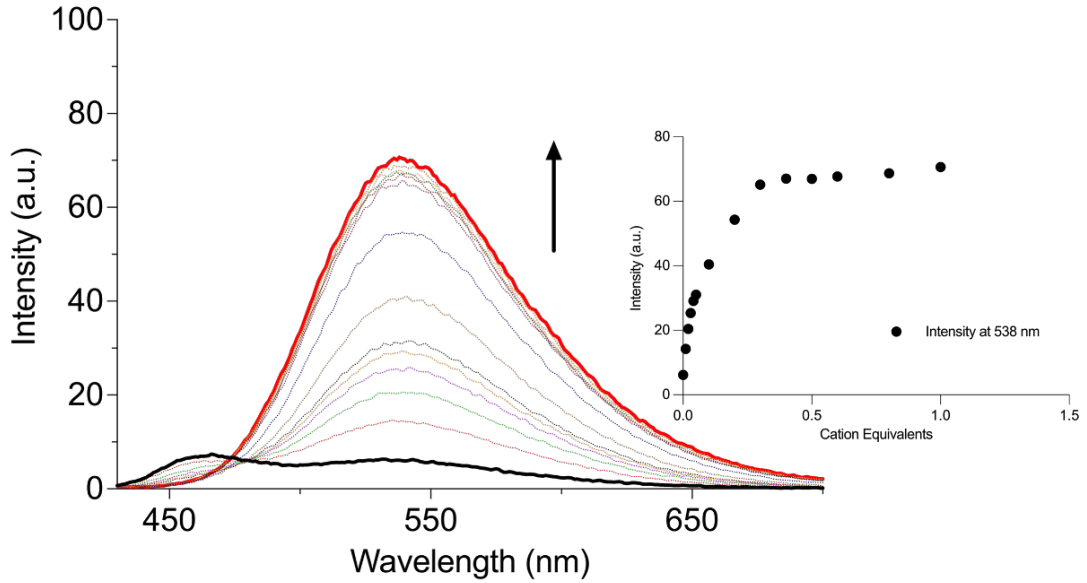

Figure SB106. Fluorescent spectra of Zn^{2+} titration of **3.4** (1 mM) in MeCN. {insert} Fitplot for fluorescence intensity at 538 nm.

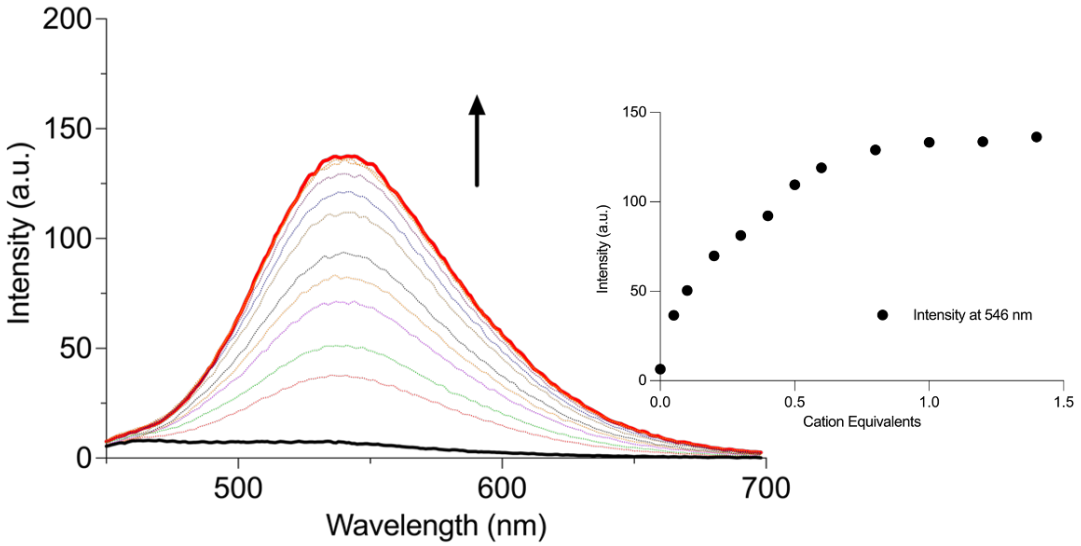

Figure SB107. Fluorescent spectra of Ag^{+} titration of **3.5** (1 mM) in MeCN. {insert} Fitplot for fluorescence intensity at 546 nm.

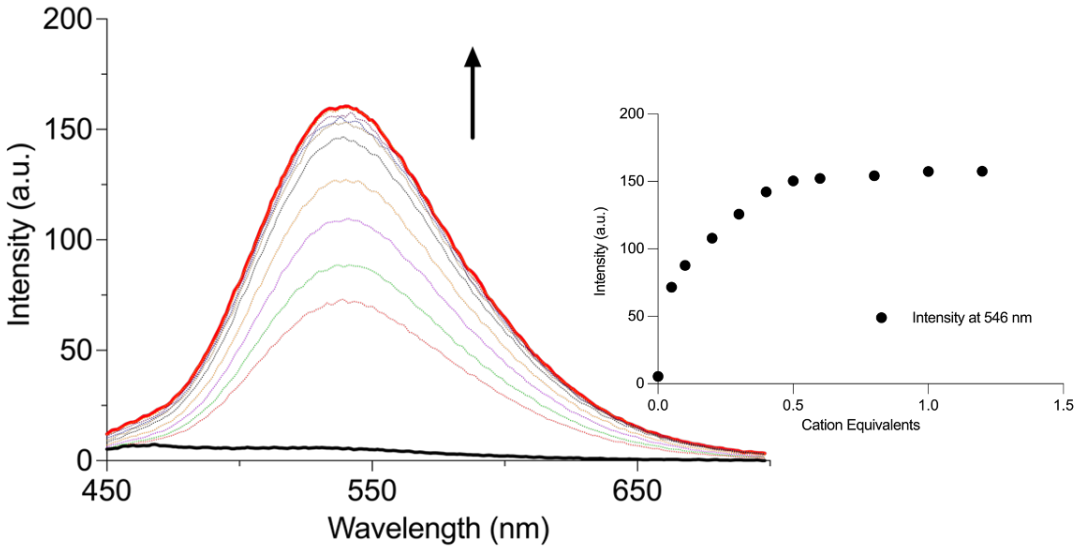

Figure SB108. Fluorescent spectra of Cd^{2+} titration of **3.5** (1 mM) in MeCN. {insert} Fitplot for fluorescence intensity at 546 nm.

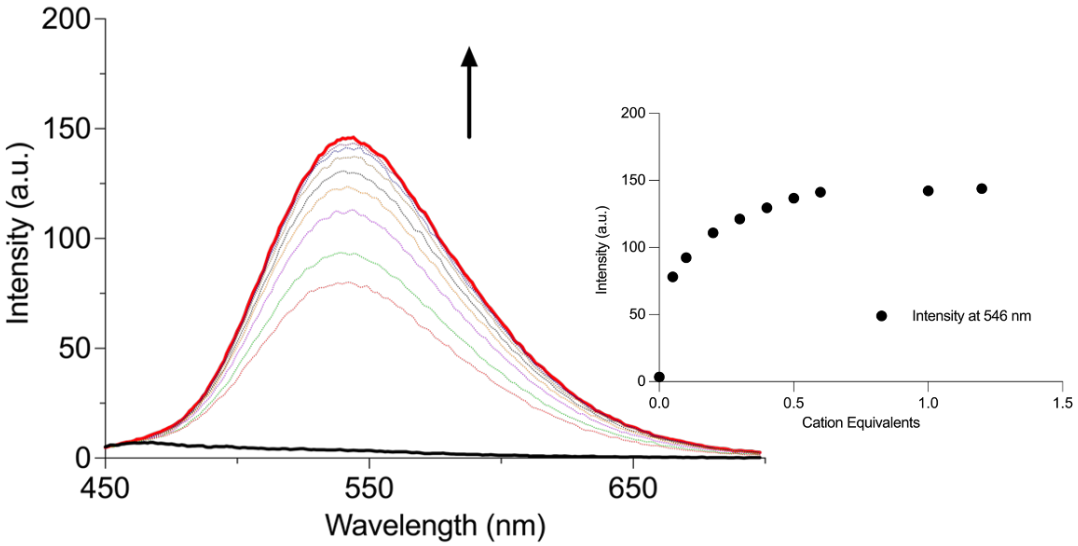

Figure SB109. Fluorescent spectra of Co^{2+} titration of **3.5** (1 mM) in MeCN. {insert} Fitplot for fluorescence intensity at 546 nm.

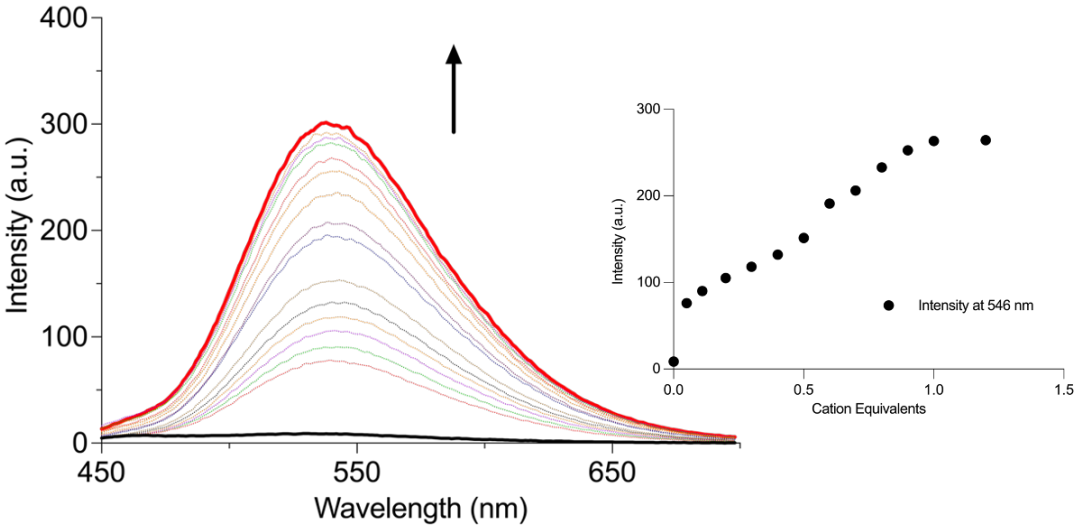

Figure SB110. Fluorescent spectra of Cu^{2+} titration of **3.5** (1 mM) in MeCN. {insert} Fitplot for fluorescence intensity at 546 nm.

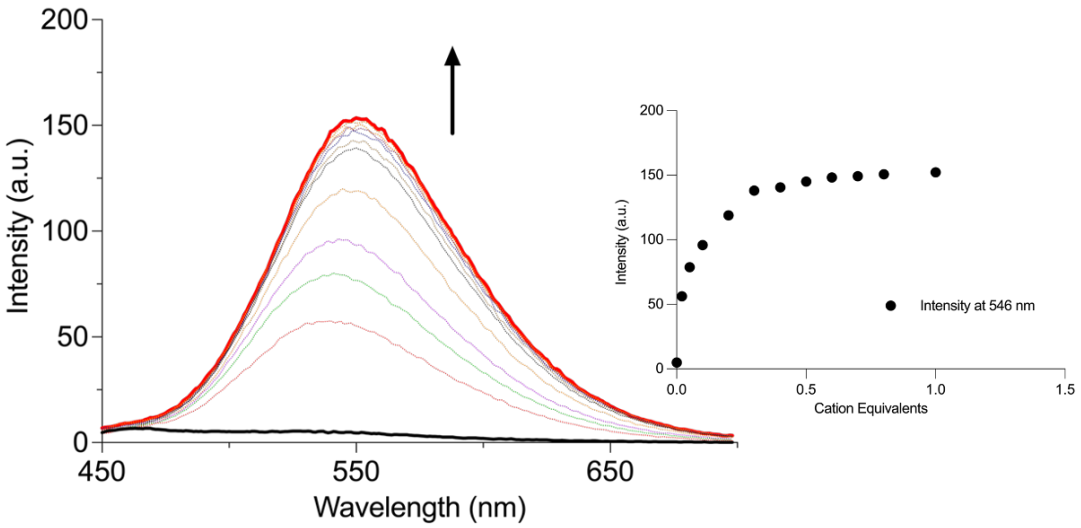

Figure SB111. Fluorescent spectra of Ni^{2+} titration of **3.5** (1 mM) in MeCN. {insert} Fitplot for fluorescence intensity at 546 nm.

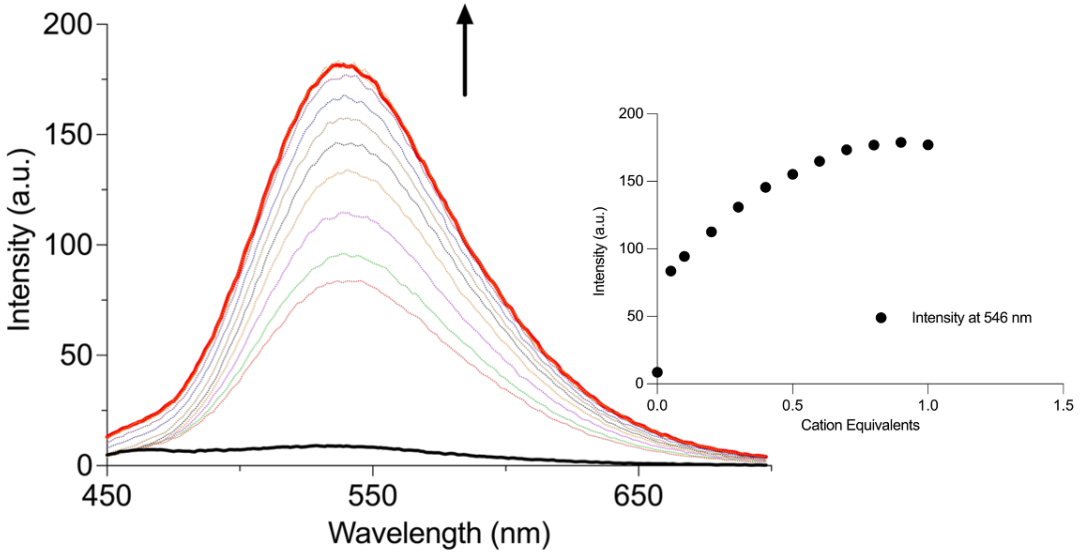

Figure SB112. Fluorescent spectra of Pb^{2+} titration of **3.5** (1 mM) in MeCN. {insert} Fitplot for fluorescence intensity at 546 nm.

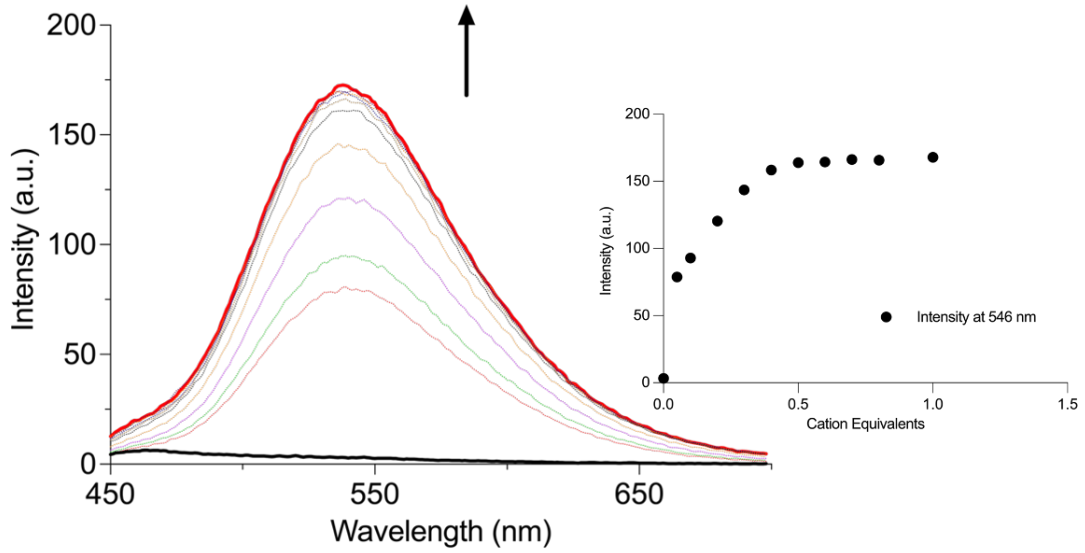

Figure SB113. Fluorescent spectra of Zn^{2+} titration of **3.5** (1 mM) in MeCN. {insert} Fitplot for fluorescence intensity at 546 nm.

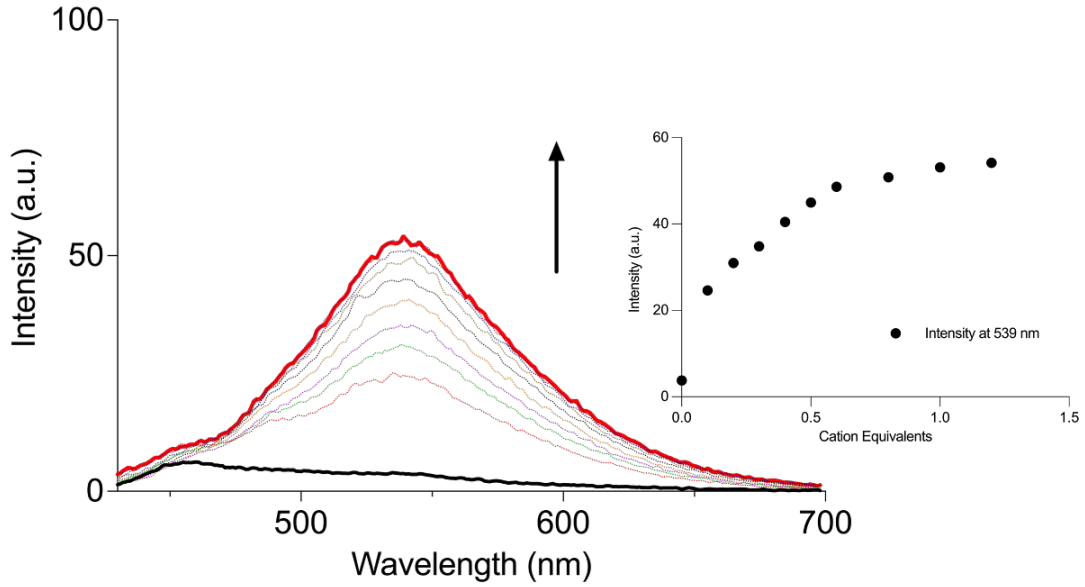

Figure SB114. Fluorescent spectra of Ag^{+} titration of **3.6** (1 mM) in MeCN. {insert} Fitplot for fluorescence intensity at 539 nm.

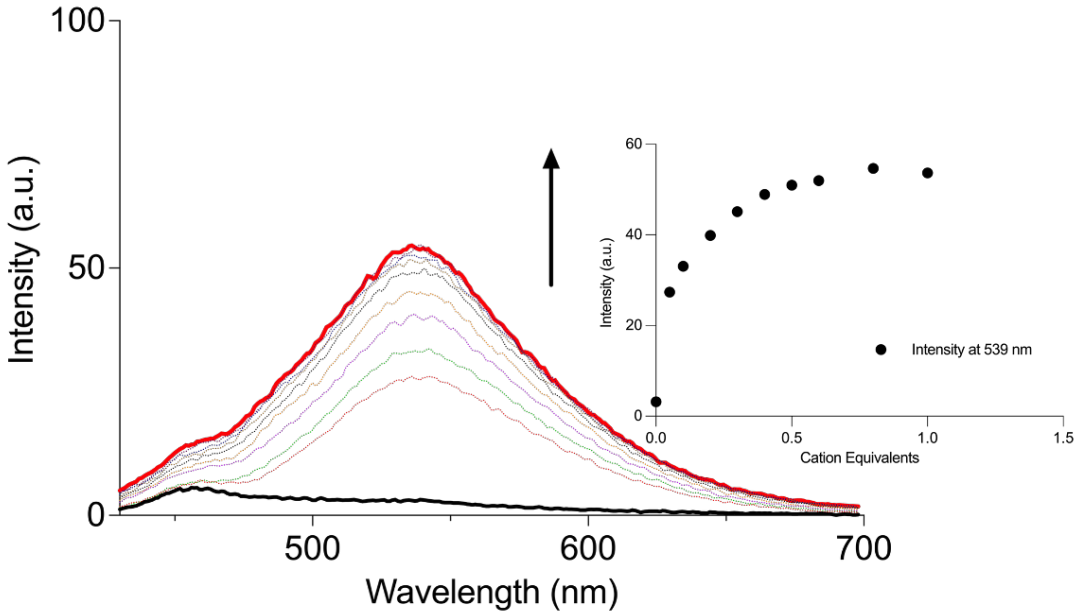

Figure SB115. Fluorescent spectra of Cd^{2+} titration of **3.6** (1 mM) in MeCN. {insert} Fitplot for fluorescence intensity at 539 nm.

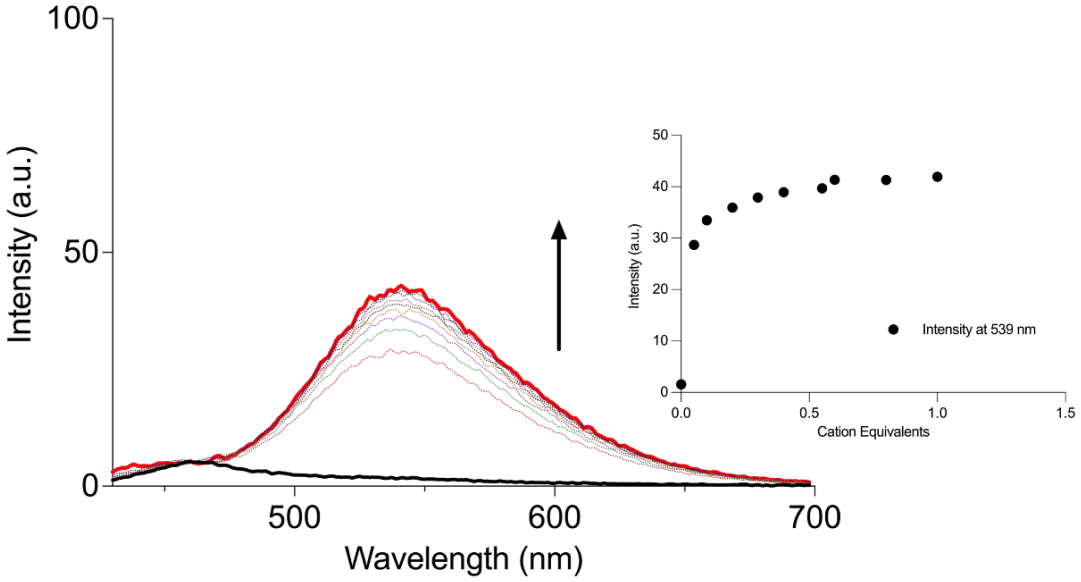

Figure SB116. Fluorescent spectra of Co^{2+} titration of **3.6** (1 mM) in MeCN. {insert} Fitplot for fluorescence intensity at 539 nm.

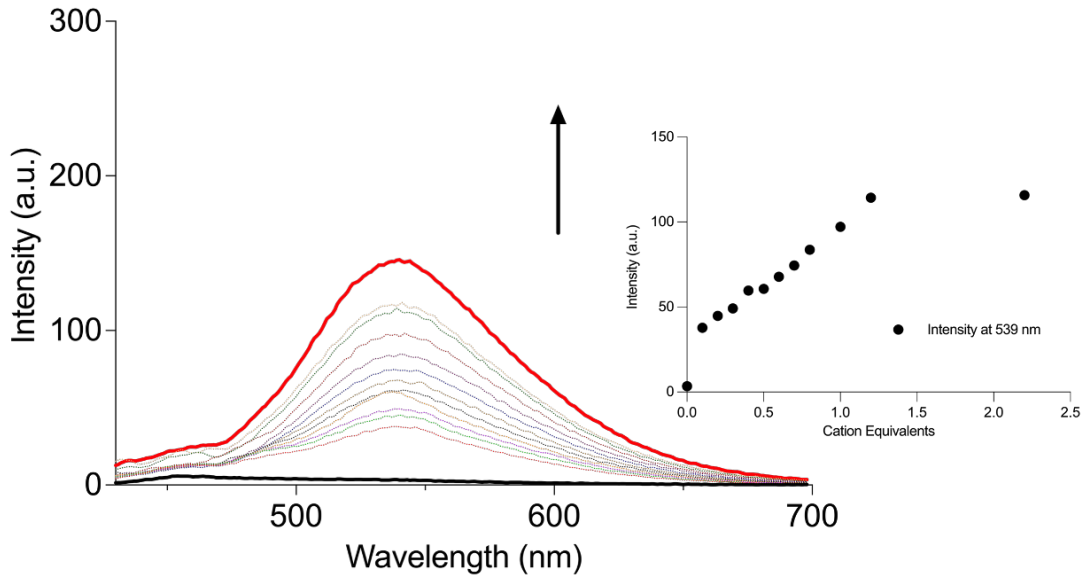

Figure SB117. Fluorescent spectra of Cu^{2+} titration of **3.6** (1 mM) in MeCN. {insert} Fitplot for fluorescence intensity at 539 nm.

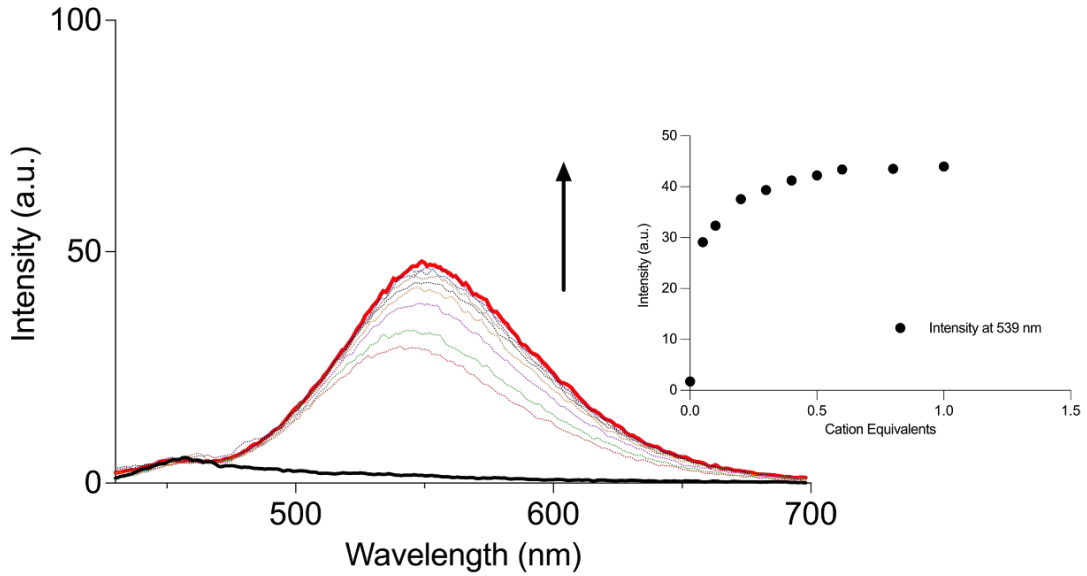

Figure SB4118. Fluorescent spectra of Ni^{2+} titration of **3.6** (1 mM) in MeCN. {insert} Fitplot for fluorescence intensity at 539 nm.

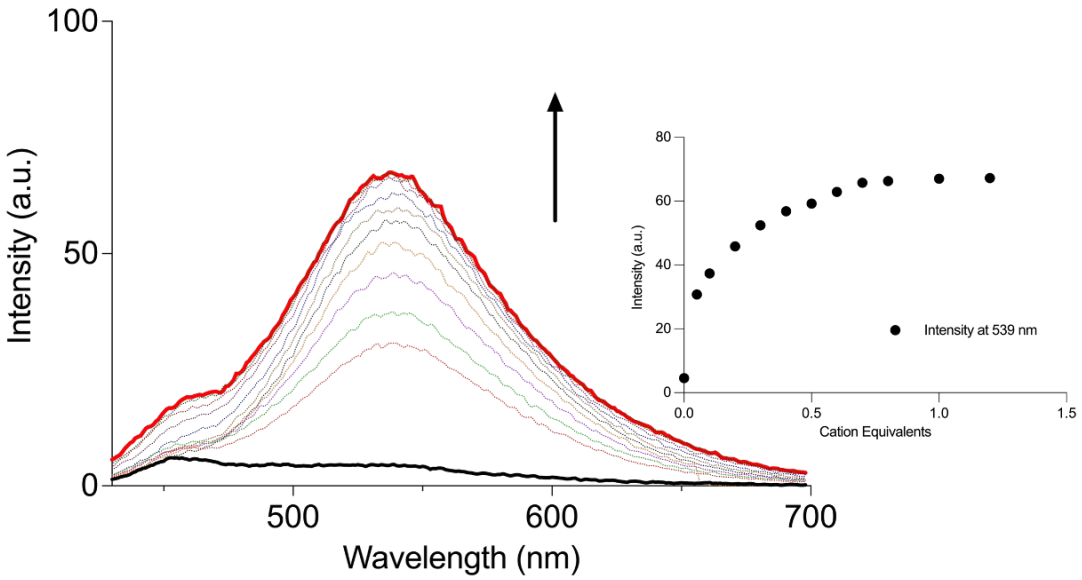

Figure SB119. Fluorescent spectra of Pb^{2+} titration of **3.6** (1 mM) in MeCN. {insert} Fitplot for fluorescence intensity at 539 nm.

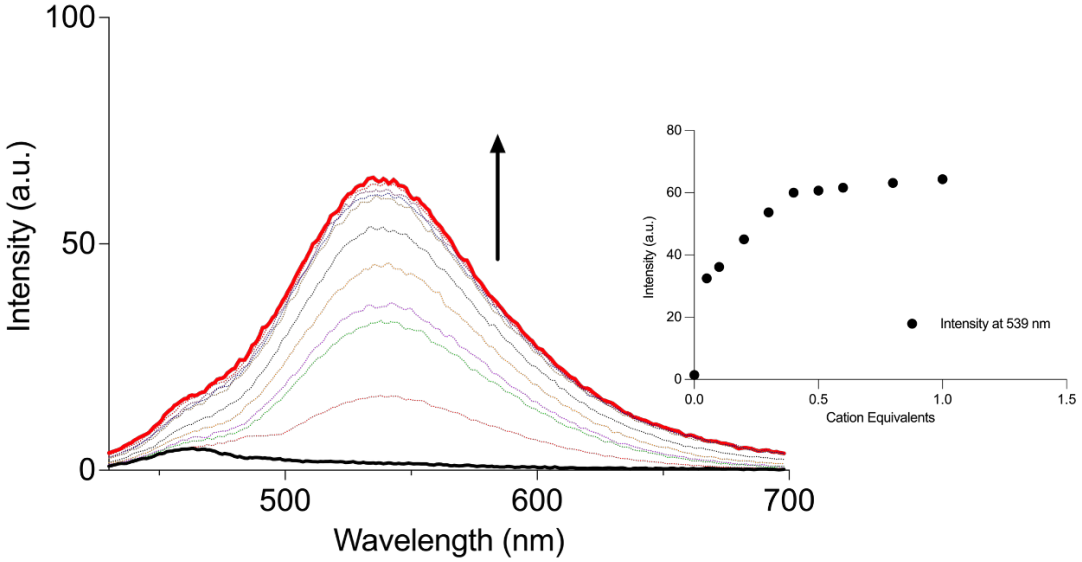

Figure SB120. Fluorescent spectra of Zn^{2+} titration of **3.6** (1 mM) in MeCN. {insert} Fitplot for fluorescence intensity at 539 nm.

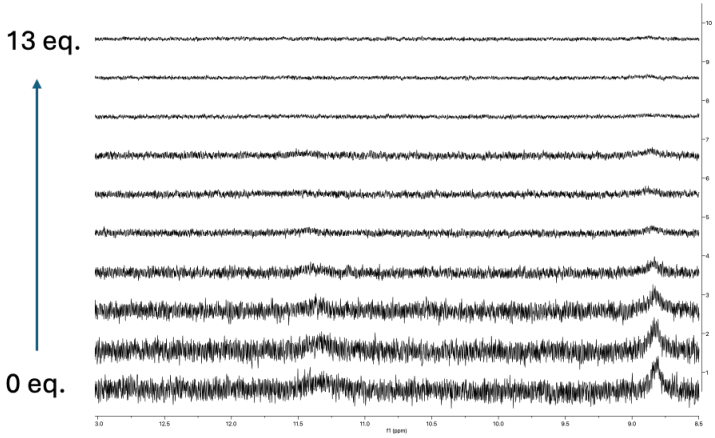

Figure SB121. ^{1}H NMR titration of **3.1** with Cl^- in DMSO-d_6. Deprotonation prevents the calculation of the K_a value.

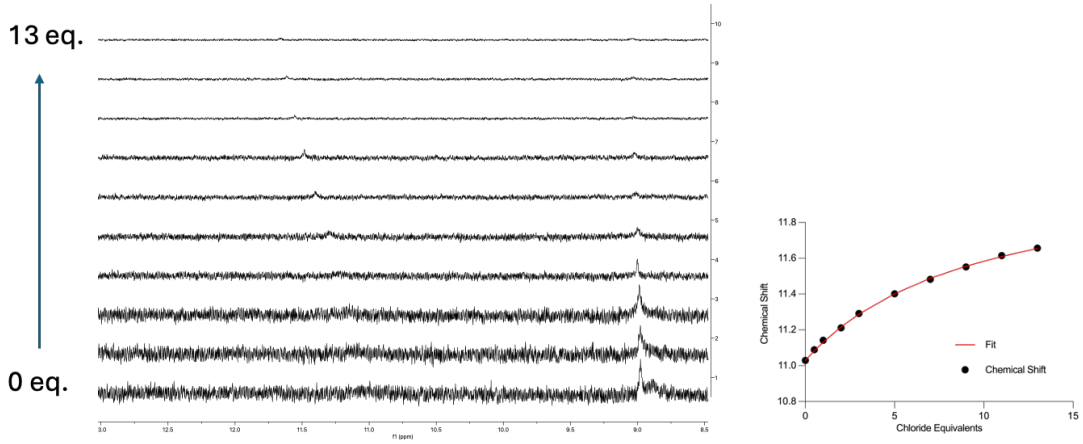

Figure SB122. (a) ^{1}H NMR titration of **3.3** with Cl^- in DMSO-d_6. (b) Fitplot for NH proton at δ = 11.03 ppm. The data were fit to a 1:1 binding model.

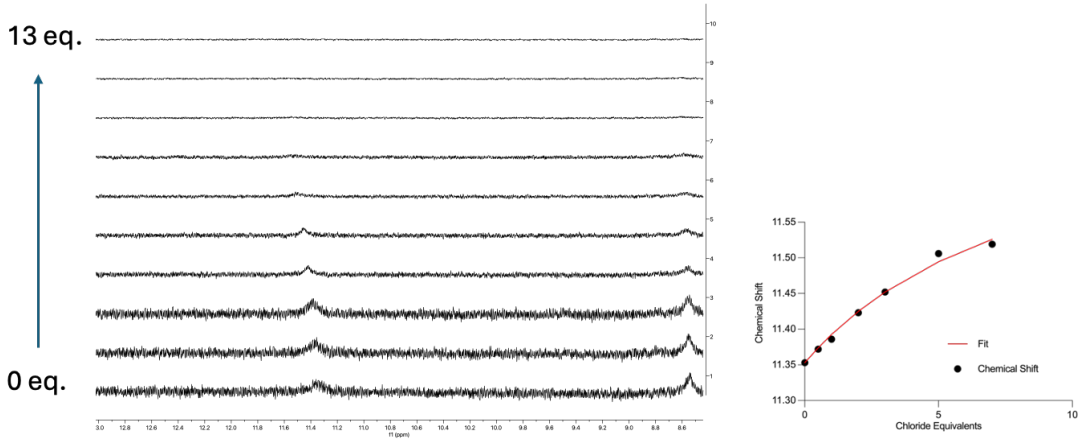

Figure SB123. (a) ^{1}H NMR titration of **3.4** with Cl^- in DMSO-d_6. (b) Fitplot for NH proton at δ = 11.35 ppm. The data were fit to a 1:1 binding model.

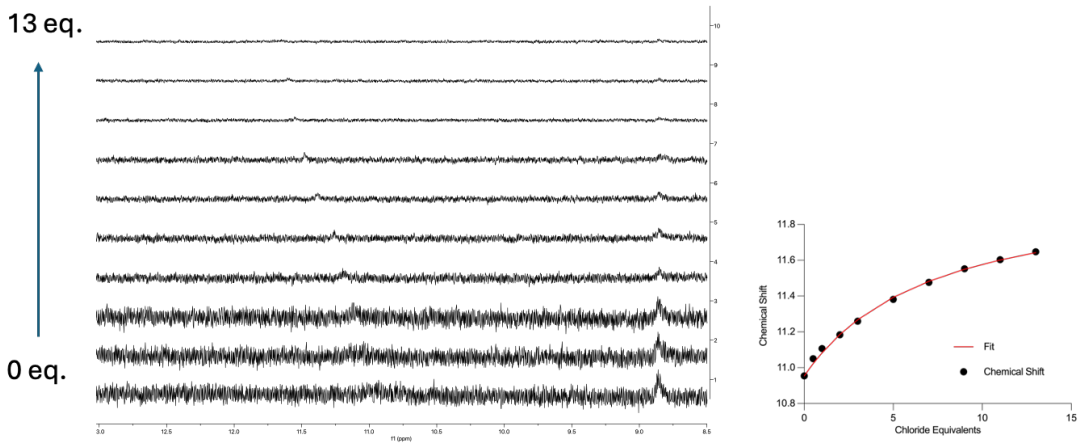

Figure SB124. (a) ^{1}H NMR titration of **3.5** with Cl^{-} in DMSO-d_6. (b) Fitplot for NH proton at δ = 10.96 ppm. The data were fit to a 1:1 binding model.

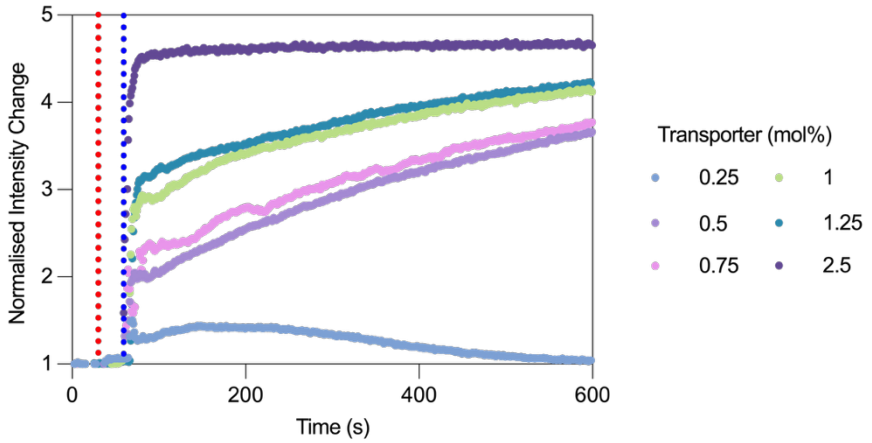

Figure SB125. Normalised intensity changes after the addition of receptor **3.2** (red line) followed by 0.1 mM Zn^{2+}(blue line). Concentration used: 0.25 mol%, 0.5 mol%, 0.75 mol%, 1 mol%, 1.25 mol%, 2.5 mol%.

Supporting information for Chapter 4

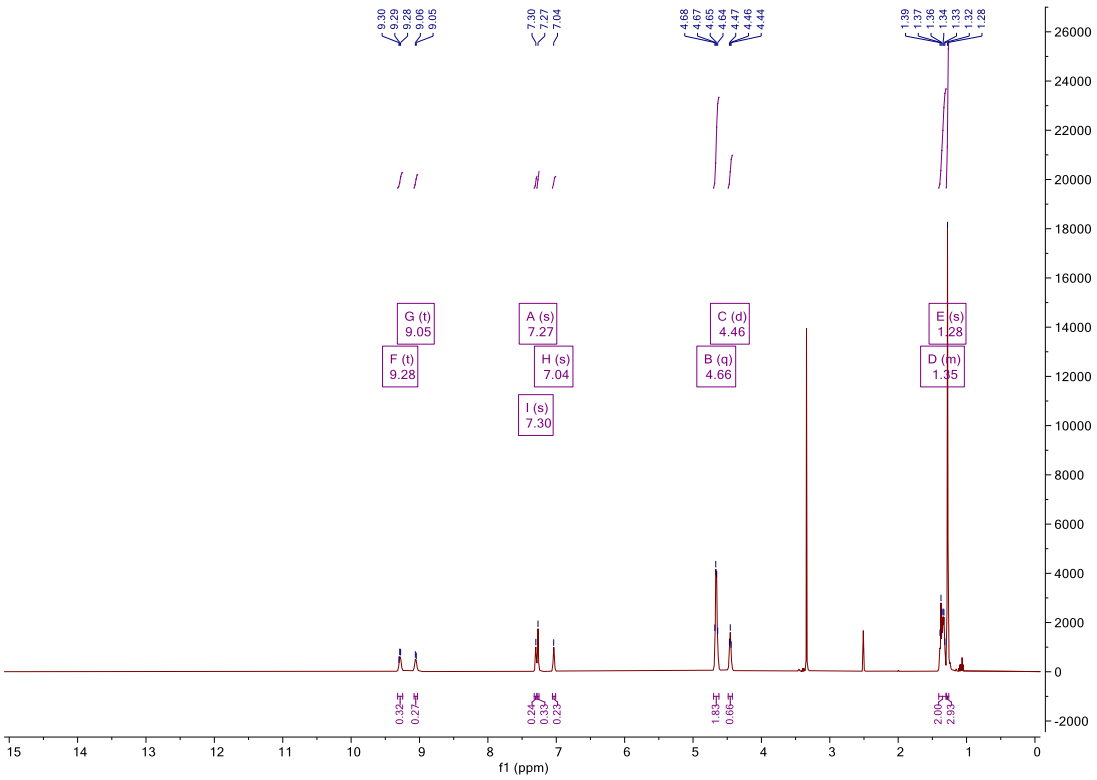

Figure SC1. ^{1}H NMR (DMSO-d_6, 500MHz) spectrum of **C3**.

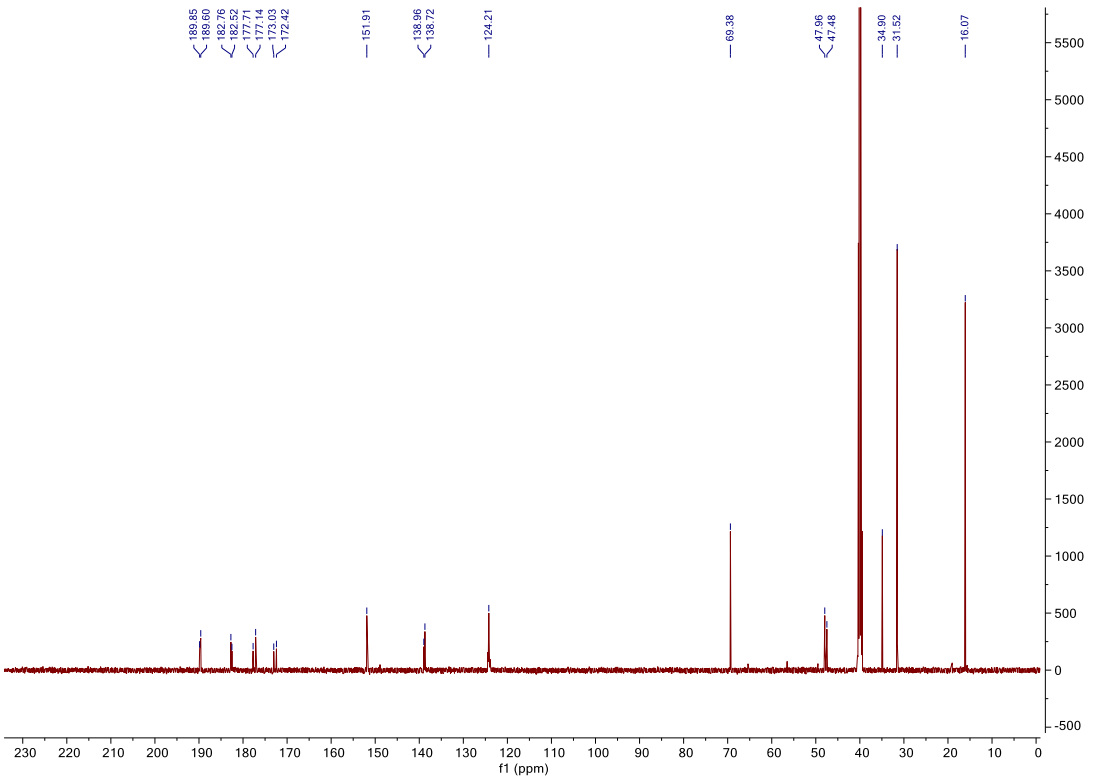

Figure SC2. ^{13}C NMR (DMSO-d_6, 126MHz) spectrum of **C3**.

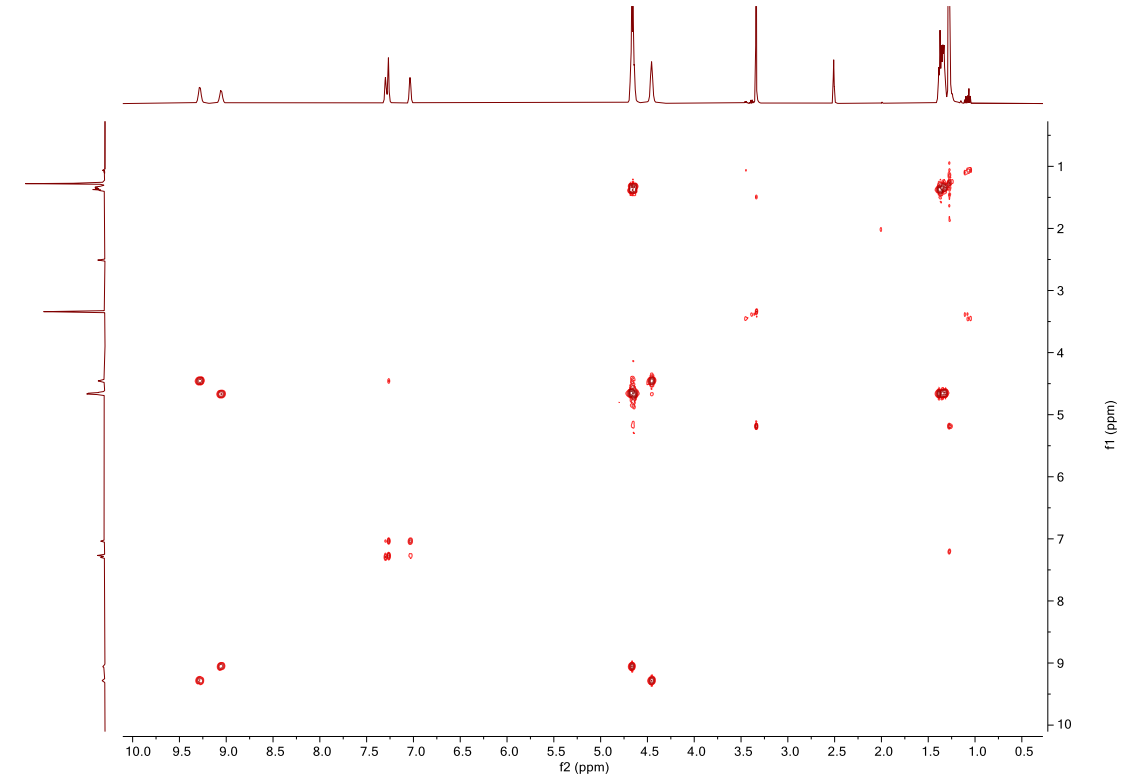

Figure SC3. COSY NMR (DMSO-d_6) spectrum of **C3**.

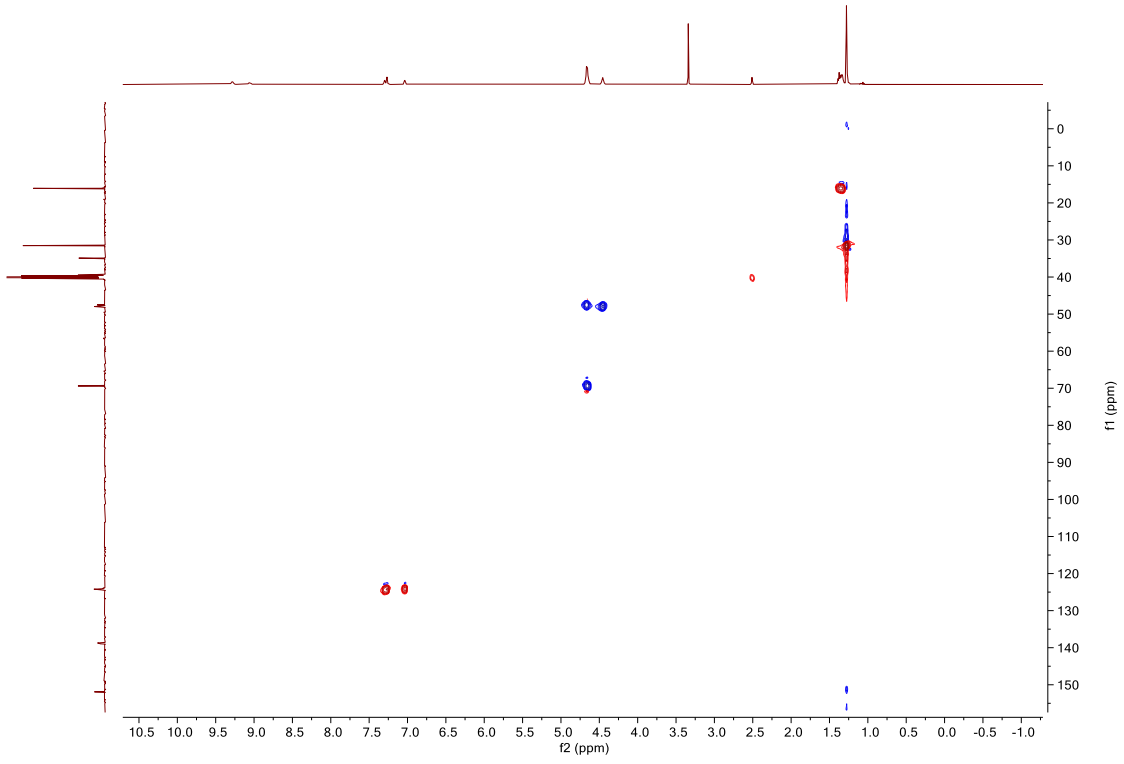

Figure SC4. HSQC NMR (DMSO-d_6) spectrum of **C3**.

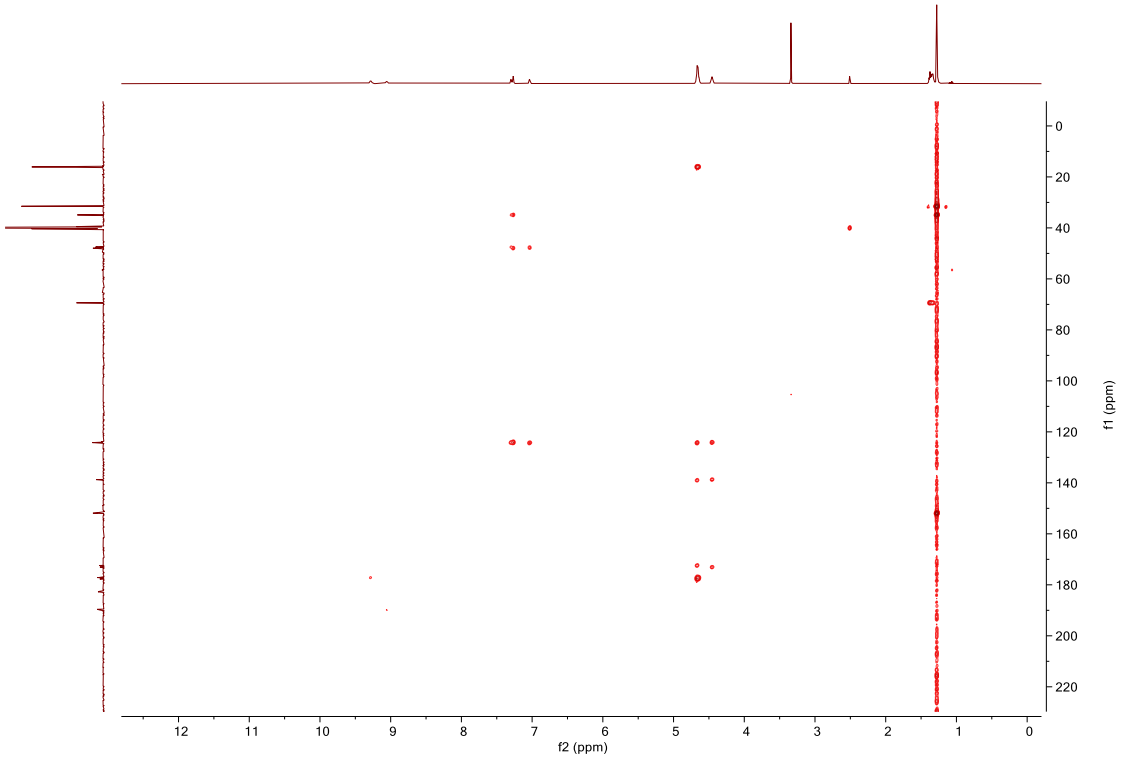

Figure SC5. HMBC NMR (DMSO-d_6) spectrum of **C3**.

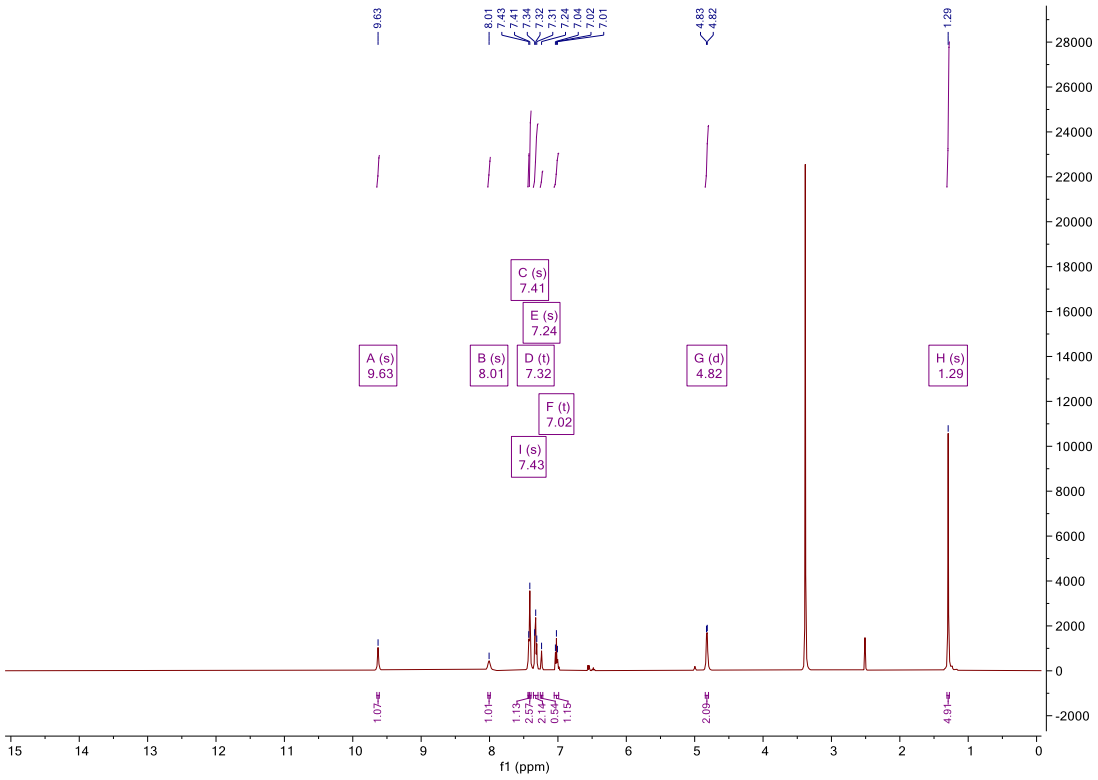

Figure SC6. ^{1}H NMR (DMSO-d_6, 500MHz) spectrum of **4.1**.

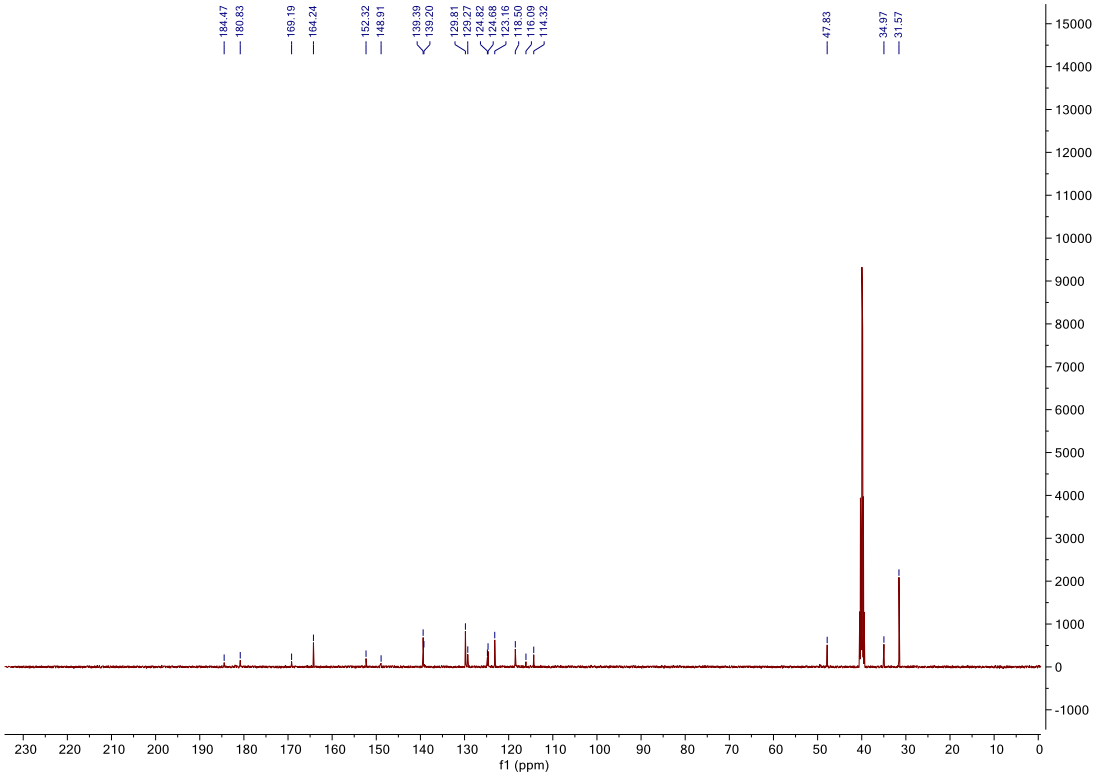

Figure SC7. ^{13}C NMR (DMSO-d_6, 126MHz) spectrum of **4.1**.

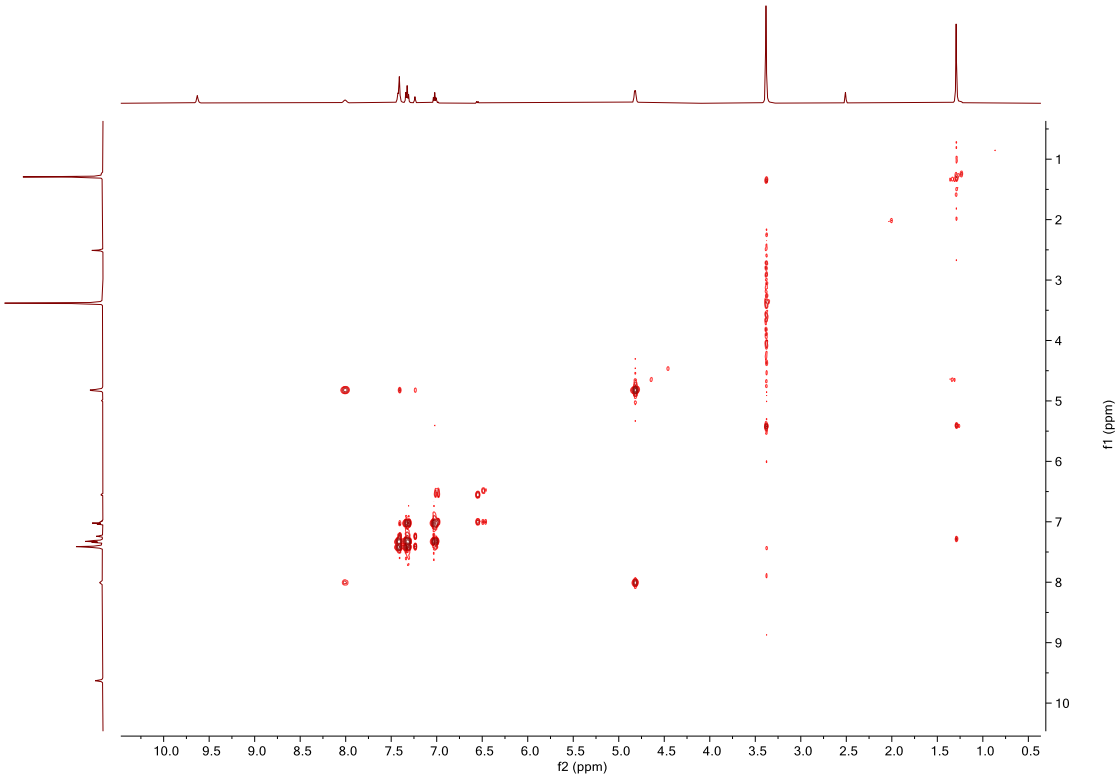

Figure SC8. COSY NMR (DMSO-d_6) spectrum of **4.1**.

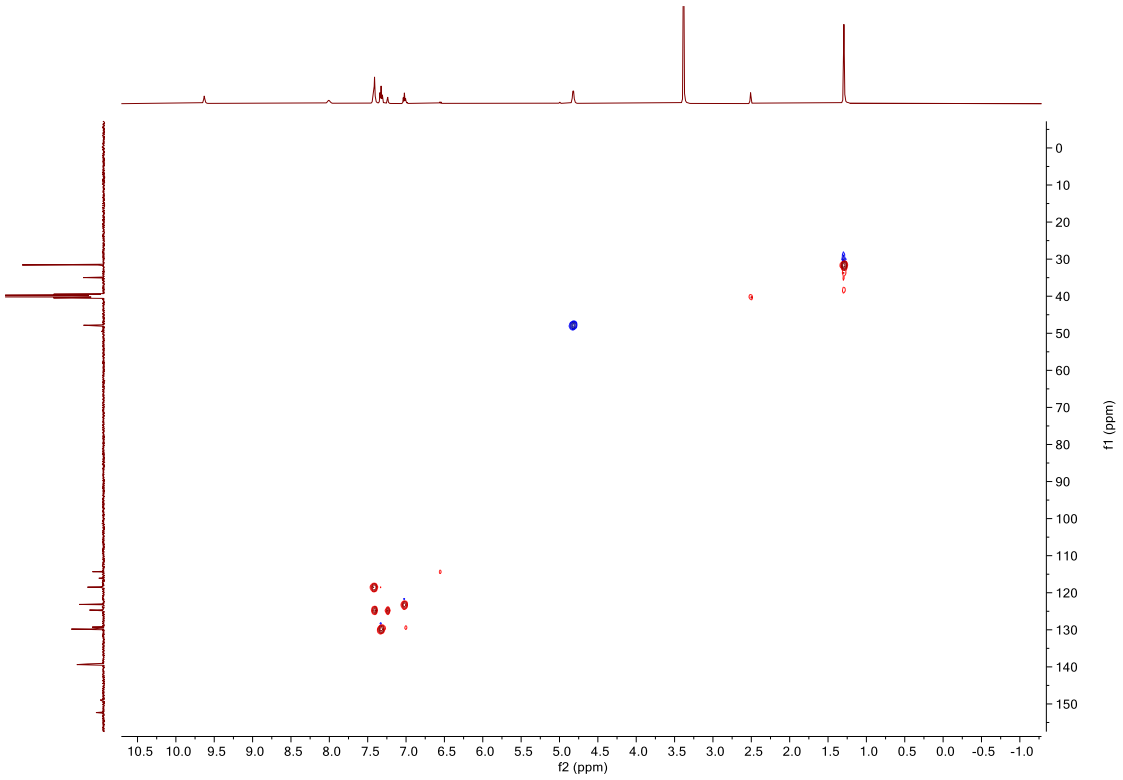

Figure SC9. HSQC NMR (DMSO-d_6) spectrum of **4.1**.

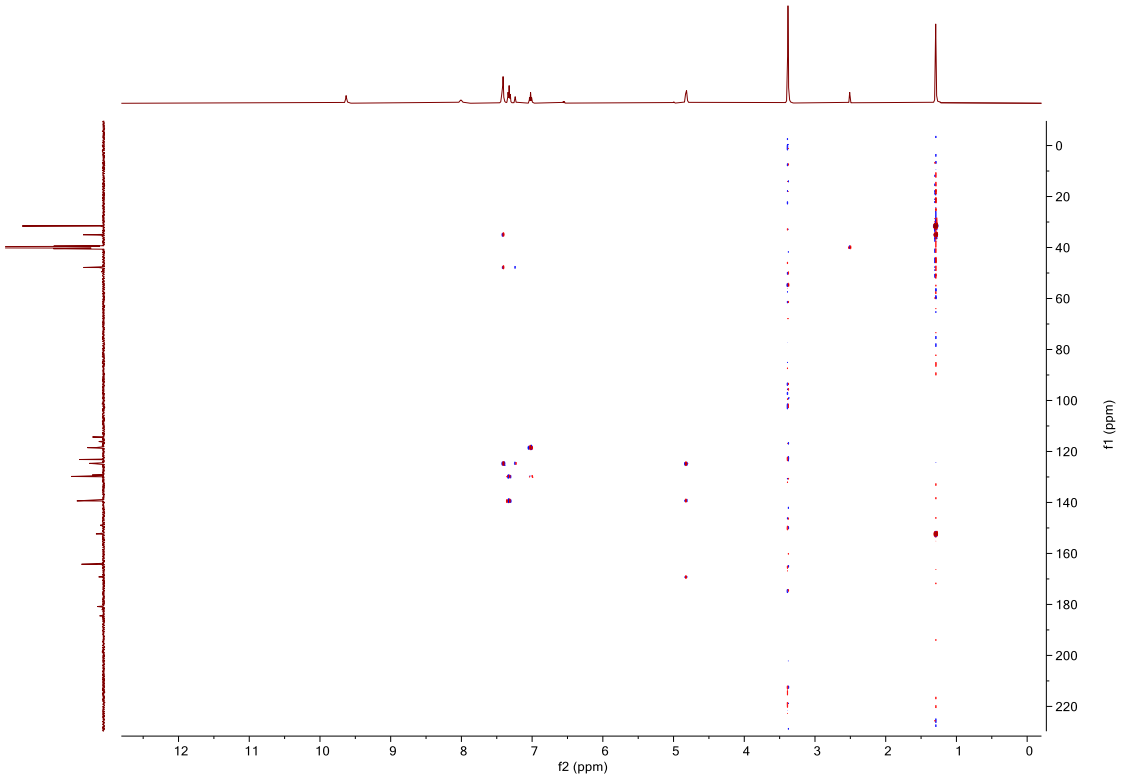

Figure SC10. HMBC NMR (DMSO-d_6) spectrum of **4.1**.

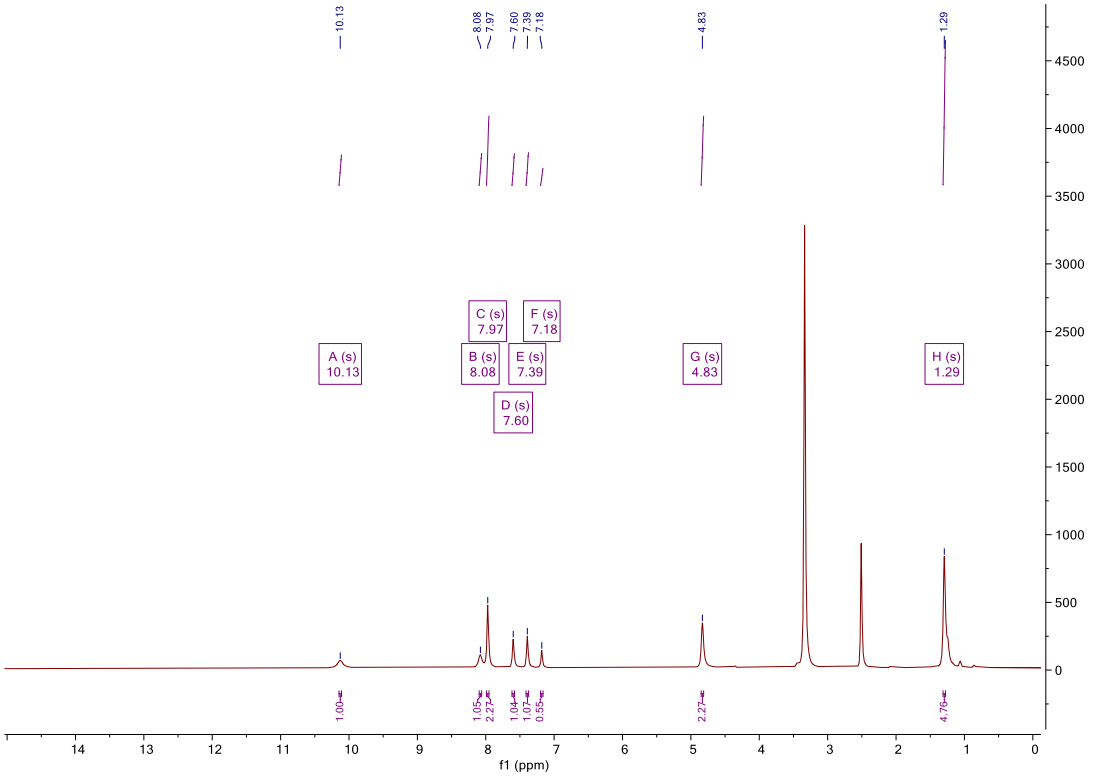

Figure SC11. ^{1}H NMR (DMSO-d_6, 500MHz) spectrum of **4.2**.

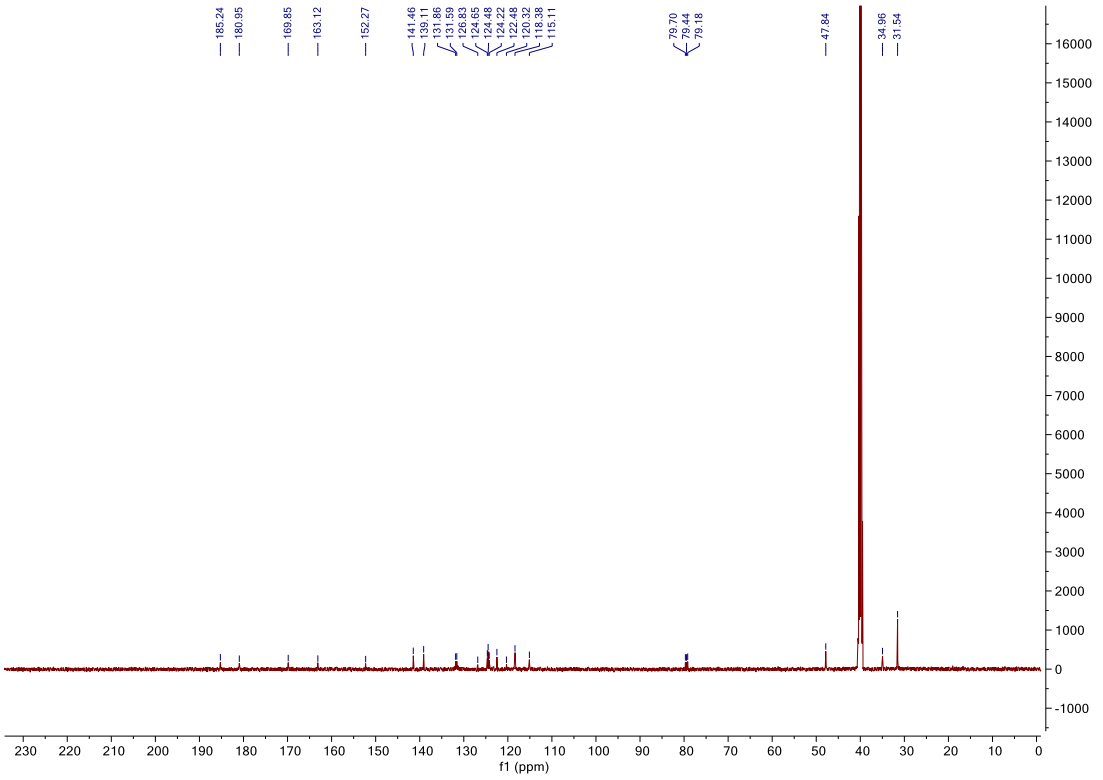

Figure SC12. ^{13}C NMR (DMSO-d_6, 126MHz) spectrum of **4.2**.

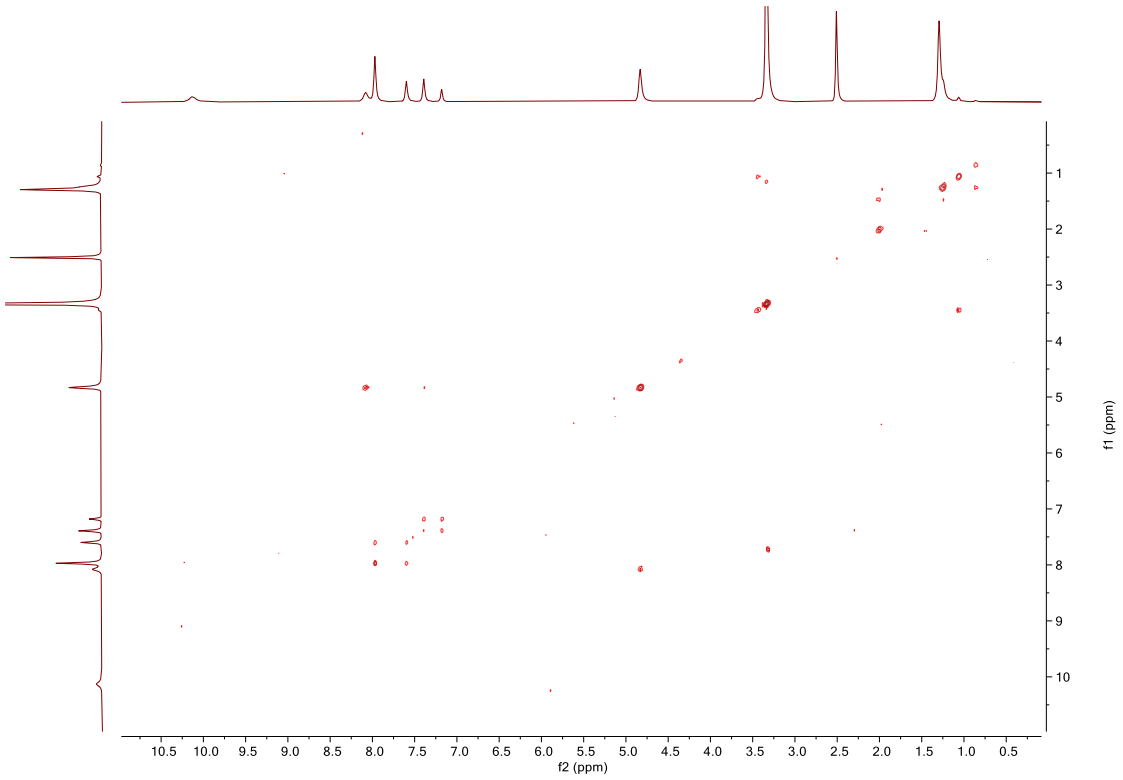

Figure SC13. COSY NMR (DMSO-d_6) spectrum of **4.2**.

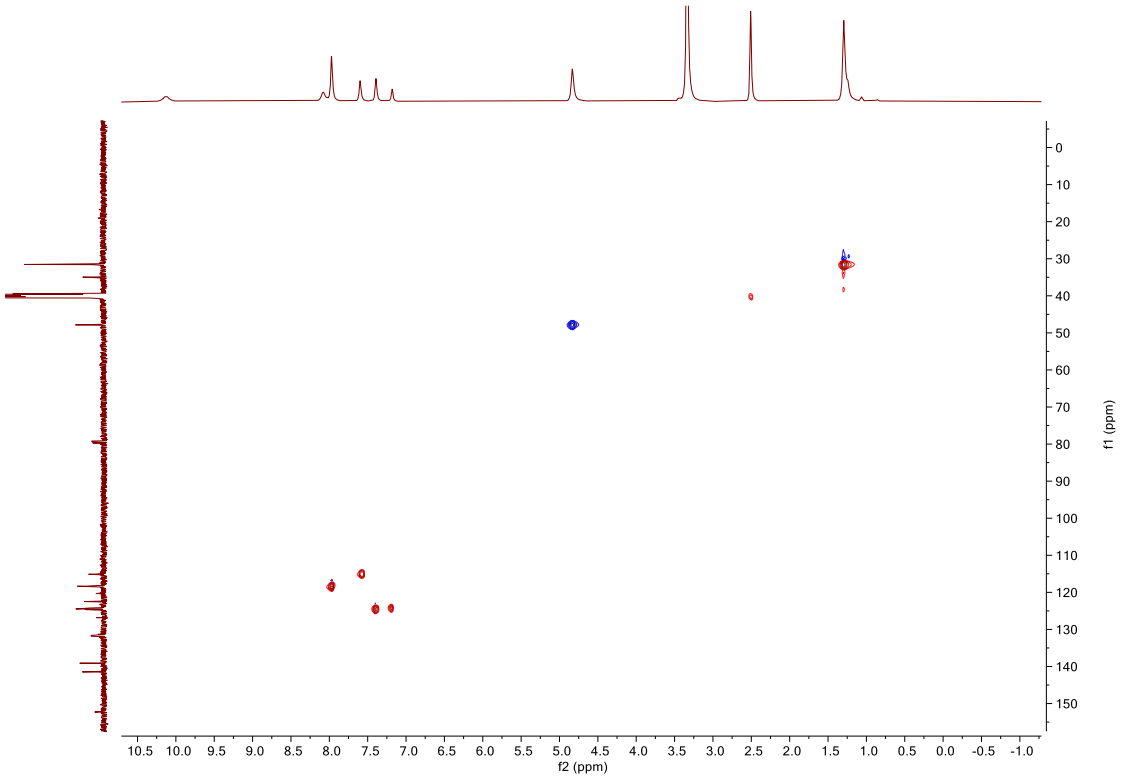

Figure SC14. HSQC NMR (DMSO-d_6) spectrum of **4.2**.

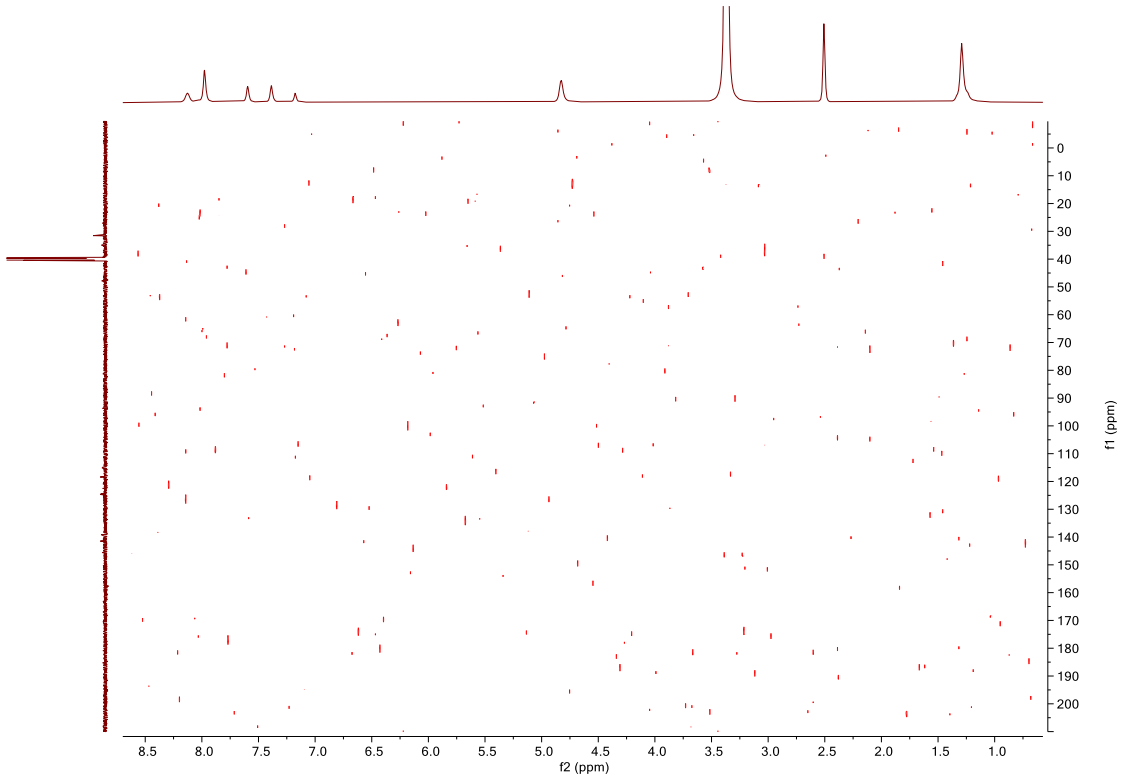

Figure SC15. HMBC NMR (DMSO-d_6) spectrum of **4.2**.

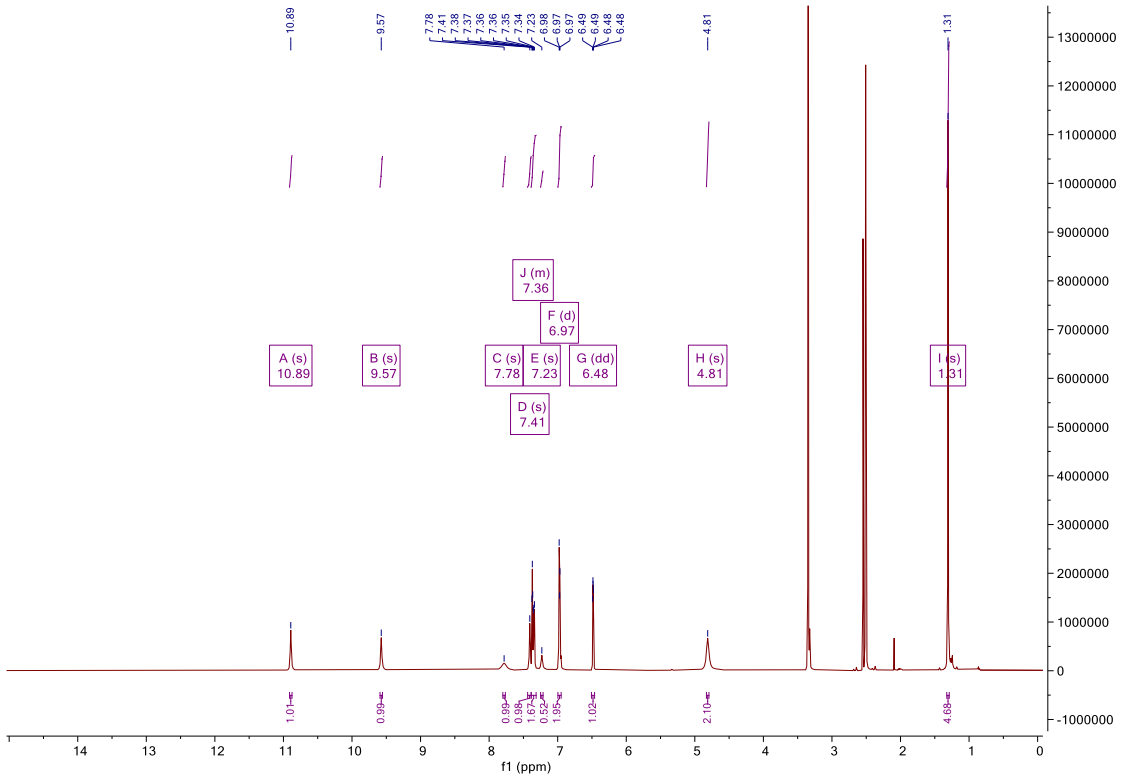

Figure SC16. ^{1}H NMR (DMSO-d_6, 500MHz) spectrum of **4.3**.

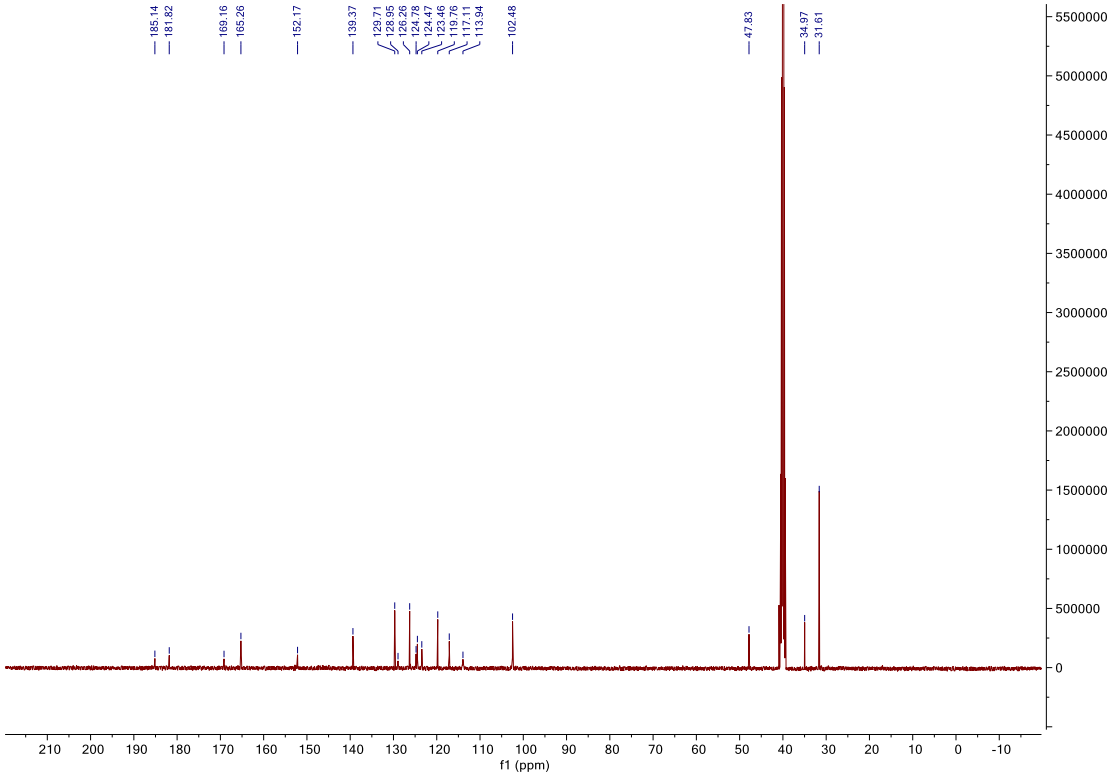

Figure SC17. ^{13}C NMR (DMSO-d_6, 126MHz) spectrum of **4.3**.

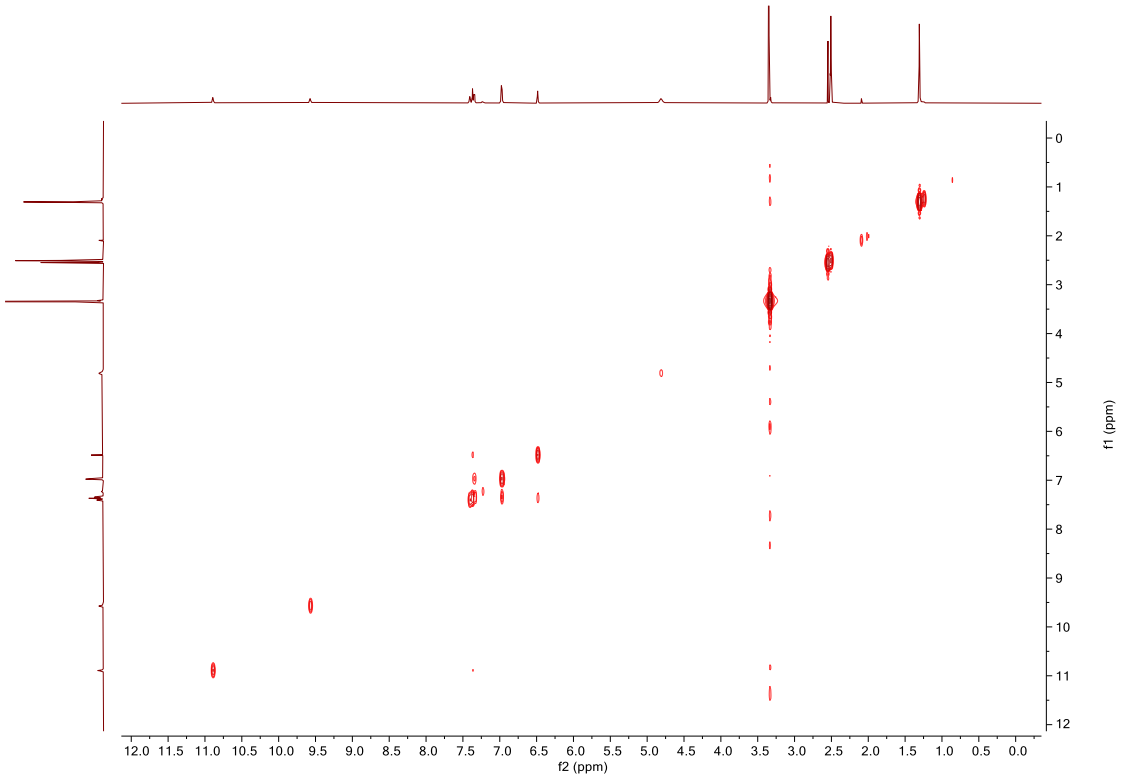

Figure SC18. COSY NMR (DMSO-d_6) spectrum of **4.3**.

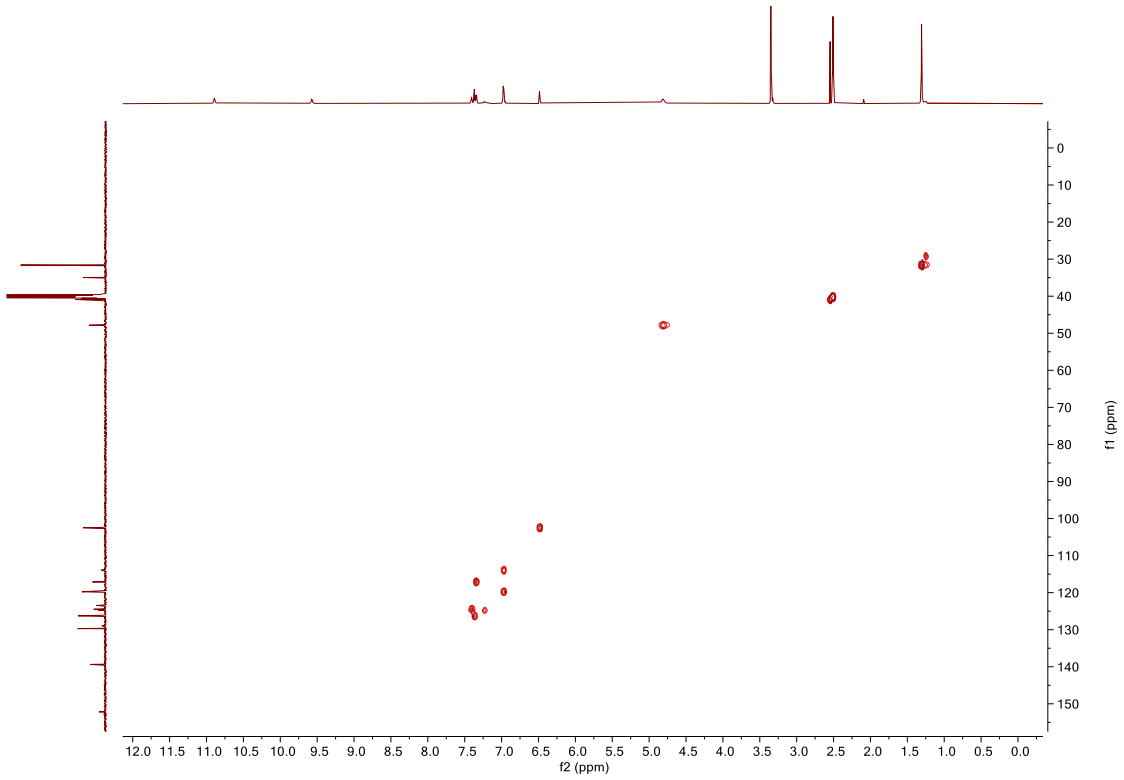

Figure SC19. HSQC NMR (DMSO-d_6) spectrum of **4.3**.

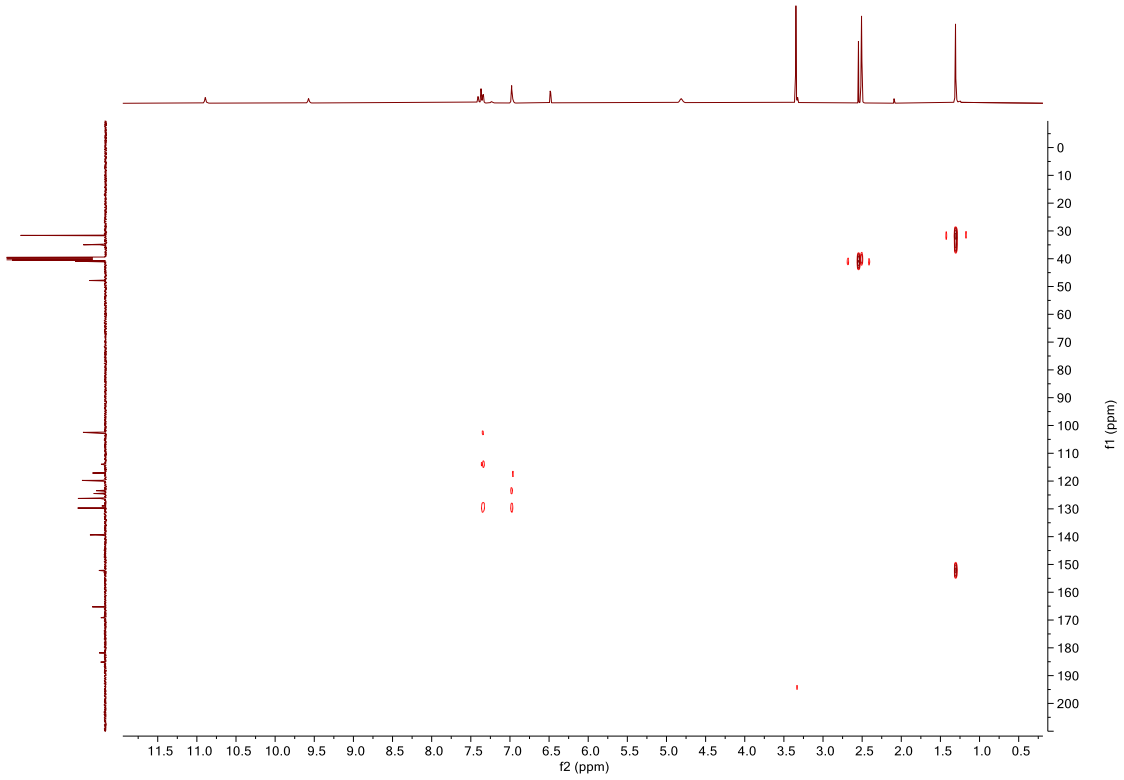

Figure SC20. HMBC NMR (DMSO-d_6) spectrum of **4.3**.

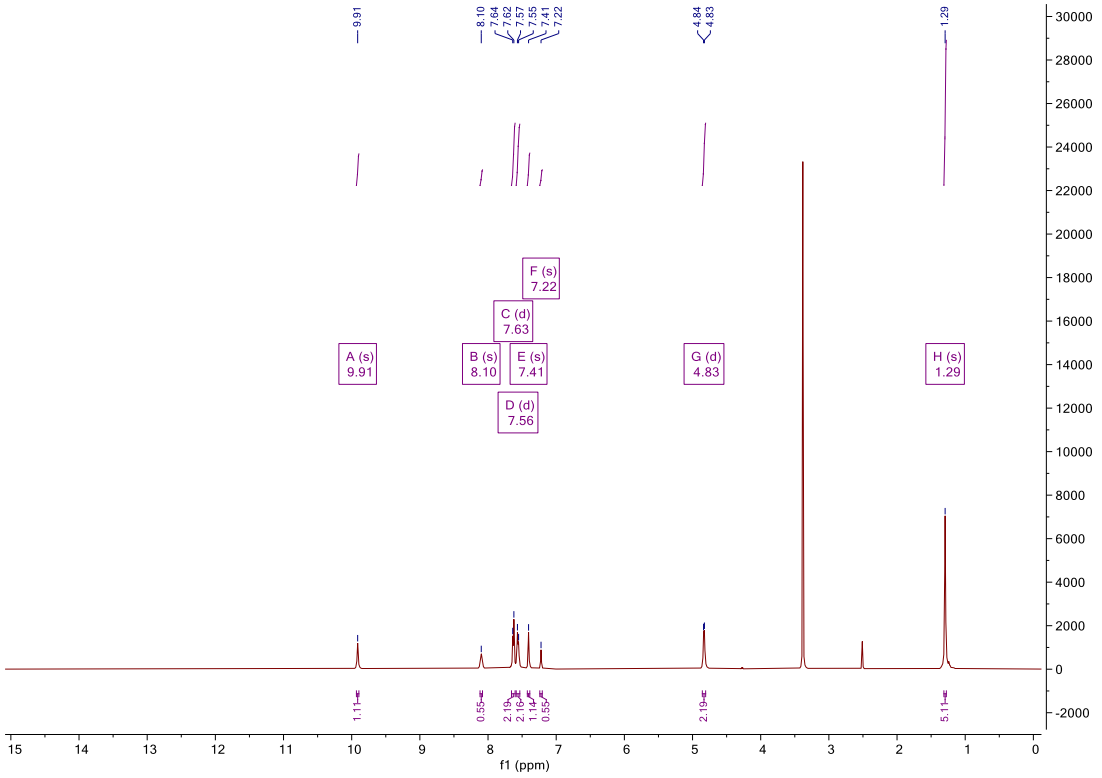

Figure SC21. ^{1}H NMR (DMSO-d_6, 500MHz) spectrum of **4.4**.

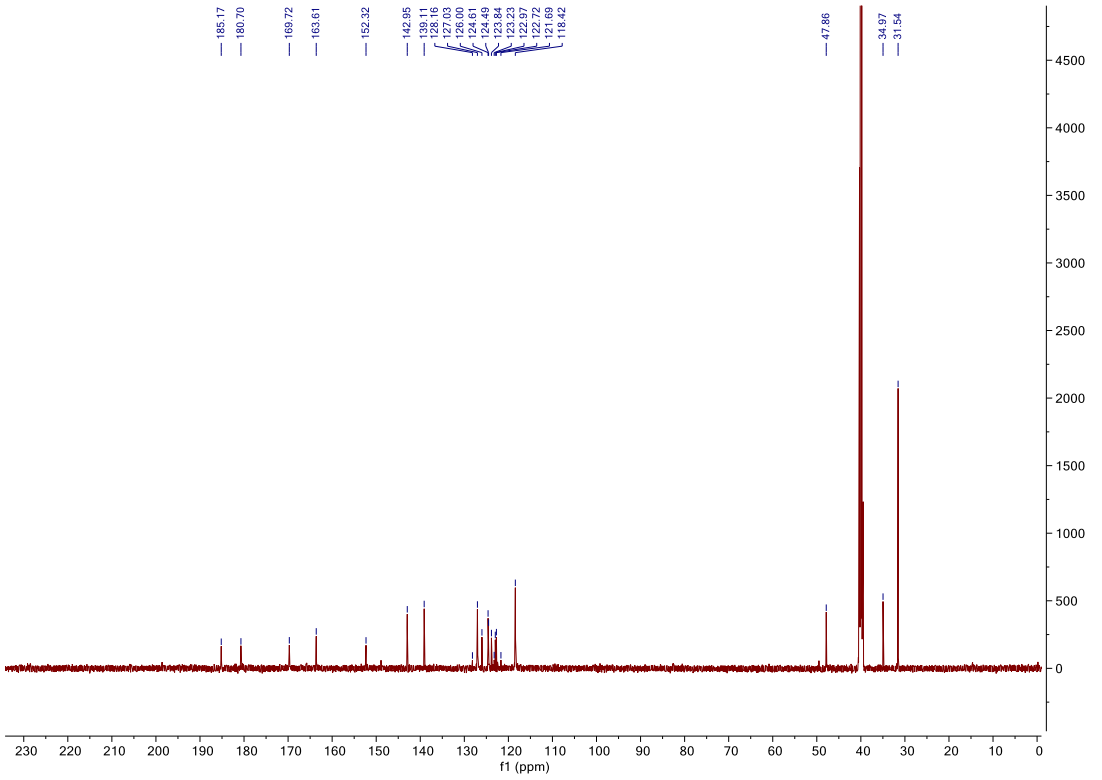

Figure SC22. ^{13}C NMR (DMSO-d_6, 126MHz) spectrum of **4.4**.

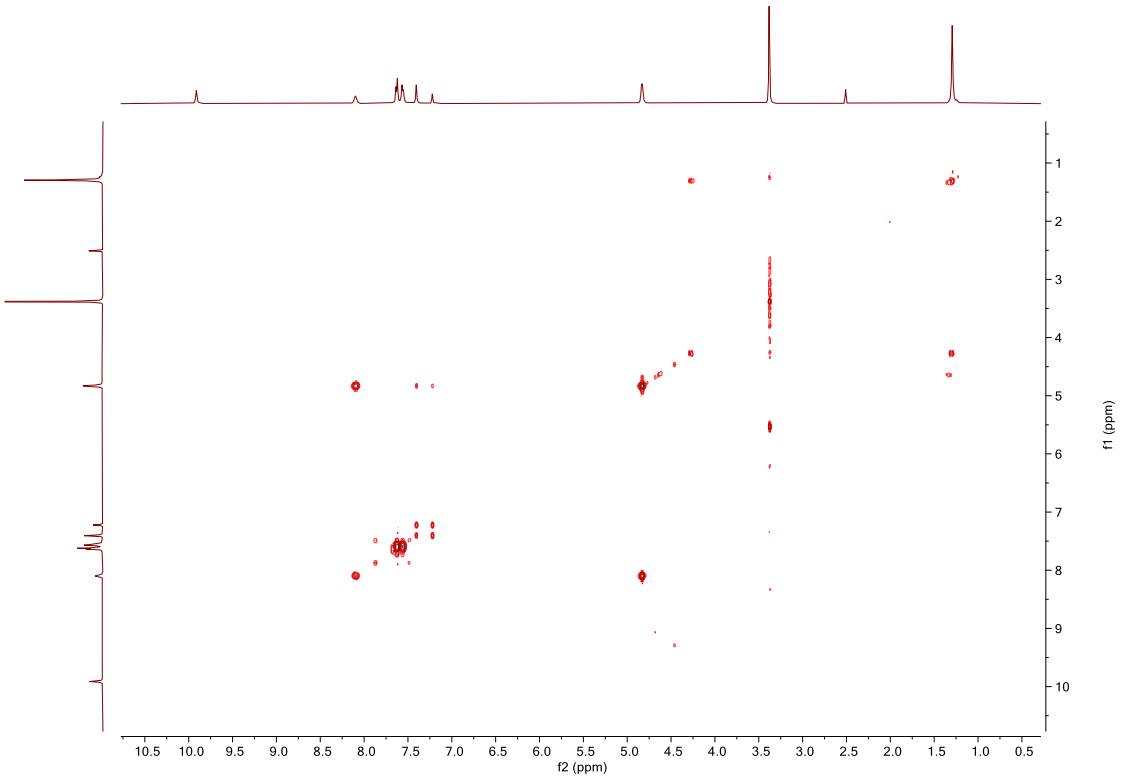

Figure SC23. COSY NMR (DMSO-d_6) spectrum of **4.4**.

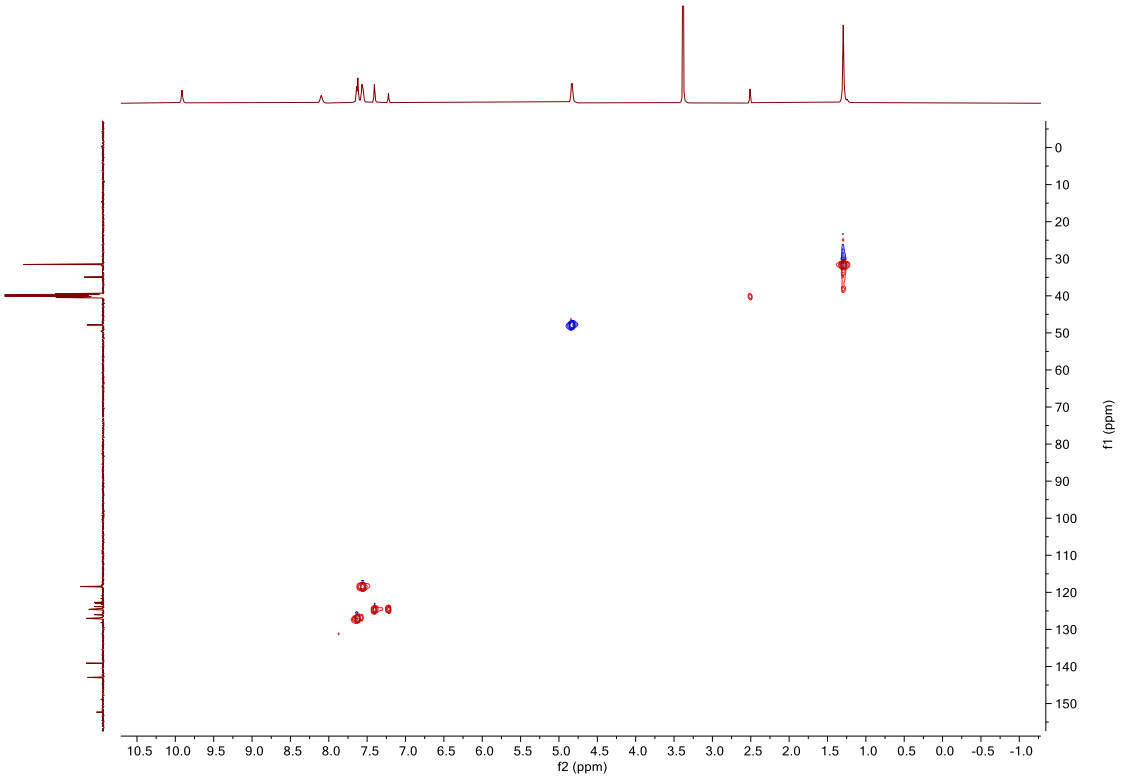

Figure SC24. HSQC NMR (DMSO-d_6) spectrum of **4.4**.

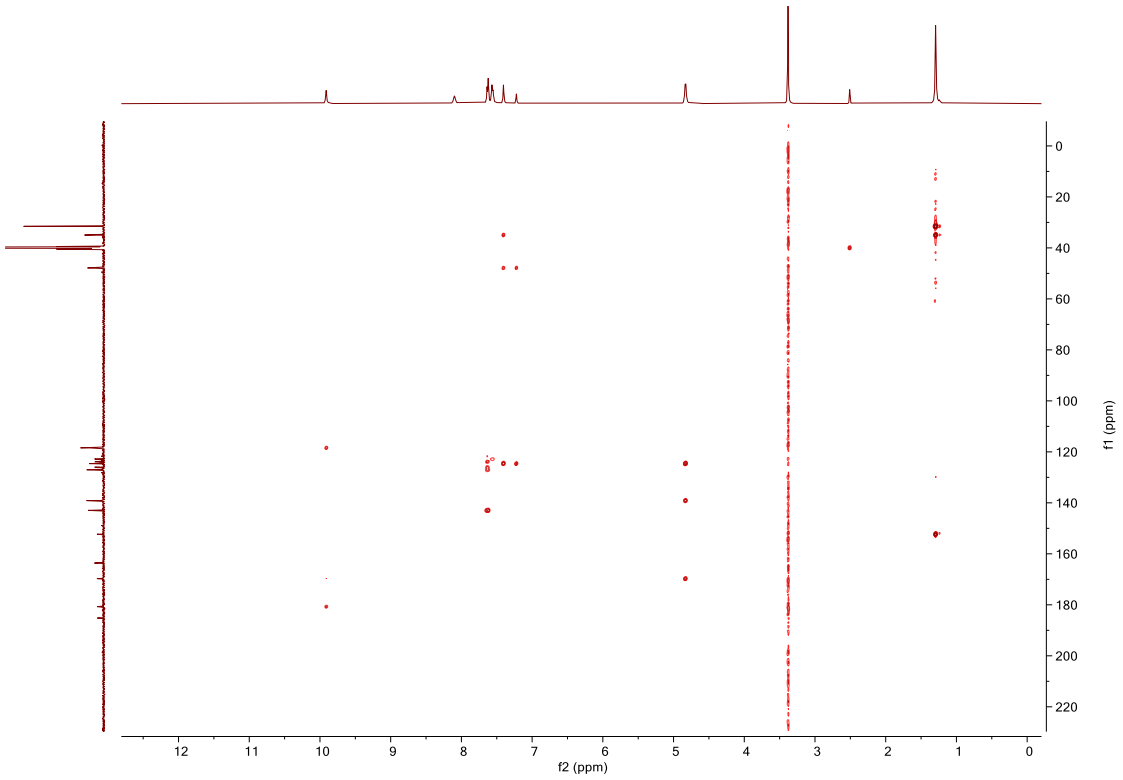

Figure SC25. HMBC NMR (DMSO-d_6) spectrum of **4.4**.

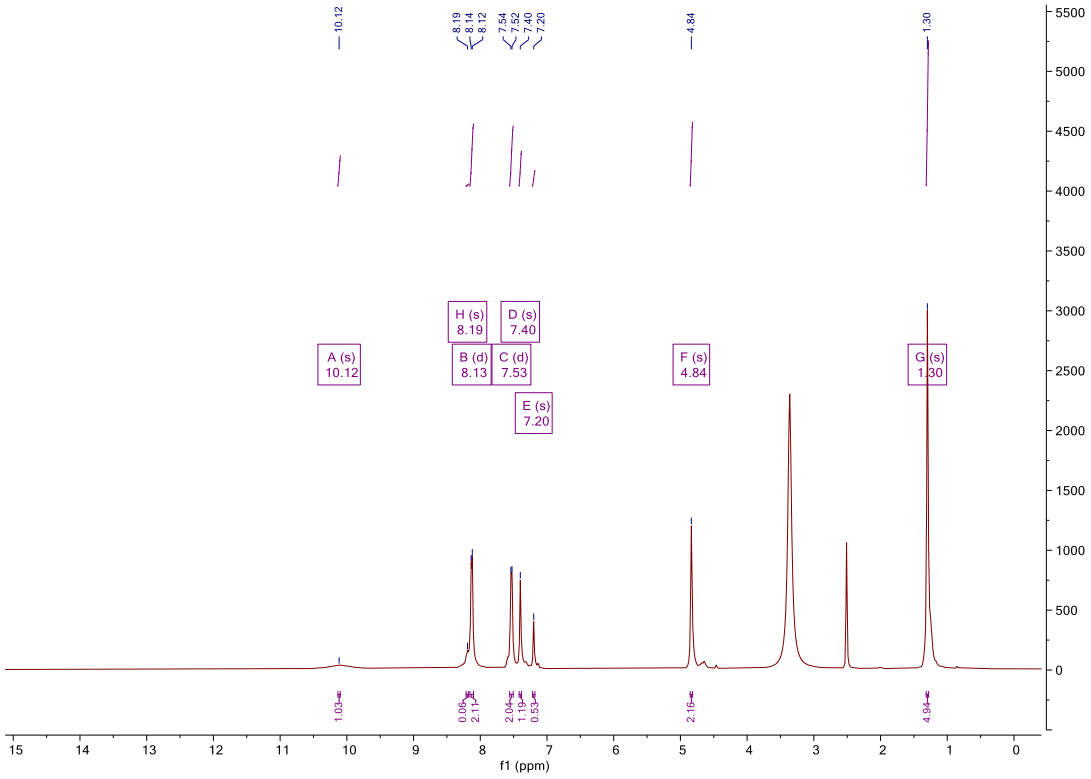

Figure SC26. ^{1}H NMR (DMSO-d_6, 500MHz) spectrum of **4.5**.

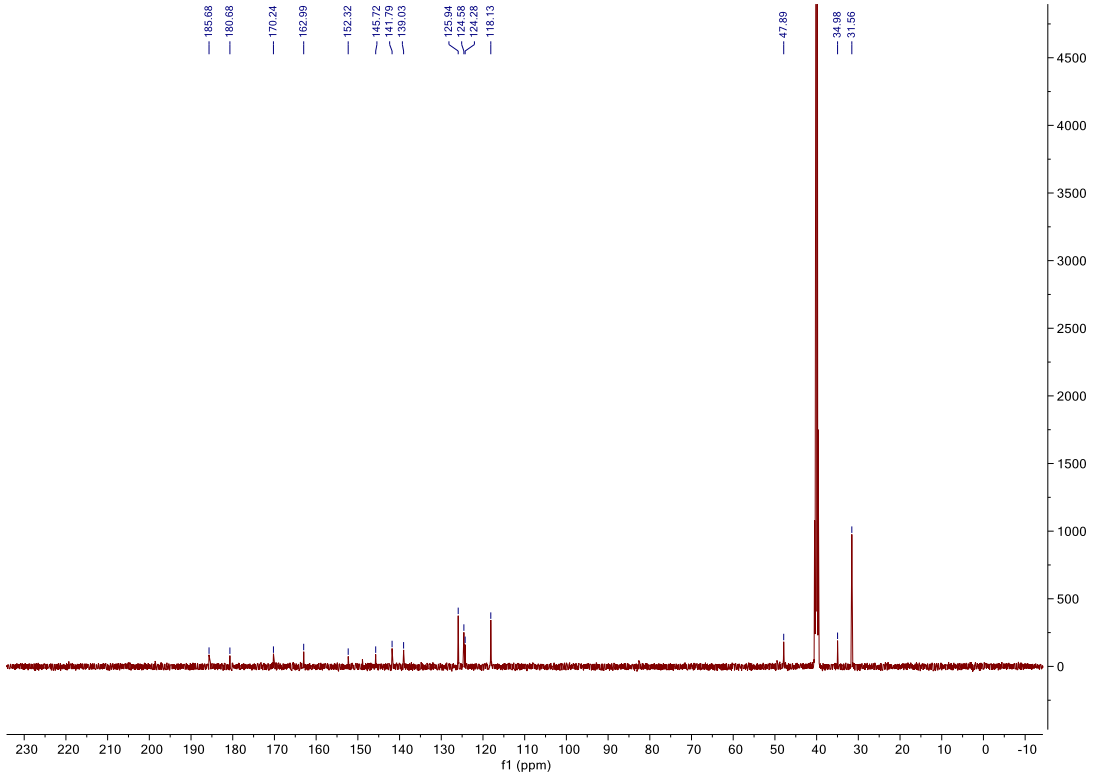

Figure SC27. ^{13}C NMR (DMSO-d_6, 126MHz) spectrum of **4.5**.

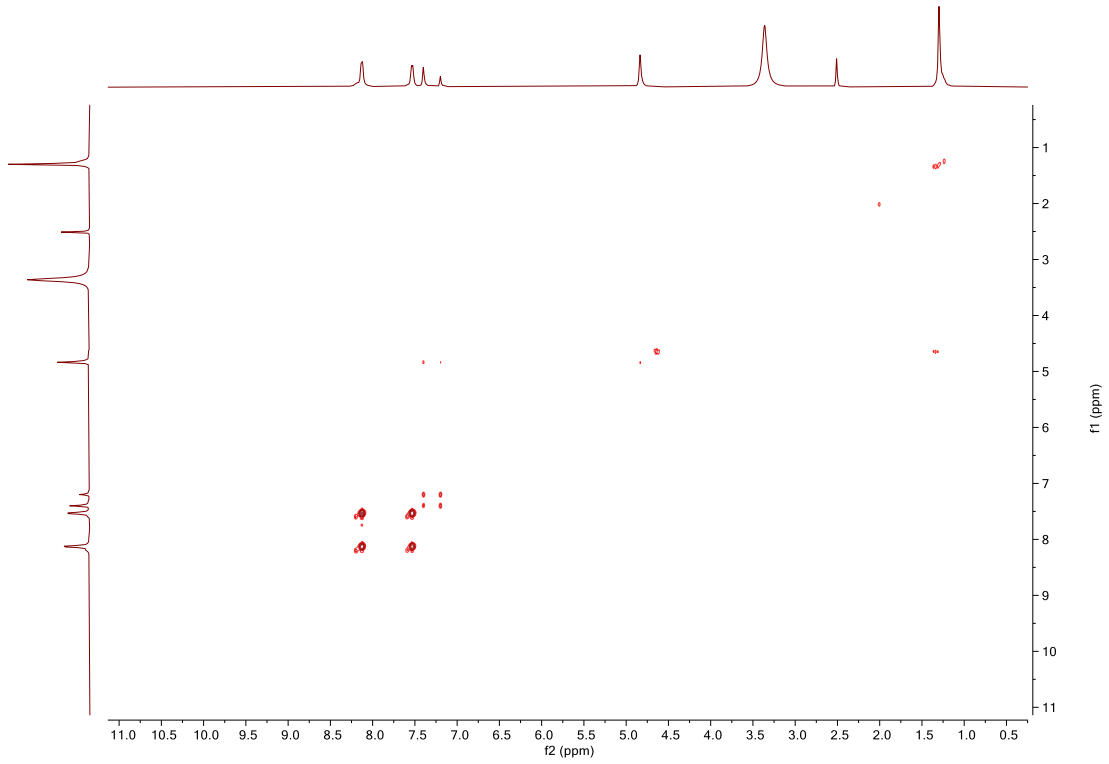

Figure SC28. COSY NMR (DMSO-d_6) spectrum of **4.5**.

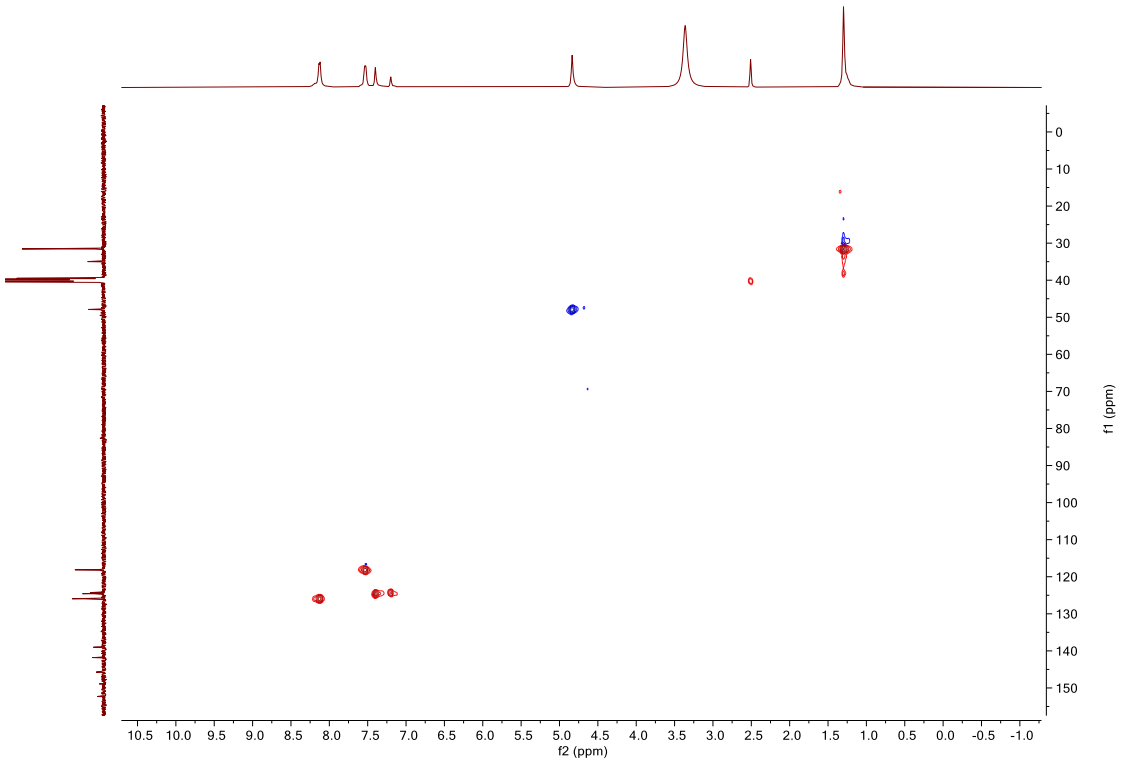

Figure SC29. HSQC NMR (DMSO-d_6) spectrum of **4.5**.

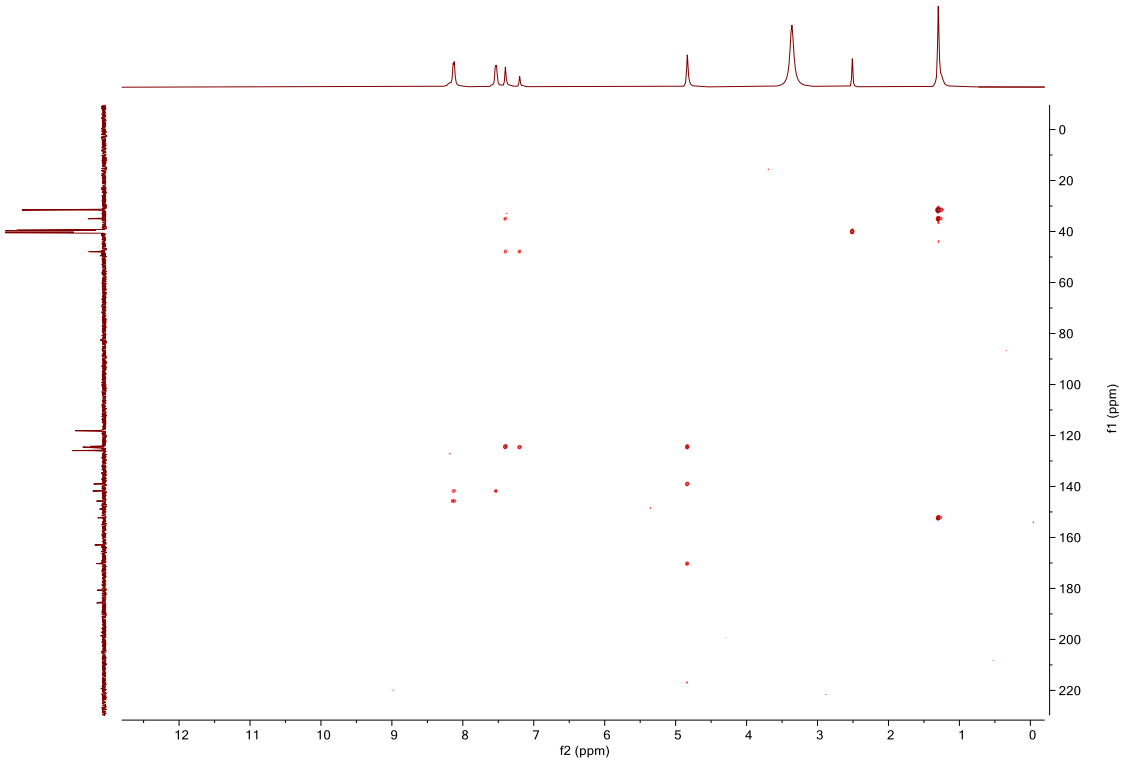

Figure SC30. HMBC NMR (DMSO-d_6) spectrum of **4.5**.

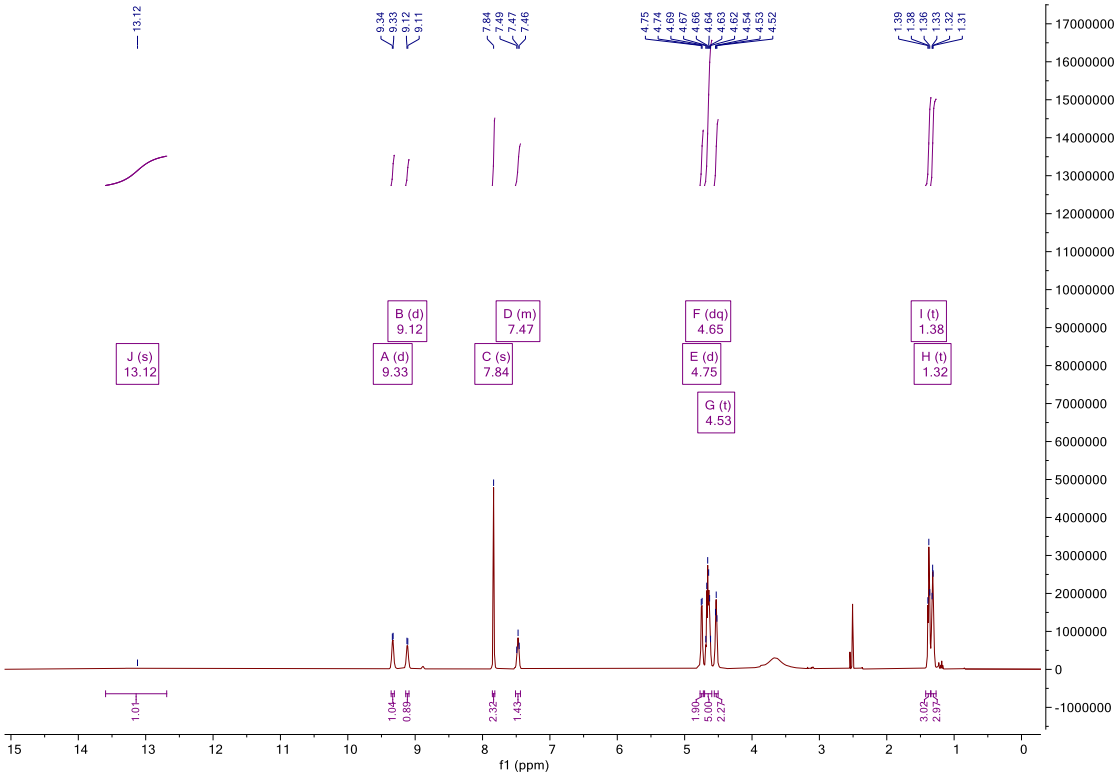

Figure SC31. ^{1}H NMR (DMSO-d_6, 500MHz) spectrum of **C4**.

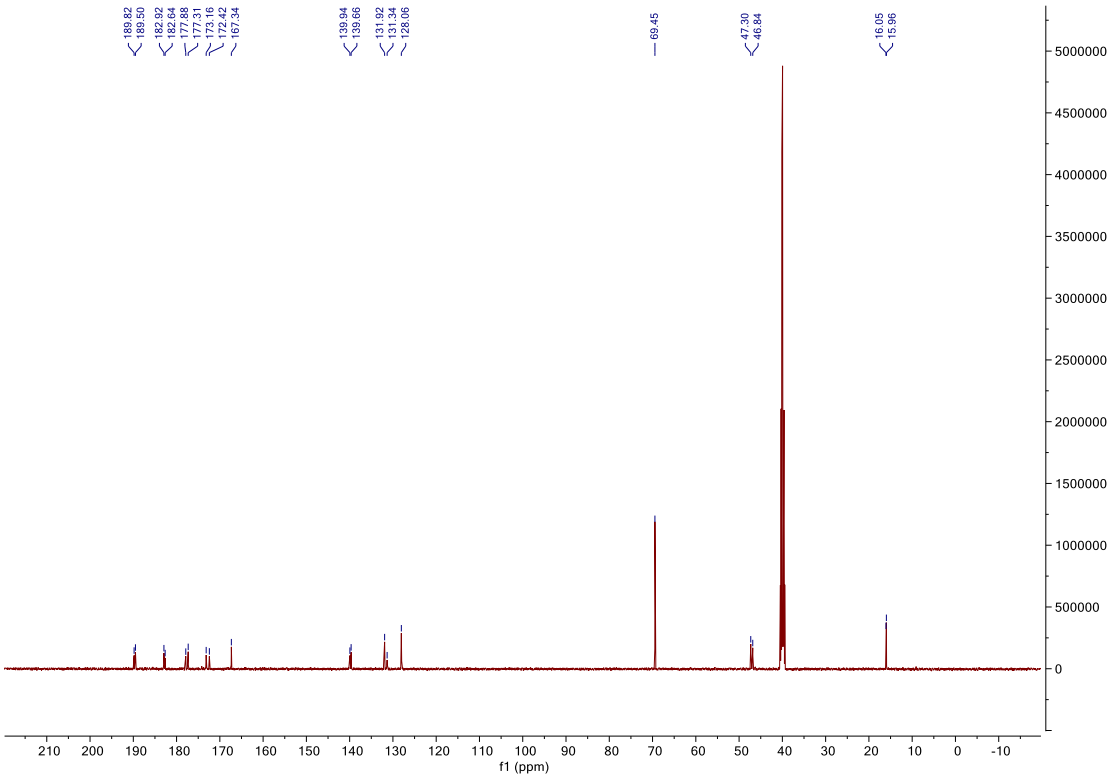

Figure SC32. ^{13}C NMR (DMSO-d_6, 126MHz) spectrum of **C4**.

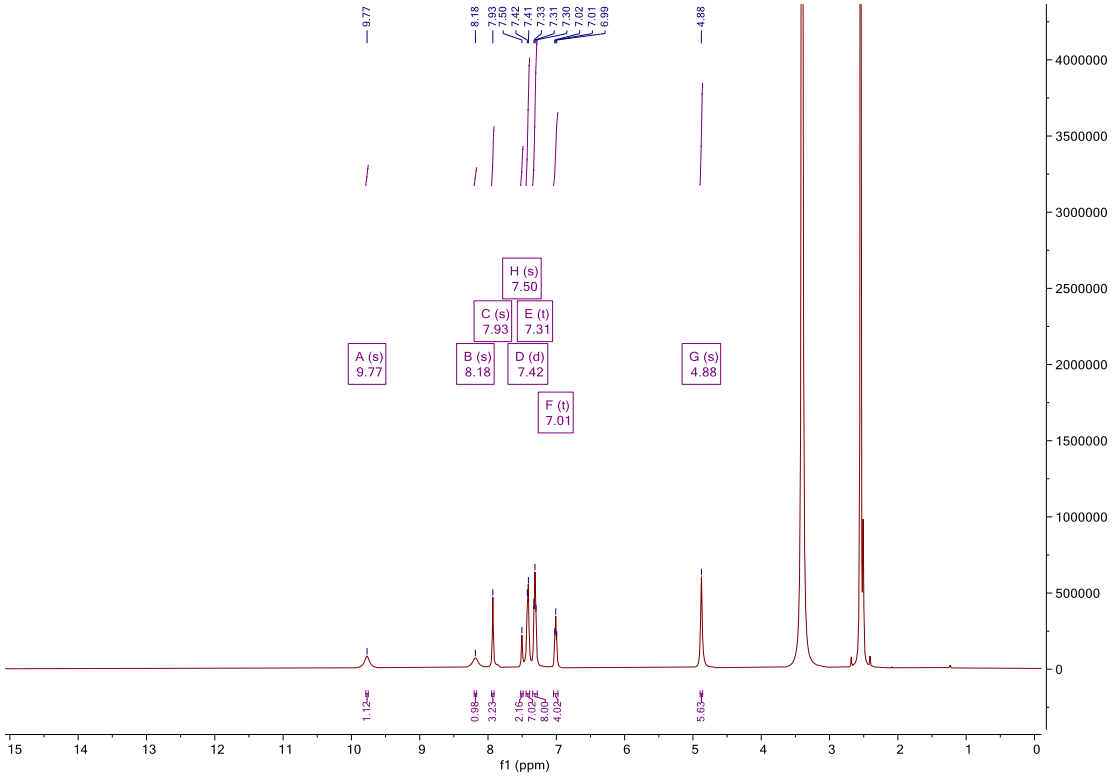

Figure SC33. ^{1}H NMR (DMSO-d_6, 500MHz) spectrum of **4.6**.

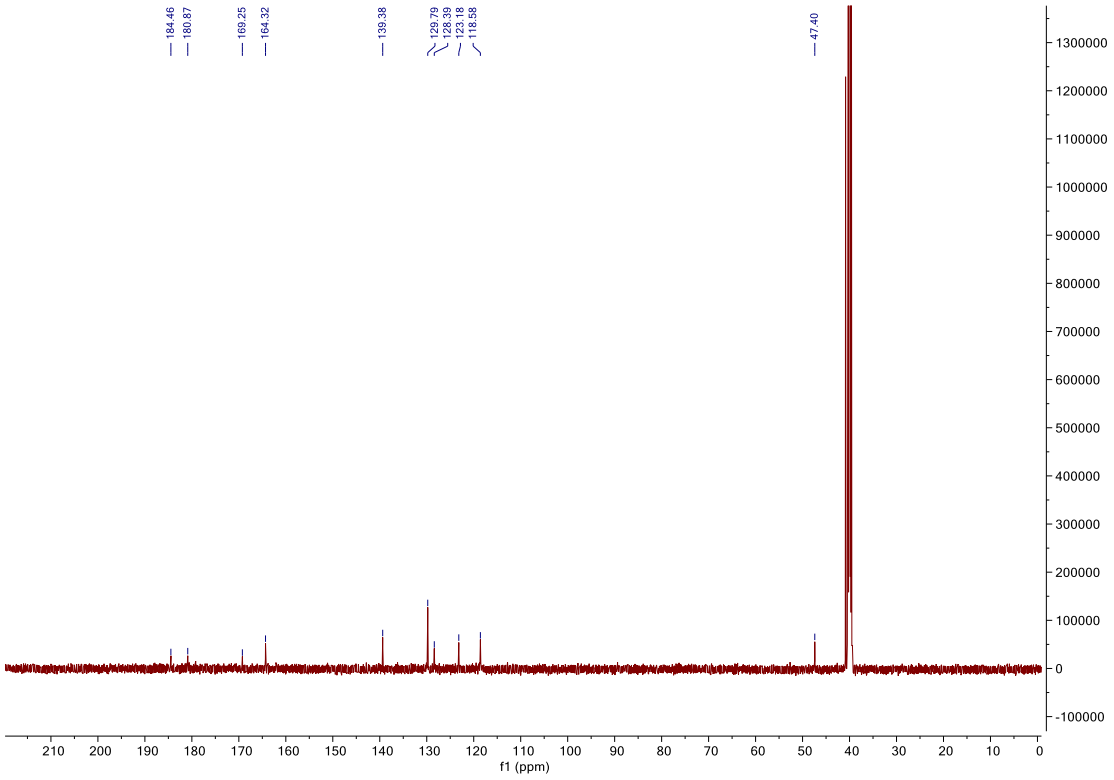

Figure SC34. ^{13}C NMR (DMSO-d_6, 126MHz) spectrum of **4.6**.

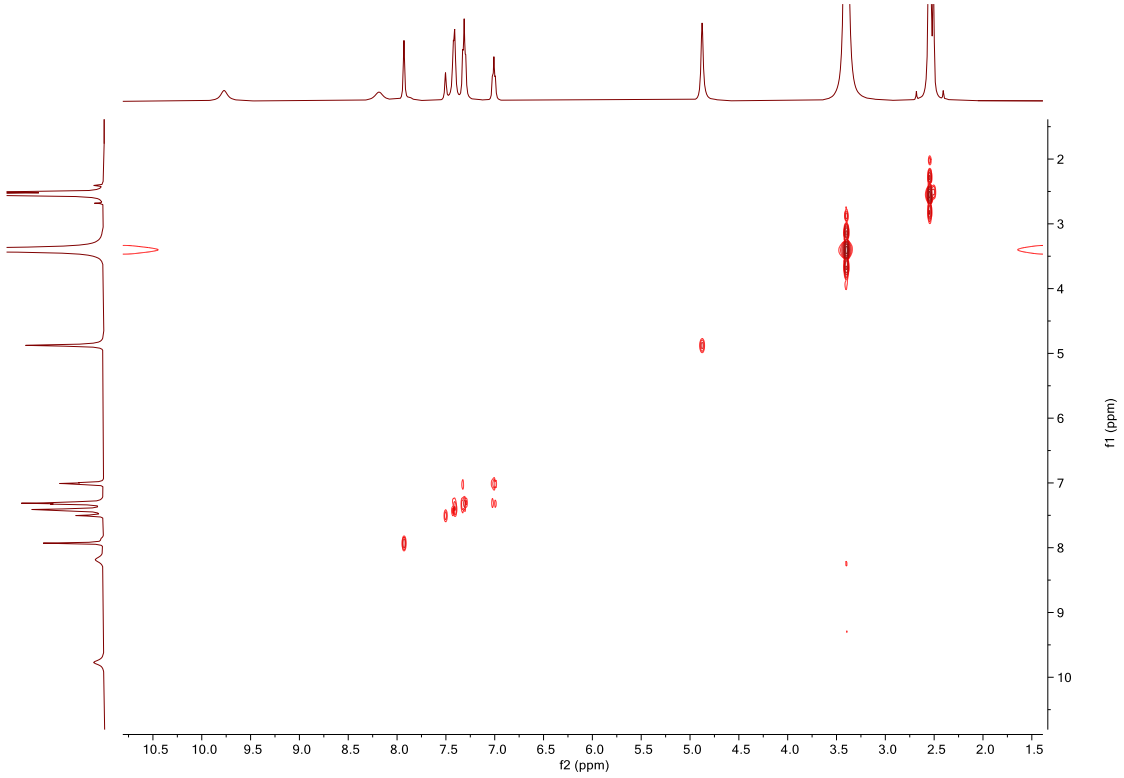

Figure SC35. COSY NMR (DMSO-d_6) spectrum of **4.6**.

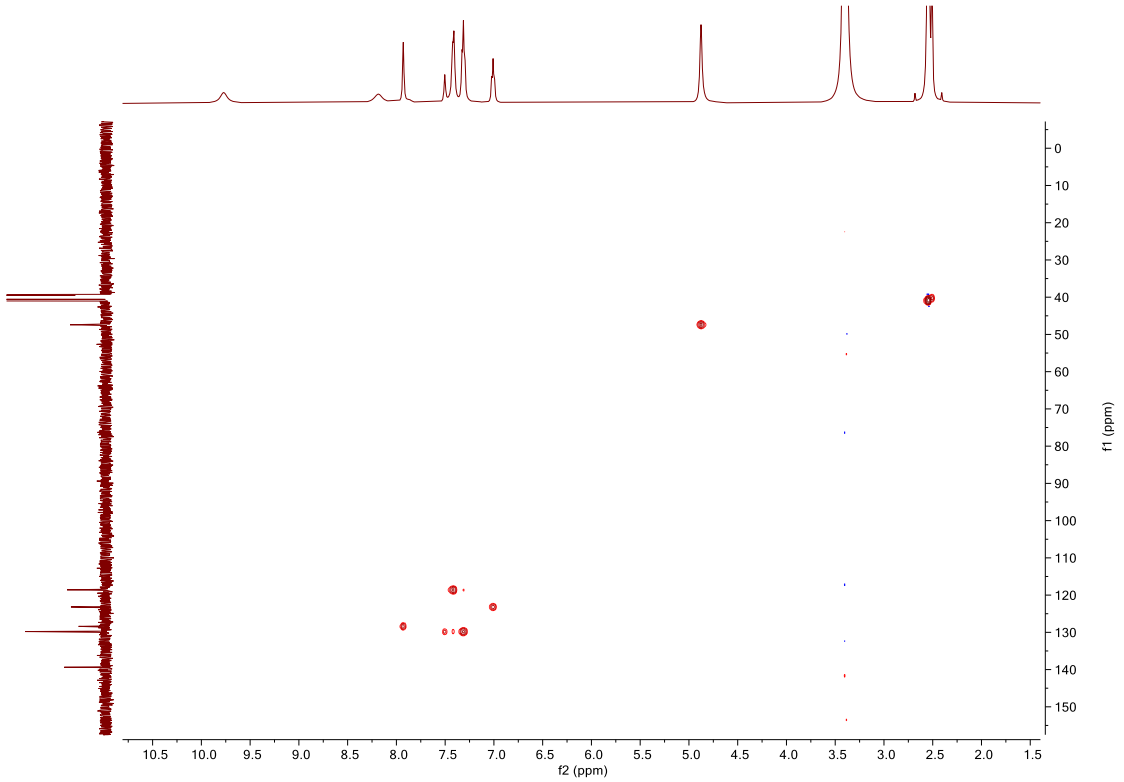

Figure SC36. HSQC NMR (DMSO-d_6) spectrum of **4.6**.

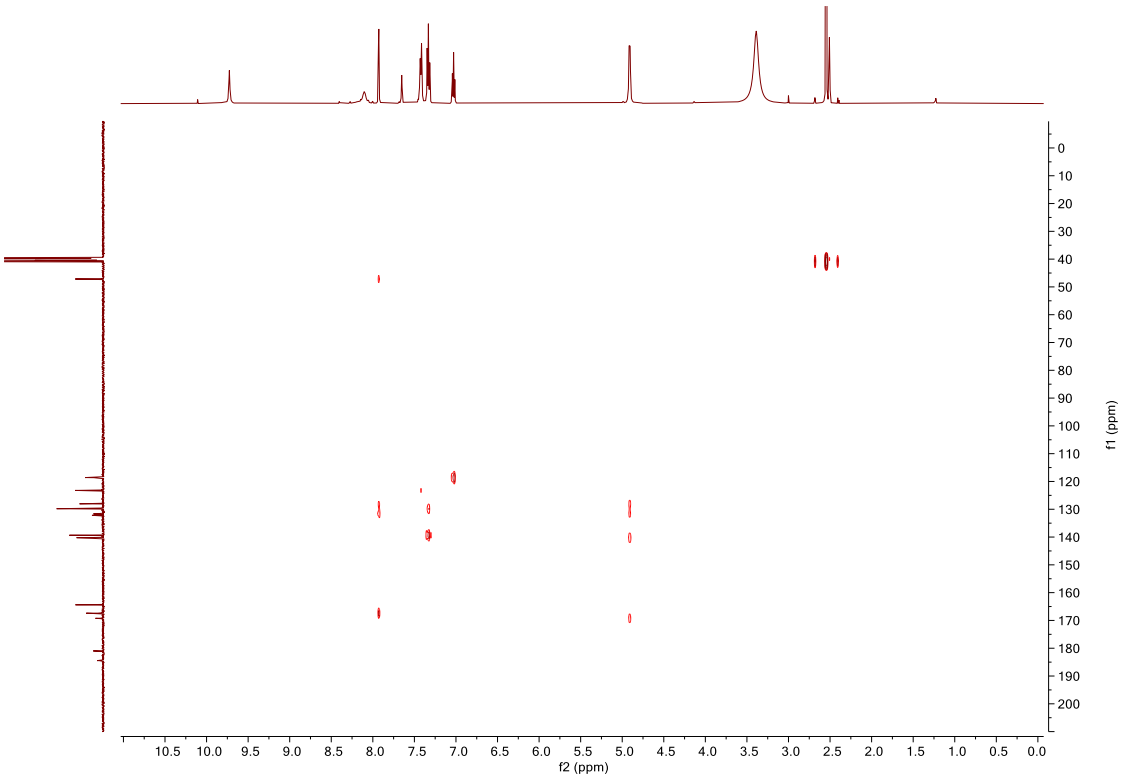

Figure SC37. HMBC NMR (DMSO-d_6) spectrum of **4.6**.

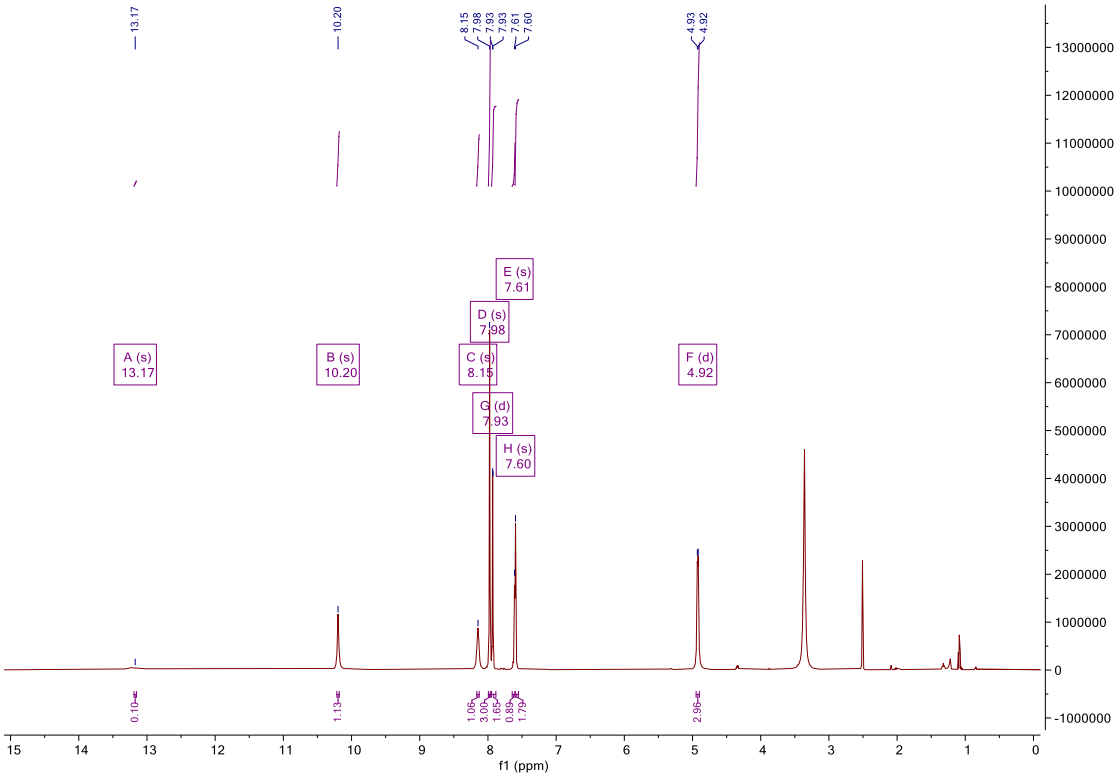

Figure SC38. ^{1}H NMR (DMSO-d_6, 500MHz) spectrum of **4.7**.

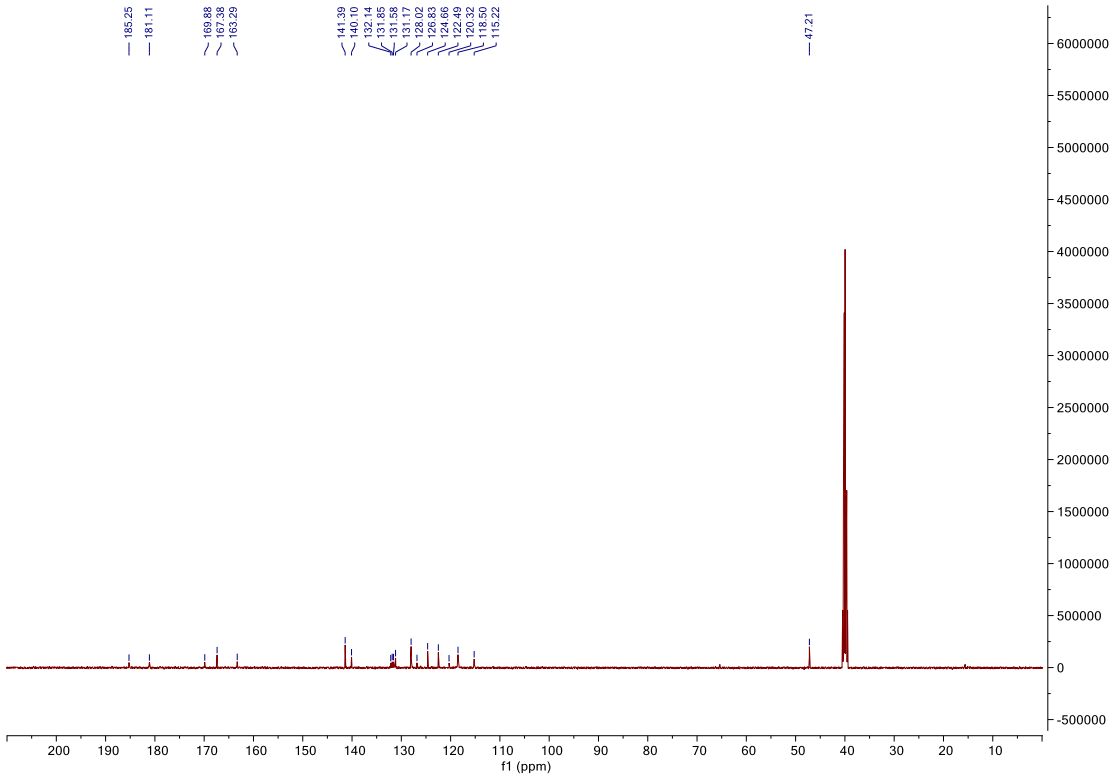

Figure SC39. ^{13}C NMR (DMSO-d_6, 126MHz) spectrum of **4.7**.

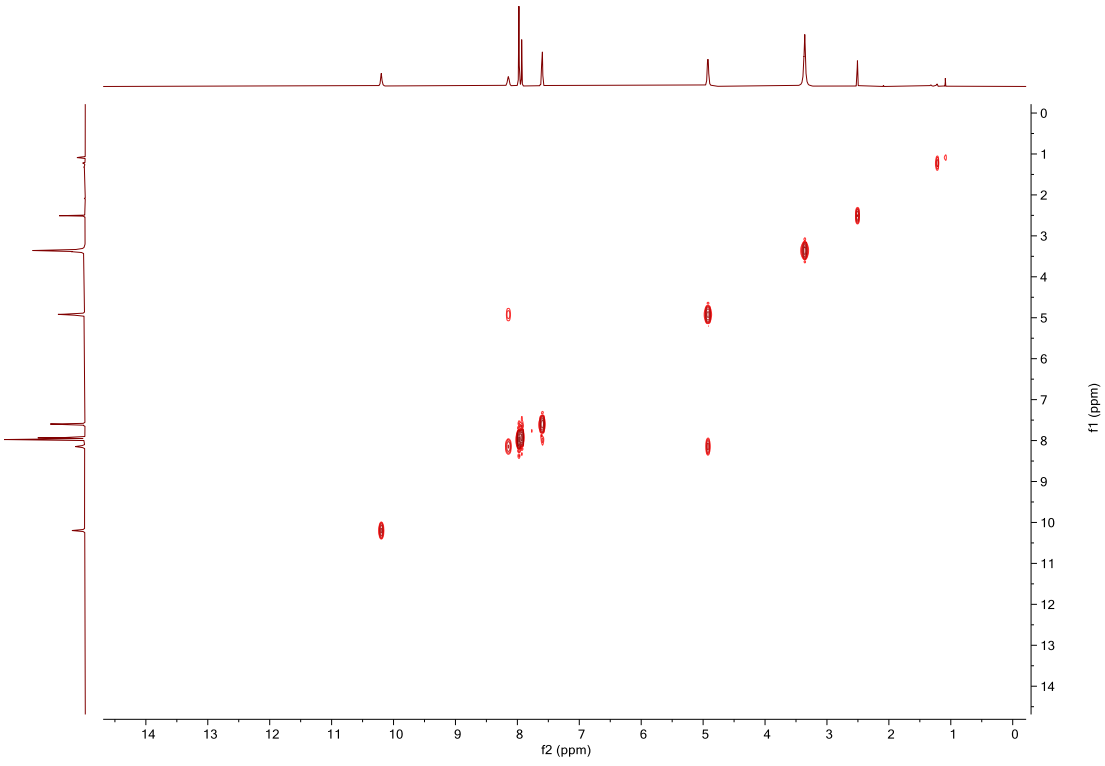

Figure SC40. COSY NMR (DMSO-d_6) spectrum of **4.7**.

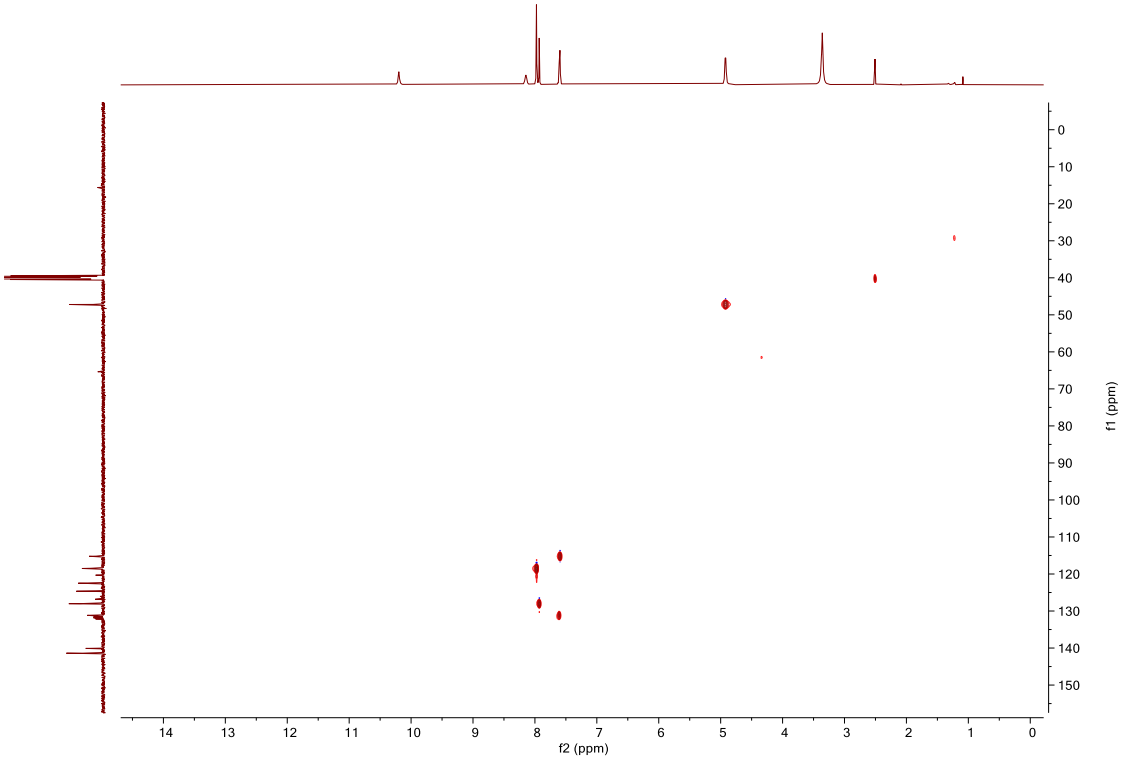

Figure SC41. HSQC NMR (DMSO-d_6) spectrum of **4.7**.

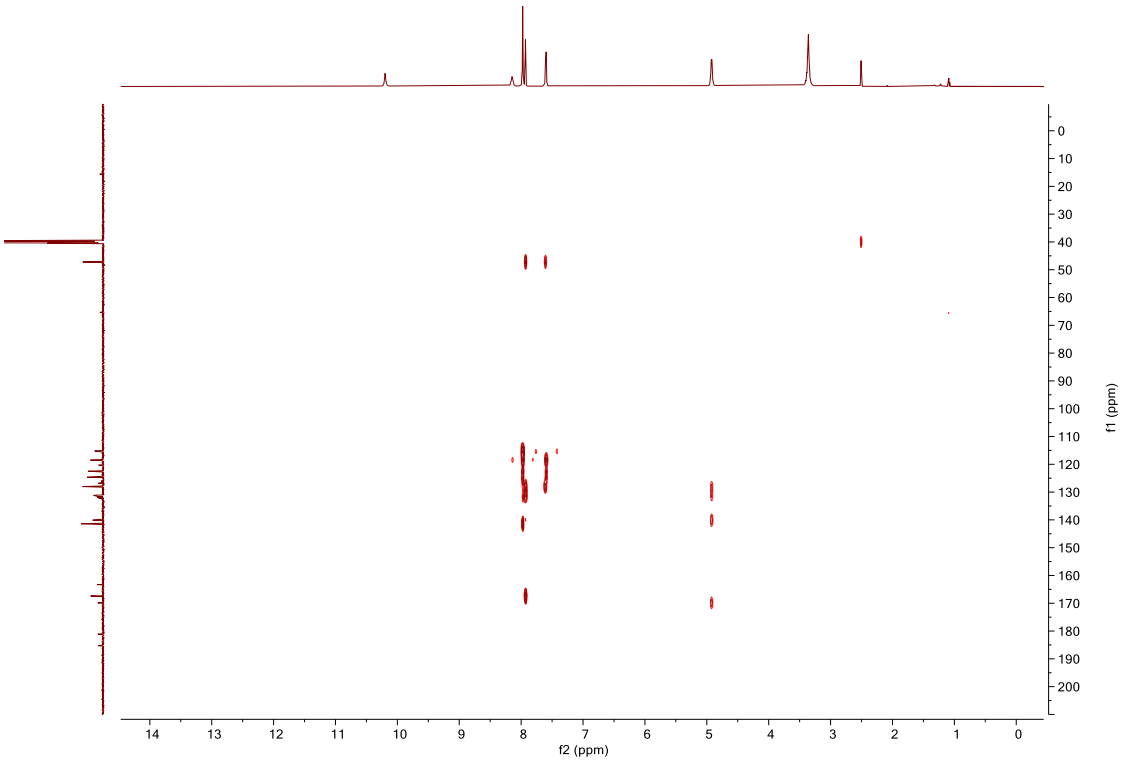

Figure SC42. HMBC NMR (DMSO-d_6) spectrum of **4.7**.

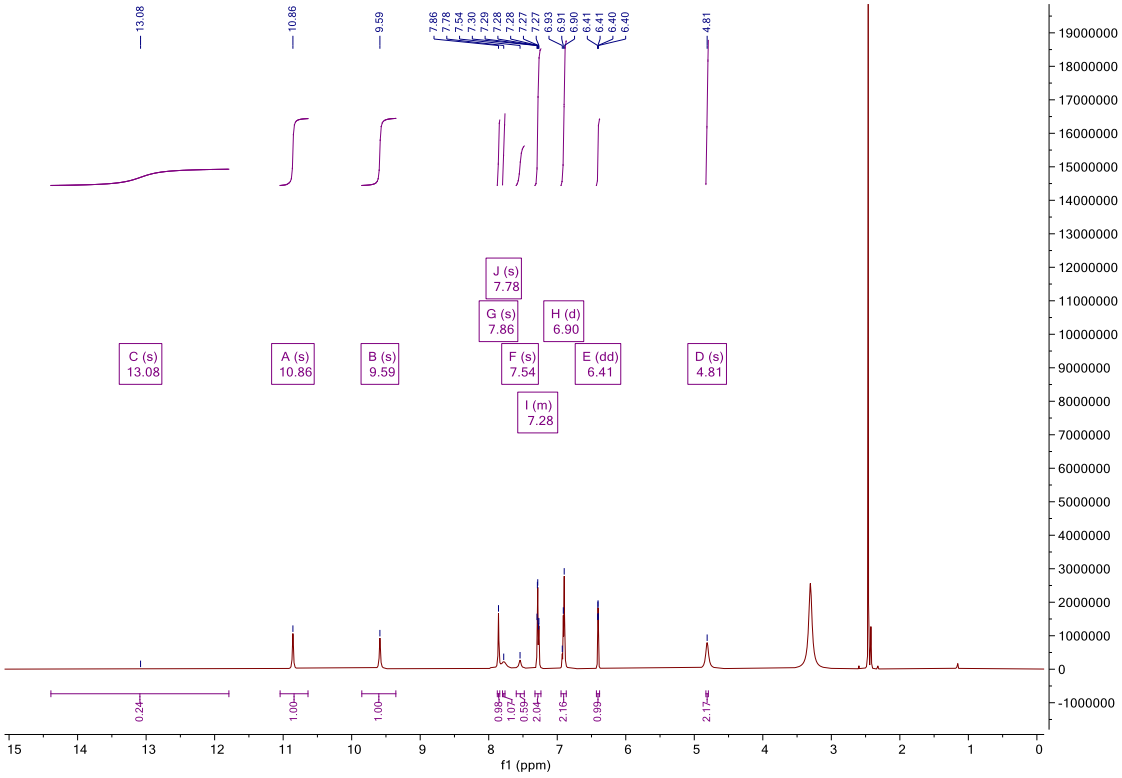

Figure SC43. ^{1}H NMR (DMSO-d_6, 500MHz) spectrum of **4.8**.

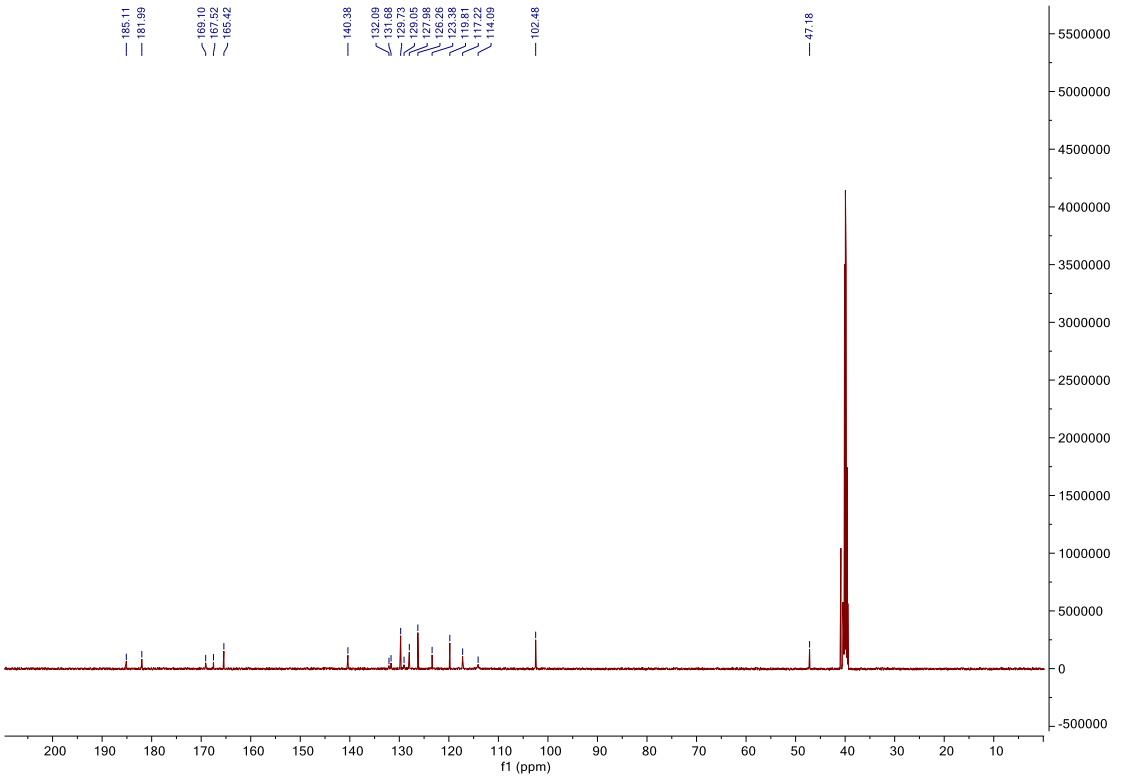

Figure SC44. ^{13}C NMR (DMSO-d_6, 126MHz) spectrum of **4.8**.

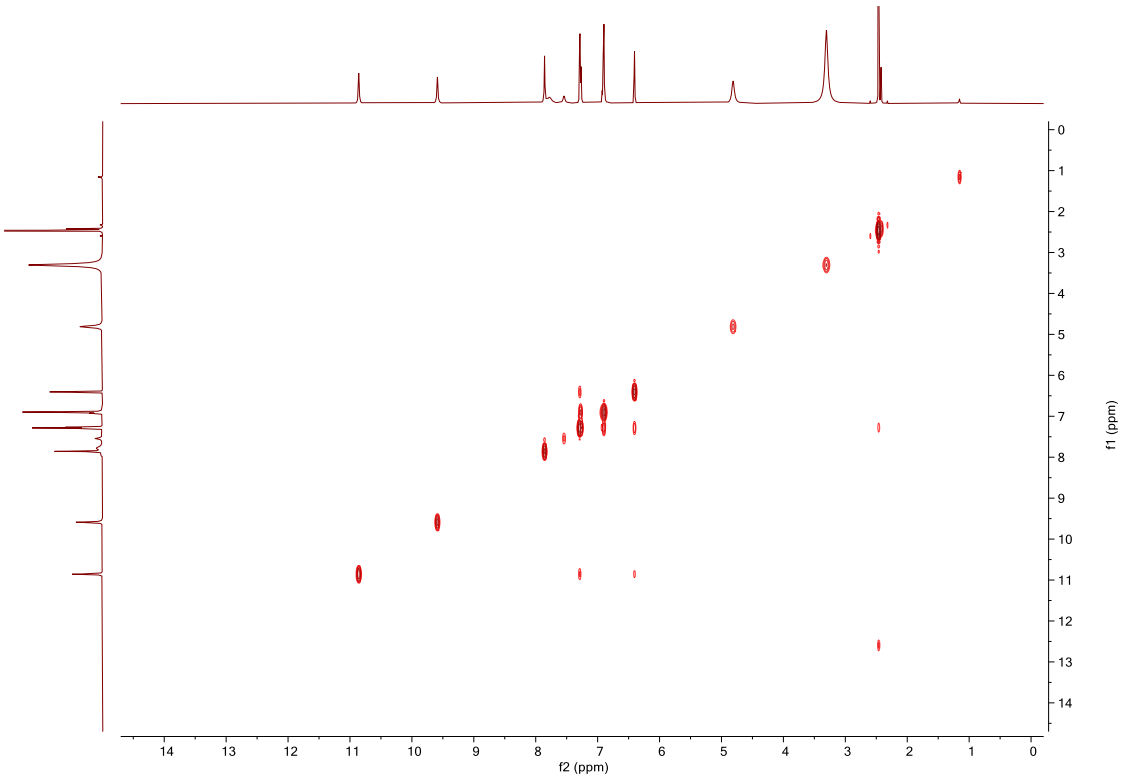

Figure SC45. COSY NMR (DMSO-d_6) spectrum of **4.8**.

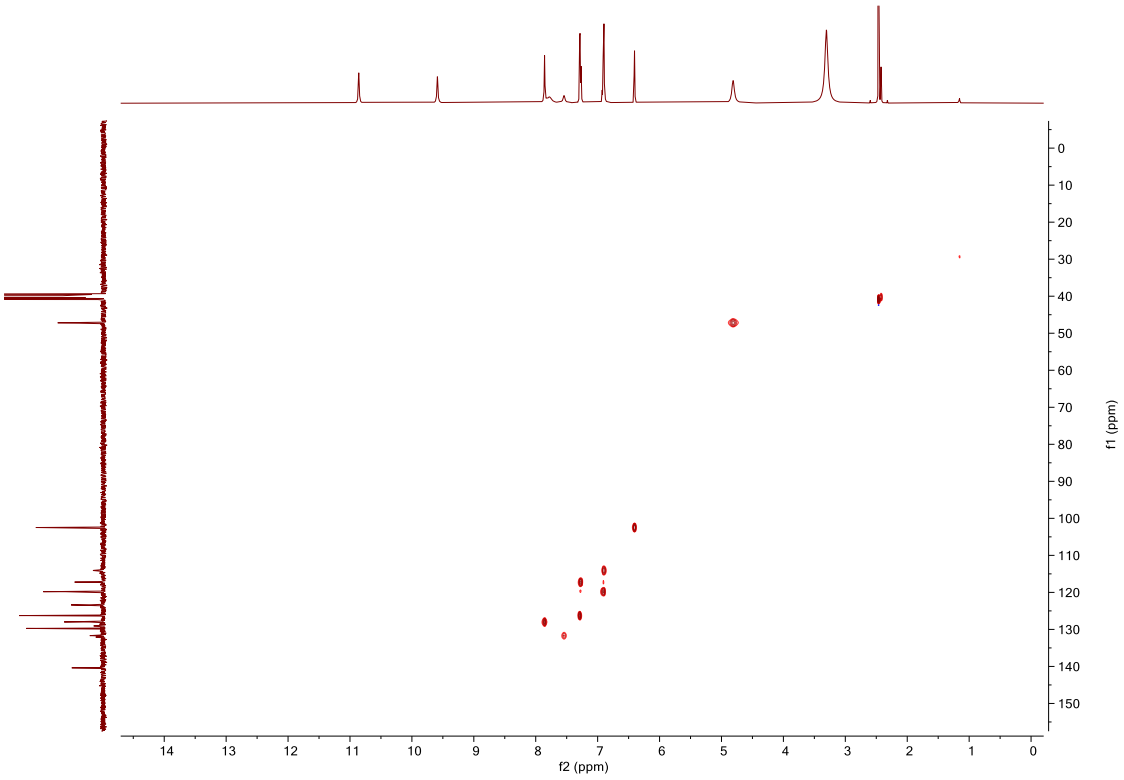

Figure SC46. HSQC NMR (DMSO-d_6) spectrum of **4.8**.

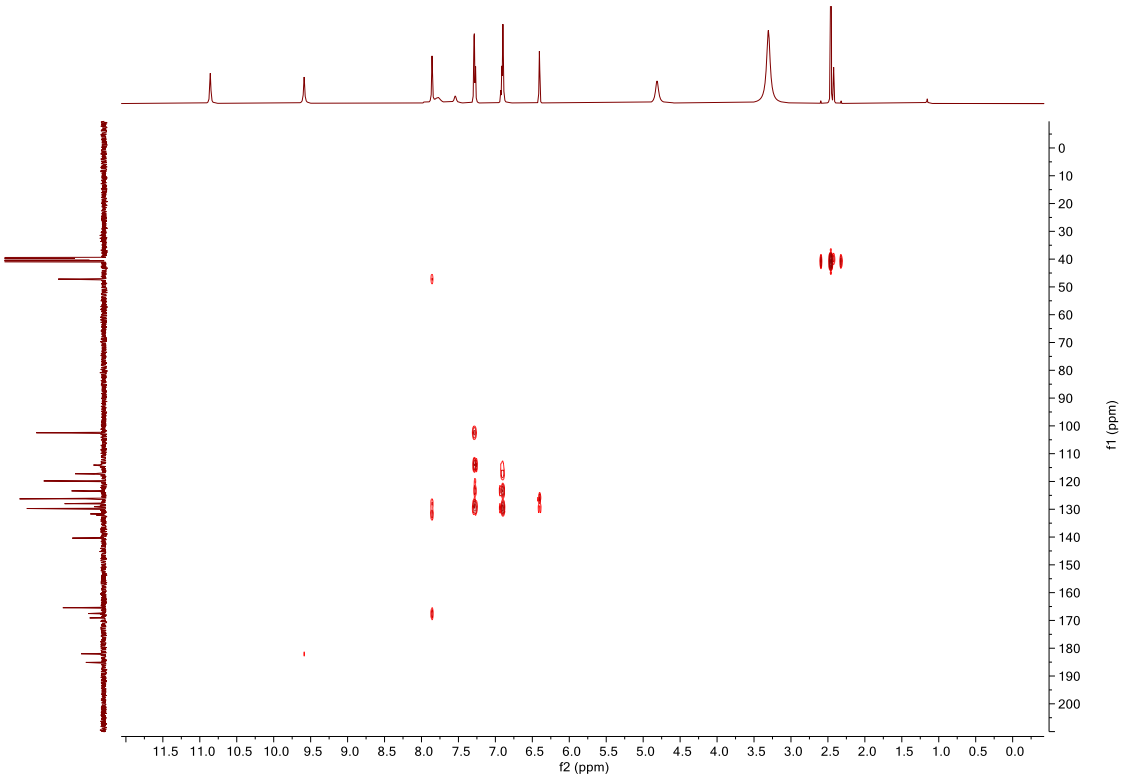

Figure SC47. HMBC NMR (DMSO-d_6) spectrum of **4.8**.

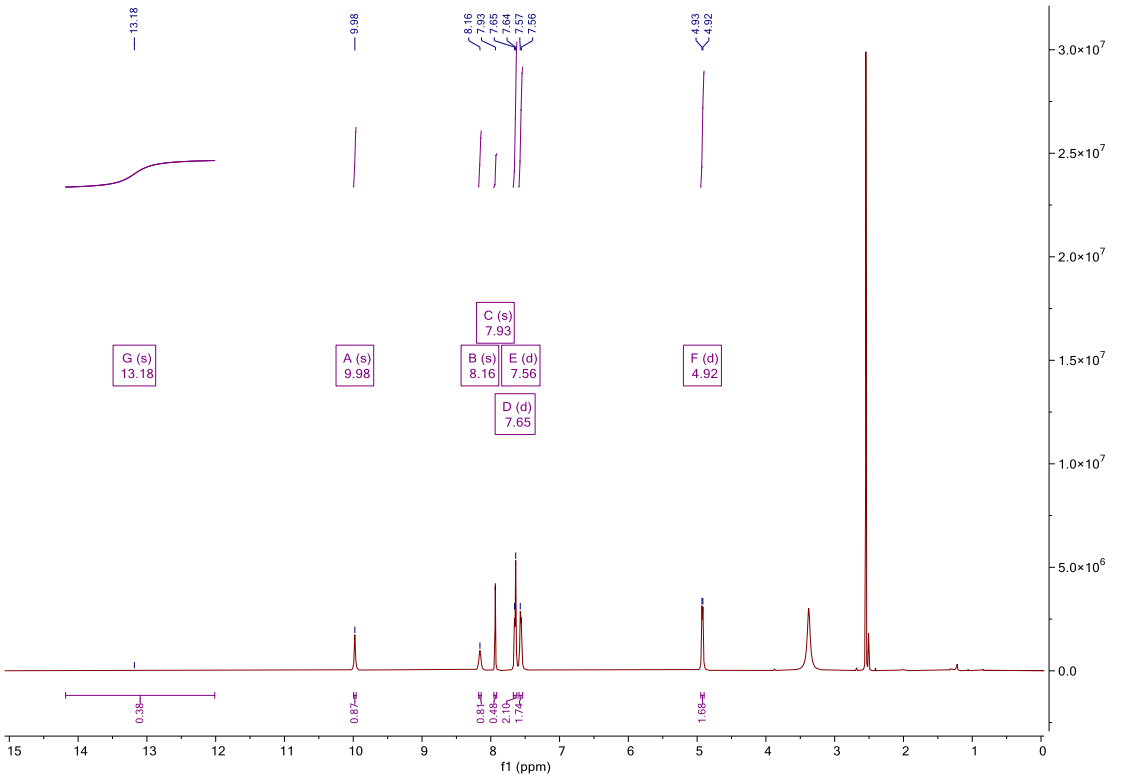

Figure SC48. ^{1}H NMR (DMSO-d_6, 500MHz) spectrum of **4.9**.

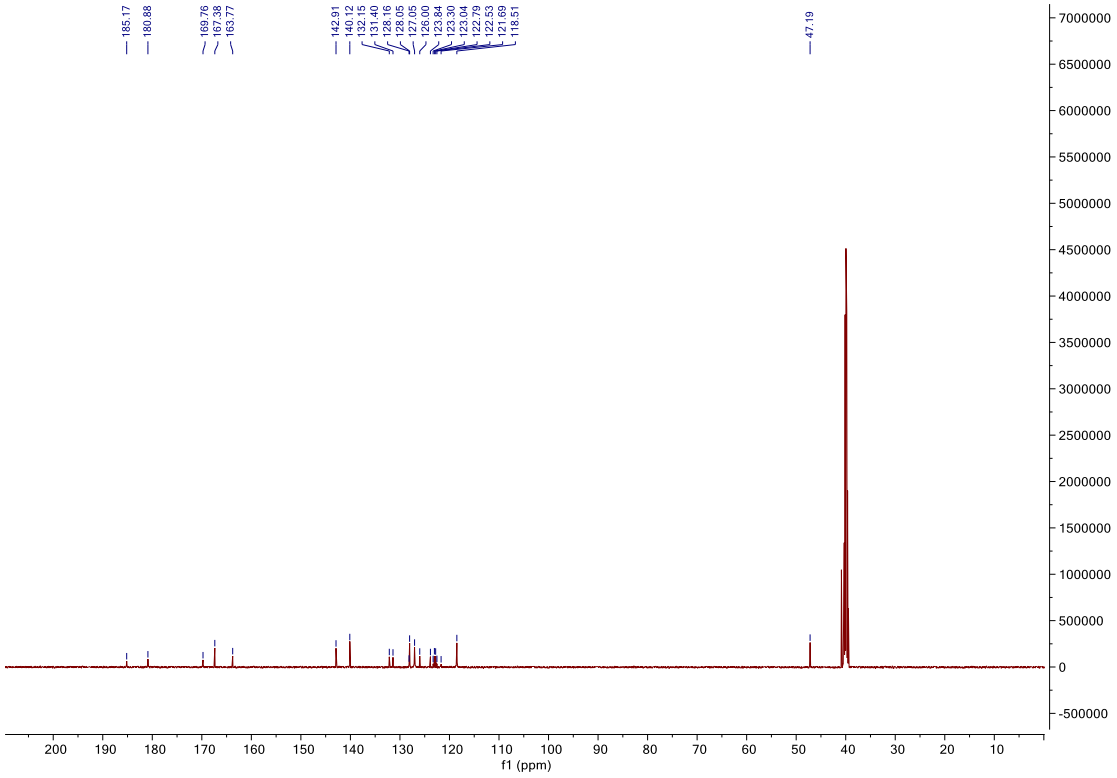

Figure SC49. ^{13}C NMR (DMSO-d_6, 126MHz) spectrum of **4.9**.

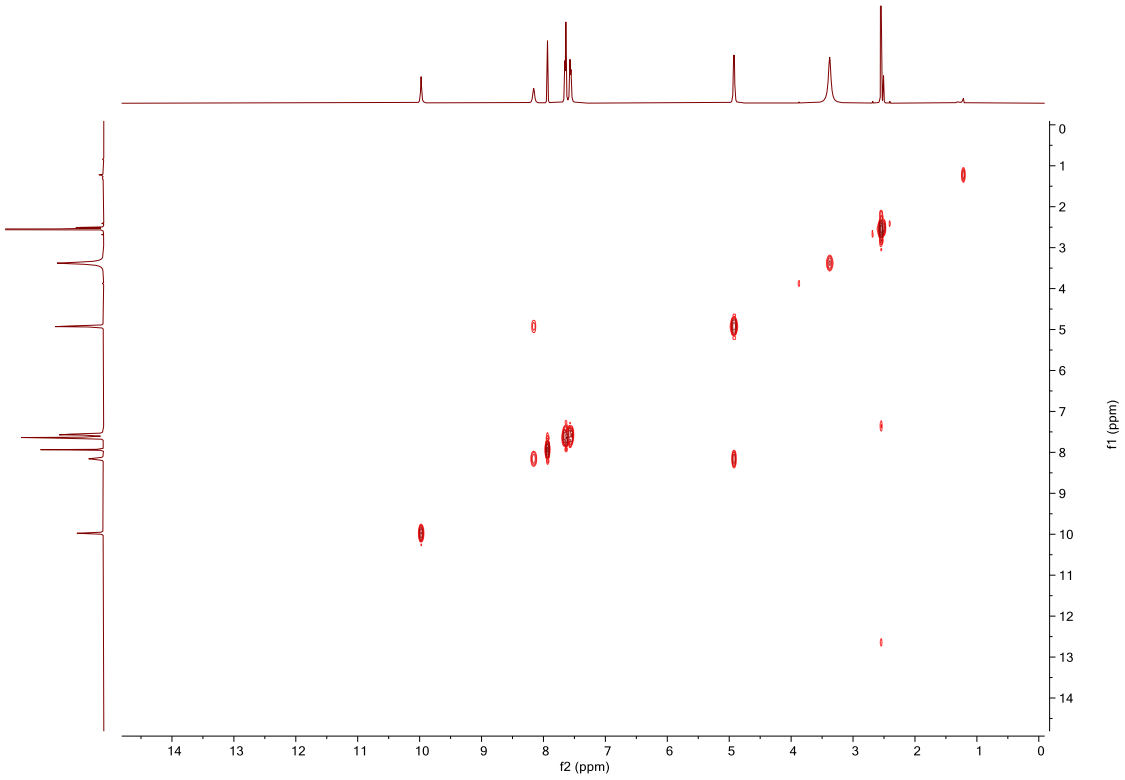

Figure SC50. COSY NMR (DMSO-d_6) spectrum of **4.9**.

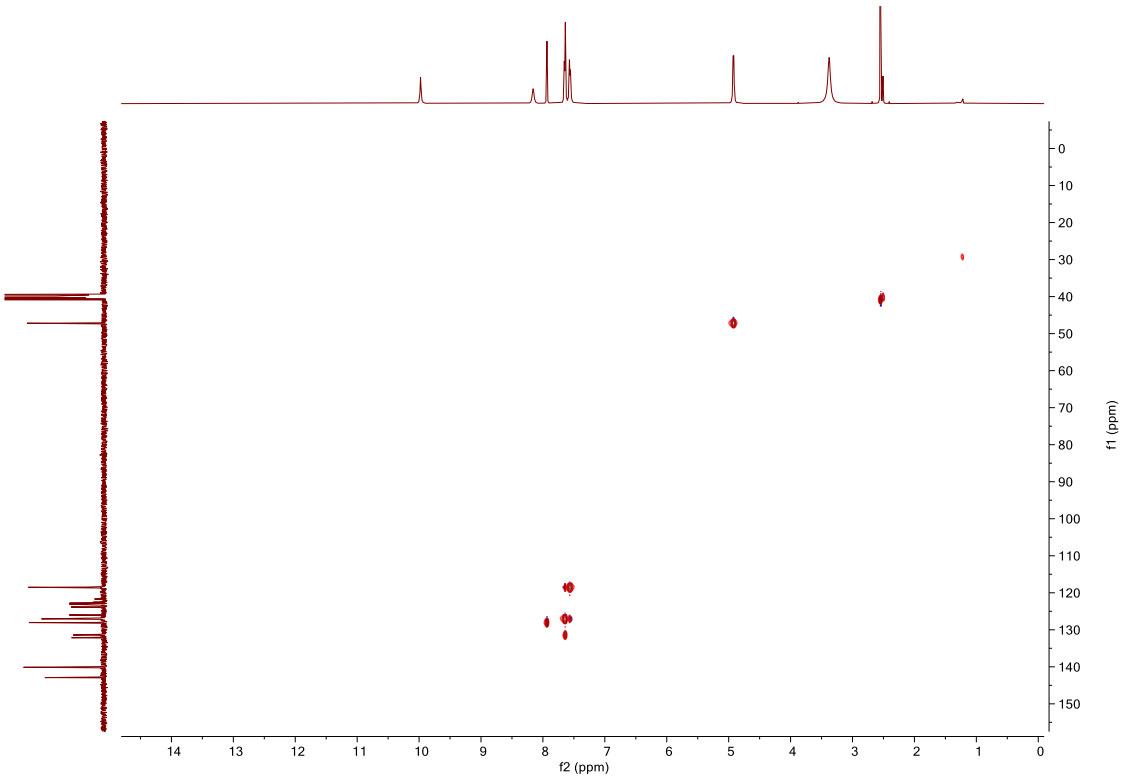

Figure SC51. HSQC NMR (DMSO-d_6) spectrum of **4.9**.

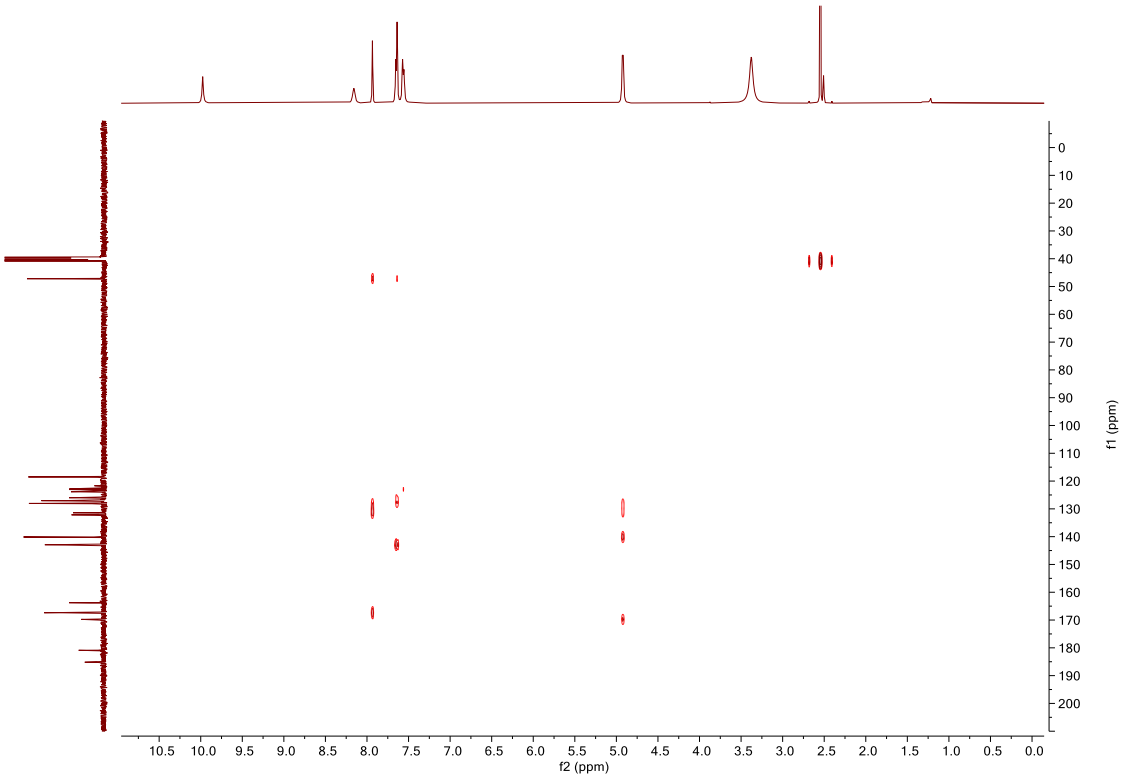

Figure SC52. HMBC NMR (DMSO-d_6) spectrum of **4.9**.

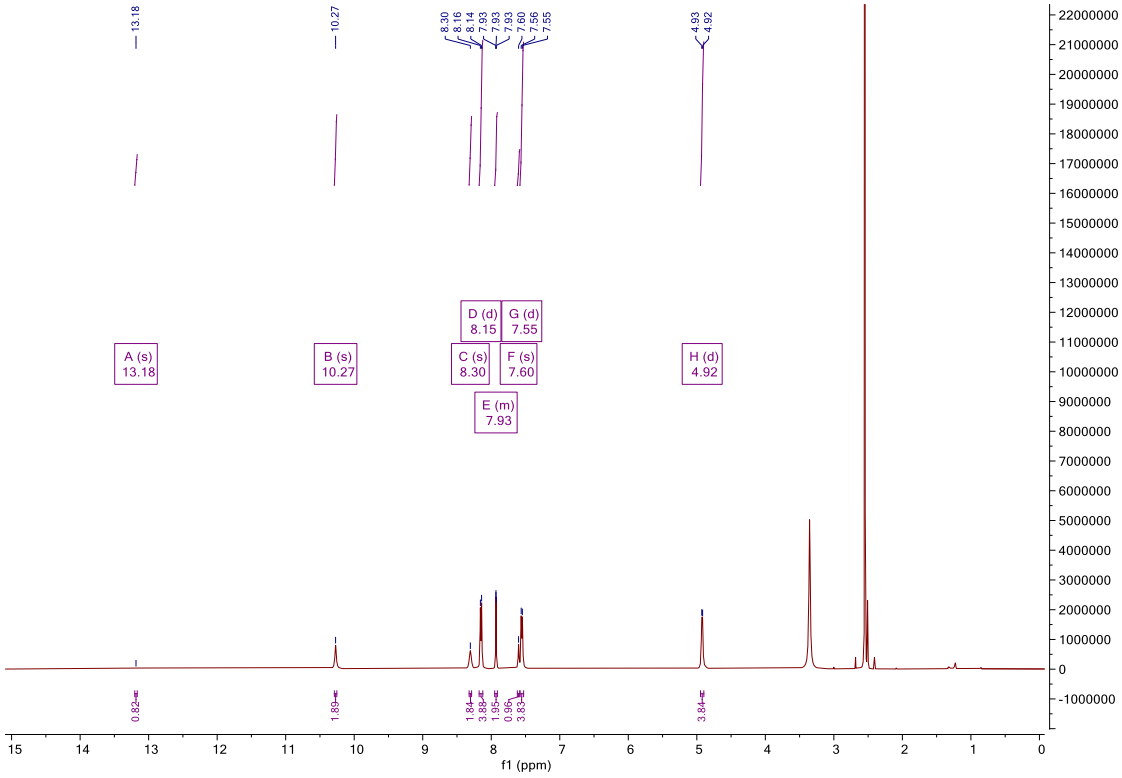

Figure SC53. ^{1}H NMR (DMSO-d_6, 500MHz) spectrum of **4.10**.

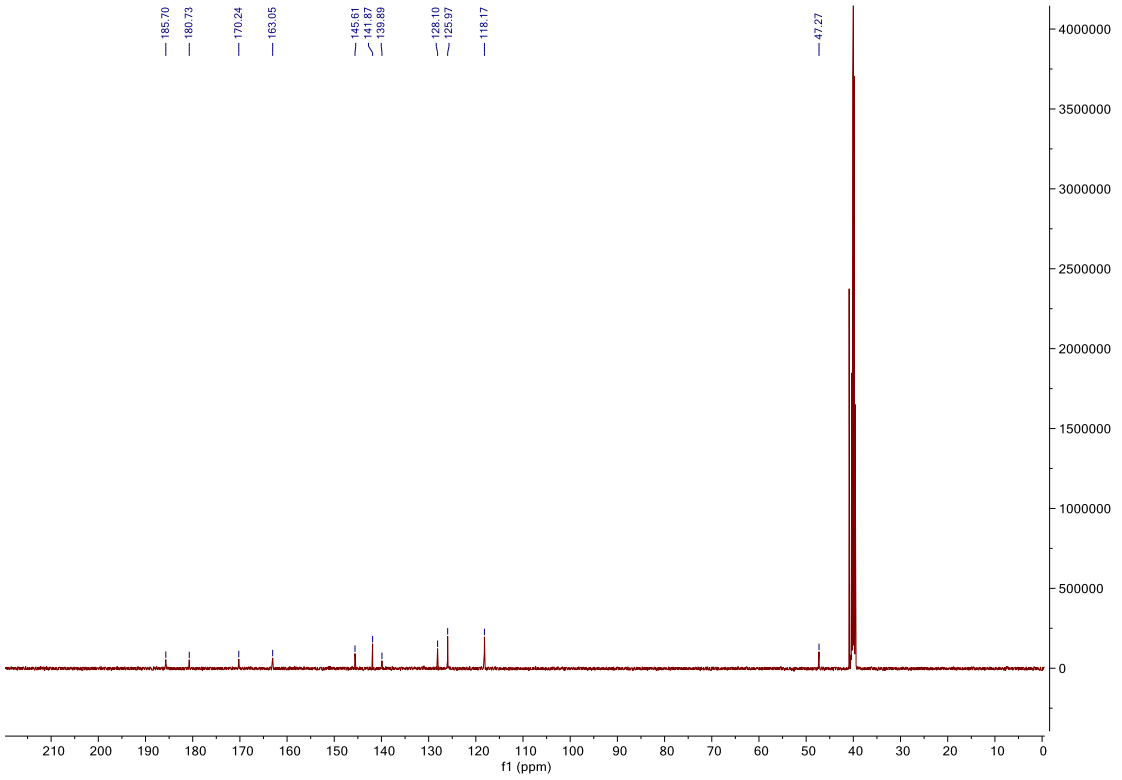

Figure SC54. ^{13}C NMR (DMSO-d_6, 126MHz) spectrum of **4.10**.

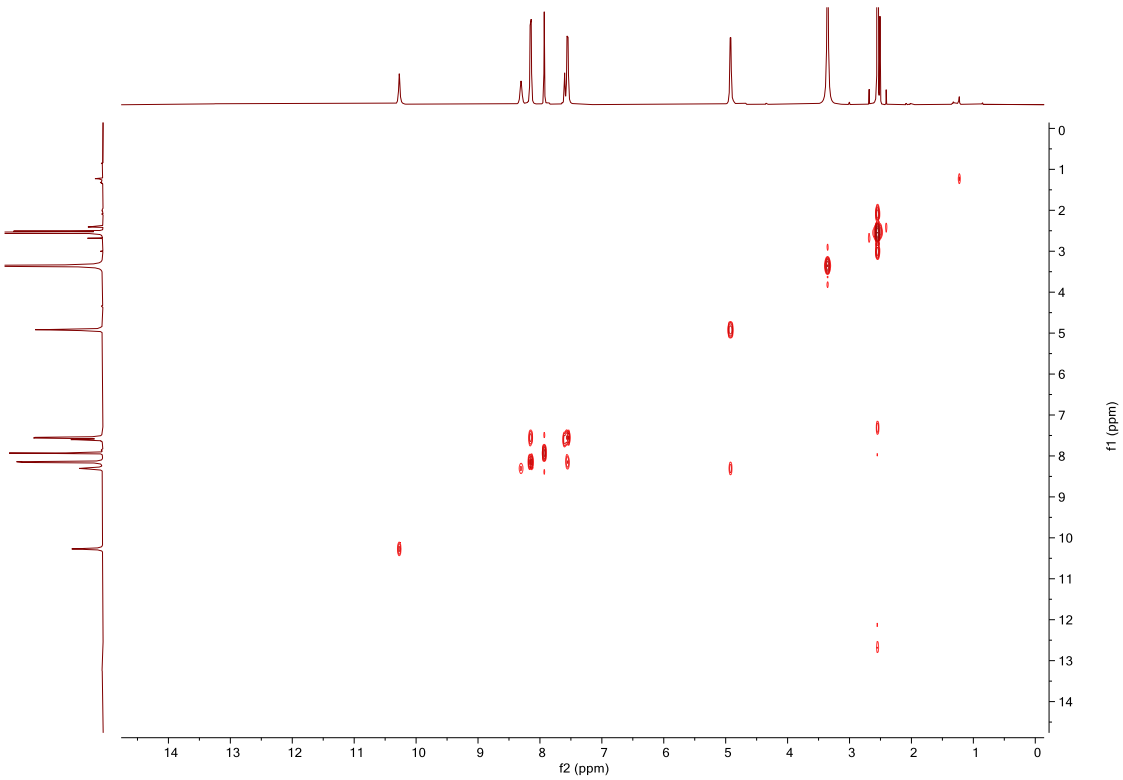

Figure SC55. COSY NMR (DMSO-d_6) spectrum of **4.10**.

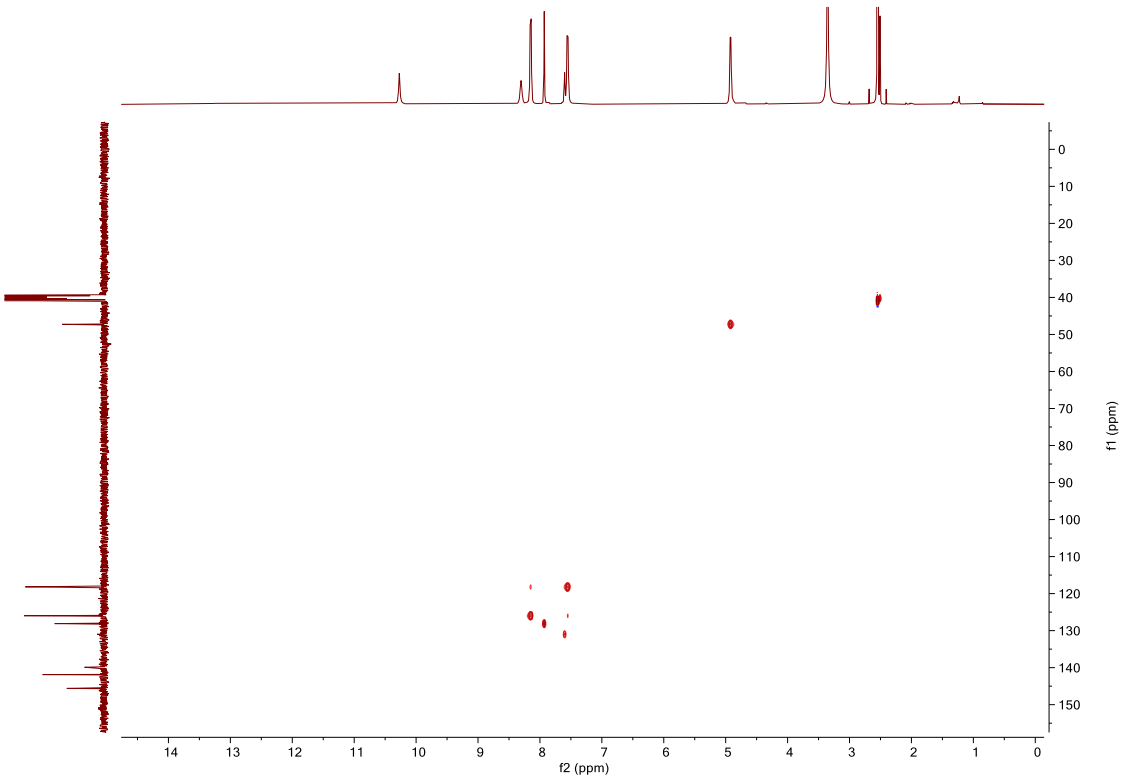

Figure SC56. HSQC NMR (DMSO-d_6) spectrum of **4.10**.

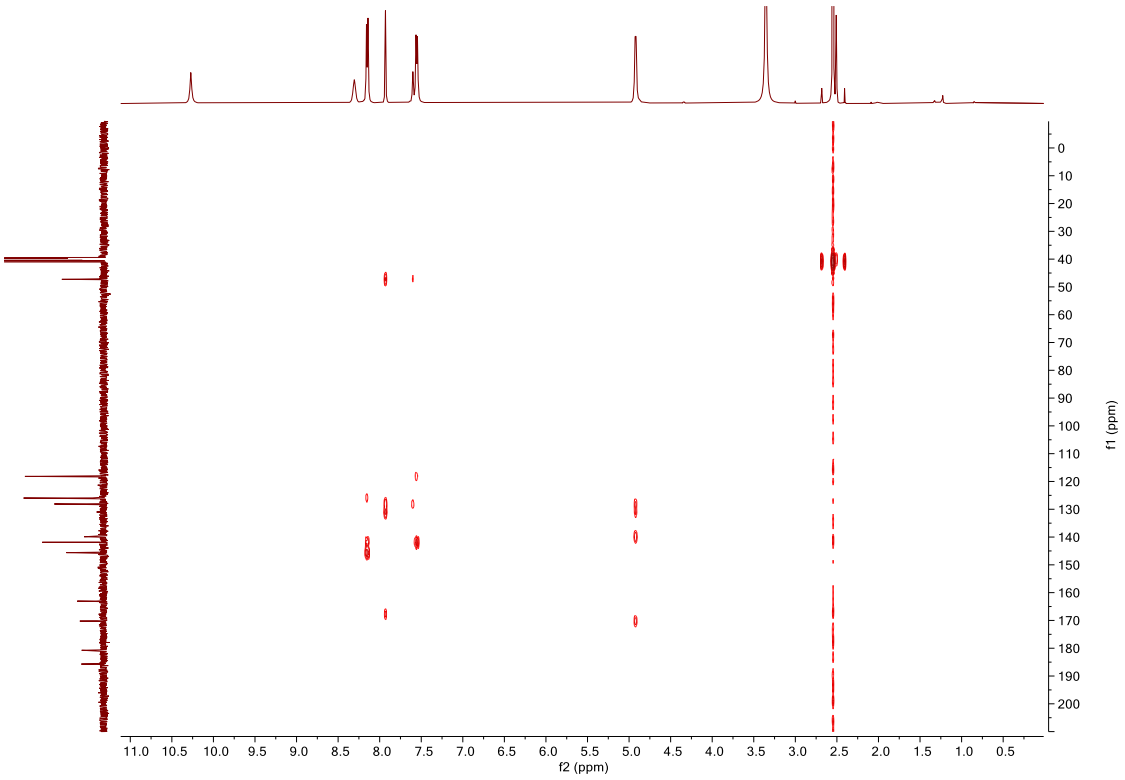

Figure SC57. HMBC NMR (DMSO-d_6) spectrum of **4.10**.

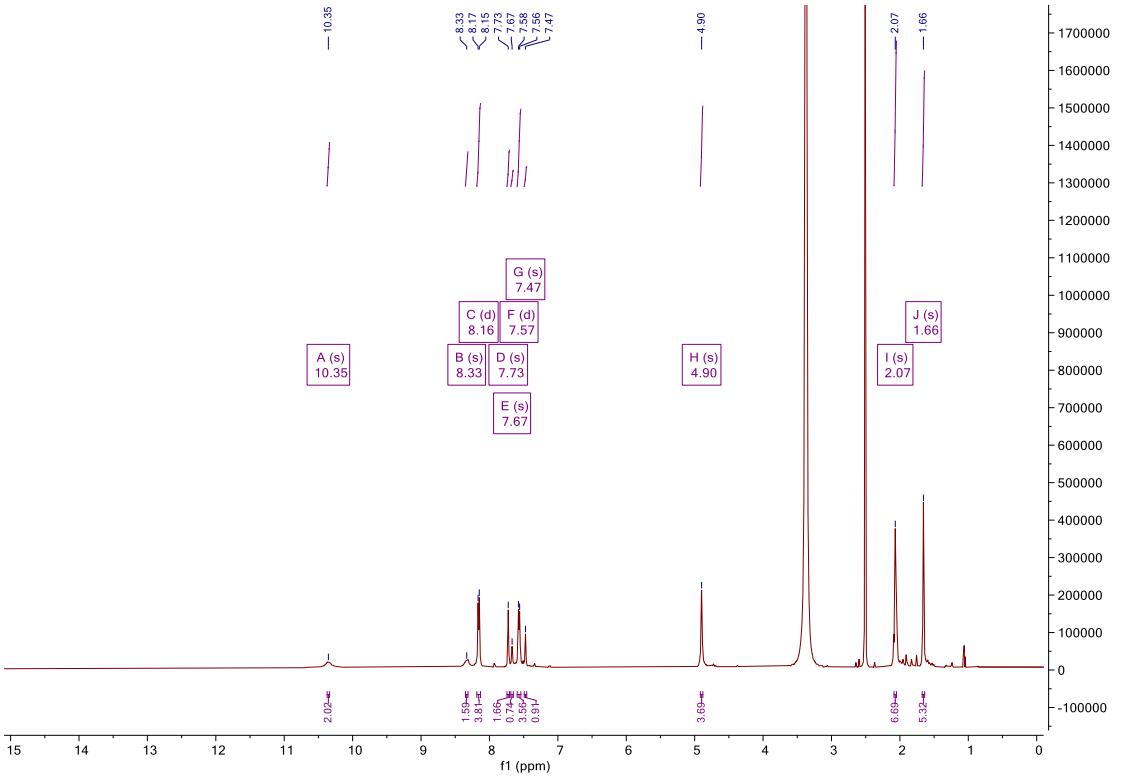

Figure SC58. ^{1}H NMR (DMSO-d_6, 500MHz) spectrum of **4.11**.

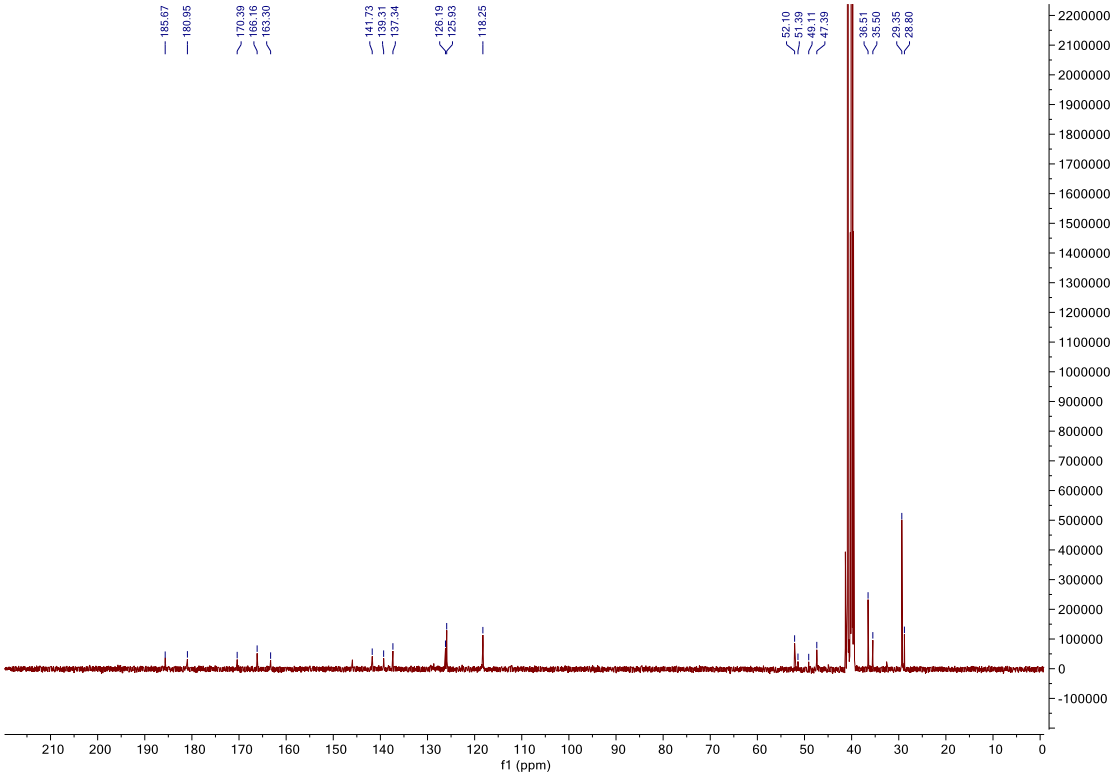

Figure SC59. ^{13}C NMR (DMSO-d_6, 126MHz) spectrum of **4.11**.

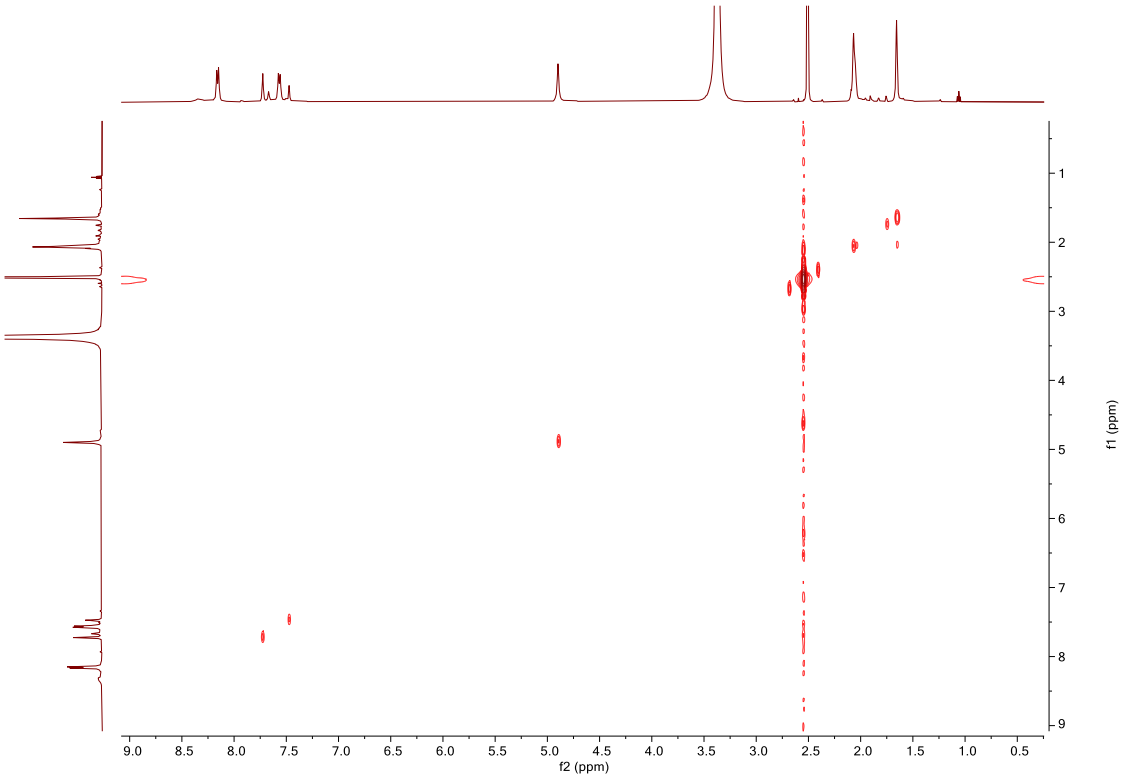

Figure SC60. COSY NMR (DMSO-d_6) spectrum of **4.11**.

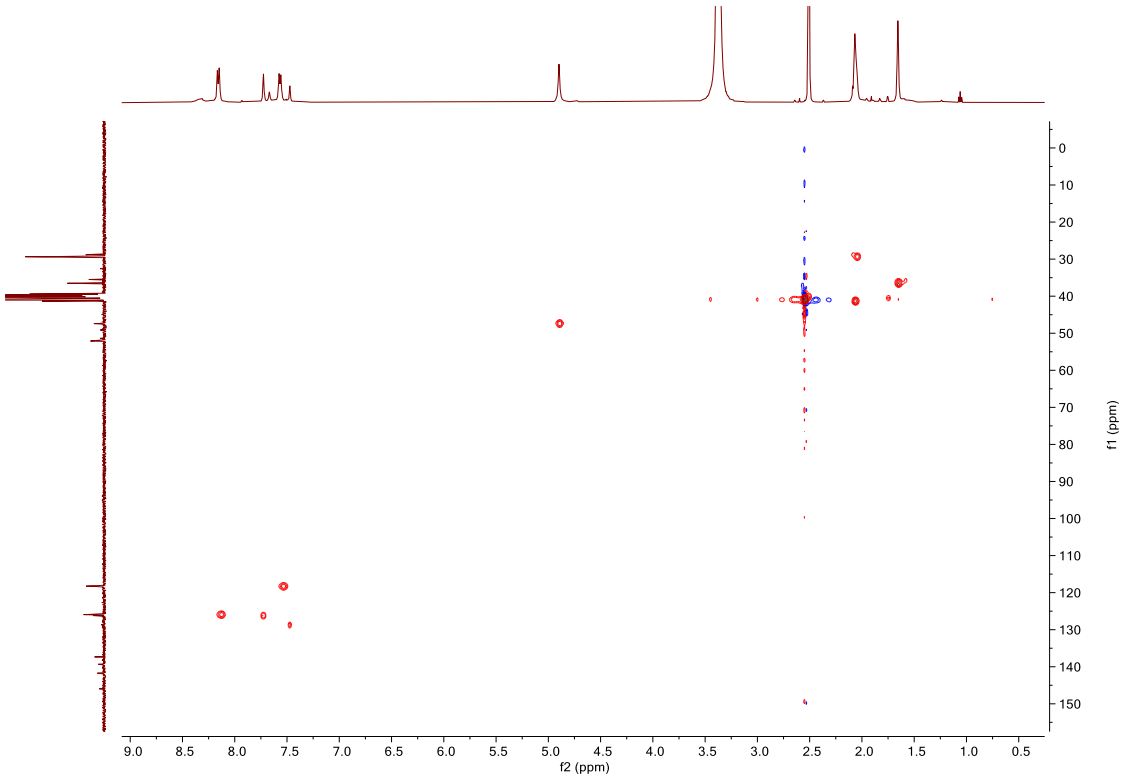

Figure SC61. HSQC NMR (DMSO-d_6) spectrum of **4.11**.

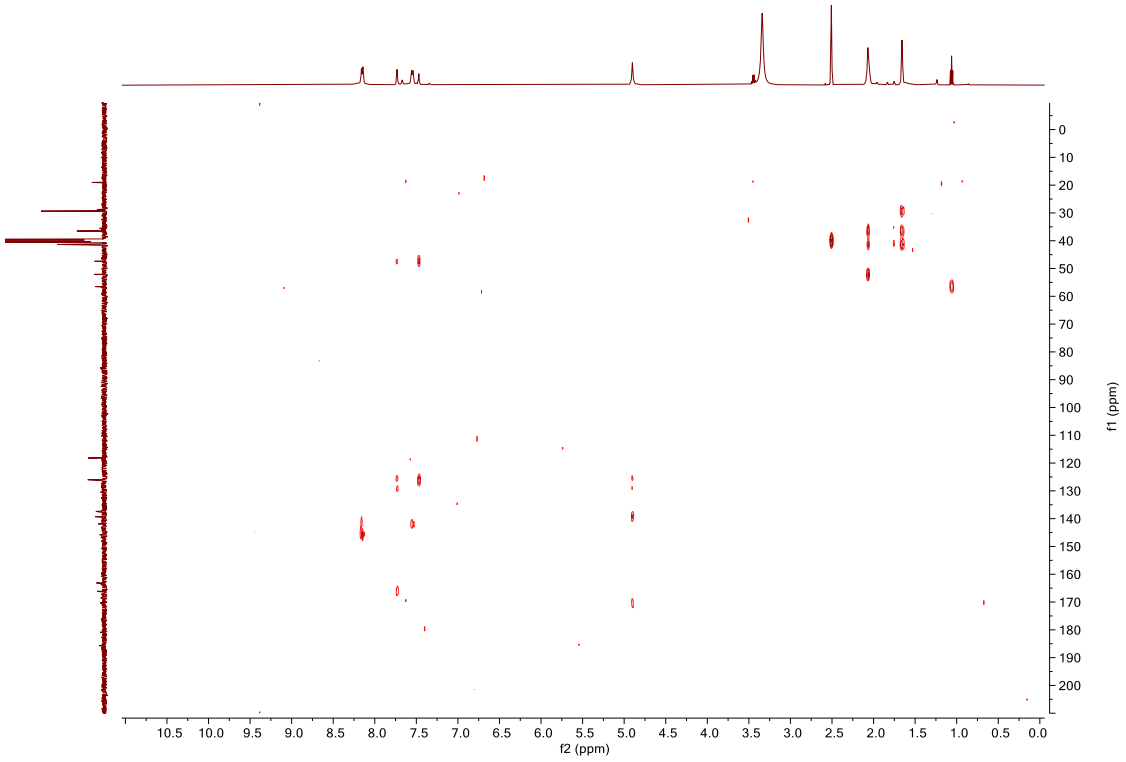

Figure SC62. HMBC NMR (DMSO-d_6) spectrum of **4.11**.

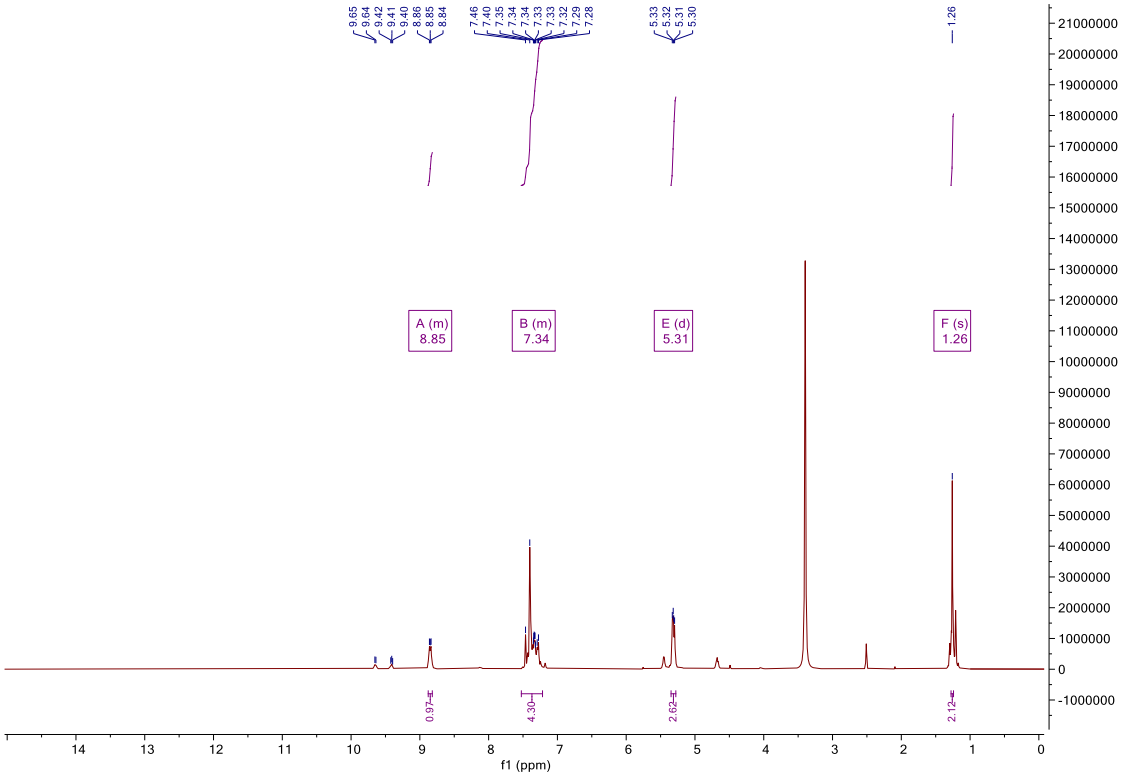

Figure SC63. ^{1}H NMR (DMSO-d_6, 500MHz) spectrum of **4.12**.

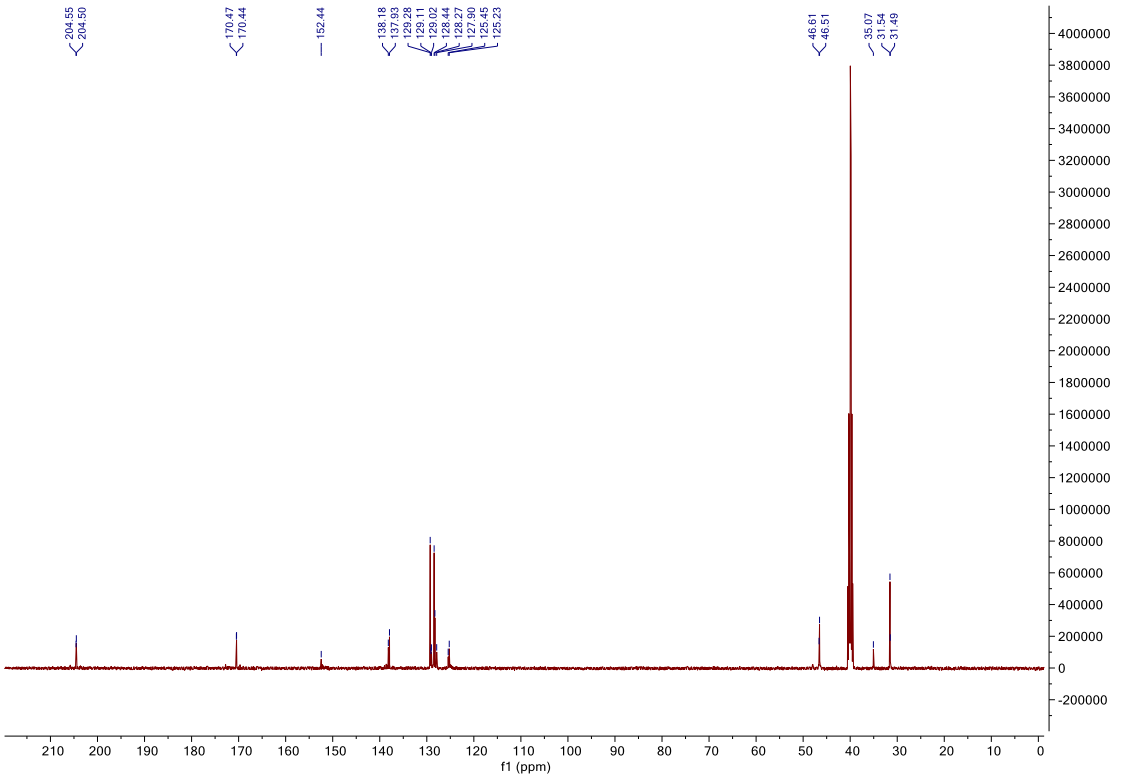

Figure SC64. ^{13}C NMR (DMSO-d_6, 126MHz) spectrum of **4.12**.

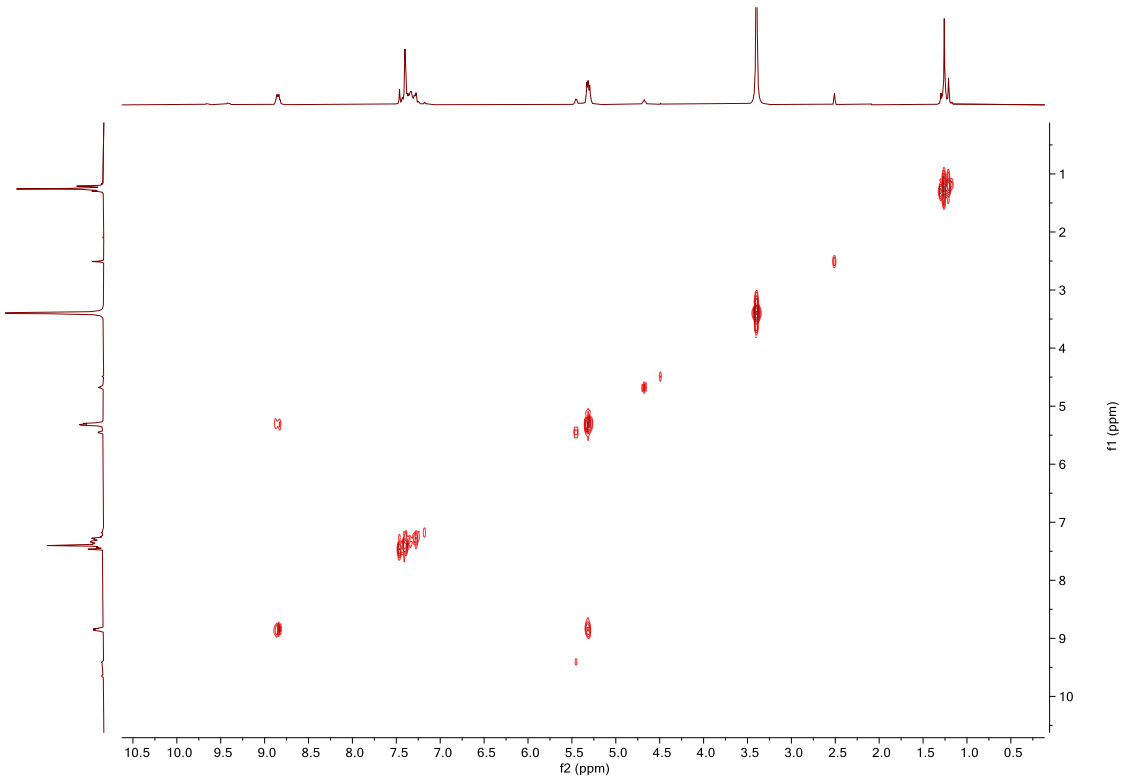

Figure SC65. COSY NMR (DMSO-d_6) spectrum of **4.12**.

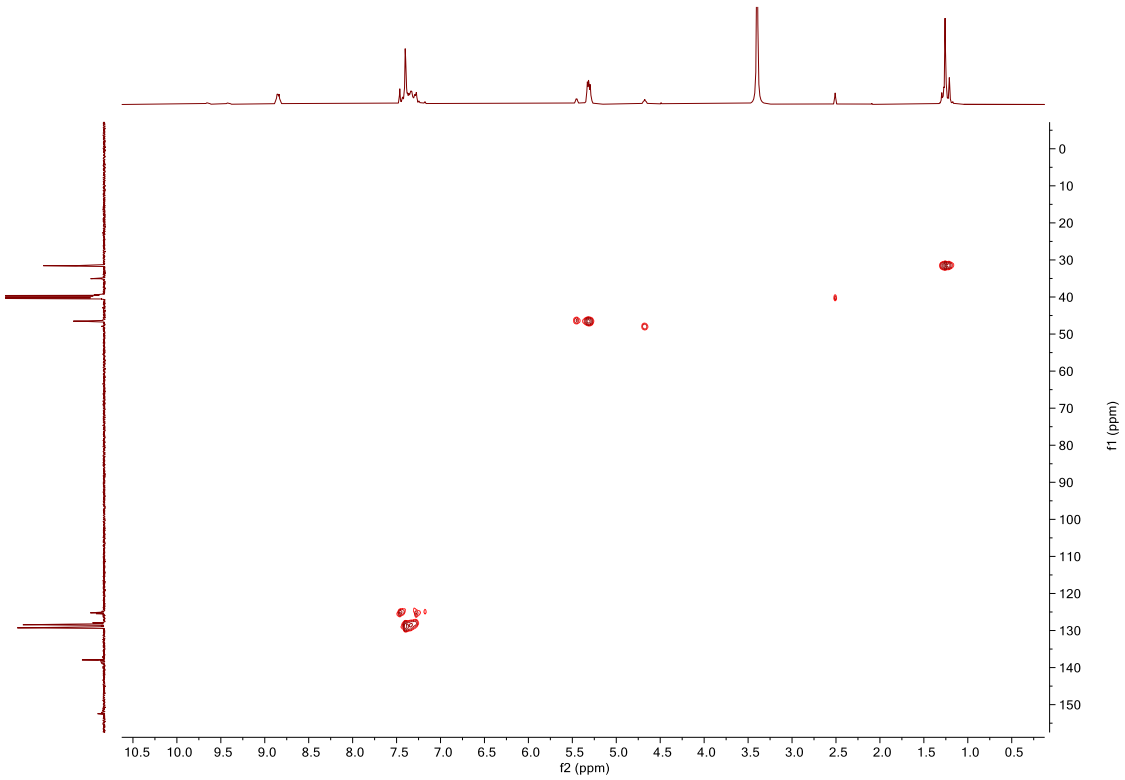

Figure SC66. HSQC NMR (DMSO-d_6) spectrum of **4.12**.

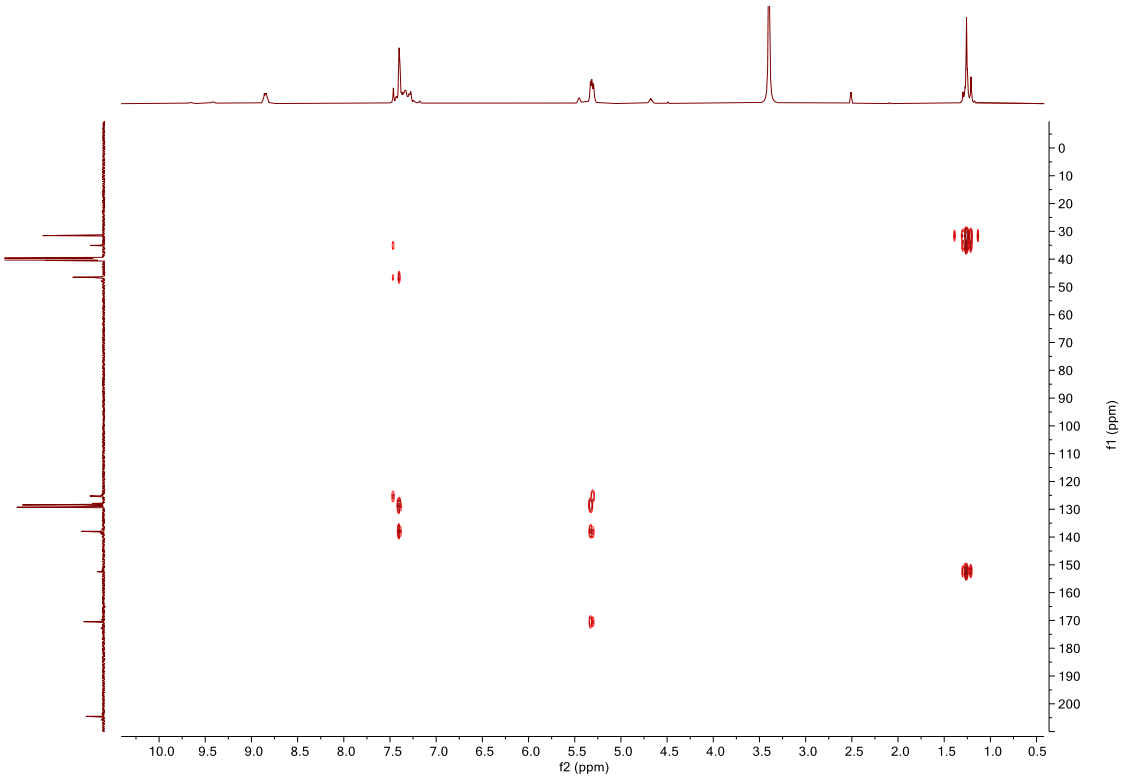

Figure SC67. HMBC NMR (DMSO-d_6) spectrum of **4.12**.

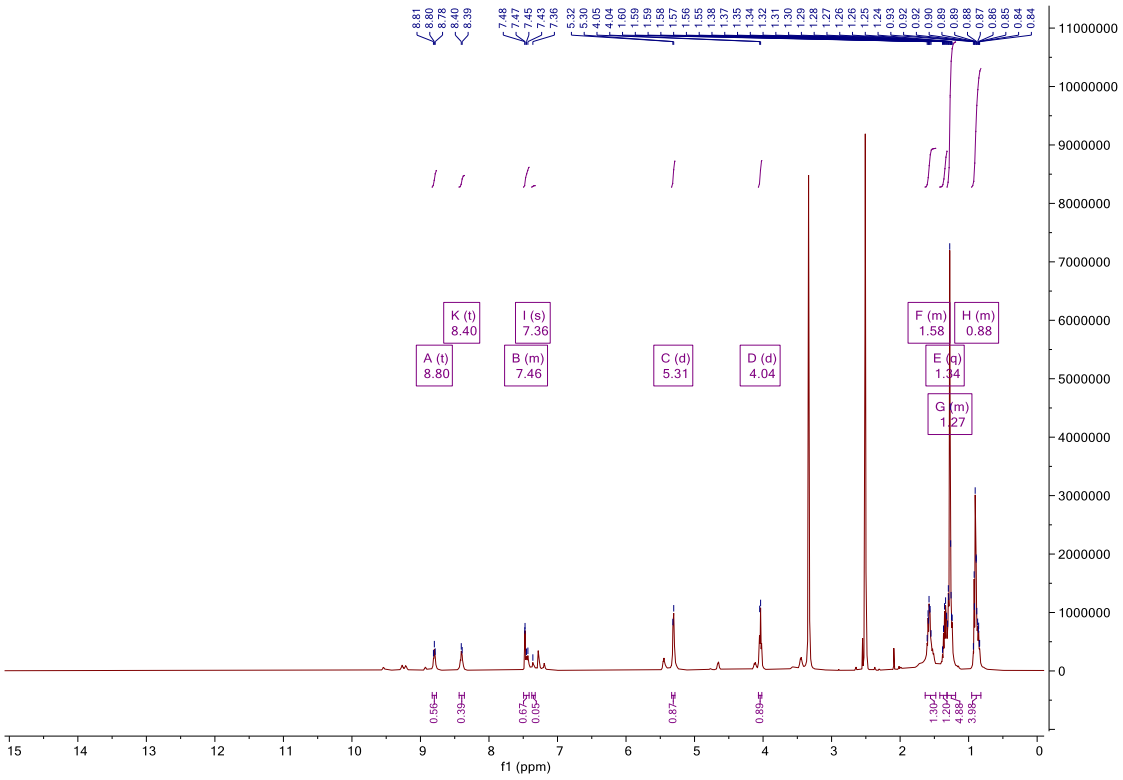

Figure SC68. ^{1}H NMR (DMSO-d_6, 500MHz) spectrum of **4.13**.

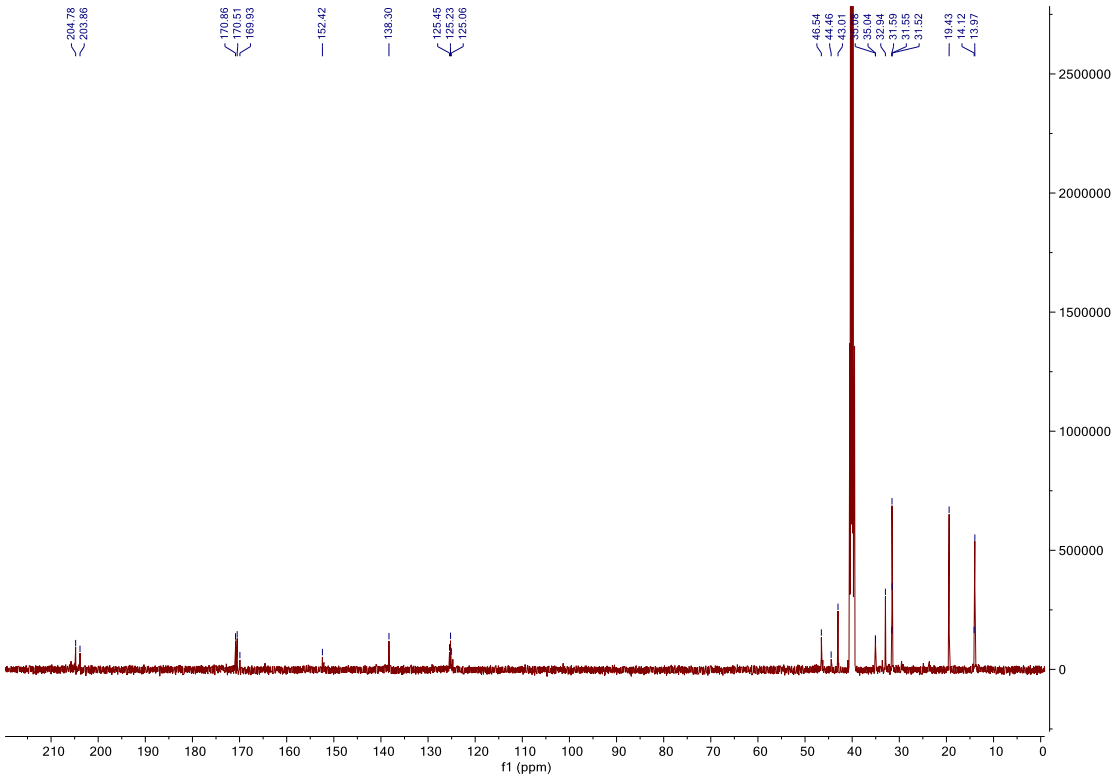

Figure SC69. ^{13}C NMR (DMSO-d_6, 126MHz) spectrum of **4.13**.

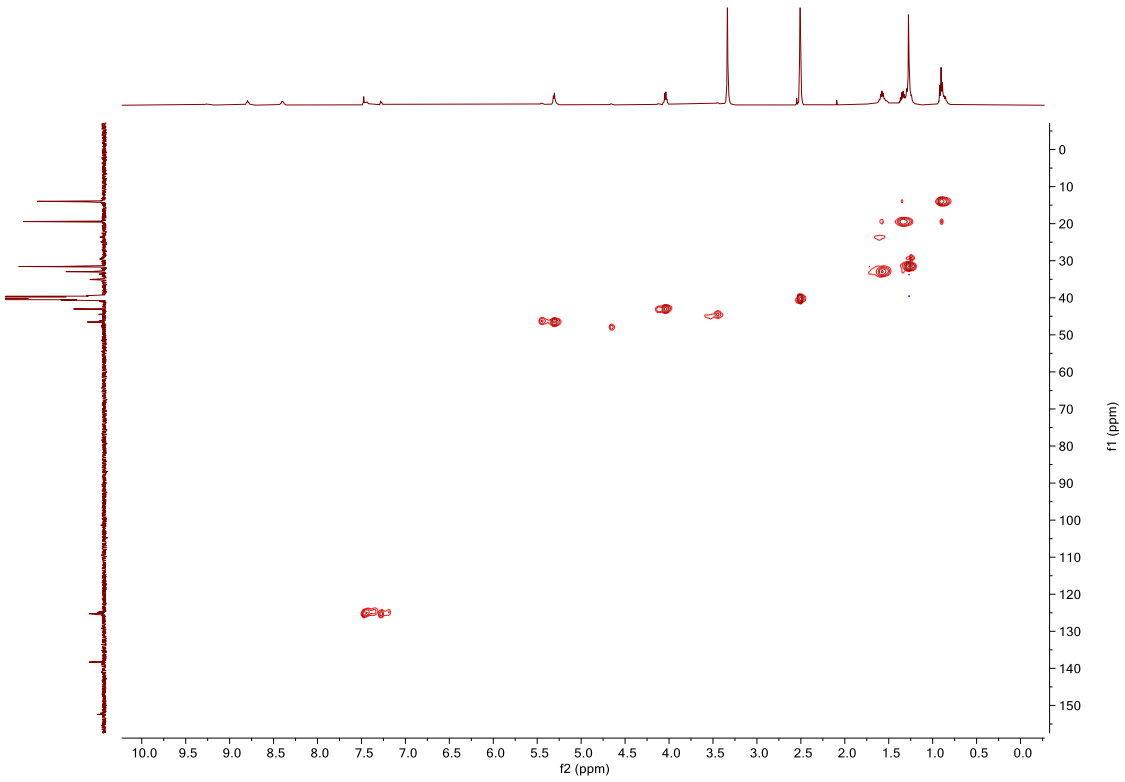

Figure SC70. COSY NMR (DMSO-d_6) spectrum of **4.13**.

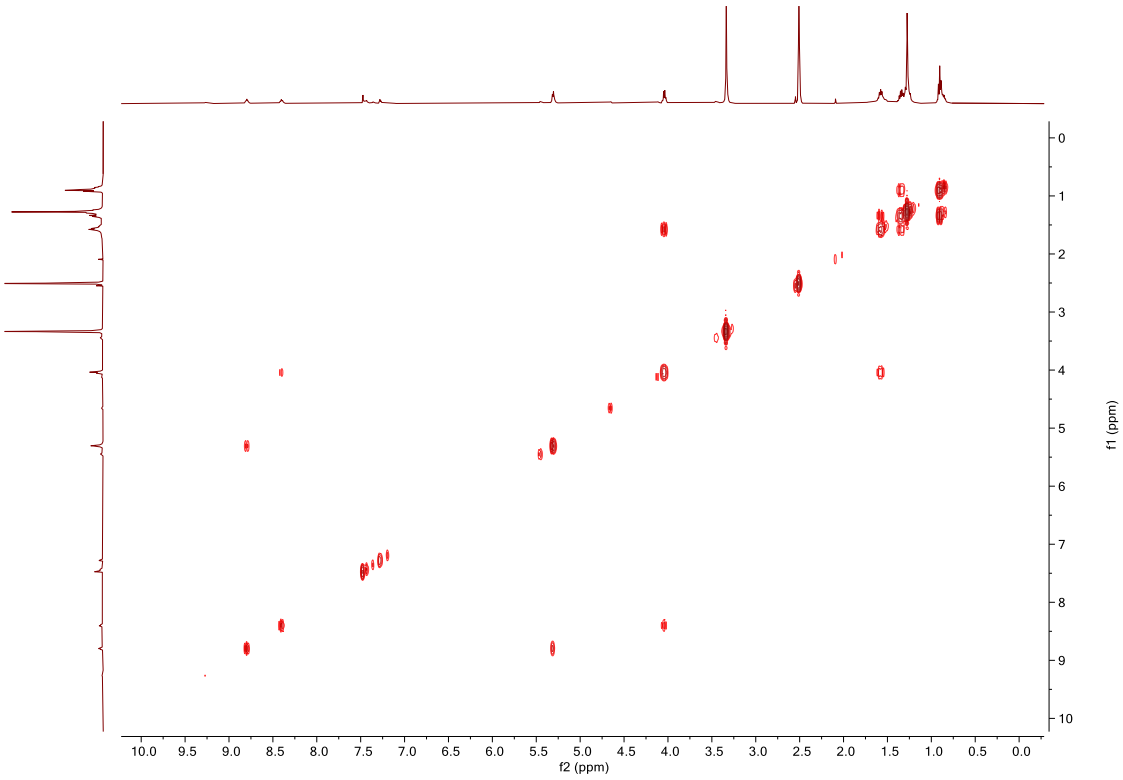

Figure SC71. HSQC NMR (DMSO-d_6) spectrum of **4.13**.

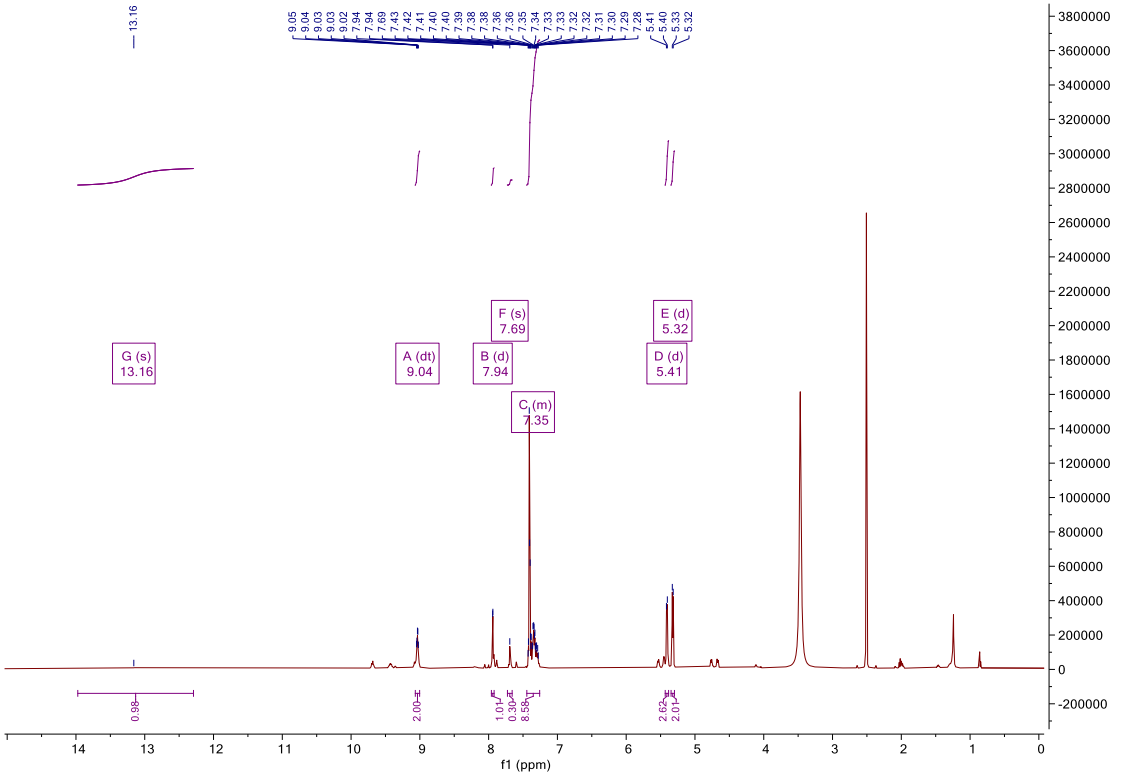

Figure SC72. ^{1}H NMR (DMSO-d_6, 500MHz) spectrum of **4.14**.

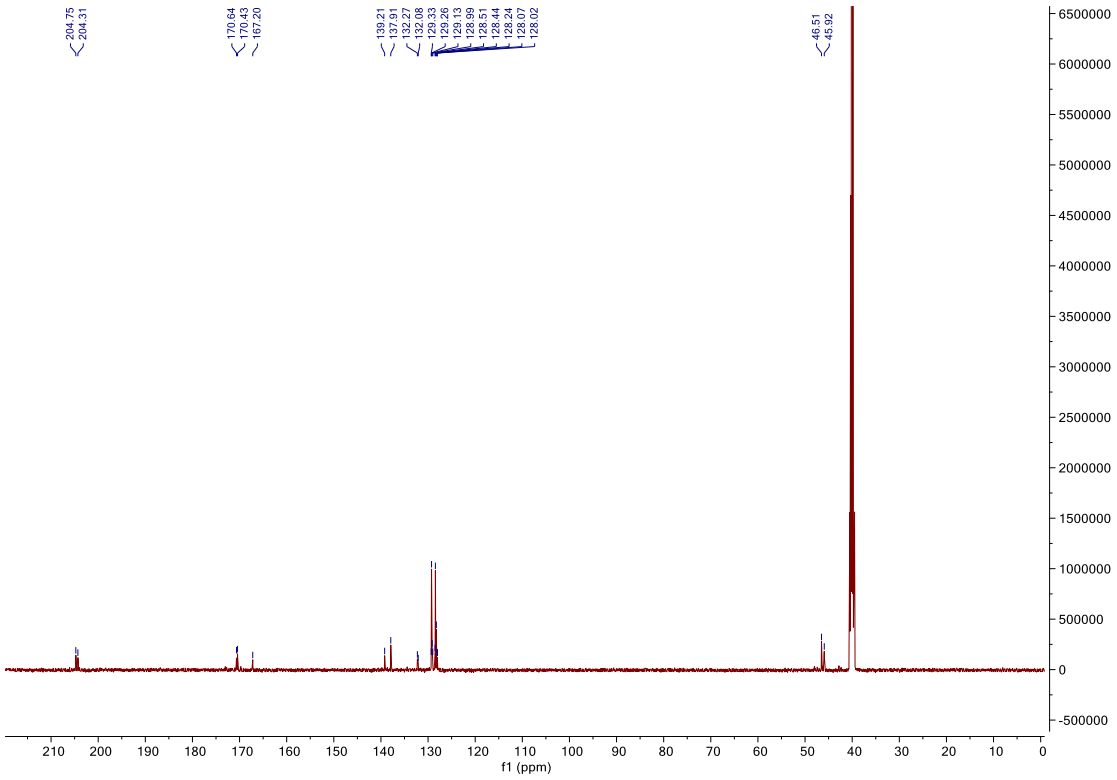

Figure SC73. ^{13}C NMR (DMSO-d_6, 126MHz) spectrum of **4.14**.

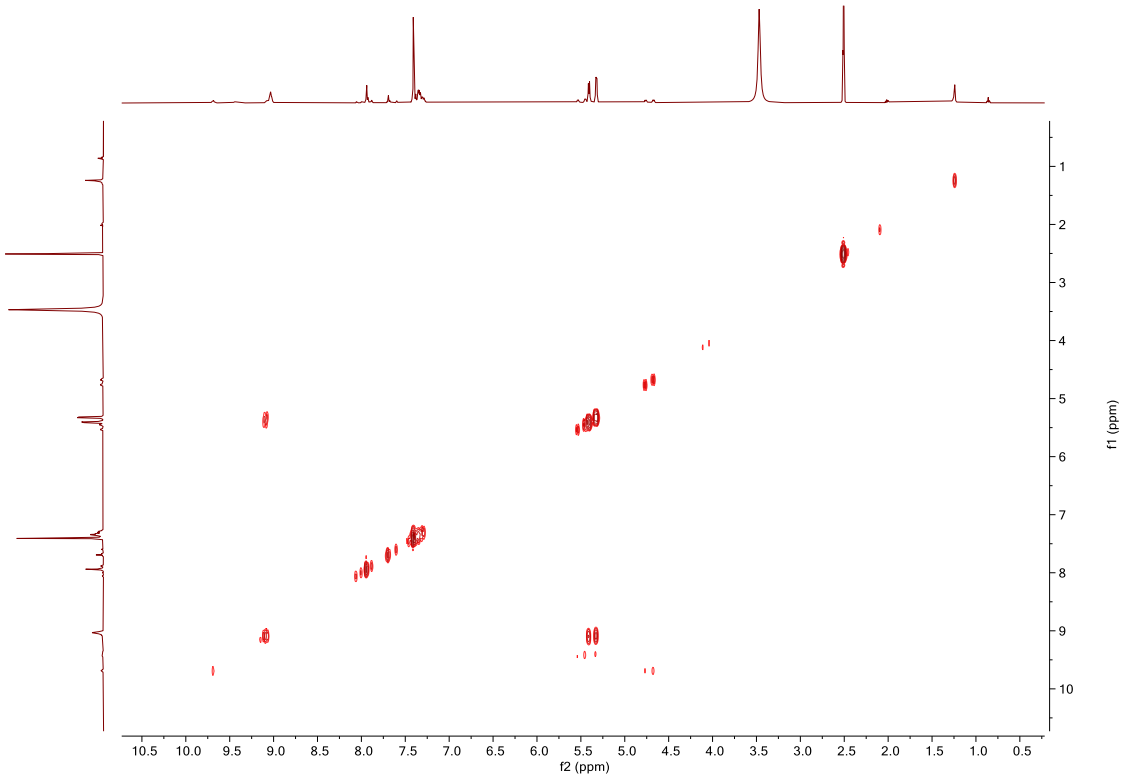

Figure SC74. COSY NMR (DMSO-d_6) spectrum of **4.14**.

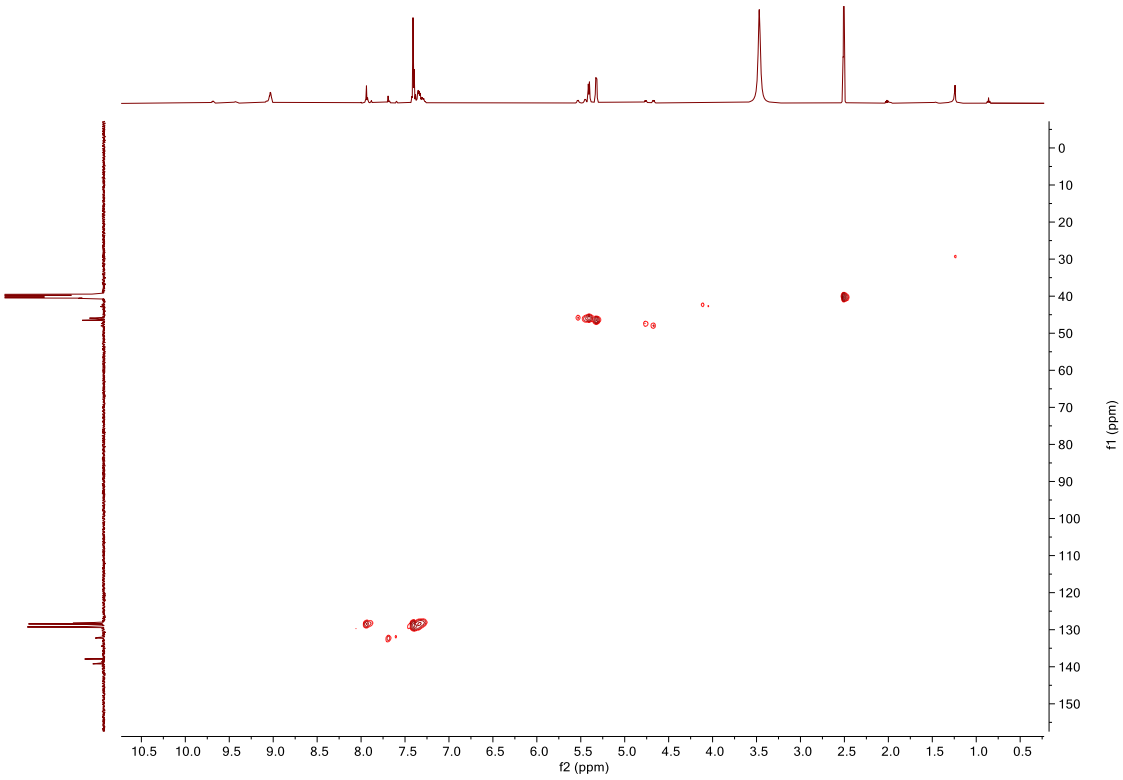

Figure SC75. HSQC NMR (DMSO-d_6) spectrum of **4.14**.

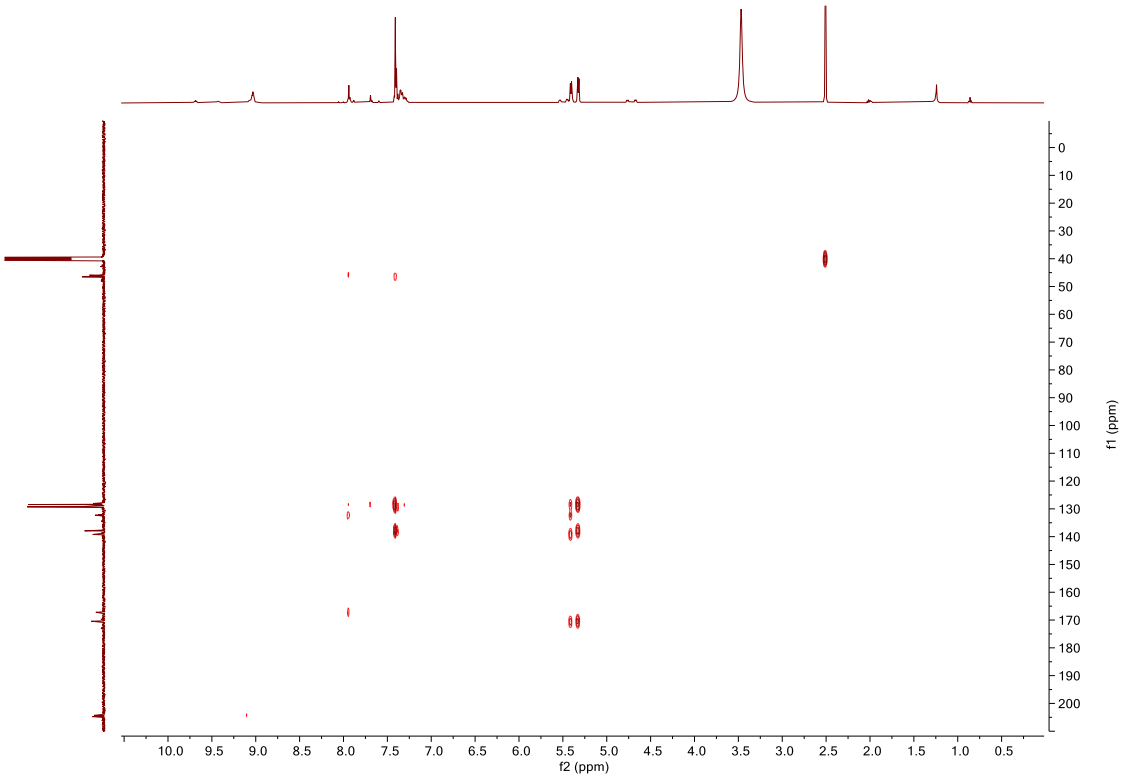

Figure SC76. HMBC NMR (DMSO-d_6) spectrum of **4.14**.

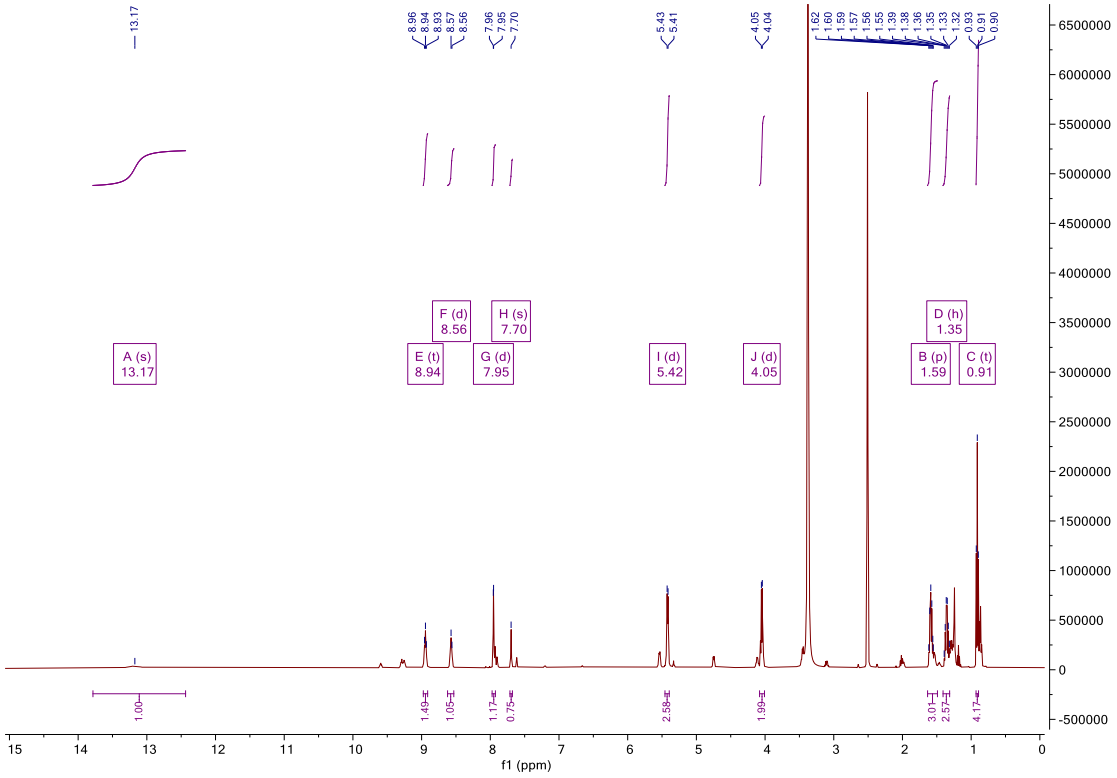

Figure SC77. ^{1}H NMR (DMSO-d_6, 500MHz) spectrum of **4.15**.

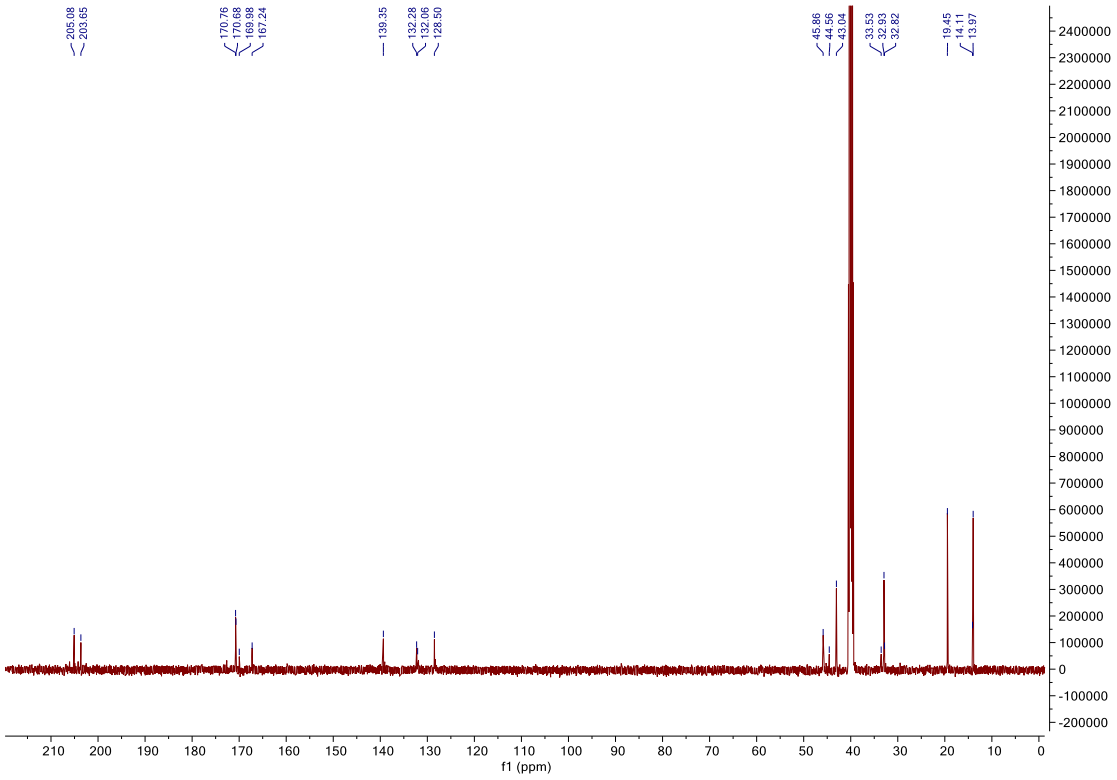

Figure SC78. ^{13}C NMR (DMSO-d_6, 126MHz) spectrum of **4.15**.

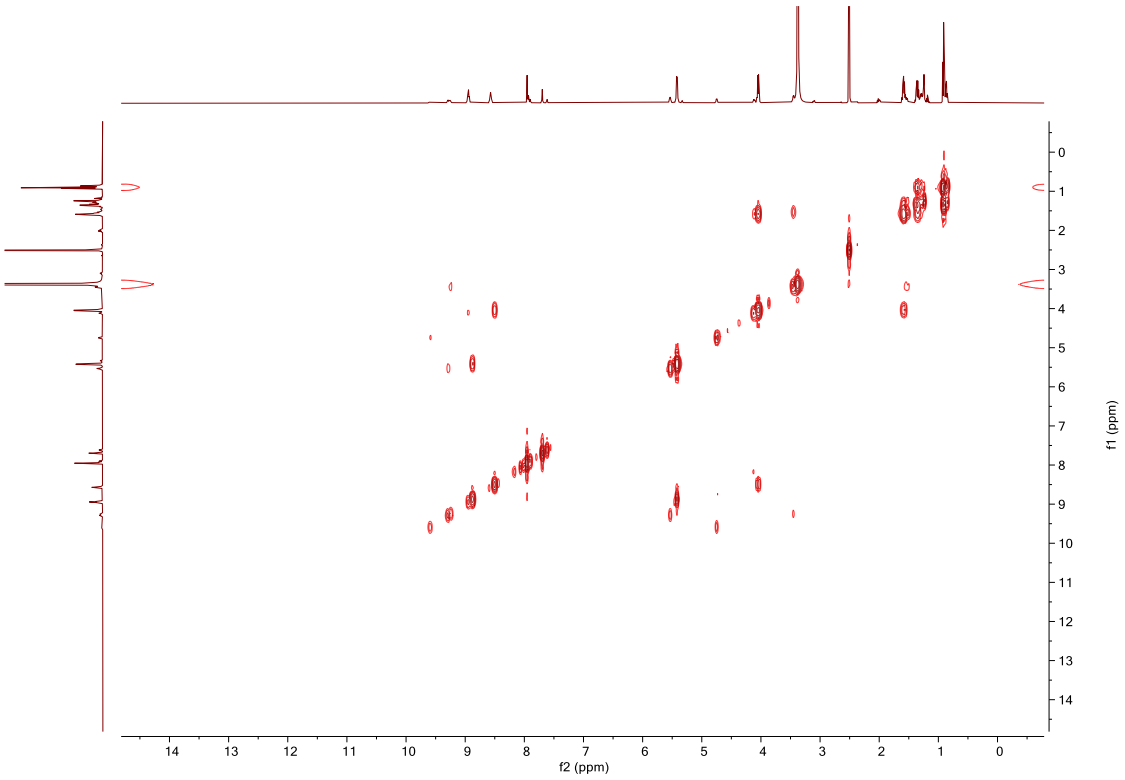

Figure SC79. COSY NMR (DMSO-d_6) spectrum of **4.15**.

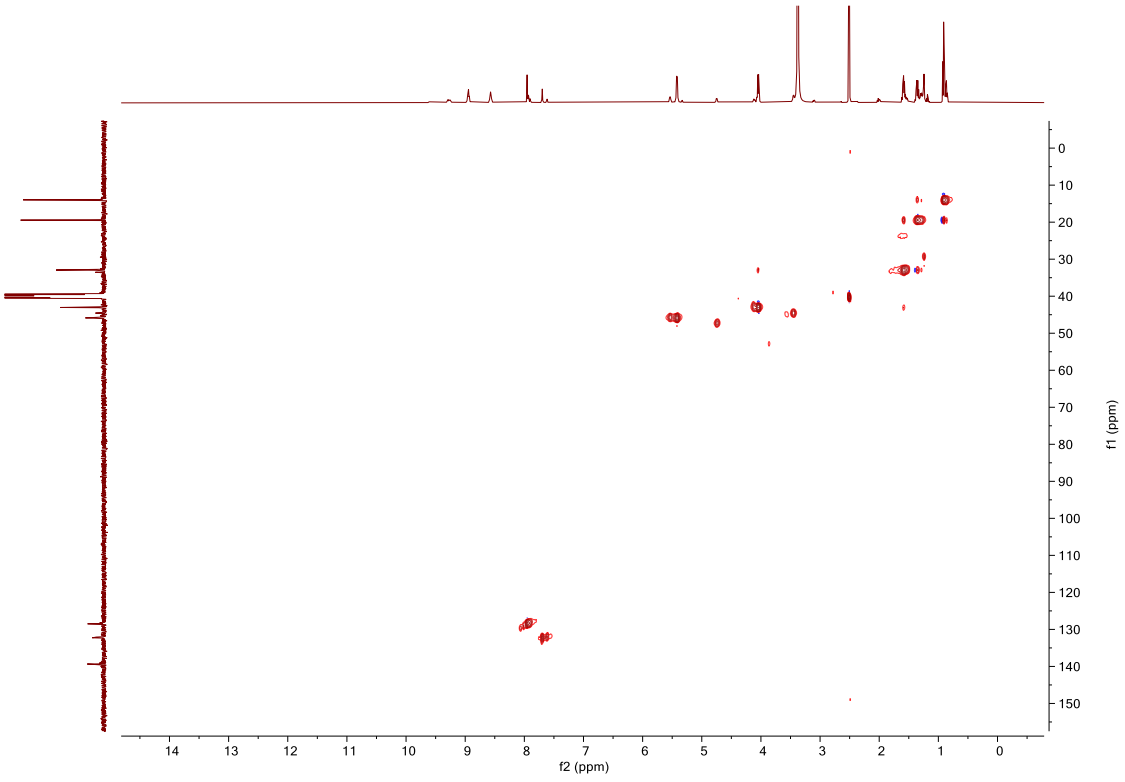

Figure SC80. HSQC NMR (DMSO-d_6) spectrum of **4.15**.

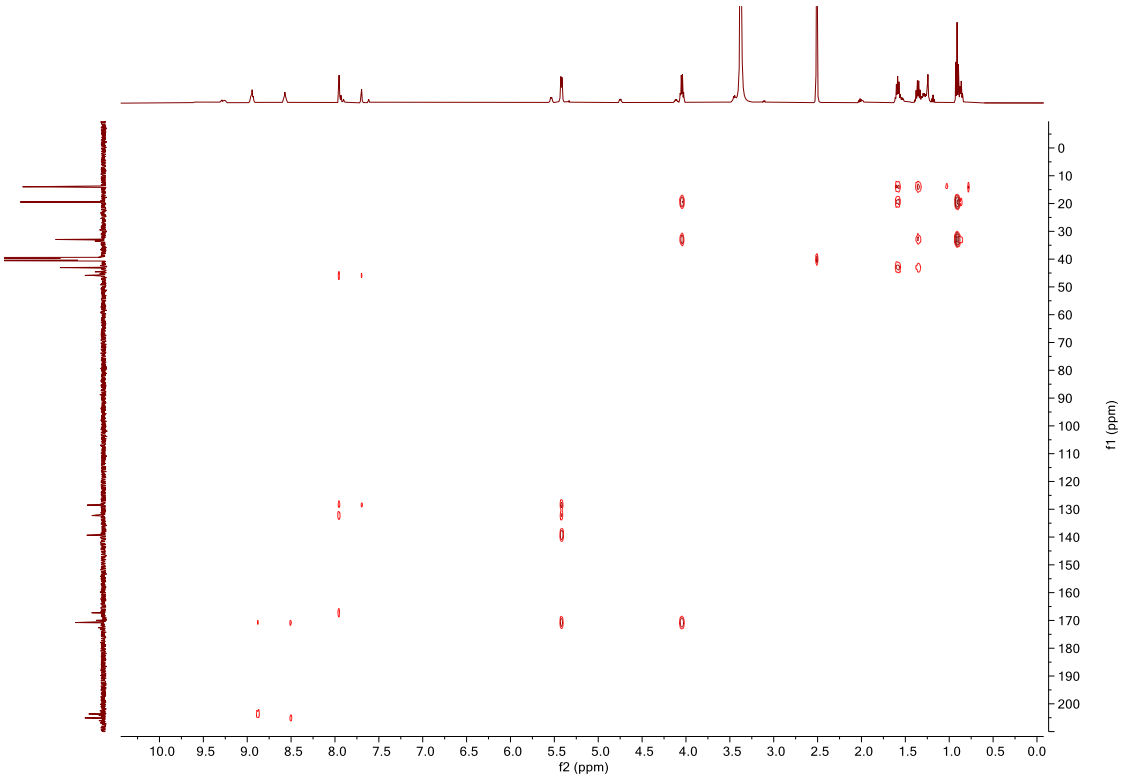

Figure SC81. HMBC NMR (DMSO-d_6) spectrum of **4.15**.

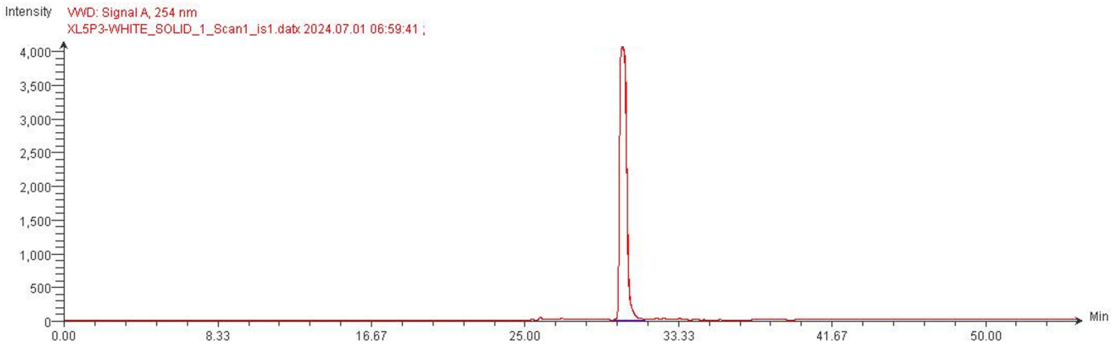

Figure SC82. Analytical LC-MS trace of **C3**.

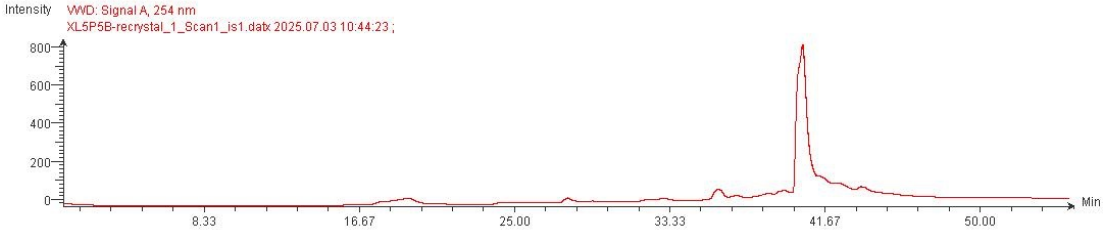

Figure SC83. Analytical LC-MS trace of **3.1**.

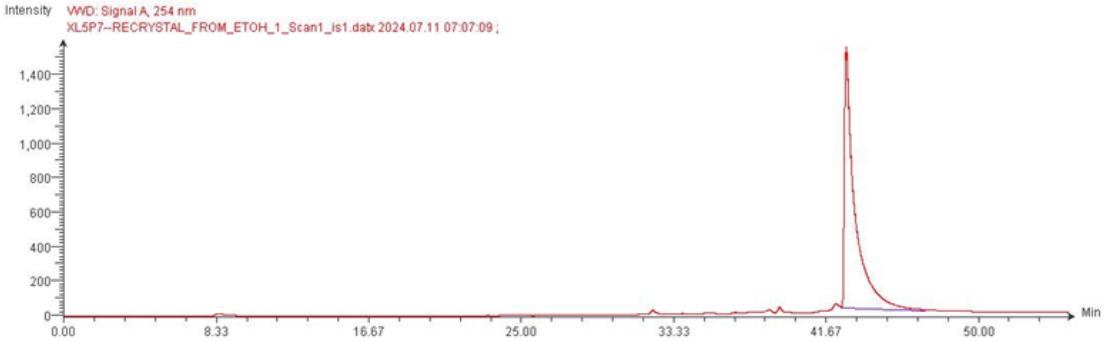

Figure SC84. Analytical LC-MS trace of **3.2**.

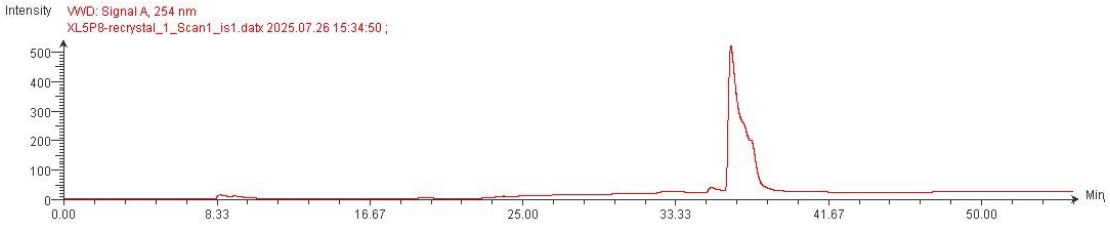

Figure SC85. Analytical LC-MS trace of **3.3**.

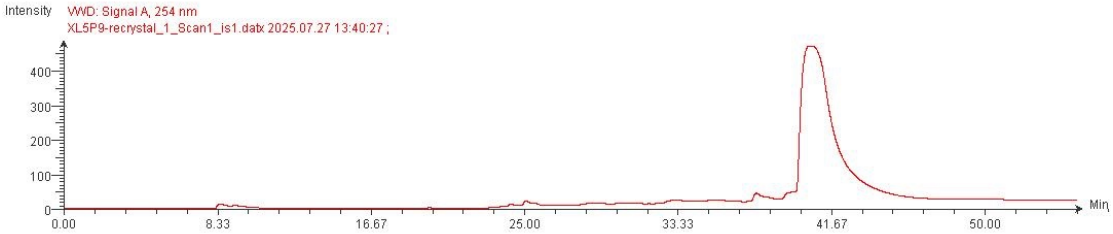

Figure SC86. Analytical LC-MS trace of **3.4**.

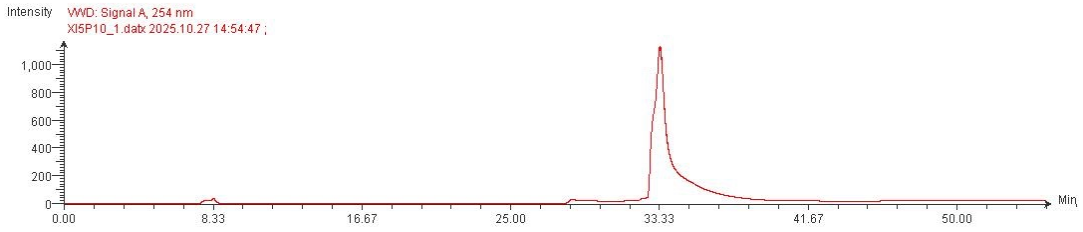

Figure SC87. Analytical LC-MS trace of **3.5**.

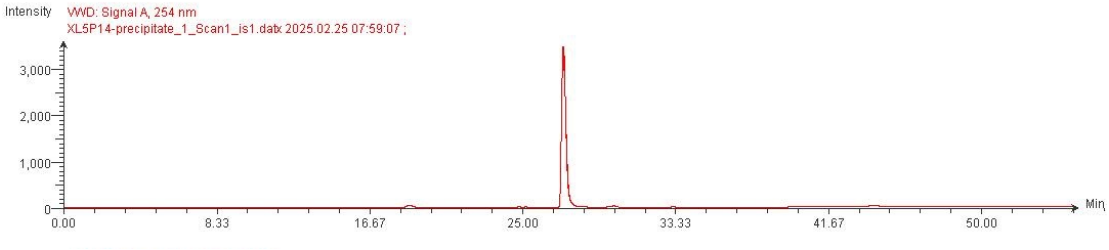

Figure SC88. Analytical LC-MS trace of **C4**.

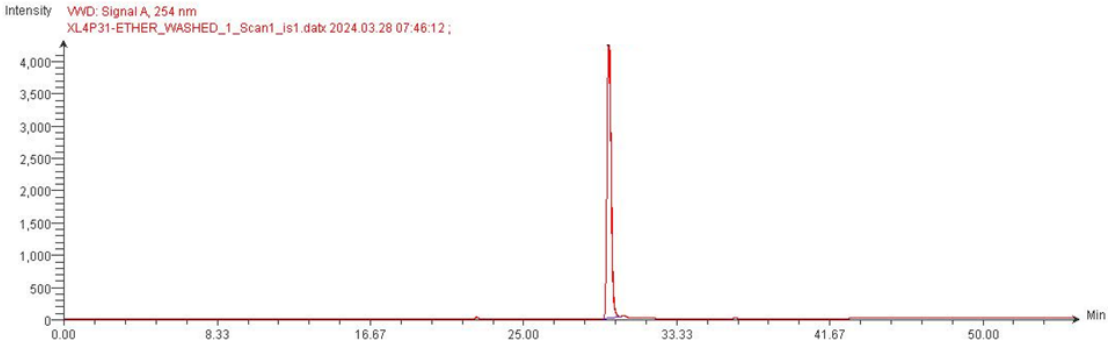

Figure SC89. Analytical LC-MS trace of **4.6**.

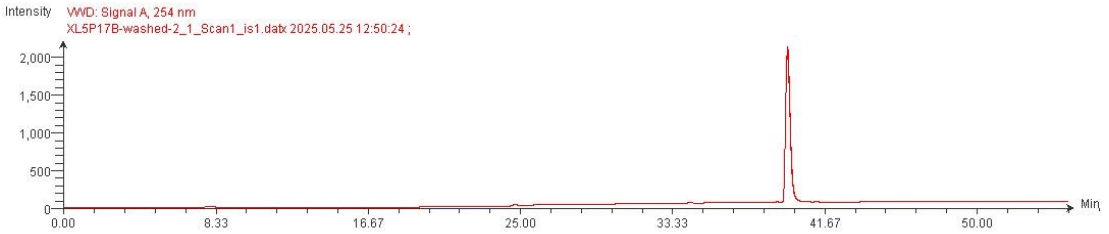

Figure SC90. Analytical LC-MS trace of **4.7**.

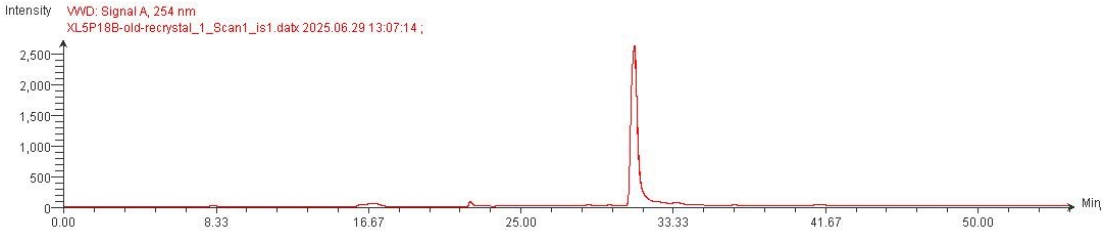

Figure SC91. Analytical LC-MS trace of **4.8**.

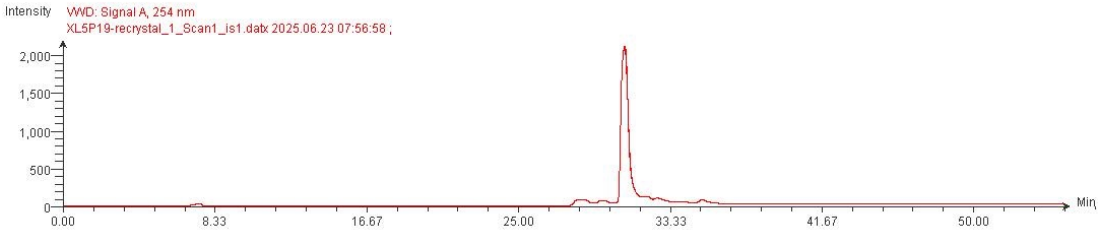

Figure SC92. Analytical LC-MS trace of **4.9**.

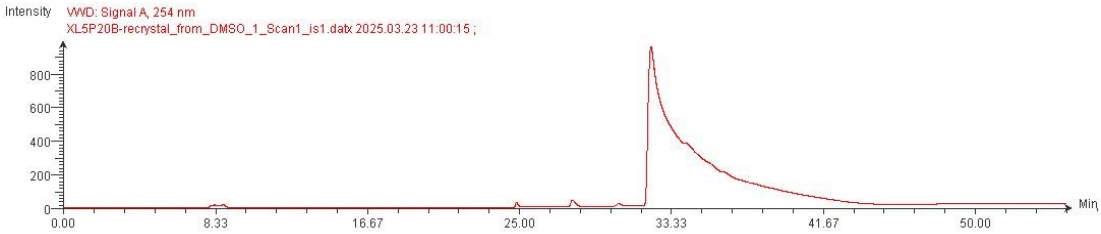

Figure SC93. Analytical LC-MS trace of **4.10**.

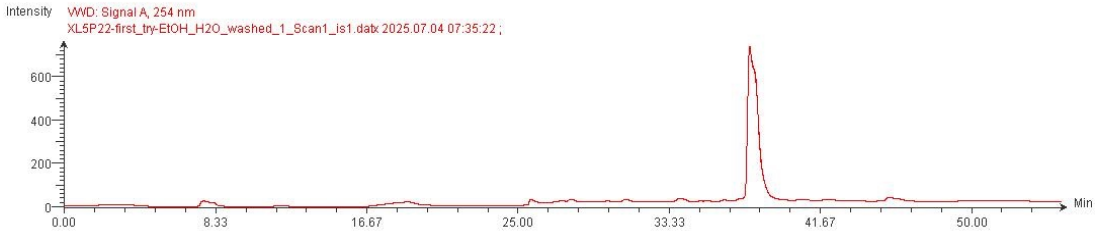

Figure SC94. Analytical LC-MS trace of **4.11**.

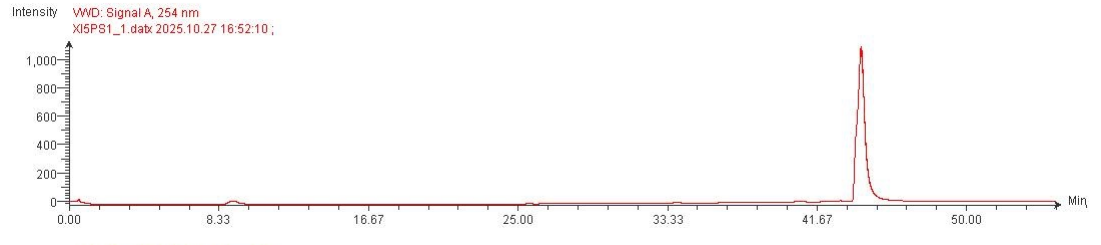

Figure SC95. Analytical LC-MS trace of **4.12**.

Figure SC96. Analytical LC-MS trace of **4.13**.

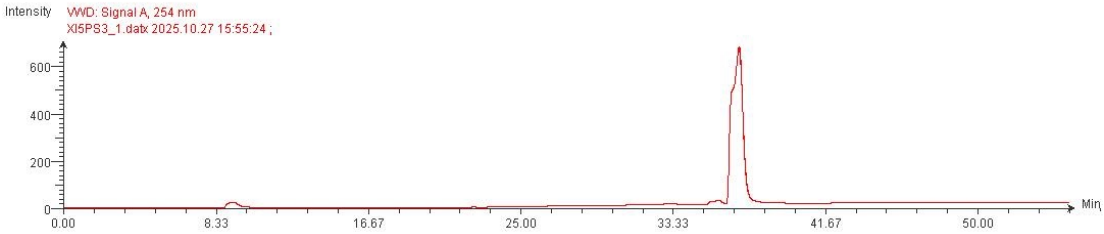

Figure SC97. Analytical LC-MS trace of **4.14**.

Figure SC98. Analytical LC-MS trace of **4.15**.

Figure: Extracted ion chromatogram (EIC) of compound.

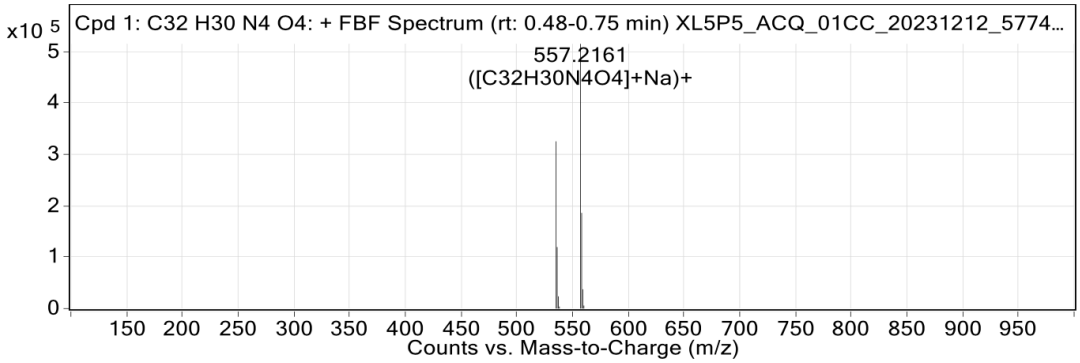

Figure: Full range view of Compound spectra and potential adducts.

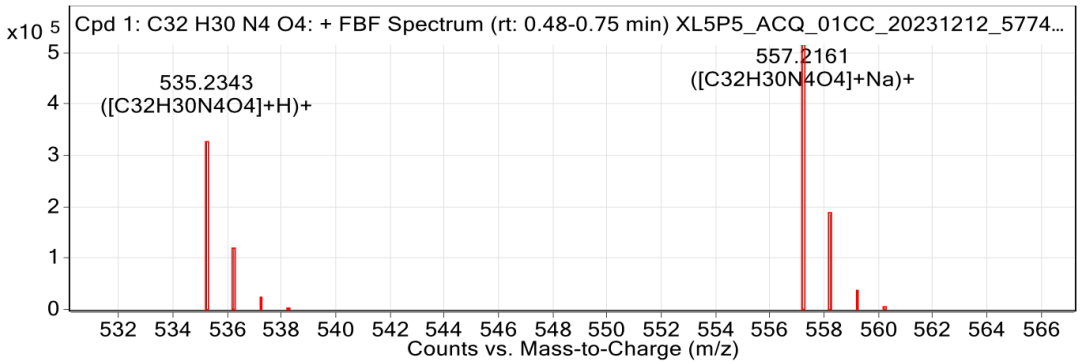

Figure SC99. Analytical HRMS trace of **4.1**.

Figure: Extracted ion chromatogram (EIC) of compound.

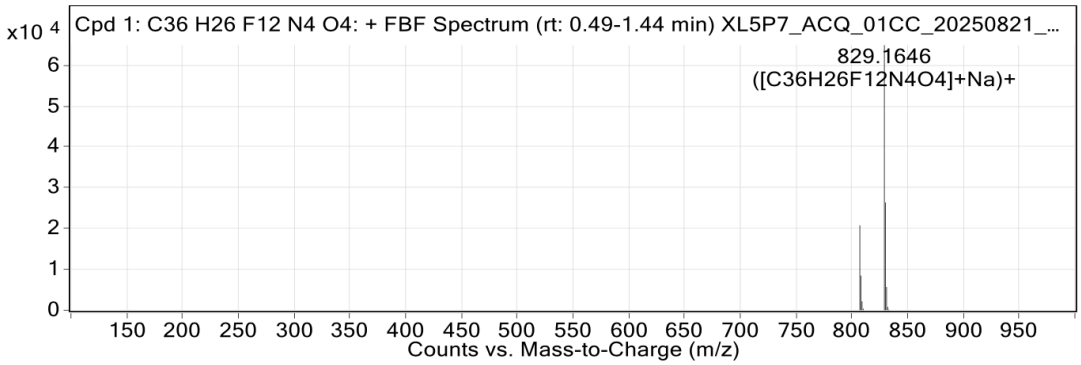

Figure: Full range view of Compound spectra and potential adducts.

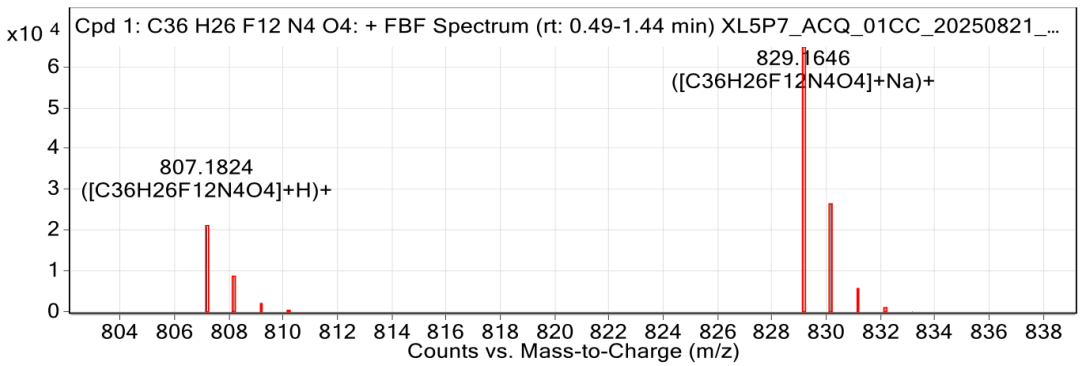

Figure SC100. Analytical HRMS trace of **4.2**.

Figure: Extracted ion chromatogram (EIC) of compound.

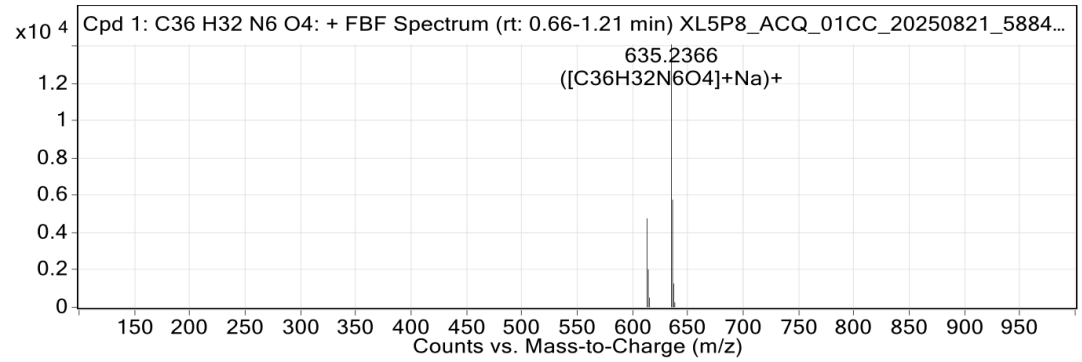

Figure: Full range view of Compound spectra and potential adducts.

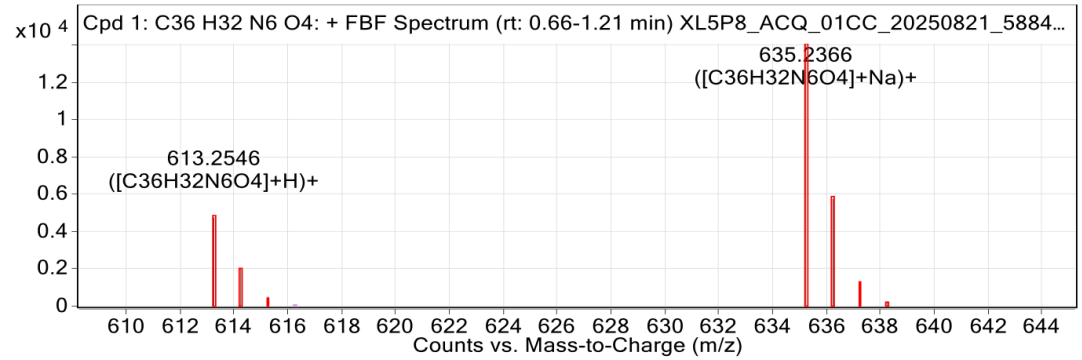

Figure SC101. Analytical HRMS trace of **4.3**.

Figure: Extracted ion chromatogram (EIC) of compound.

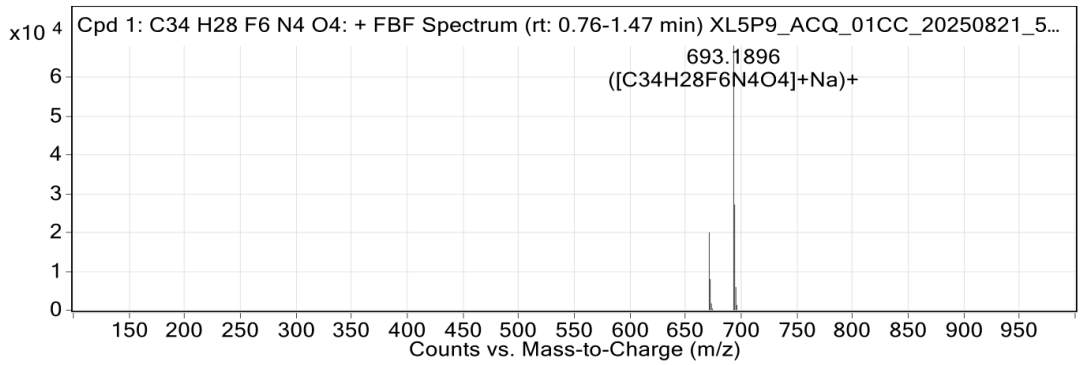

Figure: Full range view of Compound spectra and potential adducts.

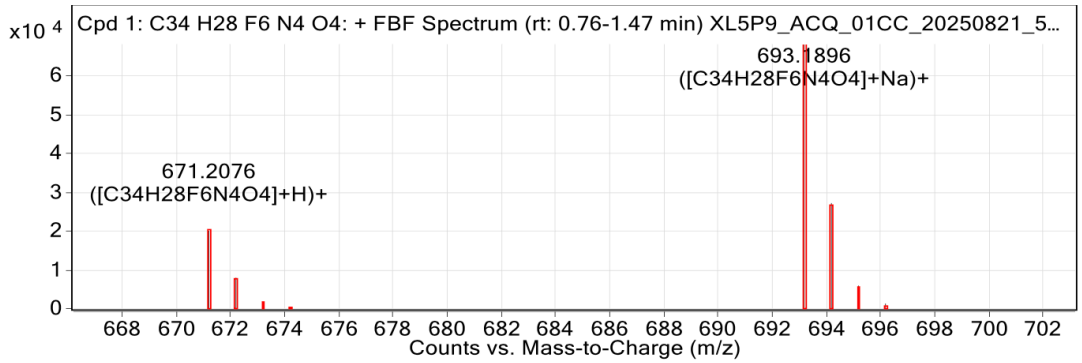

Figure SC102. Analytical HRMS trace of **4.4**.

Figure: Extracted ion chromatogram (EIC) of compound.

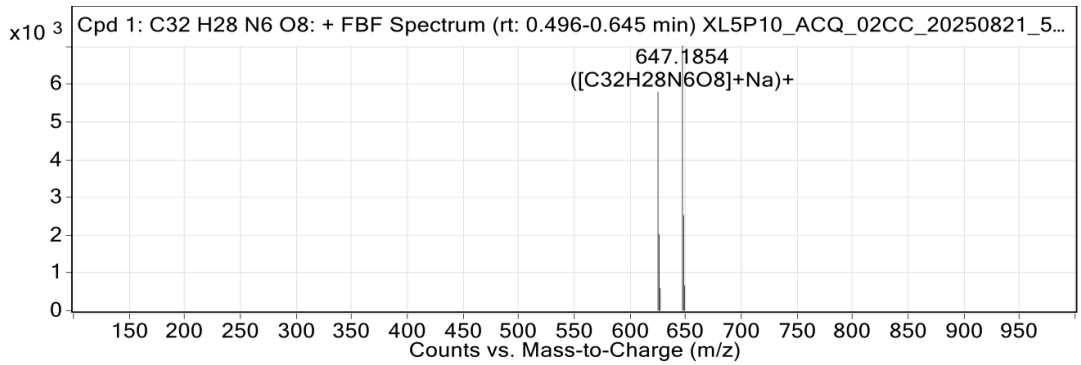

Figure: Full range view of Compound spectra and potential adducts.

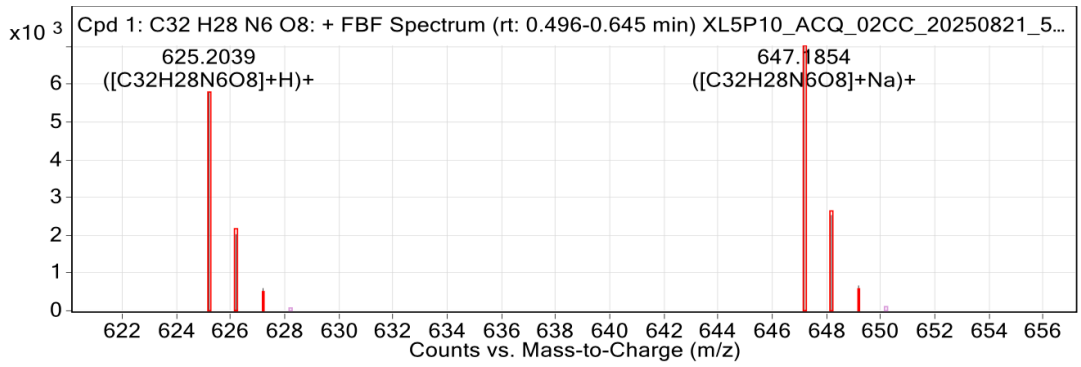

Figure SC103. Analytical HRMS trace of **4.5**.

Figure: Extracted ion chromatogram (EIC) of compound.

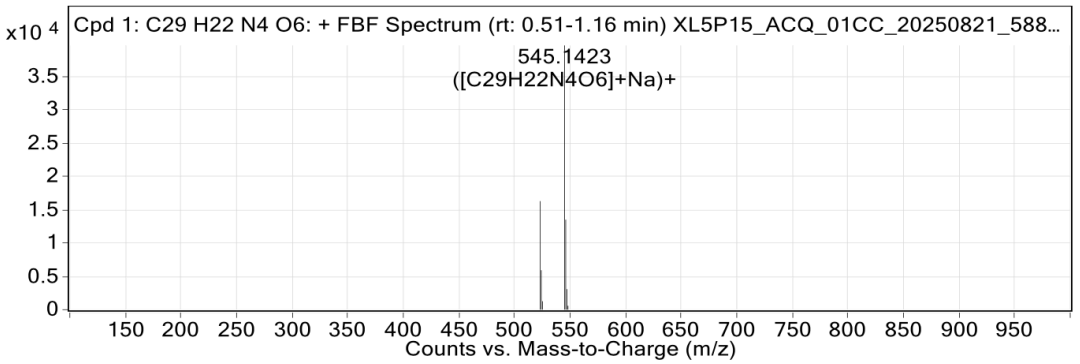

Figure: Full range view of Compound spectra and potential adducts.

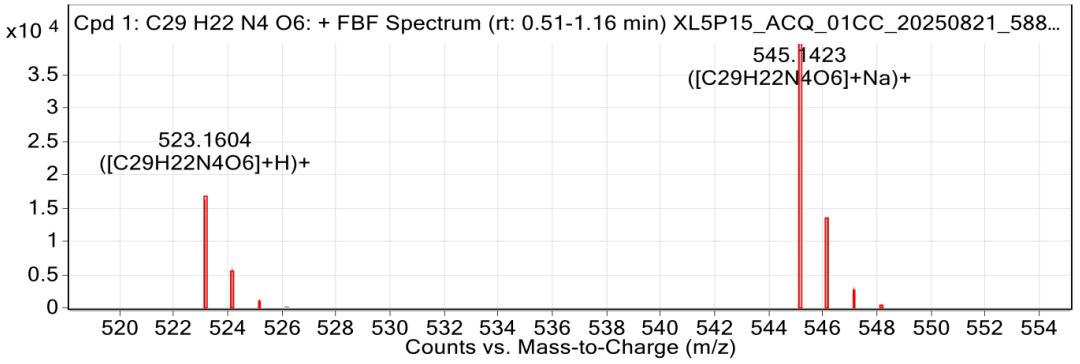

Figure SC104. Analytical HRMS trace of **4.6**.

Figure: Extracted ion chromatogram (EIC) of compound.

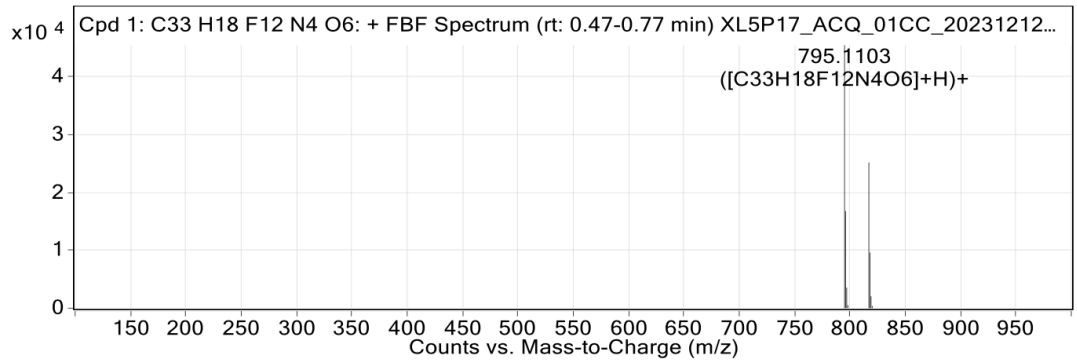

Figure: Full range view of Compound spectra and potential adducts.

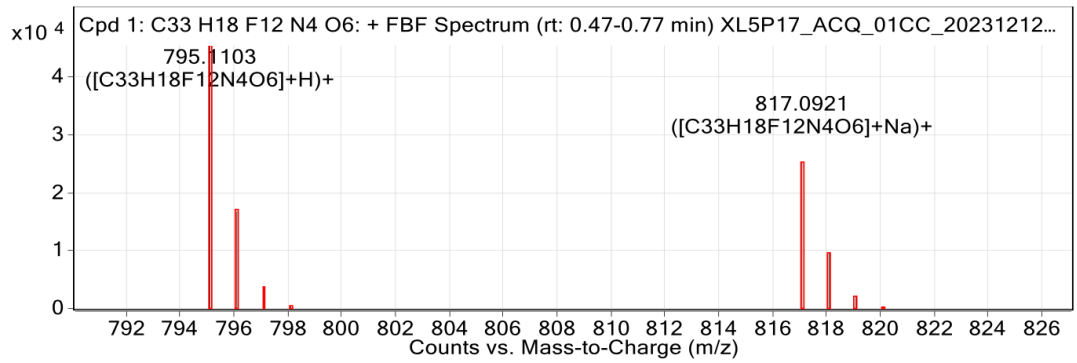

Figure SC105. Analytical HRMS trace of **4.7**.

Figure: Extracted ion chromatogram (EIC) of compound.

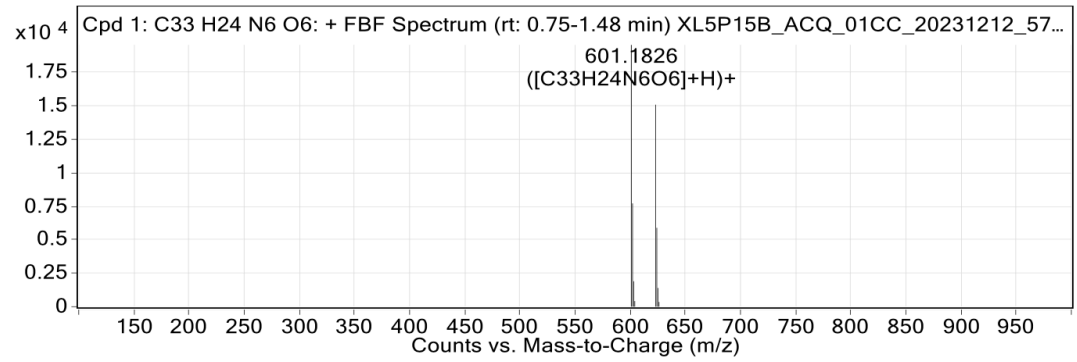

Figure: Full range view of Compound spectra and potential adducts.

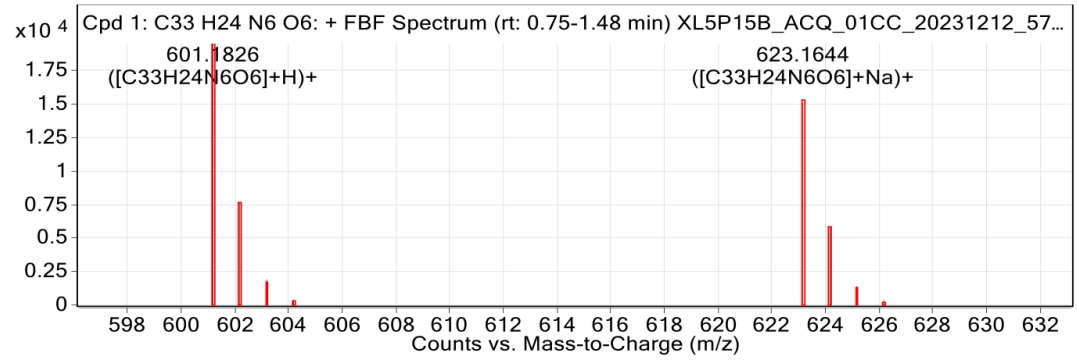

Figure SC106. Analytical HRMS trace of **4.8**.

Figure: Extracted ion chromatogram (EIC) of compound.

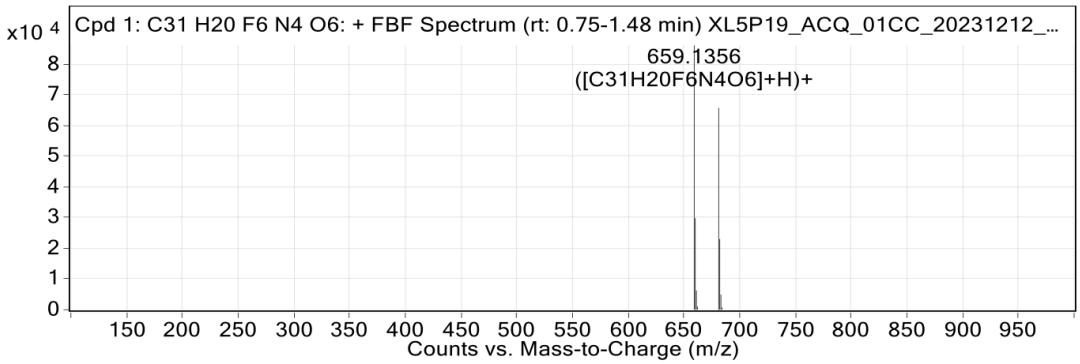

Figure: Full range view of Compound spectra and potential adducts.

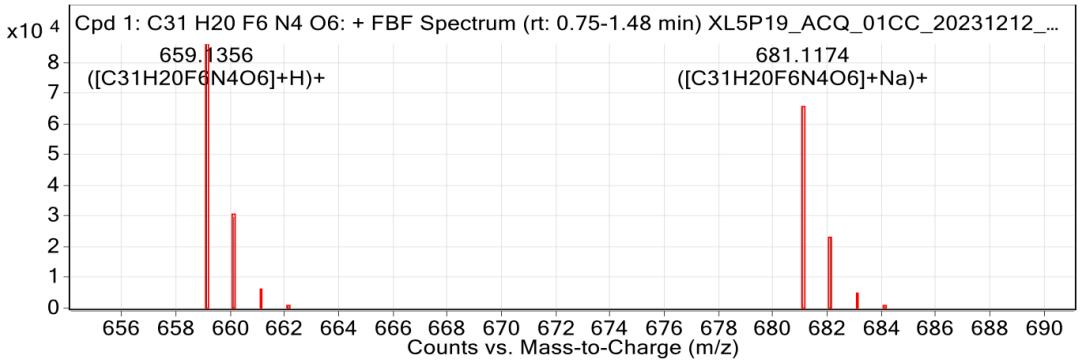

Figure SC107. Analytical HRMS trace of **4.9**.

Figure: Extracted ion chromatogram (EIC) of compound.

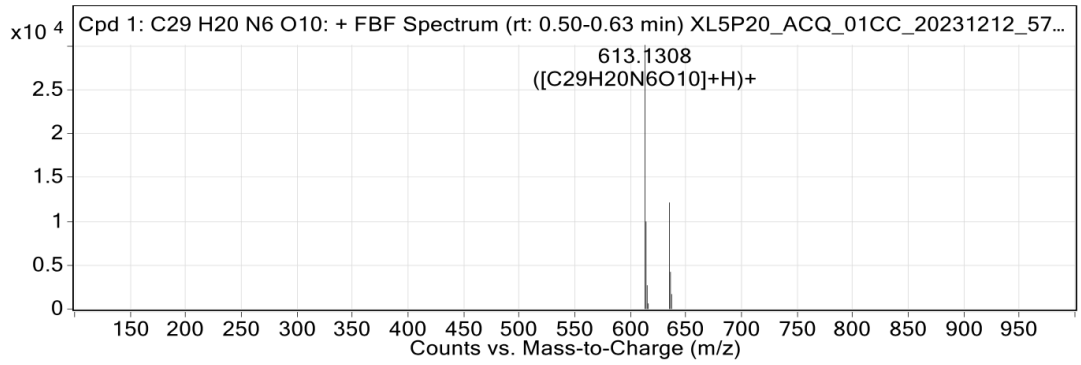

Figure: Full range view of Compound spectra and potential adducts.

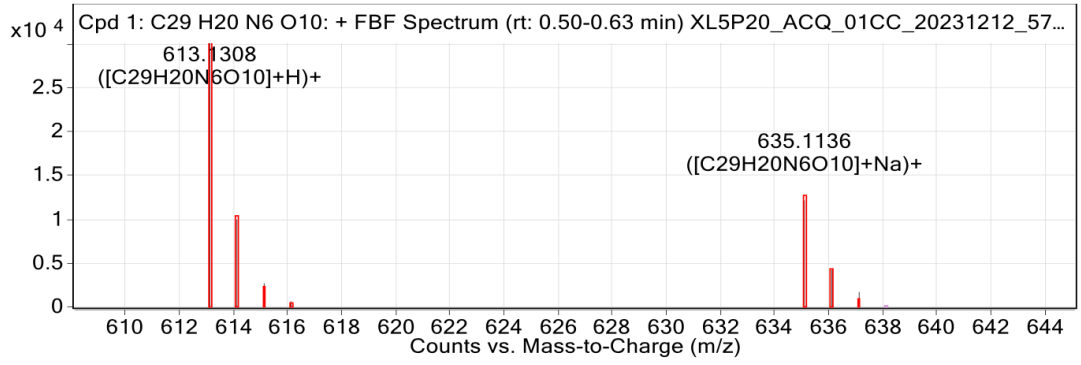

Figure SC108. Analytical HRMS trace of **4.10**.

Figure: Extracted ion chromatogram (EIC) of compound.

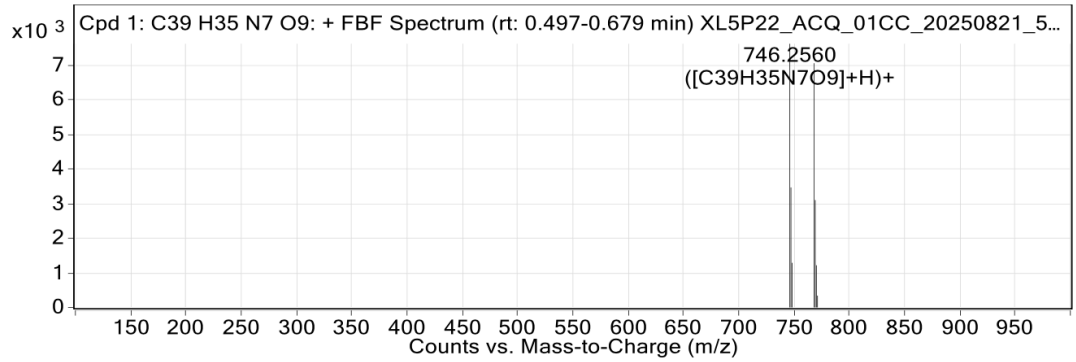

Figure: Full range view of Compound spectra and potential adducts.

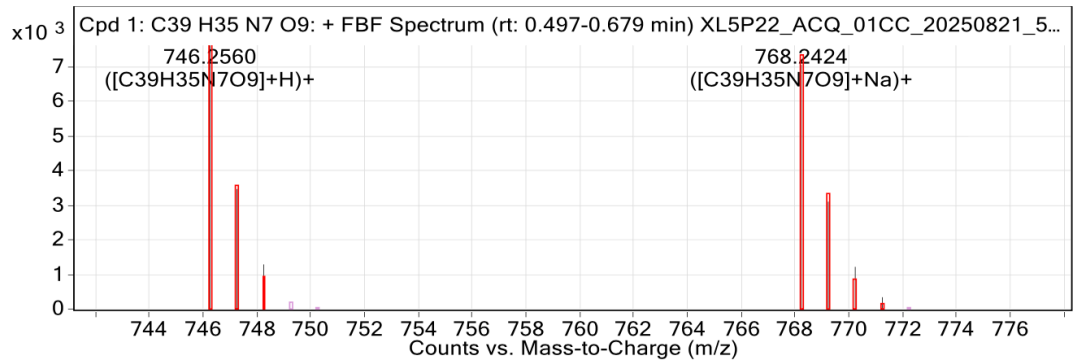

Figure SC109. Analytical HRMS trace of **4.11**.

Figure: Extracted ion chromatogram (EIC) of compound.

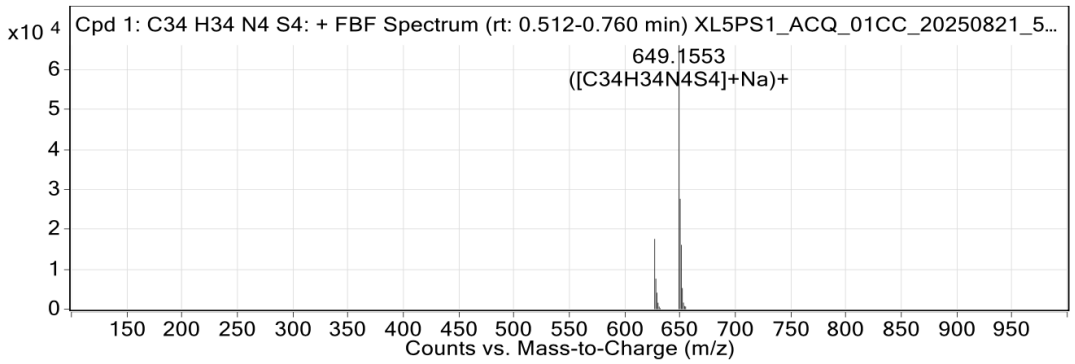

Figure: Full range view of Compound spectra and potential adducts.

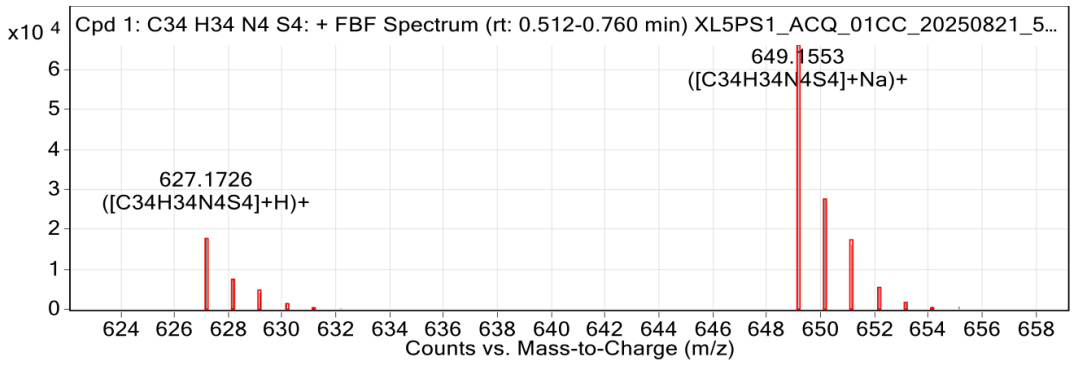

Figure SC110. Analytical HRMS trace of **4.12**.

Figure: Extracted ion chromatogram (EIC) of compound.

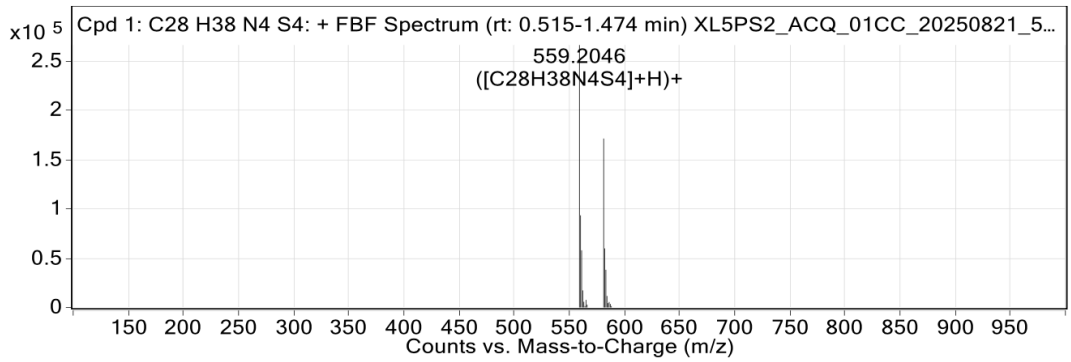

Figure: Full range view of Compound spectra and potential adducts.

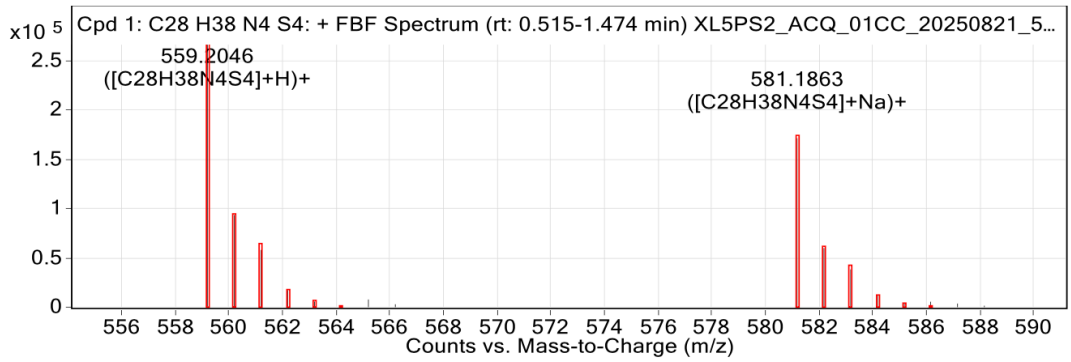

Figure SC111. Analytical HRMS trace of **4.13**.

Figure: Extracted ion chromatogram (EIC) of compound.

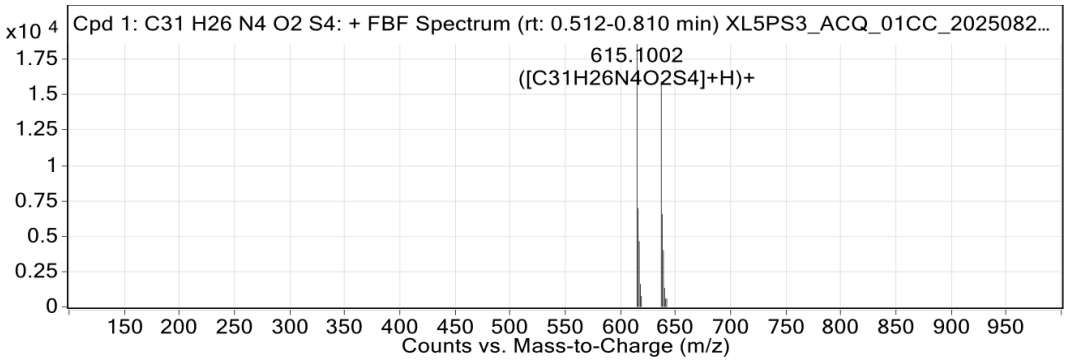

Figure: Full range view of Compound spectra and potential adducts.

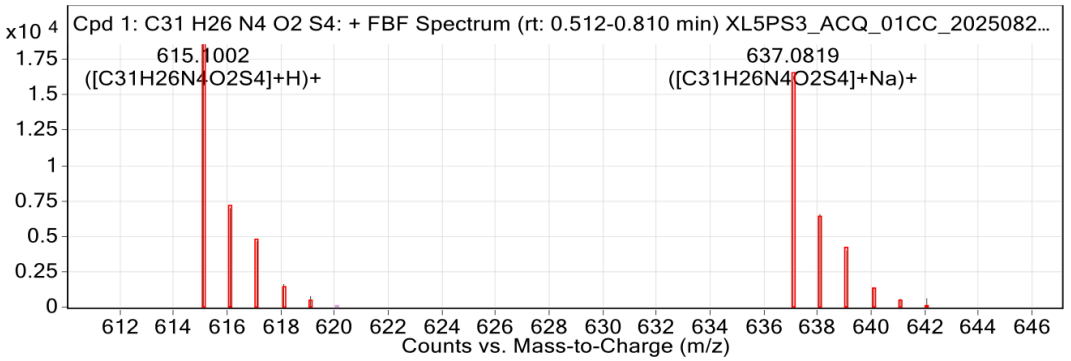

Figure SC112. Analytical HRMS trace of **4.14**.

Figure: Extracted ion chromatogram (EIC) of compound.

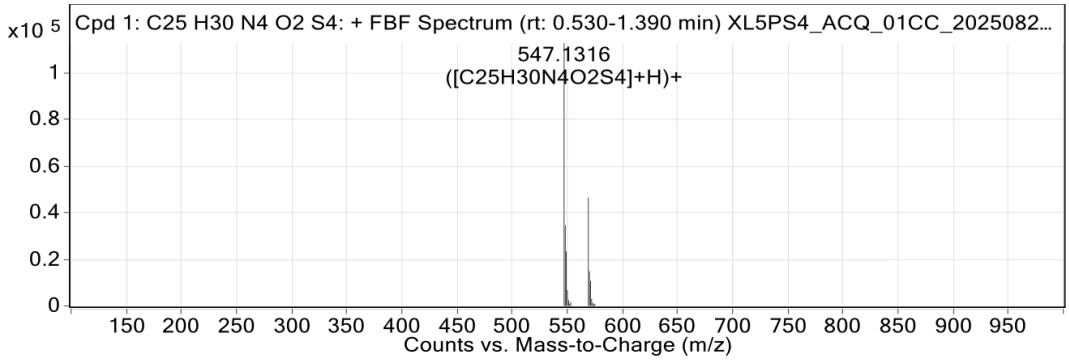

Figure: Full range view of Compound spectra and potential adducts.

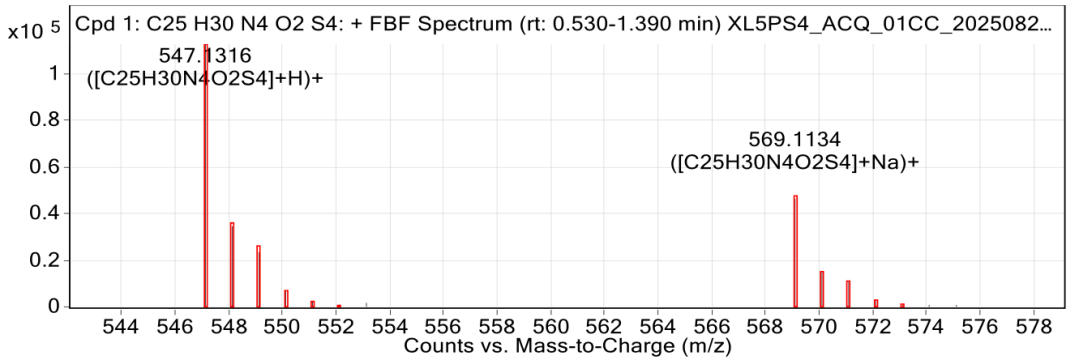

Figure SC113. Analytical HRMS trace of **4.15**.

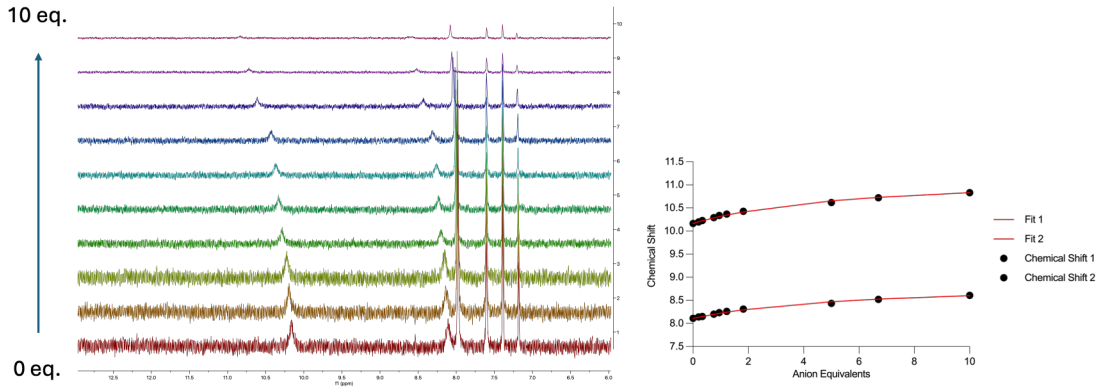

Figure SC114. ^{1}H NMR titration data for **4.2** towards Cl^{-}. {insert} ^{1}H NMR stackplot of **4.2**(0.4 mM in DMSO-d_6) upon addition of increasing molar equivalents of TBACl (0 - 10 eq.).

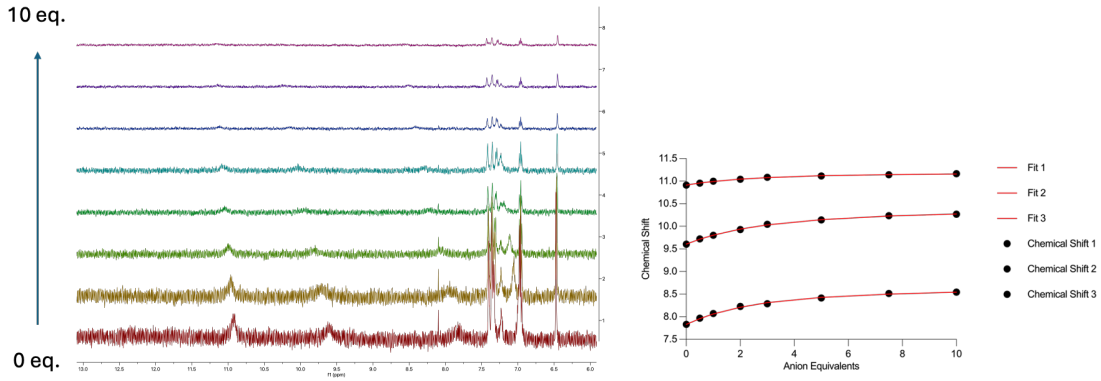

Figure SC115. ^{1}H NMR titration data for **4.3** towards Cl^{-}. {insert} ^{1}H NMR stackplot of **4.3**(0.4 mM in DMSO-d_6) upon addition of increasing molar equivalents of TBACl (0 - 10 eq.).

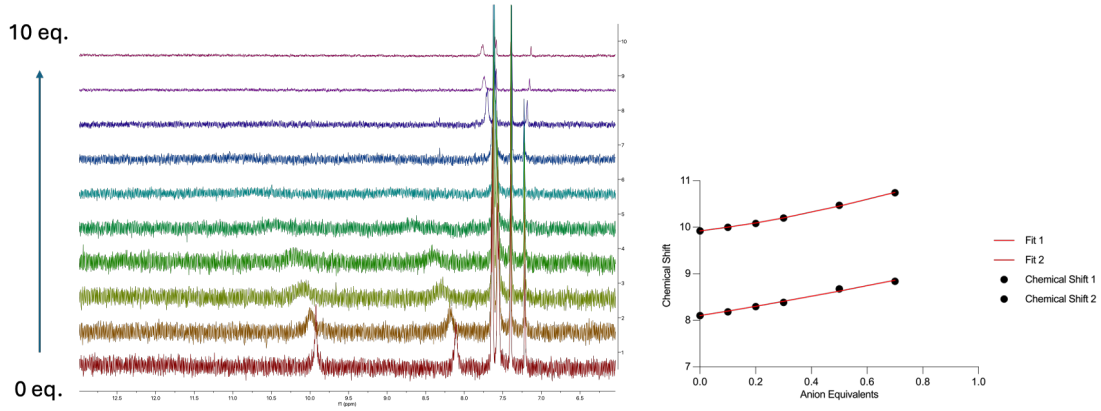

Figure SC116. ^{1}H NMR titration data for **4.4** towards Cl^{-}. {insert} ^{1}H NMR stackplot of **4.4**(0.4 mM in DMSO-d_6) upon addition of increasing molar equivalents of TBACl (0 - 10 eq.).

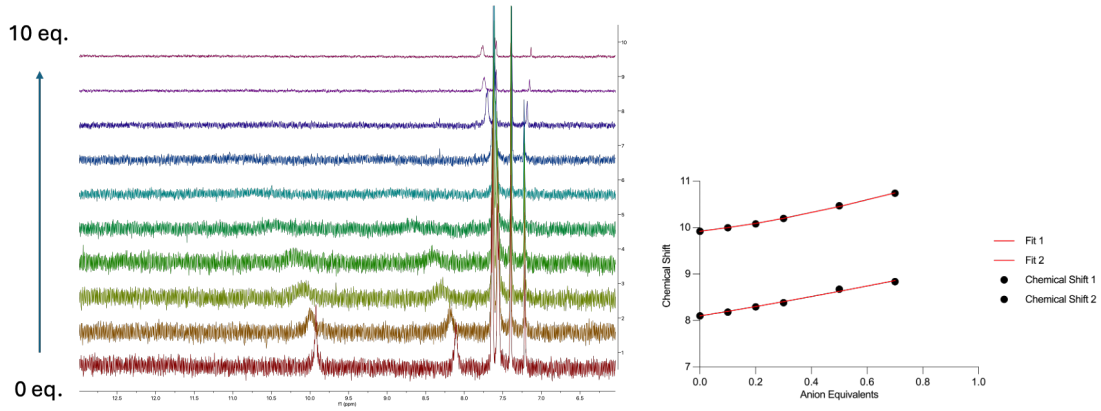

Figure SC117. ^{1}H NMR titration data for **4.4** towards AcO^{-}. {insert} ^{1}H NMR stackplot of **4.4**(0.4 mM in DMSO-d_6) upon addition of increasing molar equivalents of TBACl (0 - 10 eq.).

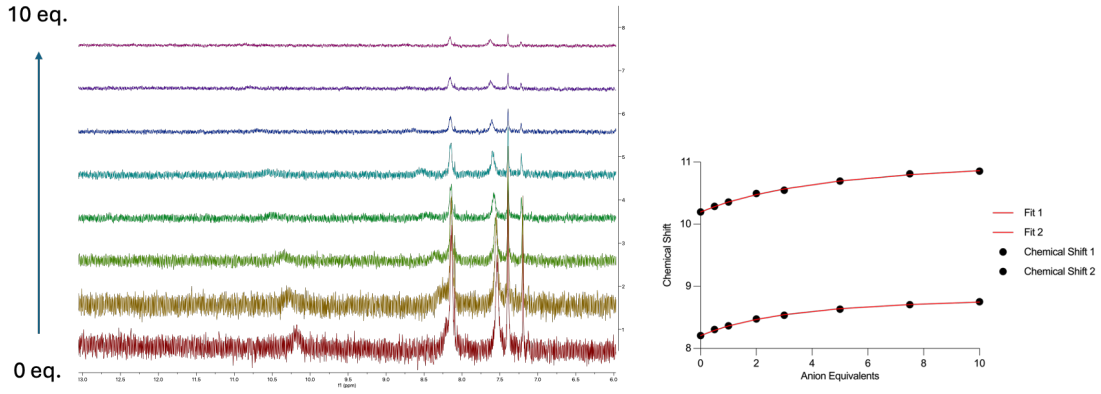

Figure SC118. ^{1}H NMR titration data for **4.5** towards Cl^{-}. {insert} ^{1}H NMR stackplot of **4.5**(0.4 mM in DMSO-d_6) upon addition of increasing molar equivalents of TBACl (0 - 10 eq.).

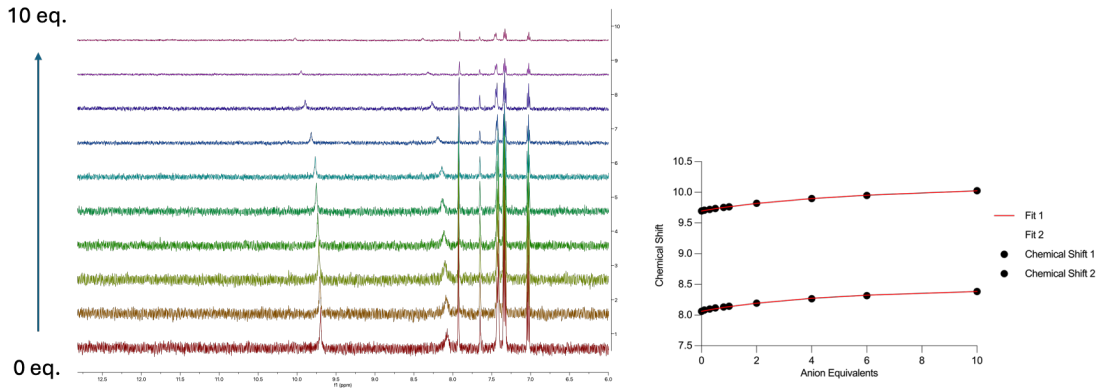

Figure SC119. ^{1}H NMR titration data for **4.6** towards Cl^{-}. {insert} ^{1}H NMR stackplot of **4.6**(0.4 mM in DMSO-d_6) upon addition of increasing molar equivalents of TBACl (0 - 10 eq.).

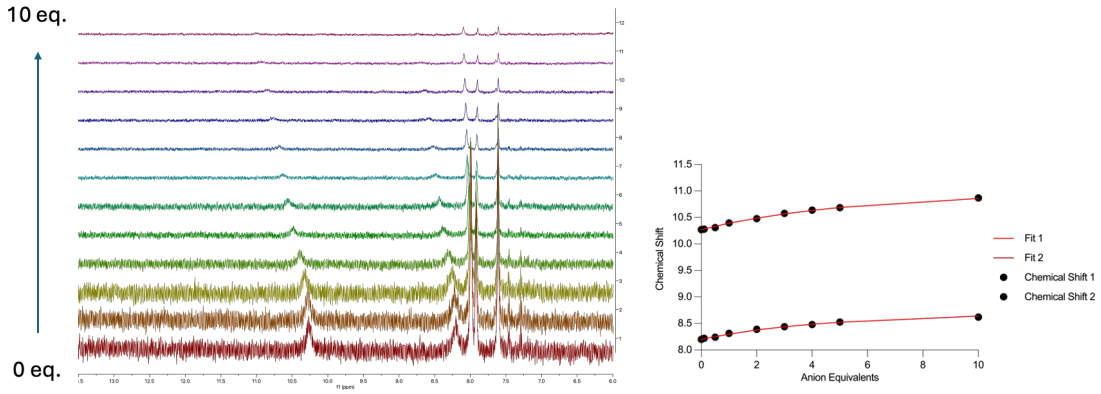

Figure SC120. ^{1}H NMR titration data for **4.7** towards Cl^{-}. {insert} ^{1}H NMR stackplot of **4.7**(0.4 mM in DMSO-d_6) upon addition of increasing molar equivalents of TBACl (0 - 10 eq.).

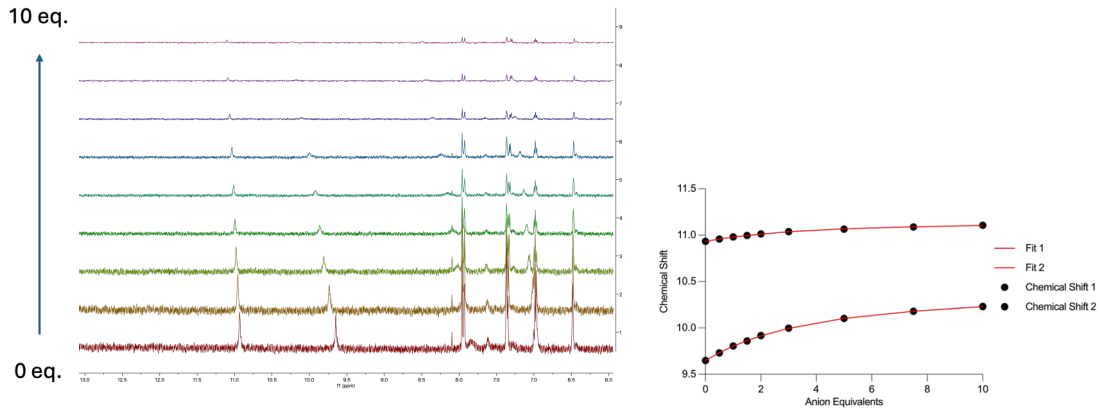

Figure SC121. ^{1}H NMR titration data for **4.8** towards Cl^{-}. {insert} ^{1}H NMR stackplot of **4.8**(0.4 mM in DMSO-d_6) upon addition of increasing molar equivalents of TBACl (0 - 10 eq.).

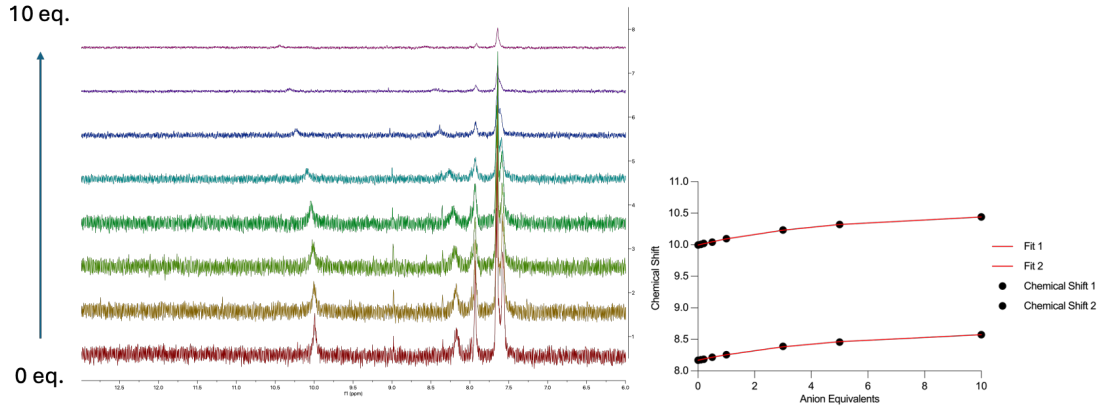

Figure SC122. ^{1}H NMR titration data for **4.9** towards Cl^{-}. {insert} ^{1}H NMR stackplot of **4.9**(0.4 mM in DMSO-d_6) upon addition of increasing molar equivalents of TBACl (0 - 10 eq.).

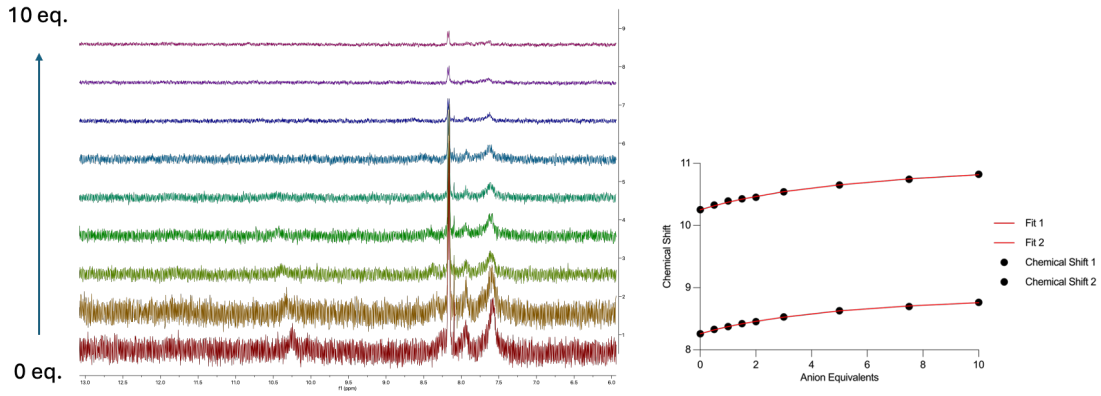

Figure SC123. ^{1}H NMR titration data for **4.10** towards Cl^{-}. {insert} ^{1}H NMR stackplot of **4.10**(0.4 mM in DMSO-d_6) upon addition of increasing molar equivalents of TBACl (0 - 10 eq.).

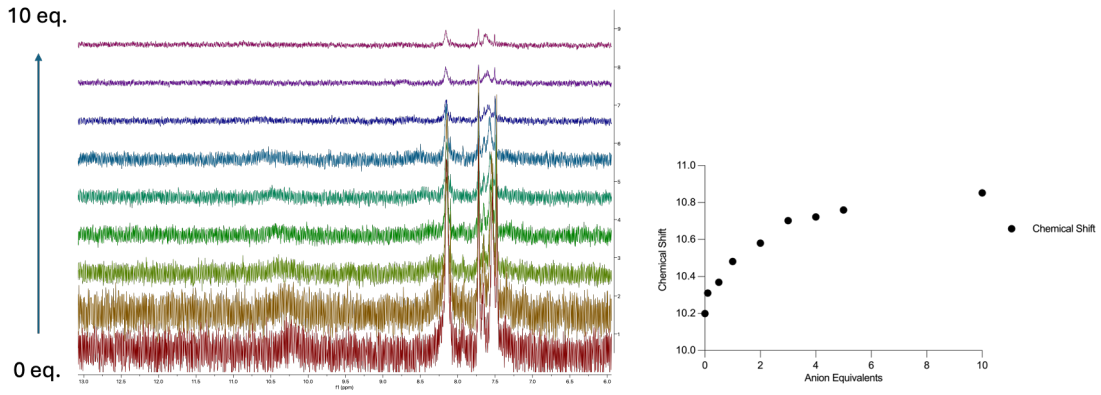

Figure SC124. ^{1}H NMR titration data for **4.11** towards Cl^{-}. {insert} ^{1}H NMR stackplot of **4.11**(0.4 mM in DMSO-d_6) upon addition of increasing molar equivalents of TBACl (0 - 10 eq.).

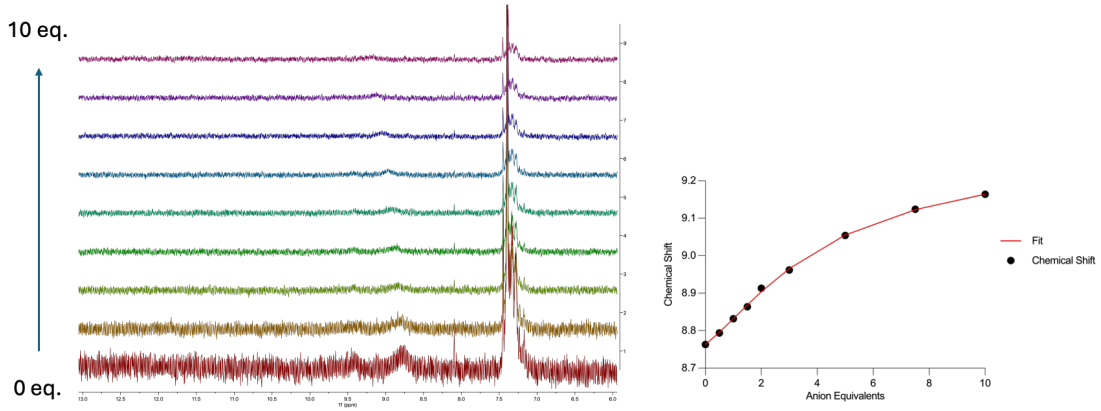

Figure SC125. ^{1}H NMR titration data for **4.12** towards Cl^{-}. {insert} ^{1}H NMR stackplot of **4.12**(0.4 mM in DMSO-d_6) upon addition of increasing molar equivalents of TBACl (0 - 10 eq.).

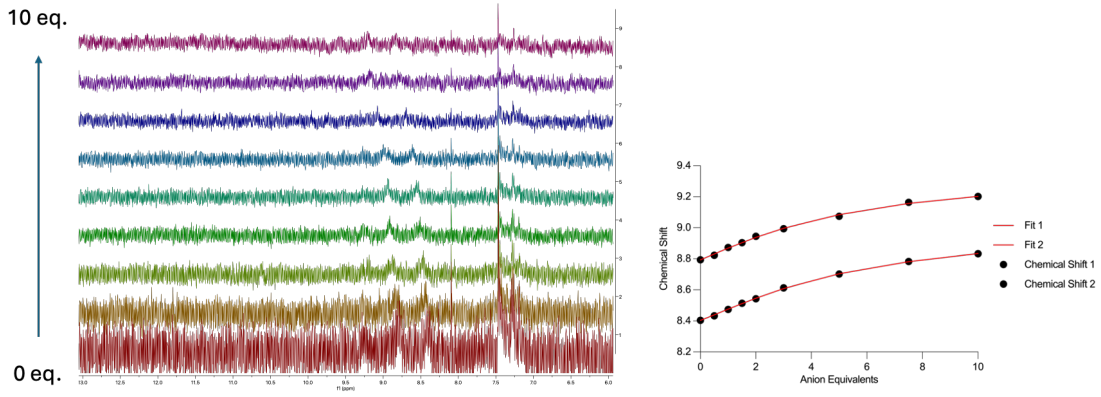

Figure SC126. ^{1}H NMR titration data for **4.13** towards Cl^{-}. {insert} ^{1}H NMR stackplot of **4.13**(0.4 mM in DMSO-d_6) upon addition of increasing molar equivalents of TBACl (0 - 10 eq.).

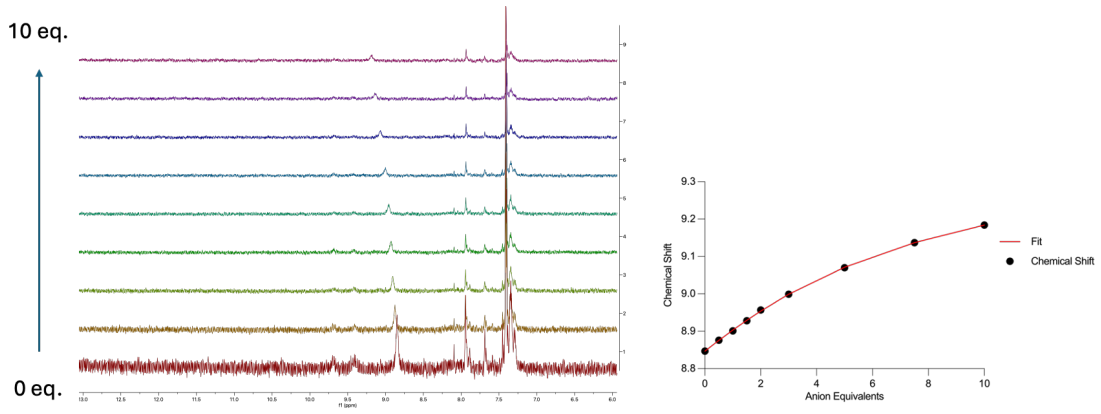

Figure SC127. ^{1}H NMR titration data for **4.14** towards Cl^{-}. {insert} ^{1}H NMR stackplot of **4.14**(0.4 mM in DMSO-d_6) upon addition of increasing molar equivalents of TBACl (0 - 10 eq.).

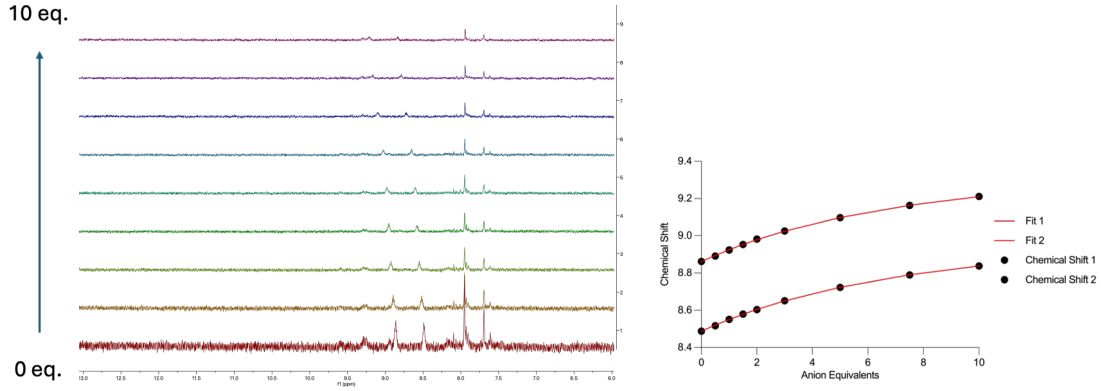

Figure SC128. ^{1}H NMR titration data for **4.15** towards Cl^{-}. {insert} ^{1}H NMR stackplot of **4.15**(0.4 mM in DMSO-d_6) upon addition of increasing molar equivalents of TBACl (0 - 10 eq.).

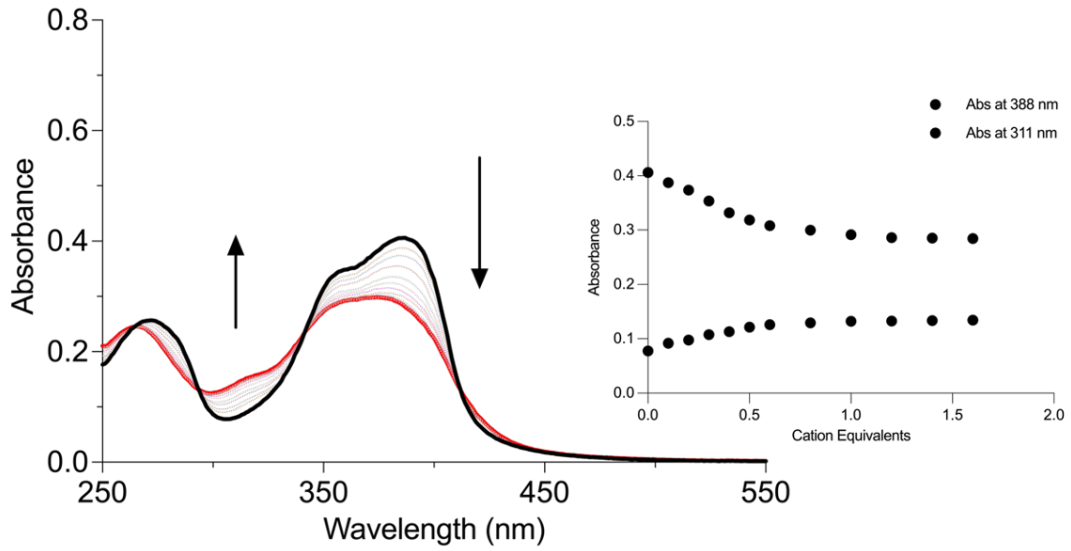

Figure SC129. UV-vis titration of **4.13** (10 μM) against $Zn(ClO_4)_2$ (0 – 1.6 eq., 1 mM) in DMSO/MeCN mixture solution (1:19). {insert} Fitplot at 388 nm and 311 nm.

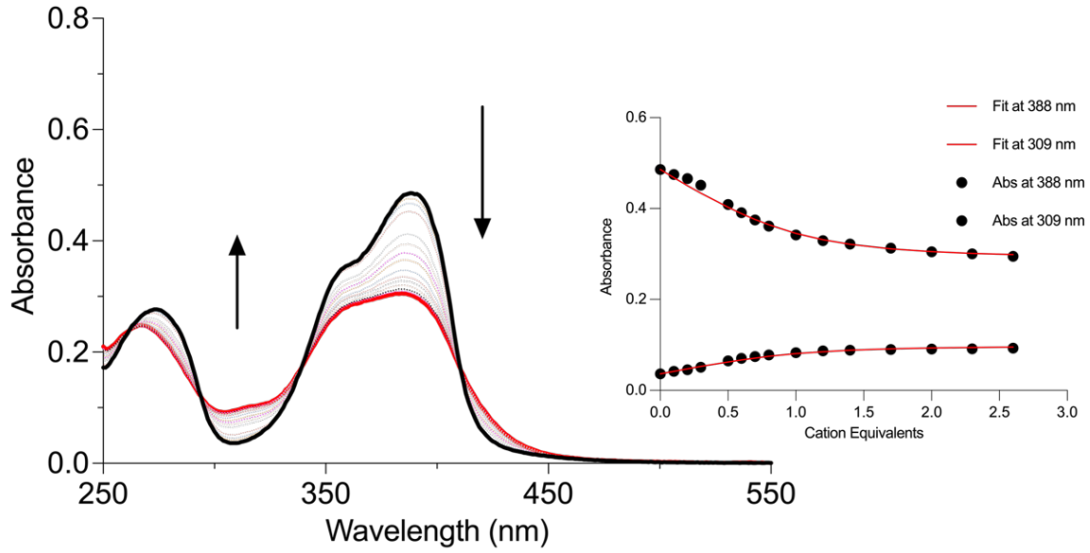

Figure SC130. UV-vis titration of **4.14** (10 μM) against $Zn(ClO_4)_2$ (0 – 2.6 eq., 1 mM) in DMSO/MeCN mixture solution (1:19). {insert} Fitplot at 388 nm and 311 nm.

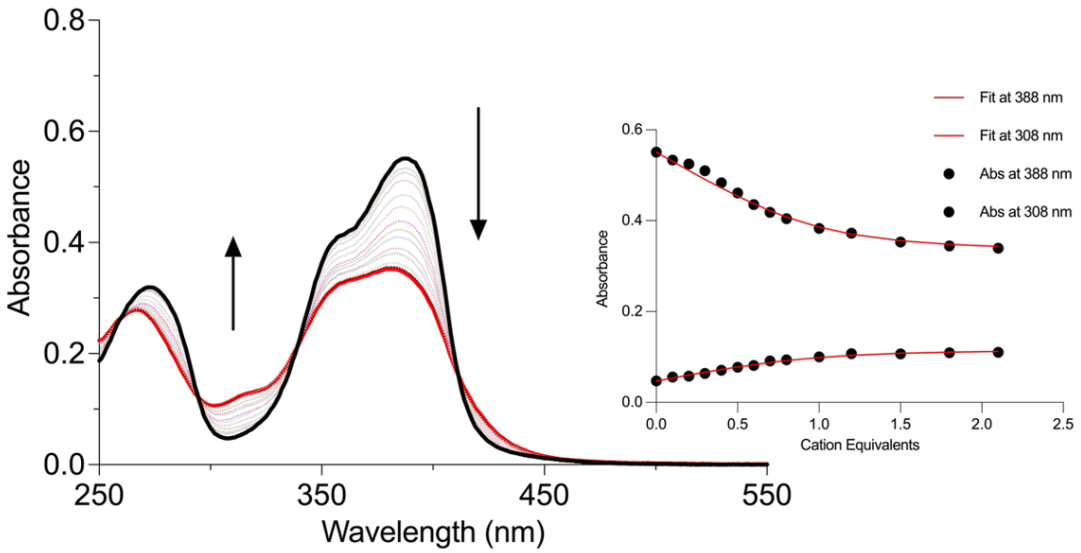

Figure SC131. UV-vis titration of **4.15** (10 μM) against $Zn(ClO_4)_2$ (0 – 2.1 eq., 1 mM) in DMSO/MeCN mixture solution (1:19). {insert} Fitplot at 388 nm and 311 nm.

The chloride transport data shown below were conducted by Prof. Roberto Quesada from the Departamento de Química at the Universidad de Burgos, Spain.

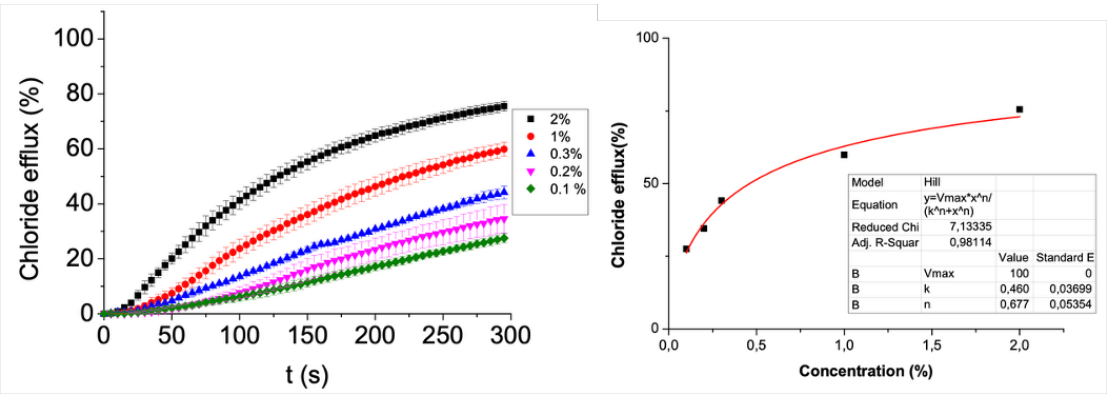

Figure SC132. Chloride efflux promoted by **4.2** compound in unilamellar POPC vesicles. Vesicles were loaded with a 489 mM NaCl solution buffered at pH 7.2 with 5 mM NaH_2PO_4 and dispersed in a 489 mM $NaNO_3$ solution buffered at pH 7.2 with 5 mM NaH_2PO_4. Each trace represents the average of at least three trials, performed with three batches of vesicles. {insert} Hill analysis for compound **4.3** (Cl^-/NO_3^- exchange).

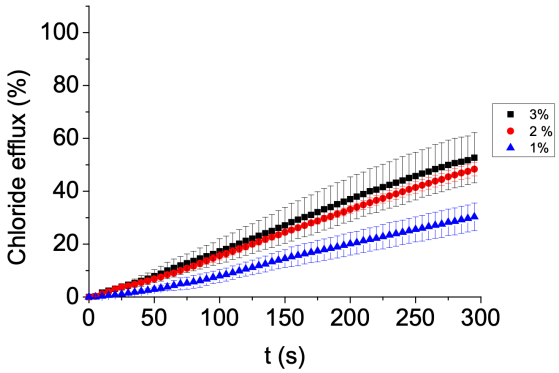

Figure SC133. Chloride efflux promoted by **4.3** compound in unilamellar POPC vesicles. Vesicles were loaded with a 489 mM NaCl solution buffered at pH 7.2 with 5 mM NaH_2PO_4 and dispersed in a 489 mM $NaNO_3$ solution buffered at pH 7.2 with 5 mM NaH_2PO_4. Each trace represents the average of at least three trials, performed with three batches of vesicles.

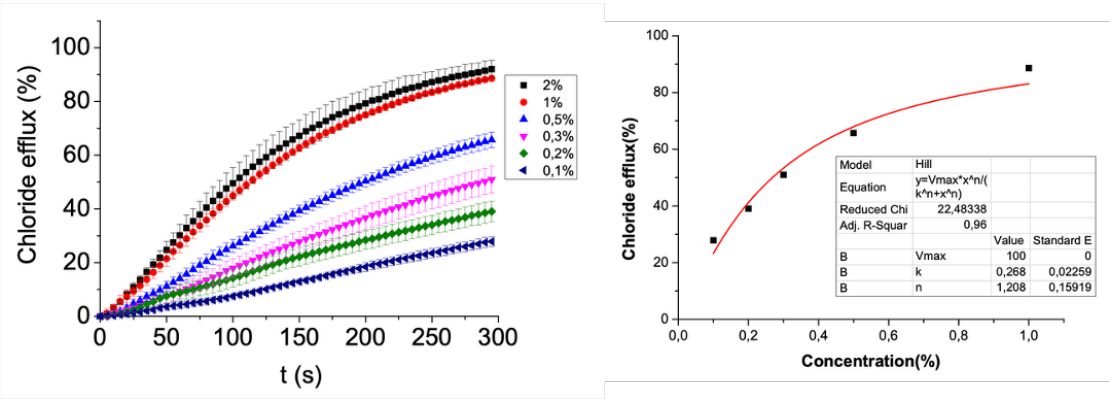

Figure SC134. Chloride efflux promoted by **4.4** compound in unilamellar POPC vesicles. Vesicles were loaded with a 489 mM NaCl solution buffered at pH 7.2 with 5 mM NaH_2PO_4 and dispersed in a 489 mM $NaNO_3$ solution buffered at pH 7.2 with 5 mM NaH_2PO_4. Each trace represents the average of at least three trials, performed with three batches of vesicles. {insert} Hill analysis for compound **4.4** (Cl^-/NO_3^- exchange).

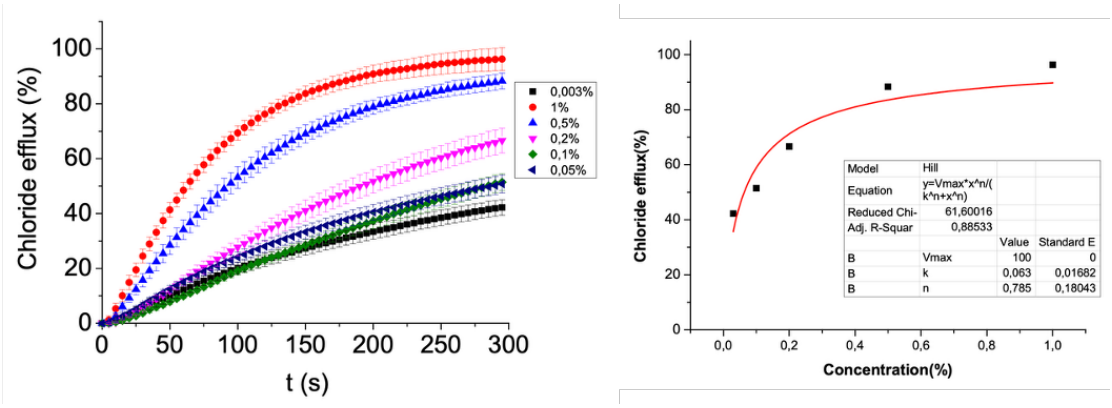

Figure SC135. Chloride efflux promoted by **4.5** compound in unilamellar POPC vesicles. Vesicles were loaded with a 489 mM NaCl solution buffered at pH 7.2 with 5 mM NaH_2PO_4 and dispersed in a 489 mM $NaNO_3$ solution buffered at pH 7.2 with 5 mM NaH_2PO_4. Each trace represents the average of at least three trials, performed with three batches of vesicles. {insert} Hill analysis for compound **4.5** (Cl^-/NO_3^- exchange).

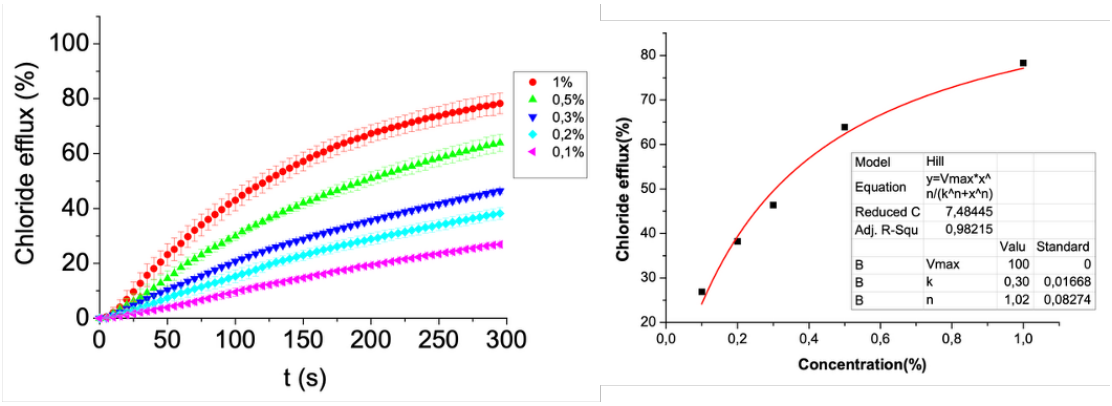

Figure SC136. Chloride efflux promoted by **4.1** compound in unilamellar POPC vesicles at various concentrations (1-3%). Vesicles, loaded with a NaCl solution (451 mM, NaCl, 20 mM NaH_2PO_4, pH 7.2), were dispersed in a $Na_2SO_4/NaHCO_3$ solution (150 mM Na_2SO_4, 40 mM $NaHCO_3$, 20 mM NaH_2PO_4, pH 7.2). Each trace represents the average of at least three trials, performed with three batches of vesicles. Bars represent mean ± SD.{insert} Hill analysis for compound **4.1** (Cl^-/HNO_3^- exchange).

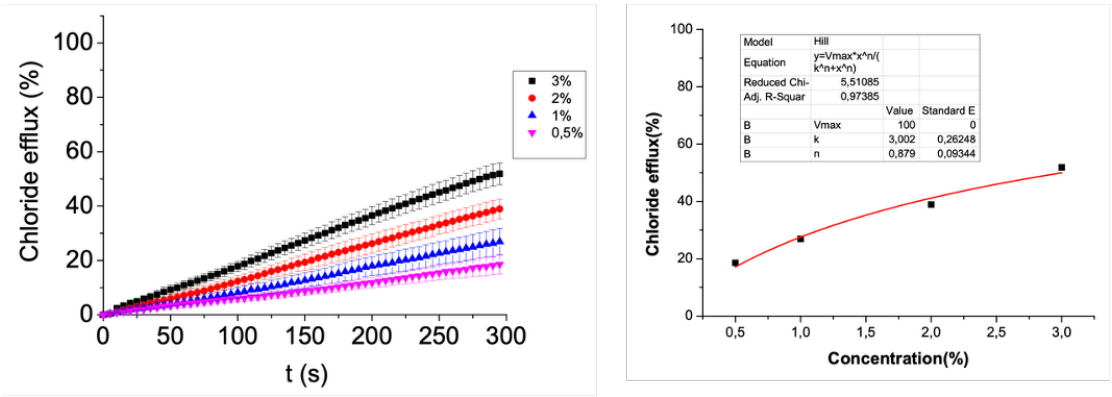

Figure SC137. Chloride efflux promoted by **4.2** compound in unilamellar POPC vesicles at various concentrations (1-3%). Vesicles, loaded with a NaCl solution (451 mM, NaCl, 20 mM NaH_2PO_4, pH 7.2), were dispersed in a Na_2SO_4/$NaHCO_3$ solution (150 mM Na_2SO_4, 40 mM $NaHCO_3$, 20 mM NaH_2PO_4, pH 7.2). Each trace represents the average of at least three trials, performed with three batches of vesicles. Bars represent mean ± SD.{insert} Hill analysis for compound **4.2** (Cl^-/HNO_3^- exchange).

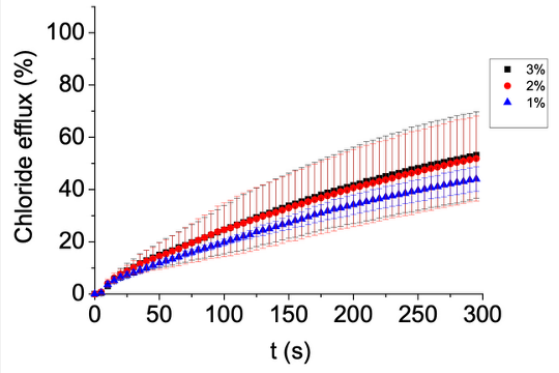

Figure SC138. Chloride efflux promoted by **4.3** compound in unilamellar POPC vesicles at various concentrations (1-3%). Vesicles, loaded with a NaCl solution (451 mM, NaCl, 20 mM NaH_2PO_4, pH 7.2), were dispersed in a Na_2SO_4/$NaHCO_3$ solution (150 mM Na_2SO_4, 40 mM $NaHCO_3$, 20 mM NaH_2PO_4, pH 7.2). Each trace represents the average of at least three trials, performed with three batches of vesicles. Bars represent mean ± SD.

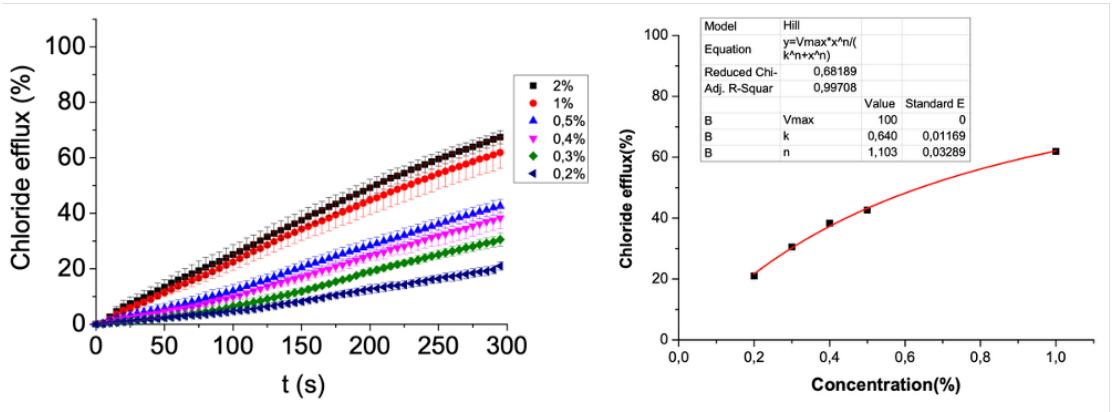

Figure SC139. Chloride efflux promoted by **4.4** compound in unilamellar POPC vesicles at various concentrations (1-3%). Vesicles, loaded with a NaCl solution (451 mM, NaCl, 20 mM NaH_2PO_4, pH 7.2), were dispersed in a Na_2SO_4/$NaHCO_3$ solution (150 mM Na_2SO_4, 40 mM $NaHCO_3$, 20 mM NaH_2PO_4, pH 7.2). Each trace represents the average of at least three trials, performed with three batches of vesicles. Bars represent mean ± SD. {insert} Hill analysis for compound **4.4** (Cl^-/HNO_3^- exchange).

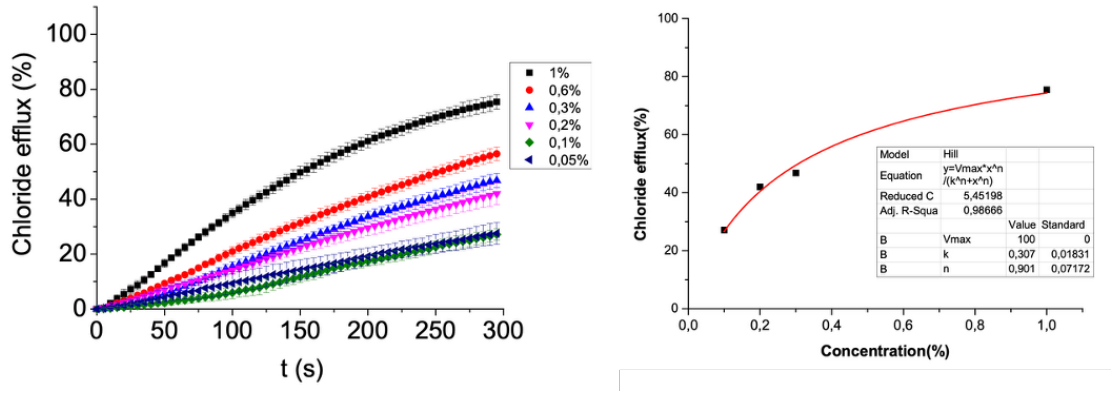

Figure SC140. Chloride efflux promoted by **4.5** compound in unilamellar POPC vesicles at various concentrations (1-3%). Vesicles, loaded with a NaCl solution (451 mM, NaCl, 20 mM NaH_2PO_4, pH 7.2), were dispersed in a Na_2SO_4/$NaHCO_3$ solution (150 mM Na_2SO_4, 40 mM $NaHCO_3$, 20 mM NaH_2PO_4, pH 7.2). Each trace represents the average of at least three trials, performed with three batches of vesicles. Bars represent mean ± SD. {insert} Hill analysis for compound **4.5** (Cl^-/HNO_3^- exchange).

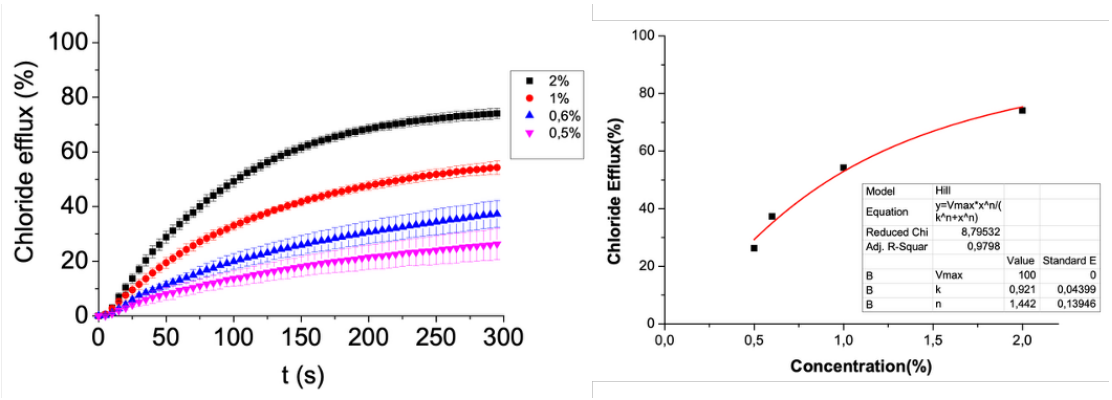

Figure SC141. Chloride efflux promoted by **4.1** compound in unilamellar POPC vesicles at various concentrations (1-3%). Vesicles were loaded with a 451 mM NaCl solution buffered at pH 7.2 with 20 mM NaH_2PO_4 and dispersed in a 150 mM Na_2SO_4 solution buffered at pH 7.2 with 20 mM NaH_2PO_4. Each trace represents the average of at least three trials, performed with three batches of vesicles. Bars represent mean ± SD. {insert} Hill analysis for compound **4.1** (Cl^-/SO_4^{2-} exchange).

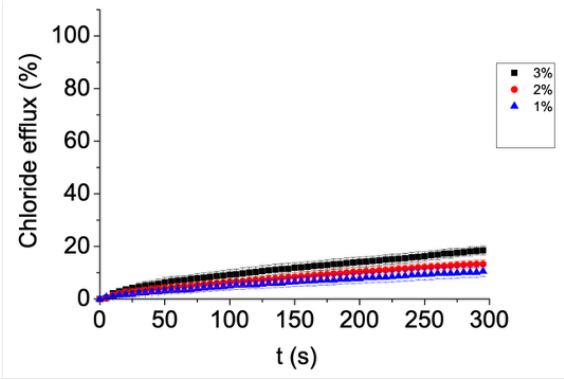

Figure SC142. Chloride efflux promoted by **4.2** compound in unilamellar POPC vesicles at various concentrations (1-3%). Vesicles were loaded with a 451 mM NaCl solution buffered at pH 7.2 with 20 mM NaH_2PO_4 and dispersed in a 150 mM Na_2SO_4 solution buffered at pH 7.2 with 20 mM NaH_2PO_4. Each trace represents the average of at least three trials, performed with three batches of vesicles. Bars represent mean ± SD.

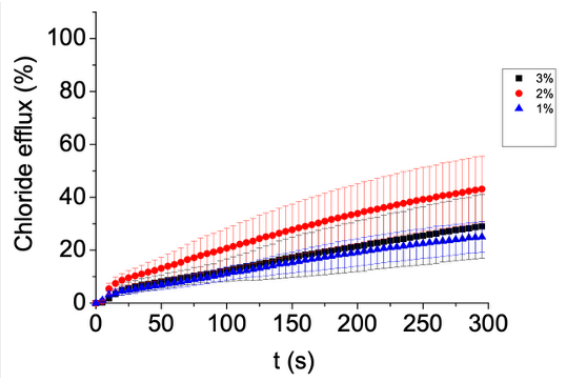

Figure SC143. Chloride efflux promoted by **4.3** compound in unilamellar POPC vesicles at various concentrations (1-3%). Vesicles were loaded with a 451 mM NaCl solution buffered at pH 7.2 with 20 mM NaH_2PO_4 and dispersed in a 150 mM Na_2SO_4 solution buffered at pH 7.2 with 20 mM NaH_2PO_4. Each trace represents the average of at least three trials, performed with three batches of vesicles. Bars represent mean ± SD.

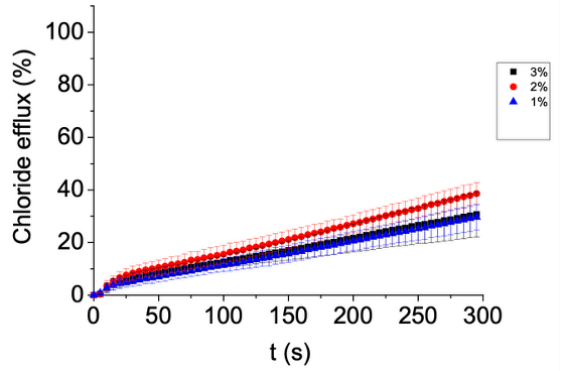

Figure SC144. Chloride efflux promoted by **4.4** compound in unilamellar POPC vesicles at various concentrations (1-3%). Vesicles were loaded with a 451 mM NaCl solution buffered at pH 7.2 with 20 mM NaH_2PO_4 and dispersed in a 150 mM Na_2SO_4 solution buffered at pH 7.2 with 20 mM NaH_2PO_4. Each trace represents the average of at least three trials, performed with three batches of vesicles. Bars represent mean ± SD.

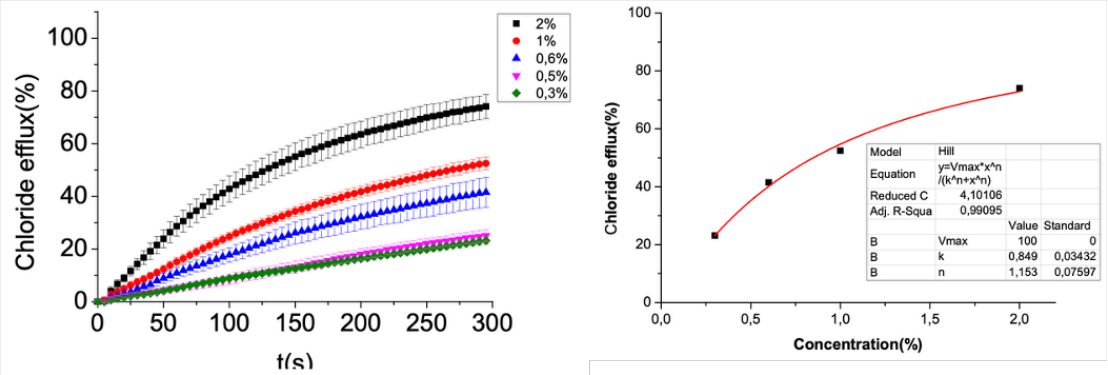

Figure SC145. Chloride efflux promoted by **4.5** compound in unilamellar POPC vesicles at various concentrations (1-3%). Vesicles were loaded with a 451 mM NaCl solution buffered at pH 7.2 with 20 mM NaH_2PO_4 and dispersed in a 150 mM Na_2SO_4 solution buffered at pH 7.2 with 20 mM NaH_2PO_4. Each trace represents the average of at least three trials, performed with three batches of vesicles. Bars represent mean ± SD. {insert} Hill analysis for compound **4.5** (Cl^-/SO_4^{2-} exchange).

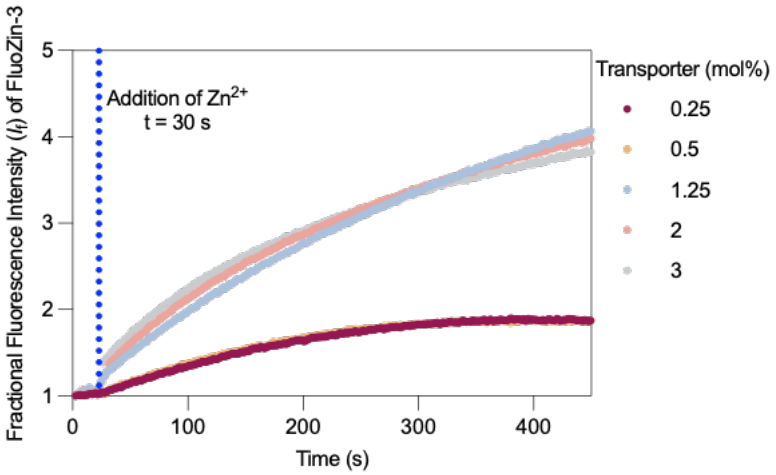

Figure SC146. The dose-dependent change in fluorescence intensity of FluoZin-3 over time of liposomes containing FluoZin-3 in PBS (0.01 M, pH=7.4) upon the addition of **4.15** at a range of increasing concentrations followed by a pulse of $Zn(ClO_4)_2$ (0.1 mM).